

OVERALL MECHANICAL RESPONSE OF SOFT COMPOSITE MATERIALS
WITH PARTICULATE MICROSTRUCTURE AT FINITE STRAINS

Reza Avazmohammadi

A DISSERTATION

in

Mechanical Engineering and Applied Mechanics

Presented to the Faculties of the University of Pennsylvania

in

Partial Fulfilment of the Requirements for the

Degree of Doctor of Philosophy

2014

Professor Pedro Ponte Castañeda
Department of Mechanical Engineering and Applied Mechanics
Supervisor of Dissertation

Associate Professor Prashant Purohit
Department of Mechanical Engineering and Applied Mechanics
Graduate Group Chairperson

Dissertation Committee:

Professor John L. Bassani,
Department of Mechanical Engineering and Applied Mechanics
Associate Professor Prashant Purohit,
Department of Mechanical Engineering and Applied Mechanics

ACKNOWLEDGEMENTS

I would like to express my gratitude to my advisor, Dr. Pedro Ponte Castañeda for his continued help and support throughout my PhD.

I would also like to thank the members of my thesis committee: Dr. John L. Bassani and Prashant Purohit.

Discussions with Morteza, Michalis, and Evan were critical to the development of this thesis.

Last but not the least, I wish to express my deepest gratitude to my family, in particular, my parents, my siblings, and my wife, Zahra, for their ceaseless love and support.

ABSTRACT

OVERALL MECHANICAL RESPONSE OF SOFT COMPOSITE MATERIALS WITH PARTICULATE MICROSTRUCTURE AT FINITE STRAINS

Reza Avazmohammadi

Pedro Ponte Castañeda

Many soft, composite materials manufactured or found in nature consist of a homogeneous matrix phase and a random distribution of micron-sized particles in the matrix. Examples among engineering materials include reinforced elastomers, microgel suspensions and polymer-matrix composites, whereas biological tissues and fluids, such as intervertebral disc and blood, provide examples of natural materials. In this thesis, we present homogenization-based models for the overall constitutive behavior of such composite materials when subjected to mechanical loadings. These models account for the constitutive nonlinearities associated with the local behavior of the matrix and particle phases, as well as for the nonlinearities associated with possible evolution of the microstructure. In this thesis, we present models for three different classes of particulate composite materials.

In the first part of this thesis, we propose a new model for the overall constitutive behavior of particle-reinforced elastomers when subjected to three-dimensional, large deformations. A key advantage of this model is that it incorporates the change in the orientation of rigid particles as the deformation proceeds, and therefore also incorporates the major influence of such changes on the development of material instabilities in the composites. We consider the application of this model to composites consisting of incompressible elastomers reinforced by aligned, spheroidal particles, undergoing non-aligned loadings.

In the second part of this work, we present a homogenization-based model for the rheological behavior of suspensions of soft viscoelastic particles in Newtonian fluids as well as in yield stress fluids under uniform, Stokes flow conditions. We investigate the effects of the shape dynamics and constitutive properties of the fluid and particle phases on the macroscopic rheological behavior of the suspensions.

In the last part of this work, we present a model to estimate the effective behavior of particulate composites consisting of elasto-viscoplastic matrices and elastic, spheroidal particles, subjected to

small strains. Here, we explore the effect of the local properties and loading conditions on the effective behavior and field statistics in these composites for the case of elastic-ideally plastic matrices.

Contents

I	Elastomeric Composites	1
1	Tangent second-order estimates for the macroscopic response of particle-reinforced elastomers	2
1.1	Introduction	3
1.2	Hyperelastic Composites	6
1.3	Tangent Second-Order Method	7
1.4	Rigidly Reinforced Composites	10
1.4.1	Tangent Second-Order Estimates	10
1.4.2	Energy Decomposition Approximation	14
1.4.3	Dilute Concentrations	19
1.4.4	Computation of the Tensor \mathbf{E}^I	20
1.5	2-D Application: Reinforced Elastomers with Elliptical Fibers	23
1.5.1	Plane-Strain Loading of Fiber-Reinforced Elastomers	24
1.5.2	Explicit Results for an Incompressible, neo-Hookean Matrix	26
1.5.3	Generalized Second-Order Estimate	28
1.5.4	Discussion of the Results	29
1.6	3-D Application: Reinforced Elastomers with Spherical Particles	33
1.6.1	Analytical Results for (Incompressible) neo-Hookean Elastomers	35
1.6.2	Results for Gent Elastomers and Discussion	39
1.7	Concluding Remarks	42
2	Application of the TSO theory to short fiber-reinforced composites: I–Analytical results	45
2.1	Introduction	46
2.2	Preliminaries on hyperelastic composites and their effective behavior	47
2.3	Tangent second-order homogenization estimates	50
2.4	Application to composites with rigid spheroidal particles	52
2.4.1	Estimates for non-aligned loadings	56
2.4.2	Estimates for aligned loadings	58
2.5	Onset of macroscopic instabilities	64
2.5.1	Axisymmetric Shear	67

2.5.2	Pure shear	70
2.6	Concluding Remarks	72
3	Application of the TSO theory to short fiber-reinforced composites: II–Representative examples	74
3.1	Introduction	75
3.2	Overall constitutive behavior	76
3.3	Applications	81
3.3.1	Aligned loadings	81
3.3.2	Non-aligned loadings	97
3.4	Concluding Remarks	107
II	Viscoelastic Suspensions	109
4	Rheology of non-dilute suspensions of soft viscoelastic particles in a Newtonian fluid	110
4.1	Introduction	111
4.2	Suspensions of viscoelastic particles in a viscous fluid	114
4.2.1	Constitutive behavior of the phases	114
4.2.2	Microstructures	117
4.3	Macroscopic response	120
4.3.1	Homogenization estimates for the instantaneous response	120
4.3.2	Evolution equations for the microstructural variables and particle elastic stress	124
4.4	Steady-state estimates for the suspensions	126
4.4.1	Steady-state solution for Kelvin-Voigt particles	128
4.5	Applications and discussion	130
4.5.1	Suspensions of initially spherical particles in an extensional flow	130
4.5.2	Suspensions of initially spherical particles in a shear flow	136
4.6	Conclusions	147
5	Rheology of non-dilute suspensions of soft viscoelastic particles in yield stress fluids	150
5.1	Introduction	151
5.2	Suspensions of viscoelastic particles in a nonlinear viscous fluid	154
5.2.1	Constitutive behavior of the phases	155
5.2.2	Microstructure	157
5.3	Macroscopic response	159
5.3.1	Homogenization estimates for the instantaneous response	159
5.3.2	Evolution equations for the microstructural variables and particle elastic stress	167
5.3.3	Steady-state estimates for the suspensions	169
5.4	Application: Shear flow	171

5.4.1	Bingham fluids	175
5.4.2	Power-law fluids	179
5.4.3	Herschel-Bulkley fluids	185
5.5	Conclusions	188
III Elasto-Viscoplastic Composites		190
6	Effective behavior of elasto-viscoplastic particle-reinforced composites	191
6.1	Introduction	192
6.2	Problem formulation	194
6.3	Variational estimates	196
6.3.1	Estimates for the linear comparison composite	198
6.3.2	Implementation of the variational procedure	202
6.4	Applications and discussions	205
6.4.1	Axisymmetric shear	207
6.4.2	Transverse and longitudinal shear loading	212
6.4.3	Combined shear loading	217
6.5	Conclusions	219
7	Closure	220
Appendices		226
Appendix		227
A		227
A.1	On the calculation of the tensor \mathbf{E}_I	228
A.2	In-plane components of the tensor \mathbf{P} for cylindrical inclusions with elliptical cross-section embedded in a compressible neo-Hookean matrix	229
A.3	The tensors \mathbf{P} and \mathbf{E} for spherical inclusions embedded in a compressible neo-Hookean matrix	231
B		234
B.1	Calculation of the tensor \mathbf{E}	235
B.2	Calculation of the tensors \mathbf{P}_r for spheroidal particles embedded in a generalized neo-Hookean matrix under non-aligned loadings	236
B.3	Normal components of the tensor \mathbf{P}_r , $r = 1, 2, 3$ for spheroidal particles embedded in a neo-Hookean matrix under general aligned loading	238
B.4	On the modulus tensor \mathbf{L}^c for the incompressible composites with the effective stored-energy function $\widehat{\Phi}(\bar{\lambda}_1, \bar{\lambda}_2, \bar{\theta}_2, \bar{\theta}_1)$ subjected to non-aligned loadings	241

C	245
C.1	The Hashin-Shtrikman-Willis variational estimates 246
C.2	Governing equations for extensional flows 249
C.3	Governing equations for shear flows 249
C.4	The tensors \mathbb{P} and \mathbb{R} for an ellipsoidal inclusion 250
D	252
D.1	Governing equations for the deformation of spherical particles in a shear flow 253
E	254
E.1	Two-Phase thermoelastic composites 255
E.2	An incremental form for the second moment of stress 255

List of Tables

6.1	Candidate materials for the elastic-ideally plastic matrix and for the elastic fibers. . .	206
-----	--	-----

List of Figures

1.1	Rigidly-reinforced composite under plane-strain loading. (a) Two-dimensional representation in the transverse plane. (b) Three-dimensional representation of a typical reinforcing fiber.	25
1.2	New tangent second-order (TSO) and generalized second-order (GSO) estimates for the effective response of a rigidly fiber-reinforced elastomer with an incompressible neo-Hookean matrix under pure shear loading. The results are shown as a function of the applied stretch $\bar{\lambda}$ for different values of the fiber volume fraction. (a) The effective energy \widehat{W} . (b) The corresponding macroscopic stress $\bar{S} = d\widehat{W}/d\bar{\lambda}$	30
1.3	The effective response of a rigidly fiber-reinforced elastomer with an incompressible neo-Hookean matrix under pure shear loading. The macroscopic stress $\bar{S} = d\widehat{W}/d\bar{\lambda}$ is plotted as a function of the applied stretch $\bar{\lambda}$ for (a) $c = 0.2$, and (b) $c = 0.3$. Comparisons are shown between the new TSO estimate (1.121), the estimate (1.126) of Lopez-Pamies and Ponte Castañeda (2006b) “GSO (2006)”, the earlier GSO results of Lopez-Pamies and Ponte Castañeda (2004b) “GSO (2004)”, the earlier TSO results of Ponte Castañeda and Tiberio (2000) “TSO (2000)”, the laminate results of deBotton (2005) “LAM”, and the FE simulations of Moraleda et al. (2009) “FEM”.	31
1.4	New tangent second-order (TSO) estimate, generalized second-order (GSO) estimate (1.126), and the FE simulations of Moraleda et al. (2009) (FEM) for the effective response of a fiber-reinforced elastomer with an incompressible Gent matrix under pure shear loading. The macroscopic stress $\bar{S} = d\widehat{W}/d\bar{\lambda}$ is depicted as a function of the applied stretch $\bar{\lambda}$, for (a) different values of the fiber volume fraction c with $J_m = 50$, and (b) different matrix lock-up parameters J_m with $c = 0.1$	32
1.5	The microstructure evolution in a rigidly fiber-reinforced elastomer with an incompressible neo-Hookean matrix under pure shear loading. The relative fiber rotation ϕ is plotted as a function of the applied stretch $\bar{\lambda}$ for three different stretching angles $\bar{\theta} = 5^\circ, 45^\circ$, and 85° . (a) Comparisons between the new TSO estimate (1.122) and the estimate (1.127) of Lopez-Pamies and Ponte Castañeda (2006b) for the volume fraction $c = 0.1$, and aspect ratios $\omega = 2$, and 10. (b) Comparisons between the new TSO estimate, the GSO estimate and the FEM simulations of Moraleda et al. (2009) for $c = 0.3$, and $\omega = 2$	33

1.6	Schematic representation of a matrix reinforced by spherical inclusions subjected to (a) Pure Shear (PS) loading, (b) Uniaxial Tension (UT) loading, and (c) Equibiaxial Tension (ET) loading.	37
1.7	New tangent second-order (TSO) estimates for the macroscopic stress $\bar{S} = d\widehat{W}/d\bar{\lambda}$ in particle-reinforced elastomers under pure shear loading ($\bar{\lambda}_3 = 1, \bar{\lambda}_2 = 1/\bar{\lambda}_1$), as functions the applied stretch $\bar{\lambda}_1 = \bar{\lambda}$. (a) neo-Hookean matrix for different values of the fiber volume fraction (b) Gent matrix for different matrix lock-up parameters.	40
1.8	New TSO estimates for the macroscopic stress $\bar{S} = d\widehat{W}/d\bar{\lambda}$ in particle-reinforced elastomers under uniaxial tension loading ($\bar{\lambda}_2 = \bar{\lambda}_3 = \bar{\lambda}_1^{-1/2}$), as functions the applied stretch $\bar{\lambda}_1 = \bar{\lambda}$. (a) neo-Hookean matrix for different values of the fiber volume fraction (b) Gent matrix for different matrix lock-up parameters.	41
1.9	New TSO estimates for the macroscopic stress $\bar{S} = d\widehat{W}/d\bar{\lambda}$ in particle-reinforced elastomers under equibiaxial tension loading ($\bar{\lambda}_3 = \bar{\lambda}_2^{-2} = \bar{\lambda}_1^{-2}$), as functions the applied stretch $\bar{\lambda}_1 = \bar{\lambda}$. (a) neo-Hookean matrix for different values of the fiber volume fraction (b) Gent matrix for different matrix lock-up parameters.	42
1.10	TSO estimates for the macroscopic stretch, $\bar{\lambda}_1^{lock}$, at which an particle-reinforced incompressible Gent elastomer locks up under three different loadings: Pure shear (PS), Uniaxial tension (UT) and Equibiaxial tension (ET). The results are shown as a function of particle concentration c for different values of the matrix lock-up parameter J_m	43
1.11	NewTSO estimates for the effective response of a rigidly particle-reinforced elastomer with an incompressible neo-Hookean matrix. (a) The effective energy \widehat{W} versus the macroscopic invariant \bar{I}_1 under three different loadings: Pure shear (PS), Uniaxial tension (UT) and Equibiaxial tension (ET) (b) The effective energy \widehat{W} versus the invariant \bar{I}_2 for two different values of the invariant \bar{I}_1	44
2.1	Schematic illustration of the microstructure of a rigid particle-reinforced elastomer in the undeformed configuration (Ω_0). Two configurations are considered. (a) Elastomers reinforced with prolate spheroidal particles ($w > 1$). (b) Elastomers reinforced with oblate spheroidal particles ($w < 1$). Note that, in both cases, the symmetry axis of the particles is initially aligned with the coordinate basis vector \mathbf{e}_3	53
2.2	Schematic orientation of the Rectangular coordinate basis \mathbf{e}'_i with respect to the basis \mathbf{e}_i after a two-step rotation. The loading (stretching) directions are aligned with the \mathbf{e}'_i basis vectors, which have a misorientation (measured by angles $\bar{\theta}_1$ and $\bar{\theta}_2$) relative to the \mathbf{e}_i basis.	54
2.3	Schematic representation of the applied loading on a rigid particle-reinforced elastomer as well as the associated evolution of microstructure. The loading (stretching) directions are aligned with \mathbf{e}'_i basis vectors which correspond to a rotation $\bar{\theta}$ about the \mathbf{e}_2 direction. (a) In the undeformed configuration (Ω_0), the particles are aligned with the \mathbf{e}_3 direction. (b) In the deformed configuration (Ω), the particles rotate (by the angle $\bar{\psi}^{(2)}$) on the $\mathbf{e}_1 - \mathbf{e}_3$ plane.	56

2.4	Schematic representation of a matrix reinforced by spheroidal particles subjected to aligned (a) axisymmetric shear loading, (b) pure shear loading.	60
3.1	Tangent second-order (TSO) estimates for the effective stored-energy function $\widehat{\phi}_0(\bar{\lambda})$ of neo-Hookean elastomers reinforced with dilute concentrations of rigid particles, as functions of the macroscopic logarithmic strain $\bar{e} = \ln(\bar{\lambda})$. Two <i>aligned</i> loadings are considered: <i>pure shear</i> (PS) ($\bar{\lambda}_1 = \bar{\lambda}, \bar{\lambda}_2 = 1$), and <i>axisymmetric shear</i> (AS) ($\bar{\lambda}_1 = \bar{\lambda}_2 = \bar{\lambda}$). (a) Prolate particles ($w \geq 1$) under PS loading, (b) oblate particles ($w < 1$) under PS loading, (c) prolate particles under AS loading, and (d) oblate particles under AS loading. The finite element (FEM) results of Lopez-Pamies et al. (2013a) for the case of spherical particles ($w = 1$) are also included for comparison.	82
3.2	TSO estimates for particle-reinforced, neo-Hookean elastomers under aligned <i>pure shear</i> loading ($\bar{\lambda}_1 = \bar{\lambda}, \bar{\lambda}_2 = 1$), as functions of the macroscopic logarithmic strain $\bar{e} = \ln(\bar{\lambda})$. The macroscopic stress \bar{S}^{PS} for: (a) spherical ($w = 1$), and (b) spheroidal ($w = 4, 0.25$) particles. Certain shear components of the effective modulus tensor \widehat{L}_{ijkl}^c for: (c) prolate ($w = 4$) and (d) oblate ($w = 0.25$) particles. Results are shown for the volume fractions $c = 0.05, 0.15$ and 0.25 . The finite element (FEM) results of Lopez-Pamies et al. (2013a) for spherical particles are also provided for comparison in part (a).	84
3.3	TSO estimates for particle-reinforced, neo-Hookean elastomers under aligned <i>axisymmetric shear</i> loading ($\bar{\lambda}_1 = \bar{\lambda}_2 = \bar{\lambda}$), as functions of the macroscopic logarithmic strain $\bar{e} = \ln(\bar{\lambda})$. The macroscopic stress \bar{S}^{PS} for: (a) spherical ($w = 1$), and (b) spheroidal particles ($w = 4, 0.25$). Certain shear components of the effective modulus tensor \widehat{L}_{ijkl}^c for: (c) prolate ($w = 4$), and (d) oblate ($w = 0.25$) particles. Results are shown for various volume fractions $c = 0.05, 0.15$ and 0.25 . The finite element (FEM) results of Lopez-Pamies et al. (2013a) for the case of spherical particles are also included for comparison in part (a).	86
3.4	TSO estimates for the macroscopic instabilities (loss of SE) in particle-reinforced neo-Hookean elastomers subjected to aligned loadings. Parts (a) and (b) show <i>pure shear</i> ($\bar{\lambda}_1 = \bar{\lambda}, \bar{\lambda}_2 = 1$) results for the critical strain (\bar{e}_{cr}^{PS}) at which loss of SE of the homogenized elastomer takes place, and the corresponding critical stress (\bar{S}_{cr}^{PS}), respectively. Parts (c) and (d) show <i>axisymmetric shear</i> ($\bar{\lambda}_1 = \bar{\lambda}_2 = \bar{\lambda}$) results for the critical strain (\bar{e}_{cr}^{AS}) and the corresponding critical stress (\bar{S}_{cr}^{AS}), respectively. The results are shown for various particle concentrations as functions of the particle aspect ratio $\ln(w)$	87

3.5	TSO estimates for the macroscopic stress \bar{S} versus the macroscopic logarithmic strain $\bar{\epsilon} = \ln(\bar{\lambda})$ for particle-reinforced Gent elastomers. The results are shown for three values of the matrix inextensibility parameter $J_m = 50, 100, \text{ and } \infty$. Four different cases are considered: (a) aligned pure shear for a prolate spheroidal shape ($w = 4$), (b) aligned pure shear for an oblate shape ($w = 0.25$), (c) aligned axisymmetric shear for a prolate shape ($w = 4$), and (d) aligned axisymmetric shear for an oblate shape ($w = 0.25$).	89
3.6	Tangent second-order (TSO) and generalized second-order (GSO) estimates for the effective response of an incompressible neo-Hookean matrix reinforced by 2-D circular (rigid) fibers ($w = 1$) subjected to transverse <i>pure shear</i> loadings. The GSO estimates correspond to the stored-energy function (1.126). The results are shown as a function of the applied stretch $\bar{\lambda}$ for different values of the fiber volume fraction. (a) The effective energy $\hat{\phi}^{PS}$. (b) The corresponding macroscopic stress $\bar{S}^{PS} = d\hat{\phi}^{PS}/d\bar{\lambda}$. . .	91
3.7	The effective response of a rigidly fiber-reinforced elastomer with an incompressible neo-Hookean matrix under pure shear loading. The macroscopic stress \bar{S}^{PS} is plotted as a function of the applied stretch $\bar{\lambda}$ for (a) $c = 0.2$, and (b) $c = 0.3$. Comparisons are shown between the new TSO estimate, the estimate (1.126) of Lopez-Pamies and Ponte Castañeda (2006b) “GSO (2006)”, the earlier TSO results of Ponte Castañeda and Tiberio (2000) “TSO (2000)”, and the FE simulations of Moraleda et al. (2009) “FEM”.	92
3.8	Comparison between the TSO estimates for the macroscopic stress \bar{S}^{PS} in 2-D and 3-D rigidly reinforced elastomers subjected to aligned <i>pure shear</i> loadings. The 2-D composite is a fiber-reinforced composite which consists of an incompressible neo-Hookean matrix and a random distribution of long, aligned (rigid) fibers with elliptical cross section, and is subjected to aligned pure shear loading. The 3-D composite is the composite studied in this work with a neo-Hookean matrix and spheroidal particles, and is subjected to aligned pure shear deformation ($\bar{\lambda}_1 = \bar{\lambda}, \bar{\lambda}_2 = 1$). The results are shown as functions of the logarithmic strain $\bar{\epsilon} = \ln(\bar{\lambda})$ for two fiber/particle aspect ratios ($w = 1$ and $w = 4$), at the fixed fiber/particle concentration $c = 0.3$. The FE simulations of Moraleda et al. (2009) for a 2-D fiber-reinforced composite with circular fibers ($w = 1$) are also included for comparison.	93

3.9	Comparisons of the predictions of TSO predictions with experimental data of Wang and Mark (1990) for composites consisting of an elastomeric matrix (made of PDMS) and prolate spheroidal particles (made of polystyrene). Parts (a) and (b) show results for uniaxial tension along \mathbf{e}_3 direction for the effective stress component \bar{S}_{33} and the strain components $\bar{e}_2 = \ln(\bar{\lambda}_2)$, $\bar{e}_3 = \ln(\bar{\lambda}_3)$, respectively, as functions of the logarithmic strain \bar{e}_3 . Parts (c) and (d) show results for uniaxial tension along \mathbf{e}_1 direction for the effective stress component \bar{S}_{11} and the strain components \bar{e}_2 , \bar{e}_3 , respectively, as functions of the strain $\bar{e}_1 = \ln(\bar{\lambda}_1)$. Parts (e) and (f) compare TSO results for uniaxial tension along \mathbf{e}_1 direction and axisymmetric deformation in $\mathbf{e}_2 - \mathbf{e}_3$ plane for the effective stress component \bar{S}_{11} and strains \bar{e}_2 , \bar{e}_3 , respectively, as functions of \bar{e}_1	94
3.10	Schematic representation of a matrix reinforced by prolate spheroidal particles subjected to (a) uniaxial tension along \mathbf{e}_1 direction, (b) tension along \mathbf{e}_1 direction with the constraint $\bar{\lambda}_2 = \bar{\lambda}_3 < 1$	95
3.11	TSO estimates for a particle-reinforced neo-Hookean composite with a dilute concentration of <i>prolate</i> particles with aspect ratio $w = 2$ subjected to <i>non-aligned</i> loadings. Parts (a) and (b) show results for <i>pure shear</i> loading ($\bar{\lambda}_1 = \bar{\lambda}$, $\bar{\lambda}_2 = 1$) for the effective stress \bar{S}_0^{PS} and the angle of rotation of the particles $\bar{\psi}^{(2)}$, respectively. Parts (c) and (d) show results for <i>axisymmetric shear</i> loading ($\bar{\lambda}_1 = \bar{\lambda}_2 = \bar{\lambda}$) for the effective stress \bar{S}_0^{AS} and the rotation $\bar{\psi}^{(2)}$, respectively. The results are shown for various angles $\bar{\theta}$ (as well as for the out-of-plane misalignment angle $\bar{\theta}_1 = 0^{+\circ}$ for the case of pure shear loading), as functions of the macroscopic logarithmic strain $\bar{e} = \ln(\bar{\lambda})$	98
3.12	TSO estimates for the incremental shear moduli of particle-reinforced neo-Hookean composites with a dilute concentration of <i>prolate</i> particles with aspect ratio $w = 2$ subjected to <i>aligned</i> loadings. (a) Results for <i>pure shear</i> loading ($\bar{\lambda}_1 = \bar{\lambda}$, $\bar{\lambda}_2 = 1$). (b) Results for <i>axisymmetric shear</i> loading ($\bar{\lambda}_1 = \bar{\lambda}_2 = \bar{\lambda}$).	99
3.13	TSO estimates for a particle-reinforced neo-Hookean composite with a dilute concentration of <i>oblate</i> particles with aspect ratio $w = 0.5$ subjected to <i>non-aligned</i> loadings. Parts (a) and (b) show results for <i>pure shear</i> loading ($\bar{\lambda}_1 = \bar{\lambda}$, $\bar{\lambda}_2 = 1$) for the effective stress \bar{S}_0^{PS} and the angle of rotation of the particles $\bar{\psi}^{(2)}$, respectively. Parts (c) and (d) show results for <i>axisymmetric shear</i> loading ($\bar{\lambda}_1 = \bar{\lambda}_2 = \bar{\lambda}$) for the effective stress \bar{S}_0^{AS} and the rotation $\bar{\psi}^{(2)}$, respectively. The results are shown for various angles $\bar{\theta}$, as functions of the macroscopic logarithmic strain $\bar{e} = \ln(\bar{\lambda})$	101
3.14	TSO estimates for particle-reinforced neo-Hookean composites with dilute concentrations of <i>prolate</i> particles subjected to <i>non-aligned</i> loadings at the fixed angle $\bar{\theta} = 25^\circ$. Parts (a) and (b) show results for the effective stress \bar{S}_0^{PS} and the angle of rotation of the particles $\bar{\psi}^{(2)}$, respectively, for <i>pure shear</i> loading ($\bar{\lambda}_1 = \bar{\lambda}$, $\bar{\lambda}_2 = 1$). Parts (c) and (d) show results for the effective stress \bar{S}_0^{AS} and the rotation $\bar{\psi}^{(2)}$, respectively, for <i>axisymmetric shear</i> ($\bar{\lambda}_1 = \bar{\lambda}_2 = \bar{\lambda}$). The results are shown for particle aspect ratios $w = 1, 1.1, 2, 4, 8$, as functions of the macroscopic logarithmic strain $\bar{e} = \ln(\bar{\lambda})$	103

3.15	TSO estimates for particle-reinforced neo-Hookean composites with dilute concentrations of <i>oblate</i> particles subjected to <i>non-aligned</i> loadings at the fixed angle $\bar{\theta} = 25^\circ$. Parts (a) and (b) show results for the effective stress \bar{S}_0^{PS} and the angle of rotation of the particles $\bar{\psi}^{(2)}$, respectively, for <i>pure shear</i> ($\bar{\lambda}_1 = \bar{\lambda}, \bar{\lambda}_2 = 1$). Parts (c) and (d) show results for the effective stress \bar{S}_0^{AS} and the rotation $\bar{\psi}^{(2)}$, respectively, for <i>axisymmetric shear</i> ($\bar{\lambda}_1 = \bar{\lambda}_2 = \bar{\lambda}$). The results are shown for particle aspect ratios $w = 1, 0.9, 0.5, 0.25, 0.125$, as functions of the macroscopic logarithmic strain $\bar{e} = \ln(\bar{\lambda})$.	105
3.16	TSO estimates for a particle-reinforced neo-Hookean composite with prolate particles of aspect ratio $w = 2$ subjected to <i>non-aligned</i> loadings at the angles $\bar{\theta} = 5^\circ$, and 25° . Parts (a) and (b) show results for the case of <i>pure shear</i> loading ($\bar{\lambda}_1 = \bar{\lambda}, \bar{\lambda}_2 = 1$), respectively for the effective stress \bar{S}_0^{PS} and the angle of rotation of the particles $\bar{\psi}^{(2)}$. Parts (c) and (d) show results for the case of <i>axisymmetric shear</i> loading ($\bar{\lambda}_1 = \bar{\lambda}_2 = \bar{\lambda}$), respectively for the effective stress \bar{S}_0^{AS} and the rotation $\bar{\psi}^{(2)}$. The results are shown for particle volume fractions $c = 0.05, 0.15$, and 0.25 , as functions of the macroscopic logarithmic strain $\bar{e} = \ln(\bar{\lambda})$.	106
4.1	Schematic illustration of the microstructure in the suspension, identifying the various microstructural variables. The particles shapes and orientations evolve with the deformation and are depicted as grey ellipses, while their two-point probability functions are depicted as larger dotted ellipses surrounding the particles. (a) At $t = 0$, the particles are spherical and distributed randomly with statistical isotropy in the Newtonian fluid. (b) At a later time t , after application of the macroscopic velocity gradient $\bar{\mathbf{L}}$, the particles have become ellipsoidal and are distributed with ellipsoidal symmetry (with the same shape and orientation). (c) The particles are described by a “representative ellipsoid” with aspect ratios $w_1 = z_2/z_1$ and $w_2 = z_3/z_1$, and with principal axes defined by the unit vectors $\mathbf{n}_1, \mathbf{n}_2$ and $\mathbf{n}_3 = \mathbf{n}_1 \times \mathbf{n}_2$ (which rotate relative to the laboratory axes $\{\mathbf{E}_i\}, i = 1, 2, 3$).	118
4.2	Results for the time-dependent response of suspensions of initially spherical neo-Hookean and Gent particles with $G = 0.3$ in an extensional flow.	132
4.3	Results for the time-dependent response of suspensions of initially spherical Kelvin-Voigt particles (with NH elastic part) for $c = 0.2$ in an extensional flow.	133
4.4	Results for the steady-state relative viscosities of suspensions of initially spherical, neo-Hookean and Gent particles in extensional flow.	135
4.5	Results for the time-dependent response of suspensions of initially spherical neo-Hookean particles with $G = 0.2$ and various values of c in a shear flow. The components of $\bar{\boldsymbol{\tau}}^{(2)}$ and $\bar{\mathbf{D}}^{(2)}$ are given relative to the principal axes of the particle.	138
4.6	Results for the time-dependent response of suspensions of initially spherical neo-Hookean and Gent particles with $c = 0.2$ and various values of the dimensionless parameter G in a shear flow. Higher values of G correspond to softer particles, or to larger shear-strain rates.	139

4.7	Results for the time-dependent response of suspensions of initially spherical Kelvin-Voigt particles (with NH elastic part) with $G = 0.2$ and various values of K in a shear flow. The components of $\bar{\tau}^{(2)}$ are given relative to the principal axes of the particle.	141
4.8	Results for the steady-state response of suspensions of initially spherical neo-Hookean particles for various values of c in a shear flow.	142
4.9	Results for the steady-state response of suspensions of initially spherical Kelvin-Voigt particles (with NH elastic part) for various values of K in a shear flow.	143
4.10	Results for the steady-state response of suspensions of initially spherical neo-Hookean, Gent and Kelvin-Voigt particles (with NH elastic part) in a shear flow.	145
4.11	Comparisons of the predictions of our model with numerical simulation results for suspensions of initially spherical capsules, as well as with experimental data for suspensions of RBCs under shear flow conditions. (a-d) Comparisons of the time-dependent response of dilute suspensions of KV particles with the simulation results of Ramanujan and Pozrikidis (1998a) for the corresponding response of dilute suspensions of capsules. (e) Comparisons of the SS response of suspensions of KV particles with the simulation results of Clausen et al. (2011) for the SS behavior of non-dilute suspensions of capsules. (f) Comparisons of the SS behavior of suspensions of KV particles with the experimental data of Brooks et al. (1970) for the effective viscosity of suspensions of normal human RBCs, as a function of the shear rate $\dot{\gamma}$, for different values of the RBC volume fraction.	146
5.1	Examples of the Herschel-Bulkley model (5.1).	152
5.2	Graphical representation of the microstructure in the suspension at a given time t . The figure shows a “representative ellipsoid” with aspect ratios $w_1 = z_2/z_1$ and $w_2 = z_3/z_1$, and with principal (orthonormal) coordinate system $\mathbf{n}_1, \mathbf{n}_2$ and $\mathbf{n}_3 = \mathbf{n}_1 \times \mathbf{n}_2$ (which rotates relative to the laboratory axes $\{\mathbf{E}_i\}, i = 1, 2, 3$).	158
5.3	Variational estimates for the time-dependent response of suspensions of initially spherical Gent particles with $G = 0.2$ in a Bingham fluid ($n = 1$) for various values of H_G under shear flow conditions. The components of $\bar{\tau}^{(1)}$ and $\bar{\tau}^{(2)}$ are given relative to the fixed coordinate system \mathbf{E}_i and the principal axes of the particles, respectively.	176
5.4	Variational estimates for the steady-state response of suspensions of initially spherical Gent particles with $G = 0.2$ in a Bingham fluid ($n = 1$) for various values of H under shear flow conditions. The components of $\bar{\tau}^{(1)}$ and $\bar{\tau}^{(2)}$ are given relative to the fixed coordinate system \mathbf{E}_i and the principal axes of the particles, respectively.	177
5.5	Variational estimates for the steady-state response of suspensions of initially spherical Gent particles with $G = 0.2$ in a Bingham fluid ($n = 1$) for various values of H_G under shear flow conditions. The components of $\bar{\tau}^{(1)}$ and $\bar{\tau}^{(2)}$ are given relative to the fixed coordinate system \mathbf{E}_i and the principal axes of the particles, respectively.	178

5.6	Variational estimates for the time-dependent response of suspensions of initially spherical Gent particles with $G = 0.2$ in a power-law fluid ($H = 0$) for various values of n under shear flow conditions. The components of $\bar{\tau}^{(1)}$ and $\bar{\tau}^{(2)}$ are given relative to the fixed coordinate system \mathbf{E}_i and the principal axes of the particles, respectively.	180
5.7	Variational estimates for the steady-state response of suspensions of initially spherical Gent particles with $G = 0.2$ in a power-law fluid ($H = 0$) for various values of n under shear flow conditions. The components of $\bar{\tau}^{(1)}$ and $\bar{\tau}^{(2)}$ are given relative to the fixed coordinate system \mathbf{E}_i and the principal axes of the particles, respectively.	181
5.8	Variational estimates for the steady-state response of suspensions of initially spherical Gent particles in a power-law fluid ($H = 0$) for various values of n under shear flow conditions. The components of $\bar{\tau}^{(1)}$ and $\bar{\tau}^{(2)}$ are given relative to the fixed coordinate system \mathbf{E}_i and the principal axes of the particles, respectively.	183
5.9	Variational estimates for the time-dependent response of suspensions of initially spherical Gent particles with $c = 0.2$ and various values of G in a Herschel-Bulkley fluid ($H = 1$ and $n = 0.5$) under shear flow conditions. Higher values of G correspond to softer particles. The components of $\bar{\tau}^{(1)}$ and $\bar{\tau}^{(2)}$ are given relative to the fixed coordinate system \mathbf{E}_i and the principal axes of the particles, respectively.	184
5.10	Variational estimates for the steady-state response of suspensions of initially spherical Gent particles with $c = 0.2$ and various values of G in a Herschel-Bulkley fluid ($n = 0.5$) under shear flow conditions. The components of $\bar{\tau}^{(1)}$ and $\bar{\tau}^{(2)}$ are given relative to the fixed coordinate system \mathbf{E}_i and the principal axes of the particles, respectively.	186
5.11	Comparisons of the effective yield stress for suspensions of rigid particles in yield stress fluids ($\bar{\tau}_0^R/\tau_0$) with experimental data in Chateau et al. (2008) (originally from Mahaut et al. (2008)), as a function of the particle volume fraction. The solid diamond and open square symbols correspond to suspensions of polystyrene and glass beads in emulsion and in bentonite, respectively, while the open circle symbols correspond to suspensions of glass beads in carbopol.	187
6.1	Schematic illustration of the microstructure in a particle-reinforced composite. The elastic particles are prolate spheroidal in shape ($w > 1$), and their symmetry axis is aligned with the coordinate basis vector \mathbf{e}_3	205
6.2	Estimates for the effective response and field statistics in the composites consisting of a elastic-ideally plastic matrix and elastic spherical particles ($w = 1$) with $c = 0.17$, $\mu^{(1)}/\sigma_0 = 30$, and $\mu^{(2)}/\mu^{(1)} = 2$, under axisymmetric shear loading. Comparisons are shown between our model, the analytical model of Lahelec and Suquet (2013) “IVP”, and the full-field simulations of Lahelec and Suquet (2013) “FFT”.	209
6.3	Variational estimates for the effective response and field statistics in the composites consisting of a elastic-ideally plastic matrix and elastic spheroidal particles with $\mu^{(1)}/\sigma_0 = 54$, $\mu^{(2)}/\mu^{(1)} = 3.8$, and $w = 3$ under axisymmetric shear loading.	210

6.4	Variational estimates for the effective response and field statistics in the composites consisting of a elastic-ideally plastic matrix and elastic spheroidal particles with $\mu^{(1)}/\sigma_0 = 54$, $\mu^{(2)}/\mu^{(1)} = 3.8$, and $c = 0.3$ under axisymmetric shear loading. The material properties correspond Sic particles and Titanium matrix.	211
6.5	Variational estimates for the effective response and field statistics in the composites consisting of a elastic-ideally plastic matrix and elastic spheroidal particles with $\mu^{(2)}/\mu^{(1)} = 2$, $c = 0.3$, and $w = 3$ under axisymmetric shear loading.	213
6.6	Variational estimates for the effective response and field statistics in the composites consisting of a elastic-ideally plastic matrix and elastic spheroidal particles with $\mu^{(1)}/\sigma_0 = 54$, $c = 0.3$, and $w = 3$ under axisymmetric shear loading.	214
6.7	Variational estimates for the effective response and field statistics in the composites consisting of a elastic-ideally plastic matrix and elastic spheroidal particles with $\mu^{(1)}/\sigma_0 = 54$, $\mu^{(2)}/\mu^{(1)} = 3.8$, and $c = 0.3$ under transverse shear loading.	215
6.8	Variational estimates for the effective response and field statistics in the composites consisting of a elastic-ideally plastic matrix and elastic spheroidal particles with $\mu^{(1)}/\sigma_0 = 54$, $\mu^{(2)}/\mu^{(1)} = 3.8$, and $c = 0.3$ under longitudinal shear loading.	216
6.9	Variational estimates for the effective response and stress phase averages in the composites consisting of a elastic-ideally plastic matrix and elastic spheroidal particles with $\mu^{(1)}/\sigma_0 = 54$, $\mu^{(2)}/\mu^{(1)} = 3.8$, and $c = 0.3$ under combined axisymmetric and longitudinal shear loading with $\alpha = 1$	218

Part I

Elastomeric Composites

Chapter 1

Tangent second-order estimates for the macroscopic response of particle-reinforced elastomers

In this chapter, we propose an approximate homogenization method to obtain estimates for the effective constitutive behavior and associated microstructure evolution in hyperelastic composites undergoing finite-strain deformations. The method is a modified version of the “tangent second-order” procedure of Ponte Castañeda and Tiberio (2000), and can be used to provide estimates for the nonlinear elastic composites in terms of corresponding estimates for suitably chosen “linear comparison composites.” The method makes use of the “tangent” moduli of the phases, evaluated at suitable averages of the deformation gradient, and yields a constitutive relation accounting for the evolution of characteristic features of the underlying microstructure in the composites, when subjected to large deformations. Satisfaction of the exact, macroscopic incompressibility constraint is ensured by means of an energy decoupling approximation splitting the elastic energy into a purely “distortional” component, together with a “dilatational” component. The method is applied to elastomers containing random distributions of aligned, rigid, ellipsoidal inclusions, and explicit analytical estimates are obtained for the special case of spherical inclusions distributed isotropically in an incompressible neo-Hookean matrix. In addition, the method is also applied to two-dimensional composites with random distributions of aligned, elliptical fibers, and the results are compared with corresponding results of earlier homogenization estimates and finite element simulations.

1.1 Introduction

Particle- and fiber-reinforced elastomers are a prominent class of soft materials that have found a wide range of applications in industry. A few examples of such applications include car tires, flexible underwater vehicles, and compliant aircraft structures. In particular, carbon-filled and silica-filled rubbers are two important groups of particle-reinforced elastomers used for technological purposes (O’connor, 1977; Bergstrom and Boyce, 1999; Wang et al., 2001; Bouchart et al., 2010; Leblanc, 2010). Also, there is a large class of thermoplastic polymers, which exhibit elastomeric behavior, and they are referred to as thermoplastic elastomers. These materials are block copolymers where the hard glassy blocks self-aggregate into a particle phase that is embedded in a matrix of the soft elastomeric blocks, thus leading to a particulate microstructure with an overall elastomeric response (Honeker and Thomas, 1996; Park et al., 2003). Moreover, elastomer-like, heterogeneous materials with particulate/fibrous microstructures are also naturally present in the form of biological tissues, such as arterial walls, ligaments, annulus fibrosus, etc. (see, e.g., Quapp and Weiss, 1998; Loocke et al., 2006; Limbert and Middleton, 2006; Chen et al., 2011; Miri et al., 2014).

As a consequence, investigations to characterize the effective behavior of elastomeric composites with *random* particulate microstructures are very timely. With this goal in mind, two different nonlinear homogenization methods have been developed recently for elastomeric composites under large deformations by means of variational principles (Ponte Castañeda, 1991), namely, the so-called “tangent second-order” (TSO) method (Ponte Castañeda and Tiberio, 2000; Lahellec et al., 2004) and the “generalized second-order” (GSO) method (Ponte Castañeda, 2002; Lopez-Pamies and Ponte Castañeda, 2004, 2006a). These methods make use of suitably designed variational principles for the properties of appropriately defined “linear comparison composites” (LCC), which are fictitious composites with the same microstructure as the original nonlinear composites, but

with linear properties. The distinguishing features of the second-order methods are that: (1) they rigorously incorporate full dependence on the nonlinear constitutive behavior of the constituent phases, (2) they are exact to second-order in the heterogeneity contrast (hence their name), and (3) they account for statistical information about the underlying microstructure in the undeformed configuration, as well as for its evolution, resulting from the finite changes in geometry caused by the applied finite deformations. The latter is essential in homogenization of hyperelastic composites as the *evolution of the microstructure* can have significant geometric softening or stiffening effects on the overall response of the material, which, in turn, may lead to the possible development of *macroscopic instabilities*.

The TSO method, which was proposed by Ponte Castañeda and Tiberio (2000) building on earlier work for viscoplastic composites (Ponte Castañeda, 1996; Ponte Castañeda and Willis, 1999), identifies the modulus tensors of the phases in the LCC with the tangent modulus tensors of the hyperelastic phases, evaluated at the phase averages of the deformation fields in the LCC. The GSO method, which was developed by Lopez-Pamies and Ponte Castañeda (2004, 2006a) building on earlier work for viscoplastic composites Ponte Castañeda and Tiberio (2000), makes use of additional information about the second moments of the fluctuations of the deformation gradients in the LCC to define an alternative linearization of the nonlinear constitutive response of the hyperelastic phases leading to more accurate predictions, especially at higher concentration of the phases. Given the highly nonlinear character of these homogenization problems in finite elasticity, the first applications of these methods were carried out in the context of two-dimensional idealizations of the microstructure. Thus, using the TSO method, elastomers with random and periodic distributions of circular particles were considered by Ponte Castañeda and Tiberio (2000) and Lahellec et al. (2004), respectively. Also, Lopez-Pamies and Ponte Castañeda (2006b) studied the application of the GSO method to two-dimensional composites containing random distributions of aligned rigid, elliptical fibers in an elastomeric matrix. More general results for fiber-reinforced elastomers subjected to three-dimensional loading conditions with periodic and random distributions of fibers have been provided by Brun et al. (2007) and Agoras et al. (2009a,b), respectively, by means of the GSO method. In addition, Bouchart et al. (2010) have presented an application of the TSO method for three-dimensional reinforced rubbers, while Racherla et al. (2010) provided an application of the TSO method for polydomain thermoplastic elastomers with lamellar microstructures.

Also, it should be mentioned that a novel homogenization approach for hyperelastic composites has been proposed recently by deBotton (2005), and developed further by deBotton et al. (2006) and Lopez-Pamies and Idiart (2010), building on earlier work for nonlinear composites with “sequentially laminated” microstructures (Ponte Castañeda, 1992; Hariton and deBotton, 2003; Idiart, 2008). This approach is based on sequential lamination, which has been used extensively for linear composites to demonstrate optimality of bounds (Milton, 2002a), and has been used more recently in the context of finite elasticity (deBotton, 2005; deBotton et al., 2006; Lopez-Pamies and Idiart, 2010). These iterated methods have the distinct advantage of producing “exact” results, unlike the linear comparison methods, which only provide variational approximations. However, the classes of microstructures that can be considered are much more restrictive and there is no precise control on the typical microstructural variables such as particle shape. Instead, use is made of two-point cor-

relation functions for the particulate phase, which typically exhibits highly distorted and physically unrealistic shapes. In addition, this technique generally leads to partial differential equations (of the Hamilton-Jacobi type) for the effective behavior, which have only been solved exactly for some very special geometric configurations and very specific constitutive models (essentially, neo-Hookean). More generally, numerical (or other types of approximations) are required to obtain explicit results by the lamination methods. By contrast, the linear comparison methods can handle much more general classes of constitutive behavior for the phases, as well as microstructures, including, for example, polydomain elastomeric systems (Racherla et al., 2010).

In spite of the significant progress that has been made to date, there are still significant barriers for the general implementation of all the presently available nonlinear homogenization methods for hyperelastic composites. The TSO method is the easiest to use, but it can give unreliable estimates for large concentrations and strongly nonlinear behavior of the constituent phases, including the failure to capture (unless appropriately modified) the overall incompressibility constraint for incompressible phases. The GSO method seems to provide the most reliable predictions, but it is more difficult to use than the TSO method and thus far has only been used for continuous fiber composites. On the other hand, the “sequentially laminated” homogenization is the most recent, and thus far it has only been used successfully for neo-Hookean phases, requiring the solution of difficult nonlinear PDE more generally.

The main goal of this chapter is to develop a general, three-dimensional model based on the TSO method of Ponte Castañeda and Tiberio (2000) for the effective behavior of elastomeric composite materials subjected to finite deformations. In particular, in this chapter, we provide analytical estimates for the effective behavior of dilute and non-dilute composites that are capable of accounting for general (ellipsoidal) particle shapes and distribution, as well as general three-dimensional loading conditions (including nonaligned loadings). In addition, evolution laws are provided for the relevant microstructural variables, including particle orientations. The new estimates recover the exact overall incompressibility constraint for the special case of rigidly reinforced elastomers with incompressible matrix phases. Furthermore, in this chapter, the principal features of this model are examined within the context of 2-D and 3-D examples. In the 2-D example, we consider elastomers reinforced with cylindrical fibers of elliptical cross-section under (transverse) plane-strain loading, while in the 3-D example, we consider class of statistically isotropic composites consisting of an incompressible, elastomeric matrix reinforced by rigid spherical inclusions. It is worth mentioning that the resulting constitutive model can be used to detect macroscopic material failure in the form of loss of strong ellipticity (or rank-one convexity) of the associated homogenized behavior (Geymonat et al., 1993), although this will be pursued in detail in Chapters 2 and 3.

This chapter is organized as follows. Sections 1.2 and 1.3 describe in some detail the tangent second-order homogenization method. Section 1.4 presents the main results of this chapter, namely, the derivation of the homogenized constitutive relation for particle-reinforced elastomers with general ellipsoidal microstructures and incompressible matrix behavior, including the development of evolution laws for the average orientation of the particles with the deformation. The principal features of this model are examined within the context of 2-D and 3-D examples, respectively, in Sections 1.5 and 1.6. Thus, Section 1.5 deals with the application to elastomers reinforced with cylindrical fibers

of elliptical cross-section under (transverse) plane-strain loading. More specific results are presented and compared with corresponding GSO estimates for composites with circular fibers, as well as with FEM results from the literature. In Section 1.6, the results of Section 1.4 are applied to the class of statistically isotropic composites consisting of an incompressible, elastomeric matrix reinforced by rigid spherical inclusions. In both examples, the influence of the particle volume fraction, matrix properties and loading conditions on the macroscopic behavior of the composite is investigated. Finally, some conclusion are drawn in Section 1.7.

1.2 Hyperelastic Composites

Consider a material consisting of N different (homogeneous) phases, which are assumed to be distributed *randomly* in a specimen occupying a volume Ω_0 with boundary $\partial\Omega_0$ in the undeformed configuration. Furthermore, the characteristic length-scale of the inhomogeneities (e.g., particles, or voids) is much smaller than the size of the specimen and the scale of variation of the loading conditions. Let the position vector of a material point in the undeformed configuration Ω_0 be denoted by \mathbf{X} , with Cartesian components X_i , $i \in \{1, 2, 3\}$ and the corresponding position vector in the deformed configuration Ω be denoted by \mathbf{x} , with components x_i . The deformation gradient tensor represented by \mathbf{F} has components $F_{ij} = \partial x_i / \partial X_j$ and is required to satisfy the material *impenetrability* condition: $J = \det \mathbf{F}(\mathbf{X}) > 0$ for all $\mathbf{X} \in \Omega_0$. In addition, let $\mathbf{F} = \mathbf{R} \mathbf{U}$ where \mathbf{U} and \mathbf{R} stand for the stretch and (*rigid-body*) rotation tensors, respectively, and let $\mathbf{C} = \mathbf{F}^T \mathbf{F} = \mathbf{U}^2$ denote the right Cauchy–Green deformation tensor.

We assume that the constitutive behavior of the phases is purely elastic and characterized by the stored-energy functions $W^{(r)}(\mathbf{F})$ ($r = 1, \dots, N$), which are taken to be *nonconvex* functions of the deformation gradient tensor \mathbf{F} , such that the local energy function of the composite may be written as

$$W(\mathbf{X}, \mathbf{F}) = \sum_{r=1}^N \chi^{(r)}(\mathbf{X}) W^{(r)}(\mathbf{F}). \quad (1.1)$$

In the above equation, the characteristic functions $\chi^{(r)}$, describing the distribution of the phases in the reference configuration, are such that they equal 1 if the position vector \mathbf{X} is inside the phase r (i.e., $\mathbf{X} \in \Omega_0^{(r)}$) and zero otherwise. The stored-energy functions $W^{(r)}(\mathbf{F})$ are assumed to be objective, namely, $W^{(r)}(\mathbf{Q}\mathbf{F}) = W^{(r)}(\mathbf{F})$ for all proper orthogonal tensors \mathbf{Q} and arbitrary deformation gradients \mathbf{F} , so that $W^{(r)}(\mathbf{F}) = W^{(r)}(\mathbf{U})$. The local or microscopic constitutive relation for the composite is then given by

$$\mathbf{S} = \frac{\partial W(\mathbf{X}, \mathbf{F})}{\partial \mathbf{F}}, \quad (1.2)$$

where \mathbf{S} stands for the first Piola-Kirchhoff stress tensor.

Following Hill (1972), the effective stored-energy function \widetilde{W} of the composite elastomer is defined

by

$$\widetilde{W}(\bar{\mathbf{F}}) = \min_{\mathbf{F} \in K(\bar{\mathbf{F}})} \langle W(\mathbf{X}, \mathbf{F}) \rangle = \min_{\mathbf{F} \in K(\bar{\mathbf{F}})} \sum_{r=1}^N c_0^{(r)} \langle W^{(r)}(\mathbf{F}) \rangle^{(r)}, \quad (1.3)$$

where $K(\bar{\mathbf{F}})$ denotes the set of kinematically admissible deformation gradients:

$$K(\bar{\mathbf{F}}) = \{ \mathbf{F} | \exists \mathbf{x} = \mathbf{x}(\mathbf{X}) \text{ with } \mathbf{F} = \text{Grad } \mathbf{x} \text{ and } J > 0 \text{ in } \Omega_0, \mathbf{x} = \bar{\mathbf{F}} \mathbf{X} \text{ on } \partial\Omega_0 \}. \quad (1.4)$$

In the above expressions, the triangular brackets $\langle \cdot \rangle$ and $\langle \cdot \rangle^{(r)}$ denote volume averages (in the undeformed configuration) over the domains Ω_0 and $\Omega_0^{(r)}$, respectively, so that the scalar $c_0^{(r)} = \langle \chi^{(r)} \rangle$ indicates the initial volume fraction of the phase r .

In the neighborhood of $\bar{\mathbf{F}} = \mathbf{I}$ (where \mathbf{I} is the second-order identity tensor), the solution of the Euler-Lagrange equations associated with the variational problem (1.3) is unique, and gives the minimum energy. As the deformation progresses into the finite deformation regime, the composite may reach a point at which this “principal” solution bifurcates into lower energy solutions. This point corresponds to the onset of an instability, beyond which the applicability of the “principal” solution becomes questionable. However, it is still possible to extract useful information from the principal solution by computing the associated macroscopic instabilities from the loss of strong ellipticity of the homogenized behavior. Based on these remarks, in this work, we will estimate the overall behavior of composite elastomers by means of the effective stored-energy function

$$\widehat{W}(\bar{\mathbf{F}}) = \text{stat}_{\mathbf{F} \in K(\bar{\mathbf{F}})} \sum_{r=1}^N c_0^{(r)} \langle W^{(r)}(\mathbf{F}) \rangle^{(r)}, \quad (1.5)$$

instead of solving the variational problem (1.3). From its definition, it is clear that $\widetilde{W}(\bar{\mathbf{F}}) = \widehat{W}(\bar{\mathbf{F}})$ from $\bar{\mathbf{F}} = \mathbf{I}$ up to the onset of the first instability, beyond which $\widetilde{W}(\bar{\mathbf{F}}) \leq \widehat{W}(\bar{\mathbf{F}})$. Moreover, it is often the case (Geymonat et al., 1993) that the first instability is indeed a long wavelength instability, as characterized by the loss of strong ellipticity of $\widetilde{W}(\bar{\mathbf{F}})$. Furthermore, it is worth stating that $\widehat{W}(\bar{\mathbf{F}})$ is an *objective* function of the macroscopic deformation gradient $\bar{\mathbf{F}}$, by virtue of its definition (1.5) and of the objectivity assumption for the $W^{(r)}$.

Noting that under the affine boundary condition $\langle \mathbf{F} \rangle = \bar{\mathbf{F}}$, and defining the average stress $\bar{\mathbf{S}} = \langle \mathbf{S} \rangle$, the effective constitutive relation for the composite is given by Hill (1972)

$$\bar{\mathbf{S}} = \frac{\partial \widetilde{W}}{\partial \bar{\mathbf{F}}}(\bar{\mathbf{F}}). \quad (1.6)$$

In the next section, we present a concise review of the “tangent second-order” homogenization procedure, including its specialization for the case of two-phase elastomeric composites.

1.3 Tangent Second-Order Method

In this section, we recall the tangent second-order (TSO) method of Ponte Castañeda and Tiberio (2000) (see also Ponte Castañeda (1996); Ponte Castañeda and Willis (1999)) in order to generate

new estimates for the effective stored-energy function $\widetilde{W}(\bar{\mathbf{F}})$ for the above-described elastomeric composite. The main concept behind the TSO method is the construction of a fictitious “linear comparison composite” (LCC), with the same microstructure (i.e., same characteristic functions $\chi^{(r)}(\mathbf{X})$) as the actual (nonlinear) composite material (in the undeformed configuration). The constituent phases of the LCC are identified with appropriate linearizations of the given nonlinear phases resulting from suitable variational principles. This allows the use of already available methods to estimate the effective behavior of linear composites to generate corresponding estimates for nonlinear composites.

Similar to relation (1.1), the local stored-energy function of the LCC can be formally expressed as

$$W_T(\mathbf{X}, \mathbf{F}) = \sum_{r=1}^N \chi^{(r)}(\mathbf{X}) W_T^{(r)}(\mathbf{F}), \quad (1.7)$$

where $W_T^{(r)}(\mathbf{F})$ is the energy potential of phase r in the LCC, which may in turn be rewritten in the form

$$W_T^{(r)}(\mathbf{F}) = f^{(r)} + \mathbf{T}^{(r)} \cdot \mathbf{F} + \frac{1}{2} \mathbf{F} \cdot \mathbf{L}^{(r)} \mathbf{F}, \quad (1.8)$$

where the “thermal stress” $\mathbf{T}^{(r)}$ and “specific heat” $f^{(r)}$ are defined as

$$\mathbf{T}^{(r)} = \mathbf{S}^{(r)}(\mathbf{F}^{(r)}) - \mathbf{L}^{(r)} \mathbf{F}^{(r)}, \quad f^{(r)} = W^{(r)}(\mathbf{F}^{(r)}) - \mathbf{T}^{(r)} \cdot \mathbf{F}^{(r)} - \frac{1}{2} \mathbf{F}^{(r)} \cdot \mathbf{L}^{(r)} \mathbf{F}^{(r)}. \quad (1.9)$$

In these expressions, the $\mathbf{F}^{(r)}$ are constant, reference, second-order tensors, while the $\mathbf{L}^{(r)}$ are uniform, (major) symmetric, fourth-order tensors, which are usually identified with the tangent modulus tensors of the phases, evaluated at the corresponding reference deformations $\mathbf{F}^{(r)}$, i.e.,

$$\mathbf{L}^{(r)} = \mathbf{L}_i^{(r)}(\mathbf{F}^{(r)}) = \frac{\partial^2 W^{(r)}}{\partial \mathbf{F} \partial \mathbf{F}}(\mathbf{F}^{(r)}). \quad (1.10)$$

In addition, use has been made of the notation

$$\mathbf{S}^{(r)} = \frac{\partial W^{(r)}}{\partial \mathbf{F}}(\mathbf{F}^{(r)}). \quad (1.11)$$

If all the phases in the LCC are characterized by potentials of the form (1.8), it follows from the linearity of the problem that the effective potential of the LCC can be written as (Ponte Castañeda and Tiberio, 2000)

$$\widetilde{W}_T(\mathbf{F}) = \tilde{f} + \tilde{\mathbf{T}} \cdot \bar{\mathbf{F}} + \frac{1}{2} \bar{\mathbf{F}} \cdot \tilde{\mathbf{L}} \bar{\mathbf{F}}, \quad (1.12)$$

where $\tilde{\mathbf{L}}$ is the effective modulus tensor of the linear-elastic comparison composite, and $\tilde{\mathbf{T}}$ and \tilde{f} are the effective thermal stress and specific heat, respectively. For two-phase composites, the expressions for $\tilde{\mathbf{T}}$ and \tilde{f} are given by Levin (1967); Ponte Castañeda and Tiberio (2000)

$$\tilde{\mathbf{T}} = \bar{\mathbf{T}} + (\tilde{\mathbf{L}} - \bar{\mathbf{L}})(\Delta \mathbf{L})^{-1} \Delta \mathbf{T}, \quad (1.13)$$

$$\tilde{f} = \bar{f} + \frac{1}{2} \Delta \mathbf{T} (\Delta \mathbf{L})^{-1} \cdot (\tilde{\mathbf{L}} - \bar{\mathbf{L}}) (\Delta \mathbf{L})^{-1} \Delta \mathbf{T}, \quad (1.14)$$

where $\Delta \mathbf{T} = \mathbf{T}^{(1)} - \mathbf{T}^{(2)}$, and $\Delta \mathbf{L} = \mathbf{L}^{(1)} - \mathbf{L}^{(2)}$. Furthermore, \bar{f} , $\bar{\mathbf{T}}$, and $\bar{\mathbf{L}}$ are the volume averages of f , \mathbf{T} and \mathbf{L} . Using Eqs. (1.13) and (1.14) in (1.12), the effective potential associated with the LCC for two-phase composites can be written as

$$\widetilde{W}_T = \bar{f} + \frac{1}{2} (\Delta \mathbf{L}_0)^{-1} \Delta \mathbf{T} \cdot (\tilde{\mathbf{L}} - \bar{\mathbf{L}}) (\Delta \mathbf{L})^{-1} \Delta \mathbf{T} + \left[\bar{\mathbf{T}} + (\tilde{\mathbf{L}} - \bar{\mathbf{L}}) (\Delta \mathbf{L})^{-1} \Delta \mathbf{T} \right] \cdot \bar{\mathbf{F}} + \frac{1}{2} \bar{\mathbf{F}} \cdot \tilde{\mathbf{L}} \bar{\mathbf{F}}. \quad (1.15)$$

Within the context of the *tangent* second-order theory, Ponte Castañeda and Tiberio (2000) made use the prescriptions $\mathbf{F}^{(r)} = \bar{\mathbf{F}}^{(r)}$ for the LCC and obtained the following estimate for the stored-energy function of N -phase, *hyperelastic composites*

$$\widehat{W}(\bar{\mathbf{F}}) = \sum_{r=1}^N c^{(r)} \left\{ W^{(r)}(\bar{\mathbf{F}}^{(r)}) + \frac{1}{2} (\bar{\mathbf{F}} - \bar{\mathbf{F}}^{(r)}) \cdot \mathbf{S}^{(r)}(\bar{\mathbf{F}}^{(r)}) \right\}, \quad (1.16)$$

where the variables $\bar{\mathbf{F}}^{(r)}$ are the phase averages of the deformation gradient field in the LCC. For two-phase composites, $\bar{\mathbf{F}}^{(1)}$ and $\bar{\mathbf{F}}^{(2)}$ are determined by means of the system of equations (Ponte Castañeda and Tiberio, 2000)

$$\bar{\mathbf{F}} = c_0^{(1)} \bar{\mathbf{F}}^{(1)} + c_0^{(2)} \bar{\mathbf{F}}^{(2)}, \quad (1.17)$$

$$\bar{\mathbf{F}}^{(2)} = \bar{\mathbf{F}} - \frac{1}{c_0^{(2)}} (\Delta \mathbf{L})^{-1} (\tilde{\mathbf{L}} - \bar{\mathbf{L}}) (\Delta \mathbf{L})^{-1} \left[\Delta \mathbf{S} + \mathbf{L}^{(1)} (\bar{\mathbf{F}} - \bar{\mathbf{F}}^{(1)}) - \mathbf{L}^{(2)} (\bar{\mathbf{F}} - \bar{\mathbf{F}}^{(2)}) \right], \quad (1.18)$$

where $\Delta \mathbf{S} = \mathbf{S}^{(1)}(\bar{\mathbf{F}}^{(1)}) - \mathbf{S}^{(2)}(\bar{\mathbf{F}}^{(2)})$, and the first equation describes as the overall average deformation condition. After some algebra, Eq. (1.18) can alternatively be written in the form

$$\bar{\mathbf{F}} - \bar{\mathbf{F}}^{(2)} = \left[c_0^{(2)} (\tilde{\mathbf{L}} - \mathbf{L}^{(1)})^{-1} + (\Delta \mathbf{L})^{-1} \right] \left[\mathbf{L}^{(1)} (\bar{\mathbf{F}}^{(1)} - \bar{\mathbf{F}}^{(2)}) - \Delta \mathbf{S} \right]. \quad (1.19)$$

In this work, we make use of the generalized estimate of the Willis type (Ponte Castañeda and Willis, 1995; Willis, 1977) for the effective modulus tensor $\tilde{\mathbf{L}}$ of the LCC. This type of estimate is known to be quite accurate for the type of “particulate” random microstructures, up to moderate concentrations of inclusions. For two-phase composites, this estimate is given by

$$\tilde{\mathbf{L}} = \mathbf{L}^{(1)} + c_0^{(2)} \left[c_0^{(1)} \mathbf{P} - (\Delta \mathbf{L})^{-1} \right]^{-1} \quad (1.20)$$

where the microstructural tensor \mathbf{P} contains information about the shape and distribution of the particles in the undeformed configuration (Ponte Castañeda and Willis, 1995). The general expression for the components of the tensor \mathbf{P} associated with an ellipsoidal inclusion, defined by

$$D_0 = \{ \mathbf{X} : \mathbf{X}^T (\mathbf{Z}_0^T \mathbf{Z}_0) \mathbf{X} < 1 \}, \quad (1.21)$$

in an infinite matrix with the elastic modulus tensor $\mathbf{L}^{(1)}$, is given by

$$P_{ijkl} = \frac{1}{4\pi |\mathbf{Z}_0|} \int_{|\xi|=1} H_{ijkl}(\xi) [\xi^T (\mathbf{Z}_0^T \mathbf{Z}_0)^{-1} \xi]^{\frac{-3}{2}} dS, \quad (1.22)$$

where the symmetric, second-order tensor \mathbf{Z}_0 serves to characterize the shape and orientation of the inclusion. In addition, \mathbf{H} is a fourth-order tensor with components $B_{ik}(\xi) \xi_j \xi_l$, and \mathbf{B} denotes the inverse of the acoustic tensor \mathbf{K} with components

$$K_{ik} = L_{ijkl}^{(1)}(\xi) \xi_j \xi_l. \quad (1.23)$$

Making use of the Willis estimate (1.20), the *implicit* tensorial equation (1.19) for the variable $\bar{\mathbf{F}}^{(2)}$ may be re-written as

$$\bar{\mathbf{F}} - \bar{\mathbf{F}}^{(2)} = (1 - c_0^{(2)}) \mathbf{P} [\mathbf{L}^{(1)}(\bar{\mathbf{F}}^{(1)} - \bar{\mathbf{F}}^{(2)}) - \Delta \mathbf{S}]. \quad (1.24)$$

In summary, the variational estimate (1.16) for two-phase composites depends explicitly only on the variables $\bar{\mathbf{F}}^{(1)}$ and $\bar{\mathbf{F}}^{(2)}$ corresponding to the average values of the deformation gradient over the phases of the chosen LCC with the strain energies defined in (1.8). Hence, the implementation of this estimate, in general, requires the calculation of the 18 unknown components of $\bar{\mathbf{F}}^{(1)}$ and $\bar{\mathbf{F}}^{(2)}$ using the relations (1.24) and (1.17), which constitute a system of 18 scalar, algebraic equations. Having computed these components for given macroscopic loading, phases characteristics and microstructure, the second-order estimate for the effective stored-energy function $\widehat{W}(\bar{\mathbf{F}})$ for particle-reinforced elastomers can be, in turn, obtained from (1.16).

1.4 Rigidly Reinforced Composites

1.4.1 Tangent Second-Order Estimates

In this section, we confine our attention to the special case of rigid particles, and our objective is to obtain a simplified form for the effective stored-energy function (1.16) and the associated kinematical equation (1.19) in this case. In order to characterize the constitutive response of the rigid particles, we assume without loss of generality that the stored-energy function of the particle phase is given by

$$W^{(2)}(\mathbf{F}) = \frac{1}{2} \mu^{(2)} [\text{tr}(\mathbf{F}^T \mathbf{F}) - 3 - 2 \ln(\det \mathbf{F})] + \frac{1}{2} \mu'^{(2)} (\det \mathbf{F} - 1)^2, \quad (1.25)$$

such that the rigid behavior of the particles is obtained by taking the limit as the Lamé moduli $\mu^{(2)}$ and $\mu'^{(2)}$ tend to infinity. It should be remarked that the stored-energy function (1.25) is zero if and only if $\mathbf{F} = \mathbf{R}$, where \mathbf{R} stands for a rotation tensor. This indicates that the particles can only undergo a rigid-body rotation in the limit $\mu^{(2)}, \mu'^{(2)} \rightarrow \infty$.

Introducing the small parameter ι , defined by

$$\iota = 1/\mu^{(2)} = \alpha/\mu'^{(2)}, \quad (1.26)$$

in which α is an arbitrary constant, we consider the following regular expansion for $\bar{\mathbf{F}}^{(2)}$ as ι tends

to zero

$$\bar{\mathbf{F}}^{(2)} = \bar{\mathbf{F}}_0^{(2)} + \iota \bar{\mathbf{F}}_1^{(2)} + O(\iota^2). \quad (1.27)$$

The corresponding asymptotic expansions for $(\bar{\mathbf{F}}^{(2)})^{-1}$ and $\bar{J}^{(2)} = \det \bar{\mathbf{F}}^{(2)}$ are given by

$$(\bar{\mathbf{F}}^{(2)})^{-1} = [\bar{\mathbf{F}}_0^{(2)} + \iota \bar{\mathbf{F}}_1^{(2)} + O(\iota^2)]^{-1} = (\bar{\mathbf{F}}_0^{(2)})^{-1} - \iota (\bar{\mathbf{F}}_0^{(2)})^{-1} \bar{\mathbf{F}}_1^{(2)} (\bar{\mathbf{F}}_0^{(2)})^{-1} + O(\iota^2), \quad (1.28)$$

$$\bar{J}^{(2)} = \bar{J}_0^{(2)} + \iota \bar{J}_1^{(2)} + O(\iota^2), \quad (1.29)$$

where

$$\bar{J}_0^{(2)} = \det \bar{\mathbf{F}}_0^{(2)}, \quad (1.30)$$

$$\bar{J}_1^{(2)} = \text{tr} \left[\left(\bar{\mathbf{F}}_0^{(2)} \right)^* \bar{\mathbf{F}}_1^{(2)} \right], \quad (1.31)$$

in which the superscript $*$ refers to the adjugate tensor.

Next, using the strain energy (1.25), along with the expansions (1.27)-(1.29), the nominal stress expansion in phase 2 is written as

$$\mathbf{S}^{(2)}(\bar{\mathbf{F}}^{(2)}) = \iota^{-1} \mathbf{S}_{-1}^{(2)} + \mathbf{S}_0^{(2)} + O(\iota), \quad (1.32)$$

where

$$\mathbf{S}_{-1}^{(2)} = \bar{\mathbf{F}}_0^{(2)} - (\bar{\mathbf{F}}_0^{(2)})^{-T} + \alpha \bar{J}_0^{(2)} (\bar{J}_0^{(2)} - 1) (\bar{\mathbf{F}}_0^{(2)})^{-T}, \quad (1.33)$$

and

$$\mathbf{S}_0^{(2)} = \bar{\mathbf{F}}_1^{(2)} + [1 - \alpha \bar{J}_0^{(2)} (\bar{J}_0^{(2)} - 1)] (\bar{\mathbf{F}}_0^{(2)})^{-T} (\bar{\mathbf{F}}_1^{(2)})^T (\bar{\mathbf{F}}_0^{(2)})^{-T} + \alpha \bar{J}_1^{(2)} (2\bar{J}_0^{(2)} - 1) (\bar{\mathbf{F}}_0^{(2)})^{-T}. \quad (1.34)$$

Moreover, the average rotational balance equation in phase 2 (which is a consequence of the objectivity of the chosen strain energy)

$$(\bar{\mathbf{F}}^{(2)})^T \mathbf{S}^{(2)} = (\mathbf{S}^{(2)})^T \bar{\mathbf{F}}^{(2)}, \quad (1.35)$$

reduces to

$$[(\bar{\mathbf{F}}_0^{(2)})^T - (\bar{\mathbf{F}}_0^{(2)})^{-1}] \bar{\mathbf{F}}_1^{(2)} + (\bar{\mathbf{F}}_1^{(2)})^T [(\bar{\mathbf{F}}_0^{(2)})^{-T} - \bar{\mathbf{F}}_0^{(2)}] + O(\iota) = \mathbf{0}, \quad (1.36)$$

by means of Eqs. (1.27) and (1.32)-(1.34).

In addition, making use of the overall average deformation condition (1.17), it follows that the average deformation gradient in the matrix is given by

$$\bar{\mathbf{F}}^{(1)} = \bar{\mathbf{F}}_0^{(1)} + O(\iota) \quad (1.37)$$

where $\bar{\mathbf{F}}_0^{(1)} = (1 - c_0^{(2)})^{-1} (\bar{\mathbf{F}} - c_0^{(2)} \bar{\mathbf{F}}_0^{(2)})$. (Note that higher-order contributions will not be needed, and will therefore not be detailed here.)

Noting the asymptotic expansion $W^{(2)}(\bar{\mathbf{F}}^{(2)}) = W^{(2)}(\bar{\mathbf{F}}_0^{(2)}) + O(\iota)$ for the stored-energy function of particles, and making use of relations (1.27), (1.32) and (1.37), the second-order estimate (1.16) for the rigidly reinforced elastomers can be shown to reduce to

$$\begin{aligned}\widehat{W}(\bar{\mathbf{F}}) &= \frac{1}{2}\iota^{-1}c_0^{(2)}(\bar{\mathbf{F}} - \bar{\mathbf{F}}_0^{(2)}) \cdot \mathbf{S}_{-1}^{(2)} \\ &\quad + (1 - c_0^{(2)})W^{(1)}(\bar{\mathbf{F}}_0^{(1)}) + c_0^{(2)}W^{(2)}(\bar{\mathbf{F}}_0^{(2)}) \\ &\quad + \frac{1}{2}c_0^{(2)}(\bar{\mathbf{F}} - \bar{\mathbf{F}}_0^{(2)}) \cdot \left[\mathbf{S}_0^{(2)} - \mathbf{S}^{(1)}(\bar{\mathbf{F}}_0^{(1)}) - \bar{\mathbf{F}}_1^{(2)} \cdot \mathbf{S}_{-1}^{(2)} \right] + O(\iota).\end{aligned}\quad (1.38)$$

Remembering that the computation of $\bar{\mathbf{F}}_0^{(1)}$ and $\mathbf{S}_{-1}^{(2)}$ requires the evaluation of the tensor $\bar{\mathbf{F}}_0^{(2)}$, and that the variable $\bar{\mathbf{F}}_1^{(2)}$ can be eliminated in favor of $\mathbf{S}_0^{(2)}$ by means of Eq. (1.34), the calculation of the above expression requires the determination of the variables $\bar{\mathbf{F}}_0^{(2)}$ and $\mathbf{S}_0^{(2)}$. To this end, we consider next the expansion of equation (1.19) to obtain a tensorial equation for the deformation gradient $\bar{\mathbf{F}}_0^{(2)}$.

Thus, setting $\mathbf{L}^{(2)}$ equal to the tangent modulus tensor (Ponte Castañeda and Tiberio, 2000) of the particle phase, $\mathbf{L}^{(2)} = \mathbf{L}_t^{(2)}(\bar{\mathbf{F}}^{(2)}) = \partial^2 W^{(2)}/\partial \mathbf{F} \partial \mathbf{F}(\bar{\mathbf{F}}^{(2)})$, it follows from the definition of the strain energy (1.25) that $\mathbf{L}^{(2)}$ can be expanded as

$$\mathbf{L}^{(2)} = \iota^{-1}\mathbf{L}_{-1}^{(2)} + O(\iota^0), \quad (1.39)$$

where

$$\mathbf{L}_{-1}^{(2)} = \left\{ (\mathcal{I} - \mathcal{X}) + \alpha [J(2J-1)\mathbf{F}^{-T} \otimes \mathbf{F}^{-T} + J(J-1)\mathcal{X}] \right\} \Big|_{\mathbf{F}=\bar{\mathbf{F}}_0^{(2)}}. \quad (1.40)$$

In this last expression, \mathcal{I} is the fourth-order identity tensor with components $\mathcal{I}_{ijkl} = \delta_{ik}\delta_{jl}$ and the components of the fourth-order tensor \mathcal{X} read as

$$\mathcal{X}_{ijkl} = -F_{li}^{-1}F_{jk}^{-1}. \quad (1.41)$$

Next, assuming that $\mathbf{L}^{(1)}$ is of order one and making use of the expression (1.39), $\Delta \mathbf{L} = \mathbf{L}^{(1)} - \mathbf{L}^{(2)}$ can be expanded as $(\Delta \mathbf{L})^{-1} = -\iota(\mathbf{L}_{-1}^{(2)})^{-1} + O(\iota^2)$. Substituting this expansion, along with relations (1.27), (1.32) and (1.37), into (1.19), it reduces after some algebra to

$$c_0^{(2)}\mathbf{S}_{-1}^{(2)}\iota^{-1} + \mathbf{T}(\bar{\mathbf{F}} - \bar{\mathbf{F}}_0^{(2)}) + c_0^{(2)}[\mathbf{S}^{(1)}(\bar{\mathbf{F}}_0^{(1)}) - \mathbf{S}_0^{(2)}] - (\tilde{\mathbf{L}}_0 - \mathbf{L}^{(1)})(\mathbf{L}_{-1}^{(2)})^{-1}\mathbf{S}_{-1}^{(2)} + O(\iota) = \mathbf{0}, \quad (1.42)$$

where we have used the notations

$$\mathbf{T} = \tilde{\mathbf{L}}_0 - (1 - c_0^{(2)})^{-1}\mathbf{L}^{(1)}, \quad (1.43)$$

and $\tilde{\mathbf{L}}_0 = \tilde{\mathbf{L}} \Big|_{\mathbf{L}^{(2)} \rightarrow \infty}$. Thus, expression (1.42) gives rise to the following system of equations

$$\mathbf{S}_{-1}^{(2)} = \bar{\mathbf{F}}_0^{(2)} - (\bar{\mathbf{F}}_0^{(2)})^{-T} + \alpha \bar{J}_0^{(2)}(\bar{J}_0^{(2)} - 1)(\bar{\mathbf{F}}_0^{(2)})^{-T} = \mathbf{0}, \quad (1.44)$$

$$\mathbf{T}(\bar{\mathbf{F}} - \bar{\mathbf{F}}_0^{(2)}) + c_0^{(2)}[\mathbf{S}^{(1)}(\bar{\mathbf{F}}_0^{(1)}) - \mathbf{S}_0^{(2)}] = \mathbf{0}. \quad (1.45)$$

Noting that equation (1.44) should be satisfied for an arbitrary constant α , it is deduced that the following equations must be satisfied

$$\bar{\mathbf{F}}_0^{(2)} - (\bar{\mathbf{F}}_0^{(2)})^{-T} = \mathbf{0}, \quad \text{and} \quad \bar{J}_0^{(2)}(\bar{J}_0^{(2)} - 1)(\bar{\mathbf{F}}_0^{(2)})^{-T} = \mathbf{0}. \quad (1.46)$$

The first equation implies that $\bar{\mathbf{F}}_0^{(2)}$ is an orthogonal matrix denoted by

$$\bar{\mathbf{F}}_0^{(2)} = \bar{\mathbf{R}}^{(2)}, \quad (1.47)$$

while, recalling the definition $\bar{J}_0^{(2)} = \det \bar{\mathbf{F}}_0^{(2)}$, it can be seen that the second equation is identically satisfied as well. This result implies that the reinforcement undergoes an average rigid rotation $\bar{\mathbf{R}}^{(2)}$, as expected on physical grounds. This result is also consistent with the expectation that the stress $\mathbf{S}^{(2)}$ given in (1.32) should remain bounded in the extreme case of rigid particles. In this connection, it is interesting to note that the average balance equation (1.36) is automatically satisfied due to the orthogonality result (1.47).

In turn, in the limit of rigid particles ($\iota \rightarrow 0$), the average deformation gradient in the matrix phase can be written as

$$\bar{\mathbf{F}}^{(1)} = \bar{\mathbf{F}}_0^{(1)} = \frac{1}{1-c}(\bar{\mathbf{F}} - c\bar{\mathbf{R}}^{(2)}), \quad (1.48)$$

where $c = c_0^{(2)}$. Accordingly, the equation (1.45) reduces to

$$\mathbf{T}(\bar{\mathbf{F}} - \bar{\mathbf{R}}^{(2)}) + c[\mathbf{S}^{(1)}(\bar{\mathbf{F}}^{(1)}) - \mathbf{S}_0^{(2)}] = \mathbf{0}, \quad (1.49)$$

which can be solved for $\mathbf{S}_0^{(2)}$ to obtain the result that

$$\mathbf{S}_0^{(2)} = c^{-1}\mathbf{T}(\bar{\mathbf{F}} - \bar{\mathbf{R}}^{(2)}) + \mathbf{S}^{(1)}(\bar{\mathbf{F}}^{(1)}). \quad (1.50)$$

Making use of the above relation together with Eqs. (1.44), (1.47) and (1.50), the second-order estimate (1.38) can now be shown to reduce to

$$\widehat{W}(\bar{\mathbf{F}}) = (1-c)W^{(1)}(\bar{\mathbf{F}}^{(1)}) + \frac{1}{2}(\bar{\mathbf{F}} - \bar{\mathbf{R}}^{(2)}) \cdot \mathbf{T}(\bar{\mathbf{F}} - \bar{\mathbf{R}}^{(2)}). \quad (1.51)$$

In order to obtain the associated equation for the average rotation tensor $\bar{\mathbf{R}}^{(2)}$ of the rigid particles, we make use of (1.47) in (1.34) to find the following expression for $\mathbf{S}_0^{(2)}$

$$\mathbf{S}_0^{(2)} = \bar{\mathbf{F}}_1^{(2)} + \bar{\mathbf{R}}^{(2)}(\bar{\mathbf{F}}_1^{(2)})^T \bar{\mathbf{R}}^{(2)} + \bar{J}_1^{(2)} \bar{\mathbf{R}}^{(2)}. \quad (1.52)$$

Substituting this expression in Eq. (1.49) and then multiplying it by $(\bar{\mathbf{R}}^{(2)})^T$ from left-hand side, we arrive at the following equation

$$(\bar{\mathbf{R}}^{(2)})^T \left[\mathbf{T}(\bar{\mathbf{F}} - \bar{\mathbf{R}}^{(2)}) \right] + c(\bar{\mathbf{R}}^{(2)})^T \mathbf{S}^{(1)}(\bar{\mathbf{F}}^{(1)}) = 2c \left\{ (\bar{\mathbf{R}}^{(2)})^T \bar{\mathbf{F}}_1^{(2)} \right\}_{Sym} + \bar{J}_1^{(2)} \mathbf{I}, \quad (1.53)$$

where the subscript *Sym* stands for the symmetric part of the relevant tensor. (We also define the

skew-symmetric part $\{\mathbf{A}\}_{Skew}$ of a second-order tensor \mathbf{A} via the relation $\mathbf{A} = \{\mathbf{A}\}_{Sym} + \{\mathbf{A}\}_{Skew}$. Thus, by taking the skew-symmetric part of both sides of expression ((1.53)), the tensorial equation for the three (generally) independent components of $\bar{\mathbf{R}}^{(2)}$ is easily obtained with the result that

$$\left\{ (\bar{\mathbf{R}}^{(2)})^T \left[\mathbf{T} (\bar{\mathbf{F}} - \bar{\mathbf{R}}^{(2)}) \right] + c (\bar{\mathbf{R}}^{(2)})^T \mathbf{S}^{(1)}(\bar{\mathbf{F}}^{(1)}) \right\}_{Skew} = \mathbf{0}. \quad (1.54)$$

The resulting estimates (1.51) and (1.54) for the rigid-reinforced elastomers can be specialized for “particulate” microstructures (Ponte Castañeda and Willis, 1995; Willis, 1977). To this end, we make use of the following Willis-type estimate for the effective modulus tensor

$$\tilde{\mathbf{L}} = \mathbf{L}^{(1)} + \frac{c}{1-c} \mathbf{P}^{-1}, \quad (1.55)$$

where the subscript 0 has been dropped from $\tilde{\mathbf{L}}_0$ for convenience. Thus, substituting this estimate for the LCC, it follows that the second-order estimate (1.51) specializes to

$$\widehat{W}(\bar{\mathbf{F}}) = (1-c) W^{(1)}(\bar{\mathbf{F}}^{(1)}) + \frac{1}{2} \frac{c}{1-c} (\bar{\mathbf{F}} - \bar{\mathbf{R}}^{(2)}) \cdot \mathbf{E} (\bar{\mathbf{F}} - \bar{\mathbf{R}}^{(2)}), \quad (1.56)$$

where

$$\mathbf{E} = \mathbf{P}^{-1} - \mathbf{L}^{(1)}. \quad (1.57)$$

Accordingly, the associated kinematical equation (1.54) for $\bar{\mathbf{R}}^{(2)}$ can be written as

$$\left\{ (\bar{\mathbf{R}}^{(2)})^T [\mathbf{E} (\bar{\mathbf{F}} - \bar{\mathbf{R}}^{(2)})] + (1-c) (\bar{\mathbf{R}}^{(2)})^T \mathbf{S}^{(1)}(\bar{\mathbf{F}}^{(1)}) \right\}_{Skew} = \mathbf{0}. \quad (1.58)$$

Having computed the tensor $\bar{\mathbf{R}}^{(2)}$ from (1.58), the second-order estimate can be calculated via (1.56).

The second-order estimate (1.56) is completely specified, except for the choice of $\mathbf{L}^{(1)}$ in the LCC. Consistent with (1.10), in the earlier version of the TSO method (Ponte Castañeda and Tiberio, 2000), $\mathbf{L}^{(1)}$ was chosen to be equal to the tangent modulus tensor of the matrix phase, evaluated at the matrix average of the deformation $\bar{\mathbf{F}}^{(1)}$, i.e., $\mathbf{L}^{(1)} = \mathbf{L}_t^{(1)}(\bar{\mathbf{F}}^{(1)})$. In this work, the prescription

$$\mathbf{L}^{(1)} = \mathbf{L}_t^{(1)}(\bar{\mathbf{F}}) = \frac{\partial^2 W^{(1)}}{\partial \mathbf{F} \partial \mathbf{F}}(\bar{\mathbf{F}}) \quad (1.59)$$

will be adopted instead. This choice is motivated by the considerable simplification in the computation of $\tilde{\mathbf{L}}$, which is an essential element in the effective energy (1.51) (through \mathbf{T}). Indeed, the computation of $\mathbf{L}^{(1)}$ by means of the prescription (1.59) is completely explicit, and does not require the calculation of the tensor $\bar{\mathbf{R}}^{(2)}$, unlike the case for the earlier prescription. On the other hand, the resulting estimates can still be shown to be exact to second-order heterogeneity contrast (for non-rigid particles).

1.4.2 Energy Decomposition Approximation

The second-order method developed in the previous section can be applied to general compressible hyperelastic composites. For the special case of the composites made up of incompressible phases,

the overall (exact) incompressibility constraint ($\bar{J} = \det(\bar{\mathbf{F}}) = 1$) must be satisfied. However, it can be verified that by taking the incompressibility limit of the effective energy function (1.51), the constraint $\bar{J} = 1$ is, in general, not satisfied. The failure to meet this constraint in the incompressibility limit, which is unacceptable, was already discussed in some detail by Ponte Castañeda and Tiberio (2000). In particular, for the special case of 2-D circular inclusions, they investigated the effect of the inclusion volume fraction on the deviation of the “approximate” macroscopic incompressibility constraint from the exact constraint $\bar{J} = 1$. The aim of this subsection is to propose a modification of method described in the last section to be able to ensure exact attainment of the exact constraint $\bar{J} = 1$ in the incompressibility limit for the composites. As mentioned before, in the earlier TSO method, the reference modulus tensor $\mathbf{L}^{(1)}$ in the LCC was set to be equal to $\mathbf{L}_t^{(1)}$. In this work, as described in the previous section, we will make use instead of the prescription (1.59) for $\mathbf{L}^{(1)}$. Indeed, making use of this prescription, it can be shown that the second term in the RHS of the estimate (1.51) is consistent with the constraint $\bar{J} = 1$ in the incompressibility limit. However, the first term in the estimate is still inconsistent with the exact incompressibility constraint. To address this issue, we propose to split up the energy functions of the constituent phases into “dilatational” and “distortional” parts, and homogenize them, separately. In this way, the dilatational contribution to the effective energy function can be obtained *exactly*, while the distortional contribution may still be computed approximately using the tangent second-order procedure, presented in Section 1.3. Despite the fact that the splitting of the energy functional in general entails an approximation in the calculation of the effective stored-energy function, satisfaction of the *exact incompressibility constraint* can be ensured. With this objective in mind and without loss of generality, it proves helpful to introduce the following form for the strain-energy function of the constituent phases, namely,

$$W^{(r)}(\mathbf{F}) = W_\mu^{(r)}(\mathbf{F}) + \frac{1}{2}\mu'^{(r)}(J - 1)^2, \quad (1.60)$$

where the parameter $\mu'^{(r)}$ denotes the Lamé modulus of the phases in the infinitesimal strain regime, which in order to recover incompressible behavior ($J \rightarrow 1$), will be taken to tend to infinity. Also, $W_\mu^{(r)}$ is that part of the stored-energy function $W^{(r)}$ not depending on $\mu'^{(r)}$. The effective stored-energy function of the nonlinear composite, defined by Eq. (1.3), may then be approximated as

$$\widehat{W}(\bar{\mathbf{F}}) \approx \widehat{W}_\mu(\bar{\mathbf{F}}) + \widehat{W}_{\mu'}(\bar{\mathbf{F}}), \quad (1.61)$$

where

$$\widehat{W}_\mu(\bar{\mathbf{F}}) = \underset{\mathbf{F} \in K(\bar{\mathbf{F}})}{\text{stat}} \sum_{r=1}^N c^{(r)} \langle W_\mu^{(r)}(\mathbf{F}) \rangle^{(r)}, \quad (1.62)$$

and

$$\widehat{W}_{\mu'}(\bar{\mathbf{F}}) = \frac{1}{2} \left(\underset{\mathbf{F} \in K(\bar{\mathbf{F}})}{\text{stat}} \sum_{r=1}^N c^{(r)} \mu'^{(r)} \langle (J - 1)^2 \rangle^{(r)} \right). \quad (1.63)$$

Making use of results from Ponte Castañeda (1989) for “elastic fluid” composites, the expression

for $\widehat{W}_{\mu'}$ can be evaluated exactly as

$$\widehat{W}_{\mu'}(\bar{\mathbf{F}}) = \frac{1}{2} \tilde{\mu}'_R (\bar{J} - 1)^2, \quad (1.64)$$

where

$$\tilde{\mu}'_R = \left[\sum_{r=1}^N c^{(r)} \left(\mu'^{(r)} \right)^{-1} \right]^{-1} \quad (1.65)$$

is the effective dilatational modulus in the ground state of the composite.

Now, by restricting attention to the two-phase rigidly reinforced composite, we apply the second-order procedure, developed in the prior subsection, to the distortional part of energy in (1.61). Thus, making use of the estimate (1.51) for $\widehat{W}_{\mu}(\bar{\mathbf{F}})$, it follows that

$$\widehat{W}_{\mu}(\bar{\mathbf{F}}) = (1 - c) W_{\mu}^{(1)}(\bar{\mathbf{F}}^{(1)}) + \frac{1}{2} (\bar{\mathbf{F}} - \bar{\mathbf{R}}^{(2)}) \cdot \mathbf{T} (\bar{\mathbf{F}} - \bar{\mathbf{R}}^{(2)}). \quad (1.66)$$

where, by means of (1.54), the kinematical equation for $\bar{\mathbf{R}}^{(2)}$, associated with (1.62), can be written as

$$\left\{ (\bar{\mathbf{R}}^{(2)})^T \left[\mathbf{T} (\bar{\mathbf{F}} - \bar{\mathbf{R}}^{(2)}) \right] + c (\bar{\mathbf{R}}^{(2)})^T \mathbf{S}_{\mu}^{(1)}(\bar{\mathbf{F}}^{(1)}) \right\}_{Skew} = \mathbf{0}, \quad (1.67)$$

where $\mathbf{S}_{\mu}^{(1)}(\mathbf{F}) = \partial W_{\mu}^{(1)}(\mathbf{F}) / \partial \mathbf{F}$. Moreover, we need an appropriate prescription for the modulus tensor $\mathbf{L}^{(1)}$ in the expression $\mathbf{T} = \tilde{\mathbf{L}} - (1 - c)^{-1} \mathbf{L}^{(1)}$ used in the estimates (1.66) and (1.67). Motivated by the choice (1.59), here we will use the prescription

$$\mathbf{L}^{(1)} = \left. \frac{\partial^2 W_{\mu}^{(1)}}{\partial \mathbf{F} \partial \mathbf{F}} \right|_{\mathbf{F}=\bar{\mathbf{F}}} + \frac{1}{2} \mu'^{(1)} \left. \frac{\partial^2 [(J - 1)^2]}{\partial \mathbf{F} \partial \mathbf{F}} \right|_{\mathbf{F}=\bar{\mathbf{F}}}. \quad (1.68)$$

Note that the second term (depending on $\mu'^{(1)}$) is needed to be able to enforce the incompressibility constraint in the LCC.

Next, specializing to rigid behavior for the inclusions in the “dilatational” part of the effective stored-energy function of the two-phase composite, we have that $\tilde{\mu}'_R = (1 - c)^{-1} \mu'^{(1)}$, and accordingly, the following estimate is obtained for $\widehat{W}_{\mu'}(\bar{\mathbf{F}})$

$$\widehat{W}_{\mu'}(\bar{\mathbf{F}}) = \frac{1}{2(1 - c)} \mu'^{(1)} (\bar{J} - 1)^2. \quad (1.69)$$

Finally, making use of expressions (1.66) and (1.69) for the two-phase, rigidly reinforced elastomers, the second-order estimate (1.61) reduces to

$$\widehat{W}(\bar{\mathbf{F}}) = (1 - c) W_{\mu}^{(1)}(\bar{\mathbf{F}}^{(1)}) + \frac{1}{2} (\bar{\mathbf{F}} - \bar{\mathbf{R}}^{(2)}) \cdot \mathbf{T} (\bar{\mathbf{F}} - \bar{\mathbf{R}}^{(2)}) + \frac{1}{2(1 - c)} \mu'^{(1)} (\bar{J} - 1)^2. \quad (1.70)$$

Note that the approximate equality has been replaced here by a standard equality, and that the particle rotation $\bar{\mathbf{R}}^{(2)}$ is still given by (1.67). Naturally, the expression (1.70) for the effective stored-energy function of the reinforced elastomer can be used, in particular, together with the

Willis estimate (1.55) for the LCC, to obtain the result

$$\widehat{W}(\bar{\mathbf{F}}) = (1 - c) W_\mu^{(1)}(\bar{\mathbf{F}}^{(1)}) + \frac{1}{2} \frac{c}{1 - c} (\bar{\mathbf{F}} - \bar{\mathbf{R}}^{(2)}) \cdot \mathbf{E} (\bar{\mathbf{F}} - \bar{\mathbf{R}}^{(2)}) + \frac{1}{2(1 - c)} \mu^{(1)} (\bar{J} - 1)^2, \quad (1.71)$$

where

$$\left\{ (\bar{\mathbf{R}}^{(2)})^T [\mathbf{E} (\bar{\mathbf{F}} - \bar{\mathbf{R}}^{(2)})] + (1 - c) (\bar{\mathbf{R}}^{(2)})^T \mathbf{S}_\mu^{(1)}(\bar{\mathbf{F}}^{(1)}) \right\}_{Skew} = \mathbf{0}, \quad (1.72)$$

and \mathbf{E} is given by expression (1.57).

At this point, it is expedient to make the following remarks concerning some features of the estimates (1.71) and (1.72) for rigidly reinforced elastomers:

1. As was also the case for the earlier tangent second-order estimate in Ponte Castañeda and Tiberio (2000), the new estimate (1.71) may blow up at some finite values of $\bar{\mathbf{F}}$. Depending on the inclusion volume fraction and initial configuration of the microstructure, the quantity $\bar{J}^{(1)} = \det(\bar{\mathbf{F}}^{(1)})$ can become zero at finite values of the deformation (see relation (1.48)), causing certain terms in the expression $W_\mu^{(1)}(\bar{\mathbf{F}}^{(1)})$ for the estimate (1.71) to blow up. As discussed by Ponte Castañeda and Tiberio (2000), this phenomenon can be interpreted as *lock up* for the composite, which is due to the fact that sufficiently large deformations would be expected to bring the rigid inclusions into contact with each other leading to strong stiffening of the composite.
2. In the limit of infinitesimal strains ($\bar{\mathbf{F}} \rightarrow \mathbf{I}$), the estimate (1.71) recovers the corresponding linear-elastic Willis estimate (Willis, 1977; Ponte Castañeda and Willis, 1995). The resulting energy can be written as $\widehat{W}(\bar{\mathbf{F}}) = 1/2 \bar{\boldsymbol{\varepsilon}} \cdot \tilde{\mathbf{L}}_L \cdot \bar{\boldsymbol{\varepsilon}}$, where $\bar{\boldsymbol{\varepsilon}}$ denotes the macroscopic infinitesimal strain tensor and $\tilde{\mathbf{L}}_L$ is the effective moduli tensor in the context of linear elasticity. Also, in this limit, the solution of equation (1.72) agrees exactly with the corresponding prediction for the infinitesimal rotation of the particles (Kailasam and Ponte Castañeda, 1998), as given by

$$\bar{\mathbf{R}}_L^{(2)} = \mathbf{I} + \bar{\boldsymbol{\omega}} - \mathbf{R}_L \mathbf{P}_L^{-1} \bar{\boldsymbol{\varepsilon}}, \quad (1.73)$$

where $\bar{\boldsymbol{\omega}}$ stands for the macroscopic infinitesimal rotation tensor, and \mathbf{R}_L and \mathbf{P}_L are the well-known Eshelby tensors in the context of small strains and rotations (see Eqs. (15) and (19) in Kailasam and Ponte Castañeda (1998)).

Incompressible Matrix

The estimate (1.70), together with (1.67), and relation (1.68) for $\mathbf{L}^{(1)}$ (used in expression (1.43) for \mathbf{T}) holds for composites with a *compressible* matrix phase characterized by the stored-energy function (1.60). However, in the limit of *incompressible* behavior for the matrix, i.e., when $\mu^{(1)} \rightarrow \infty$, the estimate (1.70) (unlike the earlier estimate (1.51)) is found to be consistent with the exact overall

incompressibility constraint ($\bar{J} = 1$), and reduces to

$$\widehat{W}(\bar{\mathbf{F}}) = (1 - c) W_\mu^{(1)}(\bar{\mathbf{F}}^{(1)}) + \frac{1}{2} (\bar{\mathbf{F}} - \bar{\mathbf{R}}^{(2)}) \cdot \mathbf{T}^I (\bar{\mathbf{F}} - \bar{\mathbf{R}}^{(2)}), \quad (1.74)$$

where

$$\mathbf{T}^I = \lim_{\mu^{(1)} \rightarrow \infty} \left[\bar{\mathbf{L}} - (1 - c)^{-1} \mathbf{L}^{(1)} \right], \quad (1.75)$$

while the equation for $\bar{\mathbf{R}}^{(2)}$ reduces to

$$\left\{ (\bar{\mathbf{R}}^{(2)})^T [\mathbf{T}^I (\bar{\mathbf{F}} - \bar{\mathbf{R}}^{(2)})] + c (\bar{\mathbf{R}}^{(2)})^T \mathbf{S}_\mu^{(1)}(\bar{\mathbf{F}}^{(1)}) \right\}_{Skew} = \mathbf{0}. \quad (1.76)$$

For the special case of the Willis estimate for $\bar{\mathbf{L}}$, the expression (1.74) further simplifies to

$$\widehat{W}(\bar{\mathbf{F}}) = (1 - c) W_\mu^{(1)}(\bar{\mathbf{F}}^{(1)}) + \frac{1}{2} \frac{c}{1 - c} (\bar{\mathbf{F}} - \bar{\mathbf{R}}^{(2)}) \cdot \mathbf{E}^I (\bar{\mathbf{F}} - \bar{\mathbf{R}}^{(2)}), \quad (1.77)$$

where

$$\mathbf{E}^I = \lim_{\mu^{(1)} \rightarrow \infty} (\mathbf{P}^{-1} - \mathbf{L}^{(1)}), \quad (1.78)$$

while the corresponding equation for the rotation $\bar{\mathbf{R}}^{(2)}$ reduces to

$$\left\{ (\bar{\mathbf{R}}^{(2)})^T [\mathbf{E}^I (\bar{\mathbf{F}} - \bar{\mathbf{R}}^{(2)})] + (1 - c) (\bar{\mathbf{R}}^{(2)})^T \mathbf{S}_\mu^{(1)}(\bar{\mathbf{F}}^{(1)}) \right\}_{Skew} = \mathbf{0}. \quad (1.79)$$

For completeness, we note that the macroscopic stress tensor $\bar{\mathbf{S}}(\bar{\mathbf{F}}) = \partial \widehat{W}(\bar{\mathbf{F}}) / \partial \bar{\mathbf{F}}$ associated with the effective stored-energy function (1.77) may be written as

$$\begin{aligned} \bar{\mathbf{S}}(\bar{\mathbf{F}}) &= \mathbf{S}_\mu^{(1)}(\bar{\mathbf{F}}^{(1)}) (\mathcal{I} - c \bar{\mathbf{g}}^{(2)}) + \dots \\ &+ \frac{c}{1 - c} \left\{ [\mathbf{E}^I (\bar{\mathbf{F}} - \bar{\mathbf{R}}^{(2)})] \bar{\mathbf{G}}^{(2)} + \frac{1}{2} (\bar{\mathbf{F}} - \bar{\mathbf{R}}^{(2)}) \left[(\bar{\mathbf{F}} - \bar{\mathbf{R}}^{(2)}) \mathbf{Y}^I \right] \right\} - p \bar{\mathbf{F}}^{-T}, \end{aligned} \quad (1.80)$$

where p stands for the arbitrary hydrostatic pressure associated with the incompressibility constraint, and \mathbf{Y}^I is the sixth-order tensor with components

$$Y_{ijklpq}^I = \left. \frac{\partial E_{ijkl}}{\partial \bar{F}_{pq}} \right|_{\mu^{(1)} \rightarrow \infty} = - \left(P_{ijmn}^{-1} \frac{\partial P_{mnrst}}{\partial \bar{F}_{pq}} P_{rstkl}^{-1} + \frac{\partial L_{ijkl}^{(1)}}{\partial \bar{F}_{pq}} \right) \Big|_{\mu^{(1)} \rightarrow \infty}. \quad (1.81)$$

In addition, $\bar{\mathbf{G}}^{(2)}$ is a fourth-order tensor with the following indicial representation

$$\bar{G}_{ijkl}^{(2)} = \mathcal{I}_{ikjl} - \bar{g}_{ijkl}^{(2)}. \quad (1.82)$$

where $\bar{g}_{ijkl}^{(2)} = \partial (\bar{R}^{(2)})_{ij} / \partial \bar{F}_{kl}$. Note that a tensorial equation for the components of the fourth-order tensor $\bar{\mathbf{g}}^{(2)}$ can be deduced from the kinematical equation (1.79), which can be written in indicial

form as

$$\left\{ \bar{g}_{pikl}^{(2)} E_{pjrs}^I (\bar{F}_{rs} - \bar{R}_{rs}^{(2)}) + \bar{R}_{pi}^{(2)} Y_{pjrskl}^I (\bar{F}_{rs} - \bar{R}_{rs}^{(2)}) + \bar{R}_{pi}^{(2)} E_{pjrs}^I \bar{G}_{rskl}^{(2)} + \left[(1-c) \bar{g}_{pikl}^{(2)} (S_\mu^{(1)})_{pj} + \bar{R}_{pi}^{(2)} (L_\mu^{(1)})_{pjrs} (\mathcal{I}_{rskl} - c \bar{g}_{rskl}^{(2)}) \right] \right\} \Big|_{[ij]kl} = 0, \quad (1.83)$$

where $A_{ijkl}|_{[ij]kl} = (A_{ijkl} - A_{jikl})/2$, and the tensors $\mathbf{S}_\mu^{(1)}$ and $\mathbf{L}_\mu^{(1)}$ are evaluated at $\bar{\mathbf{F}}^{(1)}$. On the other hand, the derivatives $\partial P_{ijkl}/\partial \bar{F}_{pq}$ in (1.81) are calculated via

$$\frac{\partial P_{ijkl}}{\partial \bar{F}_{pq}} = \frac{1}{4\pi |\mathbf{Z}_0|} \int_{|\xi|=1} \frac{\partial H_{ijkl}}{\partial \bar{F}_{pq}} [\xi^T (\mathbf{Z}_0^T \mathbf{Z}_0)^{-1} \xi]^{\frac{-3}{2}} dS. \quad (1.84)$$

In turn, in this expression the derivatives $\partial H_{ijkl}/\partial \bar{\mathbf{F}}_{pq}$ can be evaluated by recalling the relation between the tensor \mathbf{H} and $\mathbf{L}^{(1)}$ to obtain the result

$$\frac{\partial H_{ijkl}}{\partial \bar{F}_{pq}} = \frac{\partial B_{ik}}{\partial \bar{F}_{pq}} \xi_j \xi_l = -B_{im} \frac{\partial K_{mn}}{\partial \bar{F}_{pq}} B_{nk} \xi_j \xi_l = -B_{im} B_{nk} \mathcal{L}_{mrns pq}^{(1)} \xi_j \xi_l \xi_r \xi_s, \quad (1.85)$$

where $\mathcal{L}^{(1)}$ is the sixth-order elastic modulus tensor defined by $\mathcal{L}^{(1)}(\mathbf{F}) = \partial^3 W^{(1)}(\mathbf{F})/\partial \mathbf{F} \partial \mathbf{F} \partial \mathbf{F}$ (Ogden, 1997) evaluated at $\bar{\mathbf{F}}$.

1.4.3 Dilute Concentrations

Relations (1.74) and (1.76) provide TSO estimates for (rigid) particle-reinforced elastomers under general loading in the finite concentration regime. In this subsection, we specialize these results for dilute concentrations of the particles, which is an important limiting case both for theoretical and practical reasons. Mathematically speaking, we carry out an asymptotic expansion of the estimates (1.74) and (1.76) for $c \ll 1$. To this end, we assume a regular perturbation expansion for $\bar{\mathbf{F}}^{(1)}$ in c , as given by

$$\bar{\mathbf{F}}^{(1)} = \bar{\mathbf{F}} + c(\bar{\mathbf{F}} - \bar{\mathbf{R}}_0^{(2)}) + c^2(\bar{\mathbf{F}} - \bar{\mathbf{R}}_0^{(2)} - \bar{\mathbf{R}}_1^{(2)}) + O(c^3), \quad (1.86)$$

which is obtained by assuming that $\bar{\mathbf{R}}^{(2)} = \bar{\mathbf{R}}_0^{(2)} + c\bar{\mathbf{R}}_1^{(2)} + O(c^2)$ and employing Eq. (1.48) for $\bar{\mathbf{F}}^{(1)}$. In addition, keeping in mind that the tensor $\mathbf{L}^{(1)}$ is evaluated at $\bar{\mathbf{F}}$, and is therefore independent of the volume fraction, the tensor $\tilde{\mathbf{L}}$ can be assumed to have the following asymptotic expansion about $c = 0$:

$$\tilde{\mathbf{L}} = \mathbf{L}^{(1)} + c\tilde{\mathbf{L}}_1 + O(c^2). \quad (1.87)$$

Next, substituting (1.86) and (1.87) into (1.74), and expanding the resulting expression for small values of c , yields the result

$$\begin{aligned} \widehat{W}^{Dilute}(\bar{\mathbf{F}}) &= W_\mu^{(1)}(\bar{\mathbf{F}}) + c \left\{ (\bar{\mathbf{F}} - \bar{\mathbf{R}}_0^{(2)}) \cdot \mathbf{S}_\mu^{(1)}(\bar{\mathbf{F}}) - W_\mu^{(1)}(\bar{\mathbf{F}}) \right. \\ &\quad \left. + \frac{1}{2} [(\bar{\mathbf{F}} - \bar{\mathbf{R}}_0^{(2)}) \cdot (\tilde{\mathbf{L}}_1 - \mathbf{L}^{(1)})(\bar{\mathbf{F}} - \bar{\mathbf{R}}_0^{(2)})] \right\} + O(c^2). \end{aligned} \quad (1.88)$$

Similarly, the kinematical constraint (1.76) leads to

$$\left\{ (\bar{\mathbf{R}}_0^{(2)})^T \cdot [(\tilde{\mathbf{L}}_1 - \mathbf{L}^{(1)})(\bar{\mathbf{F}} - \bar{\mathbf{R}}_0^{(2)})] + (\bar{\mathbf{R}}_0^{(2)})^T \mathbf{S}_\mu^{(1)}(\bar{\mathbf{F}}) \right\}_{Skew} + O(c) = \mathbf{0}. \quad (1.89)$$

Moreover, using the Willis estimate (1.55) for the LCC, the TSO estimate (1.88) specializes to

$$\begin{aligned} \widehat{W}^{Dilute}(\bar{\mathbf{F}}) &= W_\mu^{(1)}(\bar{\mathbf{F}}) + c \left\{ (\bar{\mathbf{F}} - \bar{\mathbf{R}}_0^{(2)}) \cdot \mathbf{S}_\mu^{(1)}(\bar{\mathbf{F}}) - W_\mu^{(1)}(\bar{\mathbf{F}}) \right. \\ &\quad \left. + \frac{1}{2} [(\bar{\mathbf{F}} - \bar{\mathbf{R}}_0^{(2)}) \cdot \mathbf{E}^I(\bar{\mathbf{F}} - \bar{\mathbf{R}}_0^{(2)})] \right\} + O(c^2), \end{aligned} \quad (1.90)$$

where the equation (1.89) for $\bar{\mathbf{R}}_0^{(2)}$ takes the form

$$\left\{ (\bar{\mathbf{R}}_0^{(2)})^T [\mathbf{E}^I(\bar{\mathbf{F}} - \bar{\mathbf{R}}_0^{(2)})] + (\bar{\mathbf{R}}_0^{(2)})^T \mathbf{S}_\mu^{(1)}(\bar{\mathbf{F}}) \right\}_{Skew} + O(c) = \mathbf{0}. \quad (1.91)$$

It is worth mentioning that these results can be regarded as generalization of Eshelby results (Eshelby, 1957) for a composite material consisting of dilute concentrations of aligned, rigid ellipsoidal inclusions in a nonlinear hyperelastic matrix. As is well known, these dilute estimates depend only on the volume fraction (to first order), shape and orientation of the ellipsoidal inclusions, but not on the relative positions of the inclusions. In other words, the interactions between inclusions is neglected by the estimates (1.90) and (1.91). As a consequence, the effective stored-energy function (1.90) does not exhibit lock up at finite strains (unless the matrix does).

The corresponding expressions for the macroscopic stress tensor $\bar{\mathbf{S}}^{Dilute}(\bar{\mathbf{F}}) = \partial \widehat{W}^{Dilute}(\bar{\mathbf{F}}) / \partial \bar{\mathbf{F}}$ are given by

$$\begin{aligned} \bar{\mathbf{S}}^{Dilute}(\bar{\mathbf{F}}) &= \mathbf{S}_\mu^{(1)}(\bar{\mathbf{F}}) + \left\{ \left[\mathbf{S}_\mu^{(1)}(\bar{\mathbf{F}}) + \mathbf{E}^I(\bar{\mathbf{F}} - \bar{\mathbf{R}}_0^{(2)}) \right] \bar{\mathbf{G}}_0^{(2)} + \mathbf{L}_\mu^{(1)}(\bar{\mathbf{F}})(\bar{\mathbf{F}} - \bar{\mathbf{R}}_0^{(2)}) \right. \\ &\quad \left. - \mathbf{S}_\mu^{(1)}(\bar{\mathbf{F}}) + \frac{1}{2}(\bar{\mathbf{F}} - \bar{\mathbf{R}}_0^{(2)}) \left[(\bar{\mathbf{F}} - \bar{\mathbf{R}}_0^{(2)}) \mathbf{Y}^I \right] \right\} c - p \bar{\mathbf{F}}^{-T} + O(c^2), \end{aligned} \quad (1.92)$$

where $(\bar{G}_0^{(2)})_{ijkl} = \mathcal{I}_{ijkl} - (\bar{g}_0^{(2)})_{ijkl}$, and where the quantities $(\bar{g}_0^{(2)})_{ijkl} = \partial(\bar{R}_0^{(2)})_{ij} / \partial \bar{F}_{kl}$ are determined by the equations

$$\begin{aligned} &\left\{ (\bar{g}_0^{(2)})_{pikl} E_{pjrs}^I [\bar{F}_{rs} - (\bar{R}_0^{(2)})_{rs}] + (\bar{R}_0^{(2)})_{pi} Y_{pjrskl}^I [\bar{F}_{rs} - (\bar{R}_0^{(2)})_{rs}] \right. \\ &\quad \left. + (\bar{R}_0^{(2)})_{pi} E_{pjrs}^I (\bar{G}_0^{(2)})_{rskl} + (\bar{g}_0^{(2)})_{pikl} (S_\mu^{(1)})_{pj} + (\bar{R}_0^{(2)})_{pi} (L_\mu^{(1)})_{pjkl} \right\} \Big|_{[ij]kl} = 0. \end{aligned} \quad (1.93)$$

where the tensors $\mathbf{S}_\mu^{(1)}$ and $\mathbf{L}_\mu^{(1)}$ are now evaluated at $\bar{\mathbf{F}}$

1.4.4 Computation of the Tensor \mathbf{E}^I

The calculation of the effective stored-energy function for *incompressible*, particulate elastomeric composites, as well as the associated microstructure evolution (Eqs. (1.77) and (1.79)) under *general* (isochoric) loading conditions, requires the computation of the fourth-order, major-symmetric tensor \mathbf{E}^I . This tensor can in principle be estimated (approximately) by setting $\mu'^{(1)}$ sufficiently

large (compared to the initial shear modulus of the matrix $\mu^{(1)}$) in the definition (1.78) for \mathbf{E}^I . Nevertheless, it is possible to perform a general asymptotic analysis for the computation of the tensor \mathbf{E}^I in the incompressibility limit ($\mu^{(1)} \rightarrow \infty$), as shown next. This analysis leads to closed-form expressions for the components of the tensor \mathbf{E}^I for specific microstructures and/or loading conditions; more generally, numerical computation of the resulting integrals may be required.

Without loss of generality, and consistent with the definition of the stored-energy function for the matrix phase as given by (1.60), the modulus tensor $\mathbf{L}^{(1)}$ can be decomposed into incompressible and compressible parts, denoted by $\mathbf{L}_\mu^{(1)}$ and $\mathbf{L}_{-1}^{(1)}$ respectively, such that

$$\mathbf{L}^{(1)} = \varepsilon^{-1} \mathbf{L}_{-1}^{(1)} + \mathbf{L}_\mu^{(1)}, \quad (1.94)$$

where, by definition, $\varepsilon = \mu^{(1)}/\mu'^{(1)}$ is a small parameter, $\mathbf{L}_\mu^{(1)} = \partial^2 W_\mu^{(1)} / \partial \mathbf{F} \partial \mathbf{F}(\bar{\mathbf{F}})$ and $\mathbf{L}_{-1}^{(1)}$ is given by

$$\mathbf{L}_{-1}^{(1)} = \mu^{(1)} [J(2J-1) \mathbf{F}^{-T} \otimes \mathbf{F}^{-T} + J(J-1) \mathcal{X}] \Big|_{\mathbf{F}=\bar{\mathbf{F}}}. \quad (1.95)$$

It follows from (1.23) that the acoustic tensor associated with (1.94) takes the form

$$\mathbf{K} = \varepsilon^{-1} \mathbf{K}_{-1} + \mathbf{K}_\mu, \quad (1.96)$$

where \mathbf{K}_{-1} and \mathbf{K}_μ are the parts of the acoustic tensor associated with $\mathbf{L}_{-1}^{(1)}$ and $\mathbf{L}_\mu^{(1)}$, respectively. The inverse of the (symmetric) acoustic tensor, $\mathbf{B} = \mathbf{K}^{-1}$, can then be calculated by means of the identity

$$B_{ik} = K_{ik}^{-1} = \frac{1}{2 \det(\mathbf{K})} e_{irs} e_{kpq} K_{rp} K_{sq}, \quad (1.97)$$

where e_{ijk} is the permutating tensor of the third-order, and $\det(\mathbf{K})$ is given by

$$\det(\mathbf{K}) = \frac{1}{6} e_{ijk} e_{pqr} K_{ip} K_{jq} K_{kr}. \quad (1.98)$$

Substituting (1.96) into (1.97) together with (1.98), after some algebra, we find the following expression for \mathbf{B} ,

$$\mathbf{B} = \frac{\varepsilon \mathbf{D}_1 + \mathbf{D}_0}{\varepsilon d_1 + d_0}, \quad (1.99)$$

where d_0 and d_1 are given by

$$\begin{aligned} d_0 &= \frac{1}{6} e_{ijk} e_{pqr} [(K_\mu)_{ip} (K_\mu)_{jq} (K_{-1})_{kr} + (K_\mu)_{ip} (K_{-1})_{jq} (K_\mu)_{kr} + (K_{-1})_{ip} (K_\mu)_{jq} (K_\mu)_{kr}], \\ d_1 &= \det(\mathbf{K}_\mu) = \frac{1}{6} e_{ijk} e_{pqr} (K_\mu)_{ip} (K_\mu)_{jq} (K_\mu)_{kr}, \end{aligned} \quad (1.100)$$

and the tensors \mathbf{D}_0 and \mathbf{D}_1 have components

$$\begin{aligned} (D_0)_{ik} &= e_{irs} e_{kpq} (K_\mu)_{rp} (K_{-1})_{sq}, \\ (D_1)_{ik} &= e_{irs} e_{kpq} (K_\mu)_{rp} (K_\mu)_{sq}. \end{aligned} \quad (1.101)$$

Then, expanding Eq. (1.99) to second order in ε , we obtain

$$\mathbf{B} = \mathbf{B}_0 + \varepsilon \mathbf{B}_1 + \varepsilon^2 \mathbf{B}_2 + O(\varepsilon^3), \quad (1.102)$$

from which it is straightforward to deduce that

$$\begin{aligned} \mathbf{B}_0 &= \frac{1}{d_0} \mathbf{D}_0, \\ \mathbf{B}_1 &= \frac{1}{d_0} \left(\mathbf{D}_1 - \frac{d_1}{d_0} \mathbf{D}_0 \right), \\ \mathbf{B}_2 &= \frac{d_1}{(d_0)^3} (d_1 \mathbf{D}_0 - d_0 \mathbf{D}_1). \end{aligned} \quad (1.103)$$

The corresponding expansion for the tensor \mathbf{P} can be obtained by making use of Eq. (1.102) in the definition (1.22) for \mathbf{P} , leading to

$$\mathbf{P} = \mathbf{P}_0 + \varepsilon \mathbf{P}_1 + \varepsilon^2 \mathbf{P}_2 + O(\varepsilon^3), \quad (1.104)$$

where the tensors \mathbf{P}_0 , \mathbf{P}_1 , and \mathbf{P}_2 are given by

$$(P_q)_{ijkl} = \frac{1}{4\pi |\mathbf{Z}_0|} \int_{|\xi|=1} (B_q)_{ik} \xi_j \xi_l [\xi^T (\mathbf{Z}_0^T \mathbf{Z}_0)^{-1} \xi]^{-\frac{3}{2}} dS, \quad q = 0, 1, 2. \quad (1.105)$$

In general, a Gaussian quadrature technique can be implemented for the numerical integration over the surface of the unit sphere, $|\xi| = 1$. Note that the leading-order term in (1.104) is the limiting value of \mathbf{P} in the incompressible matrix limit. Next, we turn to the computation the tensor \mathbf{E}^I , as defined by expression (1.78).

In this connection, it is important to remark that the tensor \mathbf{P}_0 is not of full-rank, meaning there is no fourth-order tensor $(\mathbf{P}_0)^{-1}$ such that $\mathbf{P}_0 (\mathbf{P}_0)^{-1} = (\mathbf{P}_0)^{-1} \mathbf{P}_0 = \mathbf{I}$. Hence, to determine \mathbf{E}^I it is necessary to carry out an asymptotic analysis for $\mathbf{Q} = \mathbf{P}^{-1}$, about $\varepsilon = 0$. For the sake of continuity, the pertinent derivations are given in Appendix A.1, and here we only spell out the final result of the asymptotic analysis, which is given by

$$\mathbf{E}^I = \mathbf{Q}_0 - \mathbf{L}_\mu^{(1)}, \quad (1.106)$$

where

$$\mathbf{Q}_0 = \mathbf{P}_0^\dagger (\mathcal{I} - \mathbf{P}_1 \mathbf{Q}_{-1}) + \sum_{i=1}^3 \mathbf{W}_i \otimes \mathbf{V}_i^{(1)}, \quad (1.107)$$

with

$$\mathbf{Q}_{-1} = \sum_{i=1}^3 \mathbf{W}_i \otimes \mathbf{V}_i^{(0)}. \quad (1.108)$$

In the above equations, $\{\mathbf{W}_1, \mathbf{W}_2, \mathbf{W}_3\}$ is a set of second-order tensor spanning the null space of

\mathbf{P}_0 , while the second order tensors $\mathbf{V}_i^{(0)}$ and $\mathbf{V}_i^{(1)}$ are defined by (Avrachenkov et al., 2001)

$$\mathbf{V}_i^{(0)} = \frac{1}{\mathbf{W}_i \cdot \mathbf{P}_1 \mathbf{W}_i} \mathbf{W}_i \quad (1.109)$$

and

$$\mathbf{V}_i^{(1)} = -\frac{1}{\mathbf{W}_i \cdot \mathbf{P}_1 \mathbf{W}_i} \left\{ (\mathbf{P}_1 \mathbf{P}_0^\dagger)^T \mathbf{W}_i + \left[\mathbf{W}_i \cdot (\mathbf{P}_2 - \mathbf{P}_1 \mathbf{P}_0^\dagger \mathbf{P}_1) \mathbf{W}_i \right] \mathbf{V}_i^{(0)} \right\}, \quad (1.110)$$

where $i = 1, 2, 3$ (no sum), and where the superscript T denotes the usual transpose of a fourth-order tensor (i.e., $(\cdot)_{ijkl}^T = (\cdot)_{klij}$). In addition, \mathbf{P}_0^\dagger is the Moore-Penrose generalized inverse of \mathbf{P}_0 satisfying the properties

$$\begin{aligned} \mathbf{P}_0 \mathbf{P}_0^\dagger \mathbf{P}_0 &= \mathbf{P}_0, & \mathbf{P}_0^\dagger \mathbf{P}_0 \mathbf{P}_0^\dagger &= \mathbf{P}_0^\dagger, \\ (\mathbf{P}_0 \mathbf{P}_0^\dagger)^T &= \mathbf{P}_0 \mathbf{P}_0^\dagger, & (\mathbf{P}_0^\dagger \mathbf{P}_0)^T &= \mathbf{P}_0^\dagger \mathbf{P}_0. \end{aligned} \quad (1.111)$$

1.5 2-D Application: Reinforced Elastomers with Elliptical Fibers

In the previous section, we presented a general homogenization procedure to estimate the effective stored-energy function and the associated evolution of the microstructure for rigidly reinforced elastomeric composites in both the dilute and non-dilute concentration regimes. In this section and the next, we make use of this procedure to obtain some explicit estimates of the Willis-type for two specific classes of composites: (1) elastomers reinforced with aligned, cylindrical fibers subjected to general (transverse) plane-strain loading, and (2) elastomers reinforced with spherical particles subjected to general tri-axial loading. In this section, we will study the first class of composites, while the second class will be discussed in Section 1.6. (More general, non-spherical particle shapes will be considered elsewhere.) The variational estimates (1.77) and (1.79) can be employed for fairly general matrix behavior. Indeed, the stored-energy function $W^{(1)}$, characterizing the constitutive behavior of the matrix, is assumed to be objective, isotropic, strictly rank-one convex (strongly elliptic) function of the deformation gradient tensor \mathbf{F} . In this work, attention is restricted to stored-energy functions of the generalized neo-Hookean type

$$W^{(1)}(\mathbf{F}) = g(I) + h(J) + \frac{1}{2} \mu^{(1)} (J - 1)^2, \quad (1.112)$$

where $I = \text{tr}(\mathbf{C})$ and the material functions $g(I)$ and $h(J)$ are assumed to be twice continuously differentiable satisfying the conditions: $g(3) = h(1) = 0$, $g_I(3) = \mu^{(1)}/2$, $h_J(3) = -\mu^{(1)}$, and $4g_{II}(3) + h_{JJ}(1) = \mu^{(1)}$, in which the subscripts I and J stand for partial differentiation with respect to the invariants I and J , respectively. The energy form (1.112) has been shown to provide reasonably good agreement with experimental data for rubberlike materials (Ogden, 1997). A well-known example of the general form (1.112), which captures the limiting chain extensibility of elastomers,

is the (compressible) Gent model (Gent, 1996), expressed by

$$W^{(1)}(\mathbf{F}) = -\frac{J_m \mu^{(1)}}{2} \ln \left(1 - \frac{I-3}{J_m} \right) - \mu^{(1)} \ln(J) + \frac{1}{2} \left(\mu'^{(1)} - 2\frac{\mu^{(1)}}{J_m} \right) (J-1)^2, \quad (1.113)$$

where the dimensionless parameter J_m is the limiting value for $I-3$ at which the elastomer locks up. It should be remarked that the strong ellipticity of the Gent model (1.113) is satisfied for all deformations by the conditions: $\mu^{(1)} > 0$, $J_m > 0$, $\mu'^{(1)} > 2\mu^{(1)}/J_m$. Note that the Gent model (1.113) reduces to the compressible neo-Hookean model, which never locks up, in the limit as $J_m \rightarrow \infty$.

It should be emphasized that, different from the previously discussed lock-up phenomenon for the composite, the lock up associated with the parameter J_m is due to the elastomeric character of the matrix stemming from the fact that polymeric chains of the rubbery matrix become inextensible when they experience a certain strain level. Henceforth, for definiteness, we will refer to the former lock up as *geometric lock up* (GL), and to latter as *material lock up* (ML). By the same token, the macroscopic deformation gradients at which the geometric and material lock up occur are, respectively, denoted by $\bar{\mathbf{F}}^{GL}$ and $\bar{\mathbf{F}}^{ML}$. It is emphasized that the ML is already present in a homogeneous (Gent) matrix and enhanced with the reinforcement; however, the GL disappears in the limit of dilute particle concentration. It can be verified that the blow-up in the estimate (1.77) because of the GL or ML is caused only by the first term in (1.77), and, consequently, for a composite with a Gent matrix, the GL and ML respectively take place, when the following conditions are satisfied

$$\det(\bar{\mathbf{F}} - c\bar{\mathbf{R}}^{(2)}) = 0, \quad (1.114)$$

$$\text{tr} \left[\bar{\mathbf{C}} - 2c\bar{\mathbf{F}}^T \bar{\mathbf{R}}^{(2)} - 2c \left(\bar{\mathbf{R}}^{(2)} \right)^T \bar{\mathbf{F}} + c\mathbf{I} \right] = J_m + 3, \quad (1.115)$$

where $\bar{\mathbf{C}} = \bar{\mathbf{F}}^T \bar{\mathbf{F}}$. It should be remarked that both lock-up phenomena are affected by the microstructure evolution thorough $\bar{\mathbf{R}}^{(2)}$. It is obvious that the lock-up strain for the composite is determined by $\bar{\mathbf{F}}^{lock} = \min\{\bar{\mathbf{F}}^{GL}, \bar{\mathbf{F}}^{ML}\}$. In fact, depending on the underlying microstructure in the undeformed configuration and extensibility of the rubbery matrix (characterized by the parameter J_m), the composite may lock up because of either condition (1.114) or condition (1.115). It is remarked that for composites with a neo-Hookean matrix (where $J_m \rightarrow \infty$) $\bar{\mathbf{F}}^{lock} = \bar{\mathbf{F}}^{GL}$. It is also worth mentioning that, for dilute concentration conditions, the effective stored-energy function (1.90) for reinforced Gent elastomers locks up at the same deformation as the Gent matrix, as given by the condition $\text{tr}(\bar{\mathbf{C}}) = J_m + 3$.

1.5.1 Plane-Strain Loading of Fiber-Reinforced Elastomers

In this section, we obtain estimates for the effective behavior of hyperelastic composites made of a rubbery matrix and rigid and axially aligned fibers. It is assumed that the cylindrical fibers have an elliptical cross-section and are distributed with elliptical symmetry in the plane transverse to the fiber direction. Consistent with earlier discussions, the aspect ratio of both the fiber cross-section and distribution are taken to be given by ω . Furthermore, attention is restricted to macroscopic

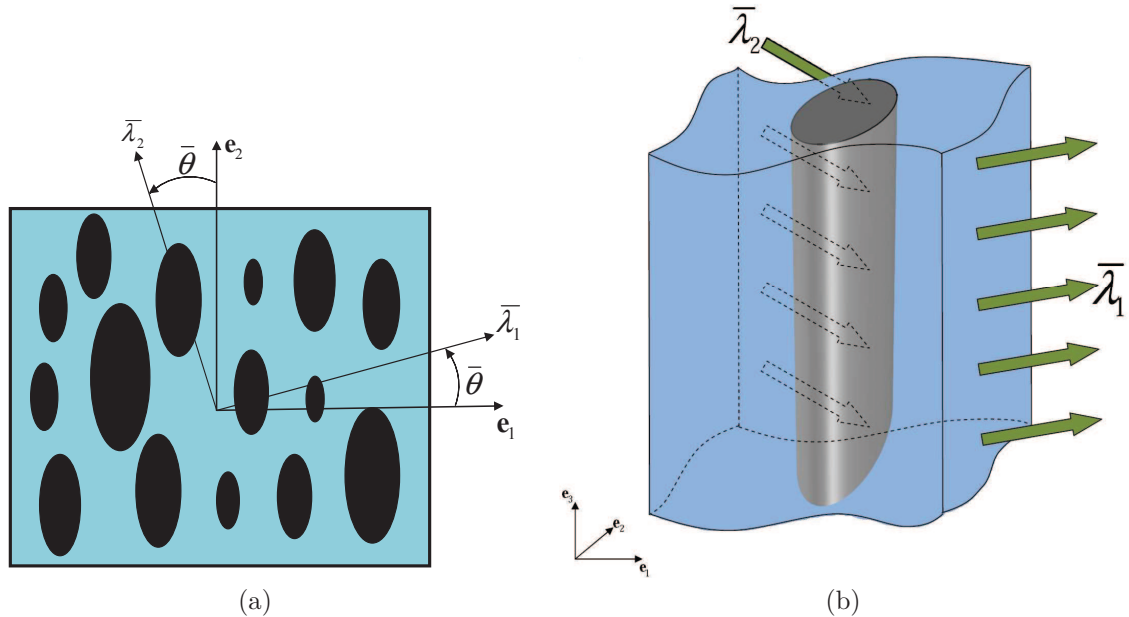


Figure 1.1: Rigidly-reinforced composite under plane-strain loading. (a) Two-dimensional representation in the transverse plane. (b) Three-dimensional representation of a typical reinforcing fiber.

plane-strain deformation. Assume that the composite undergoes a *uniform* deformation gradient $\bar{\mathbf{F}}$ with the following matrix representation

$$[\bar{\mathbf{F}}_{ij}] = \begin{pmatrix} \cos(\bar{\psi}) & -\sin(\bar{\psi}) \\ \sin(\bar{\psi}) & \cos(\bar{\psi}) \end{pmatrix} \begin{pmatrix} \cos(\bar{\theta}) & -\sin(\bar{\theta}) \\ \sin(\bar{\theta}) & \cos(\bar{\theta}) \end{pmatrix} \begin{pmatrix} \bar{\lambda}_1 & 0 \\ 0 & \bar{\lambda}_2 \end{pmatrix} \begin{pmatrix} \cos(\bar{\theta}) & \sin(\bar{\theta}) \\ -\sin(\bar{\theta}) & \cos(\bar{\theta}) \end{pmatrix}, \quad (1.116)$$

with respect to the fixed Cartesian basis $\{\mathbf{e}_i\}$, $i = 1, 2$. In the above relation, $\bar{\lambda}_1$ and $\bar{\lambda}_2$ are the principal stretches and $\bar{\theta}$ denotes the angle (positive anticlockwise) of the in-plane Lagrangean stretch axes relative to the basis $\{\mathbf{e}_i\}$. Also, $\bar{\psi}$ serves to quantify the rigid-body rotation (or “continuum spin”). A schematic representation of the composite microstructure and loading parameters is depicted in Figure 1.1(a) for $\bar{\psi} = 0$. The corresponding 3-D illustration, Figure 1.1(b) shows a typical (embedded) long cylindrical fiber under the plane-strain loading.

It should be remarked that constitutive models for this class of fiber-reinforced elastomers have already been derived by Lopez-Pamies and Ponte Castañeda (2006b) making use of the second-order (GSO) homogenization theory. Analytical results were given for general matrix behavior of the form (1.112) in the limit of an incompressible matrix. These results, which will be spelled out later, have been shown to be in good agreement with corresponding FEM numerical results available in the literature for special types of loading conditions (Moraleda et al., 2009). Hence, to gain some insight into the accuracy of the variational TSO estimates, described in the previous section, we will also show comparisons with the GSO estimates and FEM results for this class of composites in this section.

The constitutive behavior for the matrix phase is assumed to obey the Gent model given in

(1.113). The computation of the TSO estimate (1.56), requires the calculation of the components of the tensor \mathbf{P} for the cylindrical microstructure. The components of \mathbf{P} , in the rectangular Cartesian basis $\{\mathbf{e}_i\}$, $i = 1, 2, 3$, when the fibers are aligned in the direction $\mathbf{N} = \mathbf{e}_3$, are given by

$$P_{ijkl} = \frac{\omega}{2\pi} \int_0^{2\pi} \frac{H_{ijkl}(\xi_1, \xi_2, \xi_3 = 0)}{\xi_1^2 + \omega^2 \xi_2^2} d\theta, \quad (1.117)$$

where $H_{ijkl} = (L_{ipkq}^{(1)} \xi_p \xi_q)^{-1} \xi_j \xi_l$ with $\xi_1 = \cos(\theta)$, and $\xi_2 = \sin(\theta)$. In general, it is not possible to obtain analytical expressions for the components of the \mathbf{P} tensor associated with matrix form (1.113) and loading condition (1.116). But it is easy to compute numerically the tensor \mathbf{P} , as well as the associated tensor \mathbf{E} .

In this section, we will focus our attention to *incompressible* Gent matrix phases obtained from expression (1.113) in the limit as $\mu^{(1)} \rightarrow \infty$. This requires the computation of the tensor \mathbf{E}^I via the procedure given in Subsection 1.4.2. Then, the calculated components of the tensor \mathbf{E}^I can be substituted in Eqs. (1.77) and (1.79) to obtain the numerical values of the effective stored-energy function and the associated fiber rotation. It should be remarked that for the aligned loading case ($\bar{\theta} = 0$), the components of the tensor \mathbf{E}^I can be expressed explicitly, since in this case the integrals in (1.105) can be calculated analytically. This leads to a closed-form expression for the effective energy, but the expression is quite lengthy and will not be included here for brevity. It is also important to mention that when the Gent behavior (1.113) is specialized to neo-Hookean behavior (equivalent to the limit of $J_m \rightarrow \infty$), the associated integrals in (1.105) can be performed analytically. In this case, derivations of closed-form expressions for the \mathbf{E}^I -tensor components and subsequently for the effective potential energy are feasible as discussed next.

1.5.2 Explicit Results for an Incompressible, neo-Hookean Matrix

In this subsection, we assume that the matrix phase behavior is characterized by a compressible neo-Hookean stored-energy function, given by

$$W^{(1)}(\mathbf{F}) = \frac{1}{2} \mu^{(1)} (I - 2) - \mu^{(1)} \ln J + \frac{1}{2} \mu'^{(1)} (J - 1)^2, \quad (1.118)$$

where the parameters $\mu^{(1)}$ and $\mu'^{(1)}$ denote the standard Lamé moduli of the matrix at zero strain. As mentioned earlier, (1.118) is the reduced form of (1.113) for the plane-strain loading when $J_m \rightarrow \infty$. In this case, all the in-plane components of the tensor \mathbf{P} can be computed analytically and the results are provided in Appendix A.2. These results can then be used to perform an asymptotic expansion for the components of the tensor $\mathbf{E} = (\mathbf{P}^{-1} - \mathbf{L}^{(1)})|_{\mathbf{F}=\bar{\mathbf{F}}}$ in the incompressibility limit (i.e., $\mu^{(1)} \rightarrow \infty$), leading to the following expressions for the components of \mathbf{E}^I , as defined by expression (1.78), namely,

$$\begin{aligned} E_{1111}^I &= \frac{1}{2} \frac{\mu^{(1)}}{\lambda_1 \bar{\lambda}_2 \omega} \Omega_1, & E_{2222}^I &= \frac{1}{2} \frac{\mu^{(1)} \omega}{\lambda_1 \bar{\lambda}_2} \Omega_2, & E_{1212}^I &= \frac{1}{2} \frac{\mu^{(1)} \omega}{\lambda_1 \bar{\lambda}_2} \Omega_1, \\ E_{2121}^I &= \frac{1}{2} \frac{\mu^{(1)}}{\lambda_1 \bar{\lambda}_2 \omega} \Omega_2, & E_{1121}^I &= -\frac{1}{2} \frac{\mu^{(1)}}{\lambda_1 \bar{\lambda}_2 \omega} \Omega_3, & E_{2212}^I &= -\frac{1}{2} \frac{\mu^{(1)} \omega}{\lambda_1 \bar{\lambda}_2} \Omega_3, \end{aligned}$$

$$E_{1122}^I = E_{1221}^I = E_{1112}^I = E_{2221}^I = 0, \quad (1.119)$$

where

$$\begin{aligned} \Omega_{1,2} &= (\bar{\lambda}_1 + \bar{\lambda}_2) \{ \bar{\lambda}_1 + \bar{\lambda}_2 \mp (\bar{\lambda}_1 - \bar{\lambda}_2) \cos[2(\bar{\psi} + \bar{\theta})] \}, \\ \Omega_3 &= [(\bar{\lambda}_1)^2 - (\bar{\lambda}_2)^2] \sin[2(\bar{\psi} + \bar{\theta})]. \end{aligned} \quad (1.120)$$

It then follows from expression (1.77) that the effective stored-energy function $\widehat{W}(\bar{\mathbf{F}})$ of the rigidly reinforced composite reduces to

$$\begin{aligned} \widehat{W}(\bar{\mathbf{F}}) &= (1 - c) W^{(1)}(\bar{\mathbf{F}}^{(1)}) + \frac{\mu^{(1)} c (1 + \bar{\lambda}_1^2)}{4\omega (1 - c) \bar{\lambda}_1^2} \\ &\times \{ 2(1 + \omega^2)(\bar{\lambda}_1^2 - 2\bar{\lambda}_1 \cos(\phi) + 1) + (\omega^2 - 1)(\bar{\lambda}_1^2 - 1) [\cos(2\bar{\theta} - 2\phi) - \cos(2\bar{\theta})] \}, \end{aligned} \quad (1.121)$$

where

$$\begin{aligned} W^{(1)}(\bar{\mathbf{F}}^{(1)}) &= \mu^{(1)} \frac{\bar{\lambda}_1^4 - 2c\bar{\lambda}_1(1 + \bar{\lambda}_1^2) \cos(\phi) - 2\bar{\lambda}_1^2 + 4c\bar{\lambda}_1^2 + 1}{2\bar{\lambda}_1^2(1 - c)^2} \\ &- \mu^{(1)} \ln \left[\frac{(1 + c^2)\bar{\lambda}_1 - c(1 + \bar{\lambda}_1^2) \cos(\phi)}{\bar{\lambda}_1(1 - c)^2} \right]. \end{aligned}$$

In these relations, the angle ϕ , denoting the in-plane rigid body rotation of the fibers relative to the macroscopic rotation (i.e., $\phi = \bar{\psi}^{(2)} - \bar{\psi}$), is obtained from the kinematical relation

$$\begin{aligned} 2\omega (1 - c) \bar{\lambda}_1^2 \cos(\phi) \Delta_1 + 2\bar{\lambda}_1 [(\bar{\lambda}_1^2 + 1)(1 + \omega^2) + \omega (1 - c) \bar{\lambda}_1 \Delta_2] \sin(\phi) \\ + (\bar{\lambda}_1^4 - 1)(\omega^2 - 1) \sin(2\bar{\theta} - 2\phi) = 0, \end{aligned} \quad (1.122)$$

where

$$\begin{aligned} \Delta_1 &= -2c^2 \frac{\sin(\phi)[(1 + \bar{\lambda}_1^2) \cos(\phi) - 2\bar{\lambda}_1]}{(1 - c)[(1 + c^2)\bar{\lambda}_1 - c(1 + \bar{\lambda}_1^2) \cos(\phi)]}, \\ \Delta_2 &= c \frac{[\cos(\phi)(1 + \bar{\lambda}_1^2) - 2\bar{\lambda}_1][2c\bar{\lambda}_1 \cos(\phi) - \bar{\lambda}_1^2 - 1]}{(1 - c)\bar{\lambda}_1[(1 + c^2)\bar{\lambda}_1 - c(1 + \bar{\lambda}_1^2) \cos(\phi)]}. \end{aligned}$$

It is emphasized that the estimate (1.121) is consistent with the overall incompressibility constraint, which in this case reduces to $\bar{\lambda}_1 \bar{\lambda}_2 = 1$. It is also remarked that the energy function (1.121) is independent of the angle $\bar{\psi}$, which is consistent with the objectivity of the energy function $\widehat{W}(\bar{\mathbf{F}})$, requiring that $\widehat{W}(\bar{\mathbf{F}}) = \widehat{W}(\bar{\mathbf{U}})$, where $\bar{\mathbf{U}} = (\bar{\mathbf{F}}^T \bar{\mathbf{F}})^{1/2}$ is the macroscopic stretch tensor.

The above results can be easily specialized for dilute concentrations by expanding about $c = 0$. Thus, keeping terms of order c in Eq. (1.121), the estimate for the effective stored-energy function

$\widehat{W}(\bar{\mathbf{F}})$ is given by

$$\begin{aligned} \widehat{W}^{Dilute}(\bar{\mathbf{F}}) &= \frac{1}{2}\mu^{(1)}(\bar{\lambda}_1^2 + \bar{\lambda}_1^{-2} - 2) \\ &+ \frac{1}{2}\mu^{(1)} \left\{ \frac{1}{\bar{\lambda}_1^2\omega} [2\omega(1 + \bar{\lambda}_1^4) + (1 + \omega^2)(1 + \bar{\lambda}_1^2)[(1 + \bar{\lambda}_1^2) - 2\bar{\lambda}_1\cos(\phi_0)] \right. \\ &\left. + (\bar{\lambda}_1^4 - 1)(\omega^2 - 1)\sin(\phi_0)\sin(2\bar{\theta} - \phi_0) - 4\omega\bar{\lambda}_1^2 \right] - (\bar{\lambda}_1^2 + \bar{\lambda}_1^{-2} - 2) \} c + O(c^2). \end{aligned} \quad (1.123)$$

where $\phi_0 = \bar{\psi}_0^{(2)} - \bar{\psi}$ (where the angle $\bar{\psi}_0^{(2)}$ denotes the total in-plane rigid body rotation of fibers in the *dilute concentration regime*) is given by

$$2\bar{\lambda}_1(1 + \omega^2)\sin(\phi_0) - (\bar{\lambda}_1^2 - 1)(\omega^2 - 1)\sin[2(\phi_0 - \bar{\theta})] + O(c) = 0. \quad (1.124)$$

The estimates (1.123) and (1.124) are valid for arbitrary aspect ratios $\omega \geq 1$ of fibers. For the special case of the circular cross-section ($\omega = 1$) for the fibers (which also implies an isotropic distribution of the fibers), the in-plane behavior of the composite is isotropic and the stored-energy function (1.123) no longer depends on the loading angle $\bar{\theta}$. In this case, it is a simple matter to deduce that, the TSO estimate (1.123) reduces to

$$\widehat{W}^{Dilute}(\bar{\mathbf{F}}) = \frac{1}{2}\mu^{(1)} [(\bar{\lambda}_1^2 + \bar{\lambda}_1^{-2} - 2) + (2\bar{\lambda}_1^{-1} + 3\bar{\lambda}_1^{-2} + 3)(\bar{\lambda}_1 - 1)^2c] + O(c^2). \quad (1.125)$$

For comparison purposes, we recall in the next subsection the GSO results (Lopez-Pamies and Ponte Castañeda, 2006b). Although the GSO estimates are expected to be more accurate in general, they are more difficult to implement, and thus far results are only available for 2-D cases. On the other hand, as we will see in Section 1.6, the TSO can be used for general 3-D microstructures and loading conditions.

1.5.3 Generalized Second-Order Estimate

Lopez-Pamies and Ponte Castañeda (2006b) derived an expression for the effective stored-energy function of the class of fiber-reinforced composites described earlier with matrix behavior (1.112) and transverse loading conditions (1.116). In the limit of incompressible behavior for the elastomeric matrix phase ($\mu^{(1)} \rightarrow \infty$), the result simplifies to

$$\widehat{W}_{GSO}(\mathbf{F}) = (1 - c)g(\hat{I}), \quad (1.126)$$

where

$$\begin{aligned} \hat{I} &= \frac{1}{(1 - c)^2\bar{\lambda}_1^2\omega} \{ c(1 + \bar{\lambda}_1^2)^2 + [1 + 2c(c - 2)\bar{\lambda}_1^2 + \bar{\lambda}_1^4]\omega + c\omega^2(1 + \bar{\lambda}_1^2)^2 \\ &\quad - c(\bar{\lambda}_1^4 - 1)(\omega^2 - 1)\sin(\phi)\sin(\phi - 2\bar{\theta}) - 2c\bar{\lambda}_1(1 + \bar{\lambda}_1^2)(1 + \omega^2)\cos(\phi) \}. \end{aligned}$$

In this expression, the relative particle rotation angle ϕ is determined by

$$2\bar{\lambda}_1(1 + \omega^2)\sin(\phi) - (\bar{\lambda}_1^2 - 1)(\omega^2 - 1)\sin[2(\phi - \bar{\theta})] = 0. \quad (1.127)$$

The GSO estimate (1.126) is known (Lopez-Pamies and Ponte Castañeda, 2006b) to be consistent with the exact incompressibility constraint and expected to be fairly accurate for small to medium concentrations of fibers.

In the *dilute-concentration regime*, the GSO estimate (1.126) can be expanded about $c = 0$ to obtain the result that

$$\begin{aligned} \widehat{W}_{GSO}^{Dilute}(\bar{\mathbf{F}}) = g(\bar{I}) + \left\{ \frac{1}{\bar{\lambda}_1^2 \omega} g'(\bar{I}) [2\omega(1 + \bar{\lambda}_1^4) + (1 + \omega^2)(1 + \bar{\lambda}_1^2)[(1 + \bar{\lambda}_1^2) - 2\bar{\lambda}_1 \cos(\phi_0)] \right. \\ \left. + (\bar{\lambda}_1^4 - 1)(\omega^2 - 1)\sin(\phi_0)\sin(2\bar{\theta} - \phi_0) - 4\omega\bar{\lambda}_1^2 \right\} c + O(c^2), \end{aligned} \quad (1.128)$$

where $\bar{I} = \text{tr}(\bar{\mathbf{C}})$. The kinematical equation (1.127) is independent of the volume fraction of fibers and also provides the rotation of fibers in the dilute concentration regime.

Specializing the estimate (1.128) for a neo-Hookean matrix, the same second-order estimate is obtained as the dilute TSO estimate (1.123). Moreover, the estimates (1.124) and (1.127) for the particle rotation also agree exactly in this case. Consequently, the agreement of the TSO estimates (1.123) and (1.124) with the corresponding GSO results in the dilute concentration regime strongly suggests that the TSO estimates should be also be quite accurate for incompressible, rigidly-reinforced composites with more general microstructures (at least) in the dilute concentration regime. As we will see in the next subsection, differences can arise between the new TSO and GSO estimates for finite volume fractions, but only at sufficiently large stretches.

1.5.4 Discussion of the Results

In the remainder of this section, we present some illustrative results for the *new* TSO estimates for plane-strain loading of 2-D fiber-reinforced elastomers. For comparison purposes, the corresponding GSO results of Lopez-Pamies and Ponte Castañeda (2006b) are also included in the figures and shown with dashed curves. For simplicity, we restrict our attention to incompressible ($\mu^{(1)} \rightarrow \infty$) Gent and neo-Hookean matrix phases, circular fibers ($\omega = 1$) and pure shear loading ($\bar{\theta} = \bar{\psi} = 0$, $\bar{\lambda}_1 = \bar{\lambda}_2^{-1} = \bar{\lambda}$). Results are provided for several volume fractions, c , and are normalized by $\mu^{(1)}$.

Figure 1.2 shows the new TSO estimates for the effective response of the reinforced neo-Hookean elastomers, as well as the corresponding GSO estimates. Results are shown for three different fiber volume fractions $c = 0.1, 0.2, 0.3$, as a function of the macroscopic stretch $\bar{\lambda}$. Part (a) shows the effective energy \widehat{W} , and part (b), the corresponding macroscopic stress $\bar{S} = d\widehat{W}/d\bar{\lambda}$. The new TSO results are seen to be quite close to the GSO estimates for a range of $\bar{\lambda}$, but they start to deviate from the GSO results, as the average stretch approaches the “geometric” lock-up condition (1.114) for the TSO estimates (i.e., $\bar{\lambda} \rightarrow 1/c$). For instance, it is seen for $c = 0.1$ (where the lock-up stretch is 10), the TSO model predicts very similar results for the effective energy as well as the macroscopic stress to those for the GSO in the range $1 \leq \bar{\lambda} \leq 6$. On the other hand, for $c = 0.3$ (where the lock-up stretch is 3.33), the agreement is very good only up to a stretch of 2.5.

Figure 1.3 shows a more detailed comparison of the new TSO estimates with earlier analytical

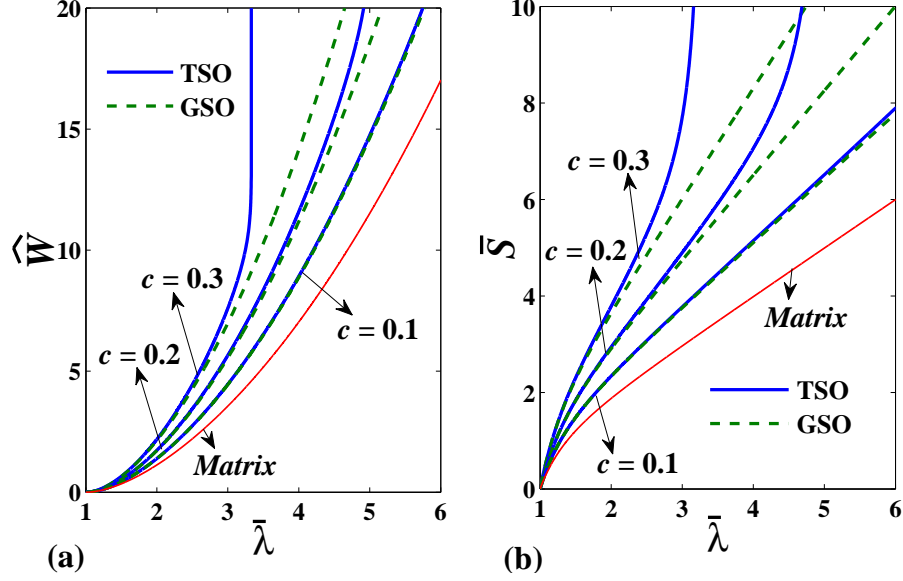


Figure 1.2: New tangent second-order (TSO) and generalized second-order (GSO) estimates for the effective response of a rigidly fiber-reinforced elastomer with an incompressible neo-Hookean matrix under pure shear loading. The results are shown as a function of the applied stretch $\bar{\lambda}$ for different values of the fiber volume fraction. (a) The effective energy $\langle \widehat{W} \rangle$. (b) The corresponding macroscopic stress $\bar{S} = d\langle \widehat{W} \rangle / d\bar{\lambda}$.

estimates and numerical simulations for neo-Hookean elastomers reinforced by rigid fibers of circular cross section. Results are provided for two volume fractions: (a) $c = 0.2$, and (b) $c = 0.3$. The GSO (2006) estimates correspond to the stored-energy function (1.126), while the GSO (2004) and TSO (2000) estimates correspond to earlier versions of the GSO (Lopez-Pamies and Ponte Castañeda, 2004b) and TSO (Ponte Castañeda and Tiberio, 2000) estimates, respectively. On the other hand, the LAM estimates refer to the sequentially laminated results of deBotton (2005), while the FEM results refer to the finite element simulations of Moraleda et al. (2009). The main observation from these plots is that while the GSO estimate provides the best agreement with the FEM simulations, the new TSO estimate also provides excellent agreement with the FEM results (up to the point where the simulations were carried out), especially for the smaller fiber concentrations. For the higher volume fraction ($c = 0.3$) the new TSO estimates tend to overestimate the FEM results at sufficiently large stretches, but are still quite good for stretches of less than 1.5. On the other hand, the LAM estimates tend to underestimate the response of the reinforced elastomers for sufficiently large strains, even if the differences relative to the FEM are relatively small. Finally, it can be seen that the new TSO estimates are much improved relative to the earlier version (Ponte Castañeda and Tiberio, 2000) of the TSO estimates, and even compared to an earlier version (Lopez-Pamies and Ponte Castañeda, 2004b) of the GSO estimates. The main conclusion from these comparisons is that the new way of handling the matrix incompressibility limit presented in Subsection 1.4.2 actually works quite well at least when the fiber concentrations and/or stretches are not too large.

Next, for completeness, we consider fiber-reinforced composites using the Gent model for the

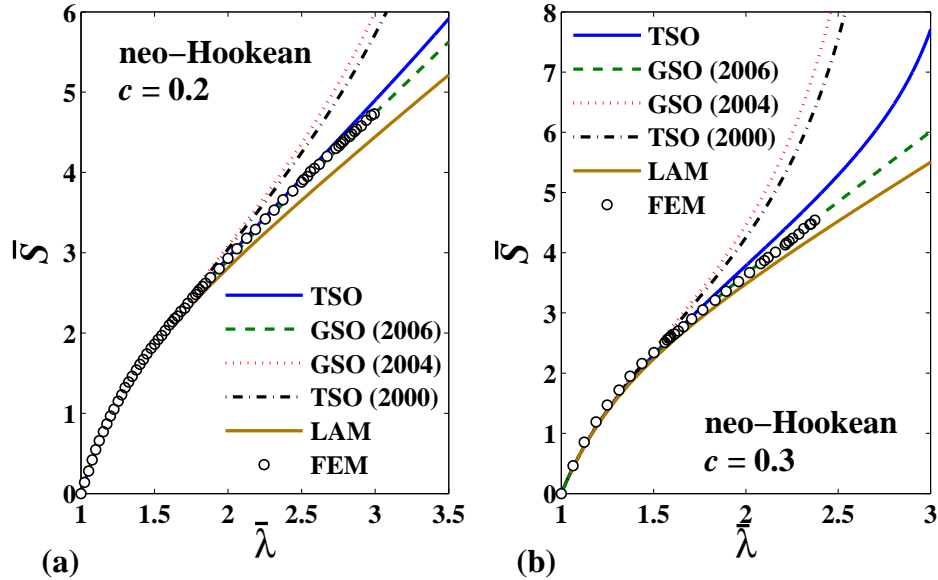


Figure 1.3: The effective response of a rigidly fiber-reinforced elastomer with an incompressible neo-Hookean matrix under pure shear loading. The macroscopic stress $\bar{S} = d\widehat{W}/d\bar{\lambda}$ is plotted as a function of the applied stretch $\bar{\lambda}$ for (a) $c = 0.2$, and (b) $c = 0.3$. Comparisons are shown between the new TSO estimate (1.121), the estimate (1.126) of Lopez-Pamies and Ponte Castañeda (2006b) “GSO (2006)”, the earlier GSO results of Lopez-Pamies and Ponte Castañeda (2004b) “GSO (2004)”, the earlier TSO results of Ponte Castañeda and Tiberio (2000) “TSO (2000)”, the laminate results of deBotton (2005) “LAM”, and the FE simulations of Moraleda et al. (2009) “FEM”.

matrix and the same loading conditions as the previous case. The results for the macroscopic stress $\bar{S} = d\widehat{W}/d\bar{\lambda}$ are presented in Figs. 1.4(a) and (b) versus the applied stretch $\bar{\lambda}$. Figure 1.4(a) shows the results for composites with fiber concentrations $c = 0.1, 0.2, 0.3$ for a fixed lock-up parameter ($J_m = 50$), while Figure 1.4(b) shows results for Gent matrices with $J_m = 50, 100, 500, \infty$ for fixed volume fraction ($c = 0.1$). The responses of the unreinforced matrix with $J_m = 50$ and $J_m = \infty$ are included respectively in Figs. 4a and 4b for comparison purposes. In addition, the results of the finite element simulations of Moraleda et al. (2009) for $J_m = 50$ are also included for comparison purposes. As can be seen from Figure 1.4(a), the agreement of the new TSO estimates for reinforced elastomers of the Gent type with the FEM results (and GSO estimates) is quite good for the range of deformations achieved in the numerical simulations. It should be noted, however, that the TSO (and GSO) predictions slightly underestimate the response, especially at the higher volume fractions. On the other hand, as show in Figure 1.4(b), the agreement of the new TSO and earlier GSO estimates for reinforced Gent elastomers is also quite good, even for fairly large stretches. However, the TSO estimates are slightly stiffer for intermediate stretches, but eventually become softer than the GSO estimates as the “constitutive” lock-up condition (1.115) is approached.

Finally, Figure 1.5 presents results for the evolution of the particle orientation under non-aligned applied loadings for neo-Hookean elastomers reinforced by rigid fibers of elliptical cross section. Results for the (average) relative rotation ϕ (see Figure 1) are shown for three different stretching

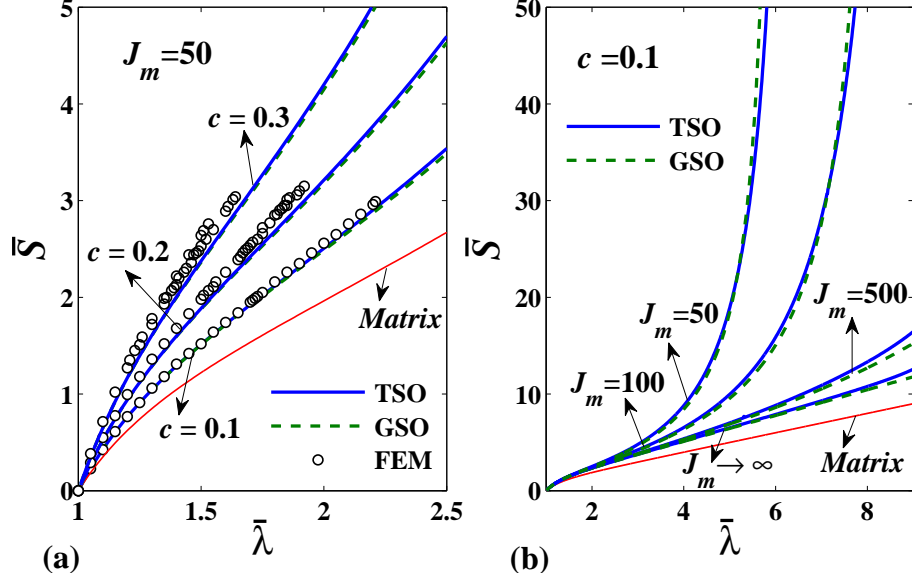


Figure 1.4: New tangent second-order (TSO) estimate, generalized second-order (GSO) estimate (1.126), and the FE simulations of Moraleda et al. (2009) (FEM) for the effective response of a fiber-reinforced elastomer with an incompressible Gent matrix under pure shear loading. The macroscopic stress $\bar{S} = d\bar{W}/d\bar{\lambda}$ is depicted as a function of the applied stretch $\bar{\lambda}$, for (a) different values of the fiber volume fraction c with $J_m = 50$, and (b) different matrix lock-up parameters J_m with $c = 0.1$.

angles ($\bar{\theta} = 5^\circ, 45^\circ$, and 85°). Figure 1.5(a) shows comparisons of the new TSO estimates with the GSO estimates (Lopez-Pamies and Ponte Castañeda, 2006b) for two different fiber aspect ratios ($\omega = 2$ and 10), and given fiber volume fraction ($c = 0.1$). The results show that the largest rotations are generated for the larger aspect ratio (i.e., for $\omega = 10$), when the compressive direction is most closely aligned with the long fiber axis (i.e., for $\bar{\theta} = 5^\circ$), although relatively large stretches are needed. In addition, the results show excellent agreement between the new TSO and GSO estimates at this fairly small value of c . This is consistent with the fact that the TSO and GSO equations ((1.127) and (1.124), respectively) for the fiber rotations agree precisely for a neo-Hookean matrix in the dilute concentration limit. Figure 1.5(b) presents additional comparisons of the new TSO estimates with the GSO estimates (Lopez-Pamies and Ponte Castañeda, 2006b), as well as with the FEM numerical simulations of Moraleda et al. (2009) for a volume fraction $c = 0.3$, and aspect ratio $\omega = 2$. It can be seen from this plot that the agreement between the TSO homogenization results, on the one hand, and the FEM numerical results, on the other, is quite good for $\bar{\theta} = 45^\circ$ and 85° , but less good for $\bar{\theta} = 5^\circ$. This may be a consequence of the fact that the FEM results made use of equisized particles, which at this relatively high value of the fiber concentration may lead to stronger interactions among the fibers than the TSO results (corresponding to polydisperse distributions of fibers) can account for. In addition, it is not clear that a sufficiently large number of configurations has been used in the FEM simulations to generate accurate results by ensemble averaging. Be that as it may, the TSO homogenization estimates, which were also found to be consistent with the corresponding GSO results at this higher value of the fiber concentration, are at least *qualitatively*

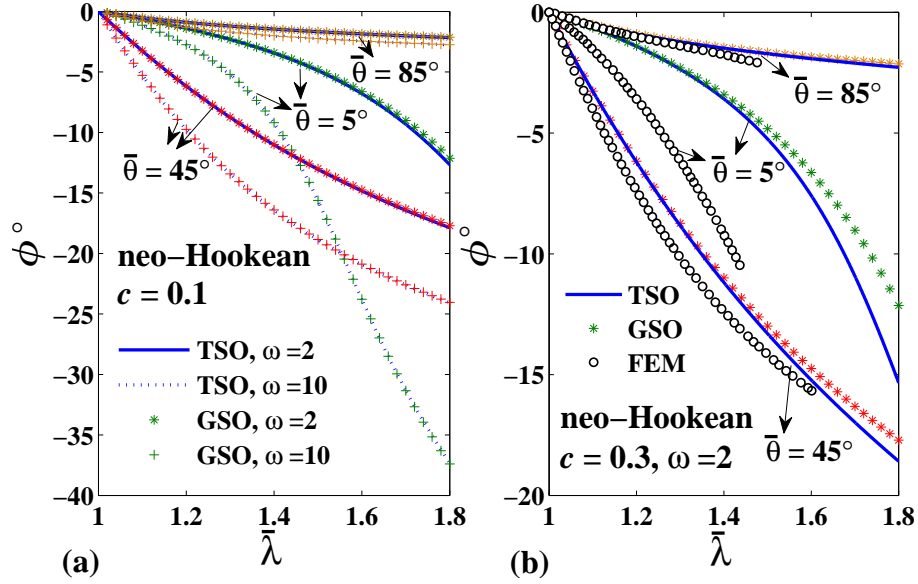


Figure 1.5: The microstructure evolution in a rigidly fiber-reinforced elastomer with an incompressible neo-Hookean matrix under pure shear loading. The relative fiber rotation ϕ is plotted as a function of the applied stretch $\bar{\lambda}$ for three different stretching angles $\bar{\theta} = 5^\circ, 45^\circ$, and 85° . (a) Comparisons between the new TSO estimate (1.122) and the estimate (1.127) of Lopez-Pamies and Ponte Castañeda (2006b) for the volume fraction $c = 0.1$, and aspect ratios $\omega = 2$, and 10. (b) Comparisons between the new TSO estimate, the GSO estimate and the FEM simulations of Moraleda et al. (2009) for $c = 0.3$, and $\omega = 2$.

consistent with the results of the numerical simulations. Clearly, more extensive numerical work will be necessary to be able to assess the accuracy of the homogenization results in the future.

1.6 3-D Application: Reinforced Elastomers with Spherical Particles

As we have seen in the previous section, the new TSO procedure can be used to obtain accurate estimates for the macroscopic response and microstructure evolution for transverse loading of fiber-reinforced elastomers at finite strains, even when the fibers are rigid, corresponding to infinite contrast, and when the matrix is incompressible, leading to a strongly nonlinear *incompressibility constraint* for the composite (which can be recovered exactly by the theory). Although the GSO procedure (Lopez-Pamies and Ponte Castañeda, 2006a) is expected to lead to even more accurate predictions, it is more difficult to implement because it makes use of additional information about the field fluctuations in the linear comparison composite. For this reason, it has not yet been implemented for general (3-D) ellipsoidal particles, especially in the limit of incompressible behavior for the matrix phase. On the other hand, the new TSO estimates of Section 1.4 for the effective stored-energy function of particle-reinforced (incompressible) elastomers are applicable for rigid particles with general ellipsoidal shape and distribution. However, for simplicity, in this section we will

focus on an application of the TSO theory to particle-reinforced elastomers consisting of a random and isotropic distribution of spherical rigid inclusions in an isotropic, incompressible matrix phase, leaving for future work an in-depth investigation of more general ellipsoidal shapes for the particles.

We begin by remarking that, in view of objectivity and the assumed isotropy of the reinforced elastomer, it suffices to restrict attention to pure stretch deformations $\bar{\mathbf{F}} = \bar{\mathbf{U}}$ (i.e., $\bar{\mathbf{R}} = \mathbf{I}$), which, in the Cartesian basis $\{\mathbf{e}_i\}$, $i = 1, 2, 3$, can be expressed in the form

$$\bar{\mathbf{F}} = \bar{\mathbf{U}} = \bar{\lambda}_1 \mathbf{e}_1 \otimes \mathbf{e}_1 + \bar{\lambda}_2 \mathbf{e}_2 \otimes \mathbf{e}_2 + \bar{\lambda}_3 \mathbf{e}_3 \otimes \mathbf{e}_3, \quad (1.129)$$

where $\bar{\lambda}_i$ is the principal stretch in the \mathbf{e}_i -direction, and the overall incompressibility constraint $\bar{\lambda}_1 \bar{\lambda}_2 \bar{\lambda}_3 = 1$ holds. Under these hypotheses, it can be shown that $\bar{\mathbf{R}}^{(2)} = \mathbf{I}$ satisfies identically equation (1.79) for the particle rotation (as expected from the symmetry of the problem), and the TSO estimate (1.77) for the effective stored-energy function of the reinforced elastomer can be shown to reduce to

$$\begin{aligned} \widehat{W}(\bar{\mathbf{F}}) &= (1 - c) W_\mu^{(1)}(\bar{\mathbf{F}}^{(1)}) + \frac{c}{2(1 - c)} [\bar{\Lambda}_{11} E_{1111}^I + \bar{\Lambda}_{22} E_{2222}^I + \bar{\Lambda}_{33} E_{3333}^I \\ &\quad + 2(\bar{\Lambda}_{12} E_{1122}^I + \bar{\Lambda}_{13} E_{1133}^I + \bar{\Lambda}_{23} E_{2233}^I)], \end{aligned} \quad (1.130)$$

where $\bar{\Lambda}_{ij} = (\bar{\lambda}_i - 1)(\bar{\lambda}_j - 1)$ ($i, j = 1, 2, 3$).

In this section, we will confine our attention to stored-energy functions of the *generalized* neo-Hookean form (1.112) for the matrix phase. As discussed in Subsection 1.4.2, the computation of the microstructural tensor \mathbf{E}^I requires the computation of the tensors \mathbf{P}_i ($i = 0, 1, 2$), as defined by (1.105), which in turn require the determination of the tensors \mathbf{B}_i via the tensors \mathbf{D}_0 , \mathbf{D}_1 and the scalars d_0 , d_1 , as provided by relations (1.103). After some algebraic manipulation, it is straightforward to deduce that the components of the symmetric, second-order tensors \mathbf{D}_0 and \mathbf{D}_1 for the matrix behavior (1.112) and the loading condition (1.129) reduce to

$$\begin{aligned} (D_0)_{11} &= \bar{\lambda}_1^2 [(\bar{\lambda}_2^2 \xi_3^2 + \bar{\lambda}_3^2 \xi_2^2) g_I + \Delta_{23}^2 g_{II} \xi_2^2 \xi_3^2], \\ (D_0)_{22} &= \bar{\lambda}_2^2 [(\bar{\lambda}_1^2 \xi_3^2 + \bar{\lambda}_3^2 \xi_1^2) g_I + \Delta_{13}^2 g_{II} \xi_1^2 \xi_3^2], \\ (D_0)_{33} &= \bar{\lambda}_3^2 [(\bar{\lambda}_1^2 \xi_2^2 + \bar{\lambda}_2^2 \xi_1^2) g_I + \Delta_{12}^2 g_{II} \xi_1^2 \xi_2^2], \\ (D_0)_{12} &= -[\bar{\lambda}_3 g_I + \Delta_{13} \Delta_{23} \bar{\lambda}_1 \bar{\lambda}_2 g_{II}] \xi_1 \xi_2, \\ (D_0)_{13} &= -[\bar{\lambda}_2 g_I + \Delta_{12} \Delta_{23} \bar{\lambda}_1 \bar{\lambda}_3 g_{II}] \xi_1 \xi_3, \\ (D_0)_{23} &= -[\bar{\lambda}_1 g_I + \Delta_{12} \Delta_{13} \bar{\lambda}_2 \bar{\lambda}_3 g_{II}] \xi_2 \xi_3, \end{aligned}$$

$$\begin{aligned}
(D_1)_{11} &= g_I^2 + (\bar{\lambda}_2^2 \xi_2^2 + \bar{\lambda}_3^2 \xi_3^2) g_I g_{II} + h_{II} (D_0)_{11}, \\
(D_1)_{22} &= g_I^2 + (\bar{\lambda}_1^2 \xi_1^2 + \bar{\lambda}_3^2 \xi_3^2) g_I g_{II} + h_{II} (D_0)_{22}, \\
(D_1)_{33} &= g_I^2 + (\bar{\lambda}_1^2 \xi_1^2 + \bar{\lambda}_2^2 \xi_2^2) g_I g_{II} + h_{II} (D_0)_{33}, \\
(D_1)_{12} &= -\bar{\lambda}_3 \xi_1 \xi_2 g_I g_{II} + h_{II} (D_0)_{12}, \\
(D_1)_{13} &= -\bar{\lambda}_2 \xi_1 \xi_3 g_I g_{II} + h_{II} (D_0)_{13}, \\
(D_1)_{23} &= -\bar{\lambda}_1 \xi_2 \xi_3 g_I g_{II} + h_{II} (D_0)_{23},
\end{aligned} \tag{1.131}$$

where $\Delta_{ij} = (\bar{\lambda}_i^2 - \bar{\lambda}_j^2)$, $i, j = 1, 2, 3$. In addition, the expressions for d_0 and d_1 are given by

$$\begin{aligned}
d_0 &= (\bar{\lambda}_2^2 \bar{\lambda}_3^2 \xi_1^2 + \bar{\lambda}_1^2 \bar{\lambda}_3^2 \xi_2^2 + \bar{\lambda}_1^2 \bar{\lambda}_2^2 \xi_3^2) g_I^2 + [\bar{\lambda}_3^2 \Delta_{12}^2 \xi_1^2 \xi_2^2 + \bar{\lambda}_2^2 \Delta_{13}^2 \xi_1^2 \xi_3^2 + \bar{\lambda}_1^2 \Delta_{23}^2 \xi_2^2 \xi_3^2] g_I g_{II}, \\
d_1 &= g_I^3 + h_{II} d_0 + (\bar{\lambda}_1^2 \xi_1^2 + \bar{\lambda}_2^2 \xi_2^2 + \bar{\lambda}_3^2 \xi_3^2) g_I^2 g_{II}.
\end{aligned} \tag{1.132}$$

For general matrix behavior, the integrals involved in the calculation of the tensors \mathbf{P}_i in expressions (1.105) cannot be performed analytically. Therefore, the double integrals are computed numerically via Gaussian quadrature, with a sufficiently high numbers of Gauss points. Thus, using expressions (1.131) and (1.132), and setting $\mathbf{Z}_0 = \mathbf{I}$ for the spherical inclusions, the integrals may be easily computed by means of polar cylindrical coordinates

$$\xi_1 = \sqrt{1 - z^2} \cos(\theta), \quad \xi_2 = \sqrt{1 - z^2} \sin(\theta), \quad \xi_3 = z, \tag{1.133}$$

which vary over the intervals $0 \leq \theta \leq \pi$ and $0 \leq z \leq 1$. After calculation of the tensors \mathbf{P}_i , the tensor \mathbf{E}^I can be calculated via the relations (1.106) to (1.110) (see also Appendix A.1). Finally, the computation of the effective stored-energy function (1.130) may be completed by means of the relevant components of the tensor \mathbf{E}^I .

Although the integrals (1.105) for the tensors \mathbf{P}_i require numerical integration in general, they can actually be computed analytically at least for Gent behavior (1.113) for the matrix phase and axisymmetric loading conditions. In this case, a closed-form estimate may be obtained for the macroscopic stored-energy function (1.130) of the particle-reinforced elastomer. However, the expressions are too lengthy to be included here. Instead, closed-form, analytical results are provided for the special case of neo-Hookean behavior for the matrix phase in the next subsection.

1.6.1 Analytical Results for (Incompressible) neo-Hookean Elastomers

In this section, we provide the specialization of the second-order estimate (1.130) for composite elastomers with *incompressible* neo-Hookean matrix phases. In fact, the microstructural tensors \mathbf{P} and \mathbf{E} , as defined by expressions (1.22) and (1.57), respectively, can be computed analytically (Lopez-Pamies and Ponte Castañeda, 2007a,b) for *compressible* neo-Hookean behavior, and are given in Appendix A.3. Therefore, the incompressible limit ($\mu^{(1)} \rightarrow \infty$) of the tensor \mathbf{E} to obtain \mathbf{E}^I can be evaluated directly in this case, without the more general procedure outlined in Subsection 1.4.2. In any event, having obtained the components of \mathbf{E}^I , the corresponding expression for the TSO estimate for the effective stored-energy function of the composite with incompressible neo-Hookean

matrix phase is obtained by substitution into (1.130). The result may be written in the form

$$\begin{aligned}
\widehat{W}(\bar{\mathbf{F}}) = & (1-c)W_\mu^{(1)}(\bar{\mathbf{F}}^{(1)}) - \frac{c\mu^{(1)}}{2(1-c)} \left\{ \{\bar{\lambda}_1^2\bar{\lambda}_2^2 [\bar{\lambda}_1^2 + \bar{\lambda}_2^2 + \bar{\lambda}_1\bar{\lambda}_2 [2 + \bar{\lambda}_1^7\bar{\lambda}_2^5 + 2\bar{\lambda}_1^6\bar{\lambda}_2^3 \right. \\
& + \bar{\lambda}_1^5\bar{\lambda}_2(\bar{\lambda}_2 + 1)(\bar{I}_{1,0}^{\bar{1},1} + \bar{\Pi}_{0,0}^{\bar{5},\bar{1}} + 1) - 2\bar{\lambda}_1^2\bar{\lambda}_2(1 + \bar{\lambda}_1^2\bar{\lambda}_2)(\bar{I}_{0,0}^{\bar{3},2} - 6\bar{\lambda}_2^2 + 2) + 2\bar{\lambda}_1^3\bar{\lambda}_2^2(\bar{I}_{0,0}^{\bar{12},\bar{3}} + \bar{\Pi}_{0,0}^{\bar{3},1} + 6) \\
& + \bar{\lambda}_2(\bar{\lambda}_2^4 - 4\bar{\lambda}_2 - 6)\bar{\lambda}_1]\} [3(\bar{\lambda}_2^4\bar{\lambda}_1^2 - 1)\Xi_e^2 + 2(\bar{\lambda}_1^4\bar{\lambda}_2^2 - 2\bar{\lambda}_1^2\bar{\lambda}_2^4 + 1)\Xi_e\Xi_f \\
& - \bar{\lambda}_1^2\bar{\lambda}_2^2(\bar{\lambda}_1^2 - \bar{\lambda}_2^2)\Xi_f^2] - (\bar{\lambda}_2^4\bar{\lambda}_1^2 - 1)(\bar{\lambda}_1^4\bar{\lambda}_2^2 - 1) [2\bar{\lambda}_1^2 + 2\bar{\lambda}_2^2 + \bar{\lambda}_1\bar{\lambda}_2 [\bar{\lambda}_2^3(3\bar{\lambda}_2^4 - 2)\bar{\lambda}_1^9 \\
& + 2\bar{\lambda}_1^8\bar{\lambda}_2^3(2\bar{\lambda}_2 + 1) + \bar{\lambda}_1^7\bar{\lambda}_2^2(\bar{I}_{0,3}^{\bar{9},\bar{8}} + \bar{\Pi}_{0,0}^{\bar{2},\bar{6}} + 4) - 2\bar{\lambda}_1^6\bar{\lambda}_2^2(\bar{I}_{3,0}^{\bar{2},\bar{3}} + \bar{\Pi}_{0,0}^{\bar{3},\bar{6}} - 1) - 2\bar{\lambda}_1^5\bar{\lambda}_2^4(\bar{I}_{0,0}^{\bar{12},4} - 3\bar{\lambda}_2^2 - 6) \\
& + 2\bar{\lambda}_1^4\bar{\lambda}_2(\bar{I}_{3,2}^{\bar{2},3} + \bar{\Pi}_{1,0}^{\bar{0},6} - 1) + \bar{\lambda}_1^3(\bar{I}_{0,9}^{\bar{9},2} + \bar{\Pi}_{4,2}^{\bar{2},0} - 2\bar{\lambda}_2^9 - 4) + 2\bar{\lambda}_1^2(\bar{\lambda}_2 - 1)(\bar{I}_{3,0}^{\bar{3},1} + \bar{\Pi}_{2,0}^{\bar{0},3} + 1) \\
& - \bar{\lambda}_1\bar{\lambda}_2^2(2\bar{\lambda}_2 - 1)(\bar{\lambda}_2 - 4) - 4\bar{\lambda}_2^3 - 2\bar{\lambda}_2^2]\} \sqrt{1 - \bar{\lambda}_1^2\bar{\lambda}_2^4 + \bar{\lambda}_1\bar{\lambda}_2(\bar{\lambda}_2^4\bar{\lambda}_1^2 - 1)} \\
& \times \{ [-4 + 2\bar{\lambda}_1\bar{\lambda}_2 [\bar{\lambda}_1^{11}\bar{\lambda}_2^5(3\bar{\lambda}_2^4 - 2) + \bar{\lambda}_1^{10}\bar{\lambda}_2^5(3\bar{\lambda}_2^2 + 4\bar{\lambda}_2 + 2) + \bar{\lambda}_1^9\bar{\lambda}_2^4(\bar{I}_{0,3}^{\bar{9},\bar{12}} + \bar{\Pi}_{0,0}^{\bar{2},\bar{9}} + 4) \\
& - \bar{\lambda}_1^8\bar{\lambda}_2^3(\bar{I}_{20,0}^{\bar{2},9} + \bar{\Pi}_{9,0}^{\bar{4},\bar{10}} + 3) + \bar{\lambda}_1^7\bar{\lambda}_2^3(\bar{I}_{10,3}^{\bar{3},20} + \bar{\Pi}_{12,0}^{\bar{0},\bar{42}} + 6) + \bar{\lambda}_1^6\bar{\lambda}_2^2(\bar{I}_{20,2}^{\bar{8},0} + \bar{\Pi}_{9,4}^{\bar{16},10} + 3) \\
& - \bar{\lambda}_1^5\bar{\lambda}_2^2(2\bar{\lambda}_2^9 + \bar{I}_{0,9}^{\bar{33},\bar{6}} + \bar{\Pi}_{4,2}^{\bar{8},0} + 16) + \bar{\lambda}_1^4\bar{\lambda}_2(\bar{I}_{16,2}^{\bar{8},18} + \bar{\Pi}_{3,4}^{\bar{16},\bar{8}} + 3) - \bar{\lambda}_1^3\bar{\lambda}_2(\bar{I}_{8,3}^{\bar{3},16} + \bar{\Pi}_{6,0}^{\bar{0},\bar{33}} - 6) \\
& + \bar{\lambda}_1^2(\bar{I}_{16,0}^{\bar{2},3} + \bar{\Pi}_{3,0}^{\bar{4},\bar{8}} - 3) + \bar{\lambda}_1(2\bar{\lambda}_2^2 + 3\bar{\lambda}_2^4 + 4 + 6\bar{\lambda}_2^3 - 12\bar{\lambda}_2) + 4\bar{\lambda}_2 - 3\bar{\lambda}_2^2 + 2]\} \Xi_e \\
& + [\bar{\lambda}_1^4 + \bar{\lambda}_2^4 + \bar{\lambda}_1\bar{\lambda}_2 [\bar{\lambda}_2^7\bar{\lambda}_1^{13} + 2\bar{\lambda}_2^5\bar{\lambda}_1^{12} - \bar{\lambda}_1^{11}\bar{\lambda}_2^3(4\bar{\lambda}_2^3 + 4\bar{\lambda}_2^2 - 1) - 4\bar{\lambda}_1^{10}\bar{\lambda}_2^4(\bar{I}_{0,0}^{\bar{1},3} - 2\bar{\lambda}_2^2 + 1) \\
& - \bar{\lambda}_1^9\bar{\lambda}_2^4(\bar{I}_{0,5}^{\bar{16},\bar{8}} + \bar{\Pi}_{0,0}^{\bar{4},\bar{12}} - 8) + 2\bar{\lambda}_1^8\bar{\lambda}_2^3(\bar{I}_{12,0}^{\bar{2},3} + \bar{\Pi}_{7,0}^{\bar{4},\bar{6}} + 1) - \bar{\lambda}_1^7\bar{\lambda}_2(4\bar{\lambda}_2^9 + \bar{I}_{24,12}^{\bar{0},4} + \bar{\Pi}_{45,16}^{\bar{8},0} + 2) \\
& - 2\bar{\lambda}_1^6\bar{\lambda}_2^2(\bar{I}_{12,2}^{\bar{2},\bar{2}} + \bar{\Pi}_{7,4}^{\bar{4},\bar{6}} - 1) + \bar{\lambda}_1^5\bar{\lambda}_2^2(4\bar{\lambda}_2^9 + \bar{I}_{0,18}^{\bar{11},0} + \bar{\Pi}_{8,4}^{\bar{4},4} + 8) - 2\bar{\lambda}_1^4\bar{\lambda}_2(\bar{I}_{8,2}^{\bar{2},10} + \bar{\Pi}_{1,4}^{\bar{4},4} + 2) \\
& + 2\bar{\lambda}_1^3\bar{\lambda}_2(\bar{I}_{4,2}^{\bar{2},8} + \bar{\Pi}_{2,0}^{\bar{0},\bar{17}} - 2) + \bar{\lambda}_1^2(\bar{I}_{16,0}^{\bar{0},4} + \bar{\Pi}_{2,0}^{\bar{0},8} + 2) - \bar{\lambda}_1\bar{\lambda}_2(\bar{\Pi}_{1,0}^{\bar{8},0} + 4\bar{\lambda}_2^3 - 2) + 2\bar{\lambda}_2^2]\} \Xi_f \} \} \\
& \times \{ \bar{\lambda}_1^2\bar{\lambda}_2^2 [[9\bar{\lambda}_1^4\bar{\lambda}_2^4(\bar{\lambda}_1^2\bar{\lambda}_2^4 - 1)\Xi_e^2 + 6\bar{\lambda}_1^4\bar{\lambda}_2^4(\bar{\lambda}_1^4\bar{\lambda}_2^2 - 2\bar{\lambda}_2^4\bar{\lambda}_1^2 + 1)\Xi_e\Xi_f \\
& - 3\bar{\lambda}_1^6\bar{\lambda}_2^6(\bar{\lambda}_1^2 - \bar{\lambda}_2^2)\Xi_f^2 - \bar{\lambda}_1^{12}\bar{\lambda}_2^8 + \bar{\lambda}_1^{10}\bar{\lambda}_2^4(1 - 3\bar{\lambda}_2^6) + \bar{\lambda}_1^8\bar{\lambda}_2^6(5 - \bar{\lambda}_2^6) - 2\bar{\lambda}_1^6\bar{\lambda}_2^2 \\
& + \bar{\lambda}_1^4\bar{\lambda}_2^4(\bar{\lambda}_2^6 - 5) + \bar{\lambda}_1^2(1 - 2\bar{\lambda}_2^6) + 5\bar{\lambda}_2^8\bar{\lambda}_1^6 + \bar{\lambda}_2^2] \sqrt{1 - \bar{\lambda}_1^2\bar{\lambda}_2^4 + 2\bar{\lambda}_1\bar{\lambda}_2(\bar{\lambda}_2^4\bar{\lambda}_1^2 - 1)} [[\bar{\lambda}_1^8\bar{\lambda}_2^4 + 5\bar{\lambda}_1^6\bar{\lambda}_2^6 \\
& + \bar{\lambda}_1^4\bar{\lambda}_2^2(\bar{\lambda}_2^6 - 4) - 4\bar{\lambda}_1^2\bar{\lambda}_2^4 + 1]\Xi_e + \bar{\lambda}_1^2\bar{\lambda}_2^2[\bar{\lambda}_1^6\bar{\lambda}_2^2 - 3\bar{\lambda}_1^4\bar{\lambda}_2^4 + \bar{\lambda}_1^2(1 - \bar{\lambda}_2^6) + 2\bar{\lambda}_2^2]\Xi_f]] \}^{-1}, \quad (1.134)
\end{aligned}$$

where

$$W_\mu^{(1)}(\bar{\mathbf{F}}^{(1)}) = \frac{\mu^{(1)}}{2} \left[\sum_{i=1}^3 \left(\frac{\bar{\lambda}_i - c}{1 - c} \right)^2 - 3 \right] - \mu^{(1)} \ln \left[\frac{(\bar{\lambda}_1 - c)(\bar{\lambda}_2 - c)(\bar{\lambda}_3 - c)}{(1 - c)^3} \right], \quad (1.135)$$

and the abbreviations

$$\bar{I}_{c,d}^{a,b} = d\bar{\lambda}_2^7 + c\bar{\lambda}_2^5 + b\bar{\lambda}_2^3 + a\bar{\lambda}_2, \quad \bar{\Pi}_{c,d}^{a,b} = d\bar{\lambda}_2^8 + c\bar{\lambda}_2^6 + b\bar{\lambda}_2^4 + a\bar{\lambda}_2^2, \quad (1.136)$$

(a barred subscript/superscript indicates the corresponding negative coefficient) have been introduced for simplicity. In addition, Ξ_f and Ξ_e are given in terms of the incomplete elliptic integrals

of the first and second kind (Abramowitz and Stegun, 1965), respectively, via

$$\Xi_f = F \left(\sqrt{1 - \bar{\lambda}_1^2 \bar{\lambda}_2^4}, \sqrt{\frac{\bar{\lambda}_1^4 \bar{\lambda}_2^2 - 1}{\bar{\lambda}_1^2 \bar{\lambda}_2^4 - 1}} \right), \quad \Xi_e = E \left(\sqrt{1 - \bar{\lambda}_1^2 \bar{\lambda}_2^4}, \sqrt{\frac{\bar{\lambda}_1^4 \bar{\lambda}_2^2 - 1}{\bar{\lambda}_1^2 \bar{\lambda}_2^4 - 1}} \right), \quad (1.137)$$

where the functions F and E are defined by

$$F(a, b) = \int_0^a \frac{1}{\sqrt{1-t^2} \sqrt{1-b^2 t^2}} dt, \quad E(a, b) = \int_0^a \frac{\sqrt{1-b^2 t^2}}{\sqrt{1-t^2}} dt. \quad (1.138)$$

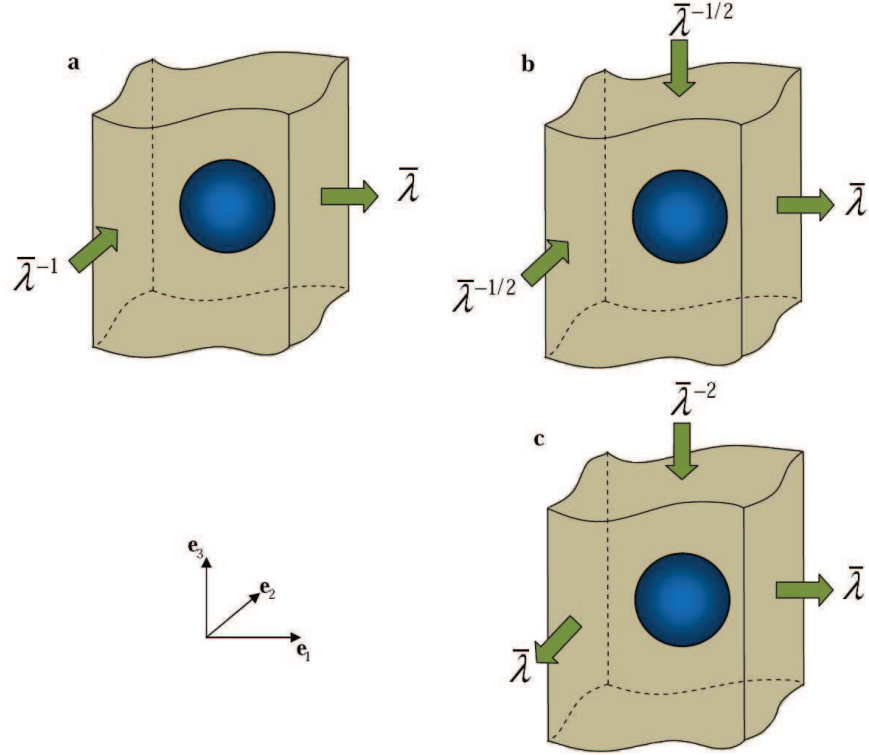


Figure 1.6: Schematic representation of a matrix reinforced by spherical inclusions subjected to (a) Pure Shear (PS) loading, (b) Uniaxial Tension (UT) loading, and (c) Equibiaxial Tension (ET) loading.

It is emphasized for completeness that the above estimate is consistent with the macroscopic incompressibility constraint $\bar{\lambda}_1 \bar{\lambda}_2 \bar{\lambda}_3 = 1$, and linearizes properly. Note also that the estimate locks up whenever any of the stretches $\bar{\lambda}_i = c$. In addition, it is well worth considering the specializations of this expression for *Pure Shear*, *Uniaxial Tension* and *Equibiaxial Tension* loading conditions, as schematically represented in Figure 1.6.

Pure Shear (PS)

For pure shear loading in the 1–3 plane (cf. Figure 1.6(a)), $\bar{\lambda}_3 = 1$ and $\bar{\lambda}_2 = 1/\bar{\lambda}_1$, and the TSO estimate (1.134) for $\widehat{W}(\bar{\mathbf{F}})$ simplifies to

$$\begin{aligned}
\widehat{W}(\bar{\mathbf{F}}) &= (1-c)W_\mu^{(1)}(\bar{\mathbf{F}}^{(1)}) - \frac{1}{2} \frac{c}{1-c} \frac{\mu^{(1)}}{\bar{\lambda}_1^2} \left\{ \left\{ 2(\bar{\lambda}_1^2 - 1) \left[(\bar{\lambda}_1^2 - 1)^3 \Xi_e + \Phi_{2,1}^{0,1} \Xi_f \right] \right. \right. \\
&\quad + \left. \left\{ 3\bar{\lambda}_1^4 \left[3\Xi_e^2 - 2(\bar{\lambda}_1^2 + 2)\Xi_e \Xi_f + (\bar{\lambda}_1^2 + 1)\Xi_f^2 \right] - (\bar{\lambda}_1^2 - 1)\Phi_{3,1}^{1,1} \right\} \sqrt{1 - \bar{\lambda}_1^{-2}} \right\}^{-1} \\
&\quad \times (\bar{\lambda}_1 - 1)^2 \left\{ (\bar{\lambda}_1^2 - 1) \left\{ \left[L_3(\bar{\lambda}_1^4 - 3) + 2\bar{\lambda}_1 \Phi_{1,5}^{2,3} \right] \Xi_f - 2(2\bar{\lambda}_1^2 + \bar{\lambda}_1 + 2)(\bar{\lambda}_1^2 - 1)^3 \Xi_e \right\} \right. \\
&\quad + \left. \left\{ \bar{\lambda}_1^2 \left[\Phi_{1,1}^{0,1} + 4\bar{\lambda}_1(\bar{\lambda}_1^4 + \bar{\lambda}_1^2 + 1) \right] \left[3\Xi_e^2 - 2(\bar{\lambda}_1^2 + 2)\Xi_e \Xi_f + (\bar{\lambda}_1^2 + 1)\Xi_f^2 \right] \right. \right. \\
&\quad \left. \left. + (\bar{\lambda}_1^2 - 1) \left[L_3(2\bar{\lambda}_1^4 - \bar{\lambda}_1^2 + 2) - 2\bar{\lambda}_1 \Phi_{0,2}^{1,2} \right] \right\} \sqrt{1 - \bar{\lambda}_1^{-2}} \right\} \Bigg\}, \tag{1.139}
\end{aligned}$$

where $L_3 = (\bar{\lambda}_1^2 - 1)^2(\bar{\lambda}_1^2 + 1)$, and the compound symbols $\Phi_{c,d}^{a,b} = a\bar{\lambda}_1^8 + b\bar{\lambda}_1^6 + c\bar{\lambda}_1^4 + d\bar{\lambda}_1^2 + 1$ are introduced for brevity (a, b, c, d are positive integer numbers, and a bar above the number indicates a negative sign). Also, Ξ_f and Ξ_e reduce to

$$\Xi_f = F \left(\sqrt{1 - \bar{\lambda}_1^{-2}}, \sqrt{-\bar{\lambda}_1^2} \right), \quad \Xi_e = E \left(\sqrt{1 - \bar{\lambda}_1^{-2}}, \sqrt{-\bar{\lambda}_1^2} \right),$$

where the functions F and E have been defined in (1.138). (Note that although $b = \sqrt{-\bar{\lambda}_1^2}$ is complex, the actual integrals in these expressions depend on b through $b^2 = -\bar{\lambda}_1^2$, which is real.)

Uniaxial Tension (UT)

For uniaxial loading in the \mathbf{e}_1 -direction (cf. Figure 1.6(b)), $\bar{\lambda}_2 = \bar{\lambda}_3 = \bar{\lambda}_1^{-1/2}$, and the TSO estimate (1.134) for $\widehat{W}(\bar{\mathbf{F}})$ reduces to

$$\begin{aligned}
\widehat{W}(\bar{\mathbf{F}}) &= (1-c)W_\mu^{(1)}(\bar{\mathbf{F}}^{(1)}) - \frac{c}{1-c}\mu^{(1)} \\
&\quad \times \left\{ \bar{\lambda}_1^{7/2} \left[-3\bar{\lambda}_1^3 \Upsilon \tanh^{-1}(\Upsilon)^2 + (\bar{\lambda}_1^3 - 1)^2 \tanh^{-1}(\Upsilon) + (\bar{\lambda}_1^3 + \bar{\lambda}_1^6 - 2)\Upsilon \right] \right\}^{-1} \\
&\quad \times \left\{ \left[2\bar{\lambda}_1^5(2\bar{\lambda}_1^3 - 6\bar{\lambda}_1^2 - 3\bar{\lambda}_1 + 1) - \bar{\lambda}_1^{7/2}(2\bar{\lambda}_1^6 - 3\bar{\lambda}_1^5 + 3\bar{\lambda}_1^4 - 15\bar{\lambda}_1^3 + 1) \right] \Upsilon \tanh^{-1}(\Upsilon)^2 \right. \\
&\quad + (\bar{\lambda}_1 - 1)^2(\bar{\lambda}_1^2 + \bar{\lambda}_1 + 1)^2 \left[2\bar{\lambda}_1^2(\bar{\lambda}_1 + 1)(2\bar{\lambda}_1 - 1) - \sqrt{\bar{\lambda}_1}(\bar{\lambda}_1^5 - \bar{\lambda}_1^4 + 5\bar{\lambda}_1^3 - 1) \right] \tanh^{-1}(\Upsilon) \\
&\quad \left. + (\bar{\lambda}_1 - 1)(\bar{\lambda}_1^2 + \bar{\lambda}_1 + 1) \left[2\bar{\lambda}_1^3(2\bar{\lambda}_1^4 + \bar{\lambda}_1^3 - 3\bar{\lambda}_1^2 + 4\bar{\lambda}_1 + 2) - \bar{\lambda}_1^{7/2}(\bar{\lambda}_1^5 - \bar{\lambda}_1^4 + 3\bar{\lambda}_1^3 + 2\bar{\lambda}_1^2 - 2\bar{\lambda}_1 + 9) \right] \Upsilon \right\} \tag{1.140}
\end{aligned}$$

where $\Upsilon = \sqrt{(\bar{\lambda}_1^3 - 1)/\bar{\lambda}_1^3}$.

Equibiaxial Tension (ET)

For equibiaxial loading (cf. Figure 1.6(c)), $\bar{\lambda}_3 = \bar{\lambda}_2^{-2} = \bar{\lambda}_1^{-2}$, and the TSO estimate (1.134) reduces to

$$\begin{aligned} \widehat{W}(\bar{\mathbf{F}}) &= (1-c) W_\mu^{(1)}(\bar{\mathbf{F}}^{(1)}) - \frac{c}{1-c} \mu^{(1)} \bar{\lambda}_1^{-4} \\ &\times \left\{ 3\bar{\lambda}_1^6 \sqrt{\bar{\lambda}_1^6 - 1} \left[\tan^{-1}(\sqrt{\bar{\lambda}_1^6 - 1}) \right]^2 + (\bar{\lambda}_1^6 - 1)^2 \left[\tan^{-1}(\sqrt{\bar{\lambda}_1^6 - 1}) \right] - (\bar{\lambda}_1^6 - 1)^{3/2} (2\bar{\lambda}_1^6 + 1) \right\}^{-1} \\ &\times \left\{ \bar{\lambda}_1^4 \sqrt{\bar{\lambda}_1^6 - 1} (\bar{\lambda}_1^{12} - 2\bar{\lambda}_1^9 + 6\bar{\lambda}_1^7 - 15\bar{\lambda}_1^6 + 12\bar{\lambda}_1^5 + 3\bar{\lambda}_1^4 - 4\bar{\lambda}_1^3 - 3\bar{\lambda}_1^2 + 2) \left[\tan^{-1}(\sqrt{\bar{\lambda}_1^6 - 1}) \right]^2 \right. \\ &+ (\bar{\lambda}_1^6 - 1)^2 (\bar{\lambda}_1^{10} - 2\bar{\lambda}_1^7 + 2\bar{\lambda}_1^5 - 5\bar{\lambda}_1^4 + 4\bar{\lambda}_1^3 + \bar{\lambda}_1^2 - 1) \left[\tan^{-1}(\sqrt{\bar{\lambda}_1^6 - 1}) \right] \\ &\left. - (\bar{\lambda}_1^6 - 1)^{3/2} (\bar{\lambda}_1 - 1)^2 (4\bar{\lambda}_1^9 - \bar{\lambda}_1^8 + 2\bar{\lambda}_1^7 + 7\bar{\lambda}_1^6 + 6\bar{\lambda}_1^5 + 3\bar{\lambda}_1^4 + 2\bar{\lambda}_1^3 - 2\bar{\lambda}_1^2 - 2\bar{\lambda}_1 - 1) \right\}. \quad (1.141) \end{aligned}$$

It is worth emphasizing that for UT and ET loadings, the expressions for the effective stored-energy functions do not contain elliptic integrals. Moreover, it should be mentioned that the effective stored-energy functions (1.139) to (1.141) are all strongly elliptic (strictly rank-one convex). This observation can be verified by means of the conditions provided by Zee and Sternberg (1983) for strong ellipticity of isotropic hyperelastic materials.

1.6.2 Results for Gent Elastomers and Discussion

In this subsection, we present some specific results for the stress-stretch relations arising from the TSO estimates for general triaxial loading of elastomeric composites consisting of Gent (or neo-Hookean) elastomers reinforced by isotropic distributions of spherical particles. As discussed in the previous section for the three particular loadings (PS, UT, ET), there is only one loading parameter, and we will depict all results here as functions of $\bar{\lambda}_1 = \bar{\lambda}$. The results correspond to several volume fractions, $c = 0.1, 0.2, 0.3$, lock-up parameters, $J_m = 50, 100, 500, \infty$, and are normalized by the ground-state shear moduli ($\mu^{(1)} = 1$). It is recalled that the case $J_m \rightarrow \infty$ corresponds to an incompressible neo-Hookean matrix, so that the corresponding results are calculated by making use of the explicit expressions (1.139) to (1.141).

Figures 1.7 to 1.9 shows plots for the new TSO estimates for the macroscopic stress $\bar{S} = \partial \widehat{W} / \partial \bar{\lambda}$ in the particles-reinforced elastomers, as functions of the applied stretch $\bar{\lambda}$, for pure shear, uniaxial tension and equibiaxial tension, respectively. Parts (a) of the figures show the results for composites with neo-Hookean matrices at various particle volume fractions, while parts (b) shows the corresponding results for composites with Gent matrices with several values of J_m , for a given volume fraction of particles $c = 0.1$. It is seen from these figures that the volume fraction of the reinforcing particles has a strong effect on the overall response of the reinforced elastomer, for all three loading types. On the other hand, the strain-locking parameter J_m in the Gent elastomers can also be seen to have a strong effect on the macroscopic response of the reinforced elastomer. In addition, it

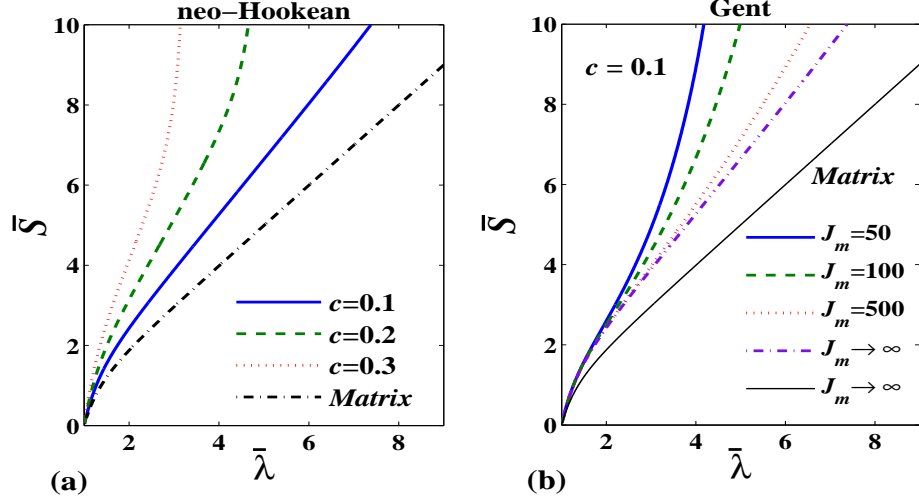


Figure 1.7: New tangent second-order (TSO) estimates for the macroscopic stress $\bar{S} = d\widehat{W}/d\bar{\lambda}$ in particle-reinforced elastomers under pure shear loading ($\bar{\lambda}_3 = 1$, $\bar{\lambda}_2 = 1/\bar{\lambda}_1$), as functions the applied stretch $\bar{\lambda}_1 = \bar{\lambda}$. (a) neo-Hookean matrix for different values of the fiber volume fraction (b) Gent matrix for different matrix lock-up parameters.

should be emphasized that the differences observed in the response of the three different loadings are due in part to the different ways in which the results are presented. Of course, the results are consistent in the limit of small strains with the results of linear elasticity, and therefore independent of the loading conditions. However, as we will see below, there is an intrinsic effect of the loading conditions for large strains.

Figure 1.10 shows plots for the “lock-up” stretch in particle-reinforced, Gent elastomers. As already mentioned in the context of the fiber-reinforced elastomers in Section 1.5, the composite may undergo either “geometric” or “material” lock up. Thus, Figure 1.10 shows plots of the stretch $\bar{\lambda}_1^{lock}$ at which lock up first takes place for a given loading path. The results are given for three particular loadings: Pure shear (PS), Uniaxial tension (UT) and Equibiaxial tension (ET). The corresponding geometric lock up condition are given by $\bar{\lambda}_1 = c^{-1}$, $\bar{\lambda}_1 = c^{-2}$ and $\bar{\lambda}_1 = c^{-1/2}$, respectively, while those for material lock up are given by

$$\begin{aligned}
 \bar{\lambda}_1^4 - 2\bar{\lambda}_1^3 c - [(1-c)^2 J_m - 4c + 2] \bar{\lambda}_1^2 - 2\bar{\lambda}_1 c + 1 &= 0, \\
 \bar{\lambda}_1^3 - 2\bar{\lambda}_1^2 c - [(1-c)^2 J_m - 6c + 3] \bar{\lambda}_1 - 4c\sqrt{\bar{\lambda}_1} + 2 &= 0, \\
 2\bar{\lambda}_1^6 - 4\bar{\lambda}_1^5 c - [(1-c)^2 J_m + 3 - 6c] \bar{\lambda}_1^4 - 2c\bar{\lambda}_1^2 + 1 &= 0,
 \end{aligned} \tag{1.142}$$

respectively. The results are shown as functions of the particle volume fraction, for fixed values of the Gent lock-up parameter $J_m = 50, 100, 500$. The main observation in this figure is the transition from material lock up to geometric lock up as the particle concentration is increased. Thus, for smaller volume fraction the lock-up stretch is associated with the material lock up (depicted as “straight” lines). On the other hand, for sufficiently large volume fraction (depending on the specific loading),

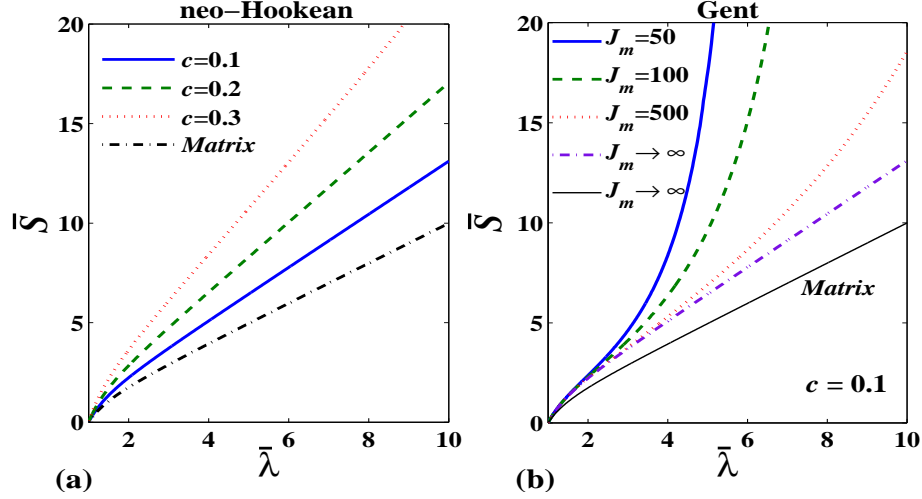


Figure 1.8: New TSO estimates for the macroscopic stress $\bar{S} = d\widehat{W}/d\bar{\lambda}$ in particle-reinforced elastomers under uniaxial tension loading ($\bar{\lambda}_2 = \bar{\lambda}_3 = \bar{\lambda}_1^{-1/2}$), as functions the applied stretch $\bar{\lambda}_1 = \bar{\lambda}$. (a) neo-Hookean matrix for different values of the fiber volume fraction (b) Gent matrix for different matrix lock-up parameters.

the lock up switches to the geometric (curved lines). It is also seen that the addition of rigid particles enhances the material lock-up effect, with respect to the homogenous matrix phase. This is related to the fact that the rigid phase cannot deform under deformation and all the deformation must be “concentrated” in the matrix, leading to a smaller effective lock-up stretch for the composite.

As discussed in Subsection 1.5.4, the accuracy of the TSO results is expected to deteriorate as geometric and material lock-up conditions are approached. For this reason, Figure 1.10 could be interpreted as providing an estimate for the range of validity of the TSO results in terms of the maximum applied stretch $\bar{\lambda}$ for given particle concentration and loading condition. Clearly, the range of validity of the estimates decreases with increasing the particle volume fraction. Thus, it is evident from the plot that UT loading has a relatively larger range of validity, while the range of validity for ET loading is more restricted with increasing values of c . For instance, for composites with a Gent matrix and fixed particle volume fraction $c=0.2$ and lock-up parameter $J_m = 500$, the range of validity for PS, UT and ET loadings can be estimated as $1 \leq \bar{\lambda} \leq 4.5$, $1 \leq \bar{\lambda} \leq 17$ and $1 \leq \bar{\lambda} \leq 2.3$, respectively.

Finally, Figures 1.11(a) and (b) present plots of the effective stored-energy function of the composite versus the macroscopic invariants $\bar{I}_1 = \bar{\lambda}_1^2 + \bar{\lambda}_2^2 + \bar{\lambda}_3^2$ and $\bar{I}_2 = \bar{\lambda}_1^2\bar{\lambda}_2^2 + \bar{\lambda}_2^2\bar{\lambda}_3^2 + \bar{\lambda}_3^2\bar{\lambda}_1^2$ of the deformation, respectively. The matrix is assumed to be neo-Hookean and results for a non-reinforced matrix are also included for comparison. It is observed in Figure 11a that the effective behavior for the composite differs noticeably for the three particular loading conditions (i.e., for PS, UT and ET loadings), while the corresponding behaviors for a homogenous neo-Hookean matrix are all identical. More specifically, it can be seen that the response for ET loading becomes increasingly stiffer with the deformation, while the responses for PS and UT loadings remain close to each other and are more compliant. Given that the material response (as gauged by the matrix response) is the same,

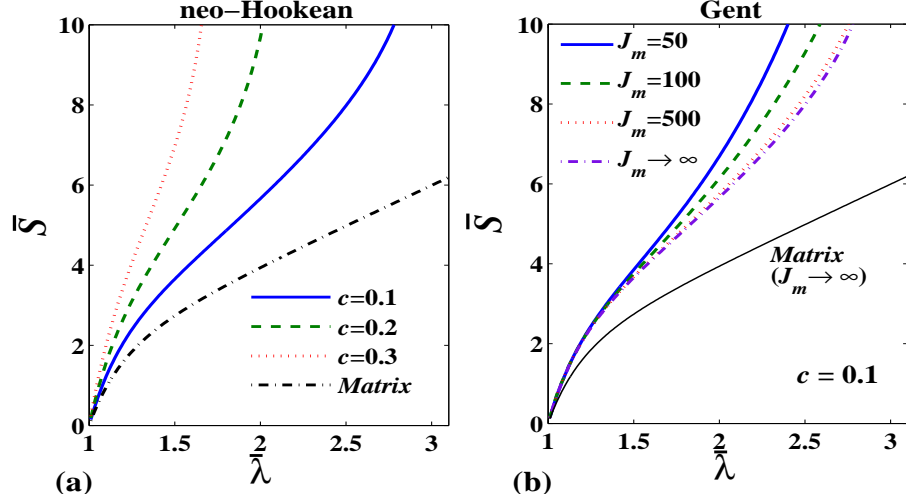


Figure 1.9: New TSO estimates for the macroscopic stress $\bar{S} = d\widehat{W}/d\bar{\lambda}$ in particle-reinforced elastomers under equibiaxial tension loading ($\bar{\lambda}_3 = \bar{\lambda}_2^{-2} = \bar{\lambda}_1^{-2}$), as functions the applied stretch $\bar{\lambda}_1 = \bar{\lambda}$. (a) neo-Hookean matrix for different values of the fiber volume fraction (b) Gent matrix for different matrix lock-up parameters.

the differences observed in the response of the composite must be attributed to the differences in the evolution of the microstructures for the different loading conditions. Figure 1.11(b) shows results for the effective stored-energy function of the composite as a function of the second invariant \bar{I}_2 , for two different, fixed values of the first invariant \bar{I}_1 . The corresponding results for the matrix phase are also included for comparison purposes. Thus, it can be seen that \bar{I}_2 has a strong effect on the macroscopic response of the composite, while the matrix material exhibits no such effect. This phenomenon is a consequence of the nonlinear response of the composite, leading to dependence on the second invariant of the deformation. (Note that dependence on third invariant would also be expected in general, but it is excluded here due to overall incompressibility of material).

1.7 Concluding Remarks

In this chapter, we have developed new constitutive models for the macroscopic response of composites with hyperelastic phases and particulate microstructures, subjected to general, three-dimensional, finite deformations. For this purpose, we have made use of a suitable extension of the tangent second-order (TSO) homogenization theory of Ponte Castañeda and Tiberio (2000), which is capable of accounting for the strongly nonlinear overall incompressibility constraint (for incompressible behavior of the phases), as well as for the reorientation of the particles with the deformation. Thus, for incompressible elastomers reinforced with random distributions of aligned, ellipsoidal, rigid inclusions, the expression (1.77) was derived for the macroscopic stored-energy function $\widehat{W}(\bar{\mathbf{F}})$ in terms of equation (1.79) for the evolution of the particle orientation $\bar{\mathbf{R}}^{(2)}$, the stored-energy function $W_\mu^{(1)}$ of the elastomeric phase (with ground-state shear modulus $\mu^{(1)}$), the initial concentration of the particles c , and a certain microstructural tensor \mathbf{E}^I , serving to characterize the particle shape, and defined

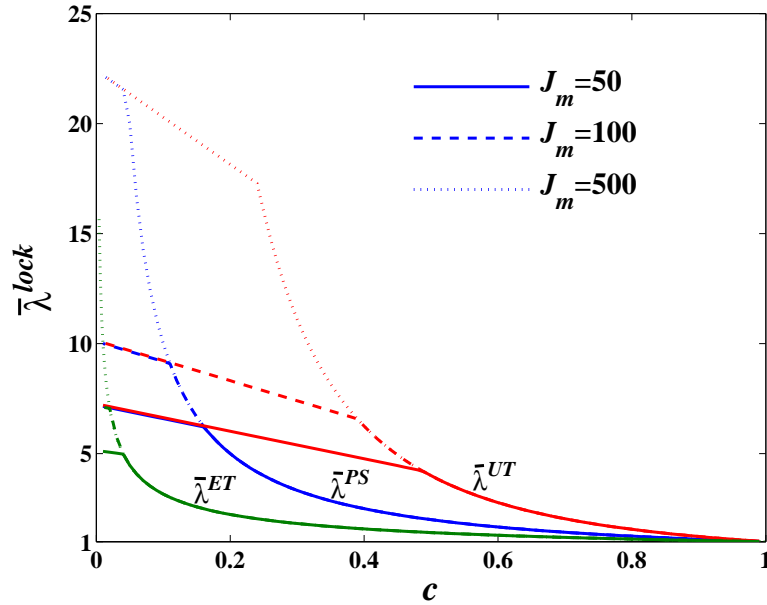


Figure 1.10: TSO estimates for the macroscopic stretch, $\bar{\lambda}_1^{lock}$, at which a particle-reinforced incompressible Gent elastomer locks up under three different loadings: Pure shear (PS), Uniaxial tension (UT) and Equibiaxial tension (ET). The results are shown as a function of particle concentration c for different values of the matrix lock-up parameter J_m .

by expression (1.106). In particular, closed-form, analytical results were obtained for neo-Hookean rubbers reinforced by isotropic distributions of spherical particles under general loading conditions (see expressions (1.134) to (1.141)). For this case, it was found that the macroscopic stored-energy function exhibits dependence on the second invariant of the right Cauchy–Green deformation tensor (even when the matrix response is assumed to depend only on the first invariant), in agreement with theoretical expectations. In addition, it was also found that the macroscopic response of Gent-type elastomers reinforced with isotropic distributions of spherical particles is strongly elliptic, and therefore shear-band localization instabilities of the type found by Lopez-Pamies and Ponte Castañeda (2006b) and Agoras et al. (2009b) for fiber-reinforced composites loaded in compression along the long axis of the fibers were not found in this case.

The TSO theory was also tested for a 2-D problem consisting of transverse shear loading of elastomers reinforced with cylindrical fibers of elliptical cross-section, where it was found to recover exactly the generalized second-order (GSO) results of Lopez-Pamies and Ponte Castañeda (2006a) for dilute concentration of elliptical fibers in a neo-Hookean elastomeric matrix. For more general material behavior (e.g., Gent) and non-dilute conditions, the new TSO theory is still in relatively good agreement with the GSO predictions, although it can lead to much stiffer predictions for neo-Hookean matrix behavior, when the TSO theory predicts “geometric” lock up, at sufficiently large deformations. However, for more realistic situations, when lock up due to the matrix behavior is present, the differences are relatively minor. In any case, comparisons with FEM simulations for

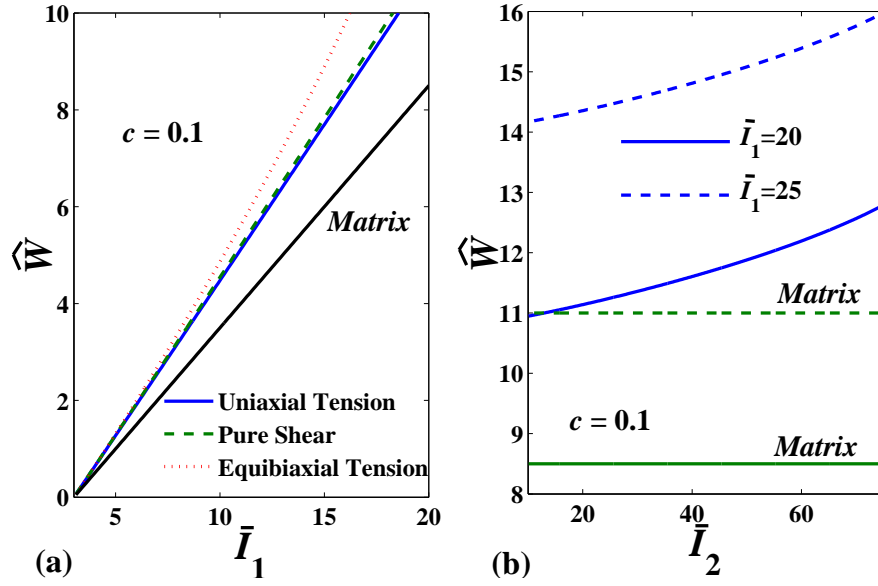


Figure 1.11: NewTSO estimates for the effective response of a rigidly particle-reinforced elastomer with an incompressible neo-Hookean matrix. (a) The effective energy $\langle \widehat{W} \rangle$ versus the macroscopic invariant \bar{I}_1 under three different loadings: Pure shear (PS), Uniaxial tension (UT) and Equibiaxial tension (ET) (b) The effective energy $\langle \widehat{W} \rangle$ versus the invariant \bar{I}_2 for two different values of the invariant \bar{I}_1 .

realistic values of the matrix locking strain and macroscopic stretches, are in excellent agreement even for relatively high concentrations (i.e., up to 30 %).

It should be emphasized that while there are presently other homogenization theories for hyperelastic composites (e.g., the GSO (Lopez-Pamies and Ponte Castañeda, 2006a) and sequentially laminated (deBotton, 2005) homogenization methods), the new TSO method developed in this work offers a good balance of generality and accuracy. Indeed, to the best of our knowledge, the TSO estimates developed in this work are the first homogenization estimates for reinforced elastomers with *general* particle shape. While only the case of spherical inclusions has been developed in detail here, results are also available for the response of elastomers reinforced with ellipsoidal inclusions under general (non-aligned) loading conditions. Due to the anisotropy of these material systems and the important effects of particle reorientation, which can lead to loss of ellipticity of the macroscopic response, the analysis of these results is quite a bit more involved and will be considered in detail in a future publication.

Chapter 2

Application of the TSO theory to short fiber-reinforced composites: I–Analytical results

In this chapter, we present a homogenization-based constitutive model for the mechanical behavior of non-spherical particle-reinforced elastomers with random microstructures subjected to finite deformations. The model is based on the improved version of the tangent second-order (TSO) method, developed in Chapter 1, for two-phase, hyperelastic composites, and is able to directly account for the shape, orientation, and concentration of the particles. After a brief summary of the TSO homogenization method, we describe its application to composites consisting of an incompressible rubber reinforced by aligned, spheroidal, rigid particles, undergoing generally non-aligned, three-dimensional loadings. While the results are valid for finite particle concentrations, in the dilute limit they can be viewed as providing a generalization of Eshelby’s results in linear elasticity. In particular, we provide analytical estimates for the overall response and microstructure evolution of the particle-reinforced composites with generalized neo-Hookean matrix phases under non-aligned loadings. For the special case of aligned pure shear and axisymmetric shear loadings, we give closed-form expressions for the effective stored-energy function of the composites with neo-Hookean matrix behavior. Moreover, we investigate the possible development of “macroscopic” (shear band-type) instabilities in the homogenized behavior of the composite at sufficiently large deformations. These instabilities whose wavelengths are much larger than the typical size of the microstructure are detected by making use of the loss of strong ellipticity condition for the effective stored-energy function of the composites. The analytical results presented in this chapter will be complemented in the next chapter by specific applications for several representative microstructures and loading configurations.

2.1 Introduction

For the purposes of the present chapter, the most relevant work was carried out by Lopez-Pamies and Ponte Castañeda (2006b) for random distributions of rigid elliptical fibers in an elastomeric phase, or more precisely for plane strain loading of continuous fiber-reinforced elastomers in the transverse plane where the fibers exhibit elliptical cross-section. These estimates demonstrated for the first time the strong effect of particle rotations, which, under certain conditions, could induce strong geometric softening leading to the possible development of macroscopic instabilities through loss of ellipticity. These homogenization estimates were also compared with full-field numerical simulations by Moraleda et al. (2009) and found to be in fairly good quantitative agreement at least for neo-Hookean matrix phases. The existence of long wave length instabilities (Geymonat et al., 1993), as well as other types of “microscopic” instabilities, in the context of two-dimensional fiber-reinforced composites with periodic microstructures has also been documented recently (Michel et al., 2010).

As already mentioned, in this chapter, we will make use of the improved version of the TSO method, developed in Chapter 1, to investigate the effect of particle shape on the macroscopic response, microstructure evolution and macroscopic instabilities in short-fiber-reinforced elastomers subjected to general finite-strain loadings. As mentioned in Chapter 1, the resulting estimates of this method for the macroscopic response of the reinforced elastomers are consistent with the overall incompressibility constraint, expected on physical grounds. Also, the TSO method is able to provide analytical estimates for the evolution of the relevant microstructural variables, including most notably the rotation of the ellipsoidal particles under general loading conditions. In particular,

we verified in Chapter 1 that the improved version of the TSO method leads to predictions that are very similar—and in some cases identical—to the predictions of the more sophisticated GSO method (Lopez-Pamies and Ponte Castañeda, 2006a), at least for the case of two-dimensional elliptical particles (Lopez-Pamies and Ponte Castañeda, 2006b). In this context, it should be noted that the GSO method requires the use of the field fluctuations in the linear comparison composite and is therefore more difficult to implement, especially for the complex three-dimensional microstructures of interest in this work.

The structure of this chapter is as follows. For convenience and clarity, Sections 2.2 and 2.3 summarize the basic elements of the nonlinear homogenization methods and, in particular, the tangent second-order theory developed in Chapter 1. Section 2.4 deals with the specific application of the TSO theory for elastomers reinforced with aligned, rigid, spheroidal particles. This section includes closed-form, analytical expressions for the homogenized stored-energy function of transversely isotropic, reinforced elastomers with neo-Hookean matrix phases under aligned, triaxial loading conditions (see expressions (2.35), (2.39), and (2.42)). Section 2.5 spells out the general conditions of strong ellipticity used to determine the “macroscopic” instabilities for incompressible, transversely isotropic, hyperelastic composites under aligned and non-aligned loading conditions. These conditions are provided in terms of appropriate traces of the associated effective incremental modulus tensor, which, in turn, can be written in terms of the derivatives of the associated effective stored-energy function with respect to the macroscopic kinematical variables. Then, these conditions are specialized for the class of (rigid) particle-reinforced elastomers undergoing *axisymmetric* and *pure* shear loading conditions. Finally, some conclusions are drawn in Section 2.6. In the next chapter, use will be made of the analytical results presented in Sections 2.4 and 2.5 of this chapter to investigate in more detail the influence of the microgeometry, matrix properties, and loading conditions on the effective constitutive behavior of the reinforced elastomers, including the associated microstructure evolution and the possible development of macroscopic instabilities.

2.2 Preliminaries on hyperelastic composites and their effective behavior

Consider a specimen consisting of several families of aligned, ellipsoidal particles, distributed randomly in a matrix phase, and occupying a volume Ω_0 with boundary $\partial\Omega_0$ in the undeformed configuration. Following the hypothesis of *separation of length scales*, we will assume that the characteristic length-scale of the particles is much smaller than the size of the specimen as well as the scale of variation of the loading conditions. Let the position vector of a material point in the undeformed configuration Ω_0 be denoted by \mathbf{X} , with Cartesian components X_i , $i \in \{1, 2, 3\}$, and the corresponding position vector in the deformed configuration Ω be denoted by \mathbf{x} , with components x_i . The deformation gradient tensor represented by \mathbf{F} has components $F_{ij} = \partial x_i / \partial X_j$ and is required to satisfy the material *impenetrability* condition: $J = \det \mathbf{F}(\mathbf{X}) > 0$ for all $\mathbf{X} \in \Omega_0$. In addition, let $\mathbf{F} = \mathbf{R}\mathbf{U}$ where \mathbf{U} and \mathbf{R} stand for the stretch and (*rigid-body*) rotation tensors, respectively, and let $\mathbf{C} = \mathbf{F}^T \mathbf{F} = \mathbf{U}^2$ denote the right Cauchy–Green deformation tensor.

We assume that the constitutive behavior of the phases is purely elastic and characterized by the stored-energy functions $W^{(r)}(\mathbf{F})$ ($r = 1, \dots, N$), which are taken to be *nonconvex* functions of the deformation gradient tensor \mathbf{F} . Also, the stored-energy functions $W^{(r)}(\mathbf{F})$ are assumed to be objective, namely, $W^{(r)}(\mathbf{Q}\mathbf{F}) = W^{(r)}(\mathbf{F})$ for all proper orthogonal tensors \mathbf{Q} and arbitrary deformation gradients \mathbf{F} , so that $W^{(r)}(\mathbf{F}) = W^{(r)}(\mathbf{U})$. In this work, we restrict our attention to the special case of composites made up of incompressible isotropic phases, and it proves useful, for later use, to introduce the following decomposition for the stored-energy function

$$W^{(r)}(\mathbf{F}) = W_{\mu}^{(r)}(\mathbf{F}) + \frac{1}{2}\mu'^{(r)}(J-1)^2, \quad (2.1)$$

where $W_{\mu}^{(r)}$ denotes the “distortional” component of $W^{(r)}$ and depends on the ground-state shear modulus $\mu^{(r)}$, while the second term depending on the Lamé parameter $\mu'^{(r)}$ characterizes the “volumetric” response of phase r . In other words, $W_{\mu}^{(r)}$ is that part of the stored-energy function $W^{(r)}$ which does not depend on $\mu'^{(r)}$. It is a simple matter to verify from (2.1) that the incompressibility constraint $J = 1$ is recovered by letting the parameter $\mu'^{(r)}$ tend to infinity.

The first Piola-Kirchhoff stress in phase r is then given by the expression

$$\mathbf{S} = \frac{\partial W^{(r)}}{\partial \mathbf{F}}(\mathbf{F}). \quad (2.2)$$

In this connection, it is useful to also define

$$\mathbf{S}_{\mu}^{(r)}(\mathbf{F}) = \frac{\partial W_{\mu}^{(r)}}{\partial \mathbf{F}}(\mathbf{F}), \quad (2.3)$$

such that

$$\mathbf{S} = \mathbf{S}_{\mu}^{(r)}(\mathbf{F}) + \mu'^{(r)}J(J-1)\mathbf{F}^{-T}. \quad (2.4)$$

In addition, consistent with the definition (2.1), the incremental *tangent* modulus tensor for the phase r can be decomposed as

$$\mathbf{L}^{(r)}(\mathbf{F}) = \frac{\partial^2 W^{(r)}}{\partial \mathbf{F} \partial \mathbf{F}} = \mathbf{L}_{\mu}^{(r)} + \mu'^{(r)}\mathbf{L}_{-1}^{(r)}, \quad (2.5)$$

where

$$\mathbf{L}_{\mu}^{(r)}(\mathbf{F}) = \frac{\partial^2 W_{\mu}^{(r)}}{\partial \mathbf{F} \partial \mathbf{F}}, \quad \text{and} \quad \mathbf{L}_{-1}^{(r)}(\mathbf{F}) = J(2J-1)\mathbf{F}^{-T} \otimes \mathbf{F}^{-T} + J(J-1)\boldsymbol{\mathcal{X}}, \quad (2.6)$$

with $\boldsymbol{\mathcal{X}}$ denoting the fourth-order tensor with components $\mathcal{X}_{ijkl} = -F_{li}^{-1}F_{jk}^{-1}$.

Next, the local energy function of the composite is defined as

$$W(\mathbf{X}, \mathbf{F}) = \sum_{r=1}^N \chi^{(r)}(\mathbf{X}) W^{(r)}(\mathbf{F}), \quad (2.7)$$

where the characteristic functions $\chi^{(r)}$, describing the distribution of the phases in the reference configuration, are such that they equal 1 if the position vector \mathbf{X} is inside the phase r (*i.e.*, $\mathbf{X} \in \Omega_0^{(r)}$)

and zero otherwise. Following Hill (1972), the effective, or macroscopic stored-energy function \widetilde{W} of the composite elastomer is given by

$$\widetilde{W}(\bar{\mathbf{F}}) = \min_{\mathbf{F} \in K(\bar{\mathbf{F}})} \langle W(\mathbf{X}, \mathbf{F}) \rangle = \min_{\mathbf{F} \in K(\bar{\mathbf{F}})} \sum_{r=1}^N c_0^{(r)} \langle W^{(r)}(\mathbf{F}) \rangle^{(r)}, \quad (2.8)$$

where $K(\bar{\mathbf{F}})$ denotes the set of kinematically admissible deformation gradients defined by

$$K(\bar{\mathbf{F}}) = \{ \mathbf{F} | \exists \mathbf{x} = \mathbf{x}(\mathbf{X}) \text{ with } \mathbf{F} = \text{Grad } \mathbf{x} \text{ and } J > 0 \text{ in } \Omega_0, \mathbf{x} = \bar{\mathbf{F}} \mathbf{X} \text{ on } \partial\Omega_0 \}. \quad (2.9)$$

In the above expressions, the triangular brackets $\langle \cdot \rangle$ represent volume averages (in the undeformed configuration) over a representative volume element (RVE) Ω_0 of the composite, while $\langle \cdot \rangle^{(r)}$ denote volume averages (in the undeformed configuration) over the phases $\Omega_0^{(r)}$, so that the scalar $c_0^{(r)} = \langle \chi^{(r)} \rangle$ indicates the initial volume fraction of the phase r . Noting that under the above-defined affine boundary condition $\langle \mathbf{F} \rangle = \bar{\mathbf{F}}$, and defining the average stress $\bar{\mathbf{S}} = \langle \mathbf{S} \rangle$, the effective constitutive relation for the composite is then given by (Hill, 1972)

$$\bar{\mathbf{S}} = \frac{\partial \widetilde{W}}{\partial \bar{\mathbf{F}}}(\bar{\mathbf{F}}). \quad (2.10)$$

At this point, it should be remarked that the solution (assuming that it exists) of the Euler-Lagrange equations associated with the variational problem (2.8) is expected to be unique in some neighborhood of $\bar{\mathbf{F}} = \mathbf{I}$ (where \mathbf{I} is the second-order identity tensor), and gives the minimum energy. However, as the deformation increases into the finite deformation regime, it may reach a point at which the solution of the Euler-Lagrange equations (referred to as the ‘‘principal’’ solution and denoted by $\widehat{W}(\bar{\mathbf{F}})$) is not unique anymore, and other kinematically admissible solutions corresponding to a lower energy might exist (which, according to (2.8), is labeled \widetilde{W}). This point corresponds to the possible onset of an *instability*, beyond which the applicability of the ‘‘principal’’ solution becomes questionable. In the context of hyperelastic composites with periodic microstructures, it is known (Geymonat et al., 1993; Triantafyllidis et al., 2006) that the first instability may be ‘‘microscopic’’ with wavelengths comparable to the size of the inhomogeneities, or they may be ‘‘macroscopic’’ with wavelengths comparable to the size of the RVE. However, for composites with random microstructures, it may be expected (Michel et al., 2010) that the first instability should actually be macroscopic. On the other hand, it is also known (Triantafyllidis and Marker, 1985; Geymonat et al., 1993) that the ‘‘macroscopic’’ instabilities can be determined from the loss of *strong ellipticity* of the effective stored-energy function of the material evaluated at the above-described ‘‘principal’’ solution. For these reasons, in this work we will only be concerned with the principal solution \widehat{W} , whose range of validity will be estimated by evaluation of the associated loss of ellipticity condition.

Following up on the preceding remarks, we finish this section by spelling out the condition of strong ellipticity (SE) for the effective stored-energy function $\widehat{W}(\bar{\mathbf{F}})$. In the context of hyperelastic materials, the SE condition for the homogenized composite elastomers characterized by the stored-energy function $\widehat{W}(\bar{\mathbf{F}})$ is equivalent to the positive-definiteness of the associated acoustic tensor $\widehat{\mathbf{K}}$,

namely, $\widehat{W}(\bar{\mathbf{F}})$ is said to be *strongly elliptic* if and only if

$$\widehat{K}_{ik} m_i m_k = \widehat{L}_{ijkl} N_j N_l m_i m_k > 0, \quad (2.11)$$

for all non-zero pairs of unit vectors \mathbf{N} and \mathbf{m} . Here, $\widehat{K}_{ik} = \widehat{L}_{ijkl} N_j N_l$ is the effective acoustic tensor, and, the fourth-order tensor $\widehat{\mathbf{L}}$, defined by

$$\widehat{\mathbf{L}} = \frac{\partial^2 \widehat{W}}{\partial \bar{\mathbf{F}} \partial \bar{\mathbf{F}}}, \quad (2.12)$$

denotes the incremental effective moduli tensor of the composite material characterizing the overall incremental response of the composite elastomer. It is also worth mentioning that the tensor \widehat{L}_{ijkl} possesses major symmetry ($\widehat{L}_{ijkl} = \widehat{L}_{klij}$), but not generally minor symmetries ($\widehat{L}_{ijkl} \neq \widehat{L}_{jilk}$).

2.3 Tangent second-order homogenization estimates

In this section, we briefly recall the tangent second-order variational method developed in Chapter 1 for the effective constitutive behavior of (two-phase) particle-reinforced, hyperelastic composites consisting of aligned, ellipsoidal, rigid particles distributed randomly with volume fraction c in an incompressible matrix phase with energy function $W_\mu^{(1)}$. (Note that since particles are rigid and the matrix is incompressible, $c = c_0^{(2)}$ for all macroscopic deformations.) As already mentioned, the TSO method makes use of a fictitious “linear comparison composite” (LCC) with the same microstructure (i.e., same characteristic functions $\chi^{(r)}(\mathbf{X})$) as the actual (nonlinear) composite material (in the undeformed configuration). The moduli of the constituent phases in the LCC are identified with “tangent” linearizations of the given nonlinear phases evaluated at the macroscopic deformation gradient $\bar{\mathbf{F}}$. This allows the use of already available methods for estimating the effective behavior of linear composites to generate corresponding estimates for nonlinear composites. In Chapter 1, we made use of the generalized Hashin-Shtrikman estimates of the Willis type (Willis, 1977; Ponte Castañeda and Willis, 1995) for the effective behavior of the linear-elastic composite materials consisting of random distributions of aligned ellipsoidal particles with prescribed “ellipsoidal symmetry” for the particle centers (i.e., the two-point correlation functions). These estimates are exact to second-order in the heterogeneity contrast and to first order in the particle volume fraction, and are known to be quite accurate for the type of “particulate” microstructures of interest here, up to moderate concentrations of particles. In order to ensure compliance with the overall incompressibility constraint ($\bar{J} = \det(\bar{\mathbf{F}}) = 1$), in Chapter 1, we made use of the expression (2.1) to split the distortional and deviatoric components of the energy and arrived at the following estimate for the effective stored-energy function $\widehat{W}(\bar{\mathbf{F}})$ of the reinforced elastomers:

$$\widehat{W}(\bar{\mathbf{F}}) = (1 - c)W_\mu^{(1)}(\bar{\mathbf{F}}^{(1)}) + \frac{1}{2} \frac{c}{1 - c} (\bar{\mathbf{F}} - \bar{\mathbf{R}}^{(2)}) \cdot \mathbf{E} (\bar{\mathbf{F}} - \bar{\mathbf{R}}^{(2)}). \quad (2.13)$$

In this expression, $\bar{\mathbf{F}}$ is the macroscopic deformation which satisfies the incompressibility condition $\det(\bar{\mathbf{F}}) = 1$, $\bar{\mathbf{R}}^{(2)}$ is a second-order orthogonal tensor characterizing the average rotation of the

rigid particles under the macroscopic deformation gradient $\bar{\mathbf{F}}$, and determined by the kinematical equation

$$Skew \left\{ (\bar{\mathbf{R}}^{(2)})^T [\mathbf{E} (\bar{\mathbf{F}} - \bar{\mathbf{R}}^{(2)})] + (1 - c) (\bar{\mathbf{R}}^{(2)})^T \mathbf{S}_\mu^{(1)} (\bar{\mathbf{F}}^{(1)}) \right\} = \mathbf{0}, \quad (2.14)$$

where *Skew* denotes the skew-symmetric part of the quantities inside the curly brackets. Note that equation (2.14) provides in general a set of three scalar algebraic equations for the three independent components of $\bar{\mathbf{R}}^{(2)}$. The second-order tensor $\bar{\mathbf{F}}^{(1)}$ corresponds to the average deformation gradient in the matrix phase of the LCC, which can be expressed in terms of the macroscopic deformation gradient $\bar{\mathbf{F}}$, and the rotation tensor $\bar{\mathbf{R}}^{(2)}$ as

$$\bar{\mathbf{F}}^{(1)} = \frac{1}{1 - c} (\bar{\mathbf{F}} - c \bar{\mathbf{R}}^{(2)}), \quad (2.15)$$

Finally, \mathbf{E} is a fourth-order, microstructural tensor given by¹

$$\mathbf{E} = \lim_{\mu^{(1)} \rightarrow \infty} (\mathbf{P}^{-1} - \mathbf{L}^{(1)}). \quad (2.16)$$

In this relation, $\mathbf{L}^{(1)}$ is a fourth-order moduli tensor determined by the tangent modulus evaluated at the macroscopic deformation, such that

$$\mathbf{L}^{(1)} = \frac{\partial^2 W^{(1)}}{\partial \mathbf{F} \partial \mathbf{F}} (\bar{\mathbf{F}}), \quad (2.17)$$

while \mathbf{P} is an Eshelby-type (fourth-order) tensor containing information about the shape and distribution of the particles in the undeformed configuration (Ponte Castañeda and Willis, 1995). For ellipsoidal particles, distributed in an infinite matrix with the elastic modulus tensor $\mathbf{L}^{(1)}$, the components of \mathbf{P} read as

$$P_{ijkl} = \frac{1}{4\pi |\mathbf{Z}_0|} \int_{|\boldsymbol{\xi}|=1} B_{ik}(\boldsymbol{\xi}) \xi_j \xi_l \left[\boldsymbol{\xi}^T (\mathbf{Z}_0^T \mathbf{Z}_0)^{-1} \boldsymbol{\xi} \right]^{-\frac{3}{2}} dS, \quad (2.18)$$

where the symmetric, second-order tensor \mathbf{Z}_0 serves to characterize the “shape” and “orientation” of the particles in the undeformed configuration, and the tensor \mathbf{B} denotes the inverse of the acoustic tensor \mathbf{K} of the matrix with components $K_{ik} = L_{ijkl}^{(1)} \xi_j \xi_l$. In this work, we will also assume that the initial (in the undeformed configuration) “shape” and “orientation” of the two-point correlation function for the distribution of the ellipsoidal particles are identically the same as for the particles themselves, as specified by the tensor \mathbf{Z}_0 . It should be remarked that this assumption is not essential, and the shapes and orientations of the distribution functions could, in general, be different from those of the particles (Ponte Castañeda and Willis, 1995) leading to the use of two different \mathbf{P} tensors. It is also worth mentioning that all fourth-order tensors \mathbf{E} , \mathbf{P} , and $\mathbf{L}^{(1)}$ have major symmetry, but not generally minor symmetry. Furthermore, in view of definitions (2.16)-(2.18), together with the

¹In Chapter 1, the fourth-order tensor \mathbf{E} was labelled \mathbf{E}^I , but, for simplicity, the superscript *I* has been dropped here.

objectivity assumption for $W^{(1)}(\mathbf{F})$, it can be verified that

$$E_{ijkl}(\bar{\mathbf{F}}) = \bar{R}_{ip}\bar{R}_{kq}E_{pqjl}(\bar{\mathbf{U}}), \quad (2.19)$$

where $\bar{\mathbf{U}}$ and $\bar{\mathbf{R}}$ denote the macroscopic stretch and (rigid-body) rotation tensors, respectively (note that $\bar{\mathbf{F}} = \bar{\mathbf{R}}\bar{\mathbf{U}}$). Making use of (2.19) along with (2.14) and (2.15), it can be shown that expression (2.13) for $\widehat{W}(\bar{\mathbf{F}})$ satisfies the *objectivity* condition

$$\widehat{W}(\bar{\mathbf{F}}) = \widehat{W}(\bar{\mathbf{U}}). \quad (2.20)$$

In summary, for a given ellipsoidal microstructure, macroscopic loading $\bar{\mathbf{F}}$, and matrix strain energy $W^{(1)}$, the computation of the effective stored-energy function $\widehat{W}(\bar{\mathbf{F}})$ in (2.13), as well as of the associated rotation tensor $\bar{\mathbf{R}}^{(2)}$ in (2.14), requires the calculation of \mathbf{E} . As defined in (2.16), the tensor \mathbf{E} should be calculated in the incompressibility limit of the matrix phase ($\mu^{(1)} \rightarrow \infty$). To this end, in Chapter 1, we carried out a general asymptotic analysis for the computation of the tensor \mathbf{E} in the incompressibility limit ($\mu^{(1)} \rightarrow \infty$). For completeness and to maintain continuity, the procedure for computing the tensor \mathbf{E} is provided in Appendix B.1.

We conclude this section by noting that, in Chapter 1, we already considered the application of the above-described results for the special case of elastomers reinforced with spherical particles under triaxial loadings, and for the special case of composites with a neo-Hookean matrix, they derived closed-form expressions for the corresponding effective stored-energy function. In addition, they considered elastomers reinforced with two-dimensional fibers of elliptical cross-section under plane-strain loading. For the special case of composites with a neo-Hookean matrix and dilute concentration of fibers, they recovered exactly the results obtained by Lopez-Pamies and Ponte Castañeda (2006b) using the more sophisticated GSO method. In addition, for finite concentrations of particles and Gent-type matrices, the agreement of the TSO and GSO results was quite good. In the present work, we will consider for the first time applications for elastomers reinforced with three-dimensional spheroidal fibers.

2.4 Application to composites with rigid spheroidal particles

In the previous section, we summarized the results for estimating the effective stored-energy function and the associated evolution of the microstructure for rigidly reinforced elastomeric composites with general “ellipsoidal microstructure.” The aim of this section is to make use of these results to generate corresponding estimates of the Willis-type for elastomers reinforced with a random distribution of aligned, *spheroidal* particles subjected to finite deformations. Our goal here is to provide explicit analytical estimates when possible; otherwise, numerical calculation of the aforementioned estimates is carried out. In the following paragraphs, we provide detailed description on the microstructural configurations, constitutive behavior of the elastomeric matrix phase, and the applied macroscopic loading for the class of composites of interest in this work.

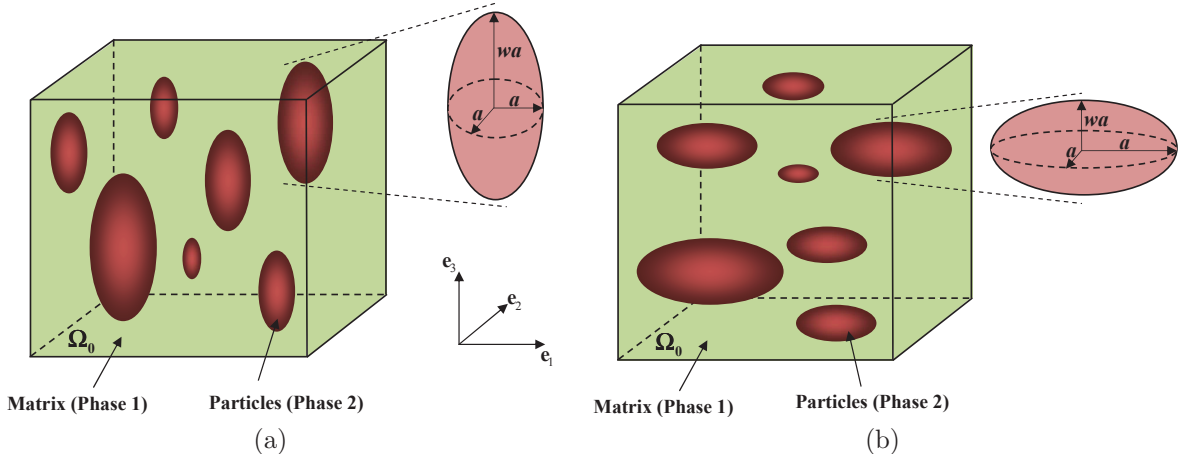


Figure 2.1: Schematic illustration of the microstructure of a rigid particle-reinforced elastomer in the undeformed configuration (Ω_0). Two configurations are considered. (a) Elastomers reinforced with prolate spheroidal particles ($w > 1$). (b) Elastomers reinforced with oblate spheroidal particles ($w < 1$). Note that, in both cases, the symmetry axis of the particles is initially aligned with the coordinate basis vector \mathbf{e}_3 .

Microstructures. The microstructures to be studied in this work are shown schematically in Figure 2.1, and are depicted in the undeformed configuration relative to the Cartesian basis $\{\mathbf{e}_i\}$ describing a fixed laboratory frame. These microstructures consists of aligned spheroidal particles of prolate and oblate shapes, in initial volume fraction $c_0^{(2)}$, which remains the same in the deformed configuration ($c = c_0^{(2)}$). As illustrated in Figure 2.1(a), the prolate spheroidal particles have aspect ratios $w > 1$, and their major (symmetry) axes are aligned with the \mathbf{e}_3 -direction. Similarly, as shown in Figure 2.1(b), the oblate spheroidal particles have aspect ratios $w < 1$, and their minor (symmetry) axes are likewise aligned with the \mathbf{e}_3 -direction. Therefore, for both cases, the circular cross-section of the particles in the undeformed configuration lies on the $\mathbf{e}_1 - \mathbf{e}_2$ plane. Moreover, consistent with earlier discussions, it is assumed that the particles are initially distributed with spheroidal symmetry (isotropic symmetry in the transverse plane), and the two-point correlation function of the particle distribution has the same aspect ratio and orientation of those of the particles.

Matrix Constitutive Behavior. The variational estimates (2.13) and (2.14) are valid for general behavior for the *incompressible* matrix phase. In this work, for definiteness, attention is restricted to stored-energy functions of the generalized neo-Hookean type, given by expression (2.1) with

$$W_\mu^{(1)}(\mathbf{F}) = g(I) + h(J). \quad (2.21)$$

In this expression, $I = \text{tr}(\mathbf{C})$ and, for proper linearization, the material functions $g(I)$ and $h(J)$ are assumed to be twice continuously differentiable satisfying the conditions: $g(3) = h(1) = 0$, $g_I(3) = \mu^{(1)}/2$, $h_J(1) = -\mu^{(1)}$, and $4g_{II}(3) + h_{JJ}(1) = \mu^{(1)}$, in which the subscripts I and J stand for partial differentiation with respect to the invariants I and J , respectively. In particular, we will consider

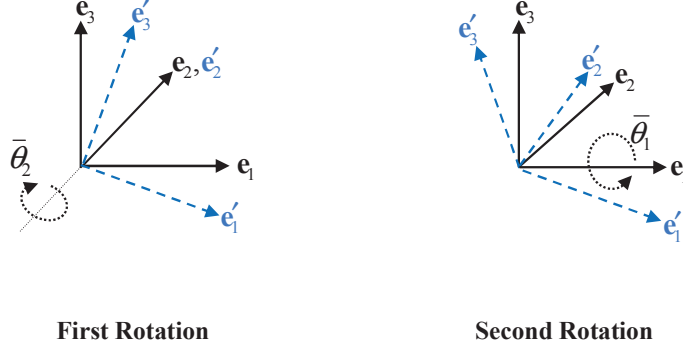


Figure 2.2: Schematic orientation of the Rectangular coordinate basis \mathbf{e}'_i with respect to the basis \mathbf{e}_i after a two-step rotation. The loading (stretching) directions are aligned with the \mathbf{e}'_i basis vectors, which have a misorientation (measured by angles $\bar{\theta}_1$ and $\bar{\theta}_2$) relative to the \mathbf{e}_i basis.

the Gent model (Gent, 1996), which has been shown to provide good agreement with experimental data for rubber-like materials (Ogden et al., 2004) and captures the limiting chain extensibility of elastomers. It is defined by

$$W_\mu^{(1)}(\mathbf{F}) = -\frac{J_m \mu^{(1)}}{2} \ln \left(1 - \frac{I - 3}{J_m} \right) + \frac{1}{2} \mu^{(1)} (J - 1)(J - 3) - \frac{\mu^{(1)}}{J_m} (J - 1)^2, \quad (2.22)$$

where $\mu^{(1)}$ is the ground-state shear modulus and J_m is a the dimensionless parameter characterizing the limiting value for $I - 3$ at which the elastomer locks up (and the argument of the logarithm vanishes). In connection with expression (2.22) for $W_\mu^{(1)}$, it should be emphasized that the terms depending on J , although vanishing for incompressible behavior at $J = 1$, are necessary for proper linearization of the deviatoric constitutive response. In addition, we should note that the form (2.22) used in this Chapter is slightly different from the more common form involving a logarithmic term in J , and indeed used in Chapter 1. The reason, as we will see below, is that this form leads to better behaved estimates for large values of the deformation.

Finally, we note that the Gent model includes the well-known neo-Hookean model in the limit as J_m approaches infinity, where $W_\mu^{(1)}$ specializes to

$$W_\mu^{(1)}(\mathbf{F}) = \frac{1}{2} \mu^{(1)} (I - 3) + \frac{1}{2} \mu^{(1)} (J - 1)(J - 3). \quad (2.23)$$

Macroscopic Loading. The isotropic distribution of the spheroidal particles in the transverse plane (here, $\mathbf{e}_1 - \mathbf{e}_2$ plane) in the undeformed configuration leads to overall *transversely isotropic* behavior for the composite with symmetry axis $\mathbf{n} = \mathbf{e}_3$. For compressible materials with transversely isotropic symmetry, the strain energy-density function can be written in terms of the 5 proper invariants of the tensor $\bar{\mathbf{C}} = \bar{\mathbf{F}}^T \bar{\mathbf{F}}$ and the vector \mathbf{n} (which reduce to 4 in the incompressibility limit). In this work, we find useful the following decomposition of the macroscopic deformation gradient

$$\bar{\mathbf{F}} = \bar{\mathbf{U}} = \bar{\mathbf{Q}} \bar{\mathbf{D}} \bar{\mathbf{Q}}^T, \quad (2.24)$$

where it has been assumed that $\bar{\mathbf{R}} = \mathbf{I}$ with recourse to the overall objectivity (2.20). In this decomposition, $\bar{\mathbf{D}}$ is a symmetric, second-order tensor given by

$$\bar{\mathbf{D}} = \bar{\lambda}_1 \mathbf{e}_1 \otimes \mathbf{e}_1 + \bar{\lambda}_2 \mathbf{e}_2 \otimes \mathbf{e}_2 + \bar{\lambda}_3 \mathbf{e}_3 \otimes \mathbf{e}_3, \quad (2.25)$$

with $\bar{\lambda}_1, \bar{\lambda}_2$ and $\bar{\lambda}_3$ identifying the principal values of $\bar{\mathbf{U}}$ (also known as the macroscopic principal stretches). In addition, $\bar{\mathbf{Q}}$ is a proper orthogonal, second-order tensor describing the orientation of the principal axes of $\bar{\mathbf{U}}$ relative to the (fixed) laboratory frame of reference $\{\mathbf{e}_i\}$. Here, the principal axes of the symmetric tensor $\bar{\mathbf{U}}$, also known as the loading (stretching) directions, are identified with the (rectangular Cartesian) basis $\{\mathbf{e}'_i\}$. In general, this basis is not aligned with the basis $\{\mathbf{e}_i\}$, representing the symmetry directions of the particles in the undeformed configuration. In turn, the tensor $\bar{\mathbf{Q}}$ can be decomposed into three proper orthogonal tensor $\bar{\mathbf{Q}}_1, \bar{\mathbf{Q}}_2$, and $\bar{\mathbf{Q}}_3$ serving to characterize the rotations of the principal axes of $\bar{\mathbf{U}}$ about the *fixed* $\mathbf{e}_1, \mathbf{e}_2$ and \mathbf{e}_3 axis, respectively. Recalling that the composite has transversely isotropic symmetry with symmetry axis along \mathbf{e}_3 , the response of the composite is insensitive to rotations about \mathbf{e}_3 , and we can restrict our attention to tensors $\bar{\mathbf{Q}}$ of the form

$$\bar{\mathbf{Q}} = \bar{\mathbf{Q}}_1 \bar{\mathbf{Q}}_2. \quad (2.26)$$

It is important to emphasize that, for a general choice of $\bar{\lambda}_1, \bar{\lambda}_2$ and $\bar{\lambda}_3$, the order of the rotations in (2.26) matters, and in this work, the order given in (2.26) will be used. Also, as illustrated in Figure 2.2, we let the two (Euler) angles $\bar{\theta}_1$ and $\bar{\theta}_2$ denote respectively rotations of the principal axes of $\bar{\mathbf{U}}$ about the \mathbf{e}_1 and \mathbf{e}_2 axis, with the sign defined according to the usual right-hand rule. More explicitly,

$$\begin{aligned} \bar{\mathbf{Q}}_1 &= \cos(\bar{\theta}_1) (\mathbf{e}_2 \otimes \mathbf{e}_2 + \mathbf{e}_3 \otimes \mathbf{e}_3) + \sin(\bar{\theta}_1) (\mathbf{e}_3 \otimes \mathbf{e}_2 - \mathbf{e}_2 \otimes \mathbf{e}_3) + \mathbf{e}_1 \otimes \mathbf{e}_1, \\ \bar{\mathbf{Q}}_2 &= \cos(\bar{\theta}_2) (\mathbf{e}_1 \otimes \mathbf{e}_1 + \mathbf{e}_3 \otimes \mathbf{e}_3) + \sin(\bar{\theta}_2) (\mathbf{e}_1 \otimes \mathbf{e}_3 - \mathbf{e}_3 \otimes \mathbf{e}_1) + \mathbf{e}_2 \otimes \mathbf{e}_2. \end{aligned} \quad (2.27)$$

Finally, as mentioned earlier, attention is restricted here to incompressible composite materials satisfying the overall incompressibility constraint, so that

$$\bar{\lambda}_3 = (\bar{\lambda}_1 \bar{\lambda}_2)^{-1}. \quad (2.28)$$

In terms of the above-defined loading parameters, the effective stored-energy function \widehat{W} may be written in the form

$$\widehat{W}(\bar{\mathbf{F}}) = \widehat{\Phi}(\bar{\lambda}_1, \bar{\lambda}_2, \bar{\theta}_1, \bar{\theta}_2). \quad (2.29)$$

Moreover, for simplicity, in this work we confine our attention to a subclass of loadings, characterized by the condition $\bar{\theta}_1 = 0^\circ$, as schematically shown in Figure 3.3.2. In this case, the effective stored-energy function simplifies further and takes the form

$$\widehat{\phi}(\bar{\lambda}_1, \bar{\lambda}_2, \bar{\theta}) = \widehat{\Phi}(\bar{\lambda}_1, \bar{\lambda}_2, 0, \bar{\theta}), \quad (2.30)$$

where the parameter $\bar{\theta}_2$ has been replaced by $\bar{\theta}$ for convenience. In this context, it is important

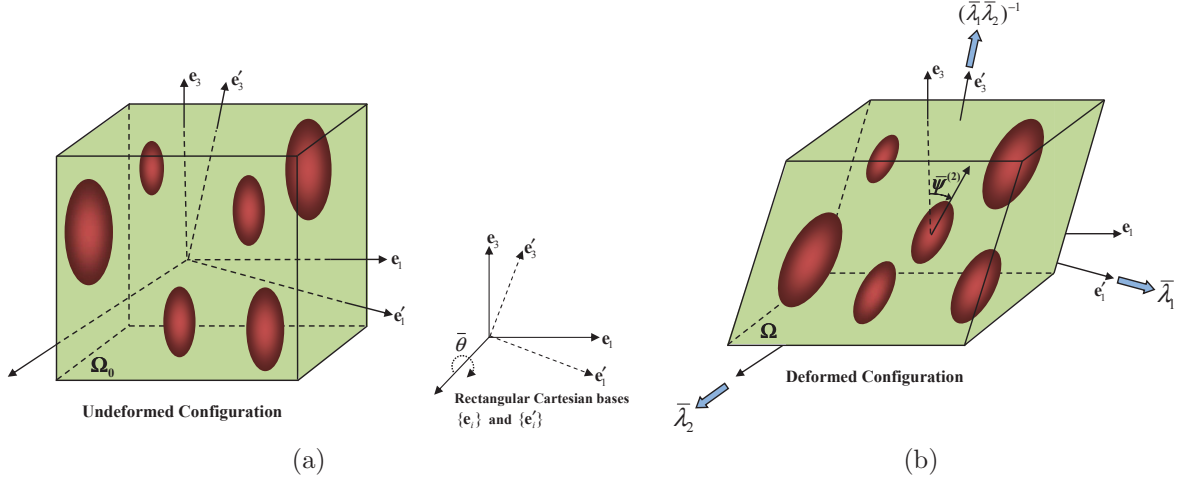


Figure 2.3: Schematic representation of the applied loading on a rigid particle-reinforced elastomer as well as the associated evolution of microstructure. The loading (stretching) directions are aligned with \bar{e}'_i basis vectors which correspond to a rotation $\bar{\theta}$ about the \mathbf{e}_2 direction. (a) In the undeformed configuration (Ω_0), the particles are aligned with the \mathbf{e}_3 direction. (b) In the deformed configuration (Ω), the particles rotate (by the angle $\bar{\psi}^{(2)}$) on the $\mathbf{e}_1 - \mathbf{e}_3$ plane.

to remark that, in general, second and higher derivatives of the effective stored-energy function $\widehat{\Phi}(\bar{\lambda}_1, \bar{\lambda}_2, \bar{\theta}_1, \bar{\theta}_2)$ with respect to $\bar{\theta}_1$, calculated at $\bar{\theta}_1 = 0^\circ$, are required for the calculation of the effective incremental modulus tensor $\widehat{\mathbf{L}}$ (defined in (2.12)) needed in turn for the computation of the ellipticity condition (2.11), even for loadings where $\bar{\theta}_1 = 0^\circ$. For this reason, it will be necessary to compute $\widehat{\Phi}$ for general values of $\bar{\theta}_1$ and $\bar{\theta}_2$, even when the results presented in this work will be restricted to loading paths with $\bar{\theta}_1 = 0^\circ$.

We conclude the description of the macroscopic loading conditions by identifying two special loading conditions: (1) *Axisymmetric Shear*, characterized by the condition $\bar{\lambda}_1 = \bar{\lambda}_2 = \bar{\lambda}$, and (2) *Pure Shear*, characterized by the condition $\bar{\lambda}_2 = 1, \bar{\lambda}_1 = \bar{\lambda}$, where $\bar{\lambda}$ is a positive loading parameter.

2.4.1 Estimates for non-aligned loadings

Under the above-mentioned assumptions on the microstructure, matrix properties and the macroscopic loading, we can now determine the tangent second-order estimates (2.13) and (2.14) for the composites consisting of a generalized neo-Hookean matrix (with stored-energy function (2.21)) and aligned, rigid spheroidal particles, subjected to the applied deformation (2.24). The resulting estimates, for general stretches $\bar{\lambda}_1$ and $\bar{\lambda}_2$ and angles $\bar{\theta}_1$, and $\bar{\theta}_2$, are too lengthy to be included here, and instead, we present results only for the case of $\bar{\theta}_1 = 0^\circ$ and $\bar{\theta}_2 = \bar{\theta}$. In this case, it can be shown

that the estimate for the effective stored-energy function of the composites reduces to

$$\begin{aligned} \widehat{W}(\bar{\mathbf{F}}) &= \widehat{\Phi}(\bar{\lambda}_1, \bar{\lambda}_2, 0, \bar{\theta}) = \widehat{\phi}(\bar{\lambda}_1, \bar{\lambda}_2, \bar{\theta}) = (1-c)W_\mu^{(1)}(\bar{\mathbf{F}}^{(1)}) + \frac{c}{2(1-c)} \{ E_{11}^{11} X_1^2 + (\bar{\lambda}_2 - 1)^2 E_{22}^{22} \\ &+ E_{33}^{33} X_2^2 + E_{13}^{13} Y_1^2 + E_{31}^{31} Y_2^2 + 2 [X_1(E_{33}^{11} X_2 + E_{13}^{11} Y_1 + E_{31}^{11} Y_2) + X_2(E_{13}^{33} Y_1 + E_{31}^{33} Y_2) \\ &+ (\bar{\lambda}_2 - 1)(E_{22}^{11} X_1 + E_{33}^{22} X_2 + E_{13}^{22} Y_1 + E_{31}^{22} Y_2) + E_{31}^{13} Y_1 Y_2 \} , \end{aligned} \quad (2.31)$$

where use has been made of the notation $E_{kl}^{ij} = E_{ijkl}$ for compactness of the Cartesian components of the microstructural tensor \mathbf{E} , as defined by expression (2.16), and where

$$\begin{aligned} X_1 &= \bar{\lambda}_1 \cos^2(\bar{\theta}) + (\bar{\lambda}_1 \bar{\lambda}_2)^{-1} \sin^2(\bar{\theta}) - \cos(\bar{\psi}^{(2)}), \\ X_2 &= \bar{\lambda}_1 \sin^2(\bar{\theta}) + (\bar{\lambda}_1 \bar{\lambda}_2)^{-1} \cos^2(\bar{\theta}) - \cos(\bar{\psi}^{(2)}), \\ Y_{1,2} &= \sin(\bar{\theta}) \cos(\bar{\theta}) \left[\bar{\lambda}_1 - (\bar{\lambda}_1 \bar{\lambda}_2)^{-1} \right] \pm \sin(\bar{\psi}^{(2)}). \end{aligned} \quad (2.32)$$

In this expressions, $\bar{\psi}^{(2)}$ characterizes the average rotation of the symmetry axis of the particles about the (fixed) \mathbf{e}_2 axis (with sign determined by the right-hand rule) in the deformed configuration (see Figure 3.3.2(b)). According to expression (2.14), $\bar{\psi}^{(2)}$ is determined as the solution of the equation

$$\begin{aligned} & \left[2 e_{31} \sin(\bar{\psi}^{(2)}) - f_1 X_1 - f_3 X_2 + E_{31}^{31} Y_2 - E_{13}^{13} Y_1 - (\bar{\lambda}_2 - 1) f_2 \right] \cos(\bar{\psi}^{(2)}) \\ & - \left\{ (E_{13}^{11} + E_{13}^{33} + e_{13}) Y_1 + E_{11}^{11} X_1 + E_{33}^{33} X_2 + (\bar{\lambda}_2 - 1) (E_{33}^{22} + E_{22}^{11}) \right. \\ & \left. + \left[\bar{\lambda}_1 + (\bar{\lambda}_1 \bar{\lambda}_2)^{-1} \right] [E_{33}^{11} + (1-c)(2g_I + \bar{\lambda}_2 h_J)] \right\} \sin(\bar{\psi}^{(2)}) + 2 e_{13} \sin^2(\bar{\psi}^{(2)}) = 0, \end{aligned} \quad (2.33)$$

where $e_{ij} = E_{3i}^{11} + E_{31}^{j3}$ and $f_i = E_{13}^{ii} - E_{31}^{ii}$, with $i, j = 1, 2, 3$.

For given loading parameters $\bar{\lambda}_1$, $\bar{\lambda}_2$, and $\bar{\theta}$, and material functions g and h , the calculation of the effective stored-energy (2.31) and the associated particle rotation in (2.33) require in turn the computation of the appropriate components of the tensor \mathbf{E} , as described by expression (B.1) in Appendix B.1. The pivotal point in this procedure is the calculation of the microstructural tensors \mathbf{P}_r , $r = 1, 2, 3$, as defined by the integrals in (B.7). For the general matrix behavior (2.21), and general choice of $\bar{\lambda}_1$ and $\bar{\lambda}_2$, and $\bar{\theta}$, the analytic calculation of these integrals is a difficult task, and we must resort to the use of a Gaussian quadrature technique. To maintain continuity here, the details are provided in Appendix B.2.

At this point, it is important to emphasize that expressions ((2.31)) and ((2.33)) for the macroscopic response of the reinforced elastomers are exactly consistent with the earlier, corresponding expressions given in Chapter 1, except that a slightly different form will be used here for the term $h(J)$ in equation ((2.21)) defining the matrix behavior $W_\mu^{(1)}$. However, it can be shown that the modifications proposed in this work for the function $h(J)$, as made explicit in the context of expressions ((2.22)) and ((2.23)) for Gent and neo-Hookean elastomers, respectively, only affect the term $W_\mu^{(1)}(\bar{\mathbf{F}}^{(1)})$ in expression ((2.31)), all other terms in expressions ((2.31)) and ((2.33)) remaining the same. (This is because the other terms in these expressions depend only on up to quadratic terms in the Taylor series expansion of h about $J = 1$.)

Finally, we note that, for the special case of *aligned* loadings, in which stretching directions of the tensor $\bar{\mathbf{U}}$ are aligned with the principal axes of spheroidal particles (in the undeformed configuration), leading to orthotropic symmetry, the calculation of the tensors \mathbf{P}_r , and subsequently the corresponding function $\hat{\Phi}$, can be carried out analytically for special forms of the matrix stored-energy function (2.21). For this reason, we present in the next subsection explicit analytical results for aligned loadings.

2.4.2 Estimates for aligned loadings

In this subsection, we restrict our attention to the special case of macroscopic loadings aligned with the particle axes $\{\mathbf{e}_i\}$, and characterized by the conditions $\bar{\theta} = 0^\circ$ and $\bar{\theta} = 90^\circ$ in expression (2.24) (recall that $\bar{\theta}_1 = 0^\circ$). However, for general values of $\bar{\lambda}_1$ and $\bar{\lambda}_2$, it suffices to identify aligned loadings by the condition $\bar{\theta} = 0^\circ$. Hence, the macroscopic deformation gradient for aligned loadings is written as

$$\bar{\mathbf{F}} = \bar{\lambda}_1 \mathbf{e}_1 \otimes \mathbf{e}_1 + \bar{\lambda}_2 \mathbf{e}_2 \otimes \mathbf{e}_2 + (\bar{\lambda}_1 \bar{\lambda}_2)^{-1} \mathbf{e}_3 \otimes \mathbf{e}_3, \quad (2.34)$$

where it is recalled that the particles are aligned in the \mathbf{e}_3 direction.

For the special case of aligned loadings, i.e., $\bar{\theta} = 0^\circ$, it can be shown that $\bar{\psi}^{(2)} = 0$ satisfies identically equation (2.33), implying that the particles do not rotate for any stretch (up to the possible onset of an instability). Making use of this fact, it is easy to show that the TSO estimate (2.13) for the effective stored-energy function reduces to

$$\begin{aligned} \widehat{W}(\bar{\mathbf{F}}) = \widehat{\phi}(\bar{\lambda}_1, \bar{\lambda}_2, 0) = (1-c)W_\mu^{(1)}(\bar{\mathbf{F}}^{(1)}) + \frac{c}{2(1-c)} \{ & (\bar{\lambda}_1 - 1)^2 E_{11}^{11} + (\bar{\lambda}_2 - 1)^2 E_{22}^{22} \\ & + l^2 E_{33}^{33} + 2 \{ l(\bar{\lambda}_1 - 1)E_{33}^{11} + (\bar{\lambda}_2 - 1) [(\bar{\lambda}_1 - 1)E_{22}^{11} + l E_{33}^{22}] \} \}, \end{aligned} \quad (2.35)$$

where $l = (\bar{\lambda}_1 \bar{\lambda}_2)^{-1} - 1$, and $W_\mu^{(1)}(\bar{\mathbf{F}}^{(1)}) = g(\bar{I}^{(1)}) + h(\bar{J}^{(1)})$, in which

$$\bar{I}^{(1)} = \frac{(\bar{\lambda}_1 - c)^2 + (\bar{\lambda}_2 - c)^2 + [(\bar{\lambda}_1 \bar{\lambda}_2)^{-1} - c]^2}{(1-c)^2}, \quad \bar{J}^{(1)} = \frac{(\bar{\lambda}_1 - c)(\bar{\lambda}_2 - c)[(\bar{\lambda}_1 \bar{\lambda}_2)^{-1} - c]}{(1-c)^3}. \quad (2.36)$$

For the general matrix behavior (2.21), the analytic calculation of the relevant components of tensor \mathbf{E} in (2.35) is cumbersome, and, for practical reasons, we make use of the Gaussian quadrature technique as will be discussed in Appendix B.2. However, for some particular types of the matrix behavior (2.21), and under loading condition (2.34), derivation of closed-form expressions for the components of the tensor \mathbf{E} and, subsequently, for the effective stored-energy function (2.35) is feasible. In the next subsection, we specialize the estimate (2.35) to neo-Hookean behavior for the matrix phase, and derive closed-form expressions for the effective stored-energy function for the two particular cases of (aligned) *axisymmetric shear* and *pure shear* loadings.

Closed-form results for a neo-Hookean matrix

In this section, we consider the hyperelastic composites made of a neo-Hookean matrix phase with stored-energy function of the form (2.23) and aligned, spheroidal, rigid particles subjected to aligned

loadings of the form (2.34). Under this type of loading conditions, the TSO estimate (2.13) for the effective stored-energy function of the composites still takes the form (2.35) with the function $W_\mu^{(1)}(\bar{\mathbf{F}}^{(1)})$ now given by

$$W_\mu^{(1)}(\bar{\mathbf{F}}^{(1)}) = \frac{1}{2}\mu^{(1)} \left(\bar{I}^{(1)} - 3 \right) + \frac{1}{2}\mu^{(1)} \left(\bar{J}^{(1)} - 1 \right) \left(\bar{J}^{(1)} - 3 \right), \quad (2.37)$$

where $\bar{I}^{(1)}$ and $\bar{J}^{(1)}$ are given by expressions (2.36). Note that $W_\mu^{(1)}(\bar{\mathbf{F}}^{(1)})$ remains bounded for all finite values of the stretches. This is different from the corresponding expression originally given in Chapter 1 which tends to blow up at a finite value of the stretch depending on the particle volume fraction—a phenomenon that was labeled *geometric locking up*. In other words, the slightly modified expressions given here for the response of the matrix phase lead to no *geometric locking up*. As we will see in Part II of this work, this feature will lead to more accurate predictions for the overall response of the reinforced elastomers.

As discussed earlier, in this case, the microstructural tensors \mathbf{P}_r , $r = 1, 2, 3$, as defined by integrals (B.7), and subsequently the tensor \mathbf{E} , as defined by (B.1), can be computed analytically for general values of $\bar{\lambda}_1$ and $\bar{\lambda}_2$. However, the expressions for the pertinent components of \mathbf{E} , as well as for the final expression for the effective stored-energy function, are too cumbersome to be included here. Instead, we provide only the analytical expressions for the relevant components of the corresponding tensors \mathbf{P}_r , $r = 1, 2, 3$, although, to maintain continuity here, they are spelled out in Appendix B.3. Having these components for the tensors \mathbf{P}_r , one can conveniently obtain a closed-form expression for the corresponding effective stored-energy function \widehat{W} by first determining the analytic expressions for the relevant components of the tensor \mathbf{E} using the algebraic operations outlined in Eqs. (B.1)-(B.5), and then substituting these components along with Eq. (2.37) into Eq. (2.35). Here, we remark that the resulting expression for the effective stored-energy function simplifies considerably, when specialized to particular choices of $\bar{\lambda}_1$ and $\bar{\lambda}_2$, corresponding to (aligned) *axisymmetric shear* and *pure shear* loadings. In the remainder of this subsection, we will separately consider these two specializations, and provide the closed-form expressions for the associated effective stored-energy functions.

Axisymmetric shear loading. Here, we consider the case of the particle-reinforced neo-Hookean composite subjected to aligned axisymmetric loading of the form (see Figure 2.4(a))

$$\bar{\mathbf{F}} = \bar{\lambda} \mathbf{e}_1 \otimes \mathbf{e}_1 + \bar{\lambda} \mathbf{e}_2 \otimes \mathbf{e}_2 + \bar{\lambda}^{-2} \mathbf{e}_3 \otimes \mathbf{e}_3, \quad (2.38)$$

for which $\bar{\lambda}_1 = \bar{\lambda}_2 = \bar{\lambda}$ is a positive loading parameter. In this case, it can be shown that the effective stored-energy function (2.35) simplifies to

$$\begin{aligned} \widehat{W}(\bar{\mathbf{F}}) &= \widehat{\phi}(\bar{\lambda}, \bar{\lambda}, 0) = (1 - c)W_\mu^{(1)}(\bar{\mathbf{F}}^{(1)}) \\ &+ \frac{c}{2(1 - c)} \left\{ 2(\bar{\lambda} - 1)^2 E_{11}^{11} + (\bar{\lambda}^{-2} - 1)^2 E_{33}^{33} + 2[(\bar{\lambda} - 1)^2 E_{22}^{11} + 2(\bar{\lambda}^{-2} - 1)(\bar{\lambda} - 1)E_{33}^{11}] \right\}, \end{aligned} \quad (2.39)$$

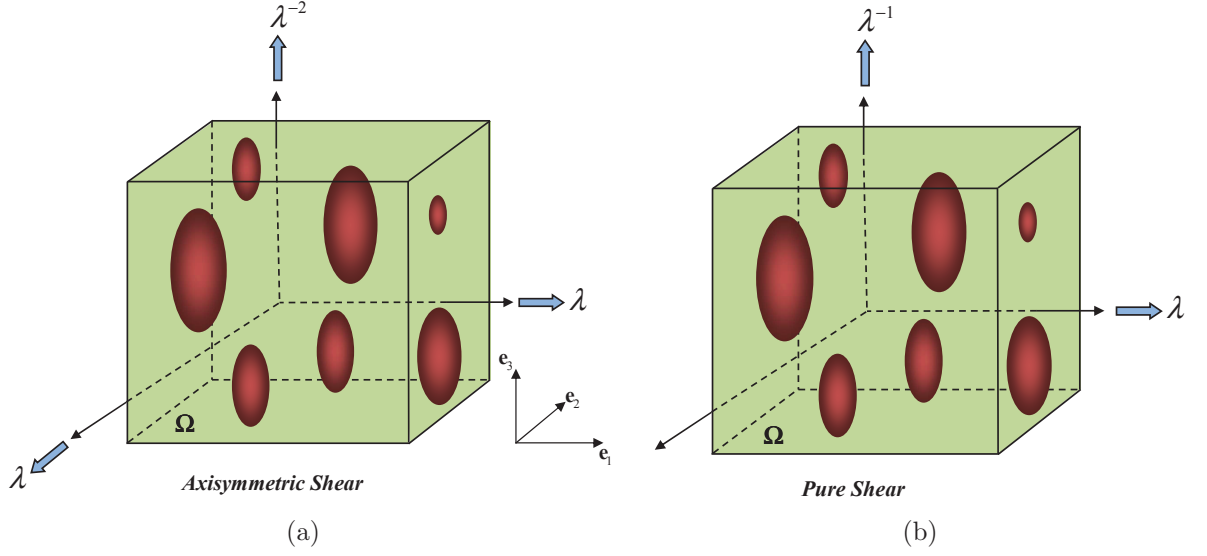


Figure 2.4: Schematic representation of a matrix reinforced by spheroidal particles subjected to aligned (a) axisymmetric shear loading, (b) pure shear loading.

where $W_{\mu}^{(1)}$ is given by expression (2.37) with

$$\bar{I}^{(1)} = \frac{2(\bar{\lambda} - c)^2 + (\bar{\lambda}^{-2} - c)^2}{(1 - c)^2}, \quad \bar{J}^{(1)} = \frac{(\bar{\lambda} - c)^2(\bar{\lambda}^{-2} - c)}{(1 - c)^3}.$$

and

$$\begin{aligned}
E_{11}^{11} &= A_3 A_4 A_5 (w \gamma_1)^{-1} \left\{ w A_1^2 A_3^3 (A_3 - w A_2) I_1^2 - w \bar{\lambda}^{12} A_2^2 A_4^4 - w A_3^2 A_4^2 A_5 [2 w^4 - w^2 I_3^2 + 4 \bar{\lambda}^6] \right. \\
&\quad + \left\{ w^2 \bar{\lambda}^{12} A_2^2 A_4^2 + w A_2 A_3 A_5 [w^4 + w^2 I_1^3 - \bar{\lambda}^6] - A_3^2 [2 w^6 - w^4 I_3^3 + w^2 I_1^8 + I_{0,0}^{1,4}] \right\} A_1 A_4 \\
&\quad \left. + A_2 A_3 A_4^2 [2 w^6 \bar{\lambda}^6 + w^4 I_{1,0}^{5,2} + (7 w^2 - 3) \bar{\lambda}^{12}] \right\}, \\
E_{33}^{33} &= A_3 A_4 A_5 w \gamma_1^{-1} \left\{ [w A_3 - \bar{\lambda}^6 A_2] A_1^2 A_3^3 I_1^2 + w \bar{\lambda}^6 A_2 A_4^2 (w A_3 I_{0,1}^{3,2} - \bar{\lambda}^{12} A_2 A_4^2) + w^3 A_3^2 A_4^2 A_5 I_{0,1}^{2,0} \right. \\
&\quad \left. + \left\{ \bar{\lambda}^{18} A_2^2 A_4^2 + 2 w \bar{\lambda}^6 A_2 A_3 A_5 I_{0,1}^{2,0} - w^2 A_3^2 [w^2 I_2^3 + I_{0,0}^{3,4}] \right\} A_1 A_4 \right\}, \\
E_{22}^{11} &= A_3 A_4 (w \bar{\lambda}^2 \gamma_1)^{-1} \left\{ A_1 \left\{ -w \bar{\lambda}^2 A_2 A_3 A_4 \left[\left(J_3^{\bar{1}} + I_{1,0}^{1,2} \right) w^4 - I_1^3 (J_1^1 + I_1^3) w^2 + \bar{\lambda}^6 \left(J_3^{\bar{1}} + I_{1,0}^{3,4} \right) \right] \right. \right. \\
&\quad \left. \left. + A_3^2 A_4 A_5 \left[(\bar{\lambda}^2 - 1) w^6 + (I_1^5 - 2 \bar{\lambda}^2) w^4 - \bar{\lambda}^2 \left(J_4^{\bar{1}} - I_1^1 \right) w^2 - \bar{\lambda}^8 \right] + w^2 \bar{\lambda}^{14} A_2^2 A_4^3 A_5 \right\} \right. \\
&\quad \left. - \bar{\lambda}^2 A_2 A_3 A_4^2 A_5 \left[\bar{\lambda}^4 (\bar{\lambda}^2 - 1) w^6 + (\bar{\lambda}^2 + 1) \left(J_{1,2}^{0,1} - I_1^2 \right) w^4 - \bar{\lambda}^6 (3 \bar{\lambda}^4 + I_4^2) w^2 - \bar{\lambda}^{12} \right] \right. \\
&\quad \left. + w^3 A_3^2 A_4^2 A_5^2 [(\bar{\lambda}^2 - 1) w^2 + \bar{\lambda}^2 (2 \bar{\lambda}^4 - 1)] + w \bar{\lambda}^{14} A_2^2 A_4^4 \left[\bar{\lambda}^4 (\bar{\lambda}^2 + 1) w^2 + I_1^2 - \bar{\lambda}^4 \right] \right. \\
&\quad \left. + w A_1^2 A_3^3 (2 \bar{\lambda}^6 - 1) \left\{ A_3 [(\bar{\lambda}^2 + 1) w^2 - \bar{\lambda}^2 q_1] - w \bar{\lambda}^2 A_2 A_5 \right\} \right\}, \\
E_{33}^{11} &= -A_3 A_4 \bar{\lambda} \gamma_1^{-1} \left\{ A_1 \left\{ w A_3^2 A_4 A_5 \left[(\bar{\lambda}^2 + 1) w^4 - w^2 \left(J_{0,2}^{0,1} + I_1^5 \right) + I_{0,0}^{1,4} + 2 \bar{\lambda}^8 \right] - w \bar{\lambda}^{14} A_2^2 A_4^3 A_5 \right. \right. \\
&\quad \left. \left. + \bar{\lambda}^2 A_2 A_3 A_4 \left[w^4 \left(J_3^{\bar{1}} + I_2^4 \right) + \bar{\lambda}^4 \left(2 \bar{\lambda}^{14} + J_{0,10}^{0,4} - I_{1,0}^{2,3} \right) w^2 + 2 \bar{\lambda}^{18} + \bar{\lambda}^{10} I_1^3 \right] \right\} \right. \\
&\quad \left. - \bar{\lambda}^{14} A_2^2 A_4^4 (w^2 q_1 - \bar{\lambda}^6 - \bar{\lambda}^4) - w \bar{\lambda}^2 A_2 A_3 A_4^2 A_5 [w^4 q_1 - (J_3^1 + 3 \bar{\lambda}^6) w^2 + 2 \bar{\lambda}^{12} + 3 \bar{\lambda}^{10}] \right. \\
&\quad \left. + w^2 A_3^2 A_4^2 A_5^2 I_{0,1}^{2,0} + A_1^2 A_3^3 I_1^2 \left\{ w \bar{\lambda}^2 A_2 A_5 - A_3 [(\bar{\lambda}^2 + 1) w^2 - \bar{\lambda}^2 q_1] \right\} \right\}. \tag{2.40}
\end{aligned}$$

In addition, in the above relations,

$$\begin{aligned}
A_1 &= \tanh^{-1} \left(\frac{\sqrt{w^2 - 1}}{w} \right), \quad A_2 = \tanh^{-1} \left(\frac{\sqrt{w^2 - \bar{\lambda}^6}}{w} \right), \quad A_3 = \sqrt{w^2 - \bar{\lambda}^6}, \\
A_4 &= \sqrt{w^2 - 1}, \quad A_5 = (\bar{\lambda}^4 + \bar{\lambda}^2 + 1)(\bar{\lambda}^2 - 1), \quad q_{1,2} = \bar{\lambda}^4 \pm 1, \\
\gamma_1 &= A_3 A_4 \left[A_1 A_3 A_4 \left(\bar{\lambda}^6 A_2 A_3^2 A_4^2 I_1^3 + w A_3^3 A_5 I_{1,1}^{4,0} \right) - A_1^2 A_3^6 I_1^2 - \bar{\lambda}^{18} A_2^2 A_4^6 \right. \\
&\quad \left. - w \bar{\lambda}^6 A_2 A_3 A_4^4 A_5 I_{0,1}^{3,0} + w^2 A_3^2 A_4^2 A_5^2 I_{0,1}^{2,0} \right] / \mu^{(1)},
\end{aligned}$$

and the abbreviations

$$I_{b,d}^{a,c} = c \bar{\lambda}^{12} + a \bar{\lambda}^6 + d w^2 + b, \quad I_b^a = I_{b,0}^{a,0}, \quad J_{b,d}^{a,c} = b \bar{\lambda}^{10} + d \bar{\lambda}^8 + a \bar{\lambda}^4 + c \bar{\lambda}^2, \quad J_b^a = J_{b,0}^{a,0},$$

have been introduced for compactness. In these last expressions, a barred subscript/superscript indicates the corresponding negative coefficient. It should be pointed out that the effective stored-energy function (2.39) is valid for both prolate ($w > 1$) and oblate ($w < 1$) spheroidal shapes for the particles. Also, when specialized to the case of $w = 1$, relation (2.39) recovers the corresponding effective stored-energy function for neo-Hookean elastomers reinforced by rigid, spherical particles provided by relation (1.141) in Chapter 1 (except that the expression for $W_\mu^{(1)}$ involves a logarithmic term in $\bar{J}^{(1)}$, because, as already noted, a slightly different form for the compressible generalization of the neo-Hookean model was used in the earlier work.). Another remarkable feature of the stored-energy function (2.39) is that it is valid for any positive loading parameter $\bar{\lambda}$. More specifically, for $\bar{\lambda} > 1$, the function (2.39) corresponds to the effective stored-energy function of the composite when subjected to *Equibiaxial Tension* loading in the $\mathbf{e}_1 - \mathbf{e}_2$ plane, while for $\bar{\lambda} < 1$, it corresponds to *Uniaxial Tension* loading in the \mathbf{e}_3 direction with tensile stretch $\bar{\lambda}_3 = 1/\bar{\lambda}^2$.

Pure shear loading. Next, we consider the case in which the (spheroidal) particle-reinforced neo-Hookean composite undergoes aligned pure shear loading (in the $\mathbf{e}_1 - \mathbf{e}_3$ plane) of the form (see Figure 2.4(b))

$$\bar{\mathbf{F}} = \bar{\lambda} \mathbf{e}_1 \otimes \mathbf{e}_1 + \mathbf{e}_2 \otimes \mathbf{e}_2 + \bar{\lambda}^{-1} \mathbf{e}_3 \otimes \mathbf{e}_3, \quad (2.41)$$

where, similar to the preceding axisymmetric case, $\bar{\lambda}_1 = \bar{\lambda}$ is a positive loading parameter. In this case, the TSO estimate (2.35) for the effective stored-energy function simplifies to

$$\begin{aligned} \widehat{W}(\bar{\mathbf{F}}) = \widehat{\phi}(\bar{\lambda}, 1, 0) &= (1 - c)W_\mu^{(1)}(\bar{\mathbf{F}}^{(1)}) + \frac{c}{2(1 - c)} \{(\bar{\lambda} - 1)^2 E_{11}^{11} + (\bar{\lambda}^{-1} - 1)^2 E_{33}^{33} \\ &+ 2(\bar{\lambda} - 1)(\bar{\lambda}^{-1} - 1)E_{33}^{11}\}, \end{aligned} \quad (2.42)$$

where $W_\mu^{(1)}$ is given by expression (2.37) with

$$\bar{I}^{(1)} = \frac{(\bar{\lambda} - c)^2 + (\bar{\lambda}^{-1} - c)^2}{(1 - c)^2} + 1, \quad \bar{J}^{(1)} = \frac{(\bar{\lambda} - c)(\bar{\lambda}^{-1} - c)}{(1 - c)^2},$$

and

$$\begin{aligned} E_{11}^{11} = &-(w \bar{\lambda} \gamma_2)^{-1} Q_1^1 \left\{ w \bar{\lambda} B_2 B_3^2 (w B_3^2 \Xi_{p2} - \bar{\lambda} B_2^3) [w B_1 Q_2^1 + B_3 (\bar{\lambda}^2 w^2 - 2 Q_1^1)] \Xi_{p1} \right. \\ &- w B_2^2 B_3^2 Q_1^1 \left[w^2 B_1^2 B_3 Q_1^1 - w \left(w^4 Q_1^1 - 4 \bar{\lambda}^2 w^2 + O_{1,1}^{1,1} \right) B_1 + \left(w^4 Q_1^1 + w^2 O_{3,1}^{1,1} + 2 \bar{\lambda}^6 \right) B_3 \right] \Xi_{p2} \\ &+ \left\{ w^2 \bar{\lambda} q_2 B_2 B_3^2 [w B_1 Q_2^1 + (\bar{\lambda}^2 w^2 - 2 Q_1^1) B_3] \Xi_{p1} - w^2 \bar{\lambda} B_2^3 B_3^2 [w B_1 Q_2^1 + (\bar{\lambda}^2 w^2 - 2 Q_1^1) B_3] \Xi_{p2} \right. \\ &- w B_2^2 \left[w^2 q_2^3 B_1^2 B_3 + w B_1 B_3^2 \left(w^2 O_{2,0,0}^{1,\bar{1},1} + O_{2,4,0}^{1,1,\bar{3}} \right) + B_3^3 \left(w^4 \bar{\lambda}^4 - w^2 O_{2,0,0}^{1,1,1} + 2 \bar{\lambda}^6 Q_1^1 \right) \right] \Xi_f \\ &\left. \left. + \bar{\lambda} B_2^5 Q_1^1 [w^2 B_1^2 B_3 Q_1^1 + w B_1 B_3^2 (w^2 Q_1^1 - Q_1^3) - B_3^3 (w^2 Q_1^1 - 2 \bar{\lambda}^2)] \right\} \right\}, \end{aligned}$$

$$\begin{aligned}
E_{33}^{33} = & -w \gamma_2^{-1} Q_1^1 \left\{ \bar{\lambda} (B_1 - w B_3) B_2 B_3^2 Q_2^1 \left(w \bar{\lambda}^3 B_3^2 \Xi_{p2} - B_2^3 \right) \Xi_{p1} - w \bar{\lambda} B_2^2 B_3^2 Q_1^1 \left\{ \bar{\lambda}^2 B_1^2 B_3 Q_1^1 \right. \right. \\
& + w \alpha B_1 - w^2 B_3 \left(2 w^2 - \bar{\lambda}^2 Q_1^1 \right) \left. \right\} \Xi_{p2} + \bar{\lambda}^3 \left\{ w \bar{\lambda} B_2 B_3^2 (B_1 - w B_3) (B_4 Q_1^1 \Xi_{p1} - B_2^2 Q_2^1 \Xi_{p2}) \right. \\
& - B_2^2 \left[w q_2^3 B_1^2 B_3 - B_1 B_3^2 \left(w^2 O_{4,2,0}^{2,0,1} + \bar{\lambda}^6 Q_2^1 \right) - w B_3^3 \left(w^2 Q_1^2 - \bar{\lambda}^6 Q_2^1 \right) \right] \left. \right\} \Xi_f \\
& + B_2^5 B_3 (\bar{\lambda}^2 + 1)^2 (B_1 - w B_3)^2 \left. \right\},
\end{aligned}$$

$$\begin{aligned}
E_{33}^{11} = & \gamma_2^{-1} \left\{ \bar{\lambda} B_3^2 \left\{ B_2^4 \left[(w^2 \bar{\lambda}^2 Q_3^1 - 2 Q_1^1) B_3 - w B_1 B_4 \right] - w \bar{\lambda} B_2 B_3^2 (w B_1 B_4 + \alpha B_3) \Xi_{p2} \right\} \Xi_{p1} \right. \\
& + w \bar{\lambda} q_2 B_2^2 B_3^2 \left[w B_1^2 B_3 Q_1^1 + \left(w^4 Q_1^1 + w^2 Q_1^1 + \bar{\lambda}^2 Q_1^1 \right) B_1 + w (2 w^2 - \bar{\lambda}^2 Q_1^1) B_3 \right] \Xi_{p2} \\
& + \bar{\lambda} \left\{ B_2^2 \left[w^2 B_3 q_2^2 Q_1^1 B_1^2 + B_3^3 \left(w^4 O_{2,1,0}^{1,0,0} - w^2 O_{1,3,1}^{0,2,1} + 2 \bar{\lambda}^8 Q_1^1 \right) + w B_3^2 Q_1^1 \left(w^2 O_{5,2,0}^{2,3,1} - O_{1,6,0}^{0,3,3} \right) B_1 \right] \right. \\
& \left. - w \bar{\lambda} B_2 B_3^2 (w B_1 B_4 + \alpha B_3) (q_2 \Xi_{p1} - B_2^2 \Xi_{p2}) \right\} \Xi_f + q_2^2 B_2^5 (w B_1^2 B_3 + (w^4 - 1) B_1 + w B_3^3) \left. \right\}.
\end{aligned} \tag{2.43}$$

In addition, in the above relations,

$$\begin{aligned}
B_1 = & \tan^{-1} \left(\frac{\sqrt{1-w^2}}{w} \right), \quad B_2 = \sqrt{\bar{\lambda}^4 - w^2}, \quad B_3 = \sqrt{1-w^2}, \quad B_4 = (\bar{\lambda}^2 - 1)(\bar{\lambda}^2 + 2), \\
\gamma_2 = & \left\{ \bar{\lambda} B_3^2 \left\{ 2 w \bar{\lambda}^3 B_2 B_3^5 \Xi_{p2} - B_2^4 \left[w B_1 B_4 - B_3 (w^2 \bar{\lambda}^2 Q_1^1 - 2) \right] \right\} \Xi_{p1} + q_2 B_2^5 Q_1^1 \left[w B_1^2 B_3 \right. \right. \\
& + (w^4 - 1) B_1 - w^3 B_3 + w B_3 \left. \right] + w \bar{\lambda} q_2 B_2^2 B_3^2 \left[w (2 w^2 - \bar{\lambda}^2 Q_1^1) B_3 - (2 w^4 - \bar{\lambda}^2 Q_1^1) B_1 \right] \Xi_{p2} \\
& \left. + \bar{\lambda}^3 B_3^4 \left\{ 2 w \bar{\lambda} B_2 B_3 (q_2 \Xi_{p1} - B_2^2 \Xi_{p2}) - B_2^2 \left[w B_1 Q_1^1 O_{2,0}^{1,2} + B_3 (w^2 Q_1^1 - 2 \bar{\lambda}^6) \right] \right\} \Xi_f \right\} / \mu^{(1)}
\end{aligned}$$

and $\alpha = w^2 (\bar{\lambda}^2 Q_1^1 + 2) - 2 \bar{\lambda}^2 Q_1^1$. Also, the abbreviations

$$Q_b^a = a \bar{\lambda}^2 + b, \quad O_{b,d,f}^{a,c,e} = f \bar{\lambda}^{10} + e \bar{\lambda}^8 + d \bar{\lambda}^6 + c \bar{\lambda}^4 + b \bar{\lambda}^2 + a, \quad O_{b,d}^{a,c} = O_{b,d,0}^{a,c,0},$$

are introduced for compactness, and it is recalled that a barred subscript/superscript indicates the corresponding negative coefficient. Moreover, Ξ_f , and $\Xi_{p1,2}$ are given in terms of the incomplete elliptic integrals of the first and third kind (Abramowitz and Stegun, 1965), respectively, via

$$\Xi_f = F \left(\frac{B_2}{\bar{\lambda}^2}, q \right), \quad \Xi_{p1} = P \left(\frac{B_2}{\bar{\lambda}^2}, \frac{\bar{\lambda}^4 - 1}{w^2 - \bar{\lambda}^4}, q \right), \quad \Xi_{p2} = P \left(\frac{B_2}{\bar{\lambda}^2}, 1, q \right),$$

where $q = \bar{\lambda} \sqrt{(\bar{\lambda}^2 - 1)/(\bar{\lambda}^4 - w^2)}$, and the functions F and P are defined by

$$F(a, b) = \int_0^a \frac{1}{\sqrt{1-t^2}\sqrt{1-b^2t^2}} dt, \quad P(a, b, c) = \int_0^a \frac{1}{\sqrt{1-t^2}\sqrt{1-bt^2}\sqrt{1-c^2t^2}} dt. \quad (2.44)$$

It is important to note that, similar to relation (2.39), the effective stored-energy function (2.42) is valid for both prolate ($w > 1$) and oblate ($w < 1$) spheroidal shapes of particles. Likewise, when specialized to the case of $w = 1$, relation (2.42) reduces to the corresponding effective stored-energy function for neo-Hookean elastomers reinforced by rigid, spherical particles provided by relation (1.139) in Chapter 1 (notwithstanding the earlier comment about the logarithmic term). Finally, it is emphasized, for completeness, that the estimates (2.39) and (2.42) are consistent with the macroscopic incompressibility constraint $\bar{\lambda}_1 \bar{\lambda}_2 \bar{\lambda}_3 = 1$, and linearize properly.

2.5 Onset of macroscopic instabilities

The purpose of this section is to investigate the possible development of macroscopic instabilities in the finitely strained, particle-reinforced elastomers described in the prior section. As discussed earlier in Section 2.2, in this work, our attention is restricted to the onset of *macroscopic* (as opposed to *microscopic*) instabilities, which are characterized by wavelengths much larger than the characteristic size of the underlying microstructure. We recall from our discussion in Section 2.2 that, based on the work by Geymonat et al. (1993), the onset of macroscopic instabilities in the heterogeneous materials corresponds to the loss of strong ellipticity of the associated homogenized constitutive behavior. Recalling from (2.11), the homogenized particle-reinforced elastomer characterized by $\widehat{W}(\bar{\mathbf{F}})$ is said to be strongly elliptic if and only if

$$\widehat{L}_{ijkl} N_j N_l m_i m_k = \left(\partial^2 \widehat{W} / \partial \bar{F}_{ij} \partial \bar{F}_{kl} N_j N_l \right) m_i m_k > 0. \quad (2.45)$$

Thus, equivalently, the *first* macroscopic instability happens whenever the inequality (2.45) ceases to hold true.

For incompressible materials, however, it proves convenient to express the strong ellipticity (SE) condition in terms of the tensor $\widehat{L}_{ijkl}^c = \widehat{L}_{ipkq} \bar{F}_{jp} \bar{F}_{lq}$ which is the updated incremental moduli tensor when the undeformed configuration coincides with the deformed configuration. Correspondingly, for incompressible composites, the SE condition (2.45) can be rewritten as

$$\text{tr}\{[\widehat{\mathbf{L}}^c(\mathbf{m} \otimes \mathbf{n})](\mathbf{m} \otimes \mathbf{n})\} > 0, \quad (2.46)$$

where $\mathbf{n} = \bar{\mathbf{F}}^{-T} \mathbf{N}$ is the transformation of the unit vector \mathbf{N} in the deformed configuration. In this case, the incompressibility constraint $\det(\bar{\mathbf{F}}) = 1$ implies that the unit vectors \mathbf{n} and \mathbf{m} must satisfy $\mathbf{n} \cdot \mathbf{m} = 0$ in (2.46). In fact, due to the incompressibility constraint, some components of the moduli \mathbf{L}^c become infinite, however, the constraint $\mathbf{n} \cdot \mathbf{m} = 0$ projects the tensor \mathbf{L}^c onto the space of isochoric deformation $\det(\bar{\mathbf{F}}) = 1$, and accordingly, the condition (2.46) is expressed in terms of some traces of \mathbf{L}^c with finite values.

Since the effective strain energy (2.13) is strongly elliptic in sufficiently small neighborhoods of $\bar{\mathbf{F}} = \mathbf{I}$, one expects that the inequality (2.46) holds true in the infinitesimal-strain regime. However, as the macroscopic strain increases, the inequality may be violated at some specific critical tensor $\bar{\mathbf{F}}^{cr}$. This critical deformation gradient is associated with the critical vectors \mathbf{n}_{cr} , \mathbf{m}_{cr} . In fact, $\bar{\mathbf{F}}^{cr}$ constitutes the boundary of the domain in deformation space, including the value $\bar{\mathbf{F}} = \mathbf{I}$, inside which the SE condition holds. It is also remarked that when the condition (2.46) fails to hold, the homogenized material becomes macroscopically unstable and this corresponds to a developing *shear band* taking place on a plane with the (unit) normal vector \mathbf{n}_{cr} (in the deformed configuration) and along the direction \mathbf{m}_{cr} .

The main objective of this section is to find the $\bar{\mathbf{F}}^{cr}$ (together with the associated vectors \mathbf{n}_{cr} and \mathbf{m}_{cr}) when the composite material consisting of rigid spheroidal particles undergoes the macroscopic deformation given by (2.24). In the following, the specialization of the SE condition (2.46) for the class of *transversely isotropic* composites under non-aligned and aligned loadings are provided, and later, they are further specialized for the (rigidly) particle-reinforced composites of interest under axisymmetric and pure shear loadings.

The modulus tensor $\hat{\mathbf{L}}^c$ in (2.46), which in general has 45 independent components, simplifies when it is specialized to the class of (incompressible) transversely isotropic composites (with symmetry axis aligned with \mathbf{e}_3 direction) undergoing the macroscopic deformation field (2.24) (recall that $\bar{\theta}_1 = 0^\circ$). Accordingly, it can be shown, by making use of the orthogonality condition $\mathbf{n} \cdot \mathbf{m} = 0$ to solve for m_3 in terms of the other components of \mathbf{m} and \mathbf{n} , that the SE condition (2.46) for the stored-energy function $\widehat{W}(\bar{\mathbf{F}})$ can be written as

$$\begin{aligned}
n_3^{-2} \left\{ \right. & \left. \widehat{L}_{3131}^c n_1^4 - 2 \widehat{L}_2^* n_3 n_1^3 + \left(\widehat{L}_{3232}^c n_2^2 + \widehat{L}_3^* n_3^2 \right) n_1^2 + \left(2 \widehat{L}_1^* n_3^3 - 2 \widehat{L}_{3212}^c n_2^2 n_3 \right) n_1 + \right. \\
& \left. \widehat{L}_{1212}^c n_2^2 n_3^2 + \widehat{L}_{1313}^c n_3^4 \right\} m_1^2 + \left\{ 2 \widehat{L}_{3131}^c n_2 n_1^3 + 2 \left(\widehat{L}_7^* n_3^2 - \widehat{L}_8^* n_1^2 - \widehat{L}_{3212}^c n_2^2 \right) n_2 n_3 \right. \\
& \left. + 2 \left(\widehat{L}_{3232}^c n_2^2 + \widehat{L}_5^* n_3^2 \right) n_1 n_2 \right\} m_1 m_2 + \left[\left(\widehat{L}_{3131}^c n_2^2 + \widehat{L}_{2121}^c n_3^2 \right) n_1^2 \right. \\
& \left. + 2 \left(\widehat{L}_{2321}^c n_3^2 - \widehat{L}_6^* n_2^2 \right) n_1 n_3 + \widehat{L}_{3232}^c n_2^4 + \widehat{L}_4^* n_3^2 n_2^2 + \widehat{L}_{2323}^c n_3^4 \right] m_2^2 \left. \right\} > 0, \tag{2.47}
\end{aligned}$$

where

$$\begin{aligned}
\widehat{L}_1^* &= \widehat{L}_{1113}^c - \widehat{L}_{3313}^c, & \widehat{L}_2^* &= \widehat{L}_{1131}^c - \widehat{L}_{3331}^c, \\
\widehat{L}_3^* &= \widehat{L}_{1111}^c + \widehat{L}_{3333}^c - 2 \widehat{L}_{1133}^c - 2 \widehat{L}_{1331}^c, & \widehat{L}_4^* &= \widehat{L}_{2222}^c + \widehat{L}_{3333}^c - 2 \widehat{L}_{2233}^c - 2 \widehat{L}_{2332}^c \\
\widehat{L}_5^* &= \widehat{L}_{1122}^c + \widehat{L}_{1221}^c + \widehat{L}_{3333}^c - \widehat{L}_{1133}^c - \widehat{L}_{2233}^c - \widehat{L}_{1331}^c - \widehat{L}_{2332}^c, \\
\widehat{L}_6^* &= \widehat{L}_{2231}^c + \widehat{L}_{3221}^c - \widehat{L}'_{3331}^c, & \widehat{L}_7^* &= \widehat{L}_{2213}^c + \widehat{L}_{2312}^c - \widehat{L}_{3313}^c, & \widehat{L}_8^* &= \widehat{L}_{2231}^c + \widehat{L}_{3221}^c + \widehat{L}_{1131}^c - 2 \widehat{L}_{3331}^c,
\end{aligned} \tag{2.48}$$

The loss of strong ellipticity of the (incompressible) composite elastomer can be determined by monitoring the sign of the LHS expression in inequality (2.47) for all possible unit vectors \mathbf{n} and \mathbf{m} satisfying the constraint $\mathbf{n} \cdot \mathbf{m} = 0$, and detecting the point at which the expression first vanishes.

As mentioned earlier in this section, for an incompressible composite, some of the components of the corresponding effective incremental modulus tensor $\widehat{\mathbf{L}}^c$ become unbounded, however, the traces of this modulus tensor which appear in the strong ellipticity condition (2.47) (the expressions of \widehat{L}_{ijkl}^c terms multiplying n_i 's components) have finite values. These traces can be derived in terms of loading parameters $\bar{\lambda}_1$, $\bar{\lambda}_2$, and $\bar{\theta}_2$ as well as the first and second derivatives of the effective stored-energy function $\widehat{\Phi}(\bar{\lambda}_1, \bar{\lambda}_2, \bar{\theta}_1, \bar{\theta}_2)$ with respect to its arguments, evaluated at $\bar{\theta}_1 = 0^\circ$. To maintain continuity, the corresponding explicit expressions for the moduli traces, calculated in the rectangular Cartesian basis $\{\mathbf{e}'_i\}$, are provided in Appendix B.4.

Substituting the expressions for the moduli traces (in (B.20)-(B.24)) into (2.47), the SE condition is expressed in terms of $\widehat{\Phi}$ and can be used to detect the onset of macroscopic instabilities for the class of particle-reinforced composites described in Section 2.4. For a general choice of $\bar{\lambda}_1$, $\bar{\lambda}_2$, and $\bar{\theta} = \bar{\theta}_2$ in deformation (2.24) (recall that $\bar{\theta}_1 = 0^\circ$), the resulting condition takes the form

$$f(\widehat{\Phi}_{,\bar{\lambda}_1}, \widehat{\Phi}_{,\bar{\lambda}_2}, \widehat{\Phi}_{,\bar{\lambda}_1\bar{\lambda}_1}, \widehat{\Phi}_{,\bar{\lambda}_2\bar{\lambda}_2}, \widehat{\Phi}_{,\bar{\theta}_1\bar{\theta}_1}, \widehat{\Phi}_{,\bar{\theta}_2\bar{\theta}_2}, n_1, n_2, n_3, m_1, m_2, m_3, \bar{\lambda}_1, \bar{\lambda}_2, \bar{\theta}) > 0, \quad (2.49)$$

in which subscript commas followed by an index denote derivatives with respect to the corresponding variables. For this general choice of loading parameters, the explicit expression for function f in (2.49) is too lengthy to be included here, but it simplifies considerably for the special case of aligned loadings ($\bar{\theta} = 0^\circ$) as discussed in the following.

For the special case of macroscopic aligned loadings, given by (2.34), it can be shown that the SE condition (2.47) reduces to

$$\begin{aligned} & n_3^{-2} \left\{ \left[\widehat{L}_{3131}^c n_1^4 + \left(\widehat{L}_{3232}^c n_2^2 + \widehat{L}_3^* n_3^2 \right) n_1^2 + \widehat{L}_{1313}^c n_3^4 + \widehat{L}_{1212}^c n_2^2 n_3^2 \right] m_1^2 \right. \\ & + \left[2 \widehat{L}_{3131}^c n_1^3 n_2 + \left(2 \widehat{L}_{3232}^c n_2^3 + 2 \widehat{L}_5^* n_2 n_3^2 \right) n_1 \right] m_1 m_2 \\ & \left. + \left[\left(\widehat{L}_{2121}^c n_3^2 + \widehat{L}_{3131}^c n_2^2 \right) n_1^2 + \widehat{L}_{3232}^c n_2^4 + \widehat{L}_4^* n_2^2 n_3^2 + \widehat{L}_{2323}^c n_3^4 \right] m_2^2 \right\} > 0. \end{aligned} \quad (2.50)$$

Substituting the moduli traces in (B.25)-(B.27) (for aligned loadings) into the above condition, the corresponding SE condition for $\widehat{\Phi}$ is obtained. For general choice of $\bar{\lambda}_1$ and $\bar{\lambda}_2$ in deformation (2.34), the resulting condition can be shown to reduce to

$$\begin{aligned} & l_1^{-2} l_2^{-2} l_3^{-1} \left\{ \left\{ \bar{\lambda}_1^4 \bar{\lambda}_2^2 l_2^2 l_3 \phi_1^* n_1^4 + \left[\bar{\lambda}_1^2 \bar{\lambda}_2^4 l_1^2 l_3 \phi_2^* n_2^2 + \bar{\lambda}_1 l_2^2 l_3 \left(\bar{\lambda}_1 l_1^2 \widehat{\Phi}_{,\bar{\lambda}_1\bar{\lambda}_1} - 2 \bar{\lambda}_1^3 \bar{\lambda}_2^2 \widehat{\Phi}_{,\bar{\theta}_2\bar{\theta}_2} - 2 l_1 \widehat{\Phi}_{,\bar{\lambda}_1} \right) n_3^2 \right] n_1^2 \right. \right. \\ & + \bar{\lambda}_2^2 l_2^2 l_1^2 \phi_3^* n_2^2 n_3^2 + \bar{\lambda}_1 l_2^2 l_3 \left(l_1 \widehat{\Phi}_{,\bar{\lambda}_1} + \bar{\lambda}_1^3 \bar{\lambda}_2^2 \widehat{\Phi}_{,\bar{\theta}_2\bar{\theta}_2} \right) n_3^4 \left. \right\} m_1^2 + 2 \left\{ \bar{\lambda}_1^4 \bar{\lambda}_2^2 l_2^2 l_3 \phi_1^* n_1^3 n_2 \right. \\ & + \left\{ \left[\bar{\lambda}_1 \bar{\lambda}_2 l_3 \left(l_1^2 l_2^2 \widehat{\Phi}_{,\bar{\lambda}_1\bar{\lambda}_2} - \bar{\lambda}_1^3 \bar{\lambda}_2 l_2^2 \widehat{\Phi}_{,\bar{\theta}_2\bar{\theta}_2} - \bar{\lambda}_1 \bar{\lambda}_2^3 l_1^2 \widehat{\Phi}_{,\bar{\theta}_1\bar{\theta}_1} \right) + l_1 l_2 \left(\bar{\lambda}_1^3 l_2^2 \widehat{\Phi}_{,\bar{\lambda}_1} - \bar{\lambda}_2^3 l_1^2 \widehat{\Phi}_{,\bar{\lambda}_2} \right) \right] n_2 n_3^2 \right. \\ & + \bar{\lambda}_1^2 \bar{\lambda}_2^4 l_1^2 l_3 \phi_2^* n_2^3 \left. \right\} n_1 \left. \right\} m_1 m_2 + \left\{ \left(\bar{\lambda}_1^4 \bar{\lambda}_2^2 l_2^2 l_3 \phi_1^* n_2^2 + \bar{\lambda}_1^2 l_2^2 l_1^2 \phi_3^* n_3^2 \right) n_1^2 + \bar{\lambda}_1^2 \bar{\lambda}_2^4 l_1^2 l_3 \phi_2^* n_2^4 \right. \\ & \left. + \bar{\lambda}_2 l_1^2 l_3 \left[\left(\bar{\lambda}_2 l_2^2 \widehat{\Phi}_{,\bar{\lambda}_2\bar{\lambda}_2} - 2 \bar{\lambda}_1^2 \bar{\lambda}_2^3 \widehat{\Phi}_{,\bar{\theta}_1\bar{\theta}_1} - 2 l_2 \widehat{\Phi}_{,\bar{\lambda}_2} \right) n_2^2 n_3^2 + \left(l_2 \widehat{\Phi}_{,\bar{\lambda}_2} + \bar{\lambda}_1^2 \bar{\lambda}_2^3 \widehat{\Phi}_{,\bar{\theta}_1\bar{\theta}_1} \right) n_3^4 \right] \right\} m_2^2 \left. \right\} \Bigg|_{\bar{\theta}_1=0^\circ} n_3^{-2} > 0, \end{aligned} \quad (2.51)$$

where $\phi_1^* = \bar{\lambda}_1 l_1 \widehat{\Phi}_{,\bar{\lambda}_1} + \widehat{\Phi}_{,\bar{\theta}_2 \bar{\theta}_2}$, $\phi_2^* = \bar{\lambda}_2 l_2 \widehat{\Phi}_{,\bar{\lambda}_2} + \widehat{\Phi}_{,\bar{\theta}_1 \bar{\theta}_1}$, $\phi_3^* = \bar{\lambda}_1 \widehat{\Phi}_{,\bar{\lambda}_1} - \bar{\lambda}_2 \widehat{\Phi}_{,\bar{\lambda}_2}$, and

$$l_1 = \bar{\lambda}_1^4 \bar{\lambda}_2^2 - 1, \quad l_2 = \bar{\lambda}_1^2 \bar{\lambda}_2^4 - 1, \quad l_3 = \bar{\lambda}_1^2 - \bar{\lambda}_2^2. \quad (2.52)$$

Before proceeding with the study of conditions (2.47), (2.49), (2.50), (2.51) for the particle-reinforced composites of interest, it is important to make the following remarks:

(1) The SE conditions (2.49) and (2.51) are valid for any stored-energy function of the form $\Phi(\bar{\lambda}_1, \bar{\lambda}_2, \bar{\theta}_1, \bar{\theta}_2)$ corresponding to a transversely isotropic material whose axis of symmetry is aligned with the \mathbf{e}_3 direction and subjected to a deformation field of the form (2.24) (with the condition $\bar{\theta}_1 = 0^\circ$) and (2.34), respectively.

(2) In the remainder of this section, we will examine the SE conditions (2.49) and (2.51) only for the transversely isotropic composite with the class of particulate microstructures studied in this work. For this class of composites, based on a numerical study of (2.49) and (2.51) (as will be discussed in Part II of this work), we provide the corresponding critical unit vectors \mathbf{n}_{cr} and \mathbf{m}_{cr} at which these condition are first violated.

(3) The aforementioned results for the critical vectors \mathbf{n}_{cr} , \mathbf{m}_{cr} are based on numerical investigations carried out for composites with Gent and neo-Hookean matrices. However, it is plausible that corresponding calculations for composites with other matrix models of the form (2.21) would result in the same critical unit vectors.

Keeping in mind these remarks, in the next two subsections we consider the strong ellipticity conditions (2.49) and (2.51) for two special types of loadings. In the first subsection, we consider *axisymmetric shear* (characterized by $\bar{\lambda}_1 = \bar{\lambda}_2 = \bar{\lambda}$), and provide first the SE conditions associated with expressions (2.49) and (2.51) for non-aligned and aligned loadings, respectively. In the second, we provide the corresponding specialized SE conditions for *pure shear* loadings (characterized by $\bar{\lambda}_1 = \bar{\lambda}$, $\bar{\lambda}_2 = 1$). In this context, it is useful to introduce the critical stretch $\bar{\lambda}_{cr}$, at which the strong ellipticity conditions associated with axisymmetric and pure shear loadings are first violated.

In the discussions below, it is helpful to introduce the notations

$$\widehat{\Phi}^{AS}(\bar{\lambda}, \bar{\theta}_1, \bar{\theta}_2) = \widehat{\Phi}(\bar{\lambda}, \bar{\lambda}, \bar{\theta}_1, \bar{\theta}_2), \quad \widehat{\Phi}^{PS}(\bar{\lambda}, \bar{\theta}_1, \bar{\theta}_2) = \widehat{\Phi}(\bar{\lambda}, 1, \bar{\theta}_1, \bar{\theta}_2), \quad (2.53)$$

corresponding to general *non-aligned* axisymmetric and pure shear loadings, respectively (cf., (2.29)). Similarly, we introduce the notations

$$\widehat{\phi}^{AS}(\bar{\lambda}, \bar{\theta}) = \widehat{\phi}(\bar{\lambda}, \bar{\lambda}, \bar{\theta}), \quad \widehat{\phi}^{PS}(\bar{\lambda}, \bar{\theta}) = \widehat{\phi}(\bar{\lambda}, 1, \bar{\theta}), \quad (2.54)$$

respectively for axisymmetric and pure shear loadings with $\theta_1 = 0$ (cf., (2.30)).

2.5.1 Axisymmetric Shear

Here, we begin by considering the SE condition for *non-aligned* axisymmetric loadings, characterized by $\bar{\lambda}_1 = \bar{\lambda}_2 = \bar{\lambda}$ in the loading form (2.24). For this case, the numerical results show that the critical unit vectors at which the inequality (2.47) cease to hold, take the form $\mathbf{m}_{cr} = \mathbf{e}_2$ and

$\mathbf{n}_{cr} = \cos(\alpha_{cr})\mathbf{e}_1 + \sin(\alpha_{cr})\mathbf{e}_3$. In view of these results for the critical vectors \mathbf{m}_{cr} and \mathbf{n}_{cr} , it is inferred that the macroscopic instability, under non-aligned loading condition, consistently takes places through development of *localized* shear deformations (also known as “*shear bands*”) on all planes whose normal lies in the $\mathbf{e}_1 - \mathbf{e}_3$ plane, and in the \mathbf{e}_2 direction. In this connection, α_{cr} serves to characterize the angle between the normal to the plane of the “shear band” and the \mathbf{e}_1 direction, *exactly* at the moment of shear band initiation. The corresponding normal vector in the undeformed configuration can be obtained from relation $\mathbf{N}_{cr} = \bar{\mathbf{F}}_{cr}^T \mathbf{n}_{cr}$. Using the resulting vectors \mathbf{n}_{cr} , and \mathbf{m}_{cr} in condition (2.47), it can be deduced that macroscopic instabilities may first develop along *non-aligned* axisymmetric shear loading paths whenever the quadratic equation

$$\widehat{L}_{2121}^c \left(\frac{n_1}{n_3} \right)^2 + 2 \widehat{L}_{2321}^c \left(\frac{n_1}{n_3} \right) + \widehat{L}_{2323}^c = 0 \quad (2.55)$$

admits real roots for n_1/n_3 . Consequently, necessary and sufficient condition for the quadratic equation to have complex roots can be expressed as

$$\widehat{L}_{2121}^c \widehat{L}_{2323}^c - \left(\widehat{L}_{2321}^c \right)^2 > 0. \quad (2.56)$$

Making use of the expressions for the L_{2121}^c , L_{2323}^c , and L_{2321}^c , provided in Appendix B.4, for axisymmetric shear loading, the associated SE condition for the effective stored-energy function $\widehat{\Phi}$ can be written as

$$\left\{ \begin{aligned} & \left[\bar{\lambda} \sin^2(\bar{\theta}) \widehat{\Phi}_{,\bar{\lambda}_1 \bar{\lambda}_1 \bar{\theta}_1 \bar{\theta}_1} - \bar{\lambda} \sin(\bar{\theta}) \cos(\bar{\theta}) \widehat{\Phi}_{,\bar{\lambda}_1 \bar{\lambda}_1 \bar{\theta}_2} + 6 \widehat{\Phi}_{,\bar{\lambda}_1 \bar{\lambda}_1} \bar{\lambda} + 2 \bar{\lambda} \widehat{\Phi}_{,\bar{\lambda}_2 \bar{\lambda}_2} + 8 \widehat{\Phi}_{,\bar{\lambda}_1} \right. \\ & \left. - 2 \bar{\lambda} \widehat{\Phi}_{,\bar{\lambda} \bar{\lambda}}^{AS} - 2 \widehat{\Phi}_{,\bar{\lambda}}^{AS} \right] \times \left[\bar{\lambda}^5 \sin(\bar{\theta}) \cos(\bar{\theta}) \widehat{\Phi}_{,\bar{\theta}_2} + \bar{\lambda}^5 \cos^2(\bar{\theta}) \widehat{\Phi}_{,\bar{\theta}_1 \bar{\theta}_1} + (\bar{\lambda}^6 - 1) \widehat{\Phi}_{,\bar{\lambda}_2} \right] \\ & - 2 \bar{\lambda}^2 (\bar{\lambda}^6 - 1)^{-2} \left\{ 2 \bar{\lambda} (2 \bar{\lambda}^6 \cos^2(\bar{\theta}) - 1) \widehat{\Phi}_{,\bar{\theta}_2} + \bar{\lambda}^2 (\bar{\lambda}^6 - 1) \cos^2(\bar{\theta}) \widehat{\Phi}_{,\bar{\lambda}_1 \bar{\theta}_2} \right. \\ & \left. - \bar{\lambda}^2 \sin(\bar{\theta}) \cos(\bar{\theta}) \left[4 \bar{\lambda}^5 \widehat{\Phi}_{,\bar{\theta}_1 \bar{\theta}_1} + (\bar{\lambda}^6 - 1) \widehat{\Phi}_{,\bar{\lambda}_1 \bar{\theta}_1 \bar{\theta}_1} \right] \right\}^2 \Bigg|_{\substack{\bar{\lambda}_1 = \bar{\lambda}_2 = \bar{\lambda}, \\ \bar{\theta}_1 = 0, \bar{\theta}_2 = \bar{\theta}}} > 0. \end{aligned} \right. \quad (2.57)$$

Recall that the above condition is calculated at $\bar{\theta}_1 = 0^\circ$, and the axisymmetric shear conditions $\bar{\lambda}_1 = \bar{\lambda}_2 = \bar{\lambda}$ should be applied to all terms after taking derivatives. Loss of ellipticity is therefore expected at the critical stretch $\bar{\lambda}_{cr}$ for which condition (2.57) is first violated. The corresponding critical angle α_{cr} can be shown to be given by

$$\alpha_{cr} = \bar{\theta} + \tan^{-1} \left\{ \bar{\lambda} \left\{ 2 \bar{\lambda} (2 \bar{\lambda}^6 \cos^2(\bar{\theta}) - 1) \widehat{\Phi}_{,\bar{\theta}_2} + \bar{\lambda}^2 (\bar{\lambda}^6 - 1) \cos^2(\bar{\theta}) \widehat{\Phi}_{,\bar{\lambda}_1 \bar{\theta}_2} \right. \right. \\ \left. \left. - \bar{\lambda}^2 \sin(\bar{\theta}) \cos(\bar{\theta}) \left[4 \bar{\lambda}^5 \widehat{\Phi}_{,\bar{\theta}_1 \bar{\theta}_1} + (\bar{\lambda}^6 - 1) \widehat{\Phi}_{,\bar{\lambda}_1 \bar{\theta}_1 \bar{\theta}_1} \right] \right\} \right. \\ \left. \times \frac{1}{2} \left[\bar{\lambda}^5 \cos(\bar{\theta}) \sin(\bar{\theta}) \widehat{\Phi}_{,\bar{\theta}_2} + \bar{\lambda}^5 \widehat{\Phi}_{,\bar{\theta}_1 \bar{\theta}_1} \cos^2(\bar{\theta}) + (\bar{\lambda}^6 - 1) \widehat{\Phi}_{,\bar{\lambda}_2} \right]^{-1} \right\} \Bigg|_{\substack{\bar{\lambda}_1 = \bar{\lambda}_2 = \bar{\lambda}_{cr}, \\ \bar{\theta}_1 = 0, \bar{\theta}_2 = \bar{\theta}}}. \quad (2.58)$$

Note that the above expression is calculated at $\bar{\lambda}_{cr}$.

Next, we consider the development of macroscopic instabilities for the composites subjected to

the *aligned* axisymmetric loading of the form (2.38). In this case, the result depends on whether the particles are *prolate* ($w > 1$), or *oblate* ($w < 1$), and these two cases are considered separately below.

Prolate particles. Here, we consider composites consisting of an incompressible matrix and aligned prolate spheroidal particles (see Figure 2.1(a)) subjected to axisymmetric shear loading (2.38). In this case, within the context of condition (2.50), and based on the numerical examination, the loss of strong ellipticity for the effective stored-energy function $\widehat{\Phi}$ takes place when the vector \mathbf{n}_{cr} is aligned with the \mathbf{e}_3 axis and the vector \mathbf{m}_{cr} lies in the $\mathbf{e}_1 - \mathbf{e}_2$ plane in the deformed configuration. That is, the homogenized composite material may develop localized shear deformations on the plane determined by the normal \mathbf{e}_3 , and in all directions in the transverse plane. Using these vectors in the condition (2.50), it can be deduced that macroscopic instabilities may first develop along axisymmetric shear loading paths whenever the following inequality is first violated

$$\widehat{L}_{1313}^c = \widehat{L}_{2323}^c > 0. \quad (2.59)$$

It should be noted that, for the case of prolate particles, the associated numerical results (to be discussed in more detail in Part II of this work) show that this type of instability occurs only when $\bar{\lambda} > 1$. This regime of $\bar{\lambda}$ corresponds to the *equibiaxial tension* loading in the $\mathbf{e}_1 - \mathbf{e}_2$ plane with the stretch $\bar{\lambda}$, which is equivalent to the *uniaxial compression* loading in the \mathbf{e}_3 direction with (compressive) stretch $1/\bar{\lambda}^2$. In other words, as the (compressive) stretching along the long axes of the particle increases, the effective incremental modulus in the transverse plane perpendicular to the particle symmetry axes ($\widehat{L}_{1313}^c = \widehat{L}_{2323}^c$) *softens* to the point that it vanishes ($\widehat{L}_{1313}^c = 0$). This point is characterized by some finite critical stretch $\bar{\lambda}_{cr} > 1$. This localized behavior can be related to the evolution of the microstructure in the particle-reinforced elastomers. Thus, as will be seen in Part II, the loss of strong ellipticity would correspond to an abrupt rotation (or *flopping*) of the particles under a sufficiently large compressive loading. Making use of the expression for L_{1313}^c given in Appendix B.4, the associated strong ellipticity condition in terms of the effective stored-energy function can be given as

$$\left[\bar{\lambda}^5 \frac{\partial^2 \widehat{\phi}^{AS}}{\partial \bar{\theta}^2} + \frac{1}{2} (\bar{\lambda}^6 - 1) \frac{\partial \widehat{\phi}^{AS}}{\partial \bar{\lambda}} \right] \Bigg|_{\bar{\theta}=0^\circ} > 0. \quad (2.60)$$

Note that all derivatives in the above conditions are taken at $\bar{\theta} = 0^\circ$.

Oblate particles. Here, we consider composites consisting of an incompressible matrix and aligned oblate spheroidal particles (see Figure 2.1(b)). In this case, along the loading path (2.38), the numerical study indicates that the strong ellipticity condition (2.50) is first violated when the vector \mathbf{n}_{cr} lies in the $\mathbf{e}_1 - \mathbf{e}_2$ plane and the vector \mathbf{m}_{cr} is aligned with the \mathbf{e}_3 direction in the deformed configuration. In other words, the homogenized composite material may develop localized shear deformations on all planes whose normal lies in the $\mathbf{e}_1 - \mathbf{e}_2$ plane, and in the \mathbf{e}_3 direction. Using these vectors in the condition (2.50), it is easy to show that the first macroscopic instabilities may

develop along axisymmetric shear loading paths whenever the following inequality is first violated

$$\widehat{L}_{3131}^c = \widehat{L}_{3232}^c > 0. \quad (2.61)$$

It is remarked that, for the case of oblate particles, the numerical results show that this instability occurs only for $0 < \bar{\lambda} < 1$. This regime of $\bar{\lambda}$ corresponds to a *equibiaxial compression* loading in the $\mathbf{e}_1 - \mathbf{e}_2$ plane with (compressive) stretch $\bar{\lambda}$, which is equivalent to the *uniaxial tension* loading in the \mathbf{e}_3 direction with (tensile) stretch $1/\bar{\lambda}^2$. That is, as the (compressive) stretching in the transverse plane increases, the effective incremental modulus in all planes with the normal vector $\mathbf{n} \in \text{Span}\{\mathbf{e}_1 - \mathbf{e}_2\}$ *softens* to the point that it vanishes ($\widehat{L}_{3131}^c = \widehat{L}_{3232}^c = 0$). Making contact with the microstructure, the loss of strong ellipticity can be identified with flopping of the oblate particles under compressive loading in the $\mathbf{e}_1 - \mathbf{e}_2$ plane. Making use of the expression for \widehat{L}_{3131}^c , given in Appendix B.4, the associated strong ellipticity condition in terms of the effective stored-energy function can be written as

$$\left[2 \frac{\partial^2 \widehat{\phi}^{AS}}{\partial \bar{\theta}^2} + \bar{\lambda}(\bar{\lambda}^6 - 1) \frac{\partial \widehat{\phi}^{AS}}{\partial \bar{\lambda}} \right] \Big|_{\bar{\theta}=0^\circ} > 0. \quad (2.62)$$

2.5.2 Pure shear

In this subsection, we consider the case of particle-reinforced elastomers subjected to pure shear deformations, characterize by $\bar{\lambda}_1 = \bar{\lambda}, \bar{\lambda}_2 = 1$ in expression (2.24). In this case, similar to the case of non-aligned axisymmetric shear loading, the strong ellipticity condition (2.47) is violated at the critical vectors $\mathbf{m}_{cr} = \mathbf{e}_2$ and $\mathbf{n}_{cr} = \cos(\alpha_{cr})\mathbf{e}_1 + \sin(\alpha_{cr})\mathbf{e}_3$. In turn, the same strong ellipticity condition (2.56) is obtained for the case of non-aligned pure shear loading. Making use of the expressions for the L_{2121}^c , L_{2323}^c , and L_{2321}^c given in Appendix B.4 for pure shear loading, the following macroscopic onset-of-failure surface $(\bar{\lambda}, \bar{\theta})$ is obtained

$$\begin{aligned} & \left\{ \left[\cos(\bar{\theta}) \sin(\bar{\theta}) \widehat{\Phi}_{,\bar{\theta}_2} - \sin^2(\bar{\theta}) \widehat{\Phi}_{,\bar{\theta}_1 \bar{\theta}_1} - (\bar{\lambda}^2 - 1) \left(\bar{\lambda} \widehat{\Phi}_{,\bar{\lambda}_1} - \widehat{\Phi}_{,\bar{\lambda}_2} \right) \right] \bar{\lambda}^2 \right. \\ & \times \left[(\bar{\lambda}^2 - 1) \widehat{\Phi}_{,\bar{\lambda}_2} + \bar{\lambda}^2 \sin(\bar{\theta}) \cos(\bar{\theta}) \widehat{\Phi}_{,\bar{\theta}_2} + \bar{\lambda}^2 \cos^2(\bar{\theta}) \widehat{\Phi}_{,\bar{\theta}_1 \bar{\theta}_1} \right] - \bar{\lambda}^4 (\bar{\lambda}^2 + 1)^{-2} \\ & \left. \times \left[(\bar{\lambda}^2 \cos^2(\bar{\theta}) - \sin^2(\bar{\theta})) \widehat{\Phi}_{,\bar{\theta}_2} - (\bar{\lambda}^2 + 1) \sin(\bar{\theta}) \cos(\bar{\theta}) \widehat{\Phi}_{,\bar{\theta}_1 \bar{\theta}_1} \right]^2 \right\} \Big|_{\substack{\bar{\lambda}_1 = \bar{\lambda}, \bar{\lambda}_2 = 1, \\ \bar{\theta}_1 = 0, \bar{\theta}_2 = \bar{\theta}}} > 0. \quad (2.63) \end{aligned}$$

Note that the SE condition (2.63) is calculated at $\bar{\theta}_1 = 0^\circ$, and the pure shear conditions $\bar{\lambda}_1 = \bar{\lambda}$, $\bar{\lambda}_2 = 1$ should be applied to all terms after taking derivatives. Also, for the cases in which the strong ellipticity condition (2.63) is violated, the corresponding critical angle α_{cr} , characterizing the angle between the \mathbf{e}_1 axis and the normal to the shear band plane at the moment of its initiation, can be

shown to be obtained by

$$\begin{aligned} \alpha_{cr} = & \bar{\theta} + \tan^{-1} \left\{ \bar{\lambda}^2 \left[(\bar{\lambda}^2 \cos^2(\bar{\theta}) - \sin^2(\bar{\theta})) \widehat{\Phi}_{,\bar{\theta}_2} - \sin(\bar{\theta}) \cos(\bar{\theta}) (\bar{\lambda}^2 + 1) \widehat{\Phi}_{,\bar{\theta}_1 \bar{\theta}_1} \right] \right. \\ & \left. \times \left\{ (\bar{\lambda}^2 + 1) \left[(\bar{\lambda}^2 - 1) \widehat{\Phi}_{,\bar{\lambda}_2} + \bar{\lambda}^2 \sin(\bar{\theta}) \cos(\bar{\theta}) \widehat{\Phi}_{,\bar{\theta}_2} + \bar{\lambda}^2 \cos^2(\bar{\theta}) \widehat{\Phi}_{,\bar{\theta}_1 \bar{\theta}_1} \right] \right\}^{-1} \right\} \Bigg|_{\substack{\bar{\lambda}_1 = \bar{\lambda}_{cr}, \bar{\lambda}_2 = 1, \\ \bar{\theta}_1 = 0, \bar{\theta}_2 = \bar{\theta}}} . \end{aligned} \quad (2.64)$$

Recall that the above expression is calculated at $\bar{\lambda}_{cr}$, corresponding to the stretch at which the shear band is initiated.

Next, we consider the development of macroscopic instabilities for the composites subjected to the aligned pure shear loading of the form (2.41). Similar to the case of axisymmetric loadings, the two classes of microstructures with *prolate* and *oblate* particles (see Figure 2.1(a), (b)) should be examined separately.

Prolate particles. For the case of prolate particles (see Figure 2.1(a)), the strong ellipticity condition (2.50) is violated at the critical vectors $\mathbf{n}_{cr} = \mathbf{e}_3$ and $\mathbf{m}_{cr} \in \text{Span}\{\mathbf{e}_1 - \mathbf{e}_2\}$. Making use of these vectors in condition (2.50), it is concluded that the particle-reinforced materials become unstable under the aligned pure shear loading whenever any of the following inequalities is violated

$$\widehat{L}_{1313}^c > 0, \quad \widehat{L}_{2323}^c > 0. \quad (2.65)$$

In fact, the “failure mechanism” for both aligned pure shear and axisymmetric shear loadings is essentially the same, which is the softening of the effective incremental shear response perpendicular to the \mathbf{e}_3 direction. However, at the point of instability in the pure shear case, the overall shear response of the composite in the transverse plane vanishes in a *particular* direction within this plane (\mathbf{e}_1 or \mathbf{e}_2), while in the axisymmetric shear case, as mentioned earlier, it vanishes in *all* directions within the transverse plane. Making contact with evolution of the microstructure, this implies that, under aligned pure shear loading, the prolate particles “flop” about either the \mathbf{e}_1 or \mathbf{e}_2 directions depending on the other microstructural variables (w and c), while, under aligned axisymmetric shear loading, the flopping of the particles about any axis $\mathbf{m} \in \text{Span}\{\mathbf{e}_1 - \mathbf{e}_2\}$ is essentially the same. Now, making use of the pertinent expressions in Appendix B.4 for aligned pure shear loading, the necessary and sufficient conditions for the associated effective stored-energy function $\widehat{\Phi}$ to be strongly elliptic can be expressed as

$$\begin{aligned} & \left\{ \bar{\lambda} \frac{\partial^2 \widehat{\phi}^{PS*}}{\partial \bar{\theta}^2} + (\bar{\lambda}^2 - 1) \left[\frac{\partial \widehat{\phi}^{PS}}{\partial \bar{\lambda}} - \left(\frac{\partial \widehat{\phi}}{\partial \bar{\lambda}_1} \right) \Big|_{\bar{\lambda}_1 = \bar{\lambda}, \bar{\lambda}_2 = 1} \right] \right\} \Bigg|_{\bar{\theta} = 0^\circ} > 0, \\ & \left[\bar{\lambda}^3 \frac{\partial^2 \widehat{\phi}^{PS}}{\partial \bar{\theta}^2} + (\bar{\lambda}^4 - 1) \frac{\partial \widehat{\phi}^{PS}}{\partial \bar{\lambda}} \right] \Bigg|_{\bar{\theta} = 0^\circ} > 0, \end{aligned} \quad (2.66)$$

where $\widehat{\phi}^{PS*}(\bar{\lambda}, \bar{\theta}) = \widehat{\phi}(1, \bar{\lambda}, \bar{\theta})$. (In the context of this last expression, it should be recalled that $\widehat{\Phi}(\bar{\lambda}_1, \bar{\lambda}_2, \bar{\theta}, 0) = \widehat{\Phi}(\bar{\lambda}_2, \bar{\lambda}_1, 0, \bar{\theta})$.) Also, note that all derivatives in the above conditions are taken at

$\bar{\theta} = 0^\circ$, and the pure shear conditions $\bar{\lambda}_1 = \bar{\lambda}$, $\bar{\lambda}_2 = 1$ should be applied to the term $\partial\widehat{\phi}/\partial\bar{\lambda}_1$.

Oblate particles. For the case of oblate particles (see Figure 2.1(b)), the strong ellipticity condition (2.50) is violated at the critical vectors $\mathbf{n}_{cr} = \mathbf{e}_1$ and $\mathbf{m}_{cr} = \mathbf{e}_3$. Making use of these vectors in condition (2.50), it is deduced that the particle-reinforced materials first become unstable under aligned pure shear loading whenever the following inequality is violated

$$\widehat{L}_{3131}^c > 0. \quad (2.67)$$

In this case, similar to the prolate particles case, the “failure mechanism” for both aligned pure shear and axisymmetric shear loadings is essentially the same, which is the softening of the effective incremental shear response along the \mathbf{e}_3 direction. The only difference is that, at the point of instability in the pure shear case, the overall shear response in the plane with normal vector \mathbf{e}_1 vanishes ($\widehat{L}_{3131}^c = 0$); however, in the axisymmetric shear case, the overall shear response of the composite in *all* planes with the normal vector in the $\mathbf{n} \in \text{Span}\{\mathbf{e}_1 - \mathbf{e}_2\}$ vanishes ($\widehat{L}_{3131}^c = \widehat{L}_{3232}^c = 0$). Now, making use of the pertinent expressions in Appendix B.4 for aligned pure shear loading, the necessary and sufficient conditions for the associated effective stored-energy function $\widehat{\Phi}$ to be strongly elliptic can be expressed as

$$\left[\frac{\partial^2 \widehat{\phi}^{PS}}{\partial \theta^2} + \bar{\lambda}(\bar{\lambda}^4 - 1) \frac{\partial \widehat{\phi}^{PS}}{\partial \lambda} \right] \Big|_{\bar{\theta}=0^\circ} > 0. \quad (2.68)$$

Finally, note that for particular case of $w = 1$, corresponding to spherical shape of particles, no loss of strong ellipticity is detected within the context of the condition (2.50). This observation, which is consistent with the results in Chapter 1 and the results of Lopez-Pamies et al. (2013a), implies that the effective stored-energy function (2.35) is *strongly elliptic* in the limiting case of *spherical* particles. The results for general spheroidal particle shapes will be discussed in more detail in the next chapter.

2.6 Concluding Remarks

In this chapter, we have made use of the tangent second-order, finite-strain homogenization framework proposed in Chapter 1 to estimate the overall response and microstructure evolution in incompressible elastomers reinforced by aligned, spheroidal, rigid particles, subject to general loading conditions. In particular, for *non-aligned* loadings, the analytical estimates (2.31) and (2.33) were derived for the effective stored-energy function of the composite and the rotation of the particles, respectively. For the special case of *aligned* loadings, explicit closed-form expressions were provided for the effective stored-energy function of particle-reinforced neo-Hookean elastomers subjected to *axisymmetric* and *pure shear* loadings, as given in (2.39) and (2.42), respectively. It should be emphasized that the analytical results developed in this work are given in a form that can be easily implemented numerically into user-defined constitutive subroutines for use with standard finite element codes.

In this work, we also have presented a detailed study of the possible development of macroscopic instabilities in the particle-reinforced composites of interest, under both aligned and non-aligned loading conditions. The onset of such instabilities in these materials is identified with the loss of strong ellipticity of the associated homogenized behavior. In this connection, general conditions for loss of ellipticity were given in (2.49) and (2.51) for non-aligned and aligned loadings, respectively. These conditions were then specialized for the class of particulate composites undergoing axisymmetric and pure shear loadings in Subsections 2.5.1 and 2.5.2.

It should be remarked that, to the best of our knowledge, the estimates provided in this work for the effective stored-energy function and the particle rotation are the first homogenization-type estimates for reinforced elastomers with general spheroidal particle shape. The results are valid for large strains provided that the interfaces between the particles and the rubber remain intact. The estimates generalize the results of Chapter 1 for spherical particles, and are consistent with earlier results for continuous-fiber-reinforced elastomers (Agoras et al., 2009a,b), as well as with simple laminates (deBotton, 2005; Lopez-Pamies and Ponte Castañeda, 2009), in the limits when the aspect ratio of the spheroidal particles tends to infinity and zero, respectively.

In the next chapter, the analytical results provided in this part for the effective stored-energy function, rotation of particles, and development of the macroscopic instabilities will be explored in more detail for particle reinforced composites with neo-Hookean and Gent matrix phases. Explicit results will be presented for axisymmetric and pure shear loadings, as well as for a wide range of particles shapes and concentrations. Where possible, comparisons with full-field numerical simulations will be carried out.

Chapter 3

Application of the TSO theory to short fiber-reinforced composites: II—Representative examples

In Chapter 2, we presented a homogenization-based constitutive model for the overall behavior of reinforced elastomers consisting of aligned, spheroidal particles distributed randomly in an incompressible, hyperelastic matrix. In particular, we provided analytical estimates for the effective stored-energy functions of the composites, as well as for the associated average particle rotations under finite deformations. The rotation of the particles is found to be very sensitive to the specific loading conditions applied, and is such that the particles tend to align themselves with the largest tensile direction. In addition, we obtained corresponding formulae for the detection of macroscopic instabilities in these composites. With the objective of illustrating the key features of the analytical results presented in Chapter 2, we conduct here a more detailed study of these results for several representative values of the microstructural and loading parameters, as well as matrix properties. More specifically, this study deals with neo-Hookean and Gent elastomers reinforced with spheroidal particles of prolate and oblate shapes with various aspect ratios and volume fractions, subjected to aligned and non-aligned macroscopic loading conditions. In addition, to assess the accuracy of the model, we compare our results with corresponding finite element results available from the literature for the special case of spherical particles, and good agreement is found. For non-spherical particles, the results indicate that the possible rotation of the particles has a major influence on the overall response of the elastomeric composites. Furthermore, it is found that the composite may develop macroscopic shear localization instabilities, as a consequence of the geometric softening induced by the sudden rotation—or flopping—of the particles, when a sufficiently large amount of compression is applied along the long axes of the particles.

3.1 Introduction

In the previous Chapter, we made use of a recently developed, improved version of the tangent second-order (TSO) homogenization method (developed in Chapter 1) to determine estimates for the macroscopic elastic behavior of short-fiber-reinforced elastomers. More specifically, the class of composites considered in this work consists of (incompressible) generalized neo-Hookean elastomers reinforced by aligned, rigid, spheroidal particles of identical aspect ratios (see Figure 2.1), exhibiting overall transversely isotropic behavior in the undeformed configuration. The composite is subjected to finite-deformation loadings whose principal stretching directions are generally not aligned with those of the particles in the undeformed configuration. The analytical estimates, presented in Chapter 2, include estimates for the effective stored-energy function of the composite, denoted by \widehat{W} , as well as the associated finite rotations of the particles, denoted by $\bar{\psi}^{(2)}$, which are a consequence of the large deformations involved. Moreover, we investigate the possible development of macroscopic instabilities in the composite, which, as discussed in Chapter 2, correspond to loss of strong ellipticity of the effective stored-energy function \widehat{W} .

Our aim in this chapter is to examine, in the context of some representative examples, the essential features of the effective constitutive model for the composites provided in Chapter 2. In particular, we investigate the influence of the relevant microstructural variables (particle aspect ratio and volume fraction), as well as nonlinear behavior of the matrix phase, on the effective stored-energy function, appropriate macroscopic stress measures and possible change in orientation

of the underlying particles. In this connection, it should be noted that the results given here for *dilute* concentrations of particles can be viewed as a generalization of the Eshelby results in linear elasticity to finite elasticity. Moreover, we investigate the influence of the microstructural variables on the possible development of macroscopic instabilities in the composites, as determined by the strong ellipticity condition. Along these lines, we will also explore the connections between the rotation of the particles and the macroscopic instabilities. Specifically, we provide results for the two special classes of macroscopic loadings discussed in Chapter 2, namely, *axisymmetric shear* and *pure shear* loading conditions. Both of these types of loadings will be considered for *aligned* and *non-aligned* conditions.

The outline of this chapter is as follows. In section 3.2, for convenience and clarity, we briefly recall the analytical results presented in Chapter 2 and lay out the key features of the results to be studied in this chapter. Making use of these results, in section 3.3 we provide and discuss examples for various microgeometries, matrix properties and loading parameters. In particular, in this section, we put into evidence the interplay between the rotation of the particles under non-aligned large deformations and the geometric softening observed in the associated macroscopic behavior. We also show that the macroscopic instabilities that develop in the particle-reinforced composites are basically caused by the collective rotation—or “*flopping*”—of the particles, when compressed along their long axes. Finally, in Section 3.4, we provide some concluding remarks.

3.2 Overall constitutive behavior

In this section, we briefly recall the analytical results presented in Chapter 2 and the associated sets of examples to be provided in this chapter. In Chapter 2, we considered two-phase composites consisting of an incompressible, elastomeric matrix phase (phase 1), characterized by the stored-energy function $W_\mu^{(1)}$, and a polydisperse family of rigid, aligned, spheroidal particles (phase 2) with aspect ratio w and volume fraction c . For definiteness, the principal directions of the particles in the undeformed configuration are defined by the rectangular Cartesian basis $\{\mathbf{e}_i\}$ such that the symmetry axis of the particles is aligned with the \mathbf{e}_3 direction in that configuration. Also, the distribution of particles is assumed to be statistically isotropic in the transverse plane, which is the plane perpendicular to the symmetry axis of particles, namely, the $\mathbf{e}_1 - \mathbf{e}_2$ plane. For convenience, the basis $\{\mathbf{e}_i\}$ is taken to define the fixed laboratory frame of reference as well, and henceforth, unless stated, the components of any tensorial quantity will be referred to $\{\mathbf{e}_i\}$. Moreover, two different geometries for the particles are assumed: (i) *prolate* ($w \geq 1$) and (ii) *oblate* ($w < 1$) spheroidal particles (see Figs. 2.1(a), (b) in Chapter 2.) Furthermore, in Chapter 2, the *local* constitutive behavior of the matrix phase was assumed to be characterized by a fairly general class of incompressible, isotropic stored-energy functions, written as

$$W_\mu^{(1)}(\mathbf{F}) = g(I) + h(J), \quad (3.1)$$

where g and h are material functions, and $I = \text{tr}(\mathbf{F}^T \mathbf{F}) = \lambda_1^2 + \lambda_2^2 + \lambda_3^2$ and $J = \det \mathbf{F} = \lambda_1 \lambda_2 \lambda_3$ denote, respectively, the first and third invariants of the deformation gradient tensor \mathbf{F} , with $\lambda_1, \lambda_2, \lambda_3$

identifying the corresponding principal stretches. Here, the deformation gradient \mathbf{F} is subject to the incompressibility constraint, implying that

$$\det \mathbf{F} = \lambda_1 \lambda_2 \lambda_3 = 1. \quad (3.2)$$

In this chapter, for calculation purposes, we make use of two simple examples of (3.1). The first material is a neo-Hookean solid whose stored-energy function is given by

$$W_\mu^{(1)}(\mathbf{F}) = \frac{1}{2}\mu^{(1)}(I - 3) + \frac{1}{2}\mu^{(1)}(J - 1)(J - 3). \quad (3.3)$$

where $\mu^{(1)}$ is the shear modulus of the solid at zero strain. The second material is an incompressible Gent solid with stored-energy function

$$W_\mu^{(1)}(\mathbf{F}) = -\frac{J_m \mu^{(1)}}{2} \ln \left(1 - \frac{I - 3}{J_m} \right) + \frac{1}{2}\mu^{(1)}(J - 1)(J - 3) - \frac{\mu^{(1)}}{J_m}(J - 1)^2, \quad (3.4)$$

where $J_m (> 0)$ is the *lock-up* parameter serving to characterize the limiting chain extensibility of elastomers. It is noted that the neo-Hookean model (3.3) corresponds to the limit as J_m approaches infinity of the Gent model (3.4), and does not lock up at finite strain. It is also recalled that the terms involving the factor $(J - 1)$ do not vanish for the homogenized behavior of the reinforced elastomers and are in fact crucial to obtain the correct linearized behavior (see Chapter 2).

The above-described particle-reinforced material is a *transversely isotropic* composite (with symmetry axis aligned with \mathbf{e}_3) in the undeformed configuration, and its macroscopic response is characterized by the effective stored-energy function $\widehat{W}(\bar{\mathbf{F}})$. The macroscopic deformation gradient $\bar{\mathbf{F}}$ is subject to the *exact* overall incompressibility constraint $\det(\bar{\mathbf{F}}) = \bar{\lambda}_1 \bar{\lambda}_2 \bar{\lambda}_3 = 1$, with $\bar{\lambda}_1, \bar{\lambda}_2, \bar{\lambda}_3$ identifying the macroscopic principal stretches. For definiteness in the analytical calculations, and motivated by possible comparisons with numerical simulations and/or experiments, we consider deformation gradients $\bar{\mathbf{F}}$ with the matrix representation

$$[\bar{F}_{ij}] = \begin{bmatrix} \cos(\bar{\theta}) & 0 & \sin(\bar{\theta}) \\ 0 & 1 & 0 \\ -\sin(\bar{\theta}) & 0 & \cos(\bar{\theta}) \end{bmatrix} \begin{bmatrix} \bar{\lambda}_1 & 0 & 0 \\ 0 & \bar{\lambda}_2 & 0 \\ 0 & 0 & (\bar{\lambda}_1 \bar{\lambda}_2)^{-1} \end{bmatrix} \begin{bmatrix} \cos(\bar{\theta}) & 0 & -\sin(\bar{\theta}) \\ 0 & 1 & 0 \\ \sin(\bar{\theta}) & 0 & \cos(\bar{\theta}) \end{bmatrix}, \quad (3.5)$$

where the conditions $\bar{\lambda}_1 = \bar{\lambda}_2 = \bar{\lambda}$ and $\bar{\lambda}_1 = \bar{\lambda}, \bar{\lambda}_2 = 1$ correspond respectively to axisymmetric and pure shear loadings, with $\bar{\lambda}$ denoting a positive loading parameter. In the above representation, $\bar{\theta}$ denotes the angle of the Lagrangian principal loading axes relative to the (fixed) basis $\{\mathbf{e}_i\}$ in the $\mathbf{e}_1 - \mathbf{e}_3$ plane. Also, for convenience, we let the directions of the principal stretches $\bar{\lambda}_1, \bar{\lambda}_2, \bar{\lambda}_3 = (\bar{\lambda}_1 \bar{\lambda}_2)^{-1}$ be identified with the Cartesian vectors $\{\mathbf{e}'_i\}$ ($i = 1, 2, 3$). A schematic representation of the particle-reinforced elastomers subjected to the class of loadings (3.5) is given in Figure 3.3.2 of Chapter 2.

In Chapter 2, we made use of the tangent second-order (TSO) procedure, developed in Chapter 1, to generate estimates for the effective stored-energy function $\widehat{W}(\bar{\mathbf{F}})$ of the above-described particle-

reinforced materials, which, under deformation gradient (3.5), takes the functional form

$$\widehat{W}(\bar{\mathbf{F}}) = \widehat{\phi}(\bar{\lambda}_1, \bar{\lambda}_2, \bar{\theta}), \quad (3.6)$$

and is given explicitly by equation (31) in Chapter 2. Also, as discussed in Chapter 2, the principal directions of loading (identified by the $\{\mathbf{e}'_i\}$ axes) are, in general, not aligned with those of the particles (identified by the $\{\mathbf{e}_i\}$ axes in the undeformed configuration), leading to finite changes in the orientation of particles as characterized by the angle $\bar{\psi}^{(2)}$. An estimate for this angle, which is an essential part in the estimate for $\widehat{\phi}$, is delivered by the TSO procedure and given by equation (33) in Chapter 2. In addition, Eqs. (59)-(62) and (65)-(68) in Chapter 2 provide the associated *strong ellipticity* (SE) conditions for the composites under aligned loadings, for axisymmetric and pure shear loading conditions, respectively. Likewise, Eqs. (57) and (63) provide the SE conditions for the composites under non-aligned loadings for axisymmetric and pure shear loading conditions, respectively. Before proceeding with the detailed examples, it proves helpful to provide a brief description of the three different types of results covered in this chapter.

Effective constitutive relation.

Recalling that the fiber-reinforced elastomers of interest in this work are incompressible, their macroscopic constitutive relation is determined by the following expression for the average Cauchy stress tensor

$$\bar{\mathbf{T}} = \frac{\partial \widehat{W}(\bar{\mathbf{F}})}{\partial \bar{\mathbf{F}}} (\bar{\mathbf{F}})^T - p \mathbf{I}, \quad (3.7)$$

where p stands for the arbitrary hydrostatic pressure associated with the incompressibility constraint.

For the specific purpose of discussing the axisymmetric and pure shear modes of loading, it is useful to introduce the scalar stress variables

$$\bar{S}^{AS} = \frac{\partial \widehat{\phi}^{AS}(\bar{\lambda}, \bar{\theta})}{\partial \bar{\lambda}}, \quad \text{and} \quad \bar{S}^{PS} = \frac{\partial \widehat{\phi}^{PS}(\bar{\lambda}, \bar{\theta})}{\partial \bar{\lambda}}, \quad (3.8)$$

where (recalling expression (3.6)) $\widehat{\phi}^{AS} = \widehat{\phi}(\bar{\lambda}, \bar{\lambda}, \bar{\theta})$ and $\widehat{\phi}^{PS} = \widehat{\phi}(\bar{\lambda}, 1, \bar{\theta})$, respectively. They can be related to the normal components of the macroscopic *Cauchy stress* tensor $\bar{\mathbf{T}}$ via the relations

$$\bar{S}^{AS} = \bar{\lambda}^{-1} [(\bar{T}'_{11} + \bar{T}'_{22}) - 2\bar{T}'_{33}], \quad \text{and} \quad \bar{S}^{PS} = \bar{\lambda}^{-1} (\bar{T}'_{11} - \bar{T}'_{33}), \quad (3.9)$$

where the \bar{T}'_{ij} denote the components of the tensor $\bar{\mathbf{T}}$ relative to the “loading” basis $\{\mathbf{e}'_i\}$ (see Figure 3.3.2 in Chapter 2), and are determined by transformation rule

$$\bar{T}'_{ij} = \bar{Q}_{pi} \bar{T}_{pq} \bar{Q}_{qj}, \quad (3.10)$$

with $\bar{\mathbf{Q}} = \cos(\bar{\theta}) (\mathbf{e}_1 \otimes \mathbf{e}_1 + \mathbf{e}_3 \otimes \mathbf{e}_3) + \sin(\bar{\theta}) (\mathbf{e}_1 \otimes \mathbf{e}_3 - \mathbf{e}_3 \otimes \mathbf{e}_1) + \mathbf{e}_2 \otimes \mathbf{e}_2$. Note that for the case of aligned loadings ($\bar{\theta} = 0^\circ$), the effective stored-energy functions $\widehat{\phi}^{AS}$ and $\widehat{\phi}^{PS}$ are explicitly given by Eqs. (39) and (42) in Chapter 2, and the associated stress measures read as $\bar{S}^{AS} = \bar{\lambda}^{-1} [(\bar{T}_{11} + \bar{T}_{22}) - 2\bar{T}_{33}]$ and $\bar{S}^{PS} = \bar{\lambda}^{-1} (\bar{T}_{11} - \bar{T}_{33})$, where it is recalled that the particles are initially aligned in the \mathbf{e}_3

direction.

Moreover, for dilute concentrations of particles, it proves useful to consider the following *modified* effective stress measures

$$\bar{S}_0^{AS} = \frac{\partial \hat{\phi}_0^{AS}(\bar{\lambda}, \bar{\theta})}{\partial \bar{\lambda}}, \quad \bar{S}_0^{PS} = \frac{\partial \hat{\phi}_0^{PS}(\bar{\lambda}, \bar{\theta})}{\partial \bar{\lambda}}, \quad (3.11)$$

where $\hat{\phi}_0^{PS}(\bar{\lambda}, \bar{\theta})$ and $\hat{\phi}_0^{AS}(\bar{\lambda}, \bar{\theta})$ are given by

$$\hat{\phi}_0^{AS} = \frac{1}{c} \left(\hat{\phi}^{AS} - \phi^{AS} \right), \quad \hat{\phi}_0^{PS} = \frac{1}{c} \left(\hat{\phi}^{PS} - \phi^{PS} \right), \quad (3.12)$$

with ϕ^{AS} and ϕ^{PS} denoting the stored-energy function of the homogeneous matrix phase evaluated at the appropriate deformation gradients.

Evolution of microstructure. As discussed in Chapter 2, the TSO procedure for estimating the effective stored-energy function $\widehat{W}(\bar{\mathbf{F}})$ also accounts for the evolution of the underlying microstructure, resulting from the finite changes in geometry that are induced by the deformation. Information on the variables characterizing the evolution of the microstructure provides deeper physical insight into the observed macroscopic behavior. For the class of particle-reinforced composites under study, the volume fraction and shape of the particles do not change (because the particles are rigid and the matrix is incompressible), and the only microstructural variables that evolve with the deformation are the orientation of the particles, and the shape and orientation of the distributional ellipsoid characterizing the angular dependence of the two-point correlation function (for the distribution of the particle centers). As we have seen, the TSO model provides us with direct access to the rotation of the particles ($\bar{\psi}^{(2)}$, as given by Eq. (33) in Chapter 2). For aligned loadings ($\bar{\theta} = 0^\circ$), the particles do not rotate ($\bar{\psi}^{(2)} = 0^\circ$), up to the possible development of an instability. On the other hand, for non-aligned loadings, the orientation of particles changes with the deformation, and this is expected to have a significant effect on the macroscopic behavior of the composite. For this reason, the evolution of the particle rotations will be included in the presentation of the results and associated discussions of the next section. On the other hand, the distributional ellipsoid, which is assumed to have initially the same shape and orientation as those of particles in the undeformed configuration, evolves with the macroscopic deformation, and can be easily computed, but is not expected to play a major role and will therefore not be discussed further here.

Onset of macroscopic instabilities. Theoretical results (Geymonat et al., 1993) suggest that composite materials can develop macroscopic (or long wavelength) instabilities at sufficiently large deformations, even when the constituent phases are *locally* strongly elliptic. Interestingly, the TSO model, developed in Chapter 2, was found to generate macroscopic instabilities under certain conditions which can be captured through loss of the SE condition for the effective stored-energy function. As discussed in Chapter 2, the onset of macroscopic instabilities in the incompressible composites correspond to development of a *localized* deformation (or *shear band*) on a plane (identified by the normal vector \mathbf{n}_{cr}) and in the direction $\mathbf{m}_{cr}(\perp \mathbf{n}_{cr})$. In particular, our aim is to in-

investigate (1) whether or not the homogenized behavior of the composites loses SE for different loading/microstructure conditions, and (2) what is the associated critical stretch (denoted by $\bar{\lambda}_{cr}$) and the pair of vectors (\mathbf{m}_{cr} and \mathbf{n}_{cr}) in case of loss of SE. For the composites under study, the local behavior of the matrix is locally strongly elliptic (models (3.3) and (3.4) are strongly elliptic for all stretches), and therefore, the loss of SE of the homogenized behavior can be related to the evolution of microstructure.

For completeness, in addition to presenting the macroscopic instability results in deformation space (given by $\bar{\lambda}_{cr}$), we also present them in stress space. To this end, we need to suitably choose the arbitrary pressure p in Eq. (3.7) depending on the applied macroscopic loading. For simplicity, we consider instability results in stress space only for aligned pure shear and axisymmetric shear loadings. The case of aligned pure shear loading ($\bar{\lambda}_1 = \bar{\lambda}$, $\bar{\lambda}_2 = 1$) can be identified with the biaxial state of stress

$$\bar{\mathbf{S}} = \bar{S}_{22}\mathbf{e}_2 \otimes \mathbf{e}_2 + \bar{S}_{33}\mathbf{e}_3 \otimes \mathbf{e}_3, \quad (3.13)$$

where the \bar{S}_{ij} denote components of the Piola-Kirchhoff stress relative to the basis $\{\mathbf{e}_i\}$. Similarly, the case of aligned axisymmetric shear loading ($\bar{\lambda}_1 = \bar{\lambda}_2 = \bar{\lambda}$) can be associated to a uniaxial state of stress in the \mathbf{e}_3 direction, written as

$$\bar{\mathbf{S}} = \bar{S}_{33}\mathbf{e}_3 \otimes \mathbf{e}_3. \quad (3.14)$$

Accordingly, we define the *critical stress* as the stress component \bar{S}_{33} at which the composite loses the strong ellipticity under these two types of loading, namely,

$$\bar{S}_{cr}^{PS} = \bar{S}_{33}(\bar{\lambda}_{cr}) = -\bar{\lambda}_{cr}^2 \frac{\partial \widehat{\phi}^{PS}(\bar{\lambda}_{cr}, 0)}{\partial \bar{\lambda}}, \quad \bar{S}_{cr}^{AS} = \bar{S}_{33}(\bar{\lambda}_{cr}) = -\frac{1}{2}\bar{\lambda}_{cr}^3 \frac{\partial \widehat{\phi}^{AS}(\bar{\lambda}_{cr}, 0)}{\partial \bar{\lambda}}. \quad (3.15)$$

In this work, we will only be concerned with macroscopic instabilities, as just described. For other types of instabilities, the reader is referred to the work of Michel et al. (2010) in the context of two-dimensional particle-reinforced composites.

As explained in Chapter 2 of this work, the calculation of the effective stored-energy function $\widehat{\phi}$, as well as of the particle rotation $\bar{\psi}^{(2)}$, requires the computation of the tensor \mathbf{E} , which, in turn, requires the calculation of the integrals associated with the tensors \mathbf{P}_r , $r = 1, 2, 3$ (see Appendix A of Chapter 2). For practical reasons, we make use here of the (numerical) Gaussian quadrature integration procedure presented in Appendix B of Chapter 2 for calculating the tensors \mathbf{P}_r . The calculation of these integrals is the most computationally intensive part of the procedure, and a high number of Gaussian points may be needed to achieve convergence, especially when the particles have aspect ratios that are far from $w = 1$. A FORTRAN program has been written for this purpose and is available upon request. In the next section, the above-mentioned sets of results will be presented and discussed in detail.

3.3 Applications

In this section, we present some representative examples for the *tangent* second-order estimates for particle-reinforced elastomers with an incompressible matrix phase and (rigid) spheroidal particles undergoing macroscopic deformations of the form (3.5). In particular, we study the TSO estimates for particle-reinforced composites with Gent (Eq. (3.4)) and neo-Hookean (Eq. (3.3)) matrix phases. For simplicity, results for the effective energy, stress and modulus tensors are normalized by the ground-state shear modulus (that is, $\mu^{(1)} = 1$), except in Figure 3.9 where the specific value for $\mu^{(1)}$ is given. Also, for the case of composites with Gent matrices, results are shown for several values of lock-up parameter J_m . We provide results for both prolate and oblate shapes of particles, and several values of the volume fraction c and particle aspect ratio w . Note that results are shown with solid and dotted lines up to the point at which the effective incremental modulus tensor loses strong ellipticity, beyond which the results are depicted by dashed and dashed-dotted lines, respectively. For the cases when no loss of SE is detected, they are truncated at some sufficiently large strain. In this connection, the circle marker ‘•’ in the plots is used to denote the point at which loss of SE first takes place (as the loading parameter $\bar{\lambda}$ is increased). Moreover, in most of the figures, the results for the pure neo-Hookean matrix are included for comparison purposes.

The results provided in this section are organized as follows. First, in subsection 3.3.1, we address the effective behavior of particle-reinforced, neo-Hookean and Gent elastomers subjected to *aligned* loadings ($\bar{\theta} = 0^\circ$). Attention is devoted to (aligned) *pure shear* and *axisymmetric shear* loadings. Next, in subsection 3.3.2, we will present representative results for the overall behavior of particle-reinforced neo-Hookean elastomers subjected to *non-aligned* loadings ($\bar{\theta} \neq 0^\circ$). In this subsection, similar to the first one, attention is restricted to (non-aligned) pure and axisymmetric shear loadings. Also, in both subsections, in order to consider exclusively the impact of the particle shape on the macroscopic behavior, results are first provided for dilute concentration of particles ($c \ll 1$), followed by results for several (finite) values of c . The theoretical significance for the dilute concentration results is that they can be interpreted as a generalization of the results of Eshelby (Eshelby, 1957) for a composite material consisting of dilute concentrations of aligned, rigid spheroidal inclusions in a nonlinear hyperelastic matrix. In fact, the nonlinear results of this chapter reduce exactly to the Eshelby results in the infinitesimal (linearized) deformation regime.

3.3.1 Aligned loadings

In this subsection, we restrict our attention to the special case of macroscopically *aligned* loadings, characterized by $\bar{\theta} = 0^\circ$. It is recalled from Chapter 2 that in this case the particles do not rotate ($\bar{\psi}^{(2)} = 0^\circ$) for any applied stretch (up to the possible development of an instability). Moreover, results are given for two specific types of aligned loadings, namely, aligned *pure shear* loading and aligned *axisymmetric shear* loading. It is important to observe that for the case of aligned axisymmetric loading, the overall behavior of the composite remains transversely isotropic in the deformed configuration with the axis of symmetry aligned with the \mathbf{e}_3 direction. On the other hand, for the case of aligned pure shear loading, the composite is initially transversely isotropic, but develops general orthotropic overall response (whose principal axes are aligned with the \mathbf{e}_i basis

directions) in the deformed configuration. It is also noted that the results in this subsection will be presented as functions of the macroscopic logarithmic strain $\bar{e} = \ln(\bar{\lambda})$. Accordingly, for the case of prolate particles, the compressive (tensile) axis of loading is aligned with the longest principal axis of particles for $\bar{e} > 0$ ($\bar{e} < 0$), while the opposite is true for the case of oblate particles. This remark will be of the essence in the physical interpretation of loss of SE results provided later in this subsection.

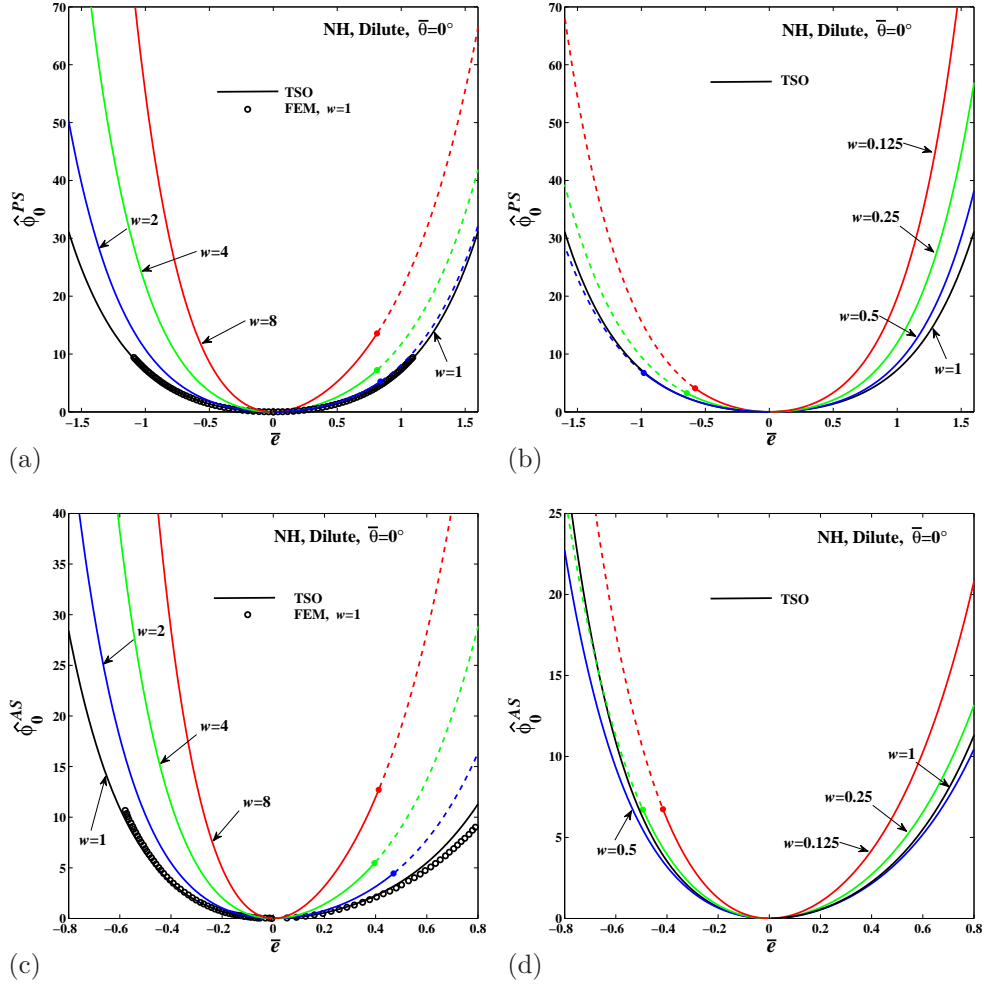


Figure 3.1: Tangent second-order (TSO) estimates for the effective stored-energy function $\hat{\phi}_0(\bar{\lambda})$ of neo-Hookean elastomers reinforced with dilute concentrations of rigid particles, as functions of the macroscopic logarithmic strain $\bar{e} = \ln(\bar{\lambda})$. Two *aligned* loadings are considered: *pure shear* (PS) ($\bar{\lambda}_1 = \bar{\lambda}, \bar{\lambda}_2 = 1$), and *axisymmetric shear* (AS) ($\bar{\lambda}_1 = \bar{\lambda}_2 = \bar{\lambda}$). (a) Prolate particles ($w \geq 1$) under PS loading, (b) oblate particles ($w \leq 1$) under PS loading, (c) prolate particles under AS loading, and (d) oblate particles under AS loading. The finite element (FEM) results of Lopez-Pamies et al. (2013a) for the case of spherical particles ($w = 1$) are also included for comparison.

Figure 3.1 presents plots for the TSO estimates for the effective stored-energy function $\hat{\phi}_0$ of the neo-Hookean elastomers reinforced with *dilute* concentrations of particles, as defined by expressions

((3.12)). Figures 3.1(a) and (b) show plots for pure shear loading ($\bar{\lambda}_1 = \bar{\lambda}$, $\bar{\lambda}_2 = 1$), as a function of the strain $\bar{\epsilon} = \ln(\bar{\lambda})$, for the cases of prolate and oblate particles, respectively, while Figure 3.1(c) and (d) show corresponding plots for axisymmetric shear loading ($\bar{\lambda}_1 = \bar{\lambda}_2 = \bar{\lambda}$). The results for prolate particles are given for aspect ratios $w = 2, 4$, and 8 , and those for oblate particles are given for aspect ratios $w = 0.5, 0.25$, and 0.125 . For comparison purposes, the finite element results (FEM) of Lopez-Pamies et al. (2013a) (obtained for a single rigid inclusion embedded in a neo-Hookean elastomer matrix), as well as the corresponding TSO results for the special case of spherical particles ($w = 1$) are also included in the plots. An immediate observation from this figure is that the aspect ratio of particles has a significant reinforcing effect on the overall response of the composite at fixed particle concentrations. We also observe that TSO estimate provides fairly good agreement with the FEM results for spherical particles (up to the point where the simulations were carried out) for both pure shear and axisymmetric shear loadings. Moreover, it is noticed from Figure 3.1 that the predictions of the TSO model for the macroscopic response of the composites with spherical particles remain *macroscopically* stable for all strains, while those of the composites with prolate and oblate particles become unstable for $\bar{\epsilon} > 0$ and for $\bar{\epsilon} < 0$, respectively, under both types of loadings. We will discuss these macroscopic instabilities and the associated failure mechanisms in more detail in the context of the next two figures.

Figure 3.2 provides plots of the TSO estimates for the overall response of the particle-reinforced elastomer with a neo-Hookean matrix phase and particle volume fractions $c = 0.05, 0.15$, and 0.25 , under *aligned pure shear* loading. Figures 3.2(a) and (b) show plots for the macroscopic stress measure \bar{S}^{PS} as a function of the logarithmic strain $\bar{\epsilon} = \ln(\bar{\lambda})$. In particular, part (a) shows the results for spherical particles ($w = 1$) and compares them with the corresponding FEM results of Lopez-Pamies et al. (2013a), while part (b) shows the results for prolate and oblate shapes of particles with fixed aspect ratios $w = 4$ and $w = 0.25$, respectively. (It should be noted that the FEM results correspond to unit cell calculations containing 30 randomly positioned spherical particles.) Also, Figs. 3.2(c) and (d) show plots for certain shear components of the effective incremental modulus tensor $\hat{\mathbf{L}}^c$, as functions of $\bar{\epsilon} = \ln(\bar{\lambda})$, for prolate particles with $w = 4$ and oblate particles with $w = 0.25$, respectively. The main observation from Figure 3.2(a) is that the TSO estimate provides fairly good agreement with the FEM results (up to the point where the simulations were carried out), especially for the smaller particle concentrations. For the higher volume fraction ($c = 0.25$), the TSO estimates tend to *underestimate* the FEM results at sufficiently large stretches, but are still in good agreement with the FEM results for stretches of less than $\bar{\lambda} = 1.4$. This is partially due to the fact that in this work the TSO model makes use of the Willis *lower bound* (Willis, 1977) for estimating the behavior of the associated linear comparison composite (Avazmohammadi and Ponte Castañeda, 2013). In addition, compared to the results for spherical particles (Figure 3.2(a)), the results in Figure 3.2(b) for spheroidal shapes show an enhanced reinforcing effect, which is due to the combined role of aspect ratio w and volume fraction c on the overall response of the composite. It is further observed from Figure 3.2(b) that, for a fixed particle volume fraction, the composite stiffening is larger for elongated particles ($w = 4$) than for oblate particles ($w = 0.25$), as long as the composite response remains strongly elliptic. Next, we observe from Figure 3.2(b) that the composites with finite concentrations of prolate and oblate particles become unstable at positive

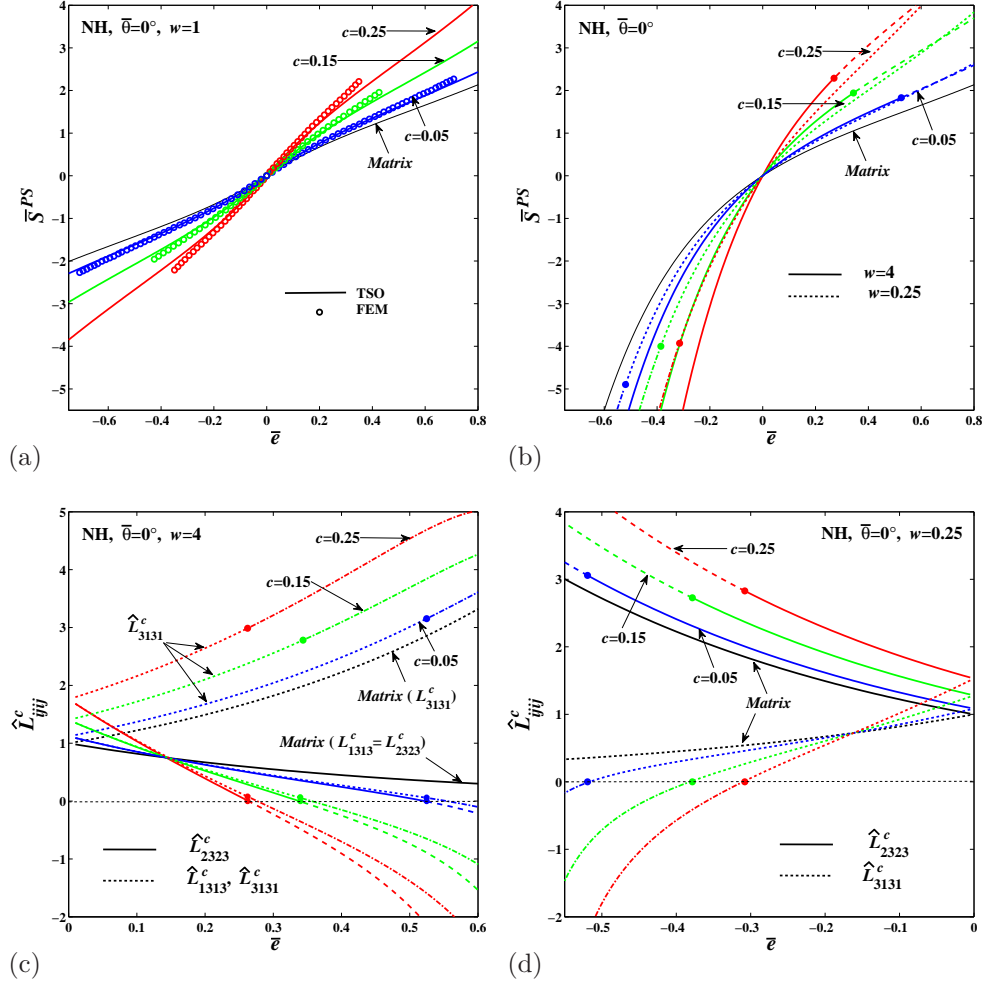


Figure 3.2: TSO estimates for particle-reinforced, neo-Hookean elastomers under aligned *pure shear* loading ($\bar{\lambda}_1 = \bar{\lambda}, \bar{\lambda}_2 = 1$), as functions of the macroscopic logarithmic strain $\bar{e} = \ln(\bar{\lambda})$. The macroscopic stress \bar{S}^{PS} for: (a) spherical ($w = 1$), and (b) spheroidal ($w = 4, 0.25$) particles. Certain shear components of the effective modulus tensor \hat{L}_{ijkl}^c for: (c) prolate ($w = 4$) and (d) oblate ($w = 0.25$) particles. Results are shown for the volume fractions $c = 0.05, 0.15$ and 0.25 . The finite element (FEM) results of Lopez-Pamies et al. (2013a) for spherical particles are also provided for comparison in part (a).

strains ($\bar{\epsilon} > 0$) and negative strains ($\bar{\epsilon} < 0$), respectively, when (for both cases) the compressive loading axis is aligned with the longest axis of the particles. Consistent with what was anticipated in Subsection 2.5.2 for prolate particles, it is seen from Figure 3.2(c) that both the shear modulus \widehat{L}_{1313}^c transverse to the long axis of the particles (and in the in-plane direction \mathbf{e}_1), as well as the shear modulus \widehat{L}_{2323}^c transverse to the long axis of the particles (but in the out-of-plane direction \mathbf{e}_2) decrease with increasing tensile strain in the \mathbf{e}_1 direction (and, therefore, increasing compressive strain the \mathbf{e}_3 direction). However, in this case with a moderate volume fraction and aspect ratio ($c \leq 0.3$ and $w \leq 5$), \widehat{L}_{2323}^c actually reaches zero before \widehat{L}_{1313}^c , and therefore the loss of ellipticity first occurs through a shear band whose normal is parallel to \mathbf{e}_3 , and whose slip direction is along the out-of-plane direction \mathbf{e}_2 (i.e., out of the loading plane). On the other hand, for the case of oblate particles, the loss of SE takes place through vanishing of the shear modulus \widehat{L}_{3131}^c (in the plane perpendicular to the long axis of the oblate particles, and in the direction of the loading axis \mathbf{e}_3). It is also observed from these figures that the reinforced elastomers lose macroscopic stability earlier for larger particle concentrations.

Similar to the previous figure, Figure 3.3 provides results for the TSO estimates for the overall response of the particle-reinforced elastomers with a neo-Hookean matrix phase and particle volume fractions $c = 0.05, 0.15,$ and 0.25 , under *aligned axisymmetric shear* loading ($\bar{\lambda}_1 = \bar{\lambda}_2 = \bar{\lambda}$). Figures 3.3(a) and (b) depict the macroscopic stress measure \bar{S}^{AS} , as a function of the logarithmic strain $\bar{\epsilon} = \ln(\bar{\lambda})$. In particular, part (a) shows the results for spherical particles ($w = 1$) in which the corresponding FEM results of Lopez-Pamies et al. (2013a) are also included for comparison purposes, while part (b) shows the results for prolate and oblate shapes of particles with fixed aspect ratios 4 and 0.25. In addition, Figs. 3.3(c) and (d) depict the variation of the moduli \widehat{L}_{1313}^c and \widehat{L}_{3131}^c versus the logarithmic strain $\bar{\epsilon} = \ln(\bar{\lambda})$ for prolate particles with aspect ratio $w = 4$ and oblate particles with aspect $w = 0.25$, respectively. Once again, we observe good agreement between the TSO estimates for spherical particles and the corresponding FEM results (up to the point where the simulations were carried out), for all three volume fractions of particles. In addition, similar to the case of pure shear loading, Figure 3.3(b) shows that, at a fixed particle volume fraction, the composites exhibit stiffer responses for elongated particles ($w = 4$) than for oblate particles ($w = 0.25$). Figure 3.3(b) also shows that, for a fixed aspect ratio of particles (e.g., $w = 4$), the behavior of composites with spheroidal particles becomes progressively less stable—as determined by loss of SE—as the volume fraction of the particles increases. Next, consistent with the results of Chapter 2 (see relations (59) and (61)), Figs. 3.3(c) and (d) show that the loss of SE in the composites subjected to aligned axisymmetric shear loading takes place through vanishing of the effective incremental shear modulus in the plane perpendicular to the major axis of particles, namely, the components $\widehat{L}_{1313}^c (= \widehat{L}_{2323}^c)$ and $\widehat{L}_{3131}^c (= \widehat{L}_{3232}^c)$, for the cases of prolate and oblate particles, respectively.

Figure 3.4 presents TSO estimates for the critical strains and stresses at which macroscopic instabilities first develop in the particle-reinforced neo-Hookean composites subjected to aligned loadings. Figures 3.4(a) and (b) show plots for the critical strain $\bar{\epsilon}_{cr}^{PS} = \ln(\bar{\lambda}_{cr})$ (at which the homogenized elastomer first loses SE) and the corresponding critical stress \bar{S}_{cr}^{PS} (as defined in (3.15)), respectively, for pure shear loading. Similarly, Figs. 3.4(c) and (d) show plots for the critical strain ($\bar{\epsilon}_{cr}^{AS}$) and the corresponding critical stress (\bar{S}_{cr}^{AS}), respectively, for axisymmetric shear loading. The

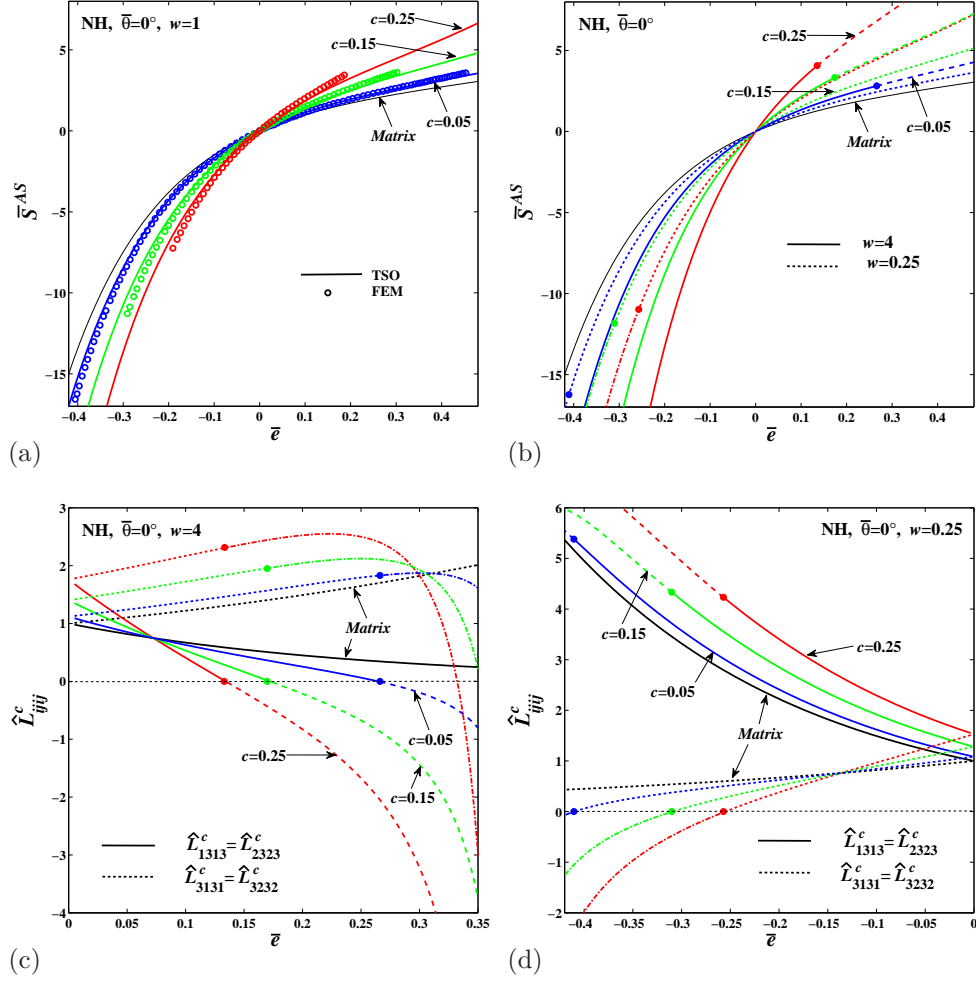


Figure 3.3: TSO estimates for particle-reinforced, neo-Hookean elastomers under aligned *axisymmetric* shear loading ($\bar{\lambda}_1 = \bar{\lambda}_2 = \bar{\lambda}$), as functions of the macroscopic logarithmic strain $\bar{e} = \ln(\bar{\lambda})$. The macroscopic stress \bar{S}^{PS} for: (a) spherical ($w = 1$), and (b) spheroidal particles ($w = 4, 0.25$). Certain shear components of the effective modulus tensor \hat{L}_{ijkl}^c for: (c) prolate ($w = 4$), and (d) oblate ($w = 0.25$) particles. Results are shown for various volume fractions $c = 0.05, 0.15$ and 0.25 . The finite element (FEM) results of Lopez-Pamies et al. (2013a) for the case of spherical particles are also included for comparison in part (a).

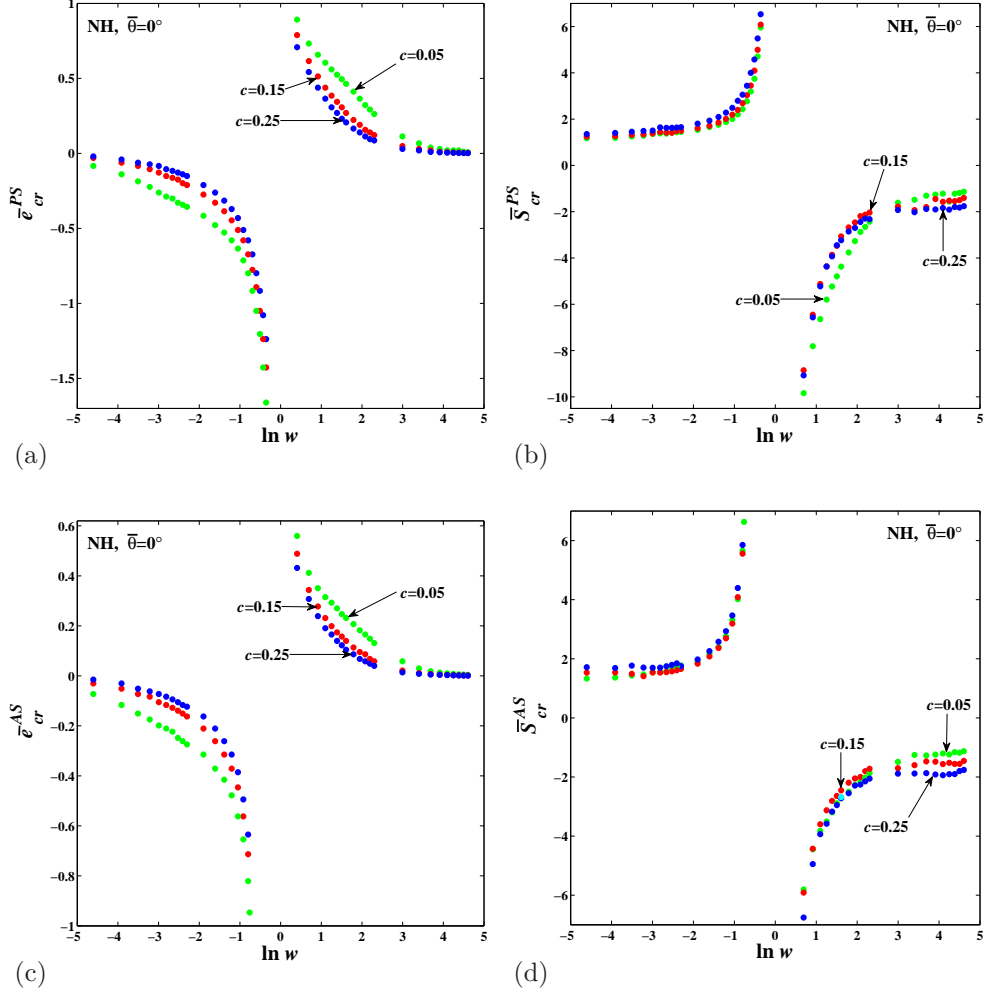


Figure 3.4: TSO estimates for the macroscopic instabilities (loss of SE) in particle-reinforced neo-Hookean elastomers subjected to aligned loadings. Parts (a) and (b) show *pure shear* ($\bar{\lambda}_1 = \bar{\lambda}$, $\bar{\lambda}_2 = 1$) results for the critical strain (\bar{e}_{cr}^{PS}) at which loss of SE of the homogenized elastomer takes place, and the corresponding critical stress (\bar{S}_{cr}^{PS}), respectively. Parts (c) and (d) show *axisymmetric shear* ($\bar{\lambda}_1 = \bar{\lambda}_2 = \bar{\lambda}$) results for the critical strain (\bar{e}_{cr}^{AS}) and the corresponding critical stress (\bar{S}_{cr}^{AS}), respectively. The results are shown for various particle concentrations as functions of the particle aspect ratio $\ln(w)$.

results are shown for several values of the concentration ($c = 0.05, 0.15$ and 0.25), as functions of the logarithm of the particle aspect ratio, $\ln(w)$. The main observation from these figures is that, for fixed volume fractions, the particle-reinforced composites become increasingly less stable in both the deformation and the stress as the value of $|\ln(w)|$ increases and the particle shape becomes progressively more prolate, or oblate. In this regard, we see from Figs. 3.4(a) and (c) that the critical strain curves have a vertical asymptote at $w = 1$ and horizontal asymptotes at $\bar{\epsilon}_{cr} = 0$ as $w \rightarrow \infty$ or $w \rightarrow 0$. The special case of $w = 1$ correspond to neo-Hookean elastomers reinforced by spherical (rigid) particles, which, as already mentioned, remain strongly elliptic for all deformations ($\bar{\epsilon}_{cr} \rightarrow \infty$). On the other hand, for the two extreme values of the particle aspect ratio, namely, the limiting cases of zero and infinite aspect ratios, the composite becomes unstable at zero strain ($\bar{\epsilon}_{cr} \rightarrow 0$), which is in consistent with the fact that the composites become rigid in these two limiting cases corresponding to a laminated material with a rigid phase and a (continuous) fiber-reinforced elastomers with rigid fibers, respectively. Similar observations can be made from Figure 3.4(b) and (d) for the critical stresses, except that the critical stresses tend to finite values, depending on the volume fraction of particles, in the limits as $w \rightarrow \infty$ and $w \rightarrow 0$.

In connection with this last observation, it is relevant to recall that Agoras et al. (2009b) derived the following results for the critical stress in composites consisting of a generalized neo-Hookean matrix and isotropic distributions of aligned, rigid, circular fibers, namely,

$$\bar{S}_{cr}^{PS} = \bar{S}_{cr}^{AS} = -\frac{1+c}{1-c} \mu^{(1)}. \quad (3.16)$$

Similarly, making use of the results provided in Appendix A of the paper Agoras et al. (2009b) for the laminate composites consisting of alternating layers of incompressible neo-Hookean materials, it can be shown that the critical stress in the limit as one phase becomes rigid is given by

$$\bar{S}_{cr}^{PS} = \bar{S}_{cr}^{AS} = \frac{1}{1-c} \mu^{(1)}. \quad (3.17)$$

Moreover, note that relations (3.16) and (3.17) are valid for both *pure shear* and *axisymmetric shear* loadings. Thus, we can check from Figure 3.4(b) and (d) that the trends in the results predicted by the TSO model for the critical stress are consistent with the corresponding results calculated from expressions (3.16) and (3.17), respectively, in the limiting cases of $w \rightarrow \infty$ and $w \rightarrow 0$.

Next, in Figure 3.5, we investigate the influence of the matrix constitutive behavior on the macroscopic stress-strain response of the composite elastomers, when subjected to aligned pure shear (PS) and axisymmetric shear (AS) loadings. Thus, Figs. 3.5(a) and (b) provide plots of the macroscopic stress \bar{S}^{PS} for prolate particles with $w = 4$ and oblate particles with $w = 0.25$, respectively, while Figs. 3.5(c) and (d) provide corresponding plots for the macroscopic stress \bar{S}^{AS} . In each figure, the volume fraction of particles is assumed to be fixed at $c = 0.25$, and results are shown for several values of the matrix lock-up parameters ($J_m = 50, 100$, and ∞). It is recalled that the case $J_m \rightarrow \infty$ corresponds to an incompressible neo-Hookean matrix. We observe from these figures that the composites with prolate particles tend to stiffen more significantly for compressive strains ($\bar{\epsilon} < 0$), resulting in tensile strains in the long fiber direction, while the composites with oblate

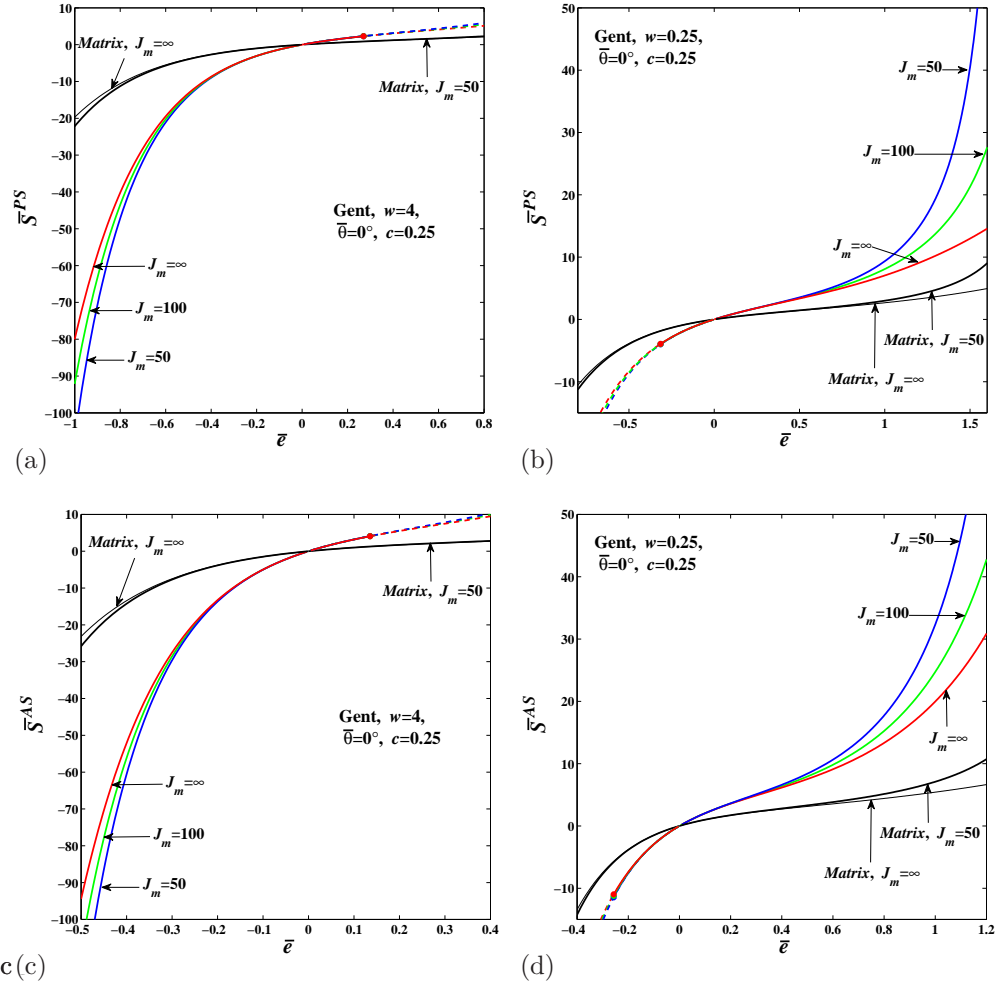


Figure 3.5: TSO estimates for the macroscopic stress \bar{S} versus the macroscopic logarithmic strain $\bar{e} = \ln(\bar{\lambda})$ for particle-reinforced Gent elastomers. The results are shown for three values of the matrix inextensibility parameter $J_m = 50, 100,$ and ∞ . Four different cases are considered: (a) aligned pure shear for a prolate spheroidal shape ($w = 4$), (b) aligned pure shear for an oblate shape ($w = 0.25$), (c) aligned axisymmetric shear for a prolate shape ($w = 4$), and (d) aligned axisymmetric shear for an oblate shape ($w = 0.25$).

particles tend to stiffen more significantly for tensile strains ($\bar{\epsilon} > 0$), corresponding to compressive strains along the short fiber direction. In addition, the amount of stiffening is more significant for larger values of J_m , as expected. Moreover, it can be shown that, the effective lock-up strain¹ for the composite materials with spheroidal particles under aligned loadings is independent of the shape of the particle and is completely determined by the values of J_m , and c . Therefore, the relations (1.142) for the composites with spherical particles, can be used to determine the lock-up stretch for the class of composites of interest here when subjected to aligned pure and axisymmetric shear loadings.

Furthermore, the plots in Figure 3.5 illustrate that, although the strain-locking parameter J_m in the Gent elastomers can have a strong influence on the macroscopic response of the reinforced elastomer, it has basically no effect on the loss of SE for the particle-reinforced composites. This is consistent with earlier findings by Lopez-Pamies and Ponte Castañeda (2006b) and Agoras et al. (2009b) that the development of macroscopic instabilities in (long) fiber-reinforced composites with Gent matrix materials subjected to 2-D and 3-D loadings becomes independent of J_m for very stiff fibers.

Elastomers reinforced with 2-D elliptical fibers

In this subsection, we provide results for the transverse effective response of a (2-D) composite consisting of an incompressible, neo-Hookean matrix reinforced by rigid, aligned, cylindrical fibers with elliptical cross section of aspect ratio w , which are subjected to pure shear aligned with the principal axes of the elliptical fibers. The response of this type of composite to pure shear loading has also been studied in Section 1.5 and in Lopez-Pamies and Ponte Castañeda (2006b).

Figure 3.6 shows the TSO estimates for the effective response of the 2-D reinforced neo-Hookean elastomers, as well as the corresponding GSO estimates calculated from the stored-energy function (1.126). Results are shown for the case of fibers with circular cross section ($w = 1$) and three different fiber volume fractions $c = 0.1, 0.2, 0.3$, as a function of the macroscopic stretch $\bar{\lambda}$. Parts (a) and (b) show the effective energy $\hat{\phi}^{PS}$ and the corresponding macroscopic stress $\bar{S}^{PS} = d\hat{\phi}^{PS}/d\bar{\lambda}$, respectively. An important observation from these figures is that the modification of the TSO estimates proposed in Chapter 2 (in terms of expression (2.22) instead of the corresponding expression (1.113) in involving a log term in the determinant) is free from the “geometric lock up” condition, and is much closer to the corresponding GSO estimates than the earlier estimate in Chapter 1 (see figure (1.2)), which were found to blow up for a sufficiently small value of the stretch $\bar{\lambda}$ (at $\bar{\lambda} = 1/c$, for the results shown in the plots).

Figure 3.7 shows a more detailed comparison of the TSO estimates with earlier analytical estimate and numerical simulations for neo-Hookean elastomers reinforced by rigid fibers of circular cross section ($w = 1$). Results are provided for two volume fractions: (a) $c = 0.2$, and (b) $c = 0.3$. The GSO (2006) and TSO (2000) estimates correspond to the stored-energy function (1.126) and the earlier version of the TSO (Ponte Castañeda and Tiberio, 2000) estimate, respectively, while the FEM results refer to the finite element simulations of Moraleta et al. (2009). We observe that the

¹The strain at which the composite locks up because of lock up in the elastomeric matrix phase

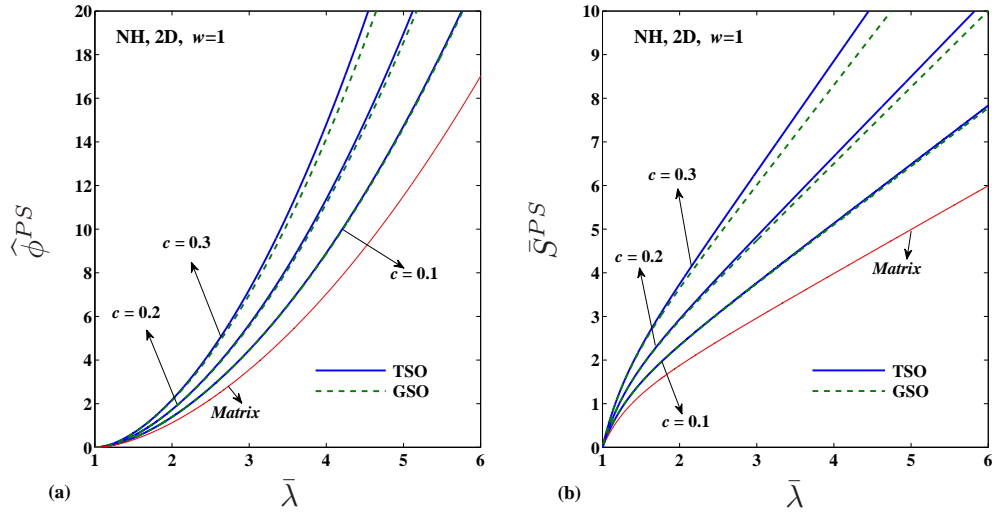


Figure 3.6: Tangent second-order (TSO) and generalized second-order (GSO) estimates for the effective response of an incompressible neo-Hookean matrix reinforced by 2-D circular (rigid) fibers ($w = 1$) subjected to transverse *pure shear* loadings. The GSO estimates correspond to the stored-energy function (1.126). The results are shown as a function of the applied stretch $\bar{\lambda}$ for different values of the fiber volume fraction. (a) The effective energy $\hat{\phi}^{PS}$. (b) The corresponding macroscopic stress $\bar{S}^{PS} = d\hat{\phi}^{PS}/d\bar{\lambda}$.

TSO estimate for the 2-D composite with circular fibers is in excellent agreement with the FEM simulations of Moraleda et al. (2009) (up to the point where the simulations were carried out), even for the case of higher fiber concentration $c = 0.3$. In fact, since the TSO estimates proposed in Chapter 2 (based on expression (2.22)) are free from the geometric lock-up, they provide closer agreement with the FEM simulations than the earlier estimates in Chapter 1 (see figure 1.3). In this connection, it also can be seen from figure 3.7 that the new TSO estimates are much more improved relative to the earlier version (Ponte Castañeda and Tiberio, 2000) of the TSO estimates in comparison with the version of the TSO shown in figure 1.3.

Finally, Figure 3.8 provides results for the transverse effective response of a (2-D) composite consisting of a neo-Hookean matrix reinforced by rigid, aligned, cylindrical fibers with elliptical cross section of aspect ratio w , which are subjected to pure shear aligned with the principal axes of the elliptical fibers. These results are compared with the corresponding results of this chapter for the (3-D) neo-Hookean elastomers reinforced with aligned, spheroidal particles with the same aspect ratio w that are subjected to the same pure shear loading, but this time in a plane including the long axis of the fibers. (It should be noted here that the results for the 2-D composite with aspect ratio $w = 1$ also correspond to the transverse shear response of the 3-D composite with aspect ratio $w \rightarrow \infty$.) More specifically, Figure 3.8 shows results for the effective stress \bar{S}^{PS} versus the logarithmic strain $\bar{e} = \ln(\bar{\lambda})$ in 2-D and 3-D composites with fiber/particle aspect ratios $w = 1$ and $w = 4$, at the fixed fiber/particle concentration $c = 0.3$. From this figure, we first observe that the response curves for the 2-D and 3-D composites with aspect ratio $w = 1$ are fairly similar, with the

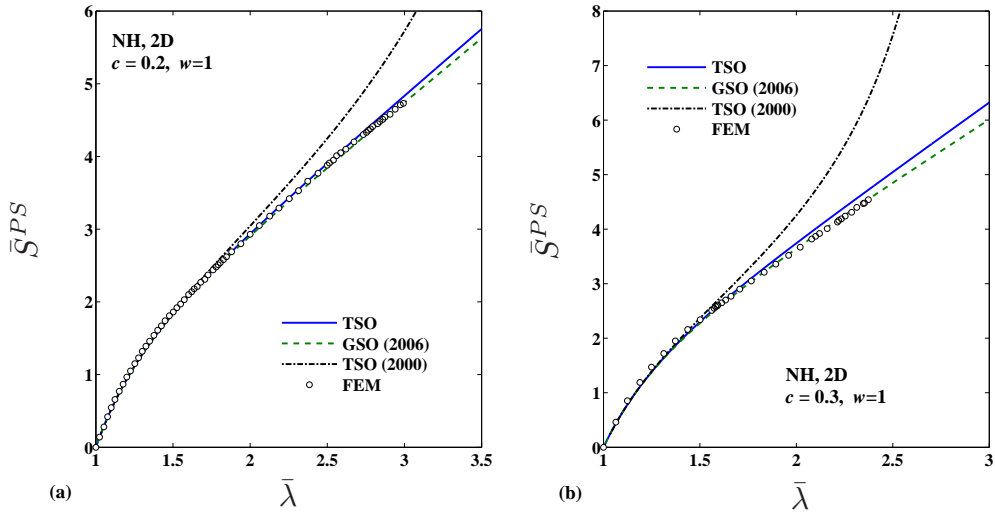


Figure 3.7: The effective response of a rigidly fiber-reinforced elastomer with an incompressible neo-Hookean matrix under pure shear loading. The macroscopic stress \bar{S}^{PS} is plotted as a function of the applied stretch $\bar{\lambda}$ for (a) $c = 0.2$, and (b) $c = 0.3$. Comparisons are shown between the new TSO estimate, the estimate (1.126) of Lopez-Pamies and Ponte Castañeda (2006b) “GSO (2006)”, the earlier TSO results of Ponte Castañeda and Tiberio (2000) “TSO (2000)”, and the FE simulations of Moraleda et al. (2009) “FEM”.

spherical particles producing a slightly stiffer response. On the other hand, the responses for the 2-D and 3-D composites with aspect ratio $w = 4$ are quite different. While the response of the 2-D composites is the same regardless of whether the extension axis is aligned with the long particle axis ($\bar{\theta} = 90^\circ$) or perpendicular to it ($\bar{\theta} = 0^\circ$), the response of the 3-D composites is quite a bit stiffer when the extension axis is aligned with the long particle axis than when it is perpendicular to it. (Recall that the unstable branches of the solutions for $\bar{\theta} = 0^\circ$ are shown in dashed and dashed-dotted lines.) However, the results for aspect ratio $w = 4$ and loading angle $\bar{\theta} = 0^\circ$ indicate that the 2-D fiber-reinforced composites are slightly more stable than the 3-D composites with the same aspect ratio.

Comparison with experimental results

For completeness, in this subsection, we provide comparisons between the predictions of the TSO model and available experimental data for the effective mechanical behavior of short-fiber reinforced composites subjected to large deformations. Figure 3.9 shows comparisons of the TSO predictions with experimental data of Wang and Mark (1990) for effective behavior of composites consisting of an elastomeric matrix and a polydisperse distribution of aligned, prolate spheroidal particles subjected to aligned, uniaxial tensions. More specifically, in the experiment of Wang and Mark (1990), the matrix is made of PDMS, a silicon-based organic polymer, and the particles are made of polystyrene, a synthetic polymer which is much stiffer than PDMS. Therefore, the particles can be approximately regarded as rigid particles. Moreover, Wang and Mark (1990) conducted experiments

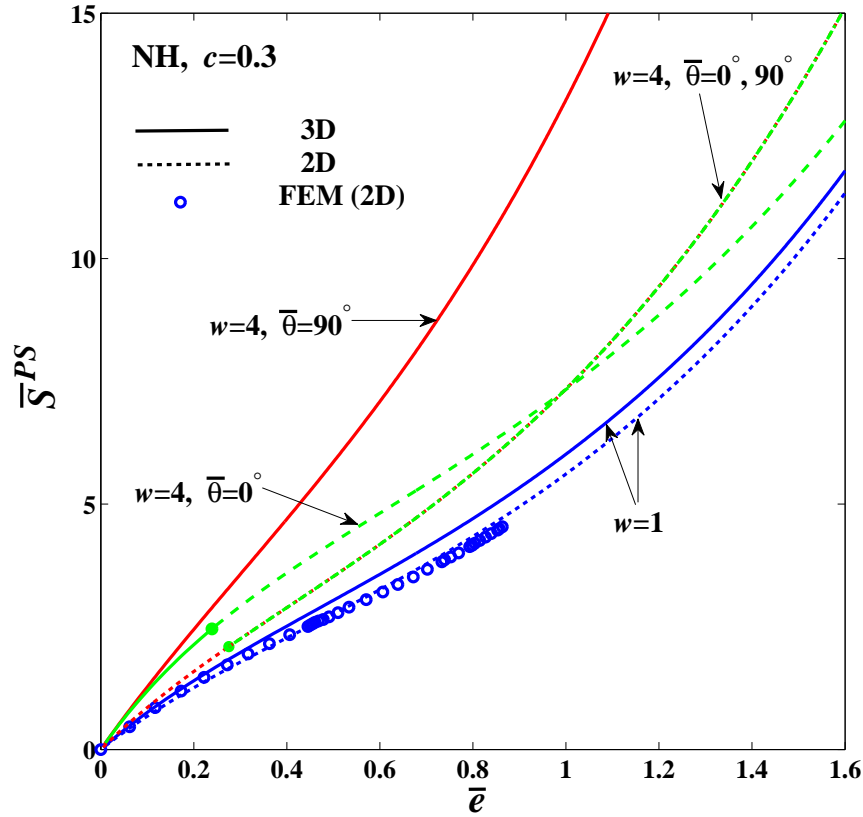


Figure 3.8: Comparison between the TSO estimates for the macroscopic stress \bar{S}^{PS} in 2-D and 3-D rigidly reinforced elastomers subjected to aligned *pure shear* loadings. The 2-D composite is a fiber-reinforced composite which consists of an incompressible neo-Hookean matrix and a random distribution of long, aligned (rigid) fibers with elliptical cross section, and is subjected to aligned pure shear loading. The 3-D composite is the composite studied in this work with a neo-Hookean matrix and spheroidal particles, and is subjected to aligned pure shear deformation ($\bar{\lambda}_1 = \bar{\lambda}$, $\bar{\lambda}_2 = 1$). The results are shown as functions of the logarithmic strain $\bar{e} = \ln(\bar{\lambda})$ for two fiber/particle aspect ratios ($w = 1$ and $w = 4$), at the fixed fiber/particle concentration $c = 0.3$. The FE simulations of Moraleda et al. (2009) for a 2-D fiber-reinforced composite with circular fibers ($w = 1$) are also included for comparison.

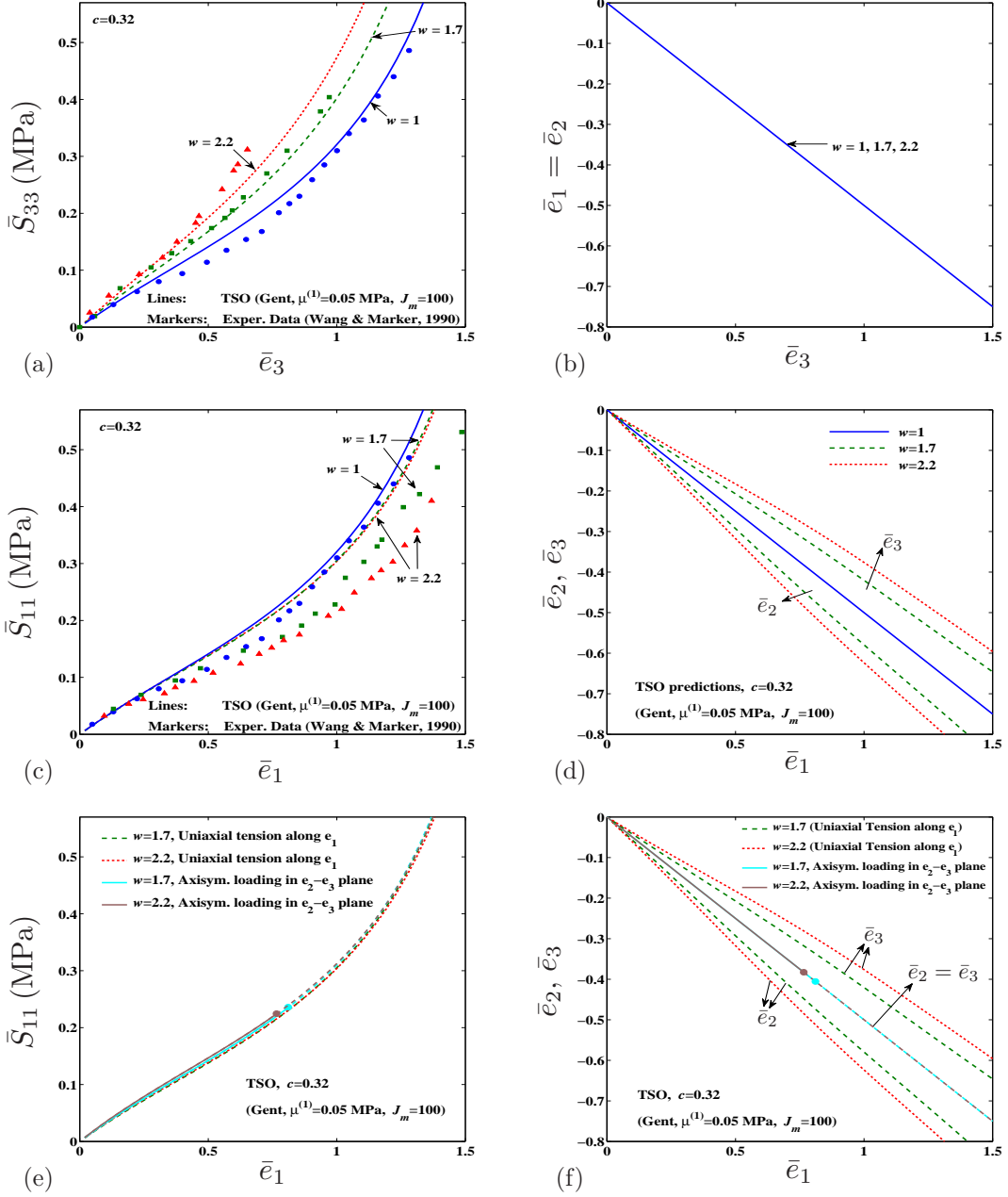


Figure 3.9: Comparisons of the predictions of TSO predictions with experimental data of Wang and Mark (1990) for composites consisting of an elastomeric matrix (made of PDMS) and prolate spheroidal particles (made of polystyrene). Parts (a) and (b) show results for uniaxial tension along \bar{e}_3 direction for the effective stress component \bar{S}_{33} and the strain components $\bar{e}_2 = \ln(\bar{\lambda}_2)$, $\bar{e}_3 = \ln(\bar{\lambda}_3)$, respectively, as functions of the logarithmic strain \bar{e}_3 . Parts (c) and (d) show results for uniaxial tension along \bar{e}_1 direction for the effective stress component \bar{S}_{11} and the strain components \bar{e}_2, \bar{e}_3 , respectively, as functions of the strain $\bar{e}_1 = \ln(\bar{\lambda}_1)$. Parts (e) and (f) compare TSO results for uniaxial tension along \bar{e}_1 direction and axisymmetric deformation in $\bar{e}_2 - \bar{e}_3$ plane for the effective stress component \bar{S}_{11} and strains \bar{e}_2, \bar{e}_3 , respectively, as functions of \bar{e}_1 .

for three particle aspect ratios ($w = 1$, $w = 1.7$ and $w = 2.2$), at the fixed particle concentration $c = 0.32$. Although the precise material properties for the elastomeric matrix (PDMS) were not provided in the work of Wang and Mark (1990), we were able to infer values of the properties in our model to achieve a reasonable match to the experimental data. More specifically, we made use of the Gent behavior (3.4) for the matrix in the TSO model with material properties $\mu^{(1)} = 0.05$ MPa and $J_m = 100$. We also note that, unlike the previous figures in this Chapter, the results for effective stress in Figure 3.9 are not normalized with the shear modulus $\mu^{(1)}$.

Figure 3.9(a) shows comparisons between the TSO estimates for the macroscopic stress component \bar{S}_{33} for the uniaxial tension along \mathbf{e}_3 direction and the corresponding experimental data for the effective behavior of the PS-PDMS composite, as functions of the logarithmic strain $\bar{e}_3 = \ln(\bar{\lambda}_3) = -\ln(\bar{\lambda}_1 \bar{\lambda}_2)$ (Note that other macroscopic stress components are zero in this case.) We observe that TSO estimates provide quite good agreement with the experimental data for the smaller aspect ratios ($w = 1, 1.7$) up to the point where the experiments were carried out, however, the TSO model tend to *underestimate* the experimental data for the higher aspect ratio ($w = 2.2$) at relatively larger stretches. As mentioned in the context of comparisons with FEM results shown in figure 3.2(a), this underestimation is partially due to the fact that the TSO model uses the Willis lower bound for estimating the behavior of the associated linear comparison composite. Nonetheless, given the uncertainties involved in the experimental data, the model does capture very well the qualitative features of the experiments for this loading condition, and overall can provide reasonably good predictive capabilities. We further note that the macroscopic response of the composite predicted by the TSO model is stable for all strains \bar{e}_3 consistent with the fact that the tensile axis of loading is aligned with the largest axis of the particles. Figure 3.9(b) shows corresponding results for the *lateral* logarithmic strain components $\bar{e}_1 = \ln(\bar{\lambda}_1)$ and $\bar{e}_2 = \ln(\bar{\lambda}_2)$, as functions of \bar{e}_3 . Clearly, the uniaxial tension along \bar{e}_3 direction produces an axisymmetric state of deformation ($\bar{\lambda}_2 = \bar{\lambda}_1 = 1/\sqrt{\bar{\lambda}_3}$), and therefore, we have $\bar{e}_1 = \bar{e}_2 = -0.5 \bar{e}_3$.

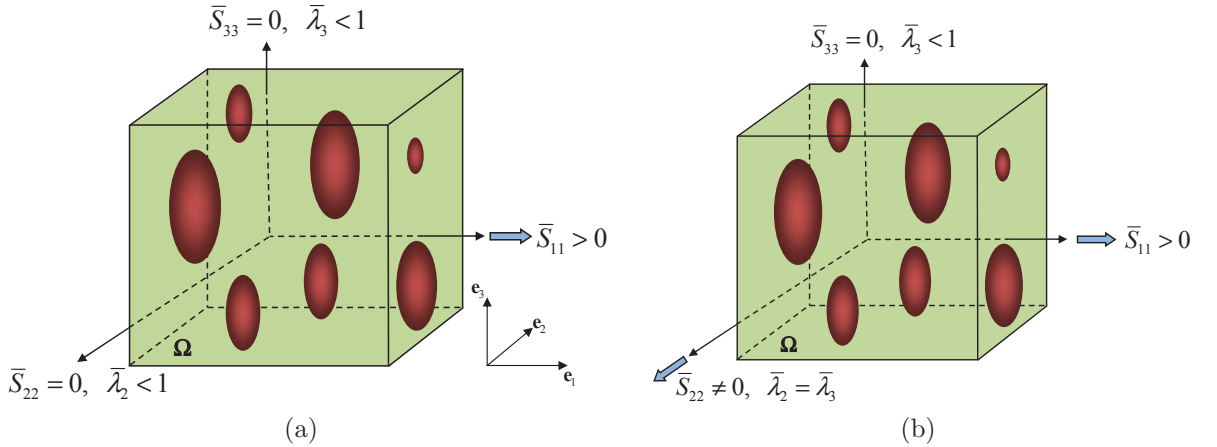


Figure 3.10: Schematic representation of a matrix reinforced by prolate spheroidal particles subjected to (a) uniaxial tension along \mathbf{e}_1 direction, (b) tension along \mathbf{e}_1 direction with the constraint $\bar{\lambda}_2 = \bar{\lambda}_3 < 1$.

Next, Figure 3.9(c) shows comparisons between the TSO model estimates for the macroscopic stress component \bar{S}_{11} for the uniaxial tension along \mathbf{e}_1 direction and the corresponding experimental data for the effective behavior of the PS-PDMS composite, as functions of the logarithmic strain $\bar{\epsilon}_1 = \ln(\bar{\lambda}_1)$ (A schematic representation of the loading condition is shown in Figure 3.10(a).) We observe from this Figure 3.9(c) that the TSO model estimates are still in quite good agreement with the experimental data up to the strain $\bar{\epsilon}_1 \approx 0.4$, beyond which the TSO model predicts a strong stiffening of the response with the increase in the strain, while the experimental data exhibit a softening in the effective response of the composite which is more pronounced for the case of $w = 2.2$. This softening, which is likely linked to the development of macroscopic shear localization instabilities (or shear bands) in the composite, is consistent with our earlier findings in the context of figures 3.2 and 3.3 for the case of pure shear and axisymmetric loading conditions, where the composite was found to become unstable under compressive strains along the largest axis of the particles. In fact, similar to these two loading conditions (with $\bar{\epsilon} > 0$), the uniaxial tension along \mathbf{e}_1 direction produces compressive strains along the largest axis of the particles (aligned with the \mathbf{e}_3 direction.) To explore this in more detail, we show in Figure 3.9(d) the corresponding TSO predictions for the *transverse* logarithmic strain components $\bar{\epsilon}_2 = \ln(\bar{\lambda}_2)$ and $\bar{\epsilon}_3 = \ln(\bar{\lambda}_3)$, as functions of $\bar{\epsilon}_1$. As can be seen from this figure, the state of macroscopic deformation is not axisymmetric (because of the non-circular geometry of the particle in the $\mathbf{e}_2 - \mathbf{e}_3$ plane, see Figure 2.1(a)), except for the case of $w = 1$ which correspond to spherical particles. In particular, we observe that the compressive strain along the largest axis of the particles (aligned with $\bar{\mathbf{e}}_3$ direction) is smaller than that along the smallest axis of the particle (aligned with \mathbf{e}_2 direction), as also intuitively expected. Note that $\bar{\epsilon}_1 + \bar{\epsilon}_2 + \bar{\epsilon}_3 = 0$ due to the macroscopic incompressibility constraint.

Going back to the TSO estimates in Figure 3.9(c), it is important to note that, we were not able to investigate the development of macroscopic instability for these estimates because our FORTRAN program for detecting the loss of SE was limited to pure shear and axisymmetric loading conditions. For this reason, we considered an “intermediate” loading condition in which the composite is subjected to a tensile stress along $\bar{\mathbf{e}}_1$ direction, and the transverse strain component $\bar{\epsilon}_2$ is enforced to be equal to $\bar{\epsilon}_3$ (therefore, the macroscopic deformation is axisymmetric in $\mathbf{e}_2 - \mathbf{e}_3$ plane). In this case, the transverse stress component \bar{S}_{22} is also non-zero (Figure 3.10(b) shows a schematic representation of the intermediate loading condition). Figures 3.9(e) and (f) show TSO estimates for this intermediate loading conditions for the macroscopic stress component \bar{S}_{11} and the corresponding transverse strain components $\bar{\epsilon}_2$ and $\bar{\epsilon}_3$, respectively, as functions of $\bar{\epsilon}_1$. Also, for comparison purposes, we have included in these figures the corresponding TSO estimates for the case of uniaxial tension along \mathbf{e}_1 direction from Figures 3.9(c) and (d). We were able to investigate the loss of SE for the case of axisymmetric loading condition, and as we observe from Figure 3.9(e), the macroscopic response of the composite becomes unstable at $\bar{\epsilon}_1 \approx 0.75$ for both aspect ratios $w = 1.7$ and $w = 2.2$ (the point of instability is denoted by a circular marker of the same color). It is worth mentioning that, in this case, the loss of SE in the composites takes place through vanishing of the effective incremental shear modulus \hat{L}_{2323}^c (in the plane perpendicular to the long axis of the particles, and in the direction of axis \mathbf{e}_2). Hence, suggested by the loss of SE for this (intermediate) axisymmetric loading condition (which occurs due to the compressive strains along the long axis of

the particles), we expect that the TSO estimates for the case of uniaxial loading become unstable as well, most likely about the same range of critical strain as for the case of axisymmetric loading. For this reason, we conclude that the discrepancy between the TSO predictions and the experimental data at large strains shown in Figure 3.9(c) is mainly due to the fact that the TSO estimates correspond to an unstable solution at those strains, and are not expected to provide very good agreement with corresponding experimental results.

3.3.2 Non-aligned loadings

In the previous subsection, we restricted our attention to cases in which the principal axes of loading are aligned with those of the particles. In this subsection, we present results for the more general case of macroscopically *non-aligned* loadings of the form (3.5). The idea behind presenting these results is to explore the effect of the evolution of the microstructure (here, the particle rotation) on the macroscopic response and stability of the reinforced elastomers. Keeping in mind the transverse isotropy of the reinforced elastomers of interest in this work, it will suffice to restrict our attention to loading orientation angles in the range $0 \leq \bar{\theta} \leq \pi/2$. Thus, in this section, results will be provided for variety of loading angles in this range, including $\bar{\theta} = 0^\circ$ and $\bar{\theta} = 0^{+\circ}$. The latter corresponds to the case in which the principal axes of loading has a very small misorientation with respect to the principal axes of the particles in the undeformed configuration. The significance of this choice will be expounded upon in the discussion below. It is also noted that all results in this subsection are for composites with neo-Hookean matrix phases of the form (3.3). Moreover, results are given for two specific types of *non-aligned* loadings: (1) *pure shear* at an angle, characterized by the choice $\bar{\lambda}_1 = \bar{\lambda}$, $\bar{\lambda}_2 = 1$ (in expression (3.5)), and (2) *axisymmetric shear* at an angle, characterized by the choices $\bar{\lambda}_1 = \bar{\lambda}_2 = \bar{\lambda}$. It is relevant to note that the transformations $\bar{\lambda} \rightarrow \bar{\lambda}^{-1}$ and $\bar{\theta} \rightarrow \bar{\theta} + \pi/2$ lead to the same pure shear loading loading. In addition, it is recalled from the formulation in Chapter 2 that the loading angle $\bar{\theta} = \bar{\theta}_2$ corresponds to rotation of the principal loading axes about the (fixed) laboratory axis \mathbf{e}_2 , while the loading angle $\bar{\theta}_1$ (which has thus far been assumed to be zero) corresponds to a rotation of the principal loading axes about the axis \mathbf{e}_1 . As will be seen below in the context of Figure 3.11 for pure shear loading conditions, we will also consider small out-of-plane misalignments ($\bar{\theta}_1 = 0^{+\circ}$) for reasons that will become evident in the discussion of said figure. Furthermore, we note that the sign convention for the angle $\bar{\psi}^{(2)}$, characterizing the average rotation of the particles, is given by the usual right-hand rule (with respect to the fixed frame of reference, see Figure (a) in Chapter 2). Finally, we note that, similar to the previous subsection, we first consider the case of dilute concentrations of particles ($c \ll 1$) in order to isolate the influence of the particle shape on the macroscopic behavior and the microstructure evolution under non-aligned loadings. After doing this, we will provide results for finite concentrations of particles.

Figure 3.11 provides results for the TSO estimates for the effective response of a neo-Hookean elastomer reinforced with prolate particles under pure and axisymmetric shear, at the fixed loadings angles $\bar{\theta} = 0^\circ, 0^{+\circ}, 5^\circ, 45^\circ, 70^\circ$ (as well as for the angle $\bar{\theta}_1 = 0^{+\circ}$, for pure shear only). Results are shown for the fixed aspect ratio $w = 2$ and a dilute concentration of particles, as functions of the macroscopic logarithmic strain $\bar{\epsilon} = \ln(\bar{\lambda})$. Figures 3.11(a) and (b) show plots for the macroscopic

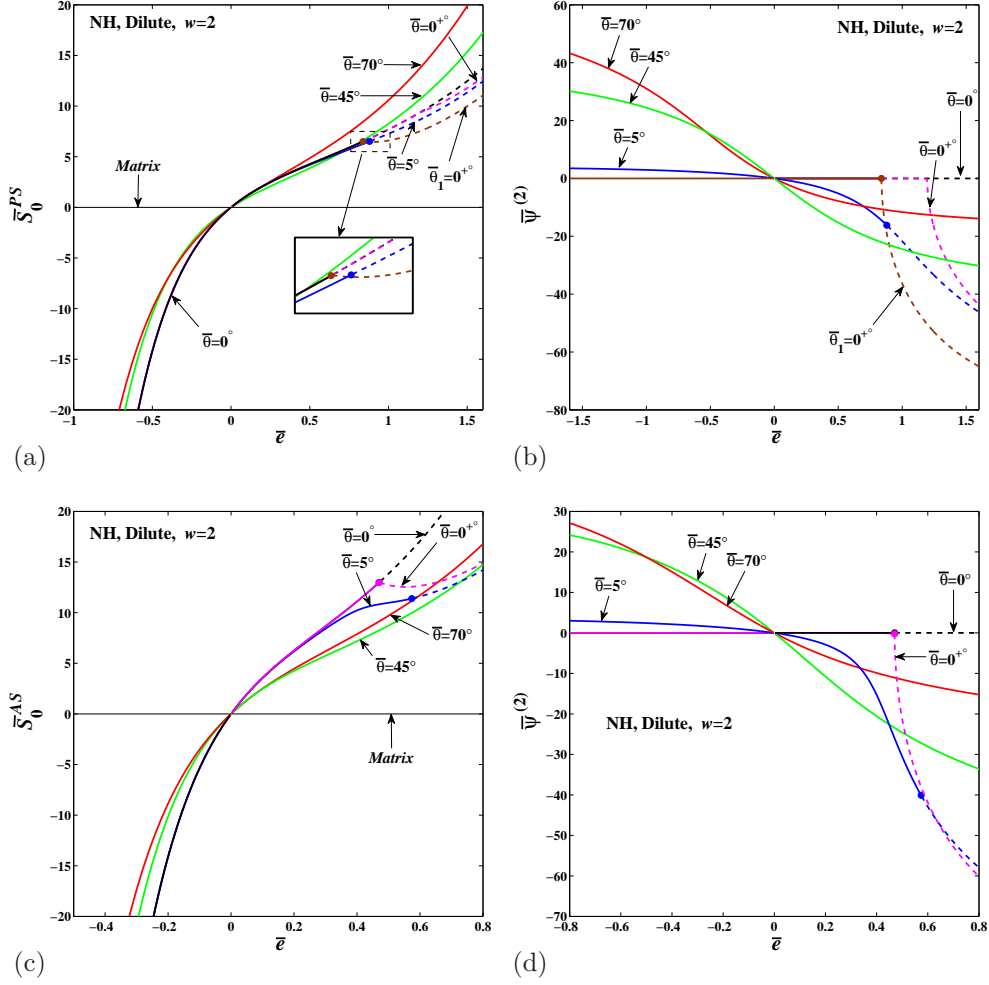


Figure 3.11: TSO estimates for a particle-reinforced neo-Hookean composite with a dilute concentration of *prolate* particles with aspect ratio $w = 2$ subjected to *non-aligned* loadings. Parts (a) and (b) show results for *pure shear* loading ($\bar{\lambda}_1 = \bar{\lambda}, \bar{\lambda}_2 = 1$) for the effective stress \bar{S}_0^{PS} and the angle of rotation of the particles $\bar{\psi}^{(2)}$, respectively. Parts (c) and (d) show results for *axisymmetric shear* loading ($\bar{\lambda}_1 = \bar{\lambda}_2 = \bar{\lambda}$) for the effective stress \bar{S}_0^{AS} and the rotation $\bar{\psi}^{(2)}$, respectively. The results are shown for various angles $\bar{\theta}$ (as well as for the out-of-plane misalignment angle $\bar{\theta}_1 = 0^{+\circ}$ for the case of pure shear loading), as functions of the macroscopic logarithmic strain $\bar{\epsilon} = \ln(\bar{\lambda})$.

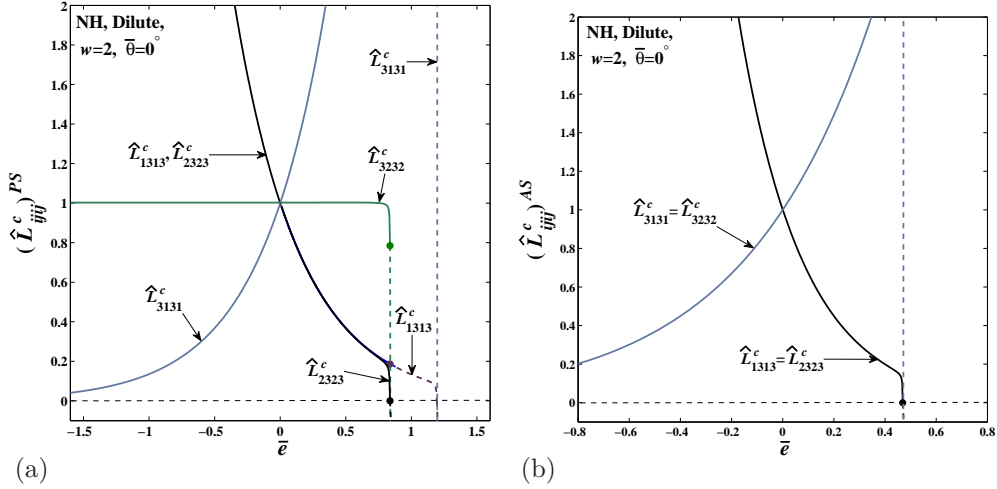


Figure 3.12: TSO estimates for the incremental shear moduli of particle-reinforced neo-Hookean composites with a dilute concentration of *prolate* particles with aspect ratio $w = 2$ subjected to *aligned* loadings. (a) Results for *pure shear* loading ($\bar{\lambda}_1 = \bar{\lambda}$, $\bar{\lambda}_2 = 1$). (b) Results for *axisymmetric shear* loading ($\bar{\lambda}_1 = \bar{\lambda}_2 = \bar{\lambda}$).

stress \bar{S}_0^{PS} and the particle rotation $\bar{\psi}^{(2)}$, respectively, for pure shear. Similarly, Figs. 3.11(c) and (d) show corresponding plots for axisymmetric shear. Recalling that \bar{S}_0^{PS} and \bar{S}_0^{AS} , as determined by expressions (3.9) and (3.11), are measures of the normal stress differences defined by the loading direction, we observe from Figs. 3.11(a) and (c) that \bar{S}_0^{PS} and \bar{S}_0^{AS} are both quite sensitive to the loading angle $\bar{\theta}$. While this is to be expected for small strains, it is interesting to note that, at finite strains, the particle rotations can have significant additional effects relative to the perfectly aligned case ($\bar{\theta} = \bar{\theta}_2 = 0^\circ$). Indeed, it can be seen that the large rotations that are produced for the cases where the long axes of the particles are nearly (but not exactly) orthogonal to the tensile loading axis ($\bar{\theta} = 0^{+\circ}, 5^\circ; \bar{\theta}_1 = 0^{+\circ}$) are associated with significant softening relative to the perfectly aligned case ($\bar{\theta} = 0^\circ$), especially for axisymmetric shear. In fact, the softening is so significant that loss of ellipticity is observed for these cases (as well as for the perfectly aligned case). In connection with the particle rotations shown in Figs. 3.11(b) and (d), it should be noted that, when the composite is subjected to non-aligned loadings, the particles tend to align their longest axis with the tensile loading direction as the deformation progresses, implying that $\bar{\psi}^{(2)} \rightarrow \bar{\theta} - 90^\circ$ for $\bar{\epsilon} \gg 0$, and $\bar{\psi}^{(2)} \rightarrow \bar{\theta}$ for $\bar{\epsilon} \ll 0$ (except for $\bar{\theta} = 0, \pi/2$, for which, the particles do not rotate and $\bar{\psi}^{(2)} = 0^\circ$). For example, for the loading angle $\bar{\theta} = 70^\circ$, $\bar{\psi}^{(2)}$ tends to the values -20° and 70° for $\bar{\epsilon} > 0$ and $\bar{\epsilon} < 0$, respectively.

At this point, it is useful to explore in more detail the possible connections between the particle rotations and the loss of SE condition. For this purpose, we show in Figure 3.12 the appropriate shear components of the incremental modulus tensor for neo-Hookean elastomers reinforced with *dilute* concentrations of *prolate* particles with $w = 2$, subjected to aligned loading conditions. Thus, we observe from Figure 3.12(a) that for *pure shear* loading conditions both \hat{L}_{1313}^c and \hat{L}_{2323}^c decrease with increasing strain and actually vanish, but at different levels of the applied strain $\bar{\epsilon}$. (Note

that the corresponding moduli \widehat{L}_{3131}^c and \widehat{L}_{3232}^c also vanish at the appropriate strains, but have very different behaviors tending to increase or remain constant before vanishing.) On the other hand, we see from Figure 3.12(b) for *axisymmetric shear* loading conditions that \widehat{L}_{1313}^c and \widehat{L}_{2323}^c are identical by symmetry and vanish at the same applied strain. (\widehat{L}_{3131}^c and \widehat{L}_{3232}^c also vanish but exhibit different trends.) In addition, it is noted that vanishing of \widehat{L}_{1313}^c implies that the particles can rotate freely about the \mathbf{e}_2 axis (in the $\mathbf{e}_1 - \mathbf{e}_3$ plane), while vanishing of \widehat{L}_{2323}^c allows the particles to rotate freely about the \mathbf{e}_1 axis (in the $\mathbf{e}_2 - \mathbf{e}_3$ plane). Moreover, the onset of the sudden rotations observed in Figs. 3.11(b) and (d) for pure shear and axisymmetric shear loading conditions, respectively, are found to coincide precisely with the vanishing of the corresponding incremental moduli (as shown in Figs. 3.12(a) and (b)). Thus, for pure shear, \widehat{L}_{1313}^c and \widehat{L}_{2323}^c vanish at different levels of the applied strain $\bar{\epsilon}$, and the particles can be seen to start rotating about the \mathbf{e}_2 and \mathbf{e}_1 axes, respectively, at the corresponding values of the applied strain $\bar{\epsilon}$. In this case, the loss of SE is associated with the first modulus to vanish (in this case, \widehat{L}_{2323}^c , corresponding to rotation of the particles out of the loading plane). On the other hand, for the case of axisymmetric shear, $\widehat{L}_{1313}^c = \widehat{L}_{2323}^c$, and the particles can start rotating about any axis in the \mathbf{e}_1 - \mathbf{e}_2 plane (because of the symmetry) at the same value of the applied strain $\bar{\epsilon}$. In conclusion, it can be seen that the sudden rotation—or *flopping*—of the fibers can be linked directly to the loss of ellipticity of the incremental elasticity tensor of the composites (at least for dilute concentrations).

Figure 3.13 provides results for the TSO estimates for the effective response of a neo-Hookean elastomer reinforced with oblate particles, under pure and axisymmetric shear loadings at the fixed loadings angles, $\bar{\theta} = 0, 0^{+\circ} 5^\circ, 45^\circ, 70^\circ$. Results are shown for the fixed aspect ratio $w = 0.5$, and a dilute concentration of particles, as functions of the macroscopic logarithmic strain $\bar{\epsilon} = \ln(\bar{\lambda})$. Figures 3.13(a) and (b) show plots for the macroscopic stress \bar{S}_0^{PS} and the rotation of the particles $\bar{\psi}^{(2)}$, respectively, for pure shear. Similarly, Figs. 3.13(c) and (d) show corresponding plots for axisymmetric shear. As discussed in the context of the previous figure for the prolate particles, the results of Figure 3.13 put into evidence the significant influence of the rotation of the particles on the effective response and macroscopic stability of the particle-reinforced composites subjected to pure and axisymmetric shear loadings. However, there are important differences between the oblate and prolate particle cases. Thus, we observe from Figure 3.13(a) that the most significant softening in the macroscopic stress-strain relation, as well as the associated loss of strong ellipticity, occur for compressive applied strains ($\bar{\epsilon} < 0$), in contrast with the prolate-particles composites (where the most pronounced softening and associated instabilities take place for tensile strains). In particular, Figure 3.13(a) shows that, when a slightly misaligned pure shear ($\bar{\theta} = 0^{+\circ}$) is applied, a burst of softening occurs starting at a certain negative value of the critical strain $\bar{\epsilon}_{cr}$, which, as mentioned earlier, is concurrent with the large particle rotations observed in Figure 3.13(b). As also discussed earlier in the context of the composites with prolate particles, this is entirely consistent with the development of flopping-type instability at the critical strain $\bar{\epsilon}_{cr}$. This softening, however, becomes less pronounced with increasing loading angle $\bar{\theta}$, due to the fact that the oblate particles will rotate more slowly and thus accommodate a smaller portion of the macroscopic compressive strain for such larger values of $\bar{\theta}$. On the contrary, when the composite is subjected to tensile strains ($\bar{\epsilon} > 0$), no *softening* phenomenon is observed (for the chosen loading angles), and the composite

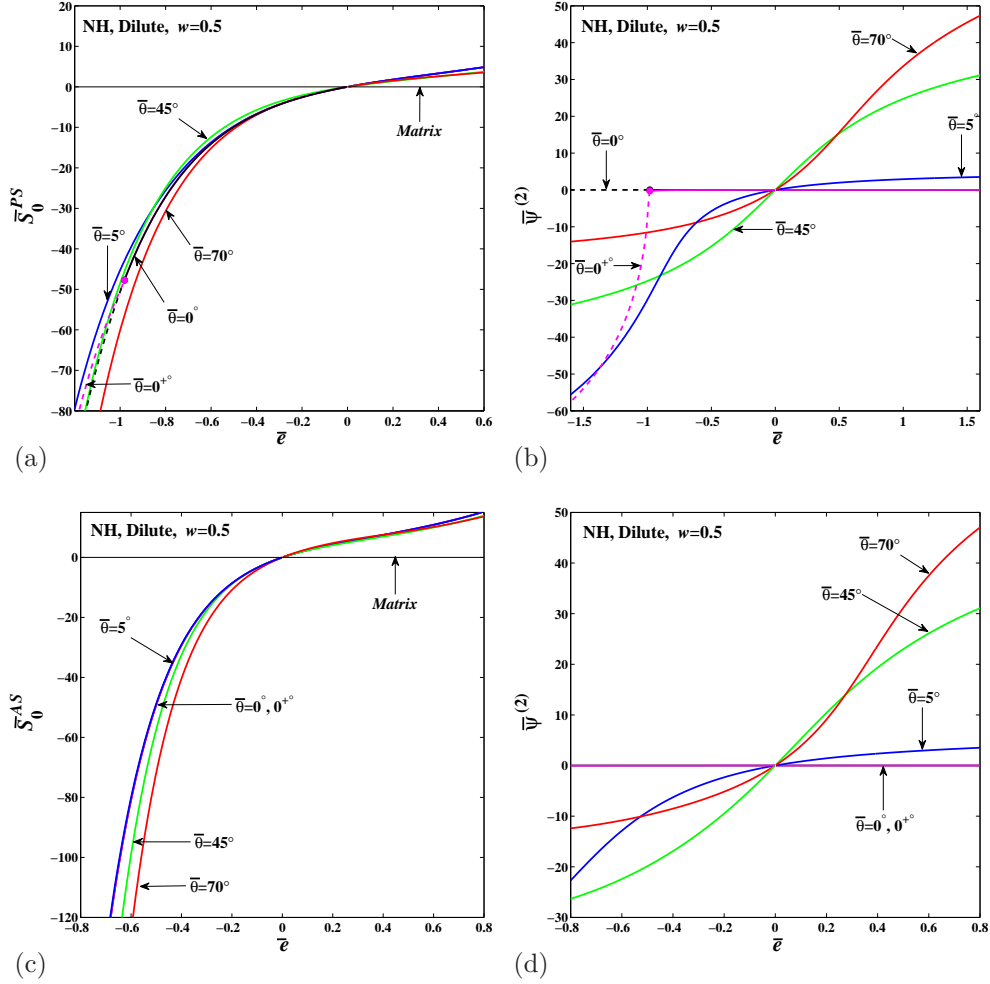


Figure 3.13: TSO estimates for a particle-reinforced neo-Hookean composite with a dilute concentration of *oblate* particles with aspect ratio $w = 0.5$ subjected to *non-aligned* loadings. Parts (a) and (b) show results for *pure shear* loading ($\bar{\lambda}_1 = \bar{\lambda}$, $\bar{\lambda}_2 = 1$) for the effective stress \bar{S}_0^{PS} and the angle of rotation of the particles $\bar{\psi}^{(2)}$, respectively. Parts (c) and (d) show results for *axisymmetric shear* loading ($\bar{\lambda}_1 = \bar{\lambda}_2 = \bar{\lambda}$) for the effective stress \bar{S}_0^{AS} and the rotation $\bar{\psi}^{(2)}$, respectively. The results are shown for various angles $\bar{\theta}$, as functions of the macroscopic logarithmic strain $\bar{e} = \ln(\bar{\lambda})$.

exhibits a consistently stiffer response for smaller loading angles, once again, due to the fact that the oblate particles rotate slower at a smaller $\bar{\theta}$ for tensile strains. On the other hand, as seen in Figure 3.13(c), no loss of ellipticity is detected for the composites under axisymmetric loading, in agreement with the results in Figure 3.1(d) for the case of $w = 0.5$. The composites, nevertheless, show a systematically softer behavior in compression ($\bar{\epsilon} < 0$) when the particles undergo a faster and larger rotation. Finally, similar to the case of prolate particles, we observe from Figure 3.13 (b) and (d) that oblate particles also tend to align (one of) their major axes with the tensile direction of the non-aligned loading as the deformation increases, and thus we deduce that in this case $\bar{\psi}^{(2)} \rightarrow \bar{\theta}$ at $\bar{\epsilon} \gg 0$, and $\bar{\psi}^{(2)} \rightarrow \bar{\theta} - 90^\circ$ at $\bar{\epsilon} \ll 0$ (except for $\bar{\theta} = 0^\circ, \pi/2$, when the particles do not rotate).

Figure 3.14 presents results for the TSO estimates for the effective response of incompressible, neo-Hookean elastomers reinforced with rigid particles in dilute concentrations, subjected to non-aligned pure and axisymmetric shear loadings at a fixed angle $\bar{\theta} = 25^\circ$. Results are shown for prolate particles with aspect ratios 1, 1.1, 2, 4 and 8, as functions of the macroscopic logarithmic strain $\bar{\epsilon} = \ln(\bar{\lambda})$. Figures 3.14(a) and (b) show plots for the case of pure shear loading for the macroscopic stress \bar{S}_0^{PS} and the rotation of the particles $\bar{\psi}^{(2)}$, respectively. Similarly, Figs. 3.14(c) and (d) show corresponding plots for the case of axisymmetric shear loading. It can be seen from Figure 3.14(a) and (c) that the effective stress-strain plots (for pure and axisymmetric shear loadings) exhibit a *softening* effect for tensile strains ($\bar{\epsilon} > 0$), which gets progressively more significant with increasing aspect ratio w . As discussed earlier, this effect is linked to the associated evolution of the microstructure. In fact, for non-aligned loadings, the finite rotation of rigid particles (see Figs. 3.14(b) and (d)) serves to *accommodate* some part of the total macroscopic deformation, so that smaller strains are produced in the elastomeric matrix phase. Interestingly, the largest particle rotations corresponding to the largest aspect ratios can be correlated with the strongest softening in the macroscopic stress-strain relations, for both pure and axisymmetric shear loadings. It also should be remarked that, at the chosen loading angle ($\bar{\theta} = 25^\circ$), no loss of SE is detected for either loading conditions. The reason behind this, as mentioned earlier, is that, at this relatively large value of $\bar{\theta}$, the compression along the major axis of particles never reaches the level required for loss of SE to occur.

In addition, consistent with earlier observations, it can be seen from Figs. 3.14(b) and (d) that the particles tend to align themselves with the tensile loading axis, so that the average rotation of the particles for this particular loading angle ($\bar{\theta} = 25^\circ$) exhibits the asymptotic behaviors: $\bar{\psi}^{(2)} \rightarrow -65^\circ$ as $\bar{\epsilon} \rightarrow \infty$, and $\bar{\psi}^{(2)} \rightarrow 25^\circ$ as $\bar{\epsilon} \rightarrow -\infty$. In this connection, it should be mentioned that results have also been included in Figs. 3.14(b) and (d) for the rotation of a ‘‘Material Line Element,’’ labeled *MLE*, for comparison purposes. These curves correspond to the rotation of a typical material line element that is initially aligned with the longest axis of the particles (in this case, the axis \mathbf{e}_3) in the undeformed configuration, and are determined by the expressions

$$\bar{\psi}_{MLE}^{PS} = -\arctan\left(\frac{\sin(\bar{\theta})\cos(\bar{\theta})(e^{2\bar{\epsilon}} - 1)}{\sin^2(\bar{\theta})e^{2\bar{\epsilon}} + \cos^2(\bar{\theta})}\right), \quad \bar{\psi}_{MLE}^{AS} = -\arctan\left(\frac{\sin(\bar{\theta})\cos(\bar{\theta})(e^{3\bar{\epsilon}} - 1)}{\sin^2(\bar{\theta})e^{3\bar{\epsilon}} + \cos^2(\bar{\theta})}\right) \quad (3.18)$$

for pure and axisymmetric shear loadings, respectively. Note that the TSO estimates for the particle rotations are consistent with these results in the limit as the prolate particles become needles ($w \rightarrow$

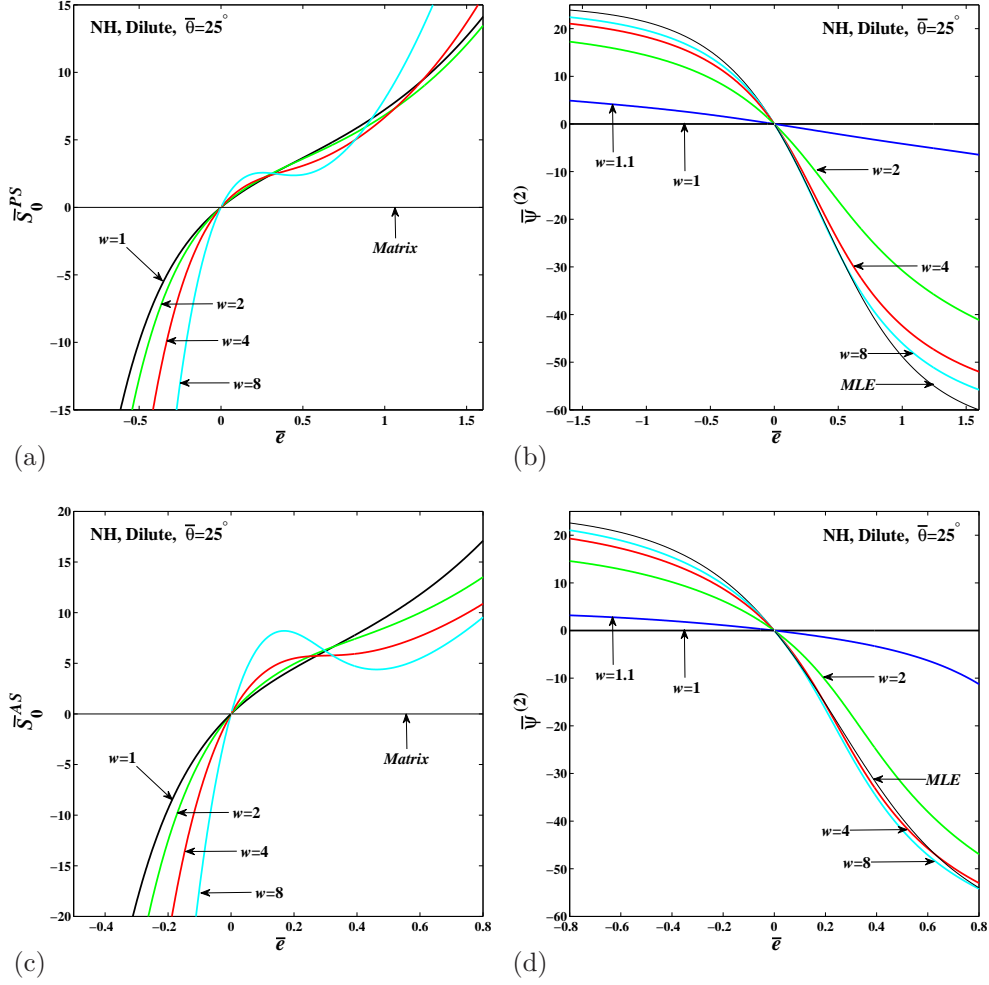


Figure 3.14: TSO estimates for particle-reinforced neo-Hookean composites with dilute concentrations of *prolate* particles subjected to *non-aligned* loadings at the fixed angle $\bar{\theta} = 25^\circ$. Parts (a) and (b) show results for the effective stress \bar{S}_0^{PS} and the angle of rotation of the particles $\bar{\psi}^{(2)}$, respectively, for *pure shear* loading ($\bar{\lambda}_1 = \bar{\lambda}_2 = 1$). Parts (c) and (d) show results for the effective stress \bar{S}_0^{AS} and the rotation $\bar{\psi}^{(2)}$, respectively, for *axisymmetric shear* ($\bar{\lambda}_1 = \bar{\lambda}_2 = \bar{\lambda}$). The results are shown for particle aspect ratios $w = 1, 1.1, 2, 4, 8$, as functions of the macroscopic logarithmic strain $\bar{e} = \ln(\bar{\lambda})$.

∞).

Figure 3.15 presents results for the TSO estimates for the effective response of incompressible, neo-Hookean elastomers reinforced with a dilute concentration of oblate rigid particles, under non-aligned pure and axisymmetric shear loadings at the fixed loading angle $\bar{\theta} = 25^\circ$. Results are shown for aspect ratios w equal to 1, 0.9, 0.5, 0.25 and 0.125, as functions of the macroscopic logarithmic strain $\bar{\epsilon} = \ln(\bar{\lambda})$. Figures 3.15(a) and (b) show plots for the macroscopic stress \bar{S}_0^{PS} and the rotation of the particles $\bar{\psi}^{(2)}$, respectively, for pure shear loading. Similarly, Figs. 3.15(c) and (d) show corresponding results for axisymmetric shear. Compared to the previous results for prolate particles, the results of Figure 3.15 for oblate particles are roughly the opposite. Thus, the particles in this case undergo the largest rotations (in the opposite direction) for compressive strains ($\bar{\epsilon} < 0$), and the rotations are faster for the smallest aspect ratios. In addition, the particles tend to the asymptotic values ($\bar{\psi}^{(2)} \rightarrow 25^\circ$ as $\bar{\epsilon} \rightarrow \infty$, and $\bar{\psi}^{(2)} \rightarrow -65^\circ$ as $\bar{\epsilon} \rightarrow -\infty$), as long as the aspect ratio w is different from unity (when the particles do not rotate). Correspondingly, the plots for the effective stress-strain relations of the composites exhibit *softening* for compressive strains ($\bar{\epsilon} < 0$), and the level of softening increases with decreasing values of the aspect ratio w . On the other hand, the (positive) particle rotations for tensile strains ($\bar{\epsilon} > 0$) can be seen to lead to a *stiffening* of the macroscopic stress-strain relation, which becomes progressively more significant, the smaller the aspect ratio.

In Figs. 3.15 (b) and (d), we have also included plots for the rotation of the normal to a “material surface element” (MSE) whose normal is initially aligned with the \mathbf{e}_3 axis. This rotation can be expressed as

$$\bar{\psi}_{MSE}^{PS} = \arctan\left(\frac{\sin(\bar{\theta})\cos(\bar{\theta})(e^{2\bar{\epsilon}} - 1)}{\sin^2(\bar{\theta}) + e^{2\bar{\epsilon}}\cos^2(\bar{\theta})}\right), \quad \bar{\psi}_{MSE}^{AS} = \arctan\left(\frac{\sin(\bar{\theta})\cos(\bar{\theta})(e^{3\bar{\epsilon}} - 1)}{\sin^2(\bar{\theta}) + \cos^2(\bar{\theta})e^{3\bar{\epsilon}}}\right) \quad (3.19)$$

for pure and axisymmetric shear loading, respectively. In this connection, it is noted that the TSO estimates for the rotation of oblate particles become consistent with these results for $MSEs$ in the limit as the aspect ratio $w \rightarrow 0$.

Finally, Figure 3.16 provides results showing the influence of the particle volume fraction on the TSO estimates for the effective response of the composites subjected to non-aligned pure and axisymmetric shear loadings. The results in this figure are shown for an incompressible, neo-Hookean elastomer reinforced with rigid, prolate particles with a fixed aspect ratio, $w = 2$, and three concentrations, $c = 0.05, 0.15, 0.25$. In addition, the results are shown for two loading angles $\bar{\theta} = 5^\circ$ and 25° , as functions of the macroscopic logarithmic strain $\bar{\epsilon} = \ln(\bar{\lambda})$. Similar to the previous figures in this subsection, parts (a) and (b) show pure shear results for the macroscopic stress \bar{S}_0^{PS} and the rotation of the particles $\bar{\psi}^{(2)}$, respectively, while parts (c) and (d) show the corresponding results for axisymmetric shear. The main observation from these figures is that the particle concentration c has a relatively small effect on the particle rotations (in fact, for small strains the particle rotations are completely insensitive to c), while it has a significant effect on the effective stress-strain relations for the composites. Thus, we can see that, as expected, increasing values of c result in stiffer responses both in tension and compression, as well as for both pure and axisymmetric shear. On the other hand, we also observe that the initial loading angle has a significant effect on the particle rotations,

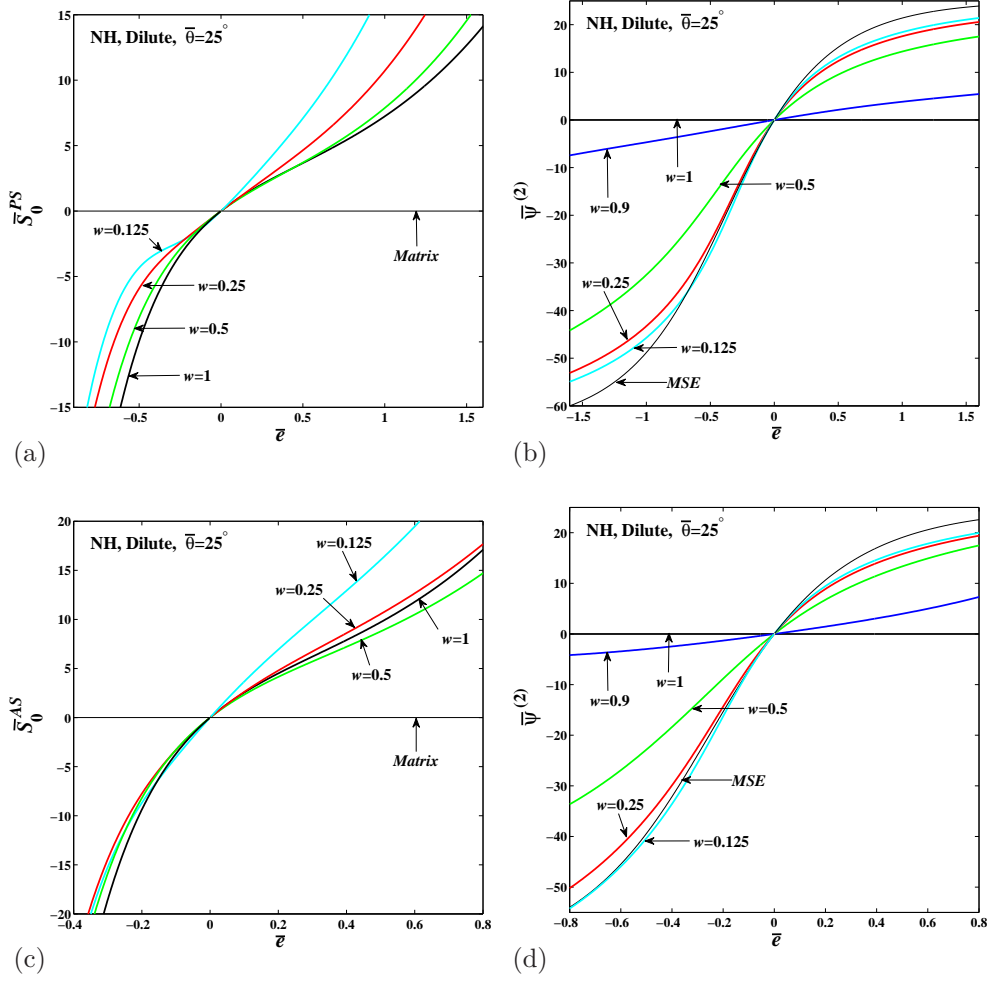


Figure 3.15: TSO estimates for particle-reinforced neo-Hookean composites with dilute concentrations of *oblate* particles subjected to *non-aligned* loadings at the fixed angle $\bar{\theta} = 25^\circ$. Parts (a) and (b) show results for the effective stress \bar{S}_0^{PS} and the angle of rotation of the particles $\bar{\psi}^{(2)}$, respectively, for *pure shear* ($\bar{\lambda}_1 = \bar{\lambda}$, $\bar{\lambda}_2 = 1$). Parts (c) and (d) show results for the effective stress \bar{S}_0^{AS} and the rotation $\bar{\psi}^{(2)}$, respectively, for *axisymmetric shear* ($\bar{\lambda}_1 = \bar{\lambda}_2 = \bar{\lambda}$). The results are shown for particle aspect ratios $w = 1, 0.9, 0.5, 0.25, 0.125$, as functions of the macroscopic logarithmic strain $\bar{\epsilon} = \ln(\bar{\lambda})$.

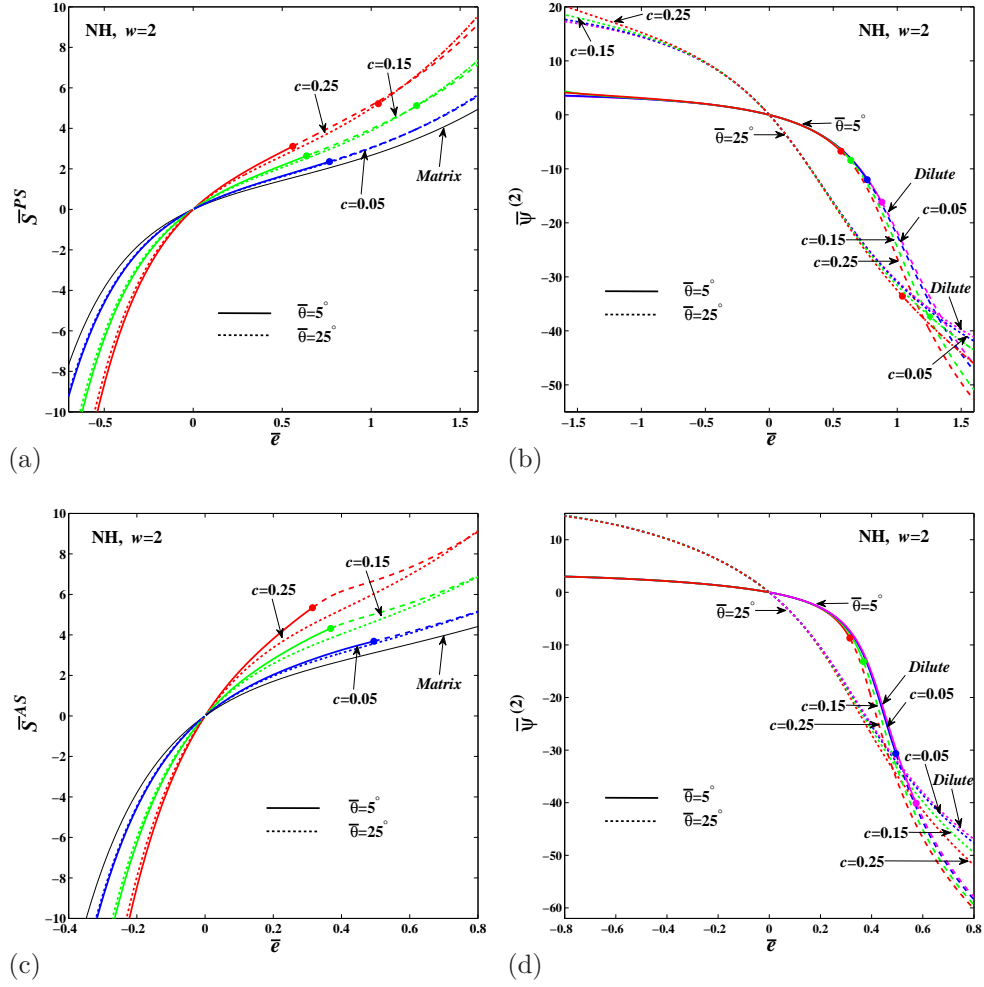


Figure 3.16: TSO estimates for a particle-reinforced neo-Hookean composite with prolate particles of aspect ratio $w = 2$ subjected to *non-aligned* loadings at the angles $\bar{\theta} = 5^\circ$, and 25° . Parts (a) and (b) show results for the case of *pure shear* loading ($\bar{\lambda}_1 = \bar{\lambda}$, $\bar{\lambda}_2 = 1$), respectively for the effective stress \bar{S}_0^{PS} and the angle of rotation of the particles $\bar{\psi}^{(2)}$. Parts (c) and (d) show results for the case of *axisymmetric shear* loading ($\bar{\lambda}_1 = \bar{\lambda}_2 = \bar{\lambda}$), respectively for the effective stress \bar{S}_0^{AS} and the rotation $\bar{\psi}^{(2)}$. The results are shown for particle volume fractions $c = 0.05, 0.15$, and 0.25 , as functions of the macroscopic logarithmic strain $\bar{e} = \ln(\bar{\lambda})$.

but a relatively small influence on the macroscopic stress-strain relation for the composite. In addition, consistent with the results of Figure 3.4, it can be seen that the reinforced elastomers become less stable with increasing particle volume fractions, while the response of these composites is more stable for the larger loading angle (25°), where loss of ellipticity is not detected for the levels of strain considered.

3.4 Concluding Remarks

In this chapter, we made use of the tangent second-order (TSO) constitutive model presented in Chapter 2 to generate estimates for the homogenized stress-strain relation, the evolution of microstructure, and the onset of macroscopic instabilities in particle-reinforced elastomeric composites consisting of an incompressible Gent/neo-Hookean matrix and random distributions of aligned spheroidal particles of aspect ratio w . The estimates presented in this chapter provide a broad picture of the influence of the macroscopic loading conditions, matrix properties and microgeometry (including particle volume fractions and shapes) on the effective behavior and the possible onset of macroscopic instabilities in the composites. Explicit results are given for composites with both *prolate* and *oblate* spheroidal shapes, subjected to *aligned* and *non-aligned* pure shear and axisymmetric shear loading conditions. These results generalize the results in Chapter 1 for elastomers reinforced with random distributions of spherical particles ($w = 1$), as well as earlier results of Lopez-Pamies and Ponte Castañeda (2006b) for 2-D composites reinforced with elliptical fibers. In addition, the results of this work are consistent with earlier results for laminated elastomers (deBotton, 2005; Lopez-Pamies and Ponte Castañeda, 2009) and for continuous-fiber-reinforced elastomers (Agoras et al., 2009a) in the limits as the aspect ratio w tend to zero and ∞ , respectively.

Concerning the results for the overall behavior, we begin by emphasizing that the TSO model predictions are in very good agreement with available numerical results (Lopez-Pamies et al., 2013a) for spherical particles ($w = 1$), up to fairly large strains. Similarly, the TSO results were found to be in excellent agreement with FEM results (Moraleda et al., 2009) for the transverse shear response of continuous-fiber-reinforced elastomers ($w \rightarrow \infty$). In particular, it should be emphasized that the new choice for the response of the neo-Hookean matrix phase, as given by expression ((3.3)), leads to estimates for the macroscopic stress-strain relation that do not lock up at finite strains. This is different from the corresponding expressions given in Chapter 1, which tend to lock up at a finite strain that becomes smaller with increasing particle volume fraction, even for neo-Hookean matrix behavior. Although a very minor change relative to the expressions originally given in Chapter 1 (nothing else changes!), the use of the new expression does give much better agreement with the available numerical results, especially at the larger volume fractions. It should be noted, however, that the corresponding results for reinforced Gent elastomers do exhibit significant stiffening due to the particles, and tend to lock up at strains that are smaller than for the elastomeric matrix material and that become smaller with increasing particle volume fraction.

Compared to the results for spherical particles, it is found that the corresponding results for prolate, or oblate particles generally result in stiffer responses when the reinforced elastomers are loaded in pure shear or axisymmetric shear aligned with the particle axes, and the amount of

stiffening increases with increasing (decreasing) aspect ratio for prolate (oblate) particles. However, when the loading axes are not aligned with the particle axes, it is found that the particles may undergo significant rotations tending to align their long axes with the tensile axes of loading; this phenomenon in turn may lead to significant softening, which becomes more pronounced as the particle shape moves away from spherical. In fact, when the tensile loading axis is nearly orthogonal to the long axes of the particles, the particles can suddenly undergo large rotations at a certain critical amount of straining, which is found to be coincident (at least for dilute concentrations) with the vanishing of the shear component of the incremental effective elasticity tensor transverse to the long particle axis of the reinforced elastomer. Thus, the reinforced elastomers with spheroidal particles can undergo shear localization instabilities, which are captured by loss of ellipticity of the associated effective incremental modulus tensors, and correspond physically to the sudden collective rotation—or flopping—of the particles to try to accommodate the imposed deformation. These flopping-type macroscopic instabilities in short-fiber-reinforced elastomers were first predicted theoretically in the context of model 2-D composites by Lopez-Pamies and Ponte Castañeda (2006b) and verified numerically by Michel et al. (2010) for the same type of 2-D composites. Although the physical mechanism for these symmetry-breaking instabilities is essentially the same for the more realistic 3-D composites considered in this work, the behavior is a bit richer for the 3-D composites when subjected to general 3-D loadings since the particles tend to flop in the softest direction (the one associated with the first transverse shear modulus to vanish). Also, consistent with earlier findings for the 2-D composites, the reinforced elastomers become more unstable (i.e., they develop instabilities for smaller strains) as the particle shape moves away from the perfectly symmetric spherical shapes and as the volume fraction of the particles increases.

Part II

Viscoelastic Suspensions

Chapter 4

Rheology of non-dilute suspensions of soft viscoelastic particles in a Newtonian fluid

In this chapter, we present a homogenization-based model for the rheological behavior of non-dilute suspensions of initially spherical, viscoelastic particles in viscous fluids under uniform, Stokes flow conditions. The particles are assumed to be neutrally buoyant, Kelvin-Voigt solids undergoing time-dependent, finite deformations, and exhibiting generalized neo-Hookean behavior in their purely elastic limit. We investigate the effects of the shape dynamics and constitutive properties of the viscoelastic particles on the macroscopic rheological behavior of the suspensions. The proposed model makes use of known homogenization estimates for composite material systems consisting of random distributions of aligned ellipsoidal particles with prescribed two-point correlation functions to generate corresponding estimates for the instantaneous (incremental) response of the suspensions, together with appropriate evolution laws for the relevant microstructural variables. To illustrate the essential features of the model, we consider two special cases: (1) extensional flow, and (2) shear flow. For each case, we provide the time-dependent response, and when available, the steady-state solution for the average particle shape and orientation, as well as for the effective viscosity and normal stress differences in the suspensions. The results exhibit shear thickening for extensional flows and shear thinning for shear flows, and it is found that the volume fraction and constitutive properties of the particles significantly influence the rheology of the suspensions under both types of flows. In particular, for the case of extensional flow, suspensions of particles with finite extensibility constraints are always found to reach a steady state, while this is only the case at sufficiently low strain rates for suspensions of neo-Hookean particles, as originally reported by Roscoe (1967) and Gao et al. (2011). For the case of shear flow, viscoelastic particles with high viscosities can experience a trembling motion of decreasing amplitude before reaching the steady state.

4.1 Introduction

Suspensions of interacting *deformable* particles in a fluid are used in numerous applications of current interest (e.g., tissue engineering, drug delivery, coatings), and they constitute a large class of naturally existing solid-fluid mixtures as well (e.g., blood). Driven by the interest in such applications, the study of the macroscopic behavior and rheology of these suspensions has received considerable attention in the past. Among them, solid-fluid mixtures consisting of large numbers of soft, micro-scaled particles suspended in Newtonian fluids are of particular importance. Well-known examples of these mixtures include suspensions of red blood cells in blood plasma which is a Newtonian fluid (Skalak et al., 1989), and suspensions of microgel particles in a solvent (Pal, 2010). When subjected to shear flows, the suspended soft particles undergo significant changes in shape and orientation, and this evolution of the microstructure is expected to have a strong influence on the macroscopic rheological properties of the suspension. It follows that sound models for the constitutive behavior of such suspensions must properly account for appropriate microstructural variables, such as the average shape and orientation of the particles, as well as for the constitutive nonlinearities associated with the mechanical response of the particles.

In the past decades, a vast amount of research has so far focused on estimating the effective viscosity of dilute and non-dilute suspensions of *rigid* particles (Einstein, 1906; Jeffery, 1922; Krieger and Dougherty, 1959; Frankel and Acrivos, 1967; Batchelor, 1970; Batchelor and Green, 1972; Krieger,

1972; Jeffrey and Acrivos, 1976; Brady and Bossis, 1985; Phung et al., 1996; Stickel and Powell, 2005, to cite only a few). By comparison, fewer studies deal with the rheology of suspensions of dilute and non-dilute concentrations of *deformable* particles in a Newtonian fluid. Among the pioneering studies, Fröhlich and Sack (1946) considered suspensions of elastic spherical particles in a Newtonian fluid undergoing a pure extensional flow and derived constitutive equations relating the macroscopic extensional stress and the applied strain rate for small deformations of the microstructure. Cerf (1952) investigated a suspension of spheres with special viscoelastic properties in a viscous liquid under oscillatory motion of small amplitude. More than a decade later, Roscoe (1967) studied the rheological behavior of *dilute* suspensions of solid viscoelastic spheres in a Newtonian fluid within the context of finite strains. In this chapter, which was limited to steady-state (SS) behaviors, Roscoe obtained the effective viscosity and normal stress differences for the suspension as functions of the solid and liquid material properties and the flow conditions. In addition, Roscoe demonstrated that, for initially spherical particles and shear-flow conditions, steady-state solutions are possible such that the particle deforms into an ellipsoid of fixed orientation, and the material within the ellipsoid undergoes a tank-treading motion deforming and rotating continuously with uniform velocity gradient and stress. In closely related work, Goddard and Miller (1967) investigated the time-dependent behavior of a viscoelastic sphere in a Newtonian fluid within the limits of small deformations of the particle. Based on the coupled solutions for the flow field around the particle and the deformation of the particle, they derived a constitutive equation for the rheological behavior of suspensions of slightly deformed spheres in the dilute limit. In the regime of non-dilute concentrations of particles but, again, within the small deformation limit, Goddard (1977) generalized the analysis of Frankel and Acrivos (1967) for highly concentrated suspensions of rigid particles to account for the effect of small deformation of the particles on the rheology of the suspension. In addition, still in the regime of small particle deformations, Snabre and Mills (1999) developed an effective medium approximation to estimate the effective shear viscosity of non-dilute suspensions of viscoelastic particles. The authors made use of the Kelvin-Voigt (KV) model to describe the deformation of particles in the suspension when subjected to a viscous shear flow. As pointed out by the authors, the KV model can be used as a first-order approximation to capture the deformation behavior in microcapsules and biological cells, as they represent an intermediate case between solid particles and fluid drops. Again, within the small deformation limit, Pal (2003) derived a semi-empirical equation for effective viscosity of non-dilute suspensions of elastic particles by means of the differential effective medium approach together with the constitutive model developed by Goddard and Miller (1967) for dilute suspensions of spherical, elastic particles. The author found good agreement with experimental data on the effective shear viscosity of un-aggregated red cells in saline solution. There has also been considerable work on suspensions of viscous droplets or emulsions (see, for example, Taylor, 1932; Oldroyd, 1953; Bilby et al., 1975; Lowenberg and Hinch, 1996; Wetzel and Tucker, 2001), where it is important to account for interfacial tension between the two fluids. In addition, numerous works have been published for suspensions of capsules and vesicles (e.g., Barthès-Biesel, 1980; Barthès-Biesel and Rallison, 1981; Keller and Skalak, 1982; Ramanujan and Pozrikidis, 1998b; Lac et al., 2004; Ghigliotti et al., 2010).

As demonstrated by several of the above-mentioned studies, the constitutive properties of the

particles strongly influence the rheology of suspensions of deformable particles in a viscous fluid. Although these studies can capture to some extent the influence of particle deformation on the effective properties of the suspensions, they are confined to small strains and/or dilute concentrations. Indeed, rheological models that can address general morphologies and particle volume fractions, as well as general constitutive behavior and finite deformations for the soft particles in the suspension are still largely lacking. Recently, Gao et al. (2011) studied the rheology of dilute suspensions of neo-Hookean particles in a Newtonian fluid under Stokes flow conditions. Making use of a polarization technique, the authors developed an *exact* analytical estimate describing the finite-strain, time-dependent response of a neo-Hookean particle in a viscous shear flow. They found that the (time-dependent) “excess” viscosity of the dilute suspensions of such particles exhibit strong coupling with the large changes in the particle shape and orientation leading to a shear thinning effect. Most recently, they made use of their model to study the rheology of dilute suspensions of neo-Hookean particles in an extensional flow (Gao et al., 2013), and found a shear-thickening effect instead. In addition Gao et al. (2012) showed that it was possible to have three types of motions—steady-state, trembling, and tumbling—for dilute concentration of elastic particles, depending on the shear rate, elastic shear modulus, and initial particle shape.

With the perspectives offered by the work of Gao et al. (2011) for *dilute* suspensions of *elastic* particles in mind, the goal of the present work is to investigate the time-dependent rheological properties of *non-dilute* suspensions of deformable *viscoelastic* particles in the regime of arbitrarily large deformations. More specifically, we study the effective rheological response, as well as the microstructure evolution, in suspensions of initially spherical, nonlinear KV viscoelastic particles with generalized neo-Hookean elastic behavior in a Newtonian viscous fluid subjected to simple flows. We assume that the characteristic size of the particles is larger than $1\ \mu\text{m}$ so that we can neglect Brownian forces acting on the particles. Also, we confine our attention to Stokes flow regime (i.e., $Re \rightarrow 0$), where viscous forces dominate over inertial effects. We develop a rigorous homogenization-based model to obtain time-dependent estimates, and when available, steady-state estimates for the rheological behavior of these suspensions. The model is based on the Hashin-Shtrikman-Willis (HSW) homogenization theory (Hashin and Shtrikman, 1963; Willis, 1977), which was originally developed for elastic composite materials. More specifically, we make use of the results of Ponte Castañeda and Willis (1995) for composites consisting of aligned ellipsoidal particles that are distributed randomly with ellipsoidal two-point correlations in a matrix of a different material. This theory was extended to two-phase viscous systems by Kailasam et al. (1997) and Kailasam and Ponte Castañeda (1998), and used to generate estimates for the deformation inside the particles, which when combined with nonlinear equations for the evolution of the stress field in the particles, as well as for the shape and orientation of the particles, can be used to characterize the macroscopic rheological behavior of the suspensions in uniform flows.

The structure of the chapter is as follows. Section 4.2 addresses the constitutive behavior of the deforming particles and the types of particulate microstructures considered in this chapter. In section 4.3, we lay out the homogenization strategy. We first provide results for the instantaneous macroscopic stress in the suspensions in terms of the average elastic stress, vorticity and deformation inside the particles, which can in turn be related to the macroscopic strain rate and vorticity in the

suspension. Next, we confine our attention to suspensions of initially spherical particles and, using the consistent homogenization estimates for the average strain-rate and vorticity tensors inside the particles, we develop evolution equations for the average particle shape and orientation. Section 4.4 provides explicit expressions for steady-state conditions for non-dilute concentration of Kelvin-Voigt and purely elastic particles, thus generalizing the results of Roscoe (1967) for dilute concentrations. In section 4.6, we apply our model for two important special cases. First, we consider the problem of suspensions of initially spherical particles in an extensional flow, and provide representative numerical examples, as well as closed-form results for steady-state conditions. Second, we consider the application of the model to suspensions of initially spherical particles in a shear flow. Finally, some conclusions are drawn in section 4.5.

4.2 Suspensions of viscoelastic particles in a viscous fluid

As already mentioned, in this chapter, we consider *random* suspensions of (soft) nonlinear viscoelastic particles in a Newtonian fluid (matrix phase). The particles and fluid phases are incompressible and have the same density, so that the particles are neutrally buoyant in the fluid. In this section, we describe in some detail the constitutive behavior of the homogeneous matrix and particle phases in the suspension, as well as for the microstructures of interest. Following this section, our aim will be to deliver estimates for the macroscopic rheological response and associated microstructure evolution in these suspensions under uniform flow conditions.

We begin with a quick review of the basic kinematic relations, in particular, to fix the notation. Under the application of mechanical loadings, a material point \mathbf{X} in the reference configuration moves to a new point \mathbf{x} at time t in the deformed configuration of the particle. In the Lagrangian description of the motion, the deformation is described by the map $\mathbf{x}(\mathbf{X}, t)$, assumed to be continuous and one-to-one. The deformation gradient tensor $\mathbf{F} = \text{Grad } \mathbf{x}$ (with Cartesian components $F_{ij} = \partial x_i / \partial X_j$) then serves to characterize the deformation of the material, and is such that $\mathbf{F} = \mathbf{R}\mathbf{U} = \mathbf{V}\mathbf{R}$, where \mathbf{R} is the rotation, and \mathbf{U} and \mathbf{V} are the right- and left-stretch tensors, respectively. We will also make use of the right and left Cauchy-Green tensors, given by $\mathbf{C} = \mathbf{F}^T \mathbf{F} = \mathbf{U}^2$ and $\mathbf{B} = \mathbf{F}\mathbf{F}^T = \mathbf{V}^2$, respectively. (\mathbf{B} is also known as the Finger tensor.) Correspondingly, in the Eulerian description, the motion is described by the velocity field $\mathbf{v}(\mathbf{x}, t)$, such that the Eulerian strain rate and vorticity tensors are given by $\mathbf{D} = \frac{1}{2}(\mathbf{L} + \mathbf{L}^T)$ and $\mathbf{W} = \frac{1}{2}(\mathbf{L} - \mathbf{L}^T)$, respectively, where $\mathbf{L} = \text{grad } \mathbf{v}$ is the velocity gradient, which is related to the deformation gradient by $\mathbf{L} = \dot{\mathbf{F}}\mathbf{F}^{-1}$, with $\dot{\mathbf{F}}$ denoting the (material) time derivative of \mathbf{F} .

4.2.1 Constitutive behavior of the phases

We assume that the suspended particles are homogeneous and made of incompressible, isotropic solids. We consider particles with viscoelastic behavior and make use of a generalized Kelvin-Voigt (KV) model to describe their constitutive response. This model consists of a hyperelastic spring and a dashpot connected in parallel. We will also consider suspensions of purely elastic particles, which are one limiting case of the KV particles. For the incompressible KV material, the Cauchy stress $\boldsymbol{\sigma}$

can be written as (Joseph, 1990)

$$\boldsymbol{\sigma} = -p'\mathbf{I} + \boldsymbol{\tau}, \quad \boldsymbol{\tau} = \boldsymbol{\tau}_e + \boldsymbol{\tau}_v, \quad (4.1)$$

where p' is an arbitrary hydrostatic pressure associated with the incompressibility constraint, and $\boldsymbol{\tau}_e$ and $\boldsymbol{\tau}_v$ are the elastic and viscous parts of the total “extra” stress tensor $\boldsymbol{\tau}$ in the particle (which need not be deviatoric in general, $\text{tr}(\boldsymbol{\tau}) \neq 0$.) Note that the actual hydrostatic pressure p is given by $p = p' - \text{tr} \boldsymbol{\tau}$.

The elastic stress may be described in terms of a stored-energy function ψ , which, on account of frame invariance, is a function of \mathbf{C} , via

$$\boldsymbol{\tau}_e = 2\mathbf{F} \frac{\partial \psi(\mathbf{C})}{\partial \mathbf{C}} \mathbf{F}^T, \quad \det(\mathbf{F}) = 1. \quad (4.2)$$

In addition, elastic isotropy (and incompressibility) implies that ψ depends on \mathbf{C} through its first two invariants. For simplicity, in this chapter, we will consider *generalized neo-Hookean* behavior such that $\psi(\mathbf{C}) = g(I)$, where $I = \text{tr}(\mathbf{C})$ and g is a generally nonlinear function of I satisfying the requirements that $g(3) = 0$, $g'(3) = \mu/2$, where μ is the ground state shear modulus of the elastic particle. Then, the elastic extra stress tensor $\boldsymbol{\tau}_e$ in (4.2) can be expressed as

$$\boldsymbol{\tau}_e = 2g'(I)\mathbf{B} - \mu\mathbf{I}, \quad (4.3)$$

where the term promotional to μ arises from the linearization requirements at the ground state (i.e., $\boldsymbol{\tau}_e(\mathbf{I}) = \mathbf{0}$).

Making use of the fact that (Joseph, 1990)

$$\overset{\nabla}{\mathbf{B}} = \frac{D\mathbf{B}}{Dt} - \mathbf{L}\mathbf{B} - \mathbf{B}\mathbf{L}^T = \mathbf{0}, \quad (4.4)$$

a *rate* (hypo-elastic) form of equation for the elastic constitutive relation (4.3) may be obtained in terms of the upper-convected (or Truesdell) time derivative such that

$$\overset{\nabla}{\boldsymbol{\tau}}_e = \dot{\boldsymbol{\tau}}_e - \mathbf{L}\boldsymbol{\tau}_e - \boldsymbol{\tau}_e\mathbf{L}^T = 4g'' \text{tr}(\mathbf{D}\mathbf{B})\mathbf{B} + 2\mu\mathbf{D}, \quad (4.5)$$

where $\dot{\boldsymbol{\tau}}_e = (\partial\boldsymbol{\tau}_e/\partial t) + \mathbf{v} \cdot \nabla\boldsymbol{\tau}_e$ denotes the material time derivative of the tensor $\boldsymbol{\tau}_e$.

The simplest possible choice for the elastic behavior of the particles is of course the neo-Hookean model with $g(I) = \frac{\mu}{2}(I - 3)$. However, this model is unrealistic at large stretches for most materials, including elastomers, as it ignores the significant stiffening that such materials exhibit at large stretches. For this reason, in the applications to be considered below, we will make use of the *Gent* model (Gent, 1996), characterized by the choice

$$g(I) = -\frac{J_m\mu}{2} \ln\left(1 - \frac{I-3}{J_m}\right), \quad (4.6)$$

where the dimensionless parameter $J_m > 0$, known as the *strain-locking* parameter, corresponds

to the limiting value of $I - 3$ at which the elastomer locks up (and the argument of the logarithm vanishes). Note that the Gent model (4.6) reduces to the neo-Hookean model in the limit as $J_m \rightarrow \infty$. The corresponding specialization of the constitutive relation (4.3) can then be written as

$$\boldsymbol{\tau}_e = \mu \left[\left(1 - \frac{I-3}{J_m} \right)^{-1} \mathbf{B} - \mathbf{I} \right], \quad (4.7)$$

which in turn leads to the following evolution equation for the elastic extra stress tensor

$$\overset{\nabla}{\boldsymbol{\tau}}_e = 2\mu \mathbf{D} + \frac{2}{\mu J_m} \text{tr}[\mathbf{D}(\boldsymbol{\tau}_e + \mu \mathbf{I})] (\boldsymbol{\tau}_e + \mu \mathbf{I}), \quad (4.8)$$

where use has been made of (4.7) to express \mathbf{B} in terms of $\boldsymbol{\tau}_e$. Note that these expressions reduce to the well-known neo-Hookean expressions (Joseph, 1990) in the limit as $J_m \rightarrow \infty$, namely,

$$\boldsymbol{\tau}_e = \mu(\mathbf{B} - \mathbf{I}), \quad \text{and} \quad \overset{\nabla}{\boldsymbol{\tau}}_e = 2\mu \mathbf{D}. \quad (4.9)$$

Going back to the general expressions for the KV material, the viscous part of the extra stress can likewise be described in terms of a dissipation potential ϕ , which, on account of incompressibility and frame invariance, is a function of the last two invariants of \mathbf{D} , via

$$\boldsymbol{\tau}_v = \frac{\partial \phi(\mathbf{D})}{\partial \mathbf{D}}, \quad \text{tr}(\mathbf{D}) = 0. \quad (4.10)$$

Although more general nonlinear forms could be considered, in this chapter, again for simplicity, we will focus our attention on linearly viscous behavior, such that

$$\boldsymbol{\tau}_v = 2\eta^{(2)} \mathbf{D}, \quad (4.11)$$

where $\eta^{(2)}$ describes the constant viscosity of the particle material.

It should be noted that the set of constitutive relations for KV particles reduce to those for purely elastic particles by taking the limit as the viscosity $\eta^{(2)}$ goes to zero. In this limit, the KV model simplifies to a hyperelastic model characterized by the stored-energy function $\psi(\mathbf{F})$. In other words, in this limit, the viscous part of the stress vanishes ($\boldsymbol{\tau}_v = \mathbf{0}$) and the elastic part coincides with the total stress ($\boldsymbol{\tau}_e = \boldsymbol{\tau}$). Therefore, for the case of (incompressible) Gent particles, the constitutive relation for the extra stress tensor ($\boldsymbol{\tau}$) and its evolution ($\overset{\nabla}{\boldsymbol{\tau}}$) are given by (4.7) and (4.8), respectively, with $\boldsymbol{\tau}_e$ being replaced by $\boldsymbol{\tau}$. These relations have been shown to provide good agreement with experimental data for rubber-like materials (Ogden et al., 2004). Similarly, for the case of neo-Hookean particles, the corresponding relations are given by (4.9) with $\boldsymbol{\tau}_e$ being replaced by $\boldsymbol{\tau}$.

The suspending fluid (or the matrix) will be assumed here to be an incompressible Newtonian fluid, with constitutive relation given by expression (4.1) with

$$\boldsymbol{\tau} = \boldsymbol{\tau}_v = 2\eta^{(1)} \mathbf{D}, \quad \text{tr}(\mathbf{D}) = 0. \quad (4.12)$$

In other words, the constitutive behavior of the matrix will be taken to be purely viscous with linear response and constant viscosity $\eta^{(1)}$.

4.2.2 Microstructures

In this chapter, we confine our attention to suspensions consisting of initially spherical, deformable, viscoelastic particles distributed isotropically in a viscous fluid (matrix). Based on earlier theoretical work for *dilute* concentrations of (non-interacting) deformable particles (Goddard and Miller, 1967; Roscoe, 1967; Gao et al., 2011), as well as numerical simulations for dilutely concentrated and moderately concentrated suspensions of capsules (Clausen and Aidun, 2010; Clausen et al., 2011), the particles are expected to change their shape and orientation when subjected to a shear flow. As already mentioned, for *dilute* concentrations, the initial spherical particles become aligned ellipsoids with a shape and orientation that evolves with the deformation until (possibly) reaching a steady state. For *non-dilute* concentrations, it may be expected that the shape assumed by the particles will not be precisely ellipsoidal—deviations would be expected due to the non-uniform deformation fields that would be generated inside the particles as a consequence of the particle interactions. In addition, it would be expected that the particle interactions would affect the orientation and relative position of individual particles in such a way that the particles in the deformed configuration would not all exhibit the same exact orientation, and the two- and higher-point correlation functions for the particle centers would cease to be isotropic. Nevertheless, in the spirit of generating simplified (homogenized) constitutive models for the instantaneous response of the non-dilute suspensions, as well as for the evolution of their microstructure, it makes sense to define suitable homogenized microstructural variables serving to characterize the evolution of the “average” shape and orientation of the particles, as well as of the particle distribution statistics, as functions of the deformation. In the context of purely viscous systems, and ignoring surface tension effects (i.e., distributions of viscous drops in a viscous fluid), Kailasam and Ponte Castañeda (1998) proposed such a model making use of a suitable application/generalization of the homogenization estimates of Ponte Castañeda and Willis (1995) for the macroscopic viscosity and average strain rate and vorticity fields in the particle phase to generate estimates for the instantaneous response of the suspension, as well as evolution laws for suitable microstructural variables characterizing the average shape and orientation of the particles, and of the two-point correlation functions describing the relative positions of the particles in the flow. In this context, it should be emphasized that the homogenization estimates of Ponte Castañeda and Willis (1995) provide a generalization of the dilute estimates of Eshelby (1957) for dispersions of non-dilute concentrations of elastic particles in an elastic matrix (with different elastic moduli)—which can be reinterpreted for viscous particles in a viscous matrix—accounting for general ellipsoidal particle shapes distributed with generally different ellipsoidal shape for the two-point probability function for the particle-center distribution. The constitutive theory of Kailasam and Ponte Castañeda (1998) applies not only for linearly viscous behavior for the phases, but can also be used for nonlinearly viscous (including ideally plastic in the rate-independent limit) phases, and generalizes earlier work in this context by Kailasam et al. (1997) for the evolution of the particle shape and distribution (with fixed orientation). In this chapter, we propose a corresponding generalization

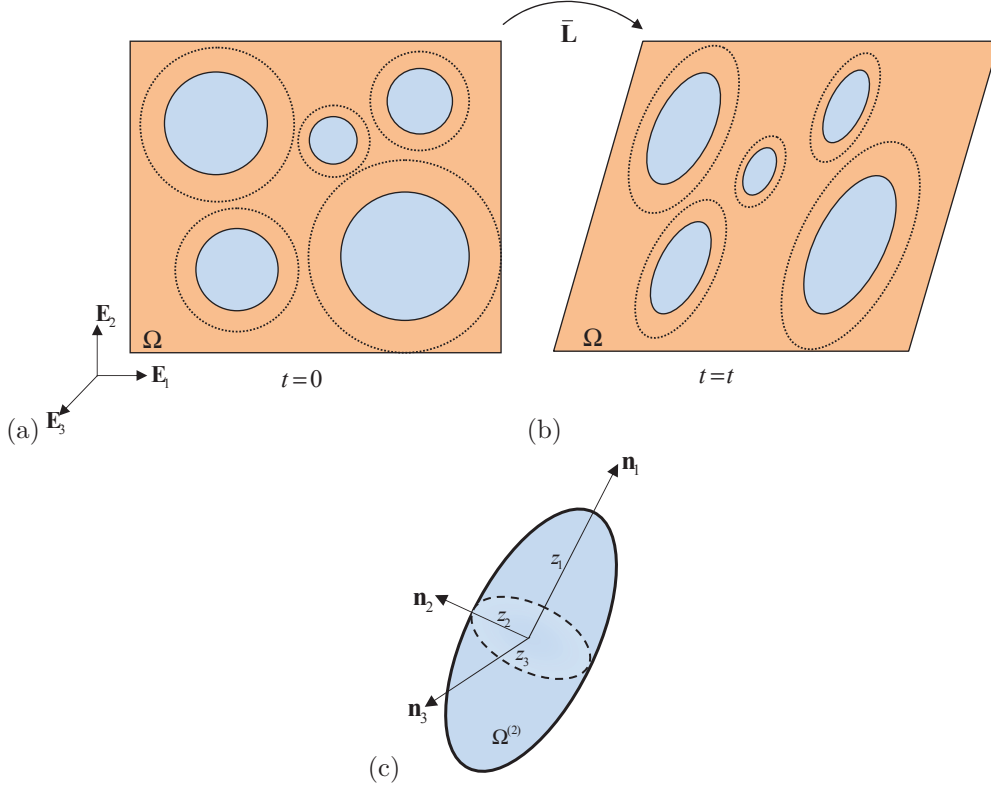


Figure 4.1: Schematic illustration of the microstructure in the suspension, identifying the various microstructural variables. The particles shapes and orientations evolve with the deformation and are depicted as grey ellipses, while their two-point probability functions are depicted as larger dotted ellipses surrounding the particles. (a) At $t = 0$, the particles are spherical and distributed randomly with statistical isotropy in the Newtonian fluid. (b) At a later time t , after application of the macroscopic velocity gradient $\bar{\mathbf{L}}$, the particles have become ellipsoidal and are distributed with ellipsoidal symmetry (with the same shape and orientation). (c) The particles are described by a “representative ellipsoid” with aspect ratios $w_1 = z_2/z_1$ and $w_2 = z_3/z_1$, and with principal axes defined by the unit vectors \mathbf{n}_1 , \mathbf{n}_2 and $\mathbf{n}_3 = \mathbf{n}_1 \times \mathbf{n}_2$ (which rotate relative to the laboratory axes $\{\mathbf{E}_i\}$, $i = 1, 2, 3$.)

of this theory to account for *viscoelastic* effects in the particles at *non-dilute* concentrations, building on the earlier work by Gao et al. (2011) for *dilute* concentration of *elastic* particles. This will require extending the notion of suitable microstructural variables to include the average elastic stress in the particles, as shall be seen in more detail later.

Consistent with the just-stated objectives, we define next a special class of microstructures characterizing the *instantaneous* state of the system. Thus, it is assumed that at the present time all the initially (at zero time) spherical particles become ellipsoidal with identical shape and orientation as described by *representative* (average) ellipsoids

$$\Omega^{(2)} = \{ \mathbf{x} : |(\mathbf{Z})^{-T} \mathbf{x}| \leq 1 \}, \quad (4.13)$$

where \mathbf{Z} is the so-called shape tensor. In addition, it will be assumed here that the relative position of the particles is described by two-point correlation functions having “ellipsoidal” symmetry. This notion was introduced by Willis (1977) to describe the shape for the angular dependence of two-point correlation functions, thus generalizing the notion of “statistical isotropy,” which corresponds to spherical angular dependence. This notion was used in the work of Ponte Castañeda and Willis (1995) to describe the shape of the two-point probabilities for the distribution of the centers of ellipsoidal particles with possibly different shapes and orientations, thus resulting in estimates depending on two Eshelby-type microstructural tensors, one describing the shape and orientation of the particles and the other that of their distribution. While in general it may be expected that the shape and orientation of the particle distribution will evolve differently from the shape and orientation of the particles themselves, in this first investigation of the problem, we will assume for simplicity that the shape and orientation of the distribution functions is identical to that of the individual particles. We expect this to be a reasonable approximation for small to moderate particle volume fractions for two reasons. First, the effect of the particle distribution is expected to be of order volume fraction squared, while that of the particle themselves is expected to be of order volume fraction. Therefore, the effect of the shape of the distribution functions is expected to be small compared to that of the particle shapes themselves, at least for small to moderate volume fractions. Second, the numerical simulations of Clausen et al. (2011) for suspensions of concentrated capsules in a simple shear flow (see figures 11 and 13 in that paper) seem to suggest that this is not a bad approximation—certainly better than assuming that the distribution of the (non-Brownian) particles remains isotropic. Another possibility would be to assume that the shape and orientation of the particles evolves with the macroscopic deformation (Kailasam et al., 1997), as would be the case for periodic distributions of particles, but such an approximation would only be accurate for small enough volume fractions, and will not be pursued in this chapter, again for simplicity, as it is much easier to work with one shape tensor than with two.

Figure 4.1(a) provides a schematic representation of the isotropic distribution of spherical particles in the suspension at $t = 0$. The spheres with solid and dotted lines represent cross sections of the particles and the distributional spheres, respectively. The triad $\{\mathbf{E}_i\}$, ($i = 1, 2, 3$) is used to characterize the fixed laboratory coordinates. Figure 4.1(b) depicts a snapshot of the suitably idealized microstructure in the suspension at a future time instant t (recall that the particles and distributional ellipsoids are assumed to have the same shape and orientation at any moment). Also, Figure 4.1(c) provides a schematic representation of the relevant microstructural variables at time t . The three orthonormal vectors \mathbf{n}_1 , \mathbf{n}_2 and $\mathbf{n}_3 = \mathbf{n}_1 \times \mathbf{n}_2$ are used to characterize the principal axes of the particle. In this principal coordinate system, the shape tensor \mathbf{Z} has the matrix representation $\mathbf{Z} = \text{diag}(z_1, z_2, z_3)$ with z_1, z_2, z_3 being the three principal semi-axes of the ellipsoid. For future reference, it is convenient to define two aspect ratios

$$w_1 = z_2/z_1 \quad \text{and} \quad w_2 = z_3/z_1, \quad (4.14)$$

which fully characterize the shape of the particle.

Consistent with the above-described microstructural model, we choose the following set of vari-

ables to characterize the state of the ellipsoidal microstructure:

$$\mathcal{S} = \{w_1, w_2, \mathbf{n}_1, \mathbf{n}_2, \mathbf{n}_3 = \mathbf{n}_1 \times \mathbf{n}_2\}. \quad (4.15)$$

4.3 Macroscopic response

The objective of this section is to determine macroscopic constitutive relations for the rheological behavior of the suspensions described in the preceding section. As we have seen, we expect the mixture to go through a sequence of microstructures, approximately consisting of aligned ellipsoids that are distributed with ellipsoidal two-point statistics (with the same shape and orientation), which evolve in time, starting from an initial state. In this chapter, we therefore break up the analysis of the macroscopic behavior of the suspensions into two parts. In the first, we assume that at a given instant the microstructure is specified, and make use of this information to estimate the *instantaneous* response of the mixture by means of a homogenization approach. In the second, we derive consistent *evolution* equations for the relevant microstructural variables making use of the corresponding instantaneous homogenization estimates for the average deformation and stress fields in the particles.

4.3.1 Homogenization estimates for the instantaneous response

We consider a *representative volume element* (RVE) of the suspension, which occupies a volume Ω with boundary $\partial\Omega$. The fluid and particle phases are in turn assumed to occupy volumes $\Omega^{(1)}$ and $\Omega^{(2)}$, respectively, such that $\Omega = \Omega^{(1)} + \Omega^{(2)}$. It is assumed that the RVE satisfies the *separation of length scales* hypothesis implying that the typical size of the neutrally buoyant particles is much smaller than the size of the RVE, as well as the Stoke's condition in the fluid phase, such that

$$Re = \frac{\rho^{(1)} \dot{\gamma} d_p^2}{\eta^{(1)}} \rightarrow 0, \quad (4.16)$$

where $\rho^{(1)}$ is the density of the fluid, $\dot{\gamma}$ is a measure of the macroscopic strain rate and d_p is a measure of the particle diameter. Noting that the microstructure of the RVE is *statistically* uniform, a uniform *macroscopic* stress field will be generated in the RVE when an *affine* velocity boundary condition is applied on the boundary of the RVE ($\partial\Omega$). Thus, the suspension is subjected to the boundary condition

$$\mathbf{v}(\mathbf{x}) = \bar{\mathbf{L}}\mathbf{x}, \quad \text{on } \partial\Omega, \quad (4.17)$$

where $\bar{\mathbf{L}}$ ($\text{tr } \bar{\mathbf{L}} = 0$) is the macroscopic, or average velocity gradient, defined by¹

$$\bar{\mathbf{L}} = \frac{1}{\text{Vol}(\Omega)} \int_{\Omega} \mathbf{L} \, dV. \quad (4.18)$$

¹The *mean value theorem for the strain rate* (e.g., Ponte Castañeda and Suquet, 1998) states that the (volume) average of the local strain-rate tensor \mathbf{L} over the RVE under the affine velocity boundary condition (4.17) is precisely $\bar{\mathbf{L}}$.

Similarly, the average or macroscopic Cauchy stress is defined as

$$\bar{\boldsymbol{\sigma}} = \frac{1}{\text{Vol}(\Omega)} \int_{\Omega} \boldsymbol{\sigma} \, dV, \quad (4.19)$$

and the instantaneous macroscopic constitutive response is determined by the relation between $\bar{\boldsymbol{\sigma}}$ and $\bar{\mathbf{L}}$.

For future reference, we also define the phase averages of the strain-rate field over phase r ($r = 1, 2$) via

$$\bar{\mathbf{D}}^{(r)} = \frac{1}{\text{Vol}(\Omega^{(r)})} \int_{\Omega^{(r)}} \mathbf{D} \, dV, \quad (4.20)$$

such that

$$\bar{\mathbf{D}} = c^{(1)} \bar{\mathbf{D}}^{(1)} + c^{(2)} \bar{\mathbf{D}}^{(2)}, \quad (4.21)$$

with the $c^{(1)}$ and $c^{(2)}$ denoting the volume fractions of fluid and particle phases, respectively. Similarly, defining $\bar{\boldsymbol{\tau}}^{(1)}$ and $\bar{\boldsymbol{\tau}}^{(2)}$ as the averages of the extra stress in the fluid and particle phases, respectively, the macroscopic stress, as defined by (4.19), can be rewritten (on account of the incompressibility of the phases) as

$$\bar{\boldsymbol{\sigma}} = -\bar{p}' \mathbf{I} + c^{(1)} \bar{\boldsymbol{\tau}}^{(1)} + c^{(2)} \bar{\boldsymbol{\tau}}^{(2)}, \quad (4.22)$$

where \bar{p}' is an indeterminate hydrostatic pressure associated with the overall incompressibility of the suspension.

Now, taking advantage of the special form of the constitutive relations for the fluid matrix and solid particle phases, as described in Section 4.2.1, *modified* dissipation potentials are introduced

$$W^{(r)}(\mathbf{D}) = \eta^{(r)} \mathbf{D} \cdot \mathbf{D} + \boldsymbol{\tau}_e \cdot \mathbf{D}, \quad \text{tr}(\mathbf{D}) = \mathbf{0}, \quad (4.23)$$

such that the local constitutive relation of the phases can be written as

$$\boldsymbol{\sigma} = -p' \mathbf{I} + \boldsymbol{\tau}, \quad \text{where} \quad \boldsymbol{\tau} = \frac{\partial W^{(r)}}{\partial \mathbf{D}} = 2\eta^{(r)} \mathbf{D} + \boldsymbol{\tau}_e, \quad (4.24)$$

where p' is an indeterminate hydrostatic pressure. It should also be emphasized that the elastic strains $\boldsymbol{\tau}_e$ are considered to be fixed in taking the derivative with respect to \mathbf{D} . Thus, it can be seen that the addition of the linear term in the strain-rate tensor \mathbf{D} to the dissipation function ϕ , defined by equation (4.10), allows the inclusion of the elastic stress $\boldsymbol{\tau}_e$, assuming that it is known at the given instant. More specifically, labeling the quantities associated with the matrix and particle phases by the superscripts (1) and (2), respectively, the local constitutive relation (4.24) can be used to recover the constitutive relations for the elastic particles and fluid matrix phases, as given by (4.1) to (4.12), provided that we let $\eta^{(1)}$ and $\eta^{(2)}$ be the viscosities of the fluid and elastic particles, respectively, and that we let $\boldsymbol{\tau}_e = \mathbf{0}$ in the fluid phase and $\boldsymbol{\tau}_e = \boldsymbol{\tau}_e^{(2)}$, as characterized by the evolution equation (4.8), in the particle phase. In addition, in this last expression, we use μ and J_m to describe the ground shear modulus and strain-locking parameter of the elastic particles, the subscript (2) having

been dropped from μ and J_m for convenience (since only the particle phase has elastic properties, thus eliminating the risk of confusion).

We define next, for compactness, the local modified dissipation potential

$$W(\mathbf{x}, \mathbf{D}) = \chi^{(1)}(\mathbf{x})W^{(1)}(\mathbf{D}) + \chi^{(2)}(\mathbf{x})W^{(2)}(\mathbf{D}), \quad (4.25)$$

where the $\chi^{(r)}(\mathbf{x})$ ($r = 1, 2$) are the characteristic functions of the two phases, such that they are equal to one if the position vector \mathbf{x} is in phase r (i.e., $\mathbf{x} \in \Omega^{(r)}$) and zero otherwise. Then, we can state the principle of minimum dissipation via

$$\min_{\mathbf{D} \in K} \int_{\Omega} W(\mathbf{x}, \mathbf{D}) \, dV, \quad (4.26)$$

where K denotes the set of kinematically admissible strain rates:

$$K = \{\mathbf{D} \mid \text{there is } \mathbf{v} \text{ such that } \mathbf{D} = (\nabla \mathbf{v} + (\nabla \mathbf{v})^T)/2, \operatorname{div} \mathbf{v} = 0 \text{ in } \Omega, \text{ and } \mathbf{v} = \bar{\mathbf{L}}\mathbf{x} \text{ on } \partial\Omega\}. \quad (4.27)$$

It is noted (see Ekeland and Témam, 1999, for the purely viscous problem) that the Euler-Lagrange equations of this variational principle are precisely the Stoke's equations for the fluid phase

$$2\eta^{(1)}\nabla^2\mathbf{v} - \nabla p = \mathbf{0}, \quad \nabla \cdot \mathbf{v} = 0, \quad (4.28)$$

together with the equilibrium equations for the solid particles, which in Eulerian form become

$$2\eta^{(2)}\nabla^2\mathbf{v} - \nabla p' + \nabla \cdot \boldsymbol{\tau}_e^{(2)} = \mathbf{0}, \quad \nabla \cdot \mathbf{v} = 0, \quad (4.29)$$

where once again the elastic extra stress $\boldsymbol{\tau}_e^{(2)}$ in the particles is assumed to be known at the present instant. Note that the variational principle also ensures continuity of the velocity \mathbf{v} and traction components of the *total* stress $\boldsymbol{\sigma}$ across the particle-fluid boundaries, as well as satisfaction of the affine boundary condition (4.17).

Finally, it is noted that the dissipation functional in equation (4.26), evaluated at the minimum, defines a function of the macroscopic strain-rate $\bar{\mathbf{D}}$, as given by the symmetric part of the average velocity gradient $\bar{\mathbf{L}}$. When normalized by the volume of the RVE Ω , it can be shown (see, for example, Ponte Castañeda and Suquet, 1998) that it provides a modified dissipation potential for the macroscopic constitutive relation, in the sense that

$$\bar{\boldsymbol{\sigma}} = -\bar{p}'\mathbf{I} + \bar{\boldsymbol{\tau}}, \quad \text{where} \quad \bar{\boldsymbol{\tau}} = \frac{\partial \widetilde{W}}{\partial \bar{\mathbf{D}}}, \quad (4.30)$$

and where \bar{p}' is the Lagrange multiplier associated with the macroscopic incompressibility constraint and

$$\widetilde{W}(\bar{\mathbf{D}}) = \min_{\mathbf{D} \in K} \frac{1}{\operatorname{Vol}(\Omega)} \int_{\Omega} W(\mathbf{x}, \mathbf{D}) \, dV. \quad (4.31)$$

The homogenization problem defined by equations (4.30) and (4.31) for the *instantaneous* re-

sponse of the viscoelastic composite characterized by (4.23)–(4.25) is mathematically analogous to the corresponding problem for an incompressible *thermoelastic* composite with elastic moduli $\eta^{(r)}$ and thermal stresses $\boldsymbol{\tau}_e$ (provided that the strain rate and velocity fields are identified with the strain and displacement fields, respectively). For the specific problem of interest here, the viscosities (moduli) $\eta^{(r)}$ are *uniform-per-phase*, and while the elastic stress (thermal stress) in the matrix phase is zero, the corresponding elastic stress (thermal stress) in the particle phase is not only non-vanishing, but in fact also non-uniform. More general situations, including the case of nonuniform thermal stresses in the matrix phase has been considered recently by Lahlouche et al. (2011).

To estimate the effective dissipation function $\widetilde{W}(\bar{\mathbf{D}})$, we make use of the Hashin-Shtrikman-Willis (HSW) variational method, which was originally developed for isotropic elastic composites by Hashin and Shtrikman (1963), and extended later for generally anisotropic elastic composites by Willis (1977, 1981). For the particulate material systems of interest in this chapter consisting of random distributions of ellipsoidal inclusions in a given matrix, more specific estimates have been given by Ponte Castañeda and Willis (1995) still making use of the HSW variational method. Applied to the above-described viscous systems, the key feature of this method is the use of a “polarization field” relative to a homogeneous “comparison fluid” (with viscosity η^0). In this way, it is possible to make use of simple, constant-per-phase trial fields for the polarization to obtain bounds and estimates for the effective response of the composite system. The application of the method of Ponte Castañeda & Willis (PCW) to the class of suspensions of thermoelastic particles of interest in this chapter was given by Ponte Castañeda (2005). For completeness, the adaptation of these results for viscoelastic particles is given in Appendix C.1. In this section, we will only provide the final results for the macroscopic response in terms of the average local fields in the particle phase.

Thus, the resulting variational estimate for the effective dissipation function $\widetilde{W}(\bar{\mathbf{D}})$ can be expressed as

$$\widetilde{W}(\bar{\mathbf{D}}) = \eta^{(1)} \bar{\mathbf{D}} \cdot \bar{\mathbf{D}} + c \left(\eta^{(2)} - \eta^{(1)} \right) \bar{\mathbf{D}}^{(2)} \cdot \bar{\mathbf{D}} + \frac{c}{2} \bar{\boldsymbol{\tau}}_e^{(2)} \cdot \left(\bar{\mathbf{D}}^{(2)} + \bar{\mathbf{D}} \right), \quad (4.32)$$

where

$$\bar{\mathbf{D}}^{(2)} = \left\{ \mathbb{I} - 2(1-c) \left(\eta^{(1)} - \eta^{(2)} \right) \mathbb{P} \right\}^{-1} \left\{ \bar{\mathbf{D}} - (1-c) \mathbb{P} \bar{\boldsymbol{\tau}}_e^{(2)} \right\} \quad (4.33)$$

is the corresponding estimate for the average strain-rate over the particles. In these expressions, it is recalled from Appendix C.1 that $c = c^{(2)}$ is the volume fraction of the particle phase, $\bar{\boldsymbol{\tau}}_e^{(2)}$ is the average elastic stress in the particles, and \mathbb{P} is a microstructural (Eshelby-type) tensor given by (C.11)₁.

For later reference, we note that the procedure also provides an estimate for the average vorticity tensor in the particle phase (see Appendix C.1), which is given by

$$\bar{\mathbf{W}}^{(2)} = \bar{\mathbf{W}} + (1-c) \mathbb{R} \left[2 \left(\eta^{(1)} - \eta^{(2)} \right) \bar{\mathbf{D}}^{(2)} - \bar{\boldsymbol{\tau}}_e^{(2)} \right], \quad (4.34)$$

where \mathbb{R} is the microstructural tensor defined by (C.11)₂.

Finally, the instantaneous macroscopic constitutive relation for the suspension of viscoelastic particles can be obtained from the estimate (4.32) for $\widetilde{W}(\bar{\mathbf{D}})$ by means of equation (4.30). However, given $\bar{\mathbf{D}}^{(2)}$ and $\bar{\boldsymbol{\tau}}_e^{(2)}$, it is simpler to make use of expression (4.21) to write the average extra stress

in the matrix phase as

$$\bar{\boldsymbol{\tau}}^{(1)} = 2\eta^{(1)}\bar{\mathbf{D}}^{(1)} = 2\eta^{(1)}(1-c)^{-1}\left(\bar{\mathbf{D}} - c\bar{\mathbf{D}}^{(2)}\right). \quad (4.35)$$

Then, substituting this expression into expression (4.22) for the macroscopic stress, we arrive at

$$\bar{\boldsymbol{\sigma}} = -\bar{p}'\mathbf{I} + 2\eta^{(1)}\bar{\mathbf{D}} + c\left(\bar{\boldsymbol{\tau}}^{(2)} - 2\eta^{(1)}\bar{\mathbf{D}}^{(2)}\right), \quad (4.36)$$

which, using (4.24)₂ to express the average extra stress over the inclusion phase in terms of the extra elastic stress over the particles, finally leads to

$$\bar{\boldsymbol{\sigma}} = -\bar{p}'\mathbf{I} + 2\eta^{(1)}\bar{\mathbf{D}} + 2c\left(\eta^{(2)} - \eta^{(1)}\right)\bar{\mathbf{D}}^{(2)} + c\bar{\boldsymbol{\tau}}_e^{(2)}. \quad (4.37)$$

Thus, it can be seen that for given macroscopic strain rate $\bar{\mathbf{D}}$, particle volume fraction c , and viscosities $\eta^{(1)}$ and $\eta^{(2)}$, the macroscopic Cauchy stress tensor $\bar{\boldsymbol{\sigma}}$ may be determined by means of expression (4.33) for $\bar{\mathbf{D}}^{(2)}$ in terms of the current values of the average of the extra stress tensor over the particle $\bar{\boldsymbol{\tau}}_e^{(2)}$, together with the current values of the average aspect ratio and orientation of the particles, as defined by expression (4.15). It should be emphasized that the above results reduce to the corresponding exact results of Gao et al. (2011) for dilute concentrations ($c \ll 1$) and vanishing viscosity ($\eta^{(2)} = 0$) of the particles. In the next subsection, we address the characterization of these variables by means of appropriate *evolution equations*, starting from an appropriate initial state where the particles are initially spherical and unstressed.

4.3.2 Evolution equations for the microstructural variables and particle elastic stress

So far, we have made use of Eulerian kinematics to describe the incremental behavior of the host fluid and particle phases, and accordingly generated estimates for the *instantaneous* response of the suspension for a given state of the microstructure. However, when subjected to simple flows, the microstructure in the suspensions generally evolves in time as the applied deformation progresses. Therefore, in order to predict the effective *time-dependent* behavior of suspensions from a given instantaneous state of the microstructure, it is crucial to first characterize the evolution of relevant microstructural variables. In addition, given that the instantaneous response depends on the current values of elastic stresses acting on the particles, which are determined by incremental constitutive equations of the type (4.8), it is also necessary to develop evolution laws for the average elastic stresses in the particles.

Recalling from Appendix C.1 that our estimates for the instantaneous response of the suspension are based on the HSW variational approximation (Ponte Castañeda and Willis, 1995) implying that the local fields are (approximately) uniform inside the particle phase, as already anticipated in section 4.2.2, it follows that the initially spherical particles will deform through a sequence of ellipsoidal shapes throughout the deformation process, in such a way that the set of equations used to determine the instantaneous stress and strain rate fields inside particles will continue to apply at each increment

of time, except that at each step the current values of the microstructural variables and of the elastic stresses in the particles will need to be used.

First, recalling that the fluid and particle phases have been assumed to be incompressible, it follows that the volume fraction of the particles will remain constant throughout any deformation process, *i.e.*,

$$c = \text{const.} \quad (4.38)$$

On the other hand, the evolution for the particle aspect ratios w_1 and w_2 , as defined by (4.14), are obtained by simple kinematic arguments (see, for example, Bilby and Kolbuszewski, 1977) via

$$\dot{w}_1 = w_1(\bar{D}_{22}^{(2)} - \bar{D}_{11}^{(2)}), \quad \dot{w}_2 = w_2(\bar{D}_{33}^{(2)} - \bar{D}_{11}^{(2)}), \quad (4.39)$$

where it is noted that the overdot here denotes simple time derivatives (since w_1 and w_2 depend only on time). It is also remarked in this context that the components of the tensorial variables associated with the particle phase, here and elsewhere, are referred to the principal axes of the ellipsoidal particle in their current state, as given by the triad $\{\mathbf{n}_1, \mathbf{n}_2, \mathbf{n}_3\}$.

Next, the evolution of the orthonormal vectors \mathbf{n}_1 , \mathbf{n}_2 and \mathbf{n}_3 , serving to characterize the orientation of particles, are determined by means of the kinematical relations

$$\dot{\mathbf{n}}_i = \boldsymbol{\Omega} \mathbf{n}_i, \quad i = 1, 2, 3, \quad (4.40)$$

where $\boldsymbol{\Omega}$ is the (antisymmetric) spin tensor of the particle, whose components in the principal coordinate system $\{\mathbf{n}_1, \mathbf{n}_2, \mathbf{n}_3\}$ are determined by means of the following relations (Ogden, 1997; Aravas and Ponte Castañeda, 2004)

$$\Omega_{ij} = \bar{W}_{ij}^{(2)} - \frac{(w_{i-1})^2 + (w_{j-1})^2}{(w_{i-1})^2 - (w_{j-1})^2} \bar{D}_{ij}^{(2)}, \quad i \neq j. \quad (4.41)$$

In this notation, when i or j is equal to 1, we define $w_{1-1} = w_0 = 1$. It should also be noted that alternative expressions for the evolution of the microstructure can be derived directly in terms of the particle shape tensors \mathbf{Z} , as shown by Goddard and Miller (1967).

As can be seen from relations (4.37), together with (4.33), the calculation of the instantaneous macroscopic stress in the suspension requires knowledge of the average elastic extra stress in the particle phase. As discussed in Appendix C.1, due to the choice of *constant-per-phase* polarization fields, together with the choice of $\eta^0 = \eta^{(1)}$, the PCW homogenization theory results in uniform stress and strain fields in the particle phase. As a consequence of this result, the constitutive relations for the average elastic stress fields in the particle phase take the same form as in the corresponding relations for the local fields. Therefore, for the case of KV particles with a Gent-type elastic stress (characterized by relations (4.7) and (4.8)), the evolution equations for the average elastic extra

stress in the particles is given by

$$\begin{aligned}\bar{\boldsymbol{\tau}}_e^{(2)\nabla} &= \dot{\bar{\boldsymbol{\tau}}}_e^{(2)} - \bar{\mathbf{L}}^{(2)}\bar{\boldsymbol{\tau}}_e^{(2)} - \bar{\boldsymbol{\tau}}_e^{(2)}(\bar{\mathbf{L}}^{(2)})^T \\ &= 2\mu\bar{\mathbf{D}}^{(2)} + \frac{2}{\mu J_m}\text{tr}\left[\bar{\mathbf{D}}^{(2)}\left(\bar{\boldsymbol{\tau}}_e^{(2)} + \mu\mathbf{I}\right)\right]\left(\bar{\boldsymbol{\tau}}_e^{(2)} + \mu\mathbf{I}\right),\end{aligned}\quad (4.42)$$

where the material time derivative $\dot{\bar{\boldsymbol{\tau}}}_e^{(2)}$ appearing in the above expression is a simple, time derivative, due to the fact that the stress field inside the particle is uniform (as already mentioned) and the convective terms hence vanishes. Note that the corresponding ‘‘total’’ form of the constitutive equation is given by

$$\bar{\boldsymbol{\tau}}_e^{(2)} = \mu\left[\left(1 - \frac{\bar{I}^{(2)} - 3}{J_m}\right)^{-1}\bar{\mathbf{B}}^{(2)} - \mathbf{I}\right], \quad \bar{\boldsymbol{\tau}}_v^{(2)} = 2\eta^{(2)}\bar{\mathbf{D}}^{(2)}.\quad (4.43)$$

where $\bar{I}^{(2)} = \text{tr}(\bar{\mathbf{B}}^{(2)})$, $\bar{\mathbf{B}}^{(2)} = \bar{\mathbf{F}}^{(2)}(\bar{\mathbf{F}}^{(2)})^T$ and $\bar{\mathbf{F}}^{(2)}$ is the average deformation gradient in the particles.

It should also be noted that, in the limit as $J_m \rightarrow \infty$ (corresponding to KV particles with a neo-Hookean elastic part), the above evolution equation simplifies to

$$\bar{\boldsymbol{\tau}}_e^{(2)\nabla} = 2\mu\bar{\mathbf{D}}^{(2)}.\quad (4.44)$$

In this context, it is important to emphasize that although the exact solution for the fields in the particles is not uniform, the uniform-field approximation is exact for dilute concentrations of particles ($c \ll 1$), as originally argued by Roscoe (1967) in the context of the steady-state solutions, and by Gao et al. (2011) for more general time-dependent motions of suspensions of purely elastic particles ($\eta^{(2)} = 0$). For non-dilute concentrations, it is expected that the approximation of uniform fields in the particles will lead to fairly accurate results provided that the concentrations are not large enough to generate strong interactions between the particles.

In summary, for a given macroscopic velocity gradient $\bar{\mathbf{L}} = \bar{\mathbf{D}} + \bar{\mathbf{W}}$, the macroscopic stress $\bar{\boldsymbol{\sigma}}$ in the suspension is given by expression (4.37), where $\bar{\mathbf{D}}^{(2)}$ is given by expression (4.33). These quantities depend on the current values of the microstructural variables \mathcal{S} , as defined by expression (4.15), and determined by the evolution equations (4.39) and (4.40) from some known initial state, as well as on the current value of the average extra elastic stress $\bar{\boldsymbol{\tau}}_e^{(2)}$ in the particles, as determined by expression (4.42). Note that the evolution equation for the particle axes (4.40) involves the average vorticity tensor in the particles, which is given in terms of other known variables by expression (4.34).

4.4 Steady-state estimates for the suspensions

It is known from earlier works (Roscoe, 1967; Goddard and Miller, 1967) that an initially spherical particle with Kelvin-Voigt viscoelastic behavior suspended in an infinite Newtonian fluid can admit, under certain conditions, steady-state (SS) solutions, where the particle becomes an ellipsoid with

fixed shape and orientation, while undergoing tank-treading motion with constant stress, strain rate and vorticity. According to the theory developed in Section 4.3, the stress and strain-rate fields are (approximately) uniform inside the particle phase, and steady-state solutions should still be possible for non-dilute concentrations of initially spherical, viscoelastic particles. In this case, existence of a SS solution will depend on flow conditions, as well as on the constitutive properties and volume fraction of the particles. For definiteness, we note that all variables in this section are evaluated at the steady state.

The SS solutions, if they exist, can be determined by setting the terms involving time derivatives equal to zero in the evolution equations for the extra stress tensor inside the particle, as well as in the evolution equations for the particle shape and orientation. The resulting expressions provide a set of algebraic equations to be solved for the six components of the extra stress tensor in the particle, $\bar{\boldsymbol{\tau}}^{(2)}$, the two aspect ratios, ω_1, ω_2 , and the three orientational angles defined by the particle axes, $\mathbf{n}_1, \mathbf{n}_2$, and \mathbf{n}_3 .

First, making use of the incompressibility constraint in the particle phase ($\text{tr}(\bar{\mathbf{D}}^{(2)}) = 0$), together with the evolution equation for the aspect ratios (4.39), we deduce that, at the steady state, the normal components of the strain-rate tensor in the particle phase, relative to the principal axes \mathbf{n}_i of the ellipsoidal particles, are equal to zero:

$$\bar{D}_{11}^{(2)} = \bar{D}_{22}^{(2)} = \bar{D}_{33}^{(2)} = 0. \quad (4.45)$$

Also, at the steady state, the evolution equations for the particle orientation, given by (4.40) and (4.41), imply that the three components of the vorticity tensor in the particle phase are given by

$$\bar{W}_{12}^{(2)} = \frac{1 + w_1^2}{1 - w_1^2} \bar{D}_{12}^{(2)}, \quad \bar{W}_{13}^{(2)} = \frac{1 + w_2^2}{1 - w_2^2} \bar{D}_{13}^{(2)}, \quad \bar{W}_{23}^{(2)} = \frac{w_1^2 + w_2^2}{w_1^2 - w_2^2} \bar{D}_{23}^{(2)}. \quad (4.46)$$

Next, recalling that the principal axes of the Finger tensor $\bar{\mathbf{B}}^{(2)} = (\bar{\mathbf{V}}^{(2)})^2$ correspond to the Eulerian axes of the deformation in the particles, so that the Eulerian axes coincide with the principal axes of the ellipsoidal particles, it follows that, at the steady state, when the particles have reached a fixed orientation, their orientation becomes fixed and is characterized by the triad $\{\mathbf{n}_1, \mathbf{n}_2, \mathbf{n}_3\}$. This implies that, at the steady-state solution, the shear components of the Finger tensor (relative to the particle axes) must all vanish:

$$\bar{B}_{12}^{(2)} = \bar{B}_{13}^{(2)} = \bar{B}_{23}^{(2)} = 0. \quad (4.47)$$

Moreover, the normal components of $\bar{\mathbf{B}}^{(2)} = (\bar{\mathbf{V}}^{(2)})^2$ (again, relative to the particle axes) correspond to the principal stretches of the deformation in the particles:

$$\bar{B}_{ii}^{(2)} = \left(\bar{\lambda}_i^{(2)}\right)^2, \quad i = 1, 2, 3 \quad (\text{no sum}), \quad (4.48)$$

where $\bar{\lambda}_i^{(2)}$ ($i = 1, 2, 3$) denote the principal stretches of the deformation in the particles, i.e., the principal values of the left stretch tensor $\bar{\mathbf{V}}^{(2)}$ in the particle. On the other hand, the shape of the

particle is described by the principal stretches as (see Figure 4.1(c) for definitions of w_1 and w_2)

$$w_1 = \bar{\lambda}_2^{(2)}/\bar{\lambda}_1^{(2)}, \quad w_2 = \bar{\lambda}_3^{(2)}/\bar{\lambda}_1^{(2)}, \quad (4.49)$$

Making use of the above relations in (4.48), together with the incompressibility constraint in the particle phase ($\bar{J}^{(2)} = \det(\bar{\mathbf{F}}^{(2)}) = \bar{\lambda}_1^{(2)} \bar{\lambda}_2^{(2)} \bar{\lambda}_3^{(2)} = 1$), we find that

$$\bar{B}_{11}^{(2)} = (w_1 w_2)^{-2/3}, \quad \bar{B}_{22}^{(2)} = (w_1)^{4/3} (w_2)^{-2/3}, \quad \bar{B}_{33}^{(2)} = (w_1)^{-2/3} (w_2)^{4/3}. \quad (4.50)$$

In this context, it is worth mentioning that the components of the tensor $\bar{\mathbf{B}}^{(2)}$ in relations (4.47) and (4.50) identically satisfy the evolution equation for the Finger tensor $\bar{\mathbf{B}}^{(2)}$ (i.e., $\bar{\mathbf{B}}^{(2)\nabla} = \mathbf{0}$) at the steady-state solution. Finally, we emphasize that the kinematical equations (4.45)-(4.50) are valid at SS solutions (if they exist) regardless of the constitutive behavior of particles. In the following subsection, we outline the additional *constitutive* equations in SS solutions for the case of KV particles.

4.4.1 Steady-state solution for Kelvin-Voigt particles

In this subsection, we consider steady-state solutions in non-dilute suspensions of Kelvin-Voigt particles, characterized by constitutive equations (4.43). Making use of (4.47) in (4.43)₁, we find that the shear components of the elastic extra stress tensor (relative to the particle axes) are zero at the SS solution:

$$(\bar{\tau}_e^{(2)})_{12} = (\bar{\tau}_e^{(2)})_{13} = (\bar{\tau}_e^{(2)})_{23} = 0. \quad (4.51)$$

Similarly, we find the three remaining (normal) components of the elastic extra stress tensor by making use of (4.50) in the constitutive relation (4.43)₁. The final results read as

$$\begin{aligned} (\bar{\tau}_e^{(2)})_{11} &= \mu d_w \left\{ J_m (w_2)^{1/3} \left[1 - (w_1 w_2)^{2/3} \right] + c_w \right\}, \\ (\bar{\tau}_e^{(2)})_{22} &= \mu d_w \left\{ J_m (w_2)^{1/3} \left[(w_1)^2 - (w_1 w_2)^{2/3} \right] + c_w \right\}, \\ (\bar{\tau}_e^{(2)})_{33} &= \mu d_w \left\{ J_m (w_2)^{1/3} \left[(w_2)^2 - (w_1 w_2)^{2/3} \right] + c_w \right\}, \end{aligned} \quad (4.52)$$

where $c_w = (w_2)^{1/3} [(w_1)^2 + (w_2)^2 + 1] - 3 (w_1)^{2/3} w_2$, and $d_w = [J_m (w_1)^{2/3} w_2 - c_w]^{-1}$. In the limit as $J_m \rightarrow \infty$ (corresponding to KV particles with neo-Hookean elastic behavior), relations (4.52) simplify to

$$\begin{aligned} (\bar{\tau}_e^{(2)})_{11} &= \mu \left[(w_1 w_2)^{-2/3} - 1 \right], \quad (\bar{\tau}_e^{(2)})_{22} = \mu \left[(w_1)^{4/3} (w_2)^{-2/3} - 1 \right], \\ (\bar{\tau}_e^{(2)})_{33} &= \mu \left[(w_1)^{-2/3} (w_2)^{4/3} - 1 \right]. \end{aligned} \quad (4.53)$$

Now, making use of (4.51) in (4.33) and (4.34), the non-zero components of the particle strain-

rate $\bar{\mathbf{D}}^{(2)}$ and vorticity $\bar{\mathbf{W}}^{(2)}$ at the steady state can be written as

$$\bar{D}_{ij}^{(2)} = \frac{\bar{D}_{ij}}{1 - \alpha \mathbb{P}_{ijij}}, \quad \bar{W}_{ij}^{(2)} = \bar{W}_{ij} + \frac{\alpha \mathbb{R}_{ijij} \bar{D}_{ij}}{1 - \alpha \mathbb{P}_{ijij}}, \quad i, j = 1, 2, 3 \text{ (no sum, } i \neq j), \quad (4.54)$$

where $\alpha = 4(1 - c)(\eta^{(1)} - \eta^{(2)})$ and all components are given relative to the particle axes.

Next, relations (4.45) together with the constitutive equation (4.43)₂ imply that, at the steady state, the normal components of the viscous part of extra stress tensor (relative to the particle axes) in the KV particles must all vanish:

$$(\bar{\tau}_v^{(2)})_{11} = (\bar{\tau}_v^{(2)})_{22} = (\bar{\tau}_v^{(2)})_{33} = 0. \quad (4.55)$$

Moreover, substituting the shear components of $\bar{\mathbf{D}}^{(2)}$ from (4.54)₁ into (4.43)₂, we find the shear components of $\bar{\tau}_v^{(2)}$ as follows

$$(\bar{\tau}_v^{(2)})_{ij} = \frac{2\eta^{(2)} \bar{D}_{ij}}{1 - 4(1 - c)(\eta^{(1)} - \eta^{(2)}) \mathbb{P}_{ijij}}, \quad i, j = 1, 2, 3 \text{ (} i \neq j). \quad (4.56)$$

Finally, the components of the total extra stress tensor in the KV particles at the steady state can be obtained in terms of the above estimates for the viscous and elastic extra stresses in the particles by means of the relation

$$\bar{\tau}_{ij}^{(2)} = (\bar{\tau}_e^{(2)})_{ij} + (\bar{\tau}_v^{(2)})_{ij}. \quad (4.57)$$

At this stage, all non-zero components of the particle stress $\bar{\boldsymbol{\tau}}^{(2)}$, strain-rate $\bar{\mathbf{D}}^{(2)}$ and vorticity $\bar{\mathbf{W}}^{(2)}$ are written in terms of steady-state values of the aspect ratios, w_1 and w_2 , and the three orientational angle defined by the particles axes, \mathbf{n}_1 , \mathbf{n}_2 , and \mathbf{n}_3 . Making use of (4.52) into (4.33), together with the three equations obtained by substituting relations (4.54) into (4.46), and expression (4.45), we obtain a system of algebraic equations for the unknowns $w_1, w_2, \mathbf{n}_1, \mathbf{n}_2, \mathbf{n}_3$.

In conclusion, it is important to remark that the SS solutions provided in this section generalize the work of Roscoe (1967) in two ways: (1) they extend the results of Roscoe to the finite concentration regime, (2) they apply for Kelvin-Voigt particles with more general elastic parts (Gent behavior), which allows these results to incorporate the dependence on the extensibility of the particles (through the parameter J_m). Indeed, in the limiting case of $c \ll 1$ and $J_m \rightarrow \infty$, the aforementioned system of equations, when applied for the cases of simple shear flow and extensional flow, will recover, respectively, the system of equations² (78)-(80) and equation (98) in Roscoe (1967), given for a dilute suspension of KV particles with neo-Hookean elastic response.

We remark that the SS solutions for suspensions of KV particles reduce to those for suspensions of elastic particles by setting $(\bar{\tau}_e^{(2)})_{ij} = \bar{\tau}_{ij}^{(2)}$ and $(\bar{\tau}_v^{(2)})_{ij} = 0$ ($i, j = 1, 2, 3$) in relations (4.51)-(4.57). For the special case of neo-Hookean particles, relations (4.53) agree exactly with the corresponding steady-state relations provided in Gao et al. (2011) for the normal components of the extra stress tensor (see relations (4.9) in the reference). In addition, in the limit as $c \rightarrow 0$, the above expressions

²We note, however, that there is a typo in the RHS of equation (79) in Roscoe's paper: the plus sign should be replaced by a minus sign. This error can be verified by doing the pertinent algebra mentioned before equation (78) in that paper.

reproduce exactly the corresponding exact estimates of Gao et al. (2011) for the particle aspect ratios and orientation angles for dilute concentration of particles.

4.5 Applications and discussion

With the objective of illustrating the physical implications of the constitutive model developed in Section 4.3, in this section we apply the model to suspensions of incompressible, viscoelastic particles in macroscopically uniform flows for representative volume fractions and constitutive properties of the particles. In particular, we consider suspensions of initially spherical particles in Newtonian fluids under two special types of flows: *extensional* and *shear* flows. For convenience, we make use of the dimensionless parameters

$$K = \frac{\eta^{(2)}}{\eta^{(1)}}, \quad \text{and} \quad G = \frac{\eta^{(1)} \dot{\gamma}}{\mu},$$

serving to characterize the particle-fluid viscosity ratio and the ratio of viscous forces in the fluid to the elastic forces in the particles, respectively.

4.5.1 Suspensions of initially spherical particles in an extensional flow

First, we consider suspensions of initially spherical particles in an extensional flow with

$$\bar{\mathbf{L}} = \bar{\mathbf{D}} = \dot{\gamma} \mathbf{E}_1 \otimes \mathbf{E}_1 - \frac{1}{2} \dot{\gamma} (\mathbf{E}_2 \otimes \mathbf{E}_2 + \mathbf{E}_3 \otimes \mathbf{E}_3), \quad (4.58)$$

where the $\{\mathbf{E}_i\}$ refer to the fixed laboratory coordinate system and $\dot{\gamma} > 0$ is the macroscopic strain rate. Because of the symmetry of the flow, as well as the incompressibility of the particles in the suspension, the particles do not rotate and the only microstructural parameter which evolves under the flow is the aspect ratio of the (axi-symmetric) particles, $w = w_1 = w_2$. In this case the microstructural tensor \mathbb{P} is explicit and we can derive correspondingly explicit expressions for the evolution of the aspect ratio w and the extra elastic stresses $\bar{\boldsymbol{\tau}}_e^{(2)}$ in the particles, as determined by (4.39) and (4.42), respectively. To maintain continuity, these equations are provided in Appendix C.2. Then, given the current values of the elastic stresses $\bar{\boldsymbol{\tau}}_e^{(2)}$ and the aspect ratio w of the particles, the macroscopic stress $\bar{\boldsymbol{\sigma}}$ can be derived by means of expression (4.37), together with (4.33).

For the purpose of efficiently describing the macroscopic response of the suspension in an extensional flow, it is useful to introduce the effective *extensional* viscosity of the suspensions via

$$\tilde{\eta}_E = \frac{3(\bar{\sigma}_{11} - \bar{\sigma}_{22})}{2(\bar{D}_{11} - \bar{D}_{22})} = \frac{1}{\dot{\gamma}}(\bar{\sigma}_{11} - \bar{\sigma}_{22}), \quad (4.59)$$

where the components of the relevant tensors are relative to the fixed laboratory axes and use has been made of $\bar{\sigma}_{33} = \bar{\sigma}_{22}$ (which follows from the flow symmetry). Also, the corresponding *intrinsic*

viscosity of the suspension is defined by

$$\tilde{\eta}'_E = \frac{1}{c} \left(\frac{\tilde{\eta}_E}{3\eta^{(1)}} - 1 \right). \quad (4.60)$$

To obtain the initial viscosity of the suspension, we make use of the (initial) condition $\bar{\tau}_e^{(2)}|_{t=0} = \mathbf{0}$, which implies that, at $t = 0$, the suspension of KV particles behaves like a suspension of spherical viscous drops with viscosity ratio $K = \eta^{(2)}/\eta^{(1)}$. Therefore, making use of the corresponding estimates of Kailasam and Ponte Castañeda (1998) for suspensions of viscous drops (which ignore surface tension effects), the initial relative viscosity can be written as

$$\left. \frac{\tilde{\eta}_E}{3\eta^{(1)}} \right|_{t=0} = \frac{3(1-c) + (2+3c)K}{3+2c+2(1-c)K}. \quad (4.61)$$

However, for the special case of purely elastic particles, the initial response of the suspension is like that of suspensions of incompressible voids ($K = 0$). Hence, in this case, the relative viscosity at $t = 0$ is given by

$$\left. \frac{\tilde{\eta}_E}{3\eta^{(1)}} \right|_{t=0} = \frac{3(1-c)}{3+2c}. \quad (4.62)$$

Figure 4.2 presents results for the time-dependent behavior of a suspension of purely elastic particles with $G = 0.3$ in extensional flow. Thus, figures 4.2(a) and (b) show respectively results for the evolution of w for suspensions of NH particles at several values of the particle volume fraction, and for suspensions of Gent particles at the fixed volume fraction $c = 0.2$ and different values of the strain-locking parameter. We observe from figure 4.2(a) that the particle volume fraction has a critical effect on the transient elongation of the NH particles. In particular, we observe that, for higher values of c ($c = 0.15, 0.2$), the time-dependent deformation of NH particles never reaches a steady state, and instead the NH particles keep elongating. On the contrary, we observe from figure 4.2(b) that the time-dependent deformation of Gent particles with $c = 0.2$ reaches a steady state, except for the case of $J_m \rightarrow \infty$ which corresponds to NH particles. This is because the *inextensibility* constraint of the Gent particles with a finite value of J_m prevents the particles from deforming indefinitely under the applied flow. Next, figures 4.2(c) and (d) show corresponding results for the non-zero components of $\bar{\tau}^{(2)}$, for the cases of NH and Gent particles, respectively. We observe from figure 4.2(c) that the continuous elongation of the NH particles for higher values of c leads to very high stresses in these particles along the extensional direction (i.e., \mathbf{E}_1 -direction), while, as observed from figure 4.2(d), all stress components reach finite values for the cases of Gent particles. Finally, figures 4.2(e) and (f) show corresponding results for the intrinsic viscosities $\tilde{\eta}'_E$ of the suspensions, for the cases of NH and Gent particles, respectively. For the case of NH particles (figures 4.2(e)), we see that the effective viscosity blows up for the higher values of c , which is a consequence of the high stresses in the NH particles. On the other hand, we observe from figure 4.2(f) that for the case of Gent particles the effective viscosity reaches finite SS values, such that the smaller the value of J_m , the smaller the SS value of the effective viscosity.

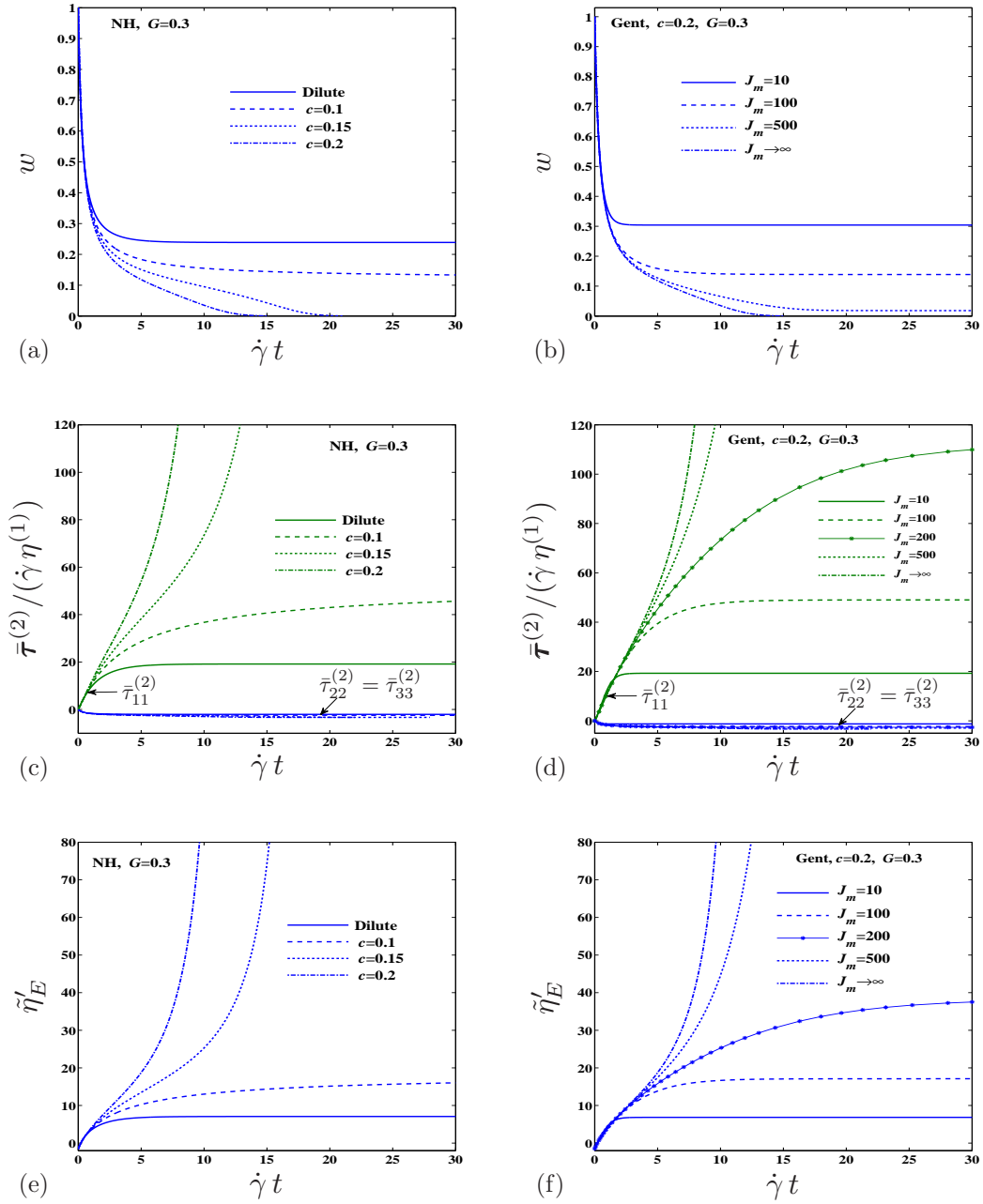


Figure 4.2: Results for the time-dependent response of suspensions of initially spherical neo-Hookean and Gent particles with $G = 0.3$ in an extensional flow.

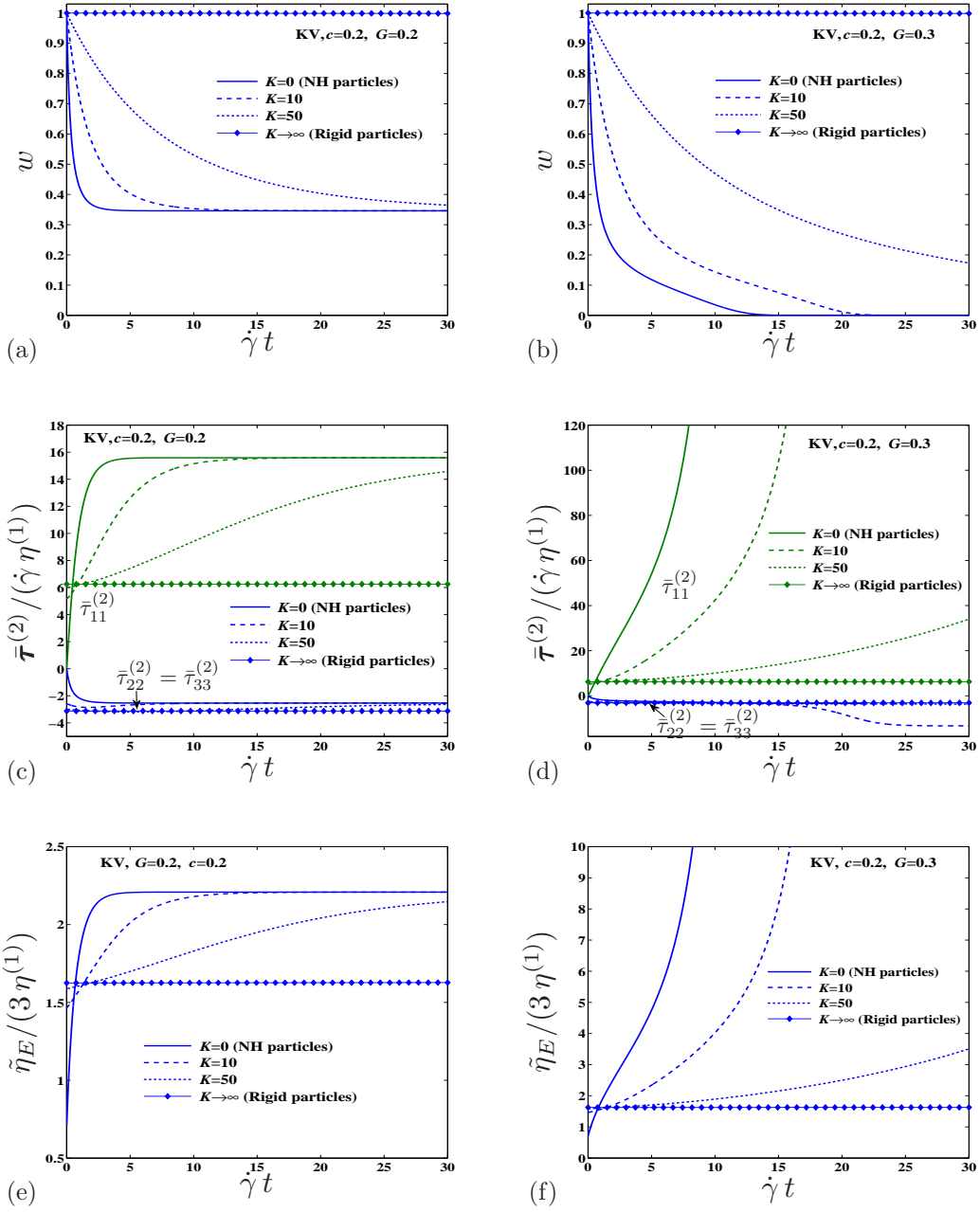


Figure 4.3: Results for the time-dependent response of suspensions of initially spherical Kelvin-Voigt particles (with NH elastic part) for $c = 0.2$ in an extensional flow.

Figure 4.3 provides estimates for the time-dependent response of the suspensions of Kelvin-Voigt particles (with a NH elastic part) in an extensional flow. Results are shown for a fixed volume fraction ($c = 0.2$) and various values of the viscosity ratio K . Figures 4.3(a) and (b) show results for evolution of w calculated at $G = 0.2$ and $G = 0.3$, respectively. In the same way, figures 4.3(c) to (d) and (e) to (f) show results for the non-zero components of $\bar{\tau}^{(2)}$ and the viscosity $\tilde{\eta}_E$, respectively. It is recalled that the extreme limits $K = 0$ and $K \rightarrow \infty$ in these figures correspond to the cases of purely elastic and rigid particles, respectively. An important observation from figures 4.3(a), (c) and (e) is that the suspensions of KV particles reach the same steady state as in suspensions of NH particles, despite the evident differences in their respective time-dependent responses (this point will be explained in more detail shortly). In particular, we can see from figure 4.3(a) that the KV particles, before reaching the steady state, exhibit decreasing deformability as K increases. This produces smaller stresses in the particles (see figure 4.3 (c)), which results in smaller extensional viscosities in the suspension (see figure 4.3 (e)). Figures 4.3(b), (d) and (f) present corresponding results for a higher value of $G (= 0.3)$. For this larger value of G , the KV particles keep deforming as long as the applied stresses are large enough, and the suspension can not reach a steady state, similar to the case of purely elastic NH particles ($K = 0$) discussed in the context of figures 4.2(a), (c) and (e).

Next, we consider the steady-state response of the suspensions of initially spherical particles in the extensional flow (4.58). It follows from the symmetry of the problem that the shear components of the stress and strain rate are zero in the particle phase. Hence, for the case of KV particles, the steady-state stress in the particle phase is purely elastic, i.e. $\bar{\tau}_{ij}^{(2)} = (\bar{\tau}_e^{(2)})_{ij}$ (this can be verified from relations (4.56) and (4.57) by noting that $\bar{D}_{ij} = 0$, $i \neq j$.) This implies that the SS values for the particle shape, stress and strain rate, in the suspensions of KV particles subjected to an extensional flow, are independent of the parameter K and, therefore, are equal to those corresponding to the elastic limit of the particles, characterized by $K = 0$. However, note that the case of $K \rightarrow \infty$ corresponds to rigid particles for which the particles do not deform. In this context, it is worthwhile to provide an expression for the steady-state value of the particle aspect ratio, denoted by w_s , in extensional flow. Thus, w_s is obtained as the acceptable root of the non-linear equation

$$4G\omega_{1s}^5 - (1-c)w_s^2 [(w_s^2 + 2)\omega_{2s} - 6\omega_{1s}] \Delta_s = 0, \quad (4.63)$$

where the variables $\omega_{1s} = \sqrt{1 - w_s^2}$ and $\omega_{2s} = 2 \ln(\omega_{1s} + 1) - 2 \ln(w_s)$ are introduced for conciseness, and

$$\Delta_s = \begin{cases} J_m (1 - w_s^2) / [(J_m + 3) w_s^{(4/3)} - (2w_s^2 + 1)], & \text{for Gent particle,} \\ w_s^{-4/3} (1 - w_s^2), & \text{for NH particle.} \end{cases} \quad (4.64)$$

The steady-state value of the effective viscosity (4.59) can also be obtained as

$$\tilde{\eta}_E = 3\eta^{(1)} \left(1 - cD_s + \frac{1}{3G} c\Delta_s \right), \quad (4.65)$$

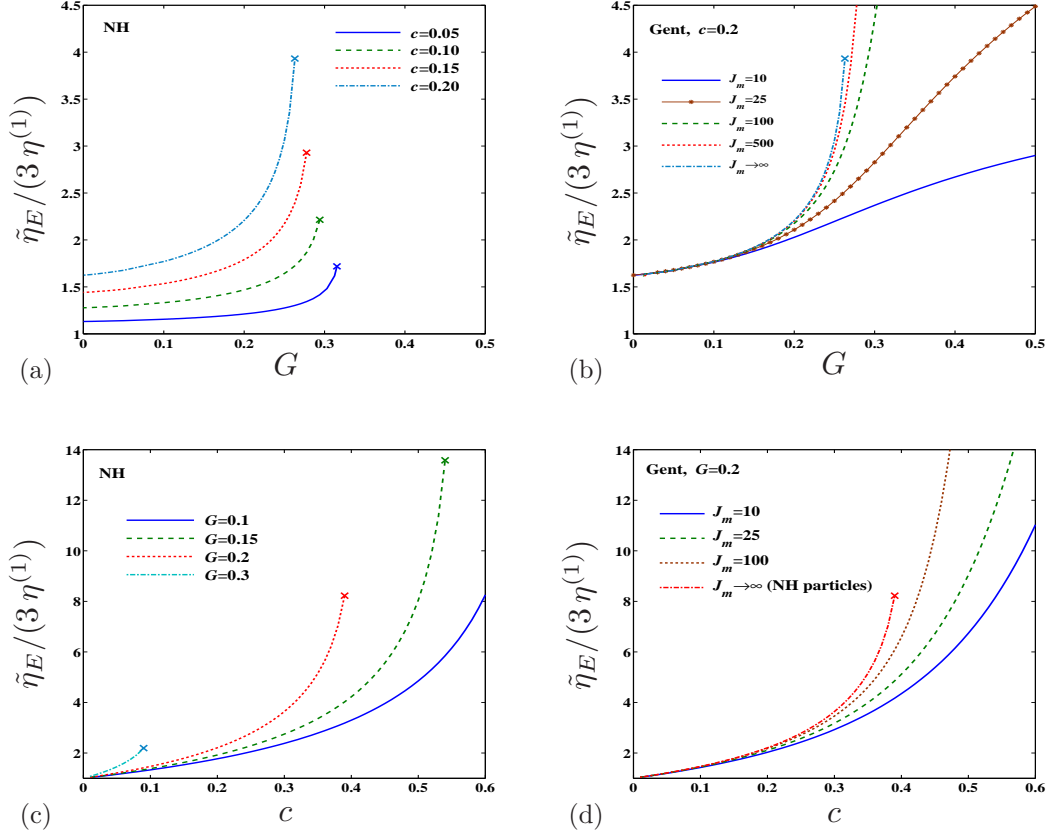


Figure 4.4: Results for the steady-state relative viscosities of suspensions of initially spherical, neo-Hookean and Gent particles in extensional flow.

where the variable D_s is given by

$$D_s = \frac{w_s^2 (1-c) [(w_s^2 + 2)\omega_{2s} - 6\omega_{1s}] \Delta_s - 4G\omega_{1s}^5}{G \{3(1-c)w_s^2(w_s^2 + 2)\omega_{2s} - 2\omega_{1s} [2\omega_{1s}^4 + 9(1-c)w_s^2]\}}, \quad (4.66)$$

with w_s being the steady-state aspect ratio.

Figure 4.4 shows estimates for the SS value of the (extensional) effective viscosity for suspensions of (initially spherical) elastic particles. Figures 4.4(a) and (b) show plots as a function of G for neo-Hookean and Gent particles, respectively, while figures 4.4(c) and (d) show plots as a function of the volume fraction for neo-Hookean and Gent particles, respectively. We observe from figures 4.4(a), (b) and (c) that $\tilde{\eta}_E$ grows monotonically as G increases, indicating a shear-thickening effect in suspensions of NH and Gent particles. This growth is stronger at higher values of the particle volume fraction. Also, for the case of NH particles, there is a critical value for G (marked with \times) beyond which the response of the suspension can not reach a steady state (refer to figure 4.2(e), and for which the time-dependent effective viscosity of the suspension tends to infinity.) However, as shown in figures 4.4(b) and (d), this unrealistic feature disappears for suspensions of Gent particles

with a finite J_m in which case the time-dependent response reaches a steady state with a finite value for $\tilde{\eta}^E$. As discussed in the context of figure 4.2, this is because the Gent model provides a more realistic constitutive description of the elastomeric particles by capturing the experimentally observed, finite extensibility of such materials.

4.5.2 Suspensions of initially spherical particles in a shear flow

Next, we consider suspensions of initially spherical particles in a simple shear flow, characterized by

$$\bar{\mathbf{L}} = \dot{\gamma} \mathbf{E}_1 \otimes \mathbf{E}_2, \quad \bar{\mathbf{D}} = \frac{1}{2} \dot{\gamma} (\mathbf{E}_1 \otimes \mathbf{E}_2 + \mathbf{E}_2 \otimes \mathbf{E}_1), \quad \bar{\mathbf{W}} = \frac{1}{2} \dot{\gamma} (\mathbf{E}_1 \otimes \mathbf{E}_2 - \mathbf{E}_2 \otimes \mathbf{E}_1), \quad (4.67)$$

where the $\{\mathbf{E}_i\}$ refer to the fixed laboratory coordinates, and $\dot{\gamma} > 0$ is the shear strain rate. In this case, the initially spherical particles deform into ellipsoids of general shape characterized by the two aspect ratios w_1 and w_2 , which in turn rotate remaining in the $\mathbf{E}_1 - \mathbf{E}_2$ plane in such a way that their current orientation may be described in terms of a single angle θ (measured positive in the counterclockwise direction from the \mathbf{E}_1 direction). Then, the evolution equations (4.39) to (4.44) can be shown to specialize to equations (C.19) in Appendix C.3. This system of equations, together with relations (4.33) and (4.34), can be integrated numerically for the time-dependent solution. For completeness, the components of the shape tensors \mathbb{P} and \mathbb{R} , required for this integration, are provided in Appendix C.4. Finally, given the current values of the elastic stresses $\bar{\boldsymbol{\tau}}_e^{(2)}$, aspect ratios w_1 and w_2 and orientation θ of the particles, the macroscopic stress $\bar{\boldsymbol{\sigma}}$ can be derived by means of expression (4.37), together with (4.33).

To conveniently describe the macroscopic response of the suspension in shear flow, we introduce the effective *shear viscosity*, as well as the first and second *normal stress differences* of the suspensions, defined by

$$\tilde{\eta}_S = \frac{1}{2 \bar{D}_{12}} \bar{\sigma}_{12} = \frac{1}{\dot{\gamma}} \bar{\sigma}_{12}, \quad (4.68)$$

and

$$\Pi_1 = \bar{\sigma}_{11} - \bar{\sigma}_{22}, \quad \Pi_2 = \bar{\sigma}_{22} - \bar{\sigma}_{33}, \quad (4.69)$$

respectively, where the components are relative to the fixed laboratory axes. Also, the corresponding *intrinsic viscosity* of the suspension is defined by

$$\tilde{\eta}'_S = \frac{1}{c} \left(\tilde{\eta}_S / \eta^{(1)} - 1 \right), \quad (4.70)$$

and similarly for the intrinsic normal stress differences Π'_1 and Π'_2 .

As was the case for extensional flow, we make use of the initial condition $\bar{\boldsymbol{\tau}}_e^{(2)} \Big|_{t=0} = \mathbf{0}$ to obtain the initial viscosity of the suspension. As already mentioned, at $t = 0$, the suspensions of KV particles behave like suspensions of spherical drops with viscosity ratio K . The initial relative viscosity ($\tilde{\eta}_S / \eta^{(1)}$) for this suspension is then given by

$$\frac{\tilde{\eta}_S}{\eta^{(1)}} \Big|_{t=0} = \frac{(3c + 2)K + 3(1 - c)}{2(1 - c)K + 2c + 3}. \quad (4.71)$$

For the case of elastic particles ($K = 0$), the above relation reduces to

$$\left. \frac{\tilde{\eta}_S}{\eta^{(1)}} \right|_{t=0} = \frac{1-c}{1+2c/3}. \quad (4.72)$$

Before proceeding with the detailed examples, it is emphasized that the components of the stress and strain rate tensors in the particle phase are shown below relative to the instantaneous principal axes of the particle.

Figure 4.5 shows estimates for the time-dependent response of dilute and non-dilute suspensions of initially spherical NH particles in a shear flow. The results are given for $G = 0.2$ and various values of particle volume fraction. Figure 4.5 (a) and (b) depict the evolutions for the aspect ratios w_1 and w_2 and the particle orientation angle θ , respectively. It is helpful to recall that w_1 and w_2 correspond to the aspect ratios of the particle in the plane of the flow and in the plane perpendicular to the short in-plane axis of the particles, respectively. The evolutions of w_1 , w_2 and θ in figures 4.5 (a) and (b) indicate that the particles in suspensions with a higher volume fraction become more elongated and their major axis becomes more aligned with the shear direction, before reaching a steady state. We emphasize that while the particle shape and orientation do not change in the steady state, material points in the particle undergo a periodic *tank-treading* motion. This motion has been frequently reported in suspensions of red blood cells (see, e.g., Keller and Skalak (1982)) and capsules (Clausen and Aidun, 2010; Clausen et al., 2011), in which the enclosing membrane continues to rotate around the interior fluid in a tank-treading motion. As can be seen from figures 4.5 (c) and (d), the normal components of the strain rate (relative to the instantaneous axes of the particle) decay to zero with the deformation, while the shear component of the strain rate and normal components of the extra elastic stress in the particles build up from zero until reaching their steady-state values. Also, we observe from figure 4.5(d) that the normal components of the average stress in the particles exhibit a progressive increase (in magnitude) as the volume fraction of the particles increases, which, correspondingly, leads to a higher intrinsic viscosity and normal stress differences, as can be seen in figures 4.5(e) and (f).

Figures 4.6(a) to (c) depict estimates for the time-dependent behavior of the particle shape and orientation in suspensions of NH particles with $c = 0.2$ in shear flows with varying values of G . The results suggest that the NH particles exhibit larger stretches, which increase monotonically with increasing values of G . For the largest value of G (i.e., $G = 1.5$ for this figure), we have also included the corresponding results for Gent particles with $J_m = 5$. For this case, we observe a significant reduction in the level of deformation resulting from the inextensibility constraint. On the other hand, figures 4.6(d) and (f) show the corresponding time-dependent results for the effective viscosity and normal stress differences. We observe from figure 4.6(d) that the initial value of the effective shear viscosity is independent of the value of G and is approximately equal to 0.7 (this matches the value calculated from (4.72) for $c = 0.2$.) We further observe that the time-dependent behavior of the effective viscosity and the first normal stress shows a more pronounced “overshoot” with increasing values of G . As explained by Gao et al. (2011), the overshoot and the subsequent decay observed in these figures are due to the fact that the particles rotation continues even after the particles have stopped elongating in the plane of shear (see figures 4.6(a) and (c).) Consistently, we notice from

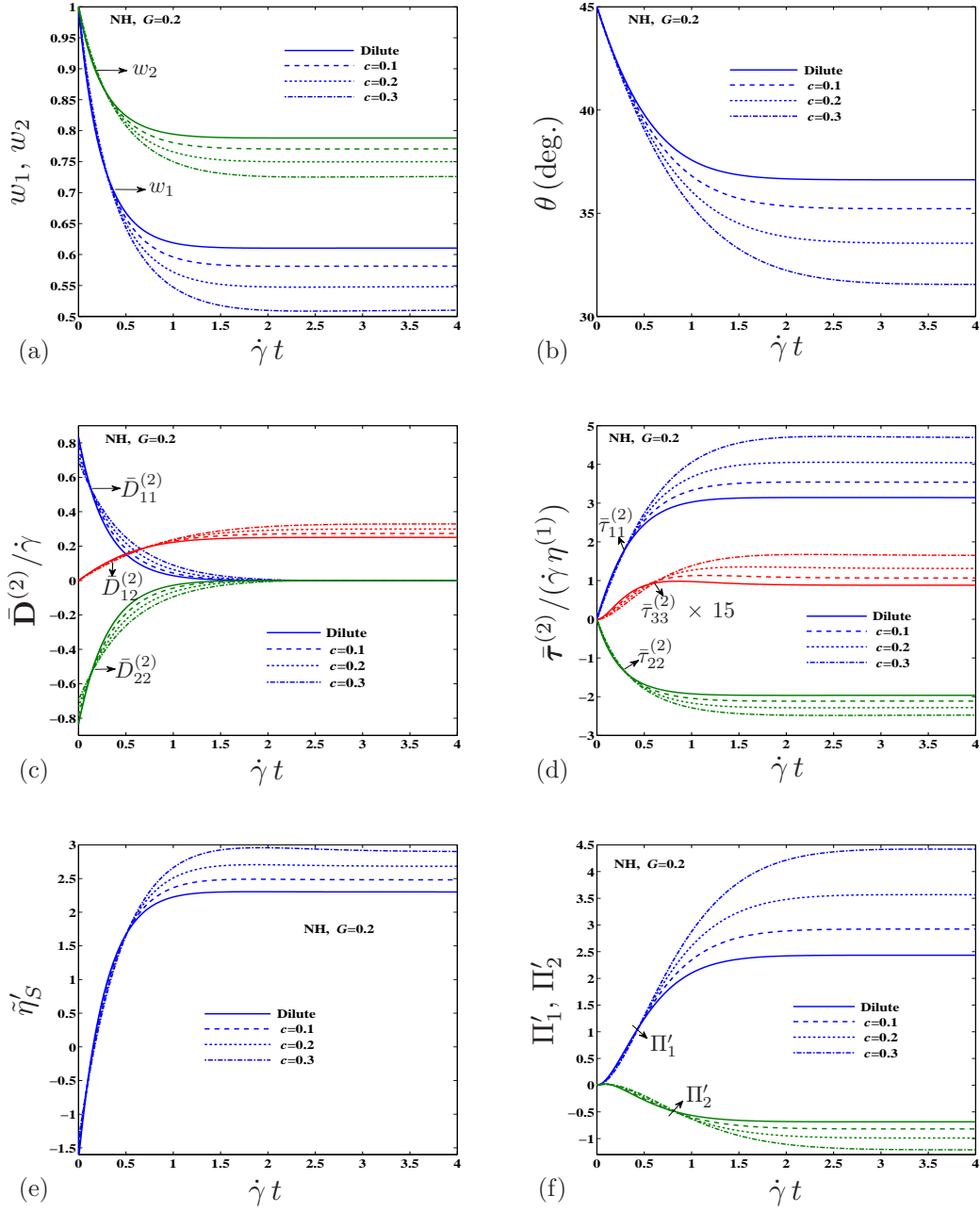


Figure 4.5: Results for the time-dependent response of suspensions of initially spherical neo-Hookean particles with $G = 0.2$ and various values of c in a shear flow. The components of $\bar{\boldsymbol{\tau}}^{(2)}$ and $\bar{\mathbf{D}}^{(2)}$ are given relative to the principal axes of the particle.

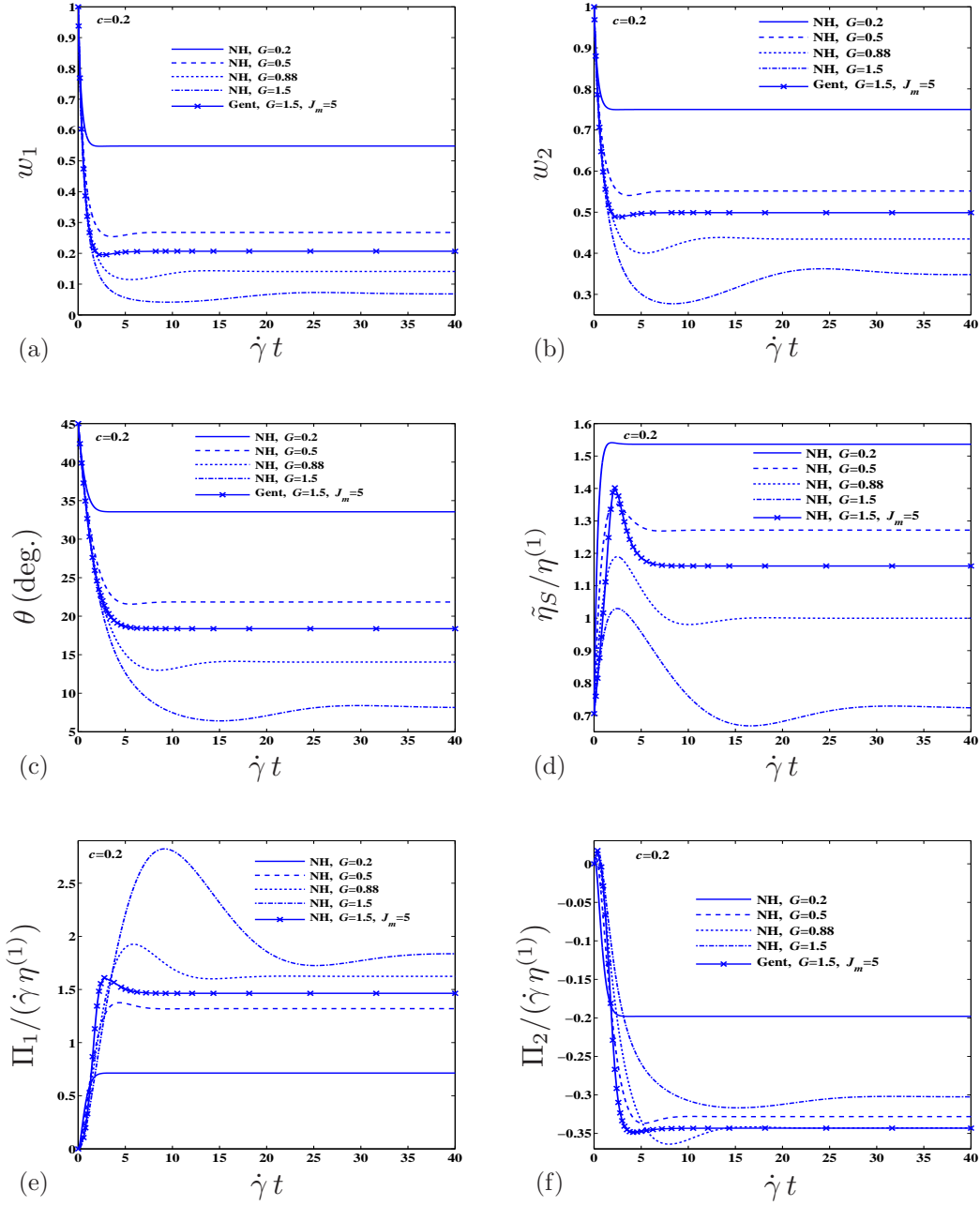


Figure 4.6: Results for the time-dependent response of suspensions of initially spherical neo-Hookean and Gent particles with $c = 0.2$ and various values of the dimensionless parameter G in a shear flow. Higher values of G correspond to softer particles, or to larger shear-strain rates.

figures 4.6(a) and (c) that the time interval between the arrest of the particles elongations in the plane of shear and the corresponding arrest of the particles rotations becomes progressively larger as G increases. Finally, we observe from figure 4.6(d) that the SS value of the effective viscosity drops as the value of G increases which suggests a *shear-thinning* effect.

Figure 4.7 shows estimates for the time-dependent rheological behavior of suspensions of KV particles in shear flow. In particular, we investigate the influence of the viscosity of the particles, characterized by the parameter $K = \eta^{(2)}/\eta^{(1)}$, on the time-dependent behavior, calculated at fixed values $G = 0.2$ and $c = 0.2$. We recall that the extreme cases $K = 0$ and $K \rightarrow \infty$ correspond to suspension of purely elastic and rigid particles, respectively. We observe from figures 4.7(a) and (b) that, for low values of K , the motion of the particles follows the same general trends as those of the purely elastic particles. However, for higher values of K , the particles undergo a *trembling* motion of decreasing amplitude before reaching the steady state. This motion is similar to that observed for capsules under similar flow conditions, as reported by Clausen et al. (2011). In the limit of rigid particles ($K \rightarrow \infty$), the rotation of particles is entirely given by the rigid body rotation of the imposed shear flow, i.e. $\theta = \pi/4 - \dot{\gamma}t/2$. Figure 4.7(c) shows the components of the extra stress tensor in the particle ($\bar{\tau}^{(2)}$) relative to the principal axes of particles. It is interesting to note that, for the case of KV particles ($K \neq 0$), the shear component $\bar{\tau}_{12}^{(2)}$ has a non-zero value, which has no contribution from the elastic part of the stress, i.e. $\bar{\tau}_{12}^{(2)} = (\bar{\tau}_v^{(2)})_{12} = 2\eta^{(2)}\bar{D}_{12}^{(2)}$. Next, figures 4.7(d), (e), and (f) show the corresponding effective viscosity, first and second normal stress differences of the suspensions, respectively. As expected, it can be seen from figure 4.7(d) that the values of the effective viscosity at $t = 0$ match the corresponding values calculated from relation (4.71). Also, we observe from figure 4.7(f) that, at higher values of K , the second normal stress difference has an initial overshoot with positive values, similar to the results for the case of suspensions of concentrated capsules, as reported by Clausen et al. (2011).

Next, we investigate the steady-state response of the suspensions of neo-Hookean particles under the shear flow conditions (4.67). Figures 4.8(a) and (b) show estimates for SS values of the aspect ratios and orientation of the particles, respectively, as a function of G , for several values of the particle volume fraction. These figures indicate that, as G increases, the NH particles reach larger elongations, as well as closer alignments with the shear direction at the steady state. This behavior of the particles is seen to be weakly affected by the value of c . Next, figure 4.8(c) and (d) show the corresponding estimates for the effective viscosity and normal stresses, respectively. We observe from figure 4.8(c) that the effective viscosity $\tilde{\eta}_S$ decreases as G increases, thus showing a shear-thinning response. Moreover, when $G \rightarrow 0$, which corresponds to suspensions of rigid spherical particles, we recover the corresponding Hashin-Shtrikman lower bound given by

$$\left. \frac{\tilde{\eta}_S}{\eta^{(1)}} \right|_{G \rightarrow 0} = \frac{1 + 3c/2}{1 - c}. \quad (4.73)$$

Another interesting observation from figure 4.8(c) is that, at approximately $G = 0.88$, the relative viscosity becomes unity. This implies that, at this value of G , the suspended elastic particles do not change the effective viscosity of the host liquid. Particles having this property have been found in other physical phenomena (Milton, 2002b) and are known in the literature as “neutral” particles.

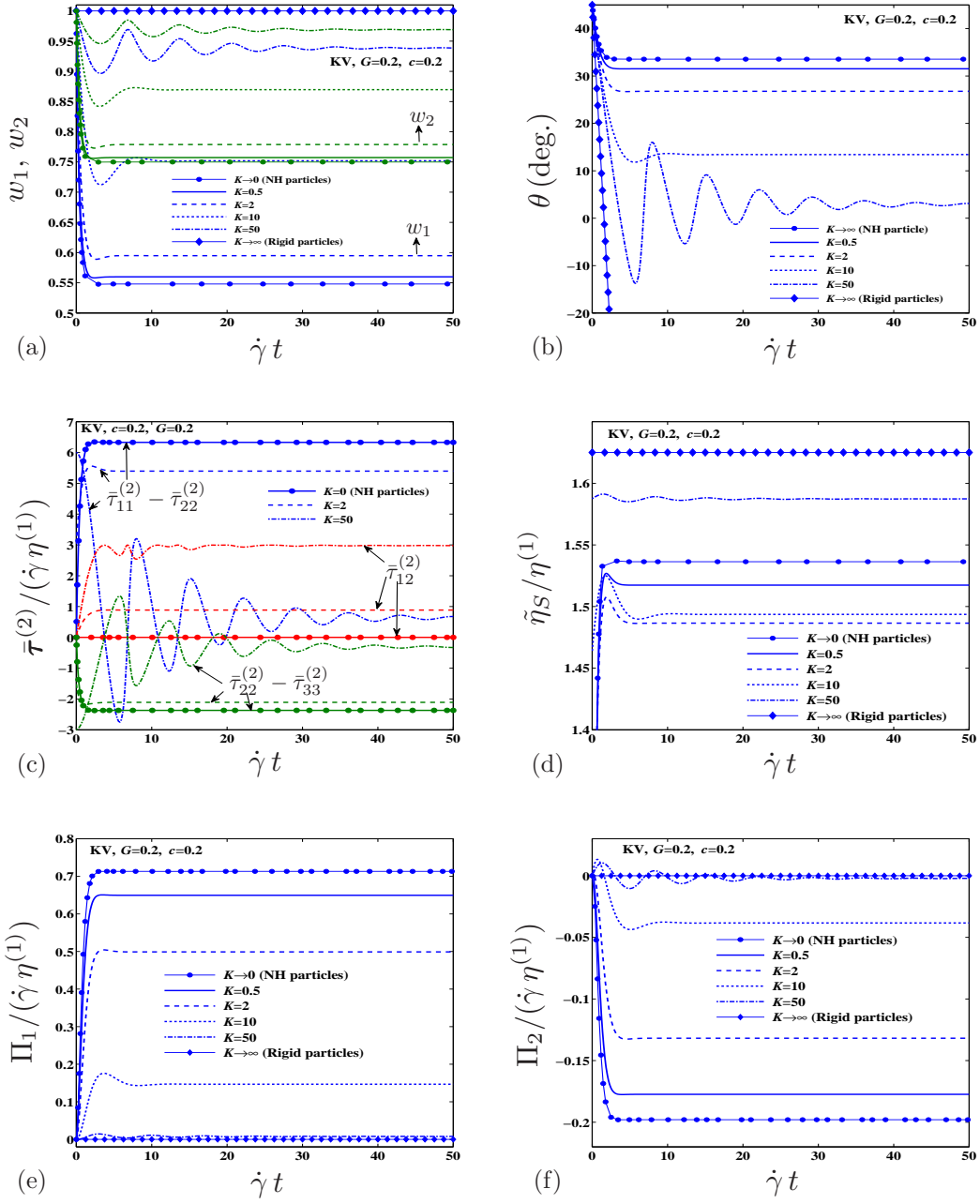


Figure 4.7: Results for the time-dependent response of suspensions of initially spherical Kelvin-Voigt particles (with NH elastic part) with $G = 0.2$ and various values of K in a shear flow. The components of $\bar{\tau}^{(2)}$ are given relative to the principal axes of the particle.

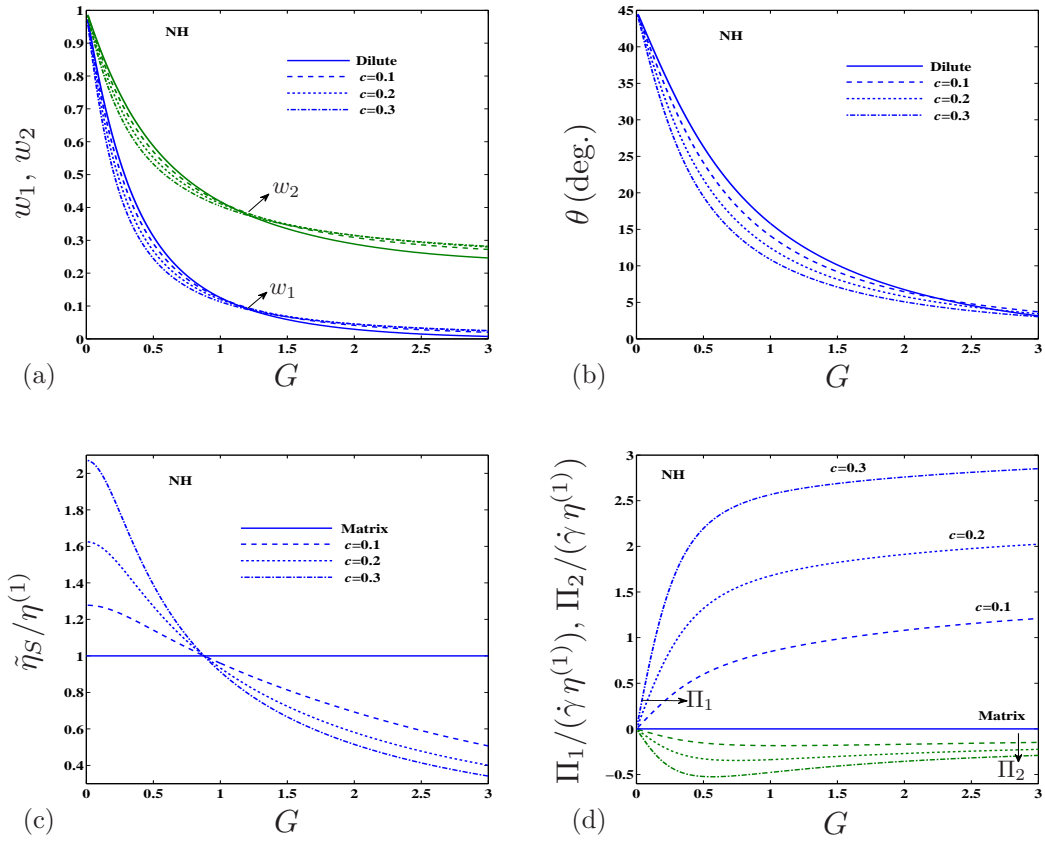


Figure 4.8: Results for the steady-state response of suspensions of initially spherical neo-Hookean particles for various values of c in a shear flow.

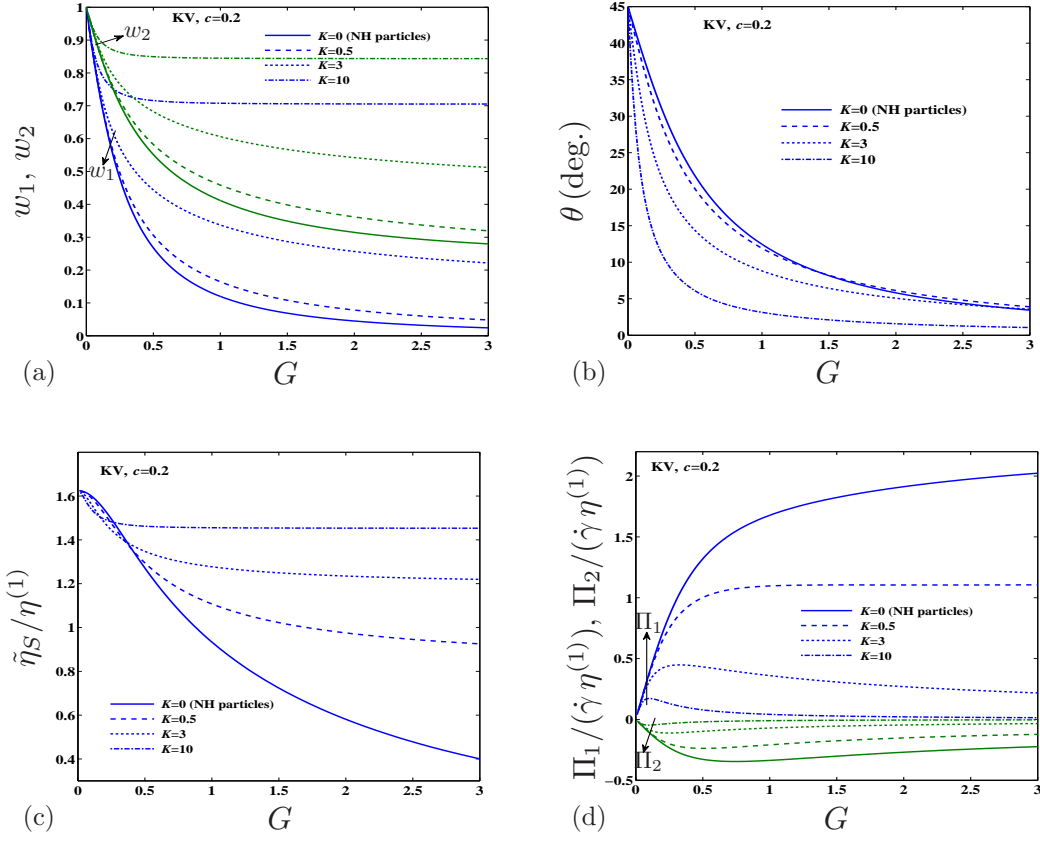


Figure 4.9: Results for the steady-state response of suspensions of initially spherical Kelvin-Voigt particles (with NH elastic part) for various values of K in a shear flow.

We observe from figure 4.8(c) that the value of G at which the NH particles become neutral, G_N say, has a weak dependence on the volume fraction of the particles (G_N is slightly smaller than 0.88 for $c > 0.3$.) For $G > G_N$, the effective viscosity of the suspension is actually less than unity, similar to the case of suspensions of viscous droplets in a more viscous liquid.

Figure 4.9 presents estimates for the SS behavior of the particles, as well as for the associated macroscopic rheological properties, of suspensions of KV particles (with NH elastic behavior) subjected to shear flow conditions. Figure 4.8(a) and (b) show results for the aspect ratios and orientations of the particles, respectively, at several values of K , for a fixed value of $c = 0.2$. As expected, we observe from these figures that, for a fixed value of G , but for increasing values of K , the particles behave more like stiff particles by deforming less and rotating more, recovering the case of rigid particles in the limit of $K \rightarrow \infty$. Figures 4.9(c) and (d) show results for the corresponding effective viscosity and normal stress differences, respectively. We observe from these figures that the viscosity of the particles (controlled by the parameter K) has a more significant effect on the steady-state behavior of the suspension at higher values of G . In addition, we observe from figure 4.9(a) that the value of G_N , at which the particles become neutral ($\tilde{\eta}_S = \eta^{(1)}$), increases with K up

to a certain value of K , beyond which the particles may never become neutral.

Next, in figure 4.10, we investigate the influence of the particle volume fractions on the SS values of the effective viscosity and normal stress differences of suspensions with different types of particles. Thus, figures 4.10(a) to (b), (c) to (d), and (e) to (f) show plots as functions of c for neo-Hookean, Gent and Kelvin-Voigt (with NH elastic behavior) particles, respectively. Consistent with earlier comments in the context of figure 4.8, we observe from figure 4.10(a) that, for suspensions of NH particles with $G < 0.88$, the relative viscosity ($\tilde{\eta}_S/\eta^{(1)}$) is greater than unity and increases with increasing particle concentration c , while for suspensions with $G > 0.88$, the relative viscosity is less than one and decreases with increasing values of c . For $G \approx 0.88$, the relative viscosity is close to one and is fairly insensitive to the particle concentration. On the other hand, we see from figure 4.10(c) that, even at a high value of $G (= 2)$, the relative viscosity of suspensions of Gent particles with a small enough value of J_m , can still be greater than unity and exhibits monotonic growth in c . Furthermore, we note from figure 4.10(e) that the viscosity of KV particles with $G = 0.2$ has a weak effect on the relative viscosity of the suspension up to moderate levels of concentration ($c < 0.3$). In addition, it is observed from figures 4.10 (b), (d) and (f) that the magnitude of the normal stresses always increases with the particle concentration c , but is fairly insensitive to the values of G and J_m , although a little more sensitive to the viscosity ratio K .

Finally, comparisons are shown in figure 4.11 of the model's predictions with numerical simulation results for suspensions of capsules, as well as with experimental data for suspensions of red blood cells (RBCs) under shear flow conditions. The initially spherical capsules are composed of a fluid-filled interior (with radius a) enclosed by a NH elastic membrane (with shear modulus μ_m), where the viscosity of the internal fluid is equal to that of the external suspending fluid. The dimensionless parameter $G_m = \eta^{(1)}\dot{\gamma} a/\mu_m$ is the counterpart of the parameter G for the capsules. While our model has been developed to describe the effective response of suspensions of "solid" viscoelastic particles, by making appropriate choices for the properties of the KV particles, it can be used to estimate the rheological behavior of suspensions of capsules (with a given value of G_m). In this case, a reasonable choice for the properties of the KV particles (with a NH elastic part) is $G = G_m$ and $K = 1$. Thus, figures 4.11(a) to (d) show comparisons between our model results for dilute suspensions of KV particles and corresponding simulation results of Ramanujan and Pozrikidis (1998a) for dilute suspensions of spherical capsules in a shear flow. Figures 4.11(a) and (b) show the comparisons for the time-dependent behavior of the Taylor deformation parameter $D = (1 - w_1)/(1 + w_1)$ and the particle orientation, respectively, while figures 4.11(c) and (d) show the comparisons for the time-dependent behavior of the excess viscosity and the normal stress differences, respectively. Although these comparisons are not entirely fair since the KV particles (corresponding to a linear dashpot connected in parallel with an NH spring) can only serve as approximate models for the capsules (consisting of a linear viscous drop enclosed by a NH membrane), we observe relatively good agreement between our results and those for the capsules, at least for these dilute concentrations. Next, in figure 4.11(e), comparisons are given between our results for the steady-state response of non-dilute suspensions of KV particles and the simulation results of Clausen et al. (2011) for suspensions of NH capsules in a shear flow. Results are shown for the effective viscosity and the normal stress differences for $c = 0.2$, as functions of $G \tilde{\eta}_S/\eta^{(1)}$. We observe from this figure that our results are still in quite good

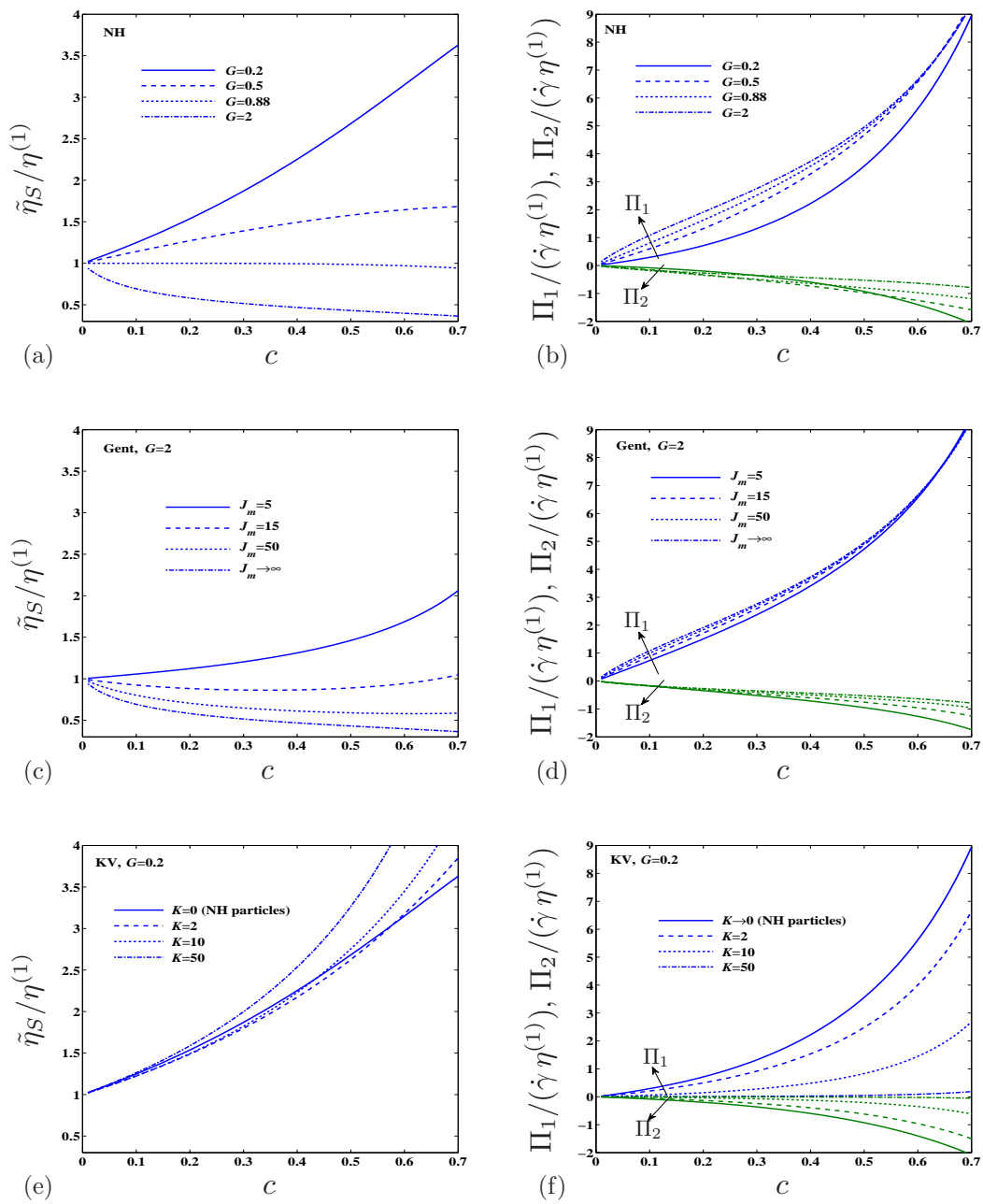


Figure 4.10: Results for the steady-state response of suspensions of initially spherical neo-Hookean, Gent and Kelvin-Voigt particles (with NH elastic part) in a shear flow.

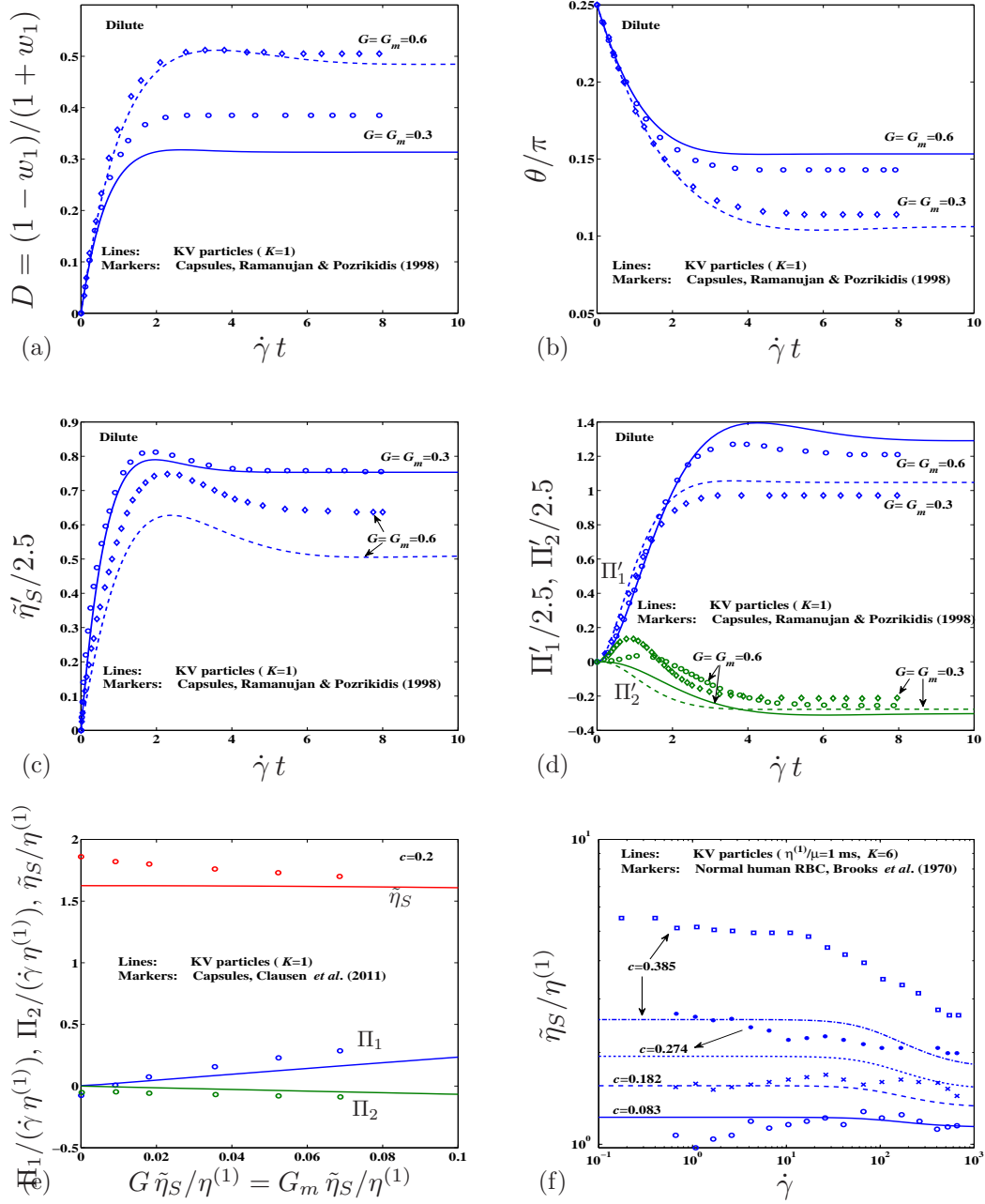


Figure 4.11: Comparisons of the predictions of our model with numerical simulation results for suspensions of initially spherical capsules, as well as with experimental data for suspensions of RBCs under shear flow conditions. (a-d) Comparisons of the time-dependent response of dilute suspensions of KV particles with the simulation results of Ramanujan and Pozrikidis (1998a) for the corresponding response of dilute suspensions of capsules. (e) Comparisons of the SS response of suspensions of KV particles with the simulation results of Clausen *et al.* (2011) for the SS behavior of non-dilute suspensions of capsules. (f) Comparisons of the SS behavior of suspensions of KV particles with the experimental data of Brooks *et al.* (1970) for the effective viscosity of suspensions of normal human RBCs, as a function of the shear rate $\dot{\gamma}$, for different values of the RBC volume fraction.

agreement with the simulation results for capsules. However, it should be remarked that the model is not expected to provide accurate predictions for rigid particles, corresponding to a zero value for G in the figure, since it has been assumed (for simplicity) that the shape of (the angular dependence of) the two-point correlation function is identical to the evolution of the particle shape. Since for rigid particles, the particle shape cannot change, this would mean that the two-point correlations function remains isotropic, which is not expected to be the case for the non-Brownian suspensions considered in this chapter. As already stated, for soft particles ($G > 0$), the change in shape of the particles is expected to dominate the higher-order effect (in c) of the changes in the particle distribution, and the model is expected to be more accurate then. Lastly, figure 4.11(f) shows comparisons between the predictions of our model and the experimental data of Brooks et al. (1970) for the effective viscosity of suspensions of normal human RBCs in a shear flow, as a function of the shear rate $\dot{\gamma}$, for different values of the RBC volume fraction. The RBCs consist of a thin elastic membrane with shear modulus $\sim 4 \times 10^{-6}$ N/m and the average radius $4 \mu\text{m}$, filled with a nearly Newtonian fluid with viscosity $6 - 7$ mPa.s. Also, the suspending fluid is a protein-free saline with the viscosity $1 - 1.2$ mPa.s. Similar to the case of capsules, we can use our model to estimate the rheological properties of suspensions of RBCs by appropriately choosing K and $\eta^{(1)}/\mu$. Consistent with the above-mentioned RBCs properties, we choose $\eta^{(1)}/\mu = 1$ s and $K = 6$. The predictions of our model in figure 4.11(f) show quite good agreement with the experimental data for small volume fractions ($c < 20\%$). For higher volume fractions, our results can still capture the shear-thinning behavior exhibited by the suspensions of RBCs at the higher shear rates. However, the magnitude of the effect is under-predicted by the model, which is probably due to the fact that the variational estimates of the HSW type tend to under-predict the strong interaction effects between the particles that develop at the higher particle concentrations ($c > 20\%$).

4.6 Conclusions

In this chapter, we have developed a homogenization-based model characterizing the finite-strain, time-dependent response of non-dilute suspensions of micro-scaled, soft particles in a Newtonian fluid under Stokes flow conditions. Although more general initial shapes and viscoelastic constitutive models could be used for the particles, we have considered here suspensions of initially spherical particles whose constitutive response is characterized by Kelvin-Voigt (KV) behavior incorporating finite extensibility of the particles in the regime of arbitrarily large deformations. Our model is based on the homogenization theory of Ponte Castañeda and Willis (1995) for linear-elastic composite materials with particulate microstructures. Extended to account for viscous behavior and finite strains, this technique has been used here to generate estimates for the averages of the strain rate and vorticity tensors in the particle phase, as given by equations (4.33) and (4.34), respectively. Such estimates, together with evolution equations for the elastic stress in the particles, as given by (4.42), and for the average particle shape and orientation, as given by (4.39) and (4.40), respectively, can then be used to obtain estimates for the macroscopic response of the suspension by means of equation (4.37). The resulting constitutive model provides a complete description for the time-dependent, macroscopic, rheological response of the non-dilute suspensions of viscoelastic particles

under macroscopically uniform flows, thus generalizing earlier work by Gao et al. (2011) for dilute suspensions of neo-Hookean (NH) particles. However, it should be recalled that the model has made use of a rather simplistic evolution law for the two-point correlation function of the particle centers, and should not be used for suspensions of (nearly) rigid particles. Improvements along these lines are certainly possible, but they would probably make most sense in the context of more sophisticated homogenization methods incorporating higher-order statistics (Milton, 2002b).

We have also used the model developed in this chapter to explore the rather rich and complex rheological behavior of the soft-particle suspensions by focusing on two types of flows: *extensional*, and *simple shear* flows. These examples provide a broad picture of the influence of the flow conditions, constitutive behaviors of the particles, and the particle volume fractions on the dynamics of the suspended particles, as well as on the macroscopic rheology of the suspension. For the case of extensional flows, we found that there is a critical value of G , beyond which suspensions of KV particles with NH elastic behavior cannot reach a steady state, and that this critical value of G decreases with increasing particle volume fraction. For dilute concentrations of the KV particles, this critical value agrees exactly with the corresponding results of Roscoe (1967). In addition, we showed that, when the value of G is subcritical and a steady state is reached, the viscosity of KV particles does not affect the rheological behavior of the suspension, although it does affect significantly the time-dependent response prior to reaching the steady state. On the other hand, for more realistic KV particles with Gent-type elastic behavior (exhibiting finite limits of extensibility characterized by the parameter J_m), the corresponding results indicate that steady-state (SS) solutions are available for the full range of values of G . In such cases, the corresponding SS values of the effective extensional viscosities exhibit shear-thickening and are lower for particles with a tighter extensibility constraint (lower values of J_m).

For simple shear flows, the viscoelastic properties of the initially spherical particles are found to have a significant effect on both the time-dependent and steady-state response of the suspension. For particles with a high viscosity ratio K , the particles exhibit a *trembling* transient motion, before reaching a steady-state, tank-treading motion with fixed particles shapes and orientations. Similar motions have also been reported in the context of suspensions of initially spherical capsules by Clausen et al. (2011). On the other hand, the results of Gao et al. (2012) for dilute concentrations of purely elastic particles showed trembling motions only for non-spherical initial shapes for the particles, indicating more complex behaviors for viscoelastic particles. Moreover, contrary to the SS results for extensional flows in which softer particles tend to increase the effective viscosity of the suspension, the corresponding SS results show that softer particles tend to reduce the effective viscosity in simple shear, leading to an overall shear-thinning effect for the suspension. However, it is interesting to note that, the shear-thickening/thinning effect is more pronounced for suspensions with higher particle volume fractions for both cases. Furthermore, in agreement with earlier results by Gao et al. (2011) for dilute concentrations, it has been found that the SS relative viscosity of the suspension in shear can become unity at some critical value $G = G_N \approx 0.88$, beyond which it becomes less than one. This result suggests that it should be possible to design suspensions of “neutral” particles (Milton, 2002b), as well as suspensions with lower viscosity than that of the suspending fluid. Our results show that the value of G_N depends weakly on the volume fraction of

particles. However, for the case of Gent-type particles, the value of G_N is strongly dependent on the value of J_m , such that the smaller the J_m , the higher the G_N .

Finally, we made comparisons of the predictions of our model with simulation results for suspensions of capsules (composed of an interior fluid enclosed by a NH membrane), as well as with the experimental data for the suspensions of RBCs, in a shear flow. It was found that the predictions of the model (for appropriate choices for the properties of the KV particles) are in a good agreement with the simulation results for dilute suspensions of capsules. For non-dilute suspensions, the corresponding predictions start to deviate from the simulation results and experimental data at sufficiently large particle concentrations, but they are still in relative good qualitative agreement with both simulation and experimental results. In any event, these comparisons suggest that simpler, *analytical* constitutive models for suspensions of viscoelastic particles (with uniform properties), such as the one developed in the present chapter, may be useful in describing at least some of the rheological features of more complex suspensions, including suspensions of capsules and vesicles.

Chapter 5

Rheology of non-dilute suspensions of soft viscoelastic particles in yield stress fluids

In this study, we present a homogenization-based model for the macroscopic, rheological behavior of non-colloidal suspensions of initially spherical, viscoelastic particles in yield stress fluids, subjected to uniform flows. The constitutive behavior of the suspending fluid is characterized by the Herschel-Bulkley (HB) model, and the particles are assumed to be neutrally buoyant solids characterized by a finite-strain Kelvin-Voigt viscoelastic behavior. The proposed model makes use of the “linear comparison composite” technique of Ponte Castañeda (1991) to transform the homogenization problem for the instantaneous response of the suspensions of viscoelastic particles in a HB fluid into the corresponding problem for the suspensions of the same particles in a Newtonian fluid with a suitably-chosen viscosity. The latter problem is then addressed by the homogenization model, developed in Chapter 4, and when combined with appropriate evolution laws for the relevant microstructural variable, the model provides a complete description for the time-dependent response of the suspensions. With the objective of illustrating the key features of our model, we consider the example of the suspensions of elastic particles in HB fluids under shear flow conditions. The results provide a broad picture of the influence of the HB fluid and particle constitutive properties as well as the particle volume fraction on the effective time-dependent as well as steady-state behaviors of the suspensions. For the special case of non-deformable particles, our model predicts that the suspensions behave like a HB fluid with modified properties, consistent with the results of Chateau et al. (2008).

5.1 Introduction

Suspensions of micron-sized, *deformable* particles in a non-Newtonian fluid constitute a large class of industrial fluids including filled polymers, food pastes, cosmetics and so on. The study of the rheological behavior of these suspensions is important in order to understand and tune the flow properties for a desired application. In particular, we are interested in suspensions of particles in yield stress fluids. These fluids exhibit a solid-like behavior before the stress reaches a threshold value (known as the yield stress), beyond which they behave as liquids with a non-linear stress-strain rate relationship. The mechanical behavior of these fluids can be well described by the Herschel-Bulkley (HB) model. Based on this model, the yield stress fluids behave as rigid solids when subjected to shear stresses lower than the yield stress, and once the yield stress is exceeded, they flow with a nonlinear stress-strain rate relationship, either as shear-thinning or as shear-thickening fluids. Roughly speaking, the HB model combines the classical Bingham model for simple rate-independent yield stress behavior with the power-law model for rate-dependent viscoplastic behavior, and therefore, it provides an enhanced constitutive description to capture both yield stress and rate-dependency behaviours of a broad class of time-independent, non-Newtonian fluids. A one-dimensional form of this model can be written as

$$\begin{cases} \dot{\gamma} = 0, & \text{if } \tau < \tau_0, \\ \dot{\gamma} = [(\tau - \tau_0)/K]^{(1/n)}, & \text{if } \tau \geq \tau_0, \end{cases} \quad (5.1)$$

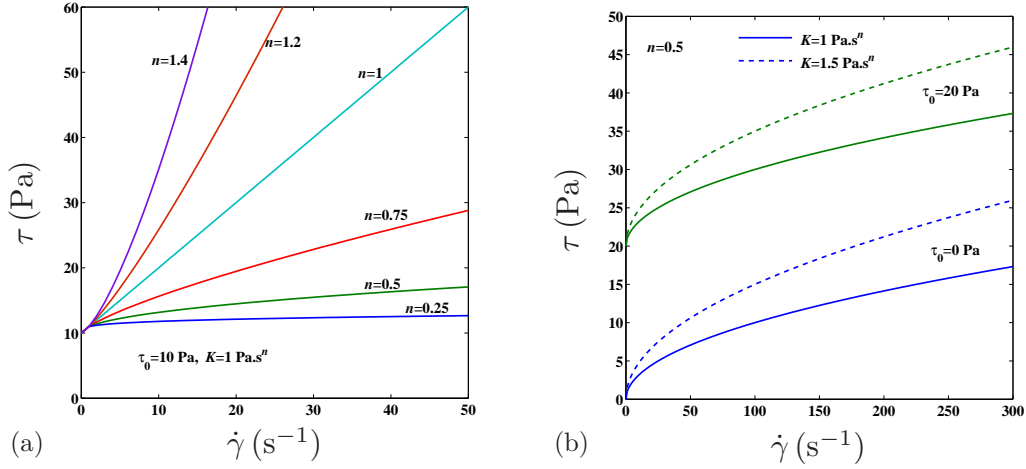


Figure 5.1: Examples of the Herschel-Bulkley model (5.1).

where τ and τ_0 denote the shear stress and the yield stress, respectively, K is the consistency constant, n is the power-law index, and $\dot{\gamma}$ denotes the shear strain-rate. Figure 5.1 presents some numerical examples of constitutive model (5.1) for representative values of material properties τ_0 , K and n .

The problem of predicting the rheological behavior of the suspension of *rigid* particles in a yield stress fluid has often been addressed in the literature through experimental and/or empirical means (see Laven and Stein, 1991; Ancey and Jorrot, 2001; Mahaut et al., 2008, to cite only a few). On the other hand, homogenization methods developed in the context of nonlinear heterogeneous media have emerged as a promising *theoretical* approach to address this problem. In particular, Ponte Castañeda (1991) proposed a *variational* principle which can be used to obtain bounds and estimates for the properties of nonlinear composite materials from the corresponding bounds and estimates for the effective properties of an optimally chosen “linear comparison composite” (LCC). In the past 20 years, applications of this method have been mainly explored for viscoplastic solid composites (Ponte Castañeda, 1991; Zaidman and Ponte Castañeda, 1996, among others). However, through the well-known analogy between the constitutive behavior for a viscoplastic solid and a yield stress fluid, some authors have applied this method to address the effective behavior of suspensions of particles in yield stress fluids. Among them, Ponte Castañeda (2003) studied application of the variational principle for suspensions of two-dimensional (circular), rigid particles in a Bingham fluid which is a special case of the HB fluid (corresponding to $n = 1$). Also, more recently, making use of the variational principle, Chateau et al. (2008) developed a homogenization-based model to provide an estimate for the effective viscosity of suspensions of rigid spherical particles in a HB fluid. In these studies, the authors investigated the purely mechanical contribution of an isotropic distribution of rigid particles to the yield stress fluids behavior, and they found that the variational estimates for the effective behavior of these suspensions predict the same type of behavior as in the corresponding plain yield stress fluid with appropriately modified constants for the fluid.

The above-mentioned studies are limited to the case of non-deformable (rigid) particles. However, when the particles are deformable, it is known that their deformability and constitutive properties can strongly influence rheology of suspensions of these particles in a viscous fluid. Therefore, it is both of theoretical and practical interests to investigate how the deformability and constitutive properties of the particles suspended in a yield stress fluid affects the homogenized behavior of the suspension. To the best of our knowledge, the theoretical investigations of this kind are not present in the literature, although there are several studies dealing with the rheology of suspensions of deformable particles in a *Newtonian* fluid. In a pioneering work, Roscoe (1967) studied the steady-state behavior of dilute suspensions of solid viscoelastic spheres in a Newtonian fluid allowing the finite strains in the particles. In closely related work, Goddard and Miller (1967) investigated the time-dependent behavior of a viscoelastic sphere in a Newtonian fluid within the limits of small deformations of the particle. Later on, Goddard (1977) studied the time-dependent rheological properties of highly concentrated suspensions of elastic particles in a Newtonian fluid, again, within the small deformation limit. In a more recent study, making use of a polarization technique, Gao et al. (2011) developed a finite-strain method to characterize the time-dependent response of dilute suspensions of neo-Hookean particles in a Newtonian fluid under Stokes flow conditions. They considered applications of their method to the dilute suspensions of neo-Hookean particles in a shear flow (Gao et al., 2012) and in an extensional flow (Gao et al., 2013). In Chapter 4, building on Gao et. al’s work, we developed a homogenization-based model to estimate the time-dependent rheological behavior of non-dilute suspensions of soft viscoelastic spheres in a Newtonian fluid, again, under Stokes flow conditions. In Chapter 4, we formulated the homogenization problem for the suspensions in terms of the corresponding problem for a composite system whose local behavior is mathematically analogous to “thermoelastic” composites. Based on this analogy, the authors made use of the Hashin–Shtrikmann–Willis (HSW) homogenization theory (Hashin and Shtrikman, 1963; Willis, 1977) and provided homogenized estimates for the *instantaneous* response of the suspensions, together with appropriate evolution laws for the relevant microstructural variables. The distinct advantage in the exact solution of Gao et al. (2011) and, similarly, in the estimates of Chapter 4, is that they account for the simultaneous deformation and rotation of particles in the macroscopic time-dependent behavior of the suspensions of the particles, when subjected to uniform flows. The results of these works at the steady state were successfully compared with those provided in the earlier work of Roscoe (1967).

Our goal in the present study is to investigate the rheological properties of non-dilute suspensions of deformable viscoelastic particles in a yield stress fluid using a homogenization approach in the regime of arbitrarily large deformations. Dense suspensions of colloidal particles is typically the origin of the yielding behavior in these fluids. In this study, however, we focus on the suspensions of the non-colloidal particles in these fluids, assuming the separation of length scale between the fluid microstructure and the non-colloidal particles. In other words, we assume that the size of the viscoelastic particles is much larger than the typical size of the colloidal particles so that we can neglect Brownian forces acting on the viscoelastic particles. Also, we confine our attention to Stokes flow regime (i.e., $Re \rightarrow 0$), where viscous forces dominate over the inertial effects. Towards our goal, we make use of the variational principle of Ponte Castañeda (1991) to replace the homogenization

problem for finding the effective (instantaneous) behavior of suspensions of viscoelastic particles in yield stress fluids by a corresponding problem for a (fictitious) LCC, consisting of the same viscoelastic particles suspended in a Newtonian fluid with a suitably-chosen viscosity, denoted by $\eta^{(1)}$. The latter problem is, in fact, the very same problem addressed in Chapter 4. Therefore, we recall pertinent estimates for the LCC from Chapter 4, which together with optimality equations for the unknown value of $\eta^{(1)}$, can be used to obtain corresponding estimates for the instantaneous response of the actual suspensions of interest. Finally, these estimates, when combined with nonlinear equations for the evolution of the stress field in the particles, as well as for the shape and orientation of the particles, can be used to characterize the macroscopic, time-dependent rheological behavior of the suspensions in uniform flows.

The structure of the paper is as follows. Section 5.2 addresses the constitutive behavior of the suspending fluid and the deformable particles as well as and the types of particulate microstructures considered in this work. We consider suspensions of Kelvin-Voigt (KV) viscoelastic particles in yield stress fluids whose rheological behavior is characterized by the HB model. In section 5.3, we lay out the homogenization strategy. We first approximate the instantaneous macroscopic stress in the suspensions by that of a suitably-chosen LCC, which can in turn be given in terms of the macroscopic strain-rate tensor and the current values of the average stress inside the particle and the relevant microstructural variables. Next, we make use of the consistent evolution equations for these variables and the particle stress to obtain the time-dependent macroscopic response of the suspensions. Lastly, in this section, we provide explicit expressions for the particle stress and the microstructural variables at a steady state. In section 5.4, we apply our model to suspensions of initially spherical, Gent hyperelastic particles (which are a special case of KV particles in the purely elastic limit) in HB fluids subjected to a shear flow, and provide representative numerical examples. Finally, some conclusions are drawn in section 5.5.

5.2 Suspensions of viscoelastic particles in a nonlinear viscous fluid

In this work, we consider *random* suspensions of viscoelastic particles in a Herschel-Bulkley (HB) fluid (matrix phase). We assume that the particles and fluid phases have the same density, so that the particles are neutrally buoyant in the fluid. In this section, we first describe in some detail the *local* constitutive behavior of the fluid and particle phases, and then define pertinent microstructural variables to characterize the *instantaneous* microstructure of the suspensions. Following this section, our aim will be to deliver estimates for the macroscopic rheological response and associated microstructure evolution in these suspensions under uniform flow conditions.

We begin with a brief review of the basic kinematic relations. Under the application of mechanical loadings, a material point \mathbf{X} in the reference configuration of the particle moves to a new point \mathbf{x} at time t in the deformed configuration of the particle. In the Lagrangian description of the motion, the deformation is described by a continuous and one-to-one mapping $\mathbf{x}(\mathbf{X}, t)$. The deformation gradient tensor $\mathbf{F} = \text{Grad } \mathbf{x}$ (with Cartesian components $F_{ij} = \partial x_i / \partial X_j$) then serves to characterize

the deformation of the material. We will also make use of the right and left Cauchy-Green tensors (the latter known as the Finger tensor), which are defined as $\mathbf{C} = \mathbf{F}^T \mathbf{F}$ and $\mathbf{B} = \mathbf{F} \mathbf{F}^T$, respectively. Correspondingly, in the Eulerian description, the motion is described by the velocity field $\mathbf{v}(\mathbf{x}, t)$, and the velocity gradient tensor $\mathbf{L} = \text{grad } \mathbf{v}$ serves to characterize the deformation rate, which is related to the deformation gradient by $\mathbf{L} = \dot{\mathbf{F}} \mathbf{F}^{-1}$, with $\dot{\mathbf{F}}$ denoting the (material) time derivative of \mathbf{F} . We will also make use of the Eulerian strain-rate and vorticity tensors, given by $\mathbf{D} = \frac{1}{2}(\mathbf{L} + \mathbf{L}^T)$ and $\mathbf{W} = \frac{1}{2}(\mathbf{L} - \mathbf{L}^T)$, respectively.

5.2.1 Constitutive behavior of the phases

Viscoelastic particles

We assume that the suspended particles are homogeneous and made of incompressible, isotropic solids. In this work, we consider viscoelastic particles whose constitutive behavior is characterized by a finite-strain Kelvin-Voigt (KV) model. This model consists of a hyperelastic spring and a dashpot connected in parallel. For the incompressible KV material, the Cauchy stress tensor $\boldsymbol{\sigma}$ can be written as (Joseph, 1990)

$$\boldsymbol{\sigma} = -p' \mathbf{I} + \boldsymbol{\tau}, \quad \boldsymbol{\tau} = \boldsymbol{\tau}_e + \boldsymbol{\tau}_v, \quad (5.2)$$

where p' is an arbitrary hydrostatic pressure due to the incompressibility constraint, \mathbf{I} is the identity tensor, and $\boldsymbol{\tau}_e$ and $\boldsymbol{\tau}_v$ are the elastic and viscous parts of the total “extra” stress tensor $\boldsymbol{\tau}$ in the particle, respectively. In general, $\boldsymbol{\tau}$ is not deviatoric ($\text{tr}(\boldsymbol{\tau}) \neq 0$), so that the actual hydrostatic pressure p is given by $p = p' - \text{tr } \boldsymbol{\tau}$.

The elastic stress $\boldsymbol{\tau}_e$ may be described in terms of a stored-energy function $\psi(\mathbf{C})$, through

$$\boldsymbol{\tau}_e = 2 \mathbf{F} \frac{\partial \psi(\mathbf{C})}{\partial \mathbf{C}} \mathbf{F}^T, \quad \det(\mathbf{F}) = 1. \quad (5.3)$$

In Chapter 4, we presented a fairly general form of the function $\psi(\mathbf{C})$, describing *generalized neo-Hookean* behavior, to characterize the elastic part of the isotropic KV particles. In this work, we make use of a special case of this form known as the *Gent* constitutive model (Gent, 1996). Making use of the Gent energy function (given by relation (4.6)), the corresponding extra stress tensor $\boldsymbol{\tau}_e$ can be expressed as

$$\boldsymbol{\tau}_e = \frac{\mu J_m}{J_m - I + 3} \mathbf{B} - \mu \mathbf{I}, \quad \det(\mathbf{F}) = 1, \quad (5.4)$$

where μ is the ground state shear modulus of the elastic particle, and $I = \text{trace}(\mathbf{B})$. The above constitutive relation has been shown to provide good agreement with experimental data for rubber-like materials (Ogden et al., 2004), as it accounts for the significant stiffening in such materials at large stretches. In particular, the dimensionless parameter $J_m > 0$ in (5.4), known as the *strain-locking* parameter, identifies limiting value for $I - 3$ at which the elastic material becomes inextensible. Note that, in the limit as $J_m \rightarrow \infty$, the Gent model (5.4) reduces to the neo-Hookean model, which ignores the stiffening at large stretches.

For our purposes in this work, it is useful to derive a *rate* (hypo-elastic) form of the constitutive relation (5.4). To this end, we make use of the upper-convected (or Truesdell) time derivative,

defined as

$$\overset{\nabla}{\mathbf{A}} = \dot{\mathbf{A}} - \mathbf{L}\mathbf{A} - \mathbf{A}\mathbf{L}^T \quad (5.5)$$

where \mathbf{A} is a symmetric second-order tensor, and $\dot{\mathbf{A}} = (\partial\mathbf{A}/\partial t) + \mathbf{v} \cdot \nabla\mathbf{A}$ denotes the material time derivative of the tensor \mathbf{A} . Taking the above time derivative from both side of relation (5.4), and making use of the fact that $\overset{\nabla}{\mathbf{B}} = \mathbf{0}$ (Joseph, 1990), $\overset{\nabla}{\boldsymbol{\tau}}_e$ for the Gent model (5.4) can be expressed as

$$\overset{\nabla}{\boldsymbol{\tau}}_e = 2\mu\mathbf{D} + \frac{2}{\mu J_m} \text{tr}[\mathbf{D}(\boldsymbol{\tau}_e + \mu\mathbf{I})](\boldsymbol{\tau}_e + \mu\mathbf{I}). \quad (5.6)$$

Also, we note that, in deriving the above relation, we have expressed the tensor \mathbf{B} in term of $\boldsymbol{\tau}_e$ by inverting the constitutive relation (5.4). It is worth mentioning that the constitutive relations (5.4) and (5.6) reduce to the well-known neo-Hookean expressions (Joseph, 1990) in the limit as $J_m \rightarrow \infty$, namely,

$$\boldsymbol{\tau}_e = \mu(\mathbf{B} - \mathbf{I}), \quad \text{and} \quad \overset{\nabla}{\boldsymbol{\tau}}_e = 2\mu\mathbf{D}. \quad (5.7)$$

Going back to the general relations (5.2) for the KV material, the viscous part of the extra stress can likewise be described in terms of a dissipation potential ϕ , which is taken to be a function of the second invariant of \mathbf{D} , via

$$\boldsymbol{\tau}_v = \frac{\partial\phi(D_{eq})}{\partial\mathbf{D}}, \quad \text{tr}(\mathbf{D}) = 0, \quad (5.8)$$

where $D_{eq} = \sqrt{2\mathbf{D} \cdot \mathbf{D}}$ is the equivalent strain-rate. In this work, for simplicity, we will restrict our attention to a quadratic form of the potential, given by $\phi(\mathbf{D}) = (\eta^{(2)}/2) D_{eq}^2$, where $\eta^{(2)}$ denotes the constant viscosity of the particle material. Making use of this form in (5.8), we find the following linear constitutive relation for $\boldsymbol{\tau}_v$

$$\boldsymbol{\tau}_v = 2\eta^{(2)}\mathbf{D}, \quad (5.9)$$

Finally, we note that the set of constitutive relations for KV particles reduce to those for purely elastic particles by taking the limit as the viscosity $\eta^{(2)}$ goes to zero. In this limit, the viscous part of the stress vanishes ($\boldsymbol{\tau}_v = \mathbf{0}$) and the elastic part coincides with the total stress ($\boldsymbol{\tau}_e = \boldsymbol{\tau}$). Therefore, for the case of (incompressible) Gent particles, the constitutive relation for the extra stress tensor ($\boldsymbol{\tau}$) and its evolution ($\overset{\nabla}{\boldsymbol{\tau}}$) are given by (5.4) and (5.6), respectively, with $\boldsymbol{\tau}_e$ being replaced by $\boldsymbol{\tau}$.

Nonlinear viscous fluid

We assume that the suspending fluid is an incompressible Herschel-Bulkley fluid. These fluids do not deform or flow until the local shear stress reaches the yield stress τ_0 . Once the yield stress is exceeded, the material flows like a fluid with a non-linear stress-strain rate relationship either as a shear-thinning fluid, or a shear-thickening one. The total (Cauchy) stress tensor $\boldsymbol{\sigma}$ in the fluid is defined by expressions (5.2) with $\boldsymbol{\tau}_e = \mathbf{0}$ and $\boldsymbol{\tau} = \boldsymbol{\tau}_v$ because the fluid does not have elastic properties. Also, the extra stress tensor $\boldsymbol{\tau}$ is deviatoric in the fluid, so that $p' = p = -\text{tr}(\boldsymbol{\sigma})/3$ defines the actual hydrostatic pressure in the fluid. Then, building on the 1-D model (5.1), the tensorial form of the constitutive relations for a HB fluid can be expressed as (Herschel and Bulkley,

1926; Alexandrou et al., 2001)

$$\begin{cases} \mathbf{D} = \mathbf{0}, & \text{if } \tau_{eq} < \tau_0, \\ \boldsymbol{\tau} = \frac{2}{D_{eq}} (\tau_0 + K D_{eq}^n) \mathbf{D}, & \text{if } \tau_{eq} \geq \tau_0, \end{cases} \quad (5.10)$$

where $\tau_{eq} = \sqrt{\boldsymbol{\tau} \cdot \boldsymbol{\tau} / 2}$ is the equivalent shear stress. Since the material is incompressible, the constraint $\text{tr}(\mathbf{D}) = 0$ is enforced. It is also important to clarify that the second constitutive relation in (5.10) is, in fact, describing the strain-rate tensor \mathbf{D} as a function of the stress tensor $\boldsymbol{\tau}$ for the condition of $\tau_{eq} \geq \tau_0$, similar to the corresponding one-dimensional form of the relation in (5.1). For the case of $\tau_0 = 0$, the constitutive model (5.10) represents the class of power-law fluids, where the cases of $n < 1$ and $n > 1$ correspond to shear-thinning (also known as pseudoplastic) and shear-thickening (also known as dilatant) fluids, respectively, while the special case of $n = 1$ corresponds to an incompressible Newtonian fluid, with K being the constant viscosity of the fluid. Also, for the case of $\tau_0 > 0$ and $n = 1$, the model reduces to a Bingham fluid.

5.2.2 Microstructure

In this chapter, we restrict our attention to suspensions consisting of initially spherical, deformable, viscoelastic particles distributed isotropically in a Herschel-Bulkley fluid matrix. Much similar to the case of suspensions of deformable particles or capsules in a Newtonian fluid (see, e.g., Roscoe, 1967; Gao et al., 2011; Clausen et al., 2011; Avazmohammadi and Ponte Castañeda, 2014), we expect that the deformable particles suspended in a non-Newtonian fluid change their shape and orientation when subjected to a shear flow. In particular, earlier theoretical studies for *dilute* concentrations of neo-Hookean particles in a Newtonian fluid (Roscoe, 1967; Gao et al., 2011) demonstrated that the initial spherical particles, when subjected to a shear flow, deform *exactly* into a series of ellipsoidal shapes- with continuously changing aspect ratios and principal directions- until they reach a final steady state with a fixed shape and orientation with respect to flow direction (if such a steady state exists.) This is because, in this case, the deformation field generated inside the particle is uniform. Interestingly, recent numerical simulations for the dilute suspensions of neo-Hookean particles in a non-Newtonian (viscoelastic) fluid (Villone et al., 2014b,a) revealed that, similar to the case of a suspending Newtonian fluid, the initial spherical particles deform into a shape very close to an ellipsoid until they reach a steady state. In particular, the authors (Villone et al., 2014b) did not observe more than 2-3% deviation of the particle shape from an exact ellipsoid throughout the deformation history of the particle. For *non-dilute* suspensions of particles in a non-Newtonian fluid, however, we may expect that the particles attain a shape with larger deviations from an ellipsoid depending on the value of the particle concentration—these deviations would be expected due to the higher fluctuation of deformation fields inside the particles as a consequence of the particle interactions. Moreover, we may expect that the particle interactions would affect the orientation and relative position of individual particles such that the particles in the deformed configuration would not all exhibit the same exact orientation, and the two- and higher-point correlation functions for the particle centers would cease to be isotropic. Nevertheless, as discussed in Chapter 4 (see subsection

4.2.2), for the purpose of providing homogenized constitutive models for the instantaneous response of the non-dilute suspensions, as well as for the evolution of their microstructure, it is reasonable to define suitable homogenized microstructural variables serving to characterize the evolution of the “average” shape and orientation of the particles, as well as of the particle distribution statistics, as functions of the deformation. Here, we adopt the microstructural model proposed in Chapter 4 to characterize microstructure of the suspensions of interest in this work. This model generalizes the earlier model proposed by Kailasam and Ponte Castañeda (1998) in the context of purely viscous systems (where the matrix and particles are characterized by general nonlinear viscous behaviors) at *moderate* concentrations of the particles to account for *elastic* effects in the particles, by including the average elastic stress in the particles as an additional microstructural variable. This model assumes that at the present time all the initially (at zero time) spherical particles become ellipsoidal with identical shape and orientation as described by a *representative* (average) ellipsoid

$$\Omega^{(2)} = \{ \mathbf{x} : |(\mathbf{Z})^{-T} \mathbf{x}| \leq 1 \}, \quad (5.11)$$

where \mathbf{Z} is the so-called shape tensor. In addition, in this microstructural model, we assume that the relative position of the particles is described by two-point correlation functions having “ellipsoidal” symmetry. As discussed subsection 4.2.2 in more detail, for simplicity, we further assume that the shape and orientation of the distribution functions are identical to those of the individual particles, described by (5.11).

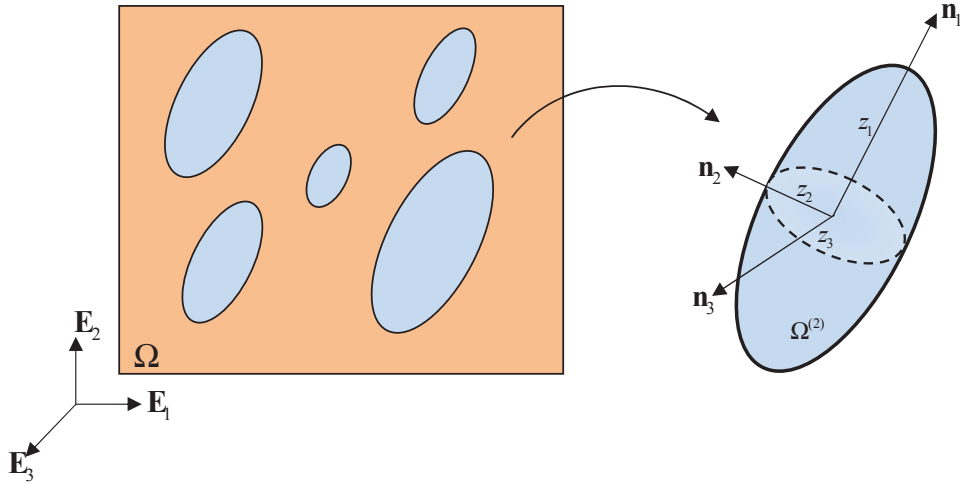


Figure 5.2: Graphical representation of the microstructure in the suspension at a given time t . The figure shows a “representative ellipsoid” with aspect ratios $w_1 = z_2/z_1$ and $w_2 = z_3/z_1$, and with principal (orthonormal) coordinate system \mathbf{n}_1 , \mathbf{n}_2 and $\mathbf{n}_3 = \mathbf{n}_1 \times \mathbf{n}_2$ (which rotates relative to the laboratory axes $\{\mathbf{E}_i\}$, $i = 1, 2, 3$.)

Figure 5.2 depicts an snapshot of the idealized microstructure in the suspension at the present time t (note that the particle are spherical at $t = 0$.) The triad \mathbf{E}_i , $i = 1, 2, 3$ denotes the fixed laboratory coordinates. A schematic representation of the relevant microstructural variables is also

shown in this figure. The three orthonormal vectors \mathbf{n}_1 , \mathbf{n}_2 and $\mathbf{n}_3 = \mathbf{n}_1 \times \mathbf{n}_2$ are used to characterize the principal axes of the particle. In this principal coordinate system, the shape tensor \mathbf{Z} has the matrix representation $\mathbf{Z} = \text{diag}(z_1, z_2, z_3)$ with z_1, z_2, z_3 being the three principal semi-axes of the ellipsoid. For future references, it is convenient to define two aspect ratios $w_1 = z_2/z_1$ and $w_2 = z_3/z_1$ which fully characterize the shape of the particle.

Consistent with the above-described microstructural model, we choose the following set of variables to characterize the state of the ellipsoidal microstructure:

$$\mathcal{S} = \{w_1, w_2, \mathbf{n}_1, \mathbf{n}_2, \mathbf{n}_3 = \mathbf{n}_1 \times \mathbf{n}_2\}. \quad (5.12)$$

5.3 Macroscopic response

In this section, our aim is to determine macroscopic constitutive relations for the rheological behaviour of the suspensions described in the previous section. As discussed in subsection 5.2.2, the suspension, under applied flow, goes through a sequence of microstructures, approximately consisting of aligned ellipsoids that are distributed with ellipsoidal two-point statistics (with the same shape and orientation), which evolve in time, starting from an initial state. Similar to our approach in Chapter 4, in this work, we break up the analysis of the macroscopic *time-dependent* behavior of the suspensions into two parts. In the first part, we assume that at the present instant the microstructure is given, and make use of this information to estimate the *instantaneous* response of the suspension by using a variational homogenization approach. In the second part, we provide consistent *evolution* equations for the relevant microstructural variables making use of the corresponding instantaneous homogenization estimates for the average deformation and stress fields in the particles. Finally, in this section, we make use of the results for the instantaneous response of the suspension and the evolution equations to provide associated estimates for the *steady-state* behavior of the suspension, if they exist. For definiteness, we use the superscripts (1) and (2) to denote variables associated with the fluid (matrix phase) and particle phase, respectively. However, for clarity, we drop these superscripts from the variables that exist only in one phase, such as μ and J_m in the particle phase and K and τ_0 in the fluid phase.

5.3.1 Homogenization estimates for the instantaneous response

We consider a *representative volume element* (RVE) of the suspension, occupying a volume Ω with boundary $\partial\Omega$. The fluid and particle phases are in turn assumed to occupy volumes $\Omega^{(1)}$ and $\Omega^{(2)}$, respectively, such that $\Omega = \Omega^{(1)} + \Omega^{(2)}$. We assume that the RVE satisfies the *separation of length scales* hypothesis implying that the average size of the neutrally buoyant particles is much smaller than the size of the RVE. We further assume the Stoke's condition in the fluid phase, such that

$$Re = \frac{\rho^{(1)} \dot{\gamma}^{2-n} d_p^2}{K} \rightarrow 0, \quad (5.13)$$

where $\rho^{(1)}$ is the density of the fluid, $\dot{\gamma}$ is a measure of the macroscopic strain rate and d_p is a measure of the particle diameter.

Noting that the microstructure of the RVE is *statistically* uniform, an *affine* velocity boundary condition on the boundary of the RVE ($\partial\Omega$) will produce a uniform *macroscopic* stress field in the RVE. Thus, the suspension is subjected to the boundary condition

$$\mathbf{v}(\mathbf{x}) = \bar{\mathbf{L}}\mathbf{x}, \quad \text{on } \partial\Omega, \quad (5.14)$$

where $\bar{\mathbf{L}}$ ($\text{tr } \bar{\mathbf{L}} = 0$) is the macroscopic, or average velocity gradient, defined by¹

$$\bar{\mathbf{L}} = \frac{1}{\text{Vol}(\Omega)} \int_{\Omega} \mathbf{L} \, dV. \quad (5.15)$$

Similarly, the average or macroscopic Cauchy stress is defined as

$$\bar{\boldsymbol{\sigma}} = \frac{1}{\text{Vol}(\Omega)} \int_{\Omega} \boldsymbol{\sigma} \, dV. \quad (5.16)$$

At this point, it is also relevant to define the phase averages of the strain-rate field over phase r ($r = 1, 2$) as

$$\bar{\mathbf{D}}^{(r)} = \frac{1}{\text{Vol}(\Omega^{(r)})} \int_{\Omega^{(r)}} \mathbf{D} \, dV, \quad (5.17)$$

such that

$$\bar{\mathbf{D}} = \frac{1}{2}(\bar{\mathbf{L}} + \bar{\mathbf{L}}^T) = c^{(1)}\bar{\mathbf{D}}^{(1)} + c^{(2)}\bar{\mathbf{D}}^{(2)}, \quad (5.18)$$

with the $c^{(1)}$ and $c^{(2)}$ denoting the volume fractions of fluid and particle phases, respectively. Similarly, defining $\bar{\boldsymbol{\tau}}^{(1)}$ and $\bar{\boldsymbol{\tau}}^{(2)}$ as the averages of the extra stress tensor in the fluid and particle phases, respectively, the macroscopic stress, as defined by (5.16), can be rewritten as

$$\bar{\boldsymbol{\sigma}} = -\bar{p}' \mathbf{I} + c^{(1)}\bar{\boldsymbol{\tau}}^{(1)} + c^{(2)}\bar{\boldsymbol{\tau}}^{(2)}, \quad (5.19)$$

where \bar{p}' is an indeterminate hydrostatic pressure associated with the overall incompressibility constraint ($\text{tr}(\bar{\mathbf{D}}) = 0$) in the suspension.

Given the local constitutive relations (5.2), (5.4), and (5.9) for the particle phase and relation (5.10) for the fluid phase, and given the instantaneous microstructure (5.12), the effective (instantaneous) behavior of the suspension can be described by the relation between the average strain-rate tensor $\bar{\mathbf{D}}$ and the average stress tensor $\bar{\boldsymbol{\sigma}}$ over the RVE Ω . The problem of finding this relation can be conveniently stated in a variational framework if we can formulate the local constitutive relations of the phases in terms of appropriate *dissipation* potentials. To this end, we introduce the following

¹This follows from the *mean value theorem for the strain rate* (e.g., Ponte Castañeda and Suquet, 1998) stating that the (volume) average of the local strain-rate tensor \mathbf{L} over the RVE under the affine velocity boundary condition (5.14) is precisely $\bar{\mathbf{L}}$.

modified dissipation potentials

$$W^{(r)}(\mathbf{D}) = \phi^{(r)}(D_{eq}) + \boldsymbol{\tau}_e^{(r)} \cdot \mathbf{D}, \quad \text{tr}(\mathbf{D}) = 0, \quad (5.20)$$

such that the local constitutive relation of the phases can be written as

$$\boldsymbol{\sigma} = -p' \mathbf{I} + \boldsymbol{\tau}, \quad \text{where} \quad \boldsymbol{\tau} = \frac{\partial W^{(r)}}{\partial \mathbf{D}} = \frac{1}{D_{eq}} \phi'^{(r)}(D_{eq}) \mathbf{D} + \boldsymbol{\tau}_e^{(r)}. \quad (5.21)$$

In the above relations, $\boldsymbol{\tau}_e^{(r)}$ is the “elastic” stress tensor in phase r which is assumed to be known at the present instant, p' is an indeterminate hydrostatic pressure, and $\phi^{(r)}$ denote (purely viscous) dissipation potentials which are only function of the equivalent strain-rate D_{eq} . We further emphasize that the elastic stresses $\boldsymbol{\tau}_e^{(r)}$ are considered to be fixed in taking the derivative with respect to \mathbf{D} . In particular, the local constitutive relation (5.21) recovers the (purely viscous) constitutive relation (5.10), by choosing the following properties for the fluid matrix (Chateau et al., 2008)

$$\phi^{(1)}(D_{eq}) = \tau_0 D_{eq} + \frac{K}{n+1} (D_{eq})^{n+1}, \quad \text{and} \quad \boldsymbol{\tau}_e^{(1)} = \mathbf{0}. \quad (5.22)$$

On the other hand, relation (5.21) recovers the (viscoelastic) constitutive relations (5.4) and (5.9) by simply choosing

$$\phi^{(2)}(D_{eq}) = \frac{\eta^{(2)}}{2} D_{eq}^2 \quad \text{and} \quad \boldsymbol{\tau}_e^{(2)} = \boldsymbol{\tau}_e, \quad (5.23)$$

where $\boldsymbol{\tau}_e$ is characterized by the evolution equation (5.6), in the particle phase.

Next, we define the local modified dissipation potential of the suspension as

$$W(\mathbf{x}, \mathbf{D}) = \chi^{(1)}(\mathbf{x}) W^{(1)}(\mathbf{D}) + \chi^{(2)}(\mathbf{x}) W^{(2)}(\mathbf{D}), \quad (5.24)$$

where the characteristic functions $\chi^{(r)}(\mathbf{x})$, $r = 1, 2$ are equal to one if the position vector \mathbf{x} is in phase r (i.e. $\mathbf{x} \in \Omega^{(r)}$) and zero otherwise. Then, making use of the *principle of minimum dissipation* (see, for example, Ponte Castañeda and Suquet, 1998; Avazmohammadi and Ponte Castañeda, 2014), we can define the macroscopic constitutive relation of the suspension, subjected to the boundary condition (5.14), in terms of the effective (modified) dissipation potential $\widetilde{W}(\bar{\mathbf{D}})$ as

$$\bar{\boldsymbol{\sigma}} = -\bar{p}' \mathbf{I} + \bar{\boldsymbol{\tau}}, \quad \text{where} \quad \bar{\boldsymbol{\tau}} = \frac{\partial \widetilde{W}}{\partial \bar{\mathbf{D}}}, \quad (5.25)$$

where \bar{p}' is the Lagrange multiplier associated with the macroscopic incompressibility constraint and $\widetilde{W}(\bar{\mathbf{D}})$ is defined as

$$\widetilde{W}(\bar{\mathbf{D}}) = \min_{\mathbf{D} \in \mathcal{K}} \frac{1}{\text{Vol}(\Omega)} \int_{\Omega} W(\mathbf{x}, \mathbf{D}) \, dV, \quad (5.26)$$

in which \mathcal{K} denotes the set of kinematically admissible strain rates:

$$\mathcal{K} = \{\mathbf{D} \mid \text{there is } \mathbf{v} \text{ such that } \mathbf{D} = (\nabla \mathbf{v} + (\nabla \mathbf{v})^T)/2, \text{ div } \mathbf{v} = 0 \text{ in } \Omega, \text{ and } \mathbf{v} = \bar{\mathbf{L}}\mathbf{x} \text{ on } \partial\Omega\}. \quad (5.27)$$

In Chapter 4, we considered the homogenization problem defined by equations (5.25) and (5.26) for the *instantaneous* response of the viscoelastic composite system characterized by relations (5.20), (5.21), and (5.24), when both dissipation potentials $\phi^{(1)}$ and $\phi^{(2)}$ have the quadratic form $\phi^{(r)}(D_{eq}) = (\eta^{(r)}/2) D_{eq}^2$, with $\eta^{(r)}$ being constant viscosity moduli. For this special case, this homogenization problem is mathematically analogous to the corresponding problem for an incompressible, linear *thermoelastic* composite with elastic moduli $\eta^{(r)}$ and thermal stresses $\tau_e^{(r)}$ (provided that the strain-rate and velocity fields are identified with the strain and displacement fields, respectively). Therefore, in this case, the authors made use of the Hashin-Shtrikman-Willis (HSW) homogenization theory (Hashin and Shtrikman, 1963; Willis, 1977, 1981) (which has been already used for thermoelastic composites), and provided an estimate for the corresponding effective (modified) dissipation function $\widetilde{W}(\bar{\mathbf{D}})$. However, for the problem of interest here, i.e. when $\phi^{(1)}(D_{eq})$ is characterized by non-quadratic form (5.22), we propose to break up the procedure for estimating the effective function $\widetilde{W}(\bar{\mathbf{D}})$ into two parts. First, in subsection 5.3.1, we make use of the variational principal of Ponte Castañeda (1991) to approximate the instantaneous behavior of the composite system, characterized by (5.20)–(5.24), by that of a *linear comparison composite* (LCC), consisting of the same particles suspended in a linear viscous matrix (characterized by a quadratic dissipation potential) with a suitably-chosen viscosity. Second, in subsection 5.3.1, we recall pertinent estimates for the LCC from Chapter 4 to estimate the instantaneous response of the actual nonlinear composite system, characterized by (5.20)–(5.24).

Variational estimates

So far, we formulated the problem of finding the effective (instantaneous) response of the suspension in terms of finding the effective potential $\widetilde{W}(\bar{\mathbf{D}})$ of the suspension, as described by relations (5.25) and (5.26). In this work, we provide an estimate for $\widetilde{W}(\bar{\mathbf{D}})$ by making use of the variational principle of Ponte Castañeda (1991). The central idea of this principle is to express the effective behavior of the nonlinear composite in terms of the effective behavior of a suitably-chosen LCC which has the same microstructure (i.e. same characteristic functions $\chi^{(r)}(\mathbf{x})$) as the actual (nonlinear) composite material. For the class of nonlinear composites (characterized by (5.20)–(5.24)), we construct a (fictitious) LCC made of a linear viscous matrix with constant viscosity $\eta^{(1)}$ and the same particle phase (as characterized by properties (5.23)). We emphasize that the volume fraction, shape and orientation of particles in the LCC are assumed to be the same as those in the nonlinear composite at the given instant. For definiteness, the subscript L has been used to denote the variables associated with the LCC.

Here, we define a LCC with local (modified) dissipation potential

$$W_L(\mathbf{x}, \mathbf{D}; \eta^{(1)}) = \chi^{(1)}(\mathbf{x}) W_L^{(1)}(\mathbf{D}; \eta^{(1)}) + \chi^{(2)}(\mathbf{x}) W_L^{(2)}(\mathbf{D}), \quad (5.28)$$

where the (modified) dissipation potentials $W_L^{(1)}(\mathbf{D}; \eta^{(1)})$ is defined as

$$W_L^{(1)}(\mathbf{D}; \eta^{(1)}) = \eta^{(1)} \mathbf{D} \cdot \mathbf{D}, \quad \text{tr}(\mathbf{D}) = 0, \quad (5.29)$$

with $\eta^{(1)}$ denoting the (as yet unknown) viscosity of the linear viscous matrix. Also, as already mentioned, the particle phase (phase 2) in the LCC is the same as in the nonlinear composite, so that $W_L^{(2)}(\mathbf{D}) = W^{(2)}(\mathbf{D})$, as defined via relations (5.20) and (5.23). Correspondingly, the local constitutive relation of the phases in the LCC can be written as

$$\boldsymbol{\sigma}_L = -p' \mathbf{I} + \boldsymbol{\tau}_L, \quad \text{where} \quad \boldsymbol{\tau}_L = \frac{\partial W_L^{(r)}}{\partial \mathbf{D}} = 2\eta^{(r)} \mathbf{D} + \boldsymbol{\tau}_e^{(r)}, \quad (5.30)$$

where $\boldsymbol{\tau}_e^{(1)} = \mathbf{0}$ and $\boldsymbol{\tau}_e^{(2)} = \boldsymbol{\tau}_e$, as characterized by the evolution equation (5.6).

Following Ponte Castañeda's variational principle, the nonlinear dissipation potential $W^{(1)}(\mathbf{D})$ can then be approximated as

$$\begin{aligned} W^{(1)}(\mathbf{D}) &= \inf_{\eta^{(1)} > 0} \left\{ W_L^{(1)}(\mathbf{D}; \eta^{(1)}) + V^{(1)}(\eta^{(1)}) \right\} \\ &= \inf_{\eta^{(1)} > 0} \left\{ \eta^{(1)} \mathbf{D} \cdot \mathbf{D} + V^{(1)}(\eta^{(1)}) \right\}, \end{aligned} \quad (5.31)$$

where the "error" function $V^{(1)}$ is defined by

$$\begin{aligned} V^{(1)}(\eta^{(1)}) &= \sup_{\mathbf{D}} \left[\widetilde{W}^{(1)}(\mathbf{D}) - \eta^{(1)} \mathbf{D} \cdot \mathbf{D} \right] \\ &= \sup_{D_{eq}} \left[\phi^{(1)}(D_{eq}) - \frac{\eta^{(1)}}{2} D_{eq}^2 \right], \end{aligned} \quad (5.32)$$

where, in the latter equation, use has been made of relation (5.20) and the fact that $\boldsymbol{\tau}_e^{(1)} = \mathbf{0}$.

Now, making use of approximation (5.31) together with relation (5.24) in definition (5.26) for the effective dissipation potential, and interchanging the order of infima over \mathbf{D} and $\eta^{(1)}$, we find the following estimate for the effective potential $\widetilde{W}(\bar{\mathbf{D}})$ (Ponte Castañeda, 1991)

$$\widetilde{W}(\bar{\mathbf{D}}) \leq \inf_{\eta^{(1)} > 0} \left\{ \widetilde{W}_L(\bar{\mathbf{D}}; \eta^{(1)}) + c^{(1)} V^{(1)}(\eta^{(1)}) \right\}, \quad (5.33)$$

where \widetilde{W}_L denotes the effective (modified) dissipation potential of the LCC consisting of the same particle phase suspended in a fictitious Newtonian fluid with viscosity $\eta^{(1)}$. Similar to definition (5.26), the effective potential \widetilde{W}_L is expressed as

$$\widetilde{W}_L(\bar{\mathbf{D}}; \eta^{(1)}) = \min_{\mathbf{D} \in \mathcal{K}} \frac{1}{\text{Vol}(\Omega)} \int_{\Omega} W_L(\mathbf{x}, \mathbf{D}; \eta^{(1)}) \, dV, \quad (5.34)$$

where the set \mathcal{K} is given by (5.27).

The optimality conditions in (5.32) and (5.33) generate a system of algebraic nonlinear equations for the optimal values of the variables $\eta^{(1)}$ and D_{eq} . First, making use of expressions (5.22) in (5.32), the function $V^{(1)}$ can be re-written as

$$V^{(1)}(\eta^{(1)}) = \sup_{D_{eq}} \left(\tau_0 D_{eq} + \frac{K}{n+1} (D_{eq})^{n+1} - \frac{\eta^{(1)}}{2} D_{eq}^2 \right). \quad (5.35)$$

The, the optimality condition in the above equation, known as the *secant* condition, leads to the following relation

$$\tau_0 + K (\hat{D}_{eq})^n = \eta^{(1)} \hat{D}_{eq}, \quad (5.36)$$

where \hat{D}_{eq} denotes the optimal value of D_{eq} in (5.35). Also, making use of (5.35) and noting the fact that $V^{(1)}$ is stationary with respect to \hat{D}_{eq} , the optimality condition in (5.33) reduces to

$$\frac{\partial \widetilde{W}_L(\bar{\mathbf{D}}; \eta^{(1)})}{\partial \eta^{(1)}} = \frac{1}{2} c^{(1)} \hat{D}_{eq}^2. \quad (5.37)$$

In summery, the system of equations (5.36) and (5.37) can be solved for two unknowns $\eta^{(1)}$ and \hat{D}_{eq} . Once these two unknowns are obtained, the effective dissipation potential $\widetilde{W}(\bar{\mathbf{D}})$ can be calculated from (5.33). In turn, noting that estimate (5.33) is stationary with respect to the variable $\eta^{(1)}$, it follows from (5.25) and (5.33) that the variational estimate for the macroscopic Cauchy stress in the suspension can be obtained as

$$\bar{\boldsymbol{\sigma}} = -\bar{p}' \mathbf{I} + \bar{\boldsymbol{\tau}}, \quad \text{where} \quad \bar{\boldsymbol{\tau}} = \frac{\partial \widetilde{W}}{\partial \mathbf{D}} = \frac{\partial \widetilde{W}_L}{\partial \bar{\mathbf{D}}} = \bar{\boldsymbol{\tau}}_L, \quad (5.38)$$

where $\bar{\boldsymbol{\tau}}_L$ denotes the macroscopic extra stress tensor in the LCC, and the second equality (in the second relation) is used instead of the inequality (in (5.33)), in the sense of an approximation. The above results imply that the macroscopic response of the actual composite (characterized by (5.20)–(5.24)) is (approximately) equal to that of the LCC (characterized by (5.28)–(5.30)), calculated at the optimized value of $\eta^{(1)}$. Also, it can be shown that (Idiart and Ponte Castañeda, 2007) the phase averages of the stress and strain-rate fields over each phase in the actual suspension are equal to the same quantities in the corresponding phase in the LCC. Indeed,

$$\bar{\mathbf{D}}^{(r)} = \bar{\mathbf{D}}_L^{(r)}, \quad \bar{\boldsymbol{\tau}}^{(r)} = \bar{\boldsymbol{\tau}}_L^{(r)}, \quad r = 1, 2. \quad (5.39)$$

Similarly, for later references, we note that the second moments of the stress and strain-rate fields in each phase in the actual suspension are also equal to the same quantities in the corresponding phase in the LCC (Idiart and Ponte Castañeda, 2007).

In conclusion, we see from relations (5.38) that the process of determining $\bar{\boldsymbol{\sigma}}$ requires the knowledge on the effective (modified) dissipation potential \widetilde{W}_L of the LCC defined in (5.34). This knowledge is available from the estimates recently provided in Chapter 4 for the effective behavior of the composite characterized by relations (5.28)–(5.30). In the next subsection, we recall the estimates for the potential $\widetilde{W}_L(\bar{\mathbf{D}})$ and the corresponding macroscopic constitutive relation of the LCC from Chapter 4. At the end, it is worth mentioning that for the case of $n \leq 1$, it can be shown that the variational estimate (5.33) is a rigorous upper bound (Ponte Castañeda, 1991) for the effective dissipation potential $\widetilde{W}(\bar{\mathbf{D}})$ (defined in (5.26)), provided that the estimate for the potential \widetilde{W}_L (which will be given in the next subsection) is also a rigorous upper bound for the effective dissipation potential of the LCC, defined in (5.34). On the other hand, for the case of $n > 1$, the estimate (5.33) is still a good *stationary* estimate for $\widetilde{W}(\bar{\mathbf{D}})$.

Estimates for the linear comparison composite

In Chapter 4, we developed a homogenization-based model for the effective behavior of suspensions of initially spherical, viscoelastic particles in a Newtonian fluid (with viscosity $\eta^{(1)}$) under simple flows. In particular, the authors constructed their model by formulating the problem of estimating the (instantaneous) effective behavior of the suspensions in terms of finding an estimate for the effective (modified) dissipation potential of a composite system, characterized by local relations (5.28)–(5.30). Then, to find this estimate, the authors made use of the HSW homogenization theory, which was originally developed for isotropic elastic composites by Hashin and Shtrikman (1963), and extended later for generally anisotropic elastic composites by Willis (1977, 1981). More specifically, the authors made use of the results of Ponte Castañeda and Willis (1995), which is based on the HSW theory, for particulate composites consisting of aligned ellipsoidal particles that are distributed randomly with ellipsoidal two-point correlations in a matrix of a different material. As described in the previous subsection, the composite system Chapter 4 (characterized by local relations (5.28)–(5.30)) is, in fact, the linear comparison composite for our problem of interest in this work. Therefore, in this subsection, we recall the relevant results for the LCC from Chapter 4 for estimating the macroscopic response of the actual suspension from (5.38). Before proceeding, we note that we drop the subscript L from the stress and strain-rate phase averages in the LCC as they are equal to the corresponding variables in the actual suspension (see relations (5.39).)

Here, we recall the final estimate for the effective potential $\widetilde{W}_L(\bar{\mathbf{D}})$ from expression (3.17) in the paper by Avazmohammadi and Ponte Castañeda (2014) which is written as

$$\widetilde{W}_L(\bar{\mathbf{D}}) = \eta^{(1)} \bar{\mathbf{D}} \cdot \bar{\mathbf{D}} + c \left(\eta^{(2)} - \eta^{(1)} \right) \bar{\mathbf{D}}^{(2)} \cdot \bar{\mathbf{D}} + \frac{c}{2} \bar{\boldsymbol{\tau}}_e^{(2)} \cdot \left(\bar{\mathbf{D}}^{(2)} + \bar{\mathbf{D}} \right), \quad (5.40)$$

where

$$\bar{\mathbf{D}}^{(2)} = \left\{ \mathbb{I} - 2(1-c) \left(\eta^{(1)} - \eta^{(2)} \right) \mathbb{P} \right\}^{-1} \left\{ \bar{\mathbf{D}} - (1-c) \mathbb{P} \bar{\boldsymbol{\tau}}_e^{(2)} \right\} \quad (5.41)$$

is the corresponding estimate for the average strain-rate tensor $\bar{\mathbf{D}}^{(2)}$ over the particle phase, available from relation (3.18) in Avazmohammadi and Ponte Castañeda (2014). In these expressions, $c = c^{(2)}$ is the volume fraction of the particle phase, $\bar{\boldsymbol{\tau}}_e^{(2)}$ is the (instantaneous) average elastic stress in the particles which is assumed to be known at the given instant², and \mathbb{P} is a microstructural (Eshelby-type) tensor which will be defined shortly. It is also relevant to provide a corresponding estimate for the average vorticity tensor in the particle phase, denoted by $\bar{\mathbf{W}}^{(2)}$, available from relation (3.19) in Avazmohammadi and Ponte Castañeda (2014). This relation is given by

$$\bar{\mathbf{W}}^{(2)} = \bar{\mathbf{W}} + (1-c) \mathbb{R} \left[2 \left(\eta^{(1)} - \eta^{(2)} \right) \bar{\mathbf{D}}^{(2)} - \bar{\boldsymbol{\tau}}_e^{(2)} \right], \quad (5.42)$$

where \mathbb{R} is the microstructural tensor. The fourth-order tensors \mathbb{P} and \mathbb{R} in the above relations can be expressed as

$$\mathbb{P} = \frac{1}{4\pi |\mathbf{Z}|} \int_{|\boldsymbol{\xi}|=1} \mathbb{H}(\boldsymbol{\xi}) |\mathbf{Z}^T \boldsymbol{\xi}|^{-3} dS, \quad \text{and} \quad (5.43)$$

²As will be shown later in this subsection, $\bar{\boldsymbol{\tau}}_e^{(2)}$ in the LCC is equal to the corresponding variable in the actual suspension, so that we do not use the superscript L for this variable.

$$\mathbb{R} = \frac{1}{4\pi |\mathbf{Z}|} \int_{|\boldsymbol{\xi}|=1} \mathbb{T}(\boldsymbol{\xi}) |\mathbf{Z}^T \boldsymbol{\xi}|^{-3} dS. \quad (5.44)$$

where the fourth-order tensor \mathbb{H} and \mathbb{T} are given by

$$H_{ijkl} = (M_{ik}\xi_j\xi_l)|_{(ij)(kl)}, \quad T_{ijkl} = (M_{ik}\xi_j\xi_l)|_{[ij](kl)}, \quad (5.45)$$

with $\mathbf{M} = \eta^{(1)}(\mathbf{I} - \boldsymbol{\xi} \otimes \boldsymbol{\xi})$. In addition, in the above relations, the parentheses and square brackets (enclosing indices) denote symmetric and anti-symmetric parts, respectively. The components of the microstructural tensors \mathbb{P} and \mathbb{R} relative to the principal axes of the ellipsoidal particles are available from Appendix C.4. These components are written in terms of the viscosity $\eta^{(1)}$ and the current values of the aspect ratios w_1 and w_2 .

As discussed in Chapter 4 (see Appendix C.1), consistent with the prediction of the HSW homogenization theory, the above estimates for the instantaneous response of the LCC are based on the approximation that the local fields are *uniform* inside the particle phase. As a consequence of this approximation, the constitutive relation for the average elastic stress field in the particle phase takes the same form as in the corresponding relation for the local field (given by (5.4)). Therefore, similar to relations (5.2), (5.4) and (5.9), the (instantaneous) average extra stress tensor in the particles in the LCC can be expressed as

$$\bar{\boldsymbol{\tau}}^{(2)} = \bar{\boldsymbol{\tau}}_e^{(2)} + \bar{\boldsymbol{\tau}}_v^{(2)}, \quad \text{where} \quad (5.46)$$

$$\bar{\boldsymbol{\tau}}_e^{(2)} = \frac{\mu J_m}{J_m - \bar{I}^{(2)} + 3} \bar{\mathbf{B}}^{(2)} - \mu \mathbf{I}, \quad \text{and} \quad \bar{\boldsymbol{\tau}}_v^{(2)} = 2\eta^{(2)} \bar{\mathbf{D}}^{(2)}, \quad (5.47)$$

with $\bar{\boldsymbol{\tau}}_v^{(2)}$ denoting the viscous part of the average stress in the particles. In the above expressions, $\bar{I}^{(2)} = \text{tr}(\bar{\mathbf{B}}^{(2)})$, $\bar{\mathbf{B}}^{(2)} = \bar{\mathbf{F}}^{(2)}(\bar{\mathbf{F}}^{(2)})^T$ and $\bar{\mathbf{F}}^{(2)}$ is the average deformation gradient in the particles. The uniform-field approximation also holds for the local fields inside the particle phase in the actual suspension, following from the fact that the second moments of the local fields (such as stress and strain-rate) inside the particle phase in the actual suspension are equal to the corresponding quantities in the LCC³. Therefore, it follows from relations (5.39) for $r = 2$ and relations (5.46) and (5.47) that the particle phase averages $\bar{\boldsymbol{\tau}}_e^{(2)}$, $\bar{\boldsymbol{\tau}}_v^{(2)}$ and $\bar{\mathbf{B}}^{(2)}$ associated with the LCC are equal to the corresponding phase averages in the actual suspension. As discussed in Chapter 4, we also note that although the exact solution for the fields in the particles is not uniform, the uniform-field approximation is expected to lead to fairly accurate results provided that the concentrations are not large enough to generate strong interactions between the particles.

At this point, the (instantaneous) macroscopic constitutive relation for the (actual) suspension of viscoelastic particles can be obtained by making use of estimate (5.40) for $\widetilde{\mathbf{W}}_L(\bar{\mathbf{D}})$ in equation (5.38). However, Avazmohammadi and Ponte Castañeda (2014) obtained a simpler (and equivalent) form of this constitutive relation (i.e., $\bar{\boldsymbol{\sigma}}_L = -\bar{p}' \mathbf{I} + \partial \widetilde{\mathbf{W}}_L / \partial \bar{\mathbf{D}}$) in terms of $\bar{\mathbf{D}}^{(2)}$ and $\bar{\boldsymbol{\tau}}_e^{(2)}$, which can

³More specifically, the uniformity of the local fields, for example the stress field, inside the particle phase in the LCC is due to fact that $\int_{\Omega^{(2)}} (\boldsymbol{\tau}_L \otimes \boldsymbol{\tau}_L) dV = \bar{\boldsymbol{\tau}}_L \otimes \bar{\boldsymbol{\tau}}_L$, and the same relation holds for the stress field inside the particle phase in the actual suspension following from relations $\bar{\boldsymbol{\tau}} = \bar{\boldsymbol{\tau}}_L$ and $\int_{\Omega^{(2)}} (\boldsymbol{\tau} \otimes \boldsymbol{\tau}) dV = \int_{\Omega^{(2)}} (\boldsymbol{\tau}_L \otimes \boldsymbol{\tau}_L) dV$.

be expressed as (see relation (3.22) in that paper)

$$\bar{\boldsymbol{\sigma}} = -\bar{p}' \mathbf{I} + 2\eta^{(1)}\bar{\mathbf{D}} + 2c\left(\eta^{(2)} - \eta^{(1)}\right)\bar{\mathbf{D}}^{(2)} + c\bar{\boldsymbol{\tau}}_e^{(2)}. \quad (5.48)$$

In summary, we see from the above constitutive relation together with expression (5.41) for $\bar{\mathbf{D}}^{(2)}$ that, for given macroscopic strain-rate $\bar{\mathbf{D}}$, particle volume fraction c , and viscosity $\eta^{(2)}$, the (*instantaneous*) macroscopic Cauchy stress tensor $\bar{\boldsymbol{\sigma}}$ may be determined in terms of the optimal value of $\eta^{(1)}$, the current value of the average elastic stress tensor over the particle $\bar{\boldsymbol{\tau}}_e^{(2)}$, and the current values of the average aspect ratio and orientation of the particles, as defined by expression (5.12). We obtain the optimal value of $\eta^{(1)}$ by making use of the expressions (5.40) in equation (5.37) and solving the (generally coupled) system of equations (5.36) and (5.37). This value is determined in terms of $\bar{\mathbf{D}}$, c , $\eta^{(2)}$, the constitutive properties of the HB fluid in the actual suspension, and the current values of the variables $\bar{\boldsymbol{\tau}}_e^{(2)}$ and $\mathcal{S} = \{w_1, w_2, \mathbf{n}_1, \mathbf{n}_2, \mathbf{n}_3 = \mathbf{n}_1 \times \mathbf{n}_2\}$. Therefore, the constitutive relation (5.48) for the instantaneous response of the actual suspension is indeed nonlinear in $\bar{\mathbf{D}}$, as expected. However, when viewed as the constitutive relation for the LCC for a given $\eta^{(1)}$, this relation (5.48) is *instantaneously* linear in $\bar{\mathbf{D}}$, since nonlinearities associated with the particle response subjected to finite strains are fully accounted for in the particle stress $\bar{\boldsymbol{\tau}}_e^{(2)}$, which is assumed to be known at any given instant. In the next subsection, we address the characterization of the variables $\bar{\boldsymbol{\tau}}_e^{(2)}$ and \mathcal{S} by means of appropriate *evolution equations*, starting from an appropriate initial state where the particles are initially spherical and unstressed.

5.3.2 Evolution equations for the microstructural variables and particle elastic stress

So far, we generated estimates for the *instantaneous* response of the suspension for the current state of the microstructure and the current value of the particle elastic stress $\bar{\boldsymbol{\tau}}_e^{(2)}$. However, when subjected to simple flows, the microstructure in the suspension as well as the value of $\bar{\boldsymbol{\tau}}_e^{(2)}$ generally evolve in time as the applied deformation progresses. Therefore, in order to predict the effective *time-dependent* behavior of suspensions from a given instantaneous state of the microstructure and the particle stress, it is crucial to establish appropriate evolution laws for relevant microstructural variables and for the stress tensor $\bar{\boldsymbol{\tau}}_e^{(2)}$. Recalling that the microstructure as well as the stress and strain-rate phase averages in the suspension are identical to those in the LCC at any given instant, henceforth, we do not distinguish between these variables in the suspension and those in the LCC.

As mentioned in the previous subsection, our estimates for the instantaneous response of the suspension are based on the approximation that the *local* fields are uniform inside the particle phase in the suspension. According to this approximation, and as already anticipated in section 5.2.2, the initially spherical particles will deform through a sequence of ellipsoidal shapes throughout the deformation process, in such a way that the set of equations used to determine the instantaneous stress and strain-rate fields inside particles will continue to apply at each increment of time, except that at each step the current values of the microstructural variables and of the stresses in the particles will need to be used.

First, it follows from the incompressibility of the fluid and particle phases that the volume fraction of the particles will remain un-changed throughout any deformation process, *i.e.*,

$$c = \text{const.} \quad (5.49)$$

Next, the evolution for the aspect ratios of the particle, w_1 and w_2 , are obtained by simple kinematic arguments (see, for example, Bilby and Kolbuszewski, 1977) as

$$\dot{w}_1 = w_1(\bar{D}_{22}^{(2)} - \bar{D}_{11}^{(2)}), \quad \dot{w}_2 = w_2(\bar{D}_{33}^{(2)} - \bar{D}_{11}^{(2)}), \quad (5.50)$$

where it is noted that the overdot here denotes simple time derivatives (since w_1 and w_2 depend only on time). It is also remarked in this context that the components of the tensorial variables associated with the particle phase, here and elsewhere, are referred to the principal directions of the ellipsoidal particle in their current state, as given by the triad $\{\mathbf{n}_1, \mathbf{n}_2, \mathbf{n}_3\}$.

Also, the evolution of the orthonormal vectors \mathbf{n}_1 , \mathbf{n}_2 and \mathbf{n}_3 , serving to characterize the orientation of particles, are determined by means of the kinematical relations

$$\dot{\mathbf{n}}_i = \boldsymbol{\Omega} \mathbf{n}_i, \quad i = 1, 2, 3, \quad (5.51)$$

where $\boldsymbol{\Omega}$ is the (antisymmetric) spin tensor of the particle, whose components in the principal coordinate system $\{\mathbf{n}_1, \mathbf{n}_2, \mathbf{n}_3\}$ are determined by means of the following relations (Ogden, 1997; Aravas and Ponte Castañeda, 2004)

$$\Omega_{ij} = \bar{W}_{ij}^{(2)} - \frac{(w_{i-1})^2 + (w_{j-1})^2}{(w_{i-1})^2 - (w_{j-1})^2} \bar{D}_{ij}^{(2)}, \quad i \neq j. \quad (5.52)$$

In this notation, when i or j is equal to 1, we define $w_{i-1} = w_0 = 1$.

Finally, an evolution equation for the particle stress $\bar{\boldsymbol{\tau}}_e^{(2)}$ can be obtained from relation (5.47)₁ by making use of the time derivative (5.5). In this connection, recalling the expression $\bar{\mathbf{B}}^{(2)} = \bar{\mathbf{F}}^{(2)}(\bar{\mathbf{F}}^{(2)})^T$ and the fact that the local fields are uniform inside the particle phase, we first find that

$$\begin{aligned} \overset{\nabla}{\bar{\mathbf{B}}}^{(2)} &= \dot{\bar{\mathbf{B}}}^{(2)} - \bar{\mathbf{L}}^{(2)}\bar{\mathbf{B}}^{(2)} - \bar{\mathbf{B}}^{(2)}(\bar{\mathbf{L}}^{(2)})^T \\ &= \dot{\bar{\mathbf{F}}}^{(2)}(\bar{\mathbf{F}}^{(2)})^T + \bar{\mathbf{F}}^{(2)}(\dot{\bar{\mathbf{F}}}^{(2)})^T - \bar{\mathbf{L}}^{(2)}\bar{\mathbf{B}}^{(2)} - \bar{\mathbf{B}}^{(2)}(\bar{\mathbf{L}}^{(2)})^T = \mathbf{0}, \end{aligned} \quad (5.53)$$

where use has been made of $\bar{\mathbf{L}}^{(2)} = \dot{\bar{\mathbf{F}}}^{(2)}(\bar{\mathbf{F}}^{(2)})^{-1}$. Making use of the above results, the evolution equation for $\bar{\boldsymbol{\tau}}^{(2)}$, defined in (5.47)₁, is expressed as

$$\begin{aligned} \overset{\nabla}{\bar{\boldsymbol{\tau}}}_e^{(2)} &= \dot{\bar{\boldsymbol{\tau}}}_e^{(2)} - \bar{\mathbf{L}}^{(2)}\bar{\boldsymbol{\tau}}_e^{(2)} - \bar{\boldsymbol{\tau}}_e^{(2)}(\bar{\mathbf{L}}^{(2)})^T \\ &= 2\mu\bar{\mathbf{D}}^{(2)} + \frac{2}{\mu J_m} \text{tr} \left[\bar{\mathbf{D}}^{(2)} \left(\bar{\boldsymbol{\tau}}_e^{(2)} + \mu\mathbf{I} \right) \right] \left(\bar{\boldsymbol{\tau}}_e^{(2)} + \mu\mathbf{I} \right). \end{aligned} \quad (5.54)$$

In the above expressions, the material time derivative $\dot{\bar{\mathbf{B}}}^{(2)}$ and $\dot{\bar{\boldsymbol{\tau}}}_e^{(2)}$ are simple, time derivative, again, due to the fact that the local fields inside the particle are uniform (as already mentioned)

and the convective terms hence vanish. Note that, following the same fact, evolution equation (5.54) takes the same form as in the corresponding equation for the local field, given by (5.6).

In summary, for a given macroscopic velocity gradient $\bar{\mathbf{L}} = \bar{\mathbf{D}} + \bar{\mathbf{W}}$, the macroscopic stress $\bar{\boldsymbol{\sigma}}$ is obtained from expression (5.48), where $\bar{\mathbf{D}}^{(2)}$ is given by expression (5.41). These quantities depend on two sets of values: (1) the current values of the microstructural variables \mathcal{S} , as defined by expression (5.12), and determined by the evolution equations (5.50) and (5.51) from some known initial state, (2) the current value of the average elastic stress $\bar{\boldsymbol{\tau}}_e^{(2)}$ in the particle, as determined by evolution equation (5.54), again from a known initial state. In this connection, note that the evolution equation for the particle axes (5.51) involves the average vorticity tensor in the particles, which is given in terms of other known variables by expression (5.42). In the next subsection, we will make use of the time-dependent solution, developed in this section, to construct steady-state solutions, when available, for the strain-rate, vorticity and stress fields inside particles.

5.3.3 Steady-state estimates for the suspensions

Based on earlier work for dilute suspensions of neo-Hookean particles in a Newtonian fluid (Roscoe, 1967; Gao et al., 2011, 2013), the initially spherical particles, subjected to simple flows, can reach, under certain conditions, a steady state in which case the particles become an ellipsoidal with a fixed shape and orientation as well as constant stress, strain-rate and vorticity. In Chapter 4, we demonstrated that, for suspensions of Kelvin-Voigt viscoelastic particles (with a Gent elastic part) in a Newtonian fluid, such a steady state can still be available for higher concentrations of initially spherical particles, following from the prediction of the HSW theory that the stress and strain-rate fields are uniform inside the particle phase. In this study, making use of the linear comparison composite technique, we generated HSW-type estimates for the instantaneous response of the non-dilute suspensions of KV particles in a HB fluid which, similarly, predict that the local fields inside the particle phase are uniform. With the same token, this prediction implies that the initially spherical KV particles, suspended in such a fluid, can still reach a steady state, when subjected to simple flows. In this subsection, we provide steady-state (SS) estimates for the kinematical and stress tensors in the particle phase. More detail on derivation of these estimates are available in Section 4.4. For definiteness, we note that all variables in this section correspond to their associated values in a steady state. Also, in this subsection, the components of all tensorial variables are referred to the principal directions of the ellipsoidal particles in its steady state, given by the triad $\{\mathbf{n}_1, \mathbf{n}_2, \mathbf{n}_3\}$.

In essence, the SS estimates can be determined by setting the terms involving time derivatives equal to zero in the evolution equation for the extra stress tensor inside the particle as well as the evolution equations for the particle shape and orientation. The resulting expressions, together with the optimality conditions (5.36) and (5.37), will provide a set of algebraic equations to be solved for the optimal values of $\eta^{(1)}$ and \hat{D}_{eq} , the six components of the extra stress tensor in the particle, $\bar{\boldsymbol{\tau}}^{(2)}$, the two aspect ratios, ω_1, ω_2 , and the three orientational angles defined by the particle axes, $\mathbf{n}_1, \mathbf{n}_2$, and \mathbf{n}_3 .

We begin with providing SS estimates for kinematical variables. Following the formulation in Section 4.4, the evolution equations (5.50)-(5.52) together with the incompressibility constraint in

the particle phase ($\text{tr}(\bar{\mathbf{D}}^{(2)}) = 0$), imply that, at a steady state, the normal components of the strain-rate tensor (relative to the particle axes) vanish,

$$\bar{D}_{11}^{(2)} = \bar{D}_{22}^{(2)} = \bar{D}_{33}^{(2)} = 0, \quad (5.55)$$

and the three components of the vorticity strain-rate tensor in the particle phase read as

$$\bar{W}_{12}^{(2)} = \frac{1 + w_1^2}{1 - w_1^2} \bar{D}_{12}^{(2)}, \quad \bar{W}_{13}^{(2)} = \frac{1 + w_2^2}{1 - w_2^2} \bar{D}_{13}^{(2)}, \quad \bar{W}_{23}^{(2)} = \frac{w_1^2 + w_2^2}{w_1^2 - w_2^2} \bar{D}_{23}^{(2)}. \quad (5.56)$$

Also, as discussed in Chapter 4 (see Section 4.4), at a steady state, the shear components of the Finger tensor $\bar{\mathbf{B}}^{(2)}$ (relative to the particle axes) are zero,

$$\bar{B}_{12}^{(2)} = \bar{B}_{13}^{(2)} = \bar{B}_{23}^{(2)} = 0. \quad (5.57)$$

and its normal components are given by

$$\bar{B}_{11}^{(2)} = (w_1 w_2)^{-2/3}, \quad \bar{B}_{22}^{(2)} = (w_1)^{4/3} (w_2)^{-2/3}, \quad \bar{B}_{33}^{(2)} = (w_1)^{-2/3} (w_2)^{4/3}. \quad (5.58)$$

Next, making use of (5.57) in (5.47)₁, we find that, at a steady state the shear components of the elastic stress tensor $\bar{\tau}_e^{(2)}$ (relative to the particle axes) are zero. In addition, we find the three remaining (normal) components of the extra stress tensor by making use of (5.58) in the constitutive relation (5.47)₁. The final results read as

$$\begin{aligned} (\bar{\tau}^{(2)})_{e11} &= \mu d_w \left\{ J_m (w_2)^{1/3} \left[1 - (w_1 w_2)^{2/3} \right] + c_w \right\}, \\ (\bar{\tau}^{(2)})_{e22} &= \mu d_w \left\{ J_m (w_2)^{1/3} \left[(w_1)^2 - (w_1 w_2)^{2/3} \right] + c_w \right\}, \\ (\bar{\tau}^{(2)})_{e33} &= \mu d_w \left\{ J_m (w_2)^{1/3} \left[(w_2)^2 - (w_1 w_2)^{2/3} \right] + c_w \right\}, \end{aligned} \quad (5.59)$$

where $c_w = (w_2)^{1/3} [(w_1)^2 + (w_2)^2 + 1] - 3 (w_1)^{2/3} w_2$, and $d_w = [J_m (w_1)^{2/3} w_2 - c_w]^{-1}$.

Now, making use of the fact that the shear components of the stress tensor $\bar{\tau}_e^{(2)}$ are zero in (5.41) and (5.42), the non-zero components of the particle strain-rate $\bar{\mathbf{D}}^{(2)}$ and vorticity $\bar{\mathbf{W}}^{(2)}$ at the steady state can be written as

$$\bar{D}_{ij}^{(2)} = \frac{\bar{D}_{ij}}{1 - \alpha \mathbb{P}_{ijij}}, \quad \bar{W}_{ij}^{(2)} = \bar{W}_{ij} + \frac{\alpha \mathbb{R}_{ijij} \bar{D}_{ij}}{1 - \alpha \mathbb{P}_{ijij}}, \quad i, j = 1, 2, 3 \text{ (no sum, } i \neq j), \quad (5.60)$$

where $\alpha = 4(1 - c)(\eta^{(1)} - \eta^{(2)})$ and all components are given relative to the particle axes.

Next, relations (5.55) together with the constitutive equation (5.47)₂ imply that, at the steady state, the normal components of the viscous part of extra stress tensor (relative to the particle axes) in the KV particles must all vanish. Moreover, substituting the shear components of $\bar{\mathbf{D}}^{(2)}$ from

(5.60)₁ into (5.47)₂, we find the (remaining) shear components of $\bar{\boldsymbol{\tau}}_v^{(2)}$ as follows

$$(\bar{\boldsymbol{\tau}}_v^{(2)})_{ij} = \frac{2\eta^{(2)}\bar{D}_{ij}}{1-4(1-c)(\eta^{(1)}-\eta^{(2)})\mathbb{P}_{ijij}}, \quad i, j = 1, 2, 3 \quad (i \neq j). \quad (5.61)$$

Finally, the components of the total extra stress tensor in the KV particles at the steady state can be obtained in terms of the above estimates for the viscous and elastic extra stresses in the particles by means of relation (5.46).

At this stage, the optimal values of $\eta^{(1)}$ and \hat{D}_{eq} , all non-zero components of the particle stress $\bar{\boldsymbol{\tau}}^{(2)}$, strain-rate $\bar{\mathbf{D}}^{(2)}$ and vorticity $\bar{\mathbf{W}}^{(2)}$ are written in terms of SS values of the aspect ratios, w_1 and w_2 , and the three orientational angle defined by the particles axes, \mathbf{n}_1 , \mathbf{n}_2 , and \mathbf{n}_3 . We obtain a system of algebraic equations for the unknowns $w_1, w_2, \mathbf{n}_1, \mathbf{n}_2, \mathbf{n}_3$ by making use of (5.59) into (5.41), together with the three equations obtained by substituting relations (5.60) into (5.56), and expression (5.55).

Finally, we remark that the SS solutions for suspensions of KV particles reduce to those for suspensions of elastic particles by setting $(\bar{\boldsymbol{\tau}}_e^{(2)})_{ij} = \bar{\tau}_{ij}^{(2)}$ and $(\bar{\boldsymbol{\tau}}_v^{(2)})_{ij} = 0$ ($i, j = 1, 2, 3$) in relations (5.59) and (5.46).

5.4 Application: Shear flow

To provide some illustrative examples for the constitutive model developed in Section 5.3, in this section we apply the model to suspensions of initially spherical, elastic particles in a Herschel-Bulkley (HB) fluid subjected to a uniform viscous flow for representative constitutive properties of the fluid and particles as well as volume fraction of particles. In particular, we consider the problem of suspensions in a simple shear flow, characterized by

$$\bar{\mathbf{L}} = \dot{\gamma} \mathbf{E}_1 \otimes \mathbf{E}_2, \quad \bar{\mathbf{D}} = \frac{1}{2} \dot{\gamma} (\mathbf{E}_1 \otimes \mathbf{E}_2 + \mathbf{E}_2 \otimes \mathbf{E}_1), \quad \bar{\mathbf{W}} = \frac{1}{2} \dot{\gamma} (\mathbf{E}_1 \otimes \mathbf{E}_2 - \mathbf{E}_2 \otimes \mathbf{E}_1), \quad (5.62)$$

where the $\{\mathbf{E}_i\}$ refer to the fixed laboratory coordinates, and $\dot{\gamma} \geq 0$ is the shear strain rate. For convenience, we make use of the dimensionless parameters

$$G = \frac{K \dot{\gamma}^n}{\mu}, \quad \text{and} \quad H = \frac{\tau_0}{K \dot{\gamma}^n},$$

which serve to characterize the ratio of viscous forces in the fluid to the elastic forces in the particles, and the ratio of the forces (exclusively) induced by the yield stress to the viscous forces induced by the application of the strain rate in the fluid, respectively. Also, for future references, it is useful to introduce a (dependent) nondimensional parameter, defined by

$$H_G = H G = \frac{\tau_0}{\mu},$$

It is relevant to mention that the special case of $G = 0$ corresponds to the suspensions of (spherical) rigid particles in a HB fluid. Also, the special cases of $H = 0$ and $n = 1$ correspond to the

suspensions of elastic particles in a power-law and Bingham fluids, respectively. All representative examples in this section are provided for the case of (purely) elastic Gent particles (i.e., $\eta^{(2)} = 0$) with a fixed strain-locking parameter ($J_m = 50$).

The initially spherical particles, when subjected to shear flow (5.62), deform into ellipsoids of general shape characterized by the two aspect ratios w_1 and w_2 , which, as defined in figure 5.2, correspond to the aspect ratios of the particle in the plane of the flow ($\mathbf{E}_1 - \mathbf{E}_2$ plane) and in the plane perpendicular to the short in-plane axis of the particles ($\mathbf{E}_1 - \mathbf{E}_3$ plane), respectively. The deformed particles also rotate remaining in the $\mathbf{E}_1 - \mathbf{E}_2$ plane in such a way that their current orientation may be described in terms of a single angle θ (measured positive in the counterclockwise direction from the \mathbf{E}_1 direction). Then, the evolution equations (5.50) to (5.54) can be shown to specialize to equations (D.1) in Appendix D.1. These equations are complemented with two more equations (5.36) and (5.37) for unknown variables $\eta^{(1)}$ and \hat{D}_{eq} associated with the LCC. The resulting system of equations, together with relations (5.41) and (5.42), can be integrated numerically for the time-dependent solution. The components of the shape tensors \mathbb{P} and \mathbb{R} , required for this integration, are not included here for brevity, but they are available from Appendix D in Avazmohammadi and Ponte Castañeda (2014). Finally, given the current values of the particle stress $\bar{\boldsymbol{\tau}}^{(2)}$, aspect ratios w_1 and w_2 and orientation θ of the particles, the macroscopic stress $\bar{\boldsymbol{\sigma}}$ can be derived by means of expression (5.48), together with (5.41).

For the specific purpose of discussing the macroscopic response of the suspensions in shear flow, we present the results for the shear component of the macroscopic Cauchy stress tensor, $\bar{\sigma}_{12}$, as well as the first and second *normal stress differences* of the suspensions, defined by

$$\Pi_1 = \bar{\sigma}_{11} - \bar{\sigma}_{22}, \quad \Pi_2 = \bar{\sigma}_{22} - \bar{\sigma}_{33}, \quad (5.63)$$

where the components are relative to the fixed laboratory axes \mathbf{E}_i .

To obtain the initial response of the suspension, we make use of the (initial) condition $\bar{\boldsymbol{\tau}}^{(2)}|_{t=0^+} = \mathbf{0}$ (we use the notation $t = 0^+$ to denote the very first instant at which the suspension flows in an average sense under the applied flow conditions). This condition for the particle stress is due to the fact that, at $t = 0^+$, the elastic particles have not had the time to respond to the applied flow, and therefore, at this instant, they behave like spherical, incompressible voids. Hence, making use of the Hashin-Shtrikman (HS) upper bound for the effective potential \widetilde{W}_L of the LCC (consisting of a viscous matrix with viscosity $\eta^{(1)}$ and random distribution of incompressible, spherical voids) in equations (5.36) and (5.37), the unknown viscosity $\eta^{(1)}$ in the LCC is obtained as

$$\eta^{(1)}|_{t=0^+} = \sqrt{\frac{3+2c}{3}} \frac{\tau_0}{\bar{D}_{eq}} + \left(\sqrt{\frac{3}{3+2c}} \right)^{n-1} K \bar{D}_{eq}^{n-1}. \quad (5.64)$$

where $\bar{D}_{eq} = \sqrt{2\bar{\mathbf{D}} \cdot \bar{\mathbf{D}}}$ denotes the macroscopic equivalent strain-rate. We note that the above relation is valid for a general uniform macroscopic flow $\bar{\mathbf{D}}$. Similarly, making use of the corresponding \widetilde{W}_L in (5.38) together with using the above relation, we find the initial macroscopic Cauchy stress

tensor as

$$\begin{aligned}\bar{\boldsymbol{\sigma}}|_{t=0^+} &= -\bar{p}' \mathbf{I} + \bar{\boldsymbol{\tau}}|_{t=0^+}, \quad \text{where} \\ \bar{\boldsymbol{\tau}}|_{t=0^+} &= \frac{6(1-c)}{3+2c} \eta^{(1)}|_{t=0^+} \bar{\mathbf{D}} = \frac{2}{D_{eq}} \left[(1-c) c^I \tau_0 + (c^I)^{n+1} K \bar{D}_{eq}^n \right] \bar{\mathbf{D}}\end{aligned}\quad (5.65)$$

where $c^I = \sqrt{3/(3+2c)}$. By comparing the above relation with the corresponding relation for the extra stress in a plain HB fluid (see relation (5.10)₂), it follows that, based on the variational method prediction, suspensions of elastic particles in a HB fluid with yield stress τ_0 and consistency constant K initially behave like a HB fluid with the same power index n as that of the suspending fluid, but with effective yield stress $\tilde{\tau}_0^I$ and consistency constant \tilde{K}^I , given by

$$\tilde{\tau}_0^I = (1-c) c^I \tau_0, \quad \tilde{K}^I = (c^I)^{n+1} K. \quad (5.66)$$

For the case of shear flow conditions (5.62), it follows from the general result (5.65) that the initial shear stress component in the suspension is given by

$$\bar{\sigma}_{12}|_{t=0^+} = \tilde{\tau}_0^I + \tilde{K}^I \dot{\gamma}^n. \quad (5.67)$$

Next, it is worthwhile to provide analytical expressions for the response of the suspension at a large enough time, specifically when the suspension reaches a steady state. Under the shear flow conditions (5.62), making use of (5.59) and (5.60)₁ in relation (5.48), the steady-state value of the macroscopic stress component $\bar{\sigma}_{12}$ is obtained as

$$\begin{aligned}\bar{\sigma}_{12}|_{SS} &= \eta^{(1)} \dot{\gamma} \left(1 - \frac{c \cos(2\theta)}{1 - 4(1-c) \eta^{(1)} \mathbb{P}_{1212}} \right) \\ &\quad + c \mu \sin(\theta) \cos(\theta) d_w \left[J_m(w_2)^{1/3} (1 - w_1^2) \right].\end{aligned}\quad (5.68)$$

where all the quantities w_1 , w_2 , θ , and $\eta^{(1)}$ are evaluated at the steady state, and the component \mathbb{P}_{1212} (relative to the particle axes) is obtained in terms of the corresponding values of w_1 , w_2 , and $\eta^{(1)}$ (see Appendix C.4).

Before proceeding with the detailed examples, it is also useful to consider the response of the suspensions in the limiting case of $G \rightarrow 0$ (under a constant strain-rate tensor $\bar{\mathbf{D}}$) which corresponds to the suspension of rigid spherical particles. In this limit, the microstructure of the suspension does not evolve because the rigid particles do not change shape and the particles distribution remain spherical based on our earlier assumption in Section 5.2.2 that the shape and orientation of the particles distribution are identical to those of the individual particles. Therefore, since there is no microstructure evolution for the case of $G \rightarrow 0$, the steady-state response of the suspension is the same as the initial response of the suspension. In this case, making use of the HS lower bound for the effective potential \widetilde{W}_L of the LCC (consisting of a viscous matrix with viscosity $\eta^{(1)}$ and random distribution of rigid spherical particles) in equations (5.36) and (5.37), the unknown viscosity $\eta^{(1)}$

in the LCC is obtained as

$$\eta^{(1)}|_{G \rightarrow 0} = (1-c) \sqrt{\frac{2}{2+3c}} \frac{\tau_0}{D_{eq}} + \left(\frac{1}{1-c} \sqrt{\frac{2+3c}{2}} \right)^{n-1} K \bar{D}_{eq}^{n-1}. \quad (5.69)$$

Similarly, making use of the corresponding \widetilde{W}_L in (5.38) together with (5.69), we find the initial macroscopic Cauchy stress tensor as

$$\begin{aligned} \bar{\sigma}|_{G \rightarrow 0} &= -\bar{p}' \mathbf{I} + \bar{\tau}|_{G \rightarrow 0}, \quad \text{where} \\ \bar{\tau}|_{G \rightarrow 0} &= \frac{2+3c}{(1-c)} \eta^{(1)}|_{G \rightarrow 0} \bar{\mathbf{D}} = \frac{2}{D_{eq}} c^R \{ \tau_0 + [c^R/(1-c)]^n K \bar{D}_{eq}^n \} \bar{\mathbf{D}} \end{aligned} \quad (5.70)$$

where $c^R = \sqrt{(2+3c)/2}$. Again, it follows from the above form for the macroscopic stress that, based on the variational method prediction, the suspension of the rigid particles in a Herschel-Bulkley fluid will exhibit a HB behavior with the same power index n as that of the suspending fluid, but with effective yield stress $\tilde{\tau}_0^R$ and consistency constant \tilde{K}^R , given by

$$\tilde{\tau}_0^R = c^R \tau_0, \quad \tilde{K}^R = (1-c) [c^R/(1-c)]^{n+1}. \quad (5.71)$$

It is worth mentioning that this prediction of the variational method is in agreement with earlier results by Chateau et al. (2008) for suspensions of rigid spherical particles in a HB fluid, as well as with the variational results reported by Ponte Castañeda (2003) for suspensions of idealized 2-D, rigid circular particles in a Bingham fluid. For the case of shear flow conditions (5.62), it follows from the general results (5.70) that the shear stress component in the suspension when $G \rightarrow 0$ is written as

$$\bar{\sigma}_{12}|_{G \rightarrow 0} = \tilde{\tau}_0^R + \tilde{K}^R \dot{\gamma}^n. \quad (5.72)$$

Finally, it is important to note that, when $n \leq 1$, it can be shown that the estimates (5.72) serves as a rigorous lower bound on the effective stress component $\bar{\sigma}_{12}$ for the case of suspensions of rigid spherical particles in a H-B fluid.

The results provided in this section are organized as follows. In Sections 5.4.1 and 5.4.2, we present the results for the suspensions of Gent particles in Bingham fluids ($n = 1$) and power-law fluids ($H = 0$), respectively. Next, in Section 5.4.3, we will present representative results for the suspensions of Gent particles in a general HB fluid. Also, in all three subsections, results are first provided for time-dependent responses of the corresponding suspensions, followed by results for steady-state (SS) behaviors of these suspension. For both groups of results, figures present results for the average particle shape (characterized by w_1 and w_2) and orientation (characterized by θ), certain components of the average extra stress tensor in the fluid phase ($\bar{\tau}^{(1)}$) and in the particle phase ($\bar{\tau}^{(2)}$), as well as the macroscopic Cauchy stresses $\bar{\sigma}_{21}$, Π_1 and Π_2 , as defined in (5.63). We emphasize that the components of the macroscopic Cauchy stress and the average stress tensor in the fluid are shown relative to the fixed laboratory axes \mathbf{E}_i , while the components of the average stress tensor in the particle are shown in the instantaneous principal axes of the particle. Finally, we note that all stress components are appropriately normalized in the results.

5.4.1 Bingham fluids

In this subsection, we present results for the case of suspensions of elastic (Gent) particles in a Bingham fluid (i.e., $n = 1$). Figure 5.3 presents variational estimates for the time-dependent behavior of suspensions of purely elastic (Gent) particles with $G = 0.2$ in a Bingham fluid under the shear flow conditions (5.62). Results are shown for a fixed volume fraction ($c = 0.2$) and various values of the non-dimensional parameter $H_G = \tau_0/\mu$. It is useful to note that the results are calculated at a constant strain rate $\dot{\gamma}$ and shear modulus μ , so that higher values of H_G correspond to the Bingham fluids with a higher yield stress τ_0 . The evolutions of w_1 , w_2 and θ in figures 5.3 (a) and (b) suggest that the particles suspended in a Bingham fluid with a higher yield stress become more elongated and their major axis becomes more aligned with the shear direction, before they reach a steady state. In fact, as we observe from figure 5.3(c), this is because, a higher yield stress of the Bingham fluid results in a larger initial stress in the fluid matrix which, in turn, induces a higher level of stress in the particles, as observed from figure 5.3(d). As a consequence, we observe from figures 5.3(f) and (e) that the macroscopic shear stress and normal stress differences exhibit a progressive increase (in magnitude) as the yield stress of the suspending fluid increases. In this connection, we note that the initial values of the (normalized) macroscopic shear stress in figure 5.3(e) define the initial yield stress of the suspension which is explicitly given in terms of τ_0 and c by relation (5.66). On the other hand, the steady-state values of the macroscopic shear stress are influenced by the evolution of the microstructure, and they can be determined from relation (5.68) in terms SS values of w_1 , w_2 and θ as well as the SS value of the viscosity $\eta^{(1)}$.

Next, we investigate the steady-state response of the suspensions of Gent particles in a Bingham fluid under the shear flow conditions (5.62). Figure 5.4 shows variational estimates for the steady-state behavior of the particle, as well as for the associated stress averages in the phases and macroscopic stresses, as a function of G . The results are given for a fixed volume fraction ($c = 0.2$) and several values of H . We note that higher values of H and G correspond to higher yield stresses of the Bingham fluid and softer particles, respectively. We realize from figures 5.4(a) and (b) that, as G increases, the Gent particles reach larger elongations, as well as closer alignments with the shear direction at the steady state. This behavior of the particles is seen to be strongly affected by the value of the yield stress of the suspending Bingham fluid. Generally, the rate of change in SS values of the aspect ratios and orientation of the particles with increasing G is higher for larger values of H . This is, once again, due to the fact that a higher yield stress τ_0 of the Bingham fluid leads to larger initial stresses in the fluid matrix and particle, as observed from figures 5.4(c) and (d), and these stresses have a stronger effect on the SS shape and orientation of the particles when G is higher, corresponding to softer particle. Next, figures 5.4(e) and (f) show the corresponding estimates for the macroscopic shear and normal stress differences, respectively. The variable $\bar{\sigma}_{12}/(K\dot{\gamma})$ in figure 5.4(e) defines the dimensionless (apparent) effective viscosity of the suspension, and its decrease with G is more pronounced for higher values of H . Moreover, when $G \rightarrow 0$, which corresponds to suspensions of rigid spherical particles, the values of the (normalized) macroscopic shear stress are in agreement with the values calculated from (5.72) for $c = 0.2$ and corresponding values of H .

In figure 5.5, we investigate the influence of the particle volume fractions on the steady-state

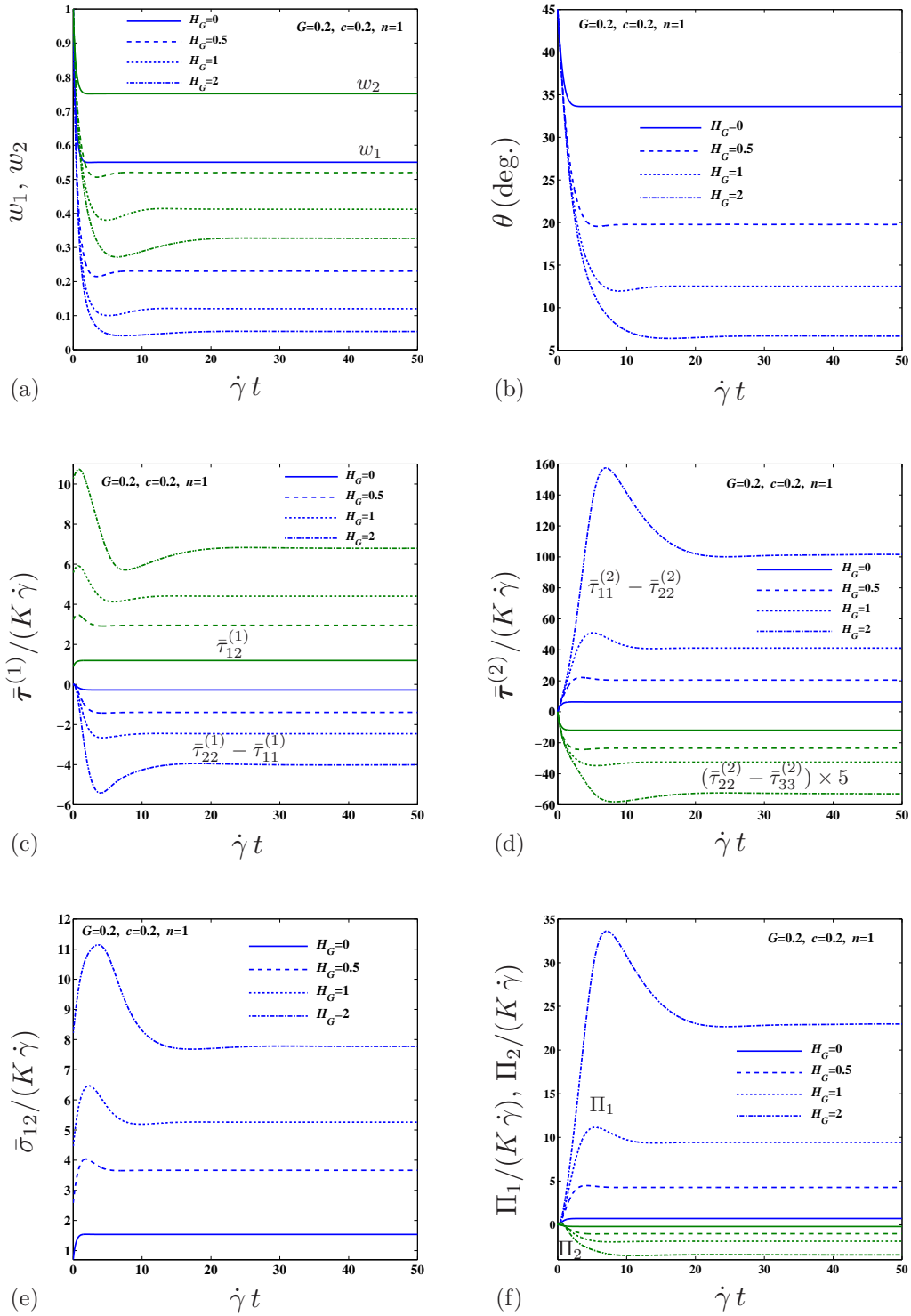


Figure 5.3: Variational estimates for the time-dependent response of suspensions of initially spherical Gent particles with $G = 0.2$ in a Bingham fluid ($n = 1$) for various values of H_G under shear flow conditions. The components of $\bar{\tau}^{(1)}$ and $\bar{\tau}^{(2)}$ are given relative to the fixed coordinate system \mathbf{E}_i and the principal axes of the particles, respectively.

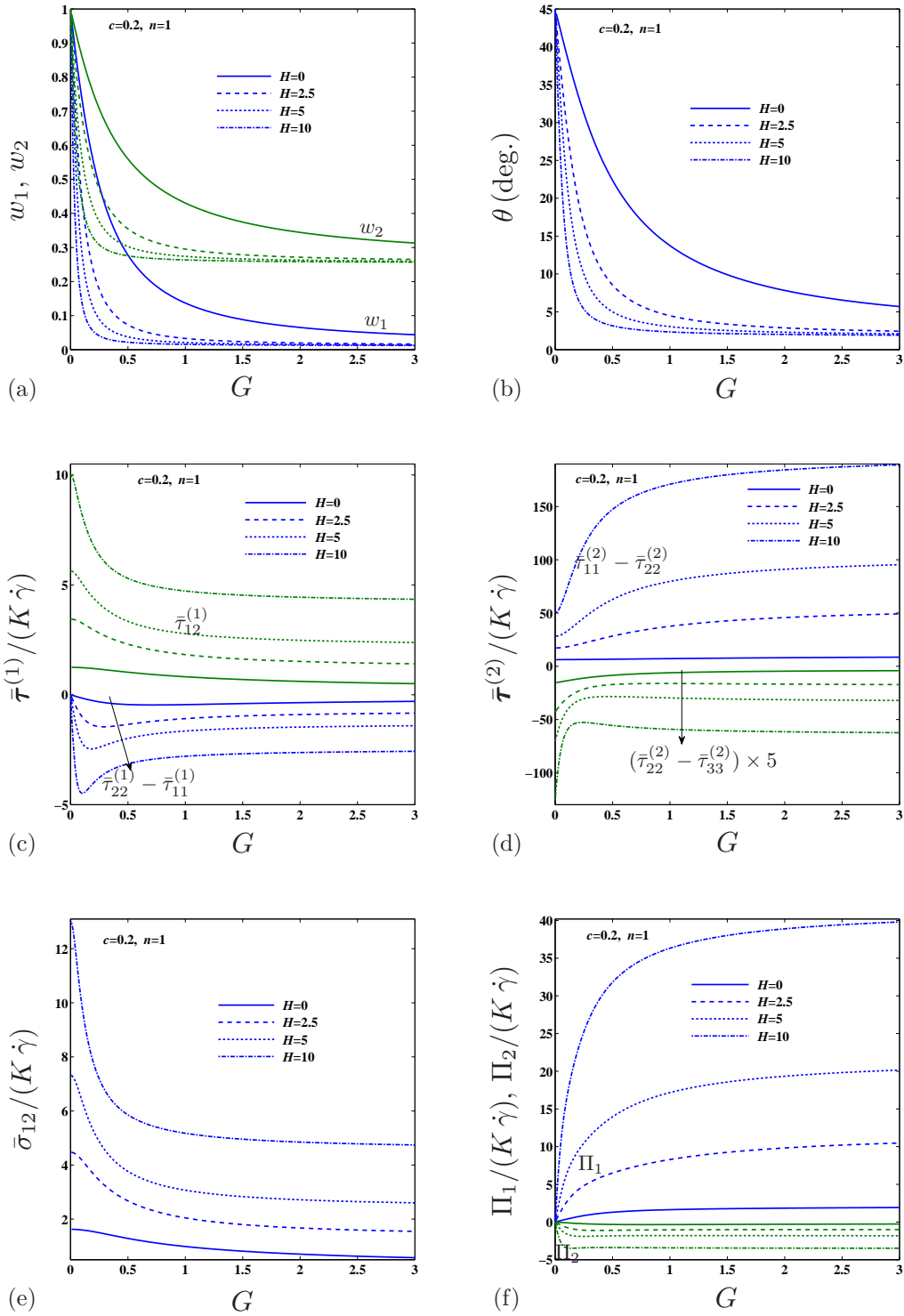


Figure 5.4: Variational estimates for the steady-state response of suspensions of initially spherical Gent particles with $G = 0.2$ in a Bingham fluid ($n = 1$) for various values of H under shear flow conditions. The components of $\bar{\tau}^{(1)}$ and $\bar{\tau}^{(2)}$ are given relative to the fixed coordinate system \mathbf{E}_i and the principal axes of the particles, respectively.

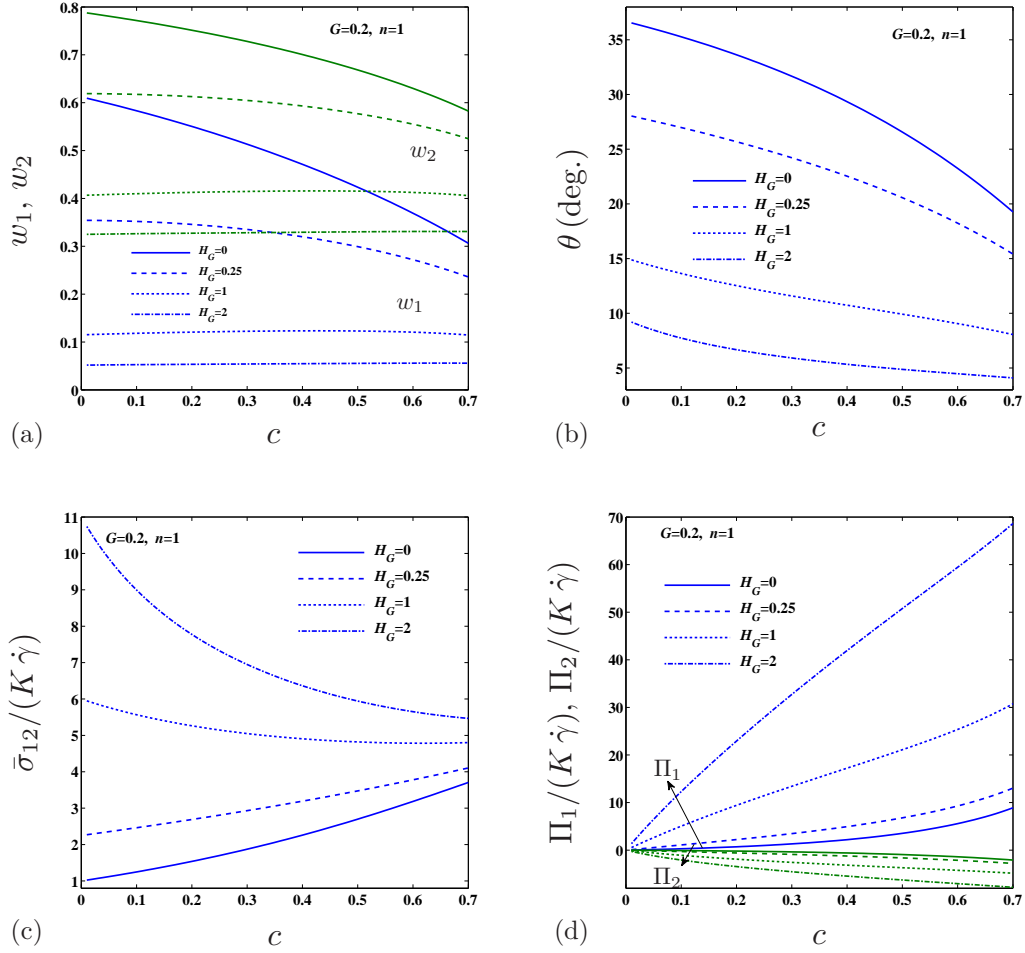


Figure 5.5: Variational estimates for the steady-state response of suspensions of initially spherical Gent particles with $G = 0.2$ in a Bingham fluid ($n = 1$) for various values of H_G under shear flow conditions. The components of $\bar{\tau}^{(1)}$ and $\bar{\tau}^{(2)}$ are given relative to the fixed coordinate system \mathbf{E}_i and the principal axes of the particles, respectively.

response of suspensions of Gent particles with $G = 0.2$ in a Bingham fluid with varying values of H_G under shear flow conditions. We recall that higher values of H_G correspond to Bingham fluids with higher yield stresses. As expected, we observe from figures 5.5 (a) and (b) that, for the case of Newtonian fluids ($H_G = 0$), the SS level of elongation and alignment of the particles with the shear direction increases with the volume fraction of particles. However, for the case of Bingham fluids with large enough values of H_G , the SS shape and orientation of the particles are seen to be weakly affected by the volume fraction. This can be explained by noting that at higher values of $H_G = \tau_0/\mu$ (corresponding to larger τ_0 at a fixed μ), the suspending Bingham fluid behaves like a very stiff material, so that the deformation in the particle is negligibly affected by increasing the concentration of the particles. Next, figures 5.5(c) and (d) show the corresponding estimates for the macroscopic shear and normal stress differences, respectively. In particular, we observe from figure 5.5(c) that, at low values of H_G , the macroscopic shear stress is increasing with the volume fraction of particles, but this trend is found to be reversed for higher values of H_G . This is, once again, due to the fact that, at higher values of H_G , the fluid matrix behaves much stiffer than the particles, so that the addition of more particles makes the suspension softer in the shear direction. On the other hand, we observe from figure 5.5(d) that the (macroscopic) normal stress differences exhibit a more pronounced increase with the volume fraction as H_G increases.

5.4.2 Power-law fluids

In this subsection, we present results for the case of suspensions of elastic (Gent) particles in a power-law fluid (i.e., $H = 0$). Figure 5.6 shows variational estimates for the time-dependent response of suspensions of Gent particles with $G = 0.2$ in a power-law fluid under shear flow. Results are shown for a fixed volume fraction ($c = 0.2$) and various values of the power-law index n . The evolutions of w_1 , w_2 and θ in figures 5.6 (a) and (b) show that over short times, say less than 3 s for $\dot{\gamma} = 1$, the particles suspended in a power-law fluid deform and rotate rapidly and then they reach a steady state. Interestingly, we further observe from these figures that, for the value of $G = 0.2$, the elastic particles exhibit smaller deformations, as well as less alignments with the shear direction at the steady state, as the value of the index n decreases. This is linked to the fact that a suspending power-law fluid with a smaller value of n exhibits a greater degree of shear-thinning, inducing smaller steady-state values of stress in the fluid and particles, as observed from figures 5.6 (c) and (d). Consistently, we observe from figures 5.6(e) and (f) that the corresponding macroscopic shear stress as well as and normal stress differences reach a smaller value at the steady state with decreasing n . Moreover, we observe from figure 5.6(e) that the normalized (macroscopic) shear stress increases with the duration of shearing, which is the characteristic of *rheopectic* fluids. It is also interesting to mention that the effect of decreasing the power-index n on the macroscopic shear stress of the suspension of elastic particle in a power-law fluid at a fixed volume fraction of the particles is (qualitatively) very similar to the effect of increasing the volume fraction of elastic particles on the shear stress of effective viscosity of the suspension of elastic particle in a Newtonian fluid ($n = 1$), which can be observed from figure 4.5(c) in Chapter 4. This can be explained by noting that both effects cause a shear-thinning behavior in the respective suspensions.

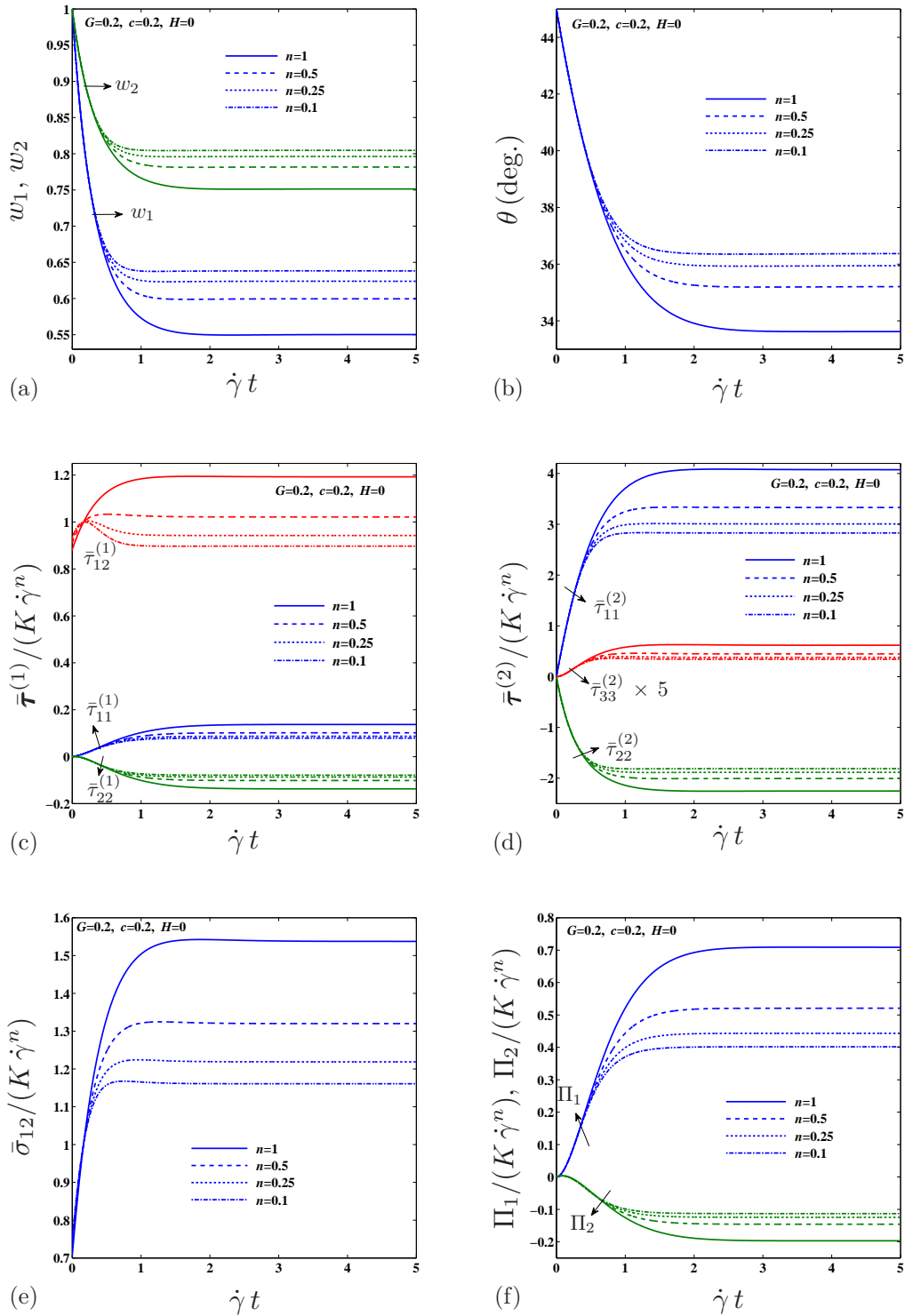


Figure 5.6: Variational estimates for the time-dependent response of suspensions of initially spherical Gent particles with $G = 0.2$ in a power-law fluid ($H = 0$) for various values of n under shear flow conditions. The components of $\bar{\tau}^{(1)}$ and $\bar{\tau}^{(2)}$ are given relative to the fixed coordinate system \mathbf{E}_i and the principal axes of the particles, respectively.

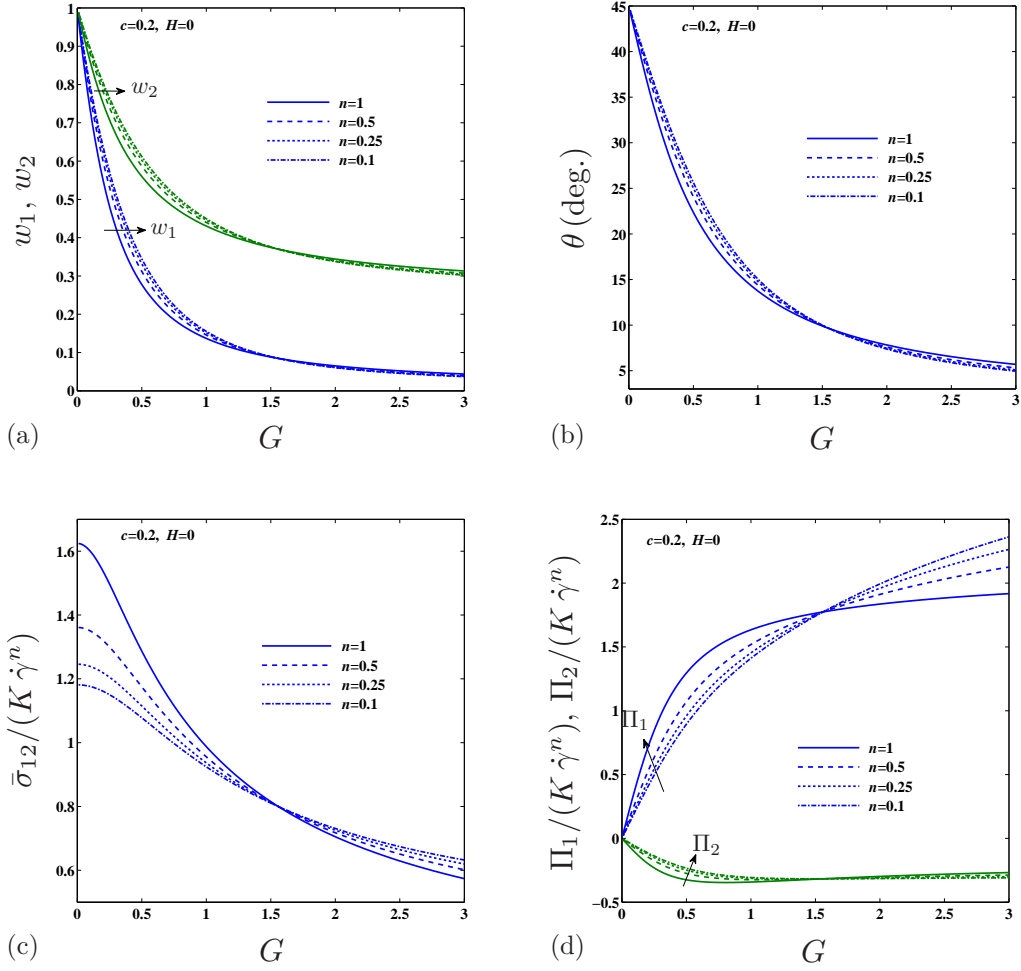


Figure 5.7: Variational estimates for the steady-state response of suspensions of initially spherical Gent particles with $G = 0.2$ in a power-law fluid ($H = 0$) for various values of n under shear flow conditions. The components of $\bar{\tau}^{(1)}$ and $\bar{\tau}^{(2)}$ are given relative to the fixed coordinate system \mathbf{E}_i and the principal axes of the particles, respectively.

Next, similar to the case of Bingham fluids discussed in the previous subsection, we investigate the steady-state response of the suspensions of Gent particles in a power-law fluid under the shear flow conditions (5.62). Figure 5.7 shows variational estimates for the steady-state behavior of the particle, as well as for the macroscopic stresses, as a function of G . The results are given for a fixed volume fraction ($c = 0.2$) and several values of n . Similar to the results in figures 5.4(a) and (b) for the case of Bingham fluids, we observe from figure 5.7 (a) and (b) that, as G increases, the elastic particles reach larger elongations, as well as closer alignments with the shear direction at the steady state. However, this behavior of the particles is seen to be weakly affected by the value of n . Next, figures 5.7(c) and (d) show the corresponding estimates for the macroscopic shear and normal stress differences, respectively. We realize from figure 5.7 (c) that the suspensions of elastic particles in power-law fluids exhibit a shear-thinning effect which is stronger for larger values of n (≤ 1). In this connection, we note that, the shear-thinning effect observed in these suspensions (and, in general, in suspensions of deformable particles in HB fluids with $n < 1$) is derived from two sources: the shear-thinning characteristic of the fluid matrix and the deformation of the particles subjected to shear flows. Another related observation from figure 5.7(c) is that the (normalized) macroscopic shear stress for the case of Newtonian fluids ($n = 1$) becomes unity at approximately $G = 0.88$. This value of G , at which the suspended elastic particles do not change the effective shear stress of the host liquid, was first reported by Gao et al. (2011) for the case of dilute concentration of elastic particle in Newtonian fluids, and was shown later by Avazmohammadi and Ponte Castañeda (2014) to be fairly insensitive to the value of the volume fraction of elastic particles. However, it is evident from figure 5.7(c), this value (denoted by G_N in earlier work), is decreasing with decreasing the value of n . Finally, we note that, when $G \rightarrow 0$, the values of the shear stress in figure 5.7(c) match the corresponding values predicted by relation (5.72).

Lastly, in this subsection, figure 5.8 presents variational estimates for the SS value of the relevant variables in suspensions of Gent particles with $G = 0.2$ in a power-law fluid with varying values of n under shear flow conditions. Consistent with earlier comments in the context of figure 5.5 for the case of Bingham fluids, we observe from figures 5.8 (a) and (b) that the elastic particles in a power-law fluid (with values of $n > 0.5$) reach larger elongations and closer alignments with the shear direction with increasing particle concentration c . However, it is interesting to observe that, for very small values of n , the particle elongation exhibits an opposite behavior and the particle orientation shows only a slight additional alignment with the shear direction as c increases from 0 to 0.7. As explained in the context of figure 5.6, this is due to the fact that a power-law suspending fluid with a lower index n exhibits a stronger shear-thinning behavior, leading to smaller SS values of stress in the fluid and particle phases, as observed from figures 5.8 (c) and (d). Consequently, we observe from figures 5.6 (e) and (f) that the effect of the particle concentration on the corresponding estimates for the macroscopic shear and normal stress differences becomes less significant as the suspending fluids becomes more shear-thinning (i.e., as n decreases).

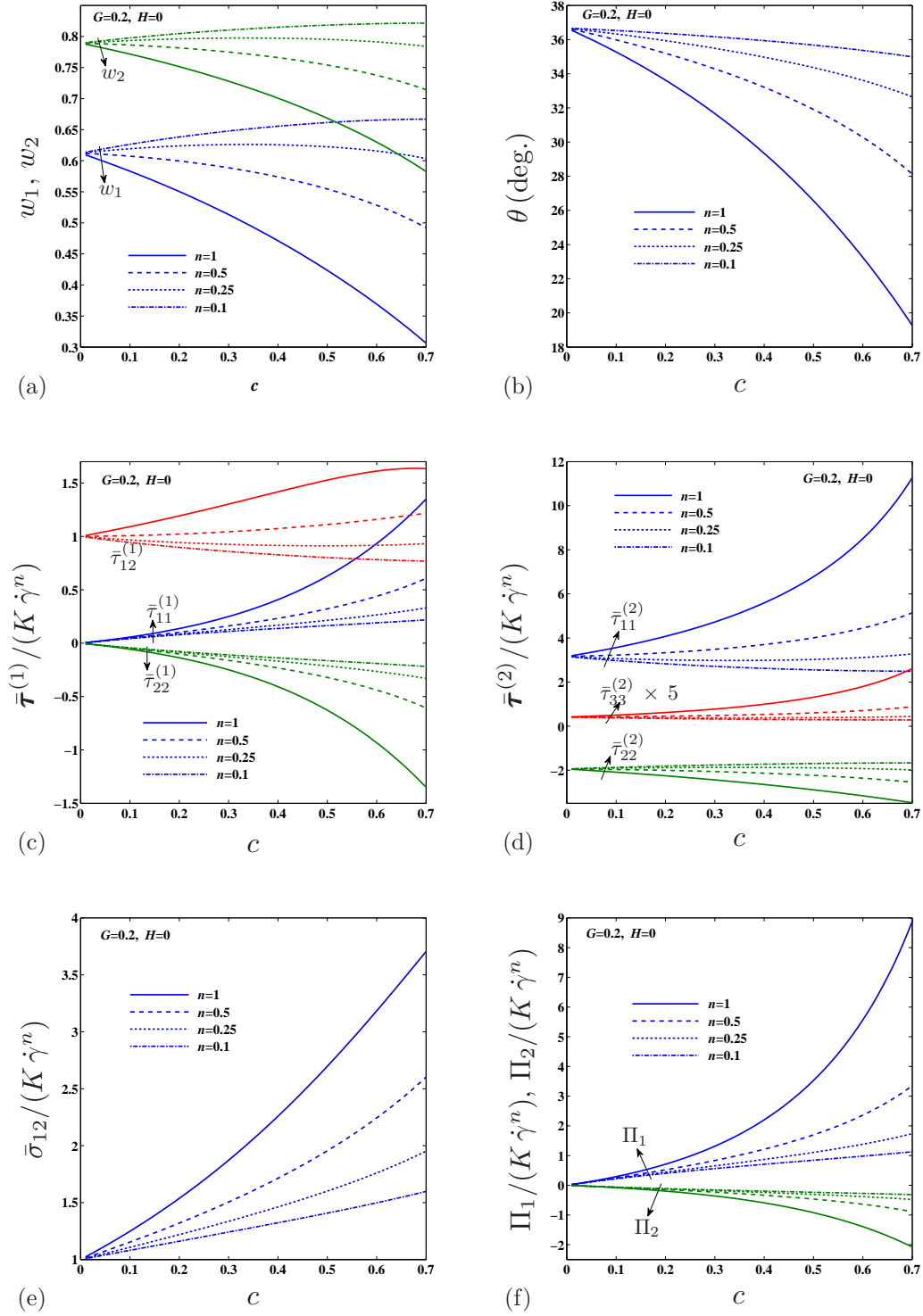


Figure 5.8: Variational estimates for the steady-state response of suspensions of initially spherical Gent particles in a power-law fluid ($H = 0$) for various values of n under shear flow conditions. The components of $\bar{\tau}^{(1)}$ and $\bar{\tau}^{(2)}$ are given relative to the fixed coordinate system \mathbf{E}_i and the principal axes of the particles, respectively.

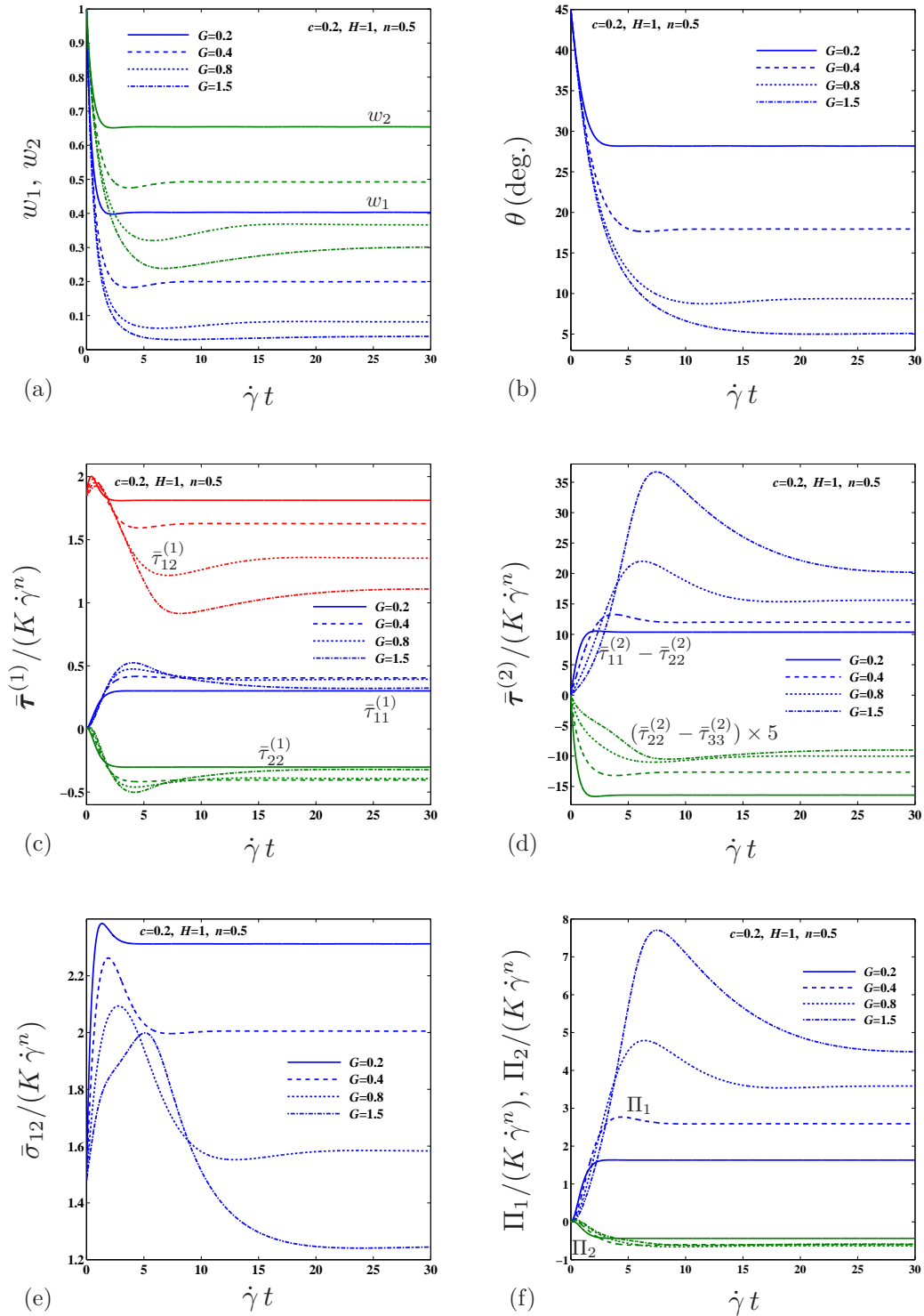


Figure 5.9: Variational estimates for the time-dependent response of suspensions of initially spherical Gent particles with $c = 0.2$ and various values of G in a Herschel-Bulkley fluid ($H = 1$ and $n = 0.5$) under shear flow conditions. Higher values of G correspond to softer particles. The components of $\bar{\tau}^{(1)}$ and $\bar{\tau}^{(2)}$ are given relative to the fixed coordinate system \mathbf{E}_i and the principal axes of the particles, respectively.

5.4.3 Herschel-Bulkley fluids

Finally, in this subsection, we present results for the case of suspensions of elastic (Gent) particles in a general Herschel-Bulkley fluid. Figure 5.9 presents variational estimates for the time-dependent behavior of suspensions of purely elastic (Gent) particles in a Herschel-Bulkley fluid ($H = 1$ and $n = 0.5$) subjected to the shear flow conditions (5.62). Results are shown for a fixed volume fraction ($c = 0.2$) and varying values of $G = K \dot{\gamma}^n / \mu$. The evolutions of w_1 , w_2 and θ in figures 5.9 (a) and (b) indicate that, as G increases, the elastic particles exhibit larger elongations, as well as closer alignment with the shear direction. In addition, we realize from these figures that, at a constant strain rate $\dot{\gamma}$, it would generally take longer for the particles with a higher G (corresponding to softer particles) to reach a steady state. In this connection, we, however, observe from these figures that particle rotation reach a steady state progressively later than the particle elongation in the plane of shear (characterized by the aspect ratio w_1) with increasing value of G . Next, we observe from figure 5.9 (c) and (d) that the shear stress component $\bar{\tau}_{12}^{(1)}$ in the fluid shows a monotonic reduction in magnitude as G increases, while the normal component $\bar{\tau}_{11}^{(2)} - \bar{\tau}_{22}^{(2)}$ in particle exhibits a rather opposite trend with increasing the value of G . This can be explained by noting that, as $G = K \dot{\gamma}^n / \mu$ increases (and if we think of this as a decrease in μ), the softer particles serve to accommodate more part of the total macroscopic deformation applied to the suspension (by exhibiting larger elongations and closer alignment with the shear direction), so that the smaller and larger stresses are produced in the fluid matrix and the particle, respectively. Moreover, figures 5.9(e) and (f) show the corresponding estimates for the macroscopic shear and normal stress differences, respectively. An interesting observation from figure 5.9(e) is presence of an “overshoot”, followed by a decay in the macroscopic shear component, as similarly reported by Gao et al. (2011) and Avazmohammadi and Ponte Castañeda (2014) for suspensions of elastic particles in Newtonian fluids. As explained in these works, this overshoot is linked to the above-mentioned fact that the time interval between the arrest of the particles elongations in the plane of shear and the corresponding arrest of the particles rotations becomes progressively larger as G increases. Finally, an important conclusion from these figures (and similarly from figures 5.3 and 5.6) is that the suspension of elastic particles in a Herschel-Bulkley fluid exhibits a time-dependent behavior upon application of a constant strain rate, although there is no time-dependency present at the level of the individual phases. In particular, the time-dependent behavior of the suspension qualitatively resemble the behavior of a *Maxwellian* viscoelastic fluid, where the stress, induced by application of a constant shear strain rate, relaxes over time.

For completeness, it is of interest to examine the influence of the yield stress of the suspending fluid on the SS behavior of the suspensions of elastic particles in a HB fluid. Figure 5.10 presents variational estimates for the steady-state response of suspensions of elastic (Gent) particles with $c = 0.2$ in a HB fluid under the shear flow conditions (5.62). Results are shown for various values of G , as a function of the non-dimensional parameter $H = \tau_0 / (K \dot{\gamma}^n)$. We observe from figures 5.10 (a) and (b) that the elastic particles in a HB fluid exhibit larger stretches as well as closer alignments with the shear direction with increasing values of H , which is consistent with the corresponding results presented in figures 5.3 and 5.4 for suspensions of elastic particles in a Bingham fluid. This trend,

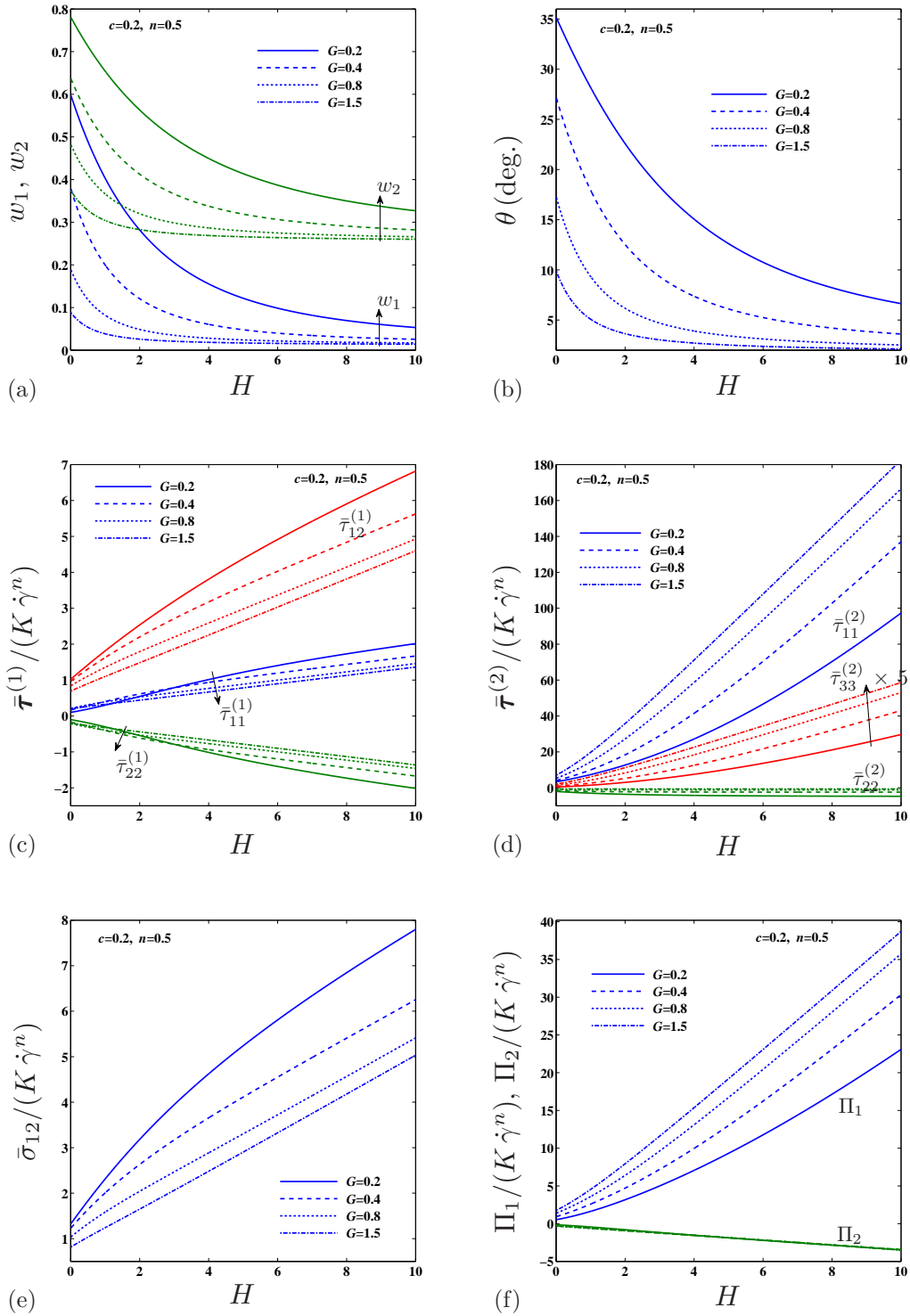


Figure 5.10: Variational estimates for the steady-state response of suspensions of initially spherical Gent particles with $c = 0.2$ and various values of G in a Herschel-Bulkley fluid ($n = 0.5$) under shear flow conditions. The components of $\bar{\tau}^{(1)}$ and $\bar{\tau}^{(2)}$ are given relative to the fixed coordinate system \mathbf{E}_i and the principal axes of the particles, respectively.

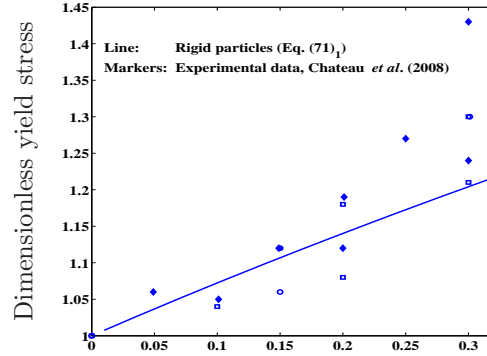


Figure 5.11: Comparisons of the effective yield stress $\tilde{\tau}_0^R$ for suspensions of rigid particles in yield stress fluids ($\tilde{\tau}_0^R/\tau_0$) with experimental data in Chateau et al. (2008) (originally from Mahaut et al. (2008)), as a function of the particle volume fraction. The solid diamond and open square symbols correspond to suspensions of polystyrene and glass beads in emulsion and in bentonite, respectively, while the open circle symbols correspond to suspensions of glass beads in carbopol.

however, is seen to be less pronounced at higher values of G corresponding to softer particles. Next, we observe from figures 5.10 (c) and (d) that increasing H leads to an increase in the stress level in both fluid and particle phases for all values of G (which is consistent with the corresponding results in figures 5.4 for the case of Bingham fluids), while increasing G leads to a reduction and increase in the stress level in the fluid and particle phases, respectively (again, in agreement with the corresponding results in figures 5.10.) Finally, figures 5.10(e) and (f) show the corresponding estimates for the macroscopic shear and normal stress differences, respectively. An interesting observation from figures 5.10(e) is that the macroscopic shear stress exhibits rather a linear increase with the parameter H at high enough values of G . This behavior of the suspension is qualitatively similar to the corresponding behavior in the suspensions of rigid spherical particles, described by relation (5.72). This is because, at high enough values of G , the SS particle shape and orientation shows only a slight variation with H , so that the SS behavior of the suspension can be approximated by that of suspensions of rigid *ellipsoidal* particles which are closely aligned with the shear direction.

Finally, in figure 5.11, we compare predictions of our model with experimental data available in the literature for suspensions of particles in yield stress fluids. This comparison is limited to the case of *rigid* particles, due to the lack of experimental data and numerical simulations on the rheology of suspension of *deformable* particles in yield stress fluids. In particular, figure 5.11 shows the comparison for the (dimensionless) effective yield stress of the suspensions of spherical rigid particles in yield stress fluids, $\tilde{\tau}_0^R/\tau_0$ (as given by (5.70)₁), with the experimental data available from Chateau et al. (2008) (originally from Mahaut et al. (2008)) for the same quantity of the suspensions of very stiff particles (polystyrene and glass beads) in yield stress fluids (including emulsion, bentonite and carbopol), as a function of c . We observe quite good agreement between our results and the experimental data up to moderate levels of particle concentration ($c < 0.25$). However, it should be noted that our model is not expected to provide accurate predictions for the case of rigid particles, since it has been assumed (for simplicity) that the shape of (the angular dependence of) the two-

point correlation function is identical to the evolution of the particle shape. Since for rigid particles, the particle shape cannot change, this would mean that the two-point correlations function remains isotropic, which is not expected to be the case for the non-colloidal suspensions considered in this work. On the other hand, for deformable particles, the change in shape of the particles is expected to dominate the higher-order effect in c of the changes in the particle distribution, and the model is expected to be more accurate then. Finally, it is relevant to mention that Chateau et al. (2008) made similar comparisons of their variational estimates for $\tilde{\tau}_0^R/\tau_0$ with the experimental data for a larger range of c , and they were able to achieve a good agreement. This is because they make use of the empirical model of Krieger and Dougherty (1959) for the effective viscosity of the corresponding LCC which has been successfully fitted to the experimental data for the case of highly concentration suspensions. We, on the other hand, made use of the HS estimate for the effective behavior of the LCC which is known to be a lower bound within the class of isotropic microstructures with two-point isotropic distributions.

5.5 Conclusions

In this chapter, we have developed a homogenization-based model to estimate the effective rheological behavior of non-colloidal suspensions of initially spherical, soft particles in yield stress fluids under Stokes flow conditions. More specifically, we considered suspensions of Kelvin-Voigt solid particles in a Herschel-Bulkley fluid which undergo time-dependent, finite deformations when subjected to uniform flows.

Our model can be summarized in four steps: (I) we formulated the problem of finding the effective (instantaneous) response of the suspension in terms of finding the effective potential $\widetilde{W}(\bar{\mathbf{D}})$ of the suspension, as described by relations (5.25) and (5.26), (II) we then made use of the variational principle of Ponte Castañeda (1991) to approximate the potential $\widetilde{W}(\bar{\mathbf{D}})$ of the actual suspension in terms of the effective potential \widetilde{W}_L of a “linear comparison composite” (LCC) consisting of the same particles distributed randomly in a (fictitious) Newtonian fluid with a suitably-chosen viscosity $\eta^{(1)}$, identified with the optimality conditions (5.36) and (5.37), (III) we recalled the relevant estimates for the LCC from Chapter 4, including an estimate for \widetilde{W}_L , as given by (5.40), (IV) we combined the solution for the instantaneous behavior of the suspension with the evolution equation for the elastic stress in the particles, as given by (5.54), and for the average particle shape and orientation, as given by (5.50) and (5.51), respectively, to complete the model for the time-dependent response of the suspensions.

We have also used our model to explore in more detail the rheology and particle dynamics in suspensions of elastic Gent particle is HB fluids under shear flow conditions, as described by (5.62). In the context of this example, we investigated the influence of constitutive properties of the HB fluids and the particles, and the particle volume fraction on the dynamics of the suspended particles, as well as on the macroscopic rheological behavior of the suspension. A general conclusion from the results is that the suspensions exhibit a time-dependent behavior upon application of a constant strain rate, although there is no time-dependency present at the level of the individual phases. Also, we found that the time-dependent behavior of the suspensions qualitatively resemble the behavior

of a *Maxwellian* viscoelastic fluid, where the stress, induced by application of a constant strain rate, relaxes over time. A similar finding has been reported in the context of suspensions of slightly deformable particles in a Newtonian fluid by Goddard (1977). In particular, for the case of power-law fluids (i.e., when $\tau_0 = 0$) with $n \leq 1$, our results indicate that the macroscopic time-dependent shear stress exhibits a *rheopectic* behavior, where the stress increases with the duration of shearing.

The results confirm that steady-state solutions are available for suspensions of Gent particles under shear flow conditions. In particular, the results show that the particles suspended in a HB fluid with a higher yield stress (τ_0) exhibit larger elongations, as well as closer alignments with the shear direction at a steady state, and this behavior is more pronounced for the case of stiffer particles. On the other hand, for the case of power-law fluids, we found that, when the elastic particles are not too soft, they exhibit smaller deformations, as well as less alignments with the shear direction at the steady state, as the value of the index n decreases. Also, for the case of Bingham fluids, we found that, at low values of τ_0 , SS values of the macroscopic shear stress is increasing with the volume fraction of particles, while the opposite is true for higher values of τ_0 . Furthermore, it has been found that the macroscopic shear stress exhibits quite a linear increase with the yield stress τ_0 for the case of very soft particles. This behavior of the suspension is qualitatively similar to the corresponding behavior in the suspensions of rigid spherical particles, described by relation (5.72).

Finally, we compared the prediction of our model with the experimental data on the effective yield stress of the suspensions of particles in yield stress fluids which were only available for the case of rigid particles. Despite the fact that our model is not expected to provide accurate estimates for the case of rigid particles, we found relatively good agreement between the model's prediction and the experimental data up to moderate concentrations of particles ($c < 0.25$). Nevertheless, we emphasize that the comparisons for the case of rigid particles can not reflect the full potential of our model in describing the rheological features of complex suspensions, and we look forward to compare the predictions of our model for the case of deformable particles when the corresponding experimental data or numerical simulations become available.

Part III

Elasto-Viscoplastic Composites

Chapter 6

Effective behavior of elasto-viscoplastic particle-reinforced composites

In this chapter, we propose an original model to study the effective behavior of particle reinforced composites consisting of an elasto-viscoplastic matrix and a random distribution of linear viscoelastic particles, subjected to small deformations. The proposed model makes use of the variational principle of Ponte Castañeda (1991) to approximate the effective behavior of the nonlinear composite by that of a *linear comparison composite* (LCC) consisting of a linear viscoelastic matrix with a suitably-chosen viscosity constant and the same particle phase as in the actual nonlinear composite. Then, making the approximation that the elastic strains in the LCC are *uniform-per-phase*, the homogenization problem for finding the effective behavior of the LCC becomes mathematically equivalent to the corresponding problem for “thermoelastic” composites with constant-per-phase thermal strains. This problem then can be solved by using the Ponte Castañeda and Willis homogenization theory (Ponte Castañeda and Willis, 1995) together with an explicit time-discretization scheme to integrate the evolution equations describing the constitutive behavior of the phases. To implement our model, we restrict our attention to the special case of incompressible composites consisting of an elastic-ideally plastic matrix and random distribution of aligned, elastic ellipsoidal particles. In this case, we propose an empirical modification of the model to improve its estimate for the purely elastic regime of the composite behavior. This modification remains consistent with the estimate of the model for the elasto-plastic regime of the composite behavior. In particular, we make use of our model to study the effective behavior of the composite with spheroidal particles subjected to isochoric loading. We investigate the effect of particle shape and volume fraction as well as the phases elastic properties on the effective behavior and field statistics in the composites

6.1 Introduction

Many engineering materials exhibit an elasto-viscoplastic behavior when subjected to mechanical loadings. Among them, the class of particle-reinforced composite materials is particularly important to study because of their numerous technological applications as well as for an understanding of the mechanics of the coupling between elastic and dissipative effects in the composite under loadings. Examples of these materials include metal-matrix and polymer-matrix composites. Our goal in this part of the thesis is to study the overall response of the particle-reinforced composite materials when the constituent phases exhibit an elasto-viscoplastic (EVP) behavior.

The problem of predicting the effective behavior of the EVP composites has often been addressed in the literature through numerical simulations (see Finlaysh and Shek, 1998; Gonzalez et al., 2004; Lee et al., 2011; Reina-Romo and Sanz-Herrera, 2011, to cite only a few). However, in the present study, our objective is to provide theoretical predictions for these composites. With this goal in mind, homogenization methods developed in the context of nonlinear heterogeneous media appear to be an promising approach to solve this problem. More specifically, these methods follow from variational principles expressing the overall response of a given nonlinear composite in terms of the behavior of an optimally chosen “linear comparison composite” (LCC). In these methods, the LCC is assumed to have the same microstructure as the nonlinear composite, and the properties of the constituent phases in the LCC are determined by appropriate linearization of the corresponding phases in the nonlinear composite. In particular, Ponte Castañeda (1991) introduced a variational method in

which the material properties in the LCC are identified by “secant” moduli of the nonlinear phases, evaluated at the second moments of the local fields over the phases. In the past 20 years, applications of this method have been mainly explored for viscoplastic or rigid-plastic composites where no elastic deformation is present in the constituent phases (Ponte Castañeda, 1991; Zaidman and Ponte Castañeda, 1996, among others). On the other hand, for EVP composites, similar methods which rely on the notion of LCCs have not been developed until more recently. More specifically, these methods follow from an “*incremental variation principal*” (IVP) which aims at recasting the elastic and dissipative potentials of the constituents phases into equivalent *condensed incremental* potentials (Lahellec and Suquet, 2007). This technique allows to extend the variational homogenization schemes originally developed for the case of viscoplastic composites to address the effective response in the EVP composites. In particular, Lahellec and Suquet (2007a) derived an incremental variation principle which is based on implicit time-discretization of the constitutive differential equations of the phases and the variational procedure of Ponte Castañeda (1992). In a similar development, Brassart et al. (2012) made use of the same incremental potential of Lahellec and Suquet (2007a) and proposed a different way of optimizing the properties of the associated LCC. More recently, Lahellec and Suquet (2013) made use of the IVP method to estimate the effective response, as well as the statistics of the stress fields in EVP composites with isotropic and kinematic hardening laws under radial and non-radial loadings.

The IVP method of Lahellec and Suquet (2007a) offers a general and accurate approach to determine the effective behavior of the EVP composites within the limit of relatively small deformations. However, the implementation of this method requires the solution of coupled nonlinear equations which often need certain regularizations to avoid the numerical problems, even for the case of an isotropic microstructure. In this work, we propose a new approach to find the effective behavior of the EVP composites which also makes use of the LCC technique. The central idea behind this approach, which is very similar to the technique used in Chapter 4, is to recast the constitutive equations of the constituent phases of the EVP composites in the form which can be described by a single *modified* dissipation potential depending on two variables: stress tensor and *elastic strain* which is assumed to be known at the present instant. In this way, we can simply use the principle of the minimum potential energy to formulate the homogenization problem for the effective behavior of the EVP composites. Then, we make use of the variational principle of Ponte Castañeda (1991) to approximate the effective behavior of the composite (with single dissipation potentials) in terms of that of a LCC. At this point, making the assumption of *uniform-per-phase* elastic strains, the local behavior of this LCC will be mathematically analogous to that of linear “thermoelastic” composites with uniform-per-phase thermal strains, and we make use of the Ponte Castañeda and Willis homogenization theory (Ponte Castañeda and Willis, 1995) to estimate the effective behavior of the LCC. This approach might not be as accurate as the IVP method, but, it is very easy to implement even for a general ellipsoidal (particulate) microstructure.

The structure of this chapter is as follows. Section 6.2 addresses the constitutive behavior of the matrix and particles considered in this work. We consider composites consisting of an elasto-viscoplastic (EVP) matrix and a random distribution of Maxwellian viscoelastic particles. In this section, we also describe the homogenization problem for this composite. Much like our homoge-

nization technique in Chapters 4 and 5, the central idea behind the homogenization approach in this chapter is to recast the constitutive equations of the constituent phases of the elasto-viscoplastic composites in the form which can be described by a single *modified* dissipation potential depending on two variables: stress tensor and *elastic strain* which is assumed to be known at the present instant. In this way, we can simply use the principle of the minimum potential energy to formulate the homogenization problem for the effective behavior of the EVP composites. In section 6.3, we lay out our strategy to solve the homogenization problem. We first replace the homogenization problem for finding the effective incremental response of the composites by the corresponding problem for a suitably-chosen LCC, consisting of a Maxwellian matrix reinforced by the same particles. Next, we make the approximation that elastic strains in the composite are uniform-per-phase, which simplifies the homogenization problem for the LCC to that for linear thermoelastic composites with uniform thermal strains. Lastly, in this section, we propose an empirical modification of the model for the purely elastic response of the composites for the case of elastic particles. In section 6.4, we apply our model to incompressible composites consisting of an elastic-ideally plastic matrix reinforced by a random distribution of aligned, elastic spheroidal particles subjected to axisymmetric, transverse and longitudinal modes of shear loading-unloading-loading cycles. Finally, some conclusions are drawn in section 6.5.

6.2 Problem formulation

In this work, we consider particle-reinforced composites consisting of an elasto-viscoplastic matrix and a random distribution of aligned, ellipsoidal linear viscoelastic particles. Both matrix and fibers phases are assumed to be isotropic. For definiteness, let Ω be a representative volume element (RVE) of this composite, and let $\Omega^{(1)}$ and $\Omega^{(2)}$ denote the complementary regions in Ω occupied by the matrix and the particles, respectively. Following the hypothesis of *separation of length scales*, we assume that the characteristic length-scale of the particles is much smaller than the size of the RVE as well as the scale of variation of the applied loading conditions. Also, it is assumed that the microstructure in the RVE is *statistically uniform*, and the characteristic functions $\chi^{(r)}(\mathbf{x})$, $r = 1, 2$ are used to describe the microstructure such that they are equal to one if the position vector \mathbf{x} is in phase r (i.e. $\mathbf{x} \in \Omega^{(r)}$) and zero otherwise. Moreover, the symbols $\langle \cdot \rangle$ and $\langle \cdot \rangle^{(r)}$ denote volume averages over the RVE (Ω) and over phase r ($\Omega^{(r)}$), respectively, so that the scalars $c^{(r)} = \langle \chi^{(r)} \rangle$ serve to denote the volume fractions of the given phases. Finally, throughout this work, we denote the quantities associated with the matrix and particle phases by the superscripts (1) and (2), respectively.

In the limit of infinitesimal strains, the total strain tensor $\boldsymbol{\epsilon}$ in the matrix phase is decomposed as

$$\boldsymbol{\epsilon}^{(1)} = \boldsymbol{\epsilon}_e^{(1)} + \boldsymbol{\epsilon}_{vp}^{(1)}, \quad (6.1)$$

where $\boldsymbol{\epsilon}_e^{(1)}$ and $\boldsymbol{\epsilon}_{vp}^{(1)}$ are the elastic and viscoplastic parts of the strain, respectively. The elasto-viscoplastic behavior of the matrix is then described by the following *rate-type* relations (Lemaitre

and Chaboche, 1994)

$$\dot{\epsilon}^{(1)} = \dot{\epsilon}_e^{(1)} + \dot{\epsilon}_{vp}^{(1)}, \quad \dot{\epsilon}_e^{(1)} = \mathbb{S}^{(1)} \dot{\sigma}, \quad \dot{\epsilon}_{vp}^{(1)} = \frac{\partial \psi(\sigma)}{\partial \sigma}, \quad \psi(\sigma) = \frac{\dot{\epsilon} \eta_0}{n+1} \left(\frac{[\sigma_{eq} - \eta_0]^+}{\sigma_0} \right)^{n+1} \quad (6.2)$$

where an overdot denotes derivation with respect to time, σ is the Cauchy stress tensor, $\psi(\sigma)$ is a stress potential, and $\sigma_{eq} = \sqrt{(3/2)\sigma_d \cdot \sigma_d}$ is the von Mises equivalent stress with σ_d denoting the deviatoric part of the stress tensor σ . Also, $\mathbb{S}^{(1)}$ is the elastic compliance tensor of the matrix, $\dot{\epsilon}_0$ is a reference strain-rate, n is a strain-rate sensitivity constant, η_0 is the flow stress of the matrix, and σ_0 is the coefficient of the plastic resistance. Moreover, $[x]^+$ denotes the positive part of x such that $[x]^+ = x$ if $x > 0$ and zero otherwise.

The particles are linear Maxwellian viscoelastic solids whose constitutive behavior is characterized by the relation

$$\dot{\epsilon}^{(2)} = \dot{\epsilon}_e^{(2)} + \mathbb{M}^{(2)} \sigma, \quad \dot{\epsilon}_e^{(2)} = \mathbb{S}^{(2)} \dot{\sigma}, \quad (6.3)$$

where $\dot{\epsilon}_e^{(2)}$ is the elastic strain-rate in the particle phase, and $\mathbb{S}^{(2)}$ and $\mathbb{M}^{(2)}$ are the elastic and viscous compliance tensors of the particle phase, respectively.

Given the microstructure of the composite and the local constitutive properties (6.2) and (6.3), the effective behavior of the composite can be described by the relation between the average strain-rate tensor $\dot{\bar{\epsilon}} = \langle \dot{\epsilon} \rangle$ and the average stress tensor $\bar{\sigma} = \langle \sigma \rangle$ over the RVE Ω . The problem of finding this relation can be conveniently stated in a variational framework if we can formulate the constitutive relations (6.2) and (6.3) in terms of appropriate free-energy density functions. To this end, we regard the elastic strain as an *internal variable* in each phase, and since we will solve the present homogenization problem in an *incremental* fashion, we assume that the elastic strain is known at the beginning of the current instant. Therefore, we introduce the *modified* free-energy functions $u^{(r)}(\sigma)$ which are written as

$$u^{(1)}(\sigma) = \psi(\sigma) + \gamma^{(1)} \cdot \sigma, \quad \text{and} \quad u^{(2)}(\sigma) = \frac{1}{2} \sigma \cdot \mathbb{M}^{(2)} \sigma + \gamma^{(2)} \cdot \sigma, \quad (6.4)$$

such that the local constitutive relation of the phases can be written as

$$\dot{\epsilon}^{(1)} = \frac{\partial u^{(1)}}{\partial \sigma} = \frac{\partial \psi(\sigma)}{\partial \sigma} + \gamma^{(1)}, \quad \text{and} \quad \dot{\epsilon}^{(2)} = \frac{\partial u^{(2)}}{\partial \sigma} = \mathbb{M}^{(2)} \sigma + \gamma^{(2)}, \quad (6.5)$$

for the matrix and particle phases, respectively. In the above relations, $\gamma^{(r)}$ is the elastic strain(-rate) tensor in phase r which is assumed to be known at the present instant, and is given by

$$\gamma^{(r)} = \dot{\epsilon}_e^{(r)} = \mathbb{S}^{(r)} \dot{\sigma}, \quad r = 1, 2. \quad (6.6)$$

Next, the local relation between the strain-rate tensor $\dot{\epsilon}$ and the stress tensor σ in the composite is given by

$$\dot{\epsilon} = \frac{\partial u}{\partial \sigma}(\mathbf{x}, \sigma), \quad u(\mathbf{x}, \sigma) = \chi^{(1)}(\mathbf{x}) u^{(1)}(\sigma) + \chi^{(2)}(\mathbf{x}) u^{(2)}(\sigma), \quad (6.7)$$

where $u(\mathbf{x}, \sigma)$ is the local stress potential.

Now, making use of the *principle of minimum complementary energy*, the relation between the average strain-rate and stress tensor is given by

$$\dot{\bar{\epsilon}} = \frac{\partial \tilde{U}(\bar{\boldsymbol{\sigma}})}{\partial \bar{\boldsymbol{\sigma}}}, \quad (6.8)$$

where $\tilde{U}(\bar{\boldsymbol{\sigma}})$ denotes the effective stress-energy potential for the composite, defined as

$$\tilde{U}(\bar{\boldsymbol{\sigma}}) = \min_{\boldsymbol{\sigma} \in S(\bar{\boldsymbol{\sigma}})} \langle u(\mathbf{x}, \boldsymbol{\sigma}) \rangle = \min_{\boldsymbol{\sigma} \in S(\bar{\boldsymbol{\sigma}})} \sum_{r=1}^2 c^{(r)} \langle u(\boldsymbol{\sigma}) \rangle^{(r)}, \quad (6.9)$$

In the above definition, $S(\bar{\boldsymbol{\sigma}})$ denotes the set of admissible stress field, given by

$$S(\bar{\boldsymbol{\sigma}}) = \{ \boldsymbol{\sigma}, \operatorname{div}(\boldsymbol{\sigma}) = 0 \text{ in } V, \boldsymbol{\sigma} \cdot \mathbf{n} = \bar{\boldsymbol{\sigma}} \cdot \mathbf{n} \text{ on } \partial V \}, \quad (6.10)$$

Thus, the problem of estimating the effective behavior of the nonlinear composite is equivalent to that of estimating the function $\tilde{U}(\bar{\boldsymbol{\sigma}})$ in relation (6.9). It should be remarked that relations (6.8) and (6.9) provide a constitutive description for the “incremental” macroscopic behavior of the composite, and the time-dependent response of the composite can be obtained by making use of a time-discretization procedure, starting from an appropriate initial state of the composite. In general, computing the function $\tilde{U}(\bar{\boldsymbol{\sigma}})$ exactly is an extremely difficult task. In the next section, we recall the variational principle of Ponte Castañeda (1991) to estimate the function $\tilde{U}(\bar{\boldsymbol{\sigma}})$.

6.3 Variational estimates

In this section, we provide an estimate for the effective potential $\tilde{U}(\bar{\boldsymbol{\sigma}})$ by making use of the variational principle of Ponte Castañeda (1991). The central idea of this principle is to express the effective potential of the nonlinear composite in terms of the effective behavior of a suitably chosen “linear comparison composite” (LCC) which has the same microstructure (i.e. same characteristic functions $\chi^{(r)}(\mathbf{x})$) as the actual (nonlinear) composite material. For the class of nonlinear composites of interest, we construct a LCC consisting of a Maxwellian matrix and the same particle phases as those in the actual nonlinear composite. In particular, we define a comparison composite with the local modified stress potential

$$u_L(\mathbf{x}, \boldsymbol{\sigma}; \eta^{(1)}) = \chi^{(1)}(\mathbf{x}) u_L^{(1)}(\boldsymbol{\sigma}; \eta^{(1)}) + \chi^{(2)}(\mathbf{x}) u_L^{(2)}(\boldsymbol{\sigma}), \quad (6.11)$$

where $u_L^{(1)}(\boldsymbol{\sigma}; \eta^{(1)})$ is the stress potential of the matrix phase in the LCC with the form similar to (6.4)₂, which can be written as

$$u_L^{(1)}(\boldsymbol{\sigma}; \eta^{(1)}) = \frac{1}{2} \boldsymbol{\sigma} \cdot \mathbb{M}^{(1)} \boldsymbol{\sigma} + \boldsymbol{\gamma}^{(1)} \cdot \boldsymbol{\sigma}, \quad (6.12)$$

In the above expressions, $\mathbb{M}^{(1)}$ denotes the (isotropic) viscous compliance tensor of the matrix phase in the LCC which takes the form

$$\mathbb{M}^{(1)} = \frac{1}{3\kappa}\mathbb{J} + \frac{1}{2\eta^{(1)}}\mathbb{K} \quad (6.13)$$

where \mathbb{J} and \mathbb{K} denote the standard fourth-order, isotropic, hydrostatic and shear projection tensors, $\eta^{(1)}$ is the (as yet unknown) viscosity of the matrix, and κ is the bulk viscosity of the matrix which is introduced to enable us to take the incompressibility in the matrix phase (i.e., $\kappa \rightarrow \infty$.) Also, $\boldsymbol{\gamma}^{(1)}$ is the elastic strain-rate tensor given by relation (6.5)₁. Moreover, as already mentioned, we choose the particle phases in the LCC to be equal to those in the nonlinear composite, so that $u^{(2)}(\boldsymbol{\sigma}) = u_L^{(2)}(\boldsymbol{\sigma})$, as defined via relations (6.4)₂ and (6.6) (for $r = 2$). We also emphasize that the volume fraction, shape and orientation of particles in the LCC are assumed to be the same as those in the nonlinear composite. Correspondingly, the local constitutive relations for the linear phases in the LCC are written as

$$\dot{\boldsymbol{\epsilon}}^{(r)} = \frac{\partial u_L^{(r)}}{\partial \boldsymbol{\sigma}} = \mathbb{M}^{(r)} \boldsymbol{\sigma} + \boldsymbol{\gamma}^{(r)}, \quad r = 1, 2. \quad (6.14)$$

Following Ponte Castañeda's variational principle Ponte Castañeda (1991), the nonlinear stress potential $u^{(1)}$ in the actual composite can then be approximated as

$$u^{(1)}(\boldsymbol{\sigma}) = \sup_{\eta^{(1)} > 0} \left\{ u_L^{(1)}(\boldsymbol{\sigma}; \eta^{(1)}) - V^{(1)}(\eta^{(1)}) \right\}, \quad (6.15)$$

where the "error" function $V^{(1)}$ is defined by

$$V^{(1)}(\eta^{(1)}) = \sup_{\sigma_{eq}} \left\{ \frac{1}{6\eta^{(1)}} (\sigma_{eq})^2 - \psi(\boldsymbol{\sigma}) \right\} \quad (6.16)$$

Now, making use of approximation (6.15) in the definition (6.9) for the effective stress potential, and interchanging the order of suprema over $\boldsymbol{\sigma}$ and $\eta^{(1)}$, we find the following estimate for the effective potential $\tilde{U}(\bar{\boldsymbol{\sigma}})$ (Ponte Castañeda, 1991)

$$\tilde{U}(\bar{\boldsymbol{\sigma}}) \geq \sup_{\eta^{(1)} > 0} \left\{ \tilde{U}_L(\bar{\boldsymbol{\sigma}}; \eta^{(1)}) - c^{(1)} V^{(1)}(\eta^{(1)}) \right\} \quad (6.17)$$

where \tilde{U}_L denotes the effective (modified) stress potential of the LCC. Similar to definition (6.8), making use of principle of minimum complementary energy, this potential is defined as

$$\tilde{U}_L(\bar{\boldsymbol{\sigma}}; \eta^{(1)}) = \inf_{\boldsymbol{\sigma} \in S(\bar{\boldsymbol{\sigma}})} \left\langle u_L(\mathbf{x}, \boldsymbol{\sigma}; \eta^{(1)}) \right\rangle. \quad (6.18)$$

The optimality conditions in (6.16) and (6.17) generate a system of algebraic nonlinear equations for the optimal values of the variables $\eta^{(1)}$ and σ_{eq} . Making use of the power-law form for the potential $\psi(\boldsymbol{\sigma})$ from (6.2), the optimality condition in (6.16), known as the *secant* condition, leads to the following relation

$$\dot{\epsilon} \left(\frac{[\hat{\sigma}_{eq} - \eta_0]^+}{\sigma_0} \right)^n = \frac{1}{3\eta^{(1)}} \hat{\sigma}_{eq}, \quad (6.19)$$

where $\hat{\sigma}_{eq}$ denotes the optimal value of σ_{eq} in (6.16). Also, the optimality condition in (6.17) reduces to

$$(\eta^{(1)})^2 \partial_{(\eta^{(1)})} \tilde{U}_L(\bar{\boldsymbol{\sigma}}) + \frac{c^{(1)}}{6} (\hat{\sigma}_{eq}^{(1)})^2 = 0. \quad (6.20)$$

In general, we need to solve the coupled algebraic equations (6.19) and (6.20) to find the unknowns $\eta^{(1)}$ and $\hat{\sigma}_{eq}$. Once these two unknowns are obtained, the effective stress potential $\tilde{U}(\bar{\boldsymbol{\sigma}})$ can be calculated from (6.17). In this study, we are particularly interested in the special case of elastic-perfectly plastic behavior for the matrix phase. In the constitutive relations (6.2) for the matrix phase, the elastic-perfectly plastic behavior is obtained by setting $\eta_0 = 0$ and taking the limit $n \rightarrow \infty$. In this case, the matrix would exhibit an elastic-perfectly plastic behavior with the yield stress σ_0 . For this special case equation (6.19) reduces to $\hat{\sigma}_{eq} = \sigma_0$ which, in turn, can be used in (6.20) to give the following equation for finding $\eta^{(1)}$

$$(\eta^{(1)})^2 \partial_{(\eta^{(1)})} \tilde{U}_L(\bar{\boldsymbol{\sigma}}) + \frac{c^{(1)}}{6} \sigma_0^2 = 0. \quad (6.21)$$

In conclusion, noting that the estimate (6.17) is stationary with respect to the variable $\eta^{(1)}$, it follows from (6.8) and (6.17) that the variational estimate for the effective behavior of the nonlinear composite can be obtained as

$$\dot{\boldsymbol{\epsilon}} = \frac{\partial \tilde{U}}{\partial \bar{\boldsymbol{\sigma}}} = \frac{\partial \tilde{U}_L}{\partial \bar{\boldsymbol{\sigma}}}, \quad (6.22)$$

where $\tilde{U}_L(\bar{\boldsymbol{\sigma}})$ is calculated at the optimized value of $\eta^{(1)}$, and the second equality (in the second relation) is used instead of the inequality (in (6.17)), in the sense of an approximation. Also, it can be shown that (Idiart and Ponte Castañeda, 2007) the first and second moments of the stress and strain fields in each phase in the LCC are equal with the same quantities in the actual nonlinear composite. The variational estimate (6.22) requires the knowledge on the effective (modified) stress potential \tilde{U}_L of the comparison composite, defined in (6.18). In the next subsection, we provide the algorithm based on an incremental formulation to obtain the potential $\tilde{U}_L(\bar{\boldsymbol{\sigma}})$ and the corresponding macroscopic constitutive relation of the LCC.

6.3.1 Estimates for the linear comparison composite

In this section, our objective is to provide an estimate for the effective stress potential of the LCC, $\tilde{U}_L(\bar{\boldsymbol{\sigma}})$. As mentioned earlier, the LCC consists of linear Maxwellian viscoelastic phases characterized by the local constitutive relations (6.14) and (6.6). Then, assuming that the elastic strain-rate tensors $\boldsymbol{\gamma}^{(r)}$ are known at the given instant, we formulated these relations in terms of the (modified) stress potentials (6.4)₂ and (6.12) in the local form (6.11). In general, the elastic strain rates tensors $\boldsymbol{\gamma}^{(r)}$ are non-uniform both in the matrix and particle phases, and we would need to use an incremental variational approach, such as the one developed by Lahellec and Suquet (2007), to find an estimate for $\tilde{U}_L(\bar{\boldsymbol{\sigma}})$. However, here, for simplicity and in order to develop a numerically feasible model, we make the approximation that the tensors $\boldsymbol{\gamma}^{(r)}$ are *uniform-per-phase*. In this case, the homogenization problem defined by equation (6.18) for the response of the viscoelastic LCC composite characterized by (6.11), (6.4)₂ and (6.12) is mathematically equivalent to the corresponding problem for a linear

thermoelastic composite with elastic moduli $\mathbb{M}^{(r)}$ and (uniform) thermal strains $\boldsymbol{\gamma}^{(r)}$ (provided that the viscosity moduli and strain rate field are identified with the elastic moduli and strain field, respectively). In this way, the effective stress potential of a the LCC can be written as

$$\tilde{U}_L(\bar{\boldsymbol{\sigma}}) = \frac{1}{2} \bar{\boldsymbol{\sigma}} \cdot \tilde{\mathbb{M}} \bar{\boldsymbol{\sigma}} + \tilde{\boldsymbol{\gamma}} \cdot \bar{\boldsymbol{\sigma}} + \tilde{g} \quad (6.23)$$

where $\tilde{\mathbb{M}}$ and $\tilde{\boldsymbol{\gamma}}$ are the effective compliance and thermal strain tensors, respectively, and \tilde{g} is the effective specific heat. The effective stress-strain-rate relation of the LCC is then given by

$$\dot{\boldsymbol{\epsilon}} = \frac{\partial \tilde{U}_L}{\partial \bar{\boldsymbol{\sigma}}} = \tilde{\mathbb{M}} \bar{\boldsymbol{\sigma}} + \tilde{\boldsymbol{\gamma}}. \quad (6.24)$$

Note that, following relation (6.22), the above relation also holds as the macroscopic constitutive relation for the actual nonlinear composite when calculated at the optimal value of $\eta^{(1)}$.

Next, it follows from linearity of the problem that the average of the strain rate over phase r , $\dot{\boldsymbol{\epsilon}}^{(r)} = \langle \dot{\boldsymbol{\epsilon}} \rangle^{(r)}$ can be written in terms of strain-rate concentration tensors, so that

$$\dot{\boldsymbol{\epsilon}}^{(r)} = \mathbb{A}^{(r)} \dot{\boldsymbol{\epsilon}} + \mathbf{a}^{(r)}, \quad r = 1, 2 \quad (6.25)$$

where $\mathbb{A}^{(r)}$ is a fourth-order tensor that exhibits minor symmetry, but not necessarily major symmetry, and $\mathbf{a}^{(r)}$ is a symmetric second-order tensor. These tensors are subject to the constrains

$$\sum_{r=1}^2 c^{(r)} \mathbb{A}^{(r)} = \mathbb{I}, \quad \sum_{r=1}^2 c^{(r)} \mathbf{a}^{(r)} = \mathbf{0}. \quad (6.26)$$

The effective properties $\tilde{\boldsymbol{\gamma}}$ and \tilde{g} as well as concentration tensors $\mathbb{A}^{(r)}$ and $\mathbf{a}^{(r)}$ can be explicitly expressed in terms of the phase properties $\mathbb{M}^{(r)}$, and $\boldsymbol{\gamma}^{(r)}$, and the effective compliance tensor $\tilde{\mathbb{M}}$. To maintain continuity, these expressions are provided in Appendix E.1.

In addition, the phase averages strain-rate $\dot{\boldsymbol{\epsilon}}^{(1)}$ can also be obtained by averaging the local (linear) constitutive relations (6.14) as follows

$$\dot{\boldsymbol{\epsilon}}^{(r)} = \mathbb{M}^{(r)} \bar{\boldsymbol{\sigma}}^{(r)} + \boldsymbol{\gamma}^{(r)}, \quad r = 1, 2. \quad (6.27)$$

where $\bar{\boldsymbol{\sigma}}^{(1)}$ and $\bar{\boldsymbol{\sigma}}^{(2)}$ are the average of the stress in the matrix and particle phases, respectively.

In this work, we make use of the generalized estimate of the Willis type (Willis, 1977, 1981) for the effective compliance tensor $\tilde{\mathbb{M}}$ of the LCC. In particular, for the composite materials with “particulate” random microstructures (which is precisely the case in this work), Ponte Castañeda and Willis (1995) provided Willis-type estimates for the composites consisting of random distributions of aligned ellipsoidal particles in a given matrix with prescribed two-point correlation functions. Although these estimates are provided for a more general case, here, for simplicity, we adopt a specialized version of them by assuming that the shape and orientation of the distribution functions are identical to those of the individual particles. Based on this assumption, for two-phase composites,

the Willis-type estimate for $\tilde{\mathbb{M}}$ is given by

$$\tilde{\mathbb{M}} = \mathbb{M}^{(1)} + c^{(2)} \left[c^{(1)} \mathbb{Q} - (\Delta \mathbb{M})^{-1} \right]^{-1}, \quad (6.28)$$

where $\Delta \mathbb{M} = \mathbb{M}^{(1)} - \mathbb{M}^{(2)}$ and the microstructural tensor \mathbb{Q} contains information about the shape and distribution of the particles. This tensor is related to the tensor \mathbb{P} via the relation

$$\mathbb{Q} = \mathbb{L}^{(1)} - \mathbb{L}^{(1)} \mathbb{P} \mathbb{L}^{(1)}, \quad (6.29)$$

where $\mathbb{L}^{(r)} = (\mathbb{M}^{(r)})^{-1}$, $r = 1, 2$, is the viscosity moduli tensor of phase r , and the fourth-order tensor \mathbb{P} is a microstructural tensor with the following expression

$$\mathbb{P} = \frac{1}{4\pi |\mathbf{Z}|} \int_{|\boldsymbol{\xi}|=1} \mathbb{H}(\boldsymbol{\xi}) |\mathbf{Z}^T \boldsymbol{\xi}|^{-3} dS, \quad (6.30)$$

where \mathbf{Z} characterizes the shape of particles. Also, the fourth-order tensor \mathbb{H} is written as

$$H_{ijkl} = (K_{ik}^{-1} \xi_j \xi_l) |_{(ij)(kl)}, \quad (6.31)$$

in which the acoustic tensor \mathbf{K} is defined as $K_{ik} = \mathbb{L}_{ijkl}^{(1)} \xi_j \xi_l$, and the indices in parentheses, such as (ij) , are to be symmetrized.

Making use of the Willis estimate $\tilde{\mathbb{M}}$ in relations (E.3), the associated concentration tensors $\mathbb{A}^{(2)}$ and $\mathbf{a}^{(2)}$ are expressed by

$$\mathbb{A}^{(2)} = \left[\mathbb{I} - c^{(1)} \mathbb{P} \Delta \mathbb{L} \right]^{-1}, \quad \mathbf{a}^{(2)} = c^{(1)} \left[\mathbb{I} - c^{(1)} \mathbb{P} \Delta \mathbb{L} \right]^{-1} \Delta \boldsymbol{\gamma} \quad (6.32)$$

where $\Delta \boldsymbol{\gamma} = \boldsymbol{\gamma}^{(1)} - \boldsymbol{\gamma}^{(2)}$. The similar expressions for $\mathbb{A}^{(1)}$ and $\mathbf{a}^{(1)}$ can be, in turn, obtained from relations (6.26). Substituting expressions (6.32) (plus those for $\mathbb{A}^{(1)}$ and $\mathbf{a}^{(1)}$) into relations (6.25) and eliminating $\boldsymbol{\gamma}^{(1)}$ and $\boldsymbol{\gamma}^{(2)}$ from relations (6.27), we obtain the following expressions for the rate of average strain in the matrix and particles phases

$$\dot{\boldsymbol{\epsilon}}^{(1)} = \dot{\boldsymbol{\epsilon}} - c^{(2)} \mathbb{E} \left(\bar{\boldsymbol{\sigma}}^{(1)} - \bar{\boldsymbol{\sigma}}^{(2)} \right), \quad \dot{\boldsymbol{\epsilon}}^{(2)} = \dot{\boldsymbol{\epsilon}} + c^{(1)} \mathbb{E} \left(\bar{\boldsymbol{\sigma}}^{(1)} - \bar{\boldsymbol{\sigma}}^{(2)} \right), \quad (6.33)$$

where $\mathbb{E} = (\mathbb{I} - \mathbb{P} \mathbb{L}^{(1)})^{-1} \mathbb{P}$.

On the other hand, we recall from relation (6.6) that the thermal strain tensor in each phase in the LCC is equal to the elastic strain tensor in the corresponding phase in the actual nonlinear composite. Therefore, the evolution equation for the average stress tensor $\bar{\boldsymbol{\sigma}}^{(1)}$ and $\bar{\boldsymbol{\sigma}}^{(2)}$ can be obtained by substituting the thermal strain from (6.6) (the second equality) and the strain-rate phase averages from (6.33) into the constitutive relations (6.27) as follows

$$\begin{aligned} \dot{\bar{\boldsymbol{\sigma}}}^{(1)} &= \mathbb{C}^{(1)} \left[\dot{\boldsymbol{\epsilon}} - c^{(2)} \mathbb{E} \left(\bar{\boldsymbol{\sigma}}^{(1)} - \bar{\boldsymbol{\sigma}}^{(2)} \right) - \mathbb{M}^{(1)} \bar{\boldsymbol{\sigma}}^{(1)} \right], \\ \dot{\bar{\boldsymbol{\sigma}}}^{(2)} &= \mathbb{C}^{(2)} \left[\dot{\boldsymbol{\epsilon}} + c^{(1)} \mathbb{E} \left(\bar{\boldsymbol{\sigma}}^{(1)} - \bar{\boldsymbol{\sigma}}^{(2)} \right) - \mathbb{M}^{(2)} \bar{\boldsymbol{\sigma}}^{(2)} \right], \end{aligned} \quad (6.34)$$

where $\mathbb{C}^{(r)} = (\mathbb{S}^{(r)})^{-1}$ is the elastic stiffness tensor of the phase r in the actual composite.

In summary, for a given macroscopic strain rate $\dot{\bar{\epsilon}}$, the set of equations (6.34) serves to fully determine the “incremental” stress tensors in the matrix and particle phases. In turn, the incremental macroscopic stress $\bar{\sigma}$ can be obtained by means of equation (6.24). However, given $\bar{\sigma}^{(1)}$ and $\bar{\sigma}^{(2)}$, it is simpler to make use of the following identity to find $\bar{\sigma}$

$$\dot{\bar{\sigma}} = c^{(1)} \dot{\bar{\sigma}}^{(1)} + c^{(2)} \dot{\bar{\sigma}}^{(2)}. \quad (6.35)$$

In addition, the phase average strain-rate, $\dot{\bar{\epsilon}}^{(r)}$, and the thermal strain (elastic strain) in each phase, $\gamma^{(r)}$, can be obtained from relations (6.33) and (6.27), respectively. Finally, after finding these variables, the effective stress potential of the LCC can be obtained from relation (6.23). In this connection, it is convenient to provide the expressions for the effective properties $\tilde{\gamma}$ and \tilde{g} associated with the Willis estimate (6.28) as follows (see Appendix E.1)

$$\tilde{\gamma} = \bar{\gamma} + c^{(1)} c^{(2)} \mathbb{F} \Delta\gamma, \quad \tilde{g} = \frac{1}{2} c^{(1)} c^{(2)} \Delta\gamma \cdot (\Delta\mathbb{M})^{-1} \mathbb{F} \Delta\gamma. \quad (6.36)$$

where $\bar{\gamma} = c^{(1)} \gamma^{(1)} + c^{(2)} \gamma^{(2)}$, and $\mathbb{F} = (c^{(1)} \Delta\mathbb{M} \mathbb{Q} - \mathbb{I})^{-1} \mathbb{Q}$.

The above formulation for the LCC can be used to generate estimate for the two-phase elasto-viscoplastic composites described in Section 6.2. In the following, we specialize this formulation to two particular cases of interest: (1) Purely elastic composites, (2) Composites with a viscoplastic matrix.

Purely elastic composites

It is of particular interest to investigate the simplification of the above formulation for the LCC to the special case of composites with purely elastic phases. In this case, the LCC simply reduces to a two-phase linear elastic composites consisting of an isotropic matrix with the stiffness tensor $\mathbb{C}^{(1)}$ and a random distribution of aligned, ellipsoidal particles made of an isotropic solid with the stiffness tensor $\mathbb{C}^{(2)}$. This special case is recovered from the above formulation by taking the limits of $\mathbb{M}^{(1)}, \mathbb{M}^{(2)} \rightarrow \mathbb{O}$. Taking this limit, relations (6.34) reduce to

$$\dot{\bar{\sigma}}^{(1)} = \mathbb{C}^{(1)} \dot{\bar{\epsilon}}, \quad \dot{\bar{\sigma}}^{(2)} = \mathbb{C}^{(2)} \dot{\bar{\epsilon}}. \quad (6.37)$$

Making use of the identity (6.35), the above relations lead to the following constitutive relation for the macroscopic response

$$\dot{\bar{\epsilon}} = \tilde{\mathbb{S}}^{Vt} \dot{\bar{\sigma}}, \quad (6.38)$$

where

$$\tilde{\mathbb{S}}^{Vt} = \left[c^{(1)} \mathbb{C}^{(1)} + c^{(2)} \mathbb{C}^{(2)} \right]^{-1}. \quad (6.39)$$

As expected, the above relations correspond to the Voigt bound for a linear elastic composite which is consistent with our earlier approximation that the elastic strain filed (in this case, the total strain filed) is constant per phase. In other words, the Voigt bound predicts no fluctuation of the strain

and stress fields in the particle and matrix phases.

Viscoplastic matrix

When the elastic deformation in the matrix phase is negligible (i.e., $\boldsymbol{\epsilon}_e^{(1)} = \mathbf{0}$), the constitutive behavior of the matrix is purely viscous. In this case, the approximation of the constant elastic strain in the particle phase is consistent with the Willis-type estimate used for the behavior of the LCC as the Willis estimate predicts no fluctuation of the local fields in the particle phase either. In other words, for the special case of a viscoplastic matrix, the only approximation involved in our homogenization method is the linearization of the matrix phase.

6.3.2 Implementation of the variational procedure

In this subsection, we discuss the implementation of the variational procedure described in this section to estimate the effective behavior of the actual nonlinear composite. In this work, we restrict our attention to the special case of two-phase *incompressible* composites consisting of an isotropic elastic-ideally plastic matrix with yield stress σ_0 and a random distribution of isotropic elastic particles, although our method can be implemented for the case of general two-phase elasto-viscoplastic composites described in Section 6.2. The limit of elastic particles requires to take the limit of $\mathbb{M}^{(2)} \rightarrow \mathbb{O}$ in the LCC formulation in Section 6.3.1. Also, we enforce the limit of incompressibility of the nonlinear matrix phase and elastic particles by taking the incompressibility limit in each phase in our formulation. Also, the case of elastic-ideally plastic matrices correspond to using the optimality condition (6.21). In this connection, in order to elucidate the implication of this condition, it is useful to write it in terms of the second moment of the equivalent stress in the matrix phase in the (thermoelastic) LCC, defined as

$$\langle \sigma_{eq}^2 \rangle^{(1)} = -\frac{6}{c^{(1)}} (\eta^{(1)})^2 \partial_{(\eta^{(1)})} \tilde{U}_L(\bar{\boldsymbol{\sigma}}), \quad (6.40)$$

Making use of the above definition in (6.21), it is written as

$$\langle \sigma_{eq}^2 \rangle^{(1)} = \sigma_0^2 \quad (6.41)$$

In fact, the above equation is an average form of the von Mises yield criteria in the matrix phase, implying that the matrix exhibits an initial purely elastic behavior to the point that the stress in the matrix phase satisfies the yield criterion in the matrix (given by (6.41)), beyond which the matrix exhibits a fully coupled elasto-plastic behavior. Therefore, since the particles are assumed to be purely elastic throughout the deformation history, the behavior of the composite is purely elastic to the point that the condition (6.41) is satisfied, beyond which the composite exhibits a coupled elasto-plastic behavior. Therefore, as will be explained in more detail in subsection 6.3.2, equation (6.41) is used to characterize the end of the purely elastic regime in the behavior of the composites. In this regard, in the next two subsections, we separately provide the set of equations need to be solved for obtaining estimates for the purely elastic and elasto-plastic parts of the composite behavior.

Followed by these subsections, we outline the general procedure to implement our model to obtain estimates for the behavior of the composite under a full cycle of loading.

Purely elastic regime: An empirical modification

As mentioned earlier, the elastic trial state can be computed from the LCC calculations by taking the limit $\mathbb{M}^{(1)}, \mathbb{M}^{(2)} \rightarrow \mathbb{O}$. The resulting relations (given by (6.37)-(6.39)) correspond to the Voigt bound for the elastic composite. However, this bound is too stiff to predict the purely elastic behavior of the composite. For this reason, instead of using relations (6.37)-(6.39), we propose to make use of the Willis-type estimate for the behavior of the two-phase composites in the purely elastic regime. The Willis estimates for the average stress in the matrix and particle phases are given by (Willis, 1977; Ponte Castañeda and Willis, 1995)

$$\begin{aligned}\dot{\boldsymbol{\sigma}}^{(1)} &= \mathbb{C}^{(1)} (\mathbb{I} - \mathbb{P}_e \Delta \mathbb{C}) \left[\mathbb{I} - c^{(1)} \mathbb{P}_e \Delta \mathbb{C} \right]^{-1} \dot{\boldsymbol{\epsilon}}, \\ \dot{\boldsymbol{\sigma}}^{(2)} &= \mathbb{C}^{(2)} \left[\mathbb{I} - c^{(1)} \mathbb{P}_e \Delta \mathbb{C} \right]^{-1} \dot{\boldsymbol{\epsilon}},\end{aligned}\tag{6.42}$$

where $\Delta \mathbb{C} = \mathbb{C}^{(1)} - \mathbb{C}^{(2)}$, and the microstructural tensor \mathbb{P}_e is defined by the same relations in (6.30) and (6.31) with $\mathbb{L}^{(1)}$ being replaced by $\mathbb{C}^{(1)}$. Making use of the identity (6.35), the above relations lead to the following constitutive relation for the macroscopic response

$$\dot{\boldsymbol{\epsilon}} = \widetilde{\mathbb{S}}^{Ws} \dot{\boldsymbol{\sigma}},\tag{6.43}$$

where

$$\widetilde{\mathbb{S}}^{Ws} = \left\{ \mathbb{C}^{(1)} + c^{(2)} \left[c^{(1)} \mathbb{P}_e - (\Delta \mathbb{C})^{-1} \right]^{-1} \right\}^{(-1)},\tag{6.44}$$

in which $\Delta \mathbb{C} = \mathbb{C}^{(1)} - \mathbb{C}^{(2)}$. According to the Willis estimate, there are field fluctuations in the matrix phase, but not in the particle phase. As mentioned earlier and also will be explained in more detail in subsection 6.3.2, we require to calculate $\langle \sigma_{eq}^2 \rangle^{(1)}$ in the purely elastic regime in order to check whether or not the yield criterion (6.41) is satisfied. Therefore, it is crucial to provide an associated incremental relation to characterize the second moment of stress in the matrix phase. An incremental relation for this quantity can be written in the form of (see Appendix E.2)

$$\overline{\langle \sigma_{eq}^2 \rangle^{(1)}} = f(\dot{\boldsymbol{\sigma}}^{(1)}, \dot{\boldsymbol{\sigma}}^{(2)}, \bar{\boldsymbol{\sigma}}^{(1)}, \bar{\boldsymbol{\sigma}}^{(2)}, \mathcal{S})\tag{6.45}$$

where \mathcal{S} is the set of variables characterizing the microstructure of the composite (such as volume fraction and shape of the particles). In fact, making use of a time-discretization scheme, the stress phase averages and the second moment of stress in the matrix are obtained by using relations (6.42) and (6.45), respectively.

Elasto-plastic regime

First, making use of relations (6.28) and (6.36) into (6.23), the effective stress potential of the LCC is expressed as

$$\begin{aligned}\tilde{U}_L(\bar{\boldsymbol{\sigma}}) &= \frac{1}{2} \bar{\boldsymbol{\sigma}} \cdot [\mathbb{M}^{(1)} (\mathbb{I} + c^{(2)} \mathbb{H})] \bar{\boldsymbol{\sigma}} + (\bar{\boldsymbol{\gamma}} + c^{(1)} c^{(2)} \mathbb{H} \mathbb{Q} \Delta \boldsymbol{\gamma}) \cdot \bar{\boldsymbol{\sigma}} \\ &\quad + \frac{1}{2} c^{(1)} c^{(2)} \Delta \boldsymbol{\gamma} \cdot \mathbb{L}^{(1)} \mathbb{H} \mathbb{Q} \Delta \boldsymbol{\gamma}\end{aligned}\quad (6.46)$$

where $\mathbb{H} = (c^{(1)} \mathbb{M}^{(1)} \mathbb{Q} - \mathbb{I})^{-1} \mathbb{Q}$. The optimal value of $\eta^{(1)}$ in the above potential is obtained by solving the algebraic equation (6.41). Making use of the definition (6.40) for the second moment and the above expression for the effective potential, equation (6.41) can be written as

$$\begin{aligned}\sigma_0^2 &= - \frac{3 (\eta^{(1)})^2}{c^{(1)}} \left\{ \bar{\boldsymbol{\sigma}} \cdot [\mathbb{M}^{(1)} (\mathbb{I} + c^{(2)} \mathbb{H})]_{,\eta^{(1)}} \bar{\boldsymbol{\sigma}} \right. \\ &\quad \left. + c^{(1)} c^{(2)} \left[2 ((\mathbb{H} \mathbb{Q})_{,\eta^{(1)}} \Delta \boldsymbol{\gamma}) \cdot \bar{\boldsymbol{\sigma}} + \Delta \boldsymbol{\gamma} \cdot (\mathbb{L}^{(1)} \mathbb{H} \mathbb{Q})_{,\eta^{(1)}} \Delta \boldsymbol{\gamma} \right] \right\}\end{aligned}\quad (6.47)$$

where the subscript comma denotes the partial derivative with respect to the following variable. Note that the differentiation in definition (6.40) is taken while the macroscopic stress $\bar{\boldsymbol{\sigma}}$ and the thermal strains $\boldsymbol{\gamma}^{(1)}$ and $\boldsymbol{\gamma}^{(2)}$ are held fixed. Next, combining relations (6.27) and (6.33), we find the following expressions for the thermal strains

$$\begin{aligned}\boldsymbol{\gamma}^{(1)} &= \dot{\boldsymbol{\epsilon}} - c^{(2)} \mathbb{E} \left(\bar{\boldsymbol{\sigma}}^{(1)} - \bar{\boldsymbol{\sigma}}^{(2)} \right) - \mathbb{M}^{(1)} \bar{\boldsymbol{\sigma}}^{(1)}, \\ \boldsymbol{\gamma}^{(2)} &= \dot{\boldsymbol{\epsilon}} + c^{(1)} \mathbb{E} \left(\bar{\boldsymbol{\sigma}}^{(1)} - \bar{\boldsymbol{\sigma}}^{(2)} \right),\end{aligned}\quad (6.48)$$

Therefore, substituting relations (6.48) into equation (6.47), this equation can be entirely written in terms of unknowns $\eta^{(1)}$, $\bar{\boldsymbol{\sigma}}^{(1)}$ and $\bar{\boldsymbol{\sigma}}^{(2)}$. Then, this equation, together with equations (6.34) for the evolution of $\bar{\boldsymbol{\sigma}}^{(1)}$ and $\bar{\boldsymbol{\sigma}}^{(2)}$, can be solved for unknowns $\eta^{(1)}$, $\bar{\boldsymbol{\sigma}}^{(1)}$ and $\bar{\boldsymbol{\sigma}}^{(2)}$. To this end, we make use of an implicit time-discretization scheme to solve the three equations.

Implementation procedure

Here, we assume a purely elastic state in the composite to the point that the stress in the matrix phase satisfies the yield criterion (6.41). The algorithm for determining the effective response of the composite can be summarized as below

1. At a given time instant $t = t_0$, the first and second moments of the stress are known in the matrix and particle phases. At this instant, we apply a macroscopic strain increment ($\dot{\boldsymbol{\epsilon}}$).

2. We calculate the phase averages $\bar{\boldsymbol{\sigma}}^{(r)}$ and the second moment $\langle \sigma_{eq}^2 \rangle^{(1)}$ at the next time increment by using incremental equations (6.42) and (6.45), respectively, corresponding to the Willis estimates for two-phase, linear elastic composites. The effective macroscopic stress is obtained by using (6.35).

- 3.1. If the second of the matrix phase calculated from step 2 satisfies the inequality $\langle \sigma_{eq}^2 \rangle^{(1)} < \sigma_0^2$, the composite behavior is purely elastic and we continue step 2. In this case, the effective behavior

of the composite is estimated by the constitutive relation (6.43).

3.2. If $\langle \sigma_{eq}^2 \rangle^{(1)} = \sigma_0^2$, the matrix phase in the composite has reached the yield stress σ_0 . At this instant, we need to use the LCC to estimate the effective behavior of the composite. In this case, we make use of an implicit time-discretization scheme to solve nonlinear equations (6.34) and (6.47) for unknowns $\eta^{(1)}$, $\bar{\sigma}^{(1)}$ and $\bar{\sigma}^{(2)}$ (note that $\mathbb{M}^{(2)} = \mathbb{O}$ in (6.34)₂ as we assumed that the particle are purely elastic). The effective macroscopic stress is obtained by using (6.35).

6.4 Applications and discussions

In this section, we investigate predictions of the homogenization procedure developed in the previous section for the effective response of an elastic-ideally plastic solids reinforced with a random distribution of aligned, prolate spheroidal elastic particles, with aspect ratio w and volume fraction c . Figure 6.1 shows a schematic view of the microstructure in the composite. For definiteness, we define the principal directions of the particles by the rectangular Cartesian basis $\{\mathbf{e}_i\}$ such that the symmetry axis of the particles is aligned with the \mathbf{e}_3 direction. Also, the distribution of particles is assumed to be statistically isotropic in the transverse plane, namely, the $\mathbf{e}_1 - \mathbf{e}_3$ plane. We further assume that the shape and orientation of the distributional spheroid characterizing the angular dependence of the two-point correlation function (for the distribution of the particle centers) are the same as those of the particles.

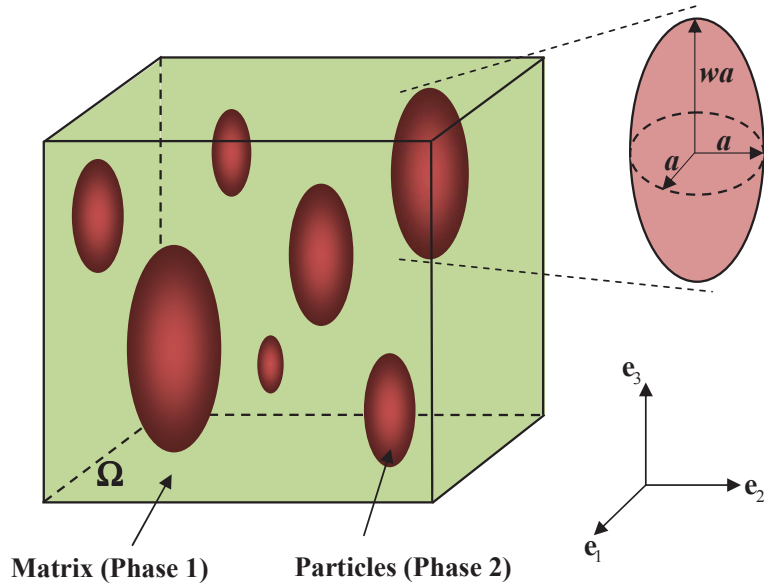


Figure 6.1: Schematic illustration of the microstructure in a particle-reinforced composite. The elastic particles are prolate spheroidal in shape ($w > 1$), and their symmetry axis is aligned with the coordinate basis vector \mathbf{e}_3 .

The matrix is an elastic-ideally plastic solid with the yield stress σ_0 . Both matrix and particles are assumed to be isotropic and incompressible. The elastic properties of the matrix and particles

Material	μ (GPa)	σ_0 (MPa)
<u>Matrix:</u>		
Aluminium	28.8	75
Titanium	44.2	818.5
Polyamide	0.8	29
<u>Ceramic Particles:</u>		
Tungsten Carbide(WC)	270.1	
Silicon Carbide (SiC)	166.7	
Nextel	83.3	

Table 6.1: Candidate materials for the elastic-ideally plastic matrix and for the elastic fibers.

are characterized by the following stiffness tensor

$$\mathbb{C}^{(r)} = 2\mu^{(r)}\mathbb{K} + \infty\mathbb{J}, \quad r = 1, 2 \quad (6.49)$$

where $\mu^{(r)}$ denote the shear modulus of the corresponding phase. Table 6.1 shows the shear modulus and yields stress properties of some common materials used in particle-reinforced metal-matrix or polymer matrix composites. We will make use of the properties in Table 6.1 in presenting the results in this section. In this connection, it is important to clarify that the materials in Table 6.1 are generally compressible, and the chosen properties for our incompressible model does not exactly represents these materials. However, the compressibility properties of the materials are not expected to have a significant effect on the overall behavior and the field statistics in the composite when subjected to isochoric loading as will be described shortly.

The effective potential for incompressible composites with transversely isotropic symmetry may be written as

$$\tilde{U}(\bar{\boldsymbol{\sigma}}) = \tilde{\phi}(\bar{\tau}_a, \bar{\tau}_n, \bar{\tau}_p), \quad (6.50)$$

where

$$\begin{aligned} \bar{\tau}_a &= \frac{1}{2\sqrt{3}}[2\bar{\sigma}_{33} - (\bar{\sigma}_{11} + \bar{\sigma}_{22})], \quad \bar{\tau}_n = \sqrt{\bar{\sigma}_{13}^2 + \bar{\sigma}_{23}^2}, \\ \text{and } \bar{\tau}_p &= \sqrt{\bar{\sigma}_{12}^2 + \frac{1}{4}(\bar{\sigma}_{11} - \bar{\sigma}_{22})^2}, \end{aligned} \quad (6.51)$$

are an appropriate set of isochoric, transversely isotropic invariants of $\bar{\boldsymbol{\sigma}}$ corresponding to axisymmetric shear, longitudinal shear and transverse shear stresses, respectively deBotton and Ponte Castañeda (1992). The macroscopic equivalent stress of the composites is then obtained as

$$\bar{\sigma}_{eq} = \sqrt{\bar{\tau}_a^2 + \bar{\tau}_n^2 + \bar{\tau}_p^2}. \quad (6.52)$$

In a similar manner, the Correspondingly, the transversely isotropic invariants of the average

stress tensors $\bar{\sigma}^{(r)}$ in the matrix and particle phase can be written as

$$\begin{aligned}\bar{\tau}_a^{(r)} &= \frac{1}{2\sqrt{3}}[2\bar{\sigma}_{33}^{(r)} - (\bar{\sigma}_{11}^{(r)} + \bar{\sigma}_{22}^{(r)})], & \bar{\tau}_n^{(r)} &= \sqrt{(\bar{\sigma}_{13}^{(r)})^2 + (\bar{\sigma}_{23}^{(r)})^2}, \\ \text{and } \bar{\tau}_p^{(r)} &= \sqrt{(\bar{\sigma}_{12}^{(r)})^2 + \frac{1}{4}(\bar{\sigma}_{11}^{(r)} - \bar{\sigma}_{22}^{(r)})^2}, & r &= 1, 2.\end{aligned}\tag{6.53}$$

In addition, it is useful to provide results for the standard deviation of the stress filed in the matrix phase, defined by

$$SD^{(1)}(\sigma_{eq}) = \sqrt{\langle \sigma_{eq}^2 - \bar{\sigma}_{eq}^2 \rangle^{(1)}}.\tag{6.54}$$

This quantity provides a convenient measure for the *intrapphase* stress field fluctuations in the matrix phase. Also, note that $SD^{(2)}(\sigma_{eq}) = 0$ within the Willis estimates.

The results provided in this section are organized as follows. First, in Sections 6.4.1, we address the effective behavior of the composites consisting of an elastic-ideally plastic matrix and spheroidal elastic particles, subjected to axisymmetric shear loading-unloading-loading cycles. In this subsection, we investigate the effect of particle volume fraction and shape as well as the effect of matrix and particle mechanical properties on the effective behavior of the composite. Here, we also compare our results with the corresponding analytical and numerical simulations available in the literature. Next, in Section 6.4.2, we will present representative results for the effective behavior of the composites subjected to transverse and longitudinal shear modes. Finally, in Section 6.4.3, we will provide representative results for the effective behavior of the composites subjected to combined axisymmetric and longitudinal shear modes. In the last two subsection, we only explore the impact of particle shape on the overall behavior of the composite for fixed value of the particle volume fraction and matrix and particle mechanical properties. In all subsections, we present results for the relevant invariant of the overall stress tensor and the average stress tensor in the matrix and particle phases, as a function of corresponding macroscopic strain component, as well as for the standard deviation of the stress field in the matrix phase (defined by (6.54)), as a function of duration of loading. Finally, we note that all the stress quantities are appropriately normalized by the yield stress of the matrix, σ_0 .

6.4.1 Axisymmetric shear

In this subsection, we study the behavior of the composite when subjected to a strain-controlled, axisymmetric shear loading of the type

$$\dot{\bar{\epsilon}}_a = \dot{\epsilon}_0(t) \left[\mathbf{e}_3 \otimes \mathbf{e}_3 - \frac{1}{2}(\mathbf{e}_1 \otimes \mathbf{e}_1 + \mathbf{e}_2 \otimes \mathbf{e}_2) \right],\tag{6.55}$$

where $\dot{\epsilon}_0(t)$ is a step function, defined as

$$\dot{\epsilon}_0(t) = \begin{cases} 6 \times 10^{-3} & \text{if } 0 \leq t \leq T, \\ -6 \times 10^{-3} & \text{if } T \leq t \leq 3T, \\ -6 \times 10^{-3} & \text{if } 3T \leq t \leq 4T, \end{cases}\tag{6.56}$$

in which $T = 10$ s. The plots in this subsection are given as a function of $\bar{\epsilon}_{33} = \int_0^t (\dot{\epsilon}_a)_{33} dt = \int_0^t \dot{\epsilon}_0(t) dt$.

Figure 6.2 shows a comparison of predictions of our model with earlier analytical estimates and numerical simulations for elastic-ideally plastic matrices reinforced by elastic spherical particles with $c = 0.17$. Results are provided for properties $\mu^{(1)}/\sigma_0 = 30$, and $\mu^{(2)}/\mu^{(1)} = 2$. The IVP estimates correspond to the predictions of an analytical homogenization model, recently developed by Lahellec and Suquet (2013). This model follows from an “*incremental variation principal*” (IVP) which aims at recasting the elastic and dissipative potentials of the constituents phases into equivalent *condensed incremental* potentials (Lahellec and Suquet, 2007). Similar to our model, this model is also based on the variational principal of Ponte Castañeda (1991), however, it accounts for the field fluctuations of the elastic strains in the matrix phase, and therefore, provides more accurate estimates compared to our model. Also, the FFT results refer to the full-field simulations carried out by Lahellec and Suquet (2013). It is important to mention that the IVP and FFT results in figure 6.2 are calculated for composites with compressible phases, however, the effect of compressibility is not expected to be significant since the composite is subjected to an isochoric loading. The main observation from these plots is that while the IVP estimate provides a very good agreement with the FFT simulations, the predictions of our model also provides quite good agreement with the FFT results, especially for the macroscopic response of the composite in figure 6.2(a). However, we observe from figures 6.2(c) and (d) that our model tends to overestimate the average stress in the particle phase and the stress field fluctuations in the matrix phase, which is due to the approximation of the uniform-per-phase elastic strains used in our model.

Figure 6.3 presents variational estimates for particle-reinforced composites consisting of an elastic-ideally plastic matrix and elastic spheroidal particles with aspect ratio $w = 3$ subjected to axisymmetric shear cycles (6.55), for various particles volume fractions ($c = 0.1, 0.2, 0.3$ and 0.4). Results are given for the mechanical properties $\mu^{(1)}/\sigma_0 = 54$ and $\mu^{(2)}/\mu^{(1)} = 3.8$, which correspond to the incompressible properties of Sic-Titanium composites. We observe from figure 6.3(a) that the composite exhibits three types of behavior in each segment of loading-unloading-loading cycles. First, the composite exhibits a linear elastic behavior (characterized by relation (6.43)) up to yielding of the matrix phase, followed by a coupled elasto-plastic behavior, which subsequently reaches a plateau. At the plateau, the overall stress in figure 6.3(a), as well as the phase averages in figures 6.3(b) and (c), coincide with the corresponding predictions of Ponte Castañeda variational procedure for the effective behavior of a rigid-ideally plastic matrix (with yield stress σ_0) reinforced by rigid particles (with volume fraction c and aspect ratio w), which is known to be a rigorous upper bound. We also observe from these figures that increasing volume fractions of the particles stiffens the effective behavior of the composite.

Figure 6.4 presents variational estimates for particle-reinforced composites consisting of an elastic-ideally plastic matrix and elastic spheroidal particles with volume fraction $c = 0.3$ subjected to axisymmetric shear cycles, for various particle aspect ratios ($w = 1, 3, 10$ and ∞). Results are, again, given for the mechanical properties $\mu^{(1)}/\sigma_0 = 54$ and $\mu^{(2)}/\mu^{(1)} = 3.8$. We note that the special case of $w = 1$ corresponds to elastic-ideally plastic matrices reinforced by spherical particles, while the special case of $w \rightarrow \infty$ corresponds to elastic-ideally plastic matrices reinforced by long cylindrical

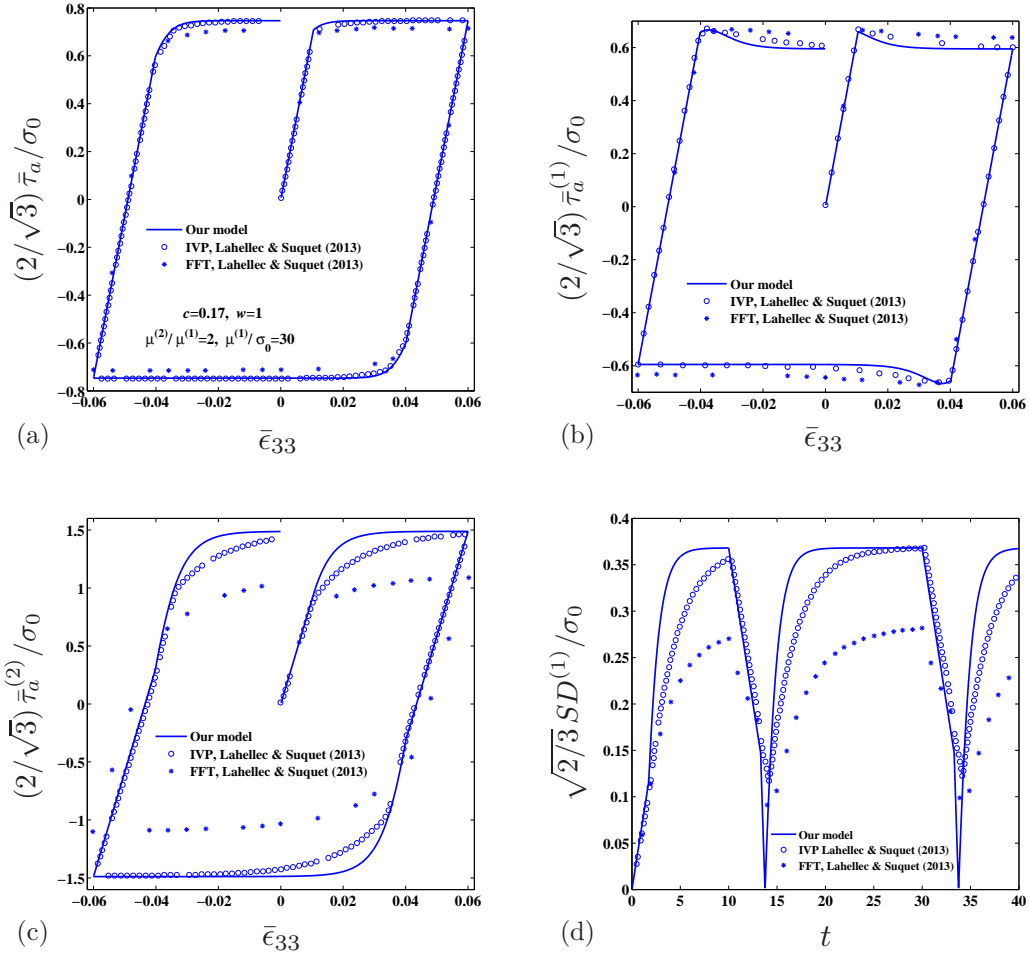


Figure 6.2: Estimates for the effective response and field statistics in the composites consisting of a elastic-ideally plastic matrix and elastic spherical particles ($w = 1$) with $c = 0.17$, $\mu^{(1)}/\sigma_0 = 30$, and $\mu^{(2)}/\mu^{(1)} = 2$, under axisymmetric shear loading. Comparisons are shown between our model, the analytical model of Lahellec and Suquet (2013) “IVP”, and the full-field simulations of Lahellec and Suquet (2013) “FFT”.

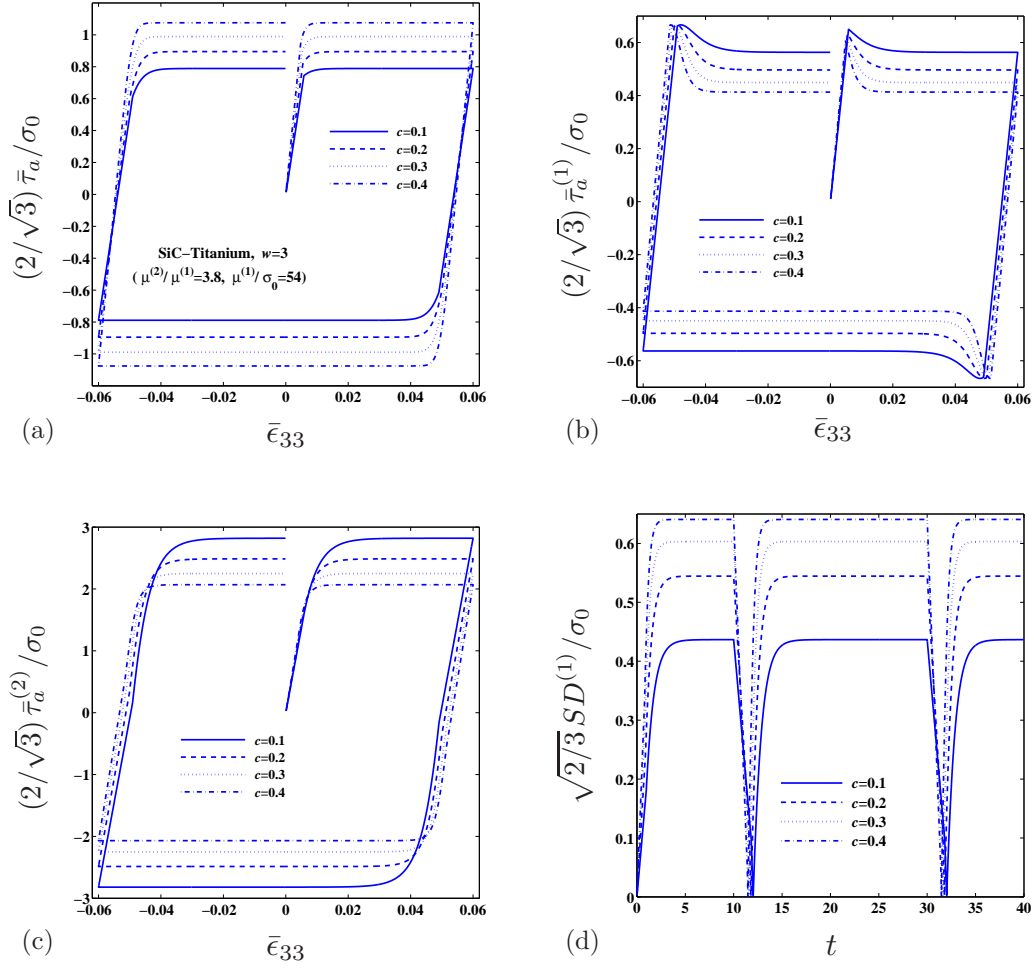


Figure 6.3: Variational estimates for the effective response and field statistics in the composites consisting of an elastic-ideally plastic matrix and elastic spheroidal particles with $\mu^{(1)}/\sigma_0 = 54$, $\mu^{(2)}/\mu^{(1)} = 3.8$, and $w = 3$ under axisymmetric shear loading.

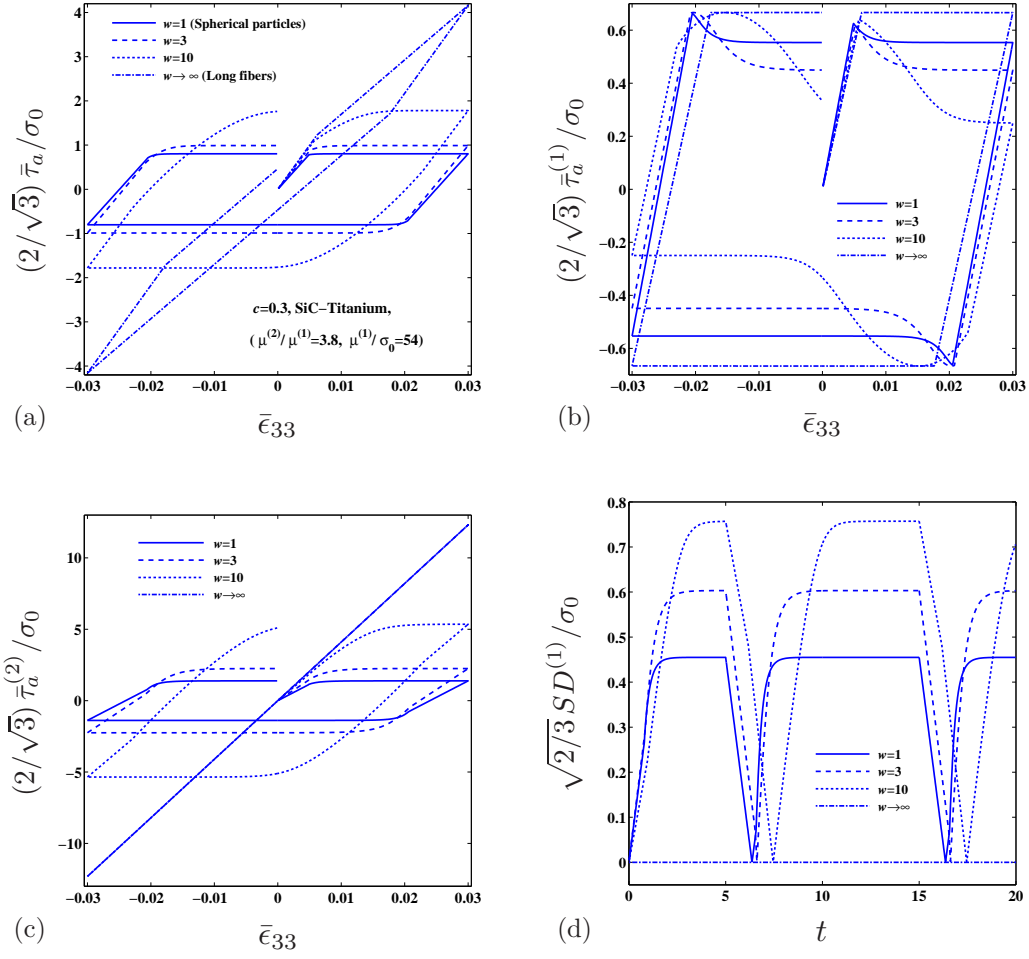


Figure 6.4: Variational estimates for the effective response and field statistics in the composites consisting of an elastic-ideally plastic matrix and elastic spheroidal particles with $\mu^{(1)}/\sigma_0 = 54$, $\mu^{(2)}/\mu^{(1)} = 3.8$, and $c = 0.3$ under axisymmetric shear loading. The material properties correspond to SiC particles and Titanium matrix.

fibers whose axis of symmetry is aligned with \mathbf{e}_3 direction. It is important to note that the results for the case of long fibers are exact and coincide with the Voigt bound for these composites. This is because, in this case, the exact solution for the local fields in the matrix and particles phase are uniform (i.e., fluctuation of local fields is zero within each phase) which is consistent with the Voigt bound. We observe from figure 6.4(a) that the composite exhibits a more pronounced elasto-plastic coupling as the aspect ratio of the particle increases. The growth of the macroscopic stress measure $\bar{\tau}_a$ becomes unbounded for the case of long fibers ($w \rightarrow \infty$) and can be shown to be proportional to $(1 - c)\bar{\epsilon}_{33}$. We observe from figure 6.4(d) that the standard deviation of the stress is identically zero for the case of long fibers which is consistent with the exact solution of uniform field-per-phase in this case.

Figure 6.5 presents variational estimates for particle-reinforced composites consisting of an elastic-ideally plastic matrix and elastic spheroidal particles with $c = 0.3$ and $w = 3$, subjected to axisymmetric shear cycles (6.55), for the fixed ratio $\mu^{(2)}/\mu^{(1)} = 2$ and various values of the ratio $\mu^{(1)}/\sigma_0$. We observe from figure 6.5(a) that all curves reach the same plateau, although the composites with higher values of $\mu^{(1)}/\sigma_0$ exhibit stiffer response and a shorter elasto-plastic coupling before they reach the plateau. As an example, as we notice from this figures, the composites with a polymeric matrix (like polyamide) show a much longer range of elasto-plastic coupling than the composites with Aluminium as the matrix with the same ratio $\mu^{(2)}/\mu^{(1)} = 2$.

Finally, in this subsection, figure 6.6 presents variational estimates for particle-reinforced composites consisting of an elastic-ideally plastic matrix and elastic spheroidal particles with $c = 0.3$ and $w = 3$, subjected to axisymmetric shear cycles (6.55), for the fixed ratio $\mu^{(1)}/\sigma_0 = 54$ and various values of the ratio $\mu^{(2)}/\mu^{(1)}$. Similar to the previous figure, we observe from figure 6.6(a) that all curves reach the same plateau, although the composites with softer fibers exhibit longer range of elasto-plastic coupling before they reach the plateau. On the other extreme, the composite with rigid particles exhibit no elasto-plastic coupling regime.

6.4.2 Transverse and longitudinal shear loading

In this subsection, we study the behavior of the composite when subjected to a strain-controlled transverse and longitudinal shear loadings of the forms

$$\dot{\epsilon}_p = \dot{\epsilon}_0(t) \left[\frac{1}{2} (\mathbf{e}_1 \otimes \mathbf{e}_1 - \mathbf{e}_2 \otimes \mathbf{e}_2) + \mathbf{e}_1 \otimes \mathbf{e}_2 + \mathbf{e}_2 \otimes \mathbf{e}_1 \right], \quad (6.57)$$

and

$$\dot{\epsilon}_n = \dot{\epsilon}_0(t) (\mathbf{e}_1 \otimes \mathbf{e}_3 + \mathbf{e}_3 \otimes \mathbf{e}_1 + \mathbf{e}_2 \otimes \mathbf{e}_3 + \mathbf{e}_3 \otimes \mathbf{e}_2), \quad (6.58)$$

respectively.

Figure 6.7 presents variational estimates for particle-reinforced composites consisting of an elastic-ideally plastic matrix and elastic spheroidal particles with $c = 0.3$, subjected to transverse shear cycles (6.57), for particle aspect ratios $w = 1, 3$ and ∞ . Results are shown for the mechanical properties $\mu^{(1)}/\sigma_0 = 54$ and $\mu^{(2)}/\mu^{(1)} = 3.8$. We observe from figures 6.7 (a-c) that the particle aspect ratio, when changing from the spherical case ($w = 1$) to the case of long fibers ($w = 1$),

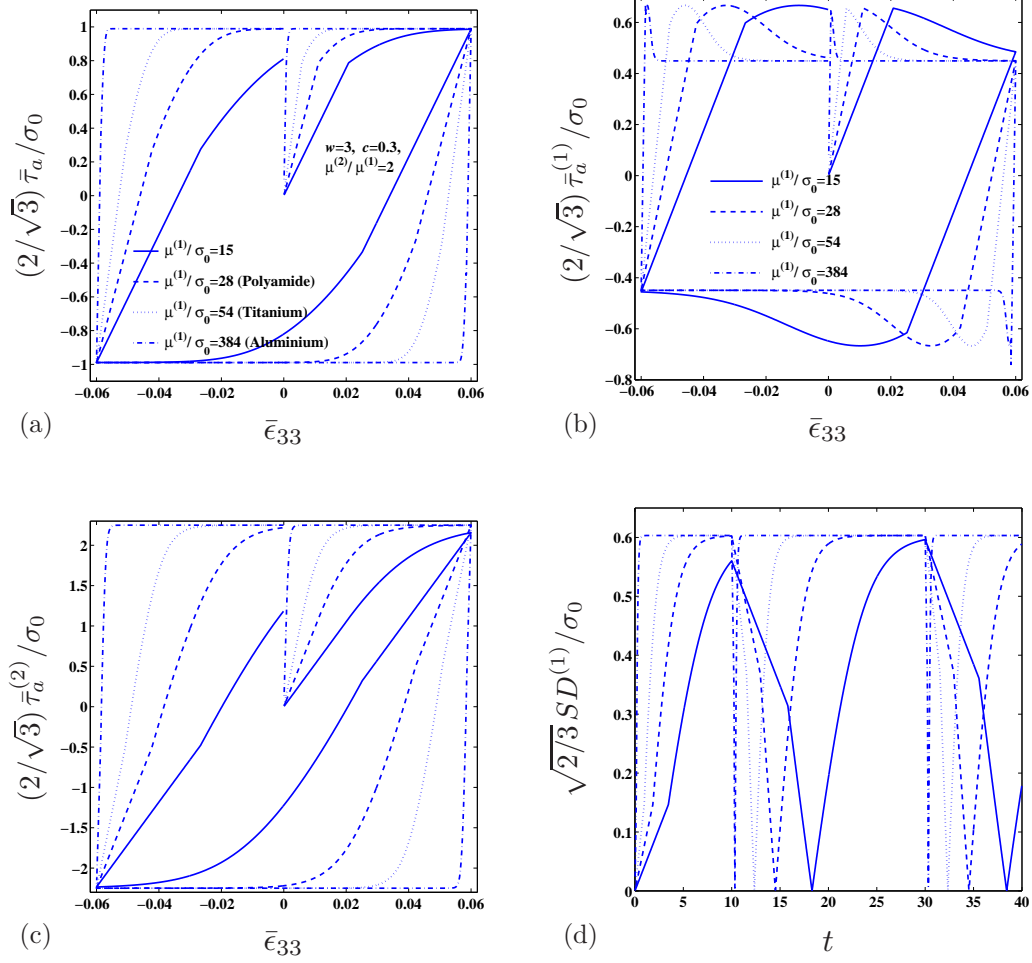


Figure 6.5: Variational estimates for the effective response and field statistics in the composites consisting of an elastic-ideally plastic matrix and elastic spheroidal particles with $\mu^{(2)}/\mu^{(1)} = 2$, $c = 0.3$, and $w = 3$ under axisymmetric shear loading.

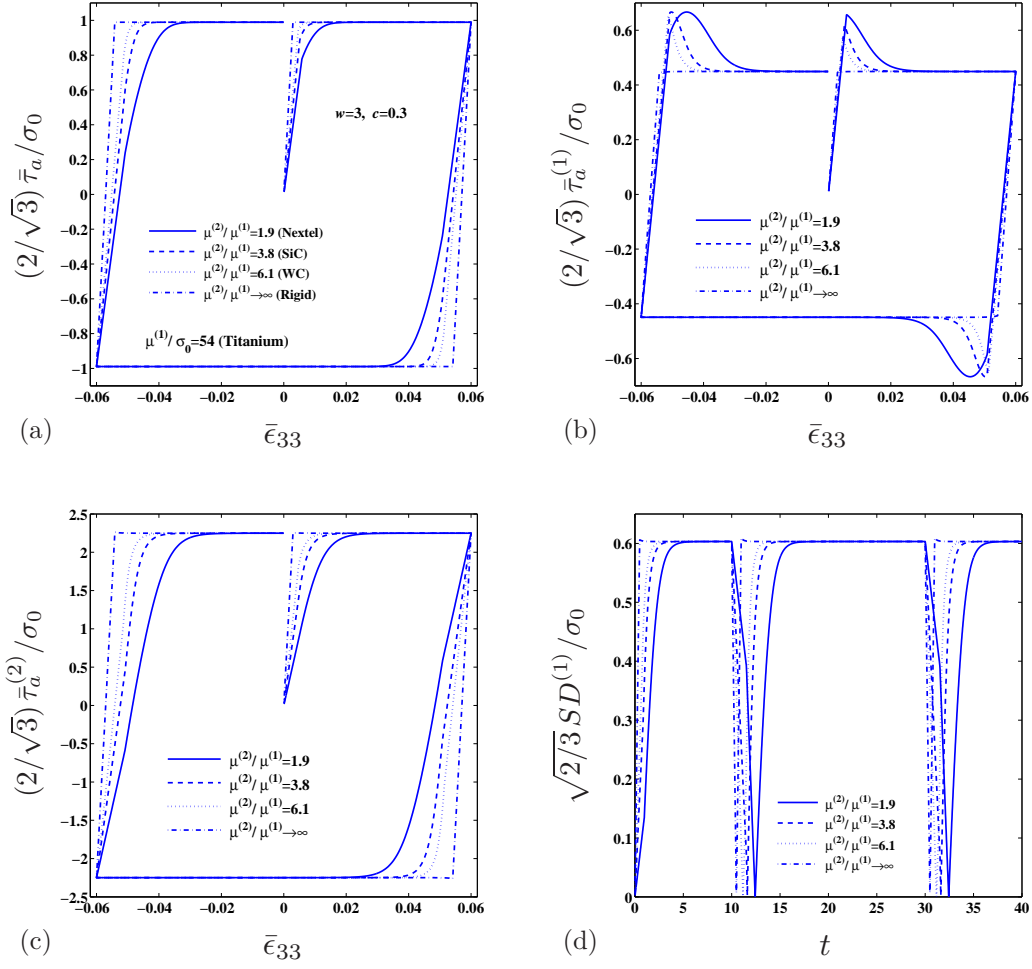


Figure 6.6: Variational estimates for the effective response and field statistics in the composites consisting of an elastic-ideally plastic matrix and elastic spheroidal particles with $\mu^{(1)}/\sigma_0 = 54$, $c = 0.3$, and $w = 3$ under axisymmetric shear loading.

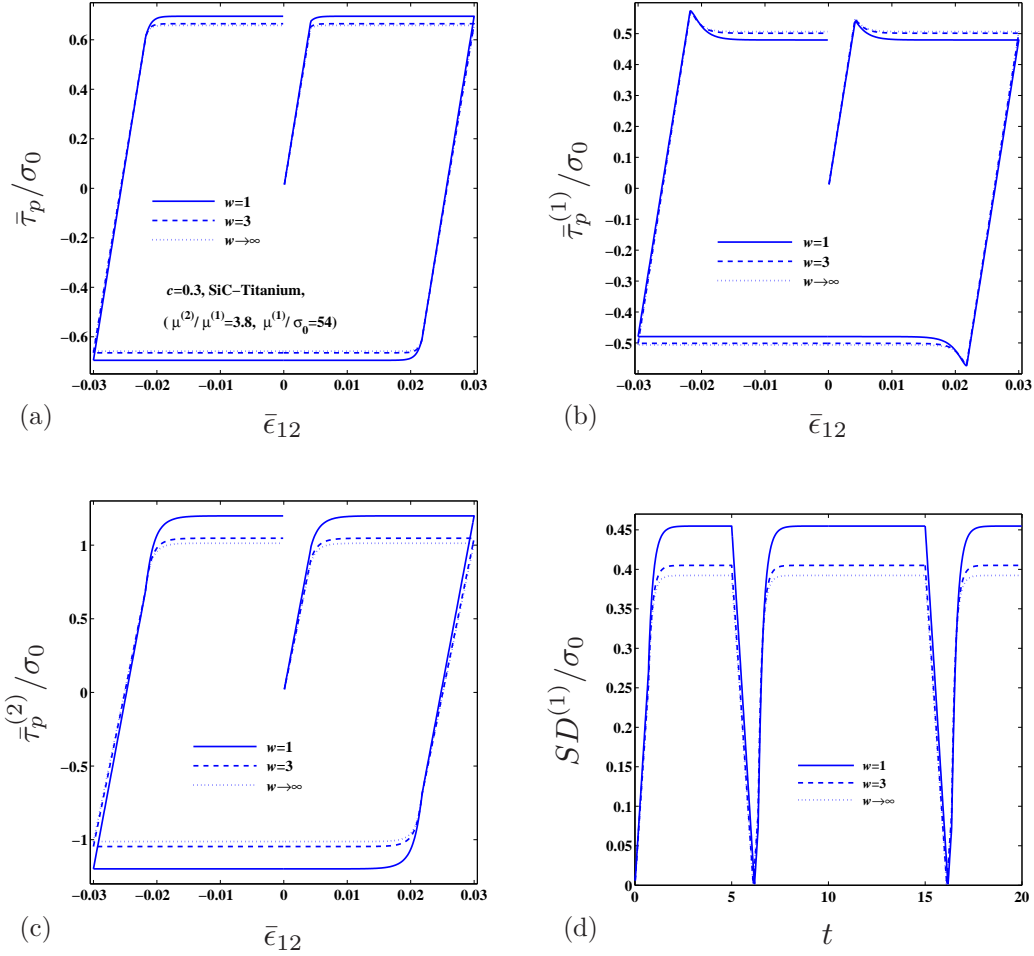


Figure 6.7: Variational estimates for the effective response and field statistics in the composites consisting of an elastic-ideally plastic matrix and elastic spheroidal particles with $\mu^{(1)}/\sigma_0 = 54$, $\mu^{(2)}/\mu^{(1)} = 3.8$, and $c = 0.3$ under transverse shear loading.

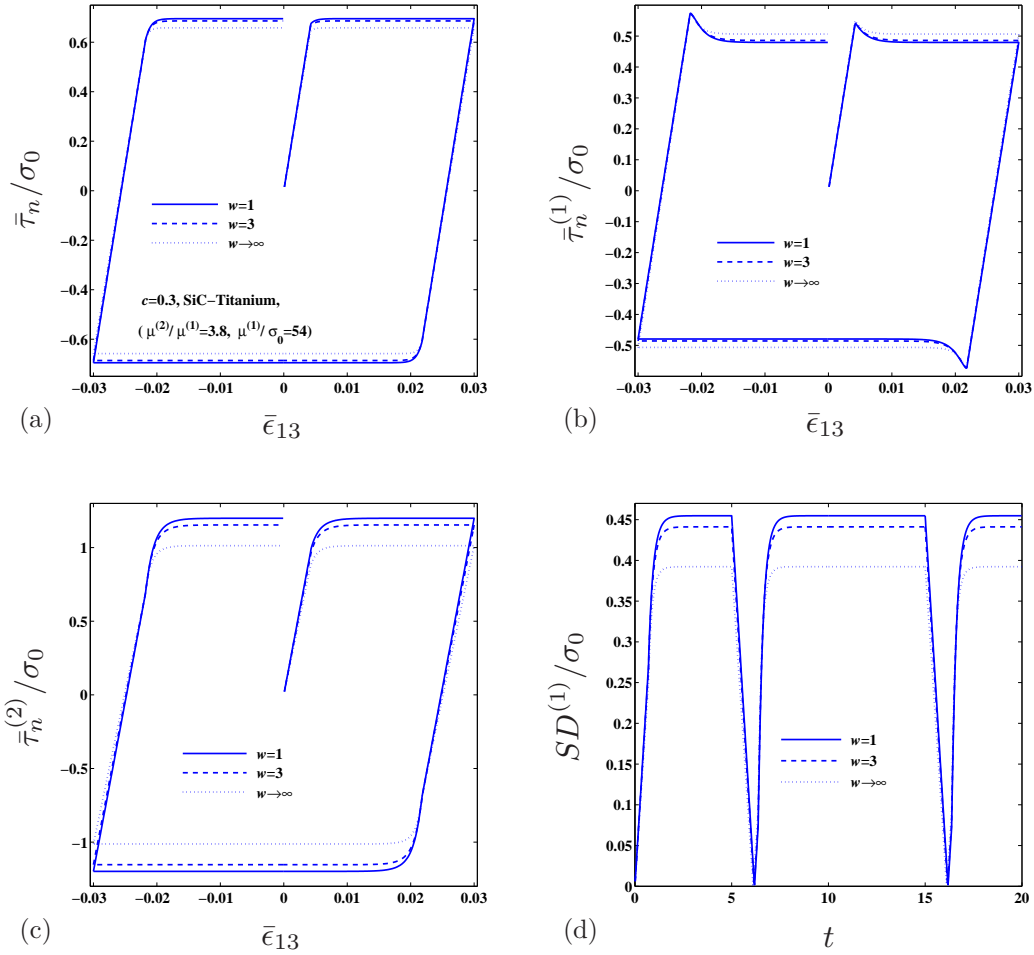


Figure 6.8: Variational estimates for the effective response and field statistics in the composites consisting of an elastic-ideally plastic matrix and elastic spheroidal particles with $\mu^{(1)}/\sigma_0 = 54$, $\mu^{(2)}/\mu^{(1)} = 3.8$, and $c = 0.3$ under longitudinal shear loading.

does not produce a significant effect on the effective behavior of the composite and the associated stress phase averages under transverse shear loading, unlike the case of axisymmetric shear loading in figure 6.4. However, we see from figures 6.7 (d) that the aspect ratio has a more noticeable effect on the standard deviation as it measures the stress field fluctuations in the matrix field.

Similar to the previous figure, figure 6.8 presents variational estimates for particle-reinforced composites consisting of an elastic-ideally plastic matrix and elastic spheroidal particles with $c = 0.3$, subjected to longitudinal shear cycles (6.58), for particle aspect ratios $w = 1, 3$ and ∞ . Results are shown for the mechanical properties $\mu^{(1)}/\sigma_0 = 54$ and $\mu^{(2)}/\mu^{(1)} = 3.8$. Similar to the case of transverse shear loading, we observe from figures 6.8 (a-c) that the effective behavior of the composite and the associated stress phase averages are weakly affected by the particle aspect ratio under longitudinal shear loading, again, unlike the case of axisymmetric shear loading. This is

because, for the case of axisymmetric shear loading, deformation is concentrated at the tips of spheroidal particles, and higher aspect ratios of the particles produces considerably larger stress concentrations at the tips and, consequently, higher field fluctuations in the matrix phase. On the other hand, for the case of transverse and longitudinal shear loadings, deformation in the matrix phase is much more homogeneous, and changing the particle aspect ratio does not significantly alter the field fluctuation in the matrix phase. Another interesting observation from figure 6.8 is that the estimates for the case of $w = 1$ and $w \rightarrow \infty$ coincide with the corresponding estimates for the case of transverse shear, presented in figure 6.7. The reason, for the case of $w = 1$, is that the composite is isotropic so that the transverse and longitudinal shear loadings are equivalent. However, for the case of long fibers ($w \rightarrow \infty$), the reason is that the Hashin-Shtrikman estimates for the effective behavior of the LCC predict the same behavior for the composite under transverse and longitudinal shear loadings.

6.4.3 Combined shear loading

In this subsection, we study the behavior of the composite when subjected to a combined, strain-controlled, axisymmetric and longitudinal mode of shear of the form

$$\dot{\boldsymbol{\epsilon}} = \dot{\epsilon}_0(t) \left\{ \left[\mathbf{e}_3 \otimes \mathbf{e}_3 - \frac{1}{2}(\mathbf{e}_1 \otimes \mathbf{e}_1 + \mathbf{e}_2 \otimes \mathbf{e}_2) \right] + \alpha (\mathbf{e}_1 \otimes \mathbf{e}_3 + \mathbf{e}_3 \otimes \mathbf{e}_1 + \mathbf{e}_2 \otimes \mathbf{e}_3 + \mathbf{e}_3 \otimes \mathbf{e}_2) \right\}, \quad (6.59)$$

where α is a constant.

Finally, figure 6.9 shows variational estimates for particle-reinforced composites consisting of an elastic-ideally plastic matrix and elastic spheroidal particles with $c = 0.3$, subjected to combined axisymmetric and longitudinal shear cycles (6.59) with $\alpha = 1$, for particle aspect ratios $w = 1, 3, 10$ and ∞ . Results are shown for the mechanical properties $\mu^{(1)}/\sigma_0 = 54$ and $\mu^{(2)}/\mu^{(1)} = 3.8$. First, by comparing the results in figure 6.9(a) and (b) with the corresponding results in figures 6.4(a) and 6.8(a), we realize that, when the axisymmetric and longitudinal shear modes are applied combined, the purely elastic regime in the overall behavior of the composite is shorter, compared to case that these modes of shear are applied individually. This is simply due to the fact that the application of a combined loading builds up a larger stress and, therefore, equation (6.41) is satisfied at a smaller applied strain. Also, we observe from figure 6.9(b) that the particle shape has a rather significant effect on the behavior of the longitudinal stress invariant $\bar{\tau}_n$, unlike the results in figure 6.8(a), although the behavior of the axisymmetric stress invariant $\bar{\tau}_a$ in figure 6.9(a) remains qualitatively very similar to that observed from figure 6.4(a). This is because the incremental stiffness of the composite in the longitudinal direction for the case of spheroidal particles can be strongly affected when the composite is simultaneously subjected to an axisymmetric mode of shear as well.

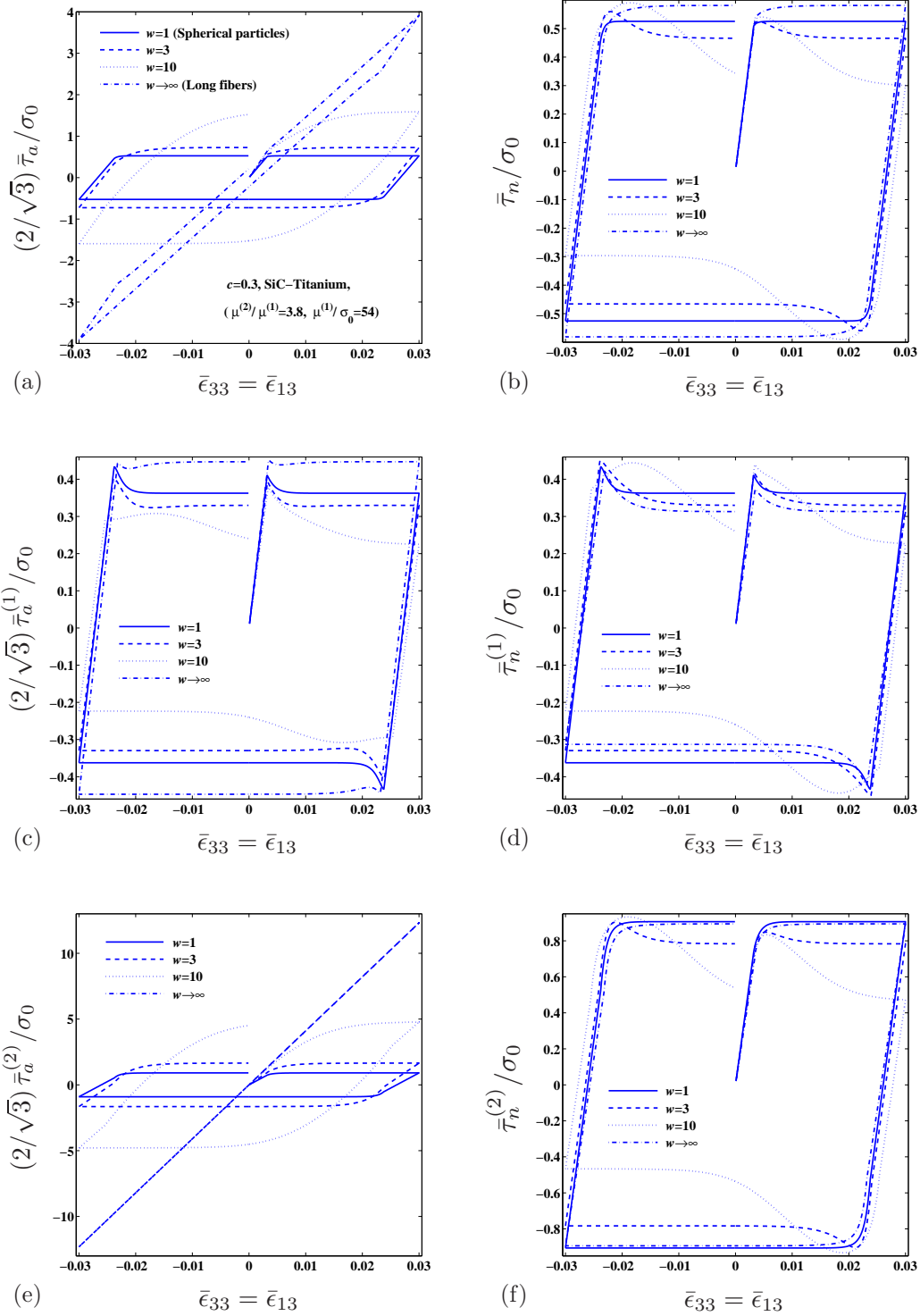


Figure 6.9: Variational estimates for the effective response and stress phase averages in the composites consisting of an elastic-ideally plastic matrix and elastic spheroidal particles with $\mu^{(1)}/\sigma_0 = 54$, $\mu^{(2)}/\mu^{(1)} = 3.8$, and $c = 0.3$ under combined axisymmetric and longitudinal shear loading with $\alpha = 1$.

6.5 Conclusions

In this chapter, we have developed a homogenization-based model to estimate the effective response of composites consisting of an elasto-viscoplastic matrix and a random distribution of aligned, ellipsoidal Maxwellian viscoelastic particles subjected to three-dimensional loading conditions in the regime of small deformations.

Our model can be summarized as follows. First, introducing the (modified) dissipation potentials in (6.4) to describe the “incremental” constitutive behavior of the local phases, we formulated the homogenization problem for the composite in a variational framework, defined in (6.8) and (6.9). Next, we made use of the variational principle of Ponte Castañeda (1991) to approximate the effective incremental response of the composites by that of a suitably-chosen LCC, consisting of a (fictitious) Maxwellian matrix reinforced by the same particles. Then, making the approximation that elastic strains in the composite are uniform-per-phase, the homogenization problem for the LCC simplifies to that for linear thermoelastic composites with uniform thermal strains, which was addressed by the homogenization theory of Ponte Castañeda and Willis (1995). Lastly, for the case of elastic particles, we proposed an empirical modification of the model for the purely elastic response of the composites.

We have also used our model to explore in more detail the effective behavior and field statistics in incompressible composites consisting of an elastic-ideally plastic matrix reinforced by a random distribution of aligned, elastic spheroidal particles subjected to axisymmetric, transverse and longitudinal modes of shear loading-unloading-loading cycles. In the context of this application, we investigated the influence of the volume fraction and shape of the particles, constitutive properties of the matrix and particle phases, and the applied loading conditions on the effective behavior and field statistics in these composites. We begin by emphasizing, although our model is based on the uniform-per-phase elastic strain approximation, its predictions were still in relatively good agreement with full-field numerical simulations of Lahellec and Suquet (2013) as well as with the corresponding predictions of IVP model (Lahellec and Suquet, 2013), for spherical particles ($w = 1$). A general observation from the results was that the composite exhibits a linear elastic behavior (characterized by relation (6.43)) up to yielding of the matrix phase, followed by a coupled elasto-plastic behavior, which subsequently approaches a plateau. Also, for the case of axisymmetric shear cycles, it is found that the particle aspect ratio has a significant effect on the effective behavior and the field statistics in the composite, while for the case of transverse and longitudinal shear loadings, the particle aspect ratio is found to weakly affect the homogenized behavior of the composite. Finally, we found that, for the case of spheroidal particles, the incremental response of the composite in the longitudinal direction can be significantly affected when the composite is simultaneously subjected to an axisymmetric mode of shear as well.

Chapter 7

Closure

In this thesis, analytical, homogenization-based models have been developed for nonlinear two-phase composites subjected to finite deformations. The models have the ability to account for the local nonlinear constitutive properties, volume fraction, shape, orientation, and distribution of the particles, as well as for the evolution of these parameters along a given macroscopic loading path.

Motivated by most applications of interest, attention has been given to two-phase composites with “particulate” microstructures and isotropic phases. In particular, we have developed our homogenizations models for the effective behavior and the microstructure evolution of two-phase composites consisting of ellipsoidal isotropic particles distributed randomly in an isotropic matrix. The use of ellipsoidal particles includes - as limiting cases - spherical particles, cylindrical fibers, as well as laminates.

Our proposed models (except the one developed in Chapter 4) make use of the technique of “linear comparison composites” (LCC), first introduced by Ponte Castañeda (1991) in the context of viscoplastic composites. This technique allows to convert available homogenization estimates for the effective behavior of linear composites into corresponding estimates for nonlinear composites. In this thesis we have developed homogenization-based models for three classes of nonlinear composite materials: (I) soft particle-reinforced elastomers, addressed in Part I of this thesis (including Chapters 1–3), (II) viscoelastic suspensions, addressed in Part II (including Chapters 4 and 5), and (III) elasto-viscoplastic composites, addressed in Part III (including Chapter 6). Next, a brief description of the main results in this thesis is provided.

In Part I of this thesis, we considered soft elastomeric composites. In Chapter 1, we have developed new constitutive models for the macroscopic response of composites with hyperelastic phases and particulate microstructures, subjected to general, three-dimensional, finite deformations. For this purpose, we have made use of a suitable extension of the tangent second-order (TSO) homogenization theory of Ponte Castañeda and Tiberio (2000), which is capable of accounting for the strongly nonlinear overall incompressibility constraint (for incompressible behavior of the phases), as well as for the reorientation of the particles with the deformation. The TSO theory was tested for 2-D problem consisting of transverse shear loading of elastomers reinforced with cylindrical fibers of elliptical cross-section, where it was found to recover exactly the generalized second-order (GSO) results of Lopez-Pamies and Ponte Castañeda (2006a) for dilute concentration of elliptical fibers in a neo-Hookean elastomeric matrix. Also, a closed-form estimate was derived for the effective stored-energy function of an incompressible neo-Hookean elastomers reinforced by spherical rigid particle subjected to general isochoric loadings.

In Chapter 2 (also published in Avazmohammadi and Ponte Castañeda (2014a)), we have made use of the tangent second-order, finite-strain homogenization framework developed in Chapter 1 to estimate the overall response and microstructure evolution in incompressible elastomers reinforced by aligned, spheroidal, rigid particles, subject to general loading conditions. In this chapter, we also have presented a detailed study of the possible development of macroscopic instabilities in the particle-reinforced composites of interest, under both aligned and non-aligned loading conditions. The onset of such instabilities in these materials is identified with the loss of strong ellipticity of the associated homogenized behavior. It should be remarked that, to the best of our knowledge, the estimates provided in this chapter for the effective stored-energy function and the particle rotation

are the first homogenization-type estimates for reinforced elastomers with general spheroidal particle shape. The results are valid for large strains provided that the interfaces between the particles and the rubber remain intact.

In Chapter 3 (also published in Avazmohammadi and Ponte Castañeda (2014b)), we made use of the TSO constitutive model presented in Chapter 2 to generate estimates for the homogenized stress-strain relation, the evolution of microstructure, and the onset of macroscopic instabilities in particle-reinforced elastomeric composites consisting of an incompressible Gent/neo-Hookean matrix and random distributions of aligned spheroidal particles of aspect ratio w . The estimates presented in this chapter provide a broad picture of the influence of the macroscopic loading conditions, matrix properties and microgeometry (including particle volume fractions and shapes) on the effective behavior and the possible onset of macroscopic instabilities in the composites. These results generalize earlier results of Lopez-Pamies and Ponte Castañeda (2006b) for 2-D composites reinforced with elliptical fibers. In addition, the results of this work are consistent with earlier results for laminated elastomers (deBotton, 2005; Lopez-Pamies and Ponte Castañeda, 2009) and for continuous-fiber-reinforced elastomers (Agoras et al., 2009a) in the limits as the aspect ratio w tend to zero and ∞ , respectively. In this chapter, we carried out comparisons between predictions of the TSO model and FEM simulations of Lopez-Pamies et al. (2013a) for spherical particles ($w = 1$), and found very good agreement up to fairly large strains. Similarly, the TSO results were found to be in excellent agreement with FEM results (Moraleda et al., 2009) for the transverse shear response of continuous-fiber-reinforced elastomers ($w \rightarrow \infty$). In contrast to the results for spherical particles in Chapter 1, it was found that the reinforced elastomers with spheroidal particles can undergo shear localization instabilities, which are captured by loss of ellipticity of the associated effective incremental modulus tensors, and correspond physically to the sudden collective rotation—or flopping—of the particles to try to accommodate the imposed deformation. These flopping-type macroscopic instabilities in short-fiber-reinforced elastomers are very similar to those predicted in the context of model 2-D composites by Lopez-Pamies and Ponte Castañeda (2006b).

Next, in Part II of this thesis, we considered viscoelastic suspensions. In Chapter 4, we have developed a homogenization-based model characterizing the finite-strain, time-dependent response of non-dilute suspensions of micro-scaled, soft particles in a Newtonian fluid under Stokes flow conditions. Although more general initial shapes and viscoelastic constitutive models could be used for the particles, we have considered here suspensions of initially spherical particles whose constitutive response is characterized by Kelvin-Voigt (KV) behavior incorporating finite extensibility of the particles in the regime of arbitrarily large deformations. The resulting constitutive model provides a complete description for the time-dependent, macroscopic, rheological response of the non-dilute suspensions of viscoelastic particles under macroscopically uniform flows, thus generalizing earlier work by Gao et al. (2011) for dilute suspensions of neo-Hookean (NH) particles. We have also used the model developed in this chapter to explore the rather rich and complex rheological behavior of the soft-particle suspensions by focusing on two types of flows: *extensional*, and *simple shear* flows. These examples provide a broad picture of the influence of the flow conditions, constitutive behaviors of the particles, and the particle volume fractions on the dynamics of the suspended particles, as well as on the macroscopic rheology of the suspension. We found that, contrary to the steady-state

(SS) results for extensional flows in which softer particles tend to increase the effective viscosity of the suspension, the corresponding SS results show that softer particles tend to reduce the effective viscosity in simple shear, leading to an overall shear-thinning effect for the suspension. This result suggests that it should be possible to design suspensions of “neutral” particles (Milton, 2002b), as well as suspensions with lower viscosity than that of the suspending fluid. Also, in this chapter, we compared the predictions of our model with simulation results for suspensions of capsules, as well as with the experimental data for the suspensions of RBCs, in a shear flow. It was found that the predictions of the model are in a good agreement with the simulation results for dilute suspensions of capsules. For non-dilute suspensions, the corresponding predictions start to deviate from the simulation results and experimental data at sufficiently large particle concentrations, but they are still in relative good qualitative agreement with both simulation and experimental results.

In Chapter 5, we have developed a homogenization-based model to estimate the effective rheological behavior of non-colloidal suspensions of initially spherical, soft particles in yield stress fluids under Stokes flow conditions. More specifically, we considered suspensions of Kelvin-Voigt solid particles in a Herschel-Bulkley fluid which undergo time-dependent, finite deformations when subjected to uniform flows. In this chapter, similar to Chapter 4, we have used our model to explore in more detail the rheology and particle dynamics in suspensions of elastic Gent particle in HB fluids under shear flow conditions. In the context of this example, we investigated the influence of constitutive properties of the HB fluids and the particles, and the particle volume fraction on the dynamics of the suspended particles, as well as on the macroscopic rheological behavior of the suspension. It should be remarked that, *analytical* constitutive models for suspensions of viscoelastic particles in Newtonian and non-Newtonian fluids, such as those developed in Chapters 4 and 5, are useful in describing some of the rheological features of complex suspensions, including suspensions of capsules and vesicles.

At this point, it worth emphasizing that although the *analytical* constitutive models developed in Part I and II of this thesis are approximate, they have significant advantages relative to full field numerical simulations. First, the numerical simulations of these problems are difficult due to the large stretches involved (requiring remeshing and other sophisticated numerical techniques) and are computationally very intensive (in practice, relatively small numbers of particles can be considered and ensemble averages would be required). Second, in practical applications, it is necessary to solve boundary value problems with non-uniform boundary conditions and complicated geometries. This requires the use of the finite element method, and for this purpose, it is crucial to be able to determine the homogenized response of the composite material accurately and efficiently under general loading conditions. Clearly, this is something that would be difficult to accomplish numerically with current codes and computational power for these highly nonlinear, anisotropic materials, but is something that would be feasible using the analytical constitutive models developed in this work. On the other hand, the analytical models are given in a form that can be easily implemented numerically into user-defined constitutive subroutines for use with standard finite element codes.

Finally, in Chapter 6 (corresponding to Part III of this thesis), we have developed a homogenization-based model to estimate the effective response of composites consisting of an elasto-viscoplastic (EVP) matrix and a random distribution of aligned, ellipsoidal Maxwellian viscoelastic particles

subjected to three-dimensional loading conditions in the regime of small deformations. We have also used our model to explore in more detail the effective behavior and field statistics in incompressible composites consisting of an elastic-ideally plastic matrix reinforced by a random distribution of aligned, elastic spheroidal particles subjected to axisymmetric, transverse and longitudinal modes of shear loading-unloading-loading cycles. It should be remarked that, for the case of axisymmetric shear cycles, it was found that predictions of our model were in relatively good agreement with full-field numerical simulations of Lahellec and Suquet (2013) as well as with the corresponding predictions of IVP model (Lahellec and Suquet, 2013), for spherical particles ($w = 1$). Also, for the case of axisymmetric shear cycles, it was found that the particle aspect ratio has a significant effect on the effective behavior and the field statistics in the composite, while for the case of transverse and longitudinal shear loadings, the particle aspect ratio is found to weakly affect the homogenized behavior of the composite.

At this stage, it is important to make a few remarks regarding future directions in connection with the results presented in this work. First, it should be mentioned that the soft elastomeric composites considered in this work offer great potential to be used as “active materials” due to their considerable flexibility in the elastic regime. These materials, which change shape and size when subjected to magnetic fields, are usually made in the form of composites consisting of an ideal dielectric and a distribution of magnetically susceptible particles, such as iron and nickel alloys. Therefore, the results of Part I of this thesis for the mechanical response of short-fiber-reinforced composites could be used to derive corresponding results for the magneto-elastic response of such composite materials when the particles are allowed to be magnetically susceptible by means of the “partial decoupling approximation” introduced recently by Ponte Castañeda and Galipeau (2011) (see also Ponte Castañeda and Siboni (2012); Siboni and Ponte Castañeda (2014); Siboni et al. (2014) for electro-active polymer composites). In addition, the models developed in this part could be generalized to account for deformability in the particle phase as well as for more general microstructures, including random particle orientations. (See, for instance, Avazmohammadi and Naghdabadi (2009); Avazmohammadi et al. (2009); Avazmohammadi and Naghdabadi (2013) for simple homogenization models for these composites with special material properties of the constituent phases, microstructures and loading conditions.) The applications of these problems can be found in constitutive modeling of biological tissues such as intervertebral disc and annulus fibrosus, which, in a simple picture, consist of an elastomer-like extracellular matrix and a random-distribution of particle-like, deformable cells.

In the context of viscoelastic suspensions, considered in Part II of this thesis, a problem of increasing interest is suspensions of microgels in Newtonian fluids which have applications in drug-delivery systems. The microgel particles are soft and deform considerably when subjected to shear flows. However, because of their highly porous nature, their mechanical deformation is strongly influenced by diffusion of the fluid through them. Therefore, the results of Chapter 4 for the rheological response of suspensions of soft particles in a Newtonian fluid can be generalized to include the effect of diffusion and permeability in the particles by making use of constitutive models for the polymer gels, recently developed by Chester and Anand (2011).

Finally, concerning our work in Part III of this thesis, it is recalled that the predictions of

our models, although very feasible to calculate, are not as accurate as the estimates of the IVP (incremental variational principle) model of Lahellec and Suquet (2013). Therefore, it is of our interest to generalize the IVP model, which so far has been developed only for spherical particles, to account for the particle shape effect on the overall behavior of the EVP composites.

Appendices

Appendix A

A.1 On the calculation of the tensor \mathbf{E}_I

In this appendix, we present a brief outline of the asymptotic analysis associated with obtaining the limiting value of the tensor \mathbf{E} ($= \mathbf{P}^{-1} - \mathbf{L}^{(1)}$) in the incompressibility limit (i.e., in the limit as $\varepsilon \rightarrow 0$). We first spell out the main steps necessary to carry out the asymptotic expansion for $\mathbf{Q} = \mathbf{P}^{-1}$ about $\varepsilon = 0$. For this purpose, we assume that the incompressibility constraint holds, and that the tensor \mathbf{Q} can be expanded in the form

$$\mathbf{Q} = \varepsilon^{-1}\mathbf{Q}_{-1} + \mathbf{Q}_0 + \varepsilon\mathbf{Q}_1 + O(\varepsilon^2), \quad (\text{A.1})$$

where $\mathbf{Q}_{-1} \neq \mathbf{0}$. In order to compute the unknown, tensorial coefficients \mathbf{Q}_{-1} and \mathbf{Q}_0 , we need to first find the null-space of \mathbf{P}_0 (the first term in the expansion (1.104)), defined by

$$\text{null } \mathbf{P}_0 = \{\mathbf{N} | \mathbf{P}_0 \mathbf{N} = \mathbf{0}\}, \quad (\text{A.2})$$

By solving $\mathbf{P}_0 \mathbf{N} = \mathbf{0}$ for the second-order tensor \mathbf{N} , we will have

$$\text{null } \mathbf{P}_0 = \text{span}\{\mathbf{W}_1, \mathbf{W}_2, \mathbf{W}_3\}, \quad (\text{A.3})$$

where $\{\mathbf{W}_1, \mathbf{W}_2, \mathbf{W}_3\}$ stands for an orthogonal basis for the set of skew-symmetric, second-order tensors such that $\mathbf{W}_i + \mathbf{W}_i^T = \mathbf{0}$ and $\mathbf{W}_i \cdot \mathbf{W}_j = 0$ ($i \neq j$), $i, j = 1, 2, 3$. Using the major symmetry of the tensor \mathbf{P}_0 ($(P_0)_{ijkl} = (P_0)_{klij}$), equations (A.3) indicate that

$$(P_0)_{ijkl} (W_p)_{kl} = (P_0)_{klij} (W_p)_{kl} = 0, \quad p = 1, 2, 3. \quad (\text{A.4})$$

By substituting the asymptotic expansions (1.104) and (A.1) into the identity $\mathbf{P} \mathbf{Q} = \mathbf{Q} \mathbf{P} = \mathcal{I}$, and collecting coefficients of the same power as ε , the following system of equations is obtained

$$\mathbf{Q}_{-1} \mathbf{P}_0 = \mathbf{P}_0 \mathbf{Q}_{-1} = \mathbf{0}, \quad (\text{A.5})$$

$$\mathbf{P}_0 \mathbf{Q}_0 + \mathbf{P}_1 \mathbf{Q}_{-1} = \mathbf{Q}_0 \mathbf{P}_0 + \mathbf{Q}_{-1} \mathbf{P}_1 = \mathcal{I}, \quad (\text{A.6})$$

$$\mathbf{P}_0 \mathbf{Q}_1 + \mathbf{P}_1 \mathbf{Q}_0 + \mathbf{P}_2 \mathbf{Q}_{-1} = \mathbf{Q}_1 \mathbf{P}_0 + \mathbf{Q}_0 \mathbf{P}_1 + \mathbf{Q}_{-1} \mathbf{P}_2 = \mathbf{0}. \quad (\text{A.7})$$

Thus, this system of linear equations for \mathbf{Q}_{-1} , \mathbf{Q}_0 , and \mathbf{Q}_1 uniquely determines the coefficients in the expansion (A.1). Noting that $\det(\mathbf{Q}_{-1}) = 0$, the general solution to the tensorial equation (A.5) can be written as (Avrachenkov et al., 2001)

$$\mathbf{Q}_{-1} = \sum_{i=1}^3 \mathbf{W}_i \otimes \mathbf{V}_i^{(0)}, \quad (\text{A.8})$$

where the arbitrary matrices $\mathbf{V}_i^{(0)}$ are determined using (A.6). To this end, by transposing (A.6) (meaning $(\cdot)_{ijkl}^T = (\cdot)_{klij}$) and then right-multiplying it with \mathbf{W}_i , it follows that

$$(P_1)_{ijkl}(Q_{-1})_{klrs}(W_p)_{ij} = (W_p)_{rs}, \quad p = 1, 2, 3, \quad (\text{A.9})$$

where use has been made of the relations (A.4). Substituting (A.8) into (A.9), it leads to

$$[(P_1)_{ijkl}(W_p)_{ij}(W_p)_{kl}](V_p^0)_{rs} = (W_p)_{rs}, \quad p = 1, 2, 3, \quad (\text{A.10})$$

from which it is concluded that

$$\mathbf{V}_i^{(0)} = \frac{1}{\mathbf{W}_i \cdot \mathbf{P}_1 \mathbf{W}_i} \mathbf{W}_i \quad i = 1, 2, 3 \quad (\text{A.11})$$

Next, the general solution of (A.6) can be represented as (Avrachenkov et al., 2001)

$$\mathbf{Q}_0 = \mathbf{P}_0^\dagger (\mathcal{I} - \mathbf{P}_1 \mathbf{Q}_{-1}) + \sum_{i=1}^3 \mathbf{W}_i \otimes \mathbf{V}_i^{(1)}, \quad (\text{A.12})$$

By the same token, in order to find $\mathbf{V}_i^{(1)}$, we take the transpose of (A.7) and then right-multiply it with \mathbf{W}_i , which leads to

$$(P_1)_{ijkl}(Q_0)_{klrs}(W_p)_{ij} + (P_2)_{ijkl}(Q_{-1})_{klrs}(W_p)_{ij} = 0, \quad p = 1, 2, 3. \quad (\text{A.13})$$

where, again, use has been made of relations (A.4). Substituting (A.12) and (A.8) into the above equation, and doing some algebra, the equations (1.110) for $\mathbf{V}_i^{(1)}$ are obtained. Finally, in the limit as $\varepsilon \rightarrow 0$, we recover $\mathbf{Q}_{-1} = \mathbf{L}_{-1}^{(1)}$ (when the isochoric deformation condition is satisfied), and along with the expansion (1.94), the tensor $\mathbf{E}^I = (\mathbf{P}^{-1} - \mathbf{L}^{(1)})|_{\mu' \rightarrow \infty}$ reduces to $\mathbf{E}^I = \mathbf{Q}_0 - \mathbf{L}_\mu^{(1)}$.

A.2 In-plane components of the tensor \mathbf{P} for cylindrical inclusions with elliptical cross-section embedded in a compressible neo-Hookean matrix

In this appendix, we present explicit expressions for the (in-plane) components of the tensor \mathbf{P} , associated with a cylindrical fiber of elliptical cross-section embedded in a generalized linear-elastic material with modulus tensor $\mathbf{L}^{(1)}$. It is recalled that the tensor \mathbf{P} , defined by (1.117), makes use of the tangent modulus tensor $\mathbf{L}^{(1)} = (\partial^2 W^{(1)} / \partial \mathbf{F} \partial \mathbf{F})|_{\mathbf{F}=\bar{\mathbf{F}}}$. Since $\mathbf{L}^{(1)}$ is characterized by the objective and isotropic stored energy function $W^{(1)}$, the following condition is known (Lopez-Pamies and Ponte Castañeda, 2006b) to be satisfied by $\mathbf{L}^{(1)}$

$$L_{ijkl}^{(1)}(\bar{\mathbf{F}}) = \bar{Q}_{rm} \bar{Q}_{jn} \bar{Q}_{sp} \bar{Q}_{lq} \bar{R}_{ir} \bar{R}_{ks} L_{mnpq}^*(\bar{\mathbf{D}}), \quad (\text{A.14})$$

where $\bar{\mathbf{R}}$ and $\bar{\mathbf{Q}}$ are the macroscopic orthogonal tensors in the decompositions $\bar{\mathbf{F}} = \bar{\mathbf{R}}\bar{\mathbf{U}} = \bar{\mathbf{R}}\bar{\mathbf{Q}}\bar{\mathbf{D}}\bar{\mathbf{Q}}^T$, given by $\bar{\mathbf{Q}} = \cos(\bar{\theta})(\mathbf{e}_1 \otimes \mathbf{e}_1 + \mathbf{e}_2 \otimes \mathbf{e}_2) + \sin(\bar{\theta})(\mathbf{e}_2 \otimes \mathbf{e}_1 - \mathbf{e}_1 \otimes \mathbf{e}_2)$ and $\bar{\mathbf{R}} = \cos(\bar{\psi})(\mathbf{e}_1 \otimes \mathbf{e}_1 + \mathbf{e}_2 \otimes \mathbf{e}_2) + \sin(\bar{\psi})(\mathbf{e}_2 \otimes \mathbf{e}_1 - \mathbf{e}_1 \otimes \mathbf{e}_2)$, with respect to the 2-D laboratory frame of reference, and $\bar{\mathbf{D}}$ is a diagonal, second-order tensor with matrix representation $\bar{\mathbf{D}} = \bar{\lambda}_1 \mathbf{e}_1 \otimes \mathbf{e}_1 + \bar{\lambda}_2 \mathbf{e}_2 \otimes \mathbf{e}_2$. The tensor \mathbf{L}^* is orthotropic relative to $\{\mathbf{e}_i\}$ and, recalling that it exhibits major symmetry $L_{ijkl}^* = L_{klij}^*$, it follows that it generally has five in-plane, independent components. However, in order to obtain simple analytical expressions for the \mathbf{P} tensor components, following Lopez-Pamies and Ponte Castañeda (2006b), we take advantage of the following constraint for the components of $\mathbf{L}^{(1)}$

$$L_{1221}^{(1)} = \sqrt{(L_{1111}^{(1)} - L_{1212}^{(1)})(L_{2222}^{(1)} - L_{1212}^{(1)}) - L_{1122}^{(1)}}, \quad (\text{A.15})$$

which is satisfied by the tangent modulus of a neo-Hookean material (but not for more general hyperelastic materials including Gent).

Following Lopez-Pamies and Ponte Castañeda (2004b, 2006b), the four independent components of $\mathbf{L}^{(1)}$ are chosen to be $L_{1111}^{(1)} = l_1^*$, $L_{2222}^{(1)} = l_2^*$, $L_{1122}^{(1)} = l_3^*$, $L_{1212}^{(1)} = l_4^*$. It can then be deduced from relation (A.14) that

$$P_{ijkl}(\bar{\mathbf{F}}) = \bar{R}_{ip}\bar{R}_{kq}P_{pqjl}^*(\bar{\mathbf{U}}) \quad (\text{A.16})$$

Now, making use of this choice of $\mathbf{L}^{(1)}$ along with the constraint (A.15), it follows that the in-plane components of \mathbf{P}^* , after some algebra, can be expressed in terms of the the variables C_j ($j = 1, \dots, 13$), and the functions P_i ($i = 1, 2, 3$), via

$$\begin{aligned} P_{1111}^* &= P_1(C_1, C_2, C_3), & P_{2222}^* &= P_2(C_4, C_5, C_6), & P_{1122}^* &= P_3(C_7, C_8, C_9) \\ P_{1212}^* &= P_2(C_1, C_2, C_{10}), & P_{1112}^* &= P_3(C_1, C_2, C_{11}), & P_{1121}^* &= P_1(C_7, -C_8, C_{12}) \\ P_{2212}^* &= P_2(C_7, -C_8, C_{12}), & P_{2221}^* &= P_3(C_4, C_5, C_6), & P_{1221}^* &= P_3(C_7, C_8, -C_2/2), & P_{2121}^* &= P_1(C_4, C_5, C_{13}) \end{aligned}$$

where

$$\begin{aligned} C_1 &= 2L^* \cos^4(\bar{\theta}) + (3l_1^* - 4l_4^* + l_2^* - 4l^*) \cos^2(\bar{\theta}) + l_4^* - l_1^*, \\ C_2 &= [L^* \cos^2(\bar{\theta}) + l_1^* - l^* - l_4^*] \sin(2\bar{\theta}), & C_3 &= -L^* \cos^4(\bar{\theta}) + 2(l_1^* - l^* - l_4^*) \cos^2(\bar{\theta}) + l_1^*, \\ C_4 &= 2L^* \cos^4(\bar{\theta}) + (3l_2^* - 4l_4^* + l_1^* - 4l^*) \cos^2(\bar{\theta}) + l_4^* - l_2^*, \\ C_5 &= [L^* \cos^2(\bar{\theta}) + l_2^* - l^* - l_4^*] \sin(2\bar{\theta}), & C_6 &= L^* \sin^2(\bar{\theta}) \cos^2(\bar{\theta}) - l_4^*, \\ C_7 &= L^* \sin(4\bar{\theta})/4, & C_8 &= L^* \sin^2(2\bar{\theta})/2 - l^*, & C_9 &= [l_1^* - l^* - l_4^* - L^* \cos^2(\bar{\theta})] \sin(\bar{\theta}) \cos(\bar{\theta}), \\ C_{10} &= L^* \cos^4(\bar{\theta}) + 2(l_4^* + l^* - l_1^*) \cos^2(\bar{\theta}) + l_1^*, & C_{11} &= 2(l_4^* + l^* - l_1^*) \cos^2(\bar{\theta}) - L^* \cos^4(\bar{\theta}) + l_1^*, \\ C_{12} &= [L^* \cos^2(\bar{\theta}) + l_1^* - l^* - l_4^*] \sin(\bar{\theta}) \cos(\bar{\theta}), & C_{13} &= L^* \sin^2(2\bar{\theta})/4 - l_4^*, \end{aligned}$$

and

$$\begin{aligned} P_1(A_1, A_2, A_3) &= \vartheta \{ \{ \varpi(A_1 a_1 + A_2 a_2) s_2 - k(a_1^2 + a_2^2)[(k a_1 - 1)A_3 + k(k a_1 - 1)A_1 + k(k a_2 - a_2)A_2] \} s_1 \\ &+ \{ (a_1^2 + a_2^2)[k(2a_1 + a_2^2) - 2]A_3 - a_2[3ka_1^2 - a_2^2 k + [(a_2^2 - 4)k - 1]a_1 + 2]A_2 \\ &+ [2ka_1^2 + 2(2a_2^2 k - 1)a_1 + ka_2^4 - (2k + 1)a_2^2]A_1 \} s_2 \}, \end{aligned}$$

$$\begin{aligned}
P_2(A_1, A_2, A_3) = & -\vartheta \{ \{ \varpi(A_1 a_1 + A_2 a_2) s_2 - (k-1)(a_1^2 + a_2^2)[(k a_1 - 1)A_3 + k(k a_1 - 1)A_1 \\
& + k(k a_2 - a_2)A_2] \} s_1 + \{ (a_1^2 + a_2^2)[k(2a_1 - 2a_1^2 - a_2^2) + 2a_1 + a_2^2 - 2]A_3 \\
& + a_2[k a_1^3 + (1-5k)a_1^2 + (1+4k)a_1 + (1-k)a_2^2 - 2]A_2 \\
& + [(2+2k - k a_2^2)a_1^2 + 2(k a_2^2 - 1)a_1 + (1-2k)a_2^2 - 2a_1^3 k]A_1 \} s_2 \},
\end{aligned}$$

$$\begin{aligned}
P_3(A_1, A_2, A_3) = & \vartheta \{ \{ \varpi(A_1 a_2 - A_2 a_1) s_2 - k(k-1)(a_1^2 + a_2^2)[a_2 k A_1 + (1 - k a_1)A_2 + a_2 A_3] \} s_1 \\
& + \{ a_2[2a_1^3 k + (a_2^2 k - 2 - 2k)a_1^2 + 2(1 - a_2^2 k)a_1 + (2k - 1)a_2^2]A_2 \\
& - a_2[3a_1^2 k + (a_2^2 k - 4k - 1)a_1 + 2 - a_2^2 k]A_1 - a_2(a_1^2 + a_2^2)(k a_1 - 2k + 1)A_3 \} s_2 \}.
\end{aligned}$$

In the above expressions,

$$\begin{aligned}
a_1 &= (l_1^* - l_2^*) \cos(2\bar{\theta})/a, \quad a_2 = (l_1^* - l_2^*) \sin(2\bar{\theta})/a, \quad a = -[l_1^* \sin^2(\bar{\theta}) + l_2^* \cos^2(\bar{\theta})] \\
\varpi &= (k a_1 - 1)^2 + k(k-1)a_2^2, \quad \vartheta = 2\pi \alpha \{ \varpi(a_1^2 + a_2^2) s_1 s_2 \}^{-1}, \quad L^* = 2l_4^* + 2l_7^* - l_2^* - l_1^* \\
l^* &= \sqrt{(l_1^* - l_4^*)(l_2^* - l_4^*)}, \quad k = \omega^2/(\omega^2 - 1).
\end{aligned}$$

For the special case of compressible neo-Hookean materials, the expression for the components of the tensor \mathbf{P} are obtained by substituting the following expressions for l_1^*, \dots, l_4^* into the above relations

$$l_i^* = \bar{\lambda}_i^{-2} \left[\mu^{(1)}(\bar{\lambda}_i^2 + 1) + \mu'^{(1)} \bar{J}^2 \right] \quad (i = 1, 2), \quad l_3^* = \mu'^{(1)}(2\bar{J} - 1), \quad \text{and} \quad l_4^* = \mu^{(1)}, \quad (\text{A.17})$$

where $\bar{J} = \det(\bar{\mathbf{F}}) = \bar{\lambda}_1 \bar{\lambda}_2$.

A.3 The tensors \mathbf{P} and \mathbf{E} for spherical inclusions embedded in a compressible neo-Hookean matrix

In this appendix, explicit analytical expressions are given for the components of the tensors \mathbf{P} and \mathbf{E} for spherical inclusions embedded in generalized linear-elastic material with moduli tensor $\mathbf{L}^{(1)}$, whose components are assumed to satisfy (Agoras et al., 2009a) the constraints

$$\begin{aligned}
L_{1212}^{(1)} &= L_{1313}^{(1)} = L_{2323}^{(1)} \\
L_{1221}^{(1)} &= \sqrt{(l_1^* - l_7^*)(l_2^* - l_7^*)} - l_4^*, \quad L_{1331}^{(1)} = \sqrt{(l_1^* - l_7^*)(l_3^* - l_7^*)} - l_5^*, \quad L_{2332}^{(1)} = \sqrt{(l_2^* - l_7^*)(l_3^* - l_7^*)} - l_6^*,
\end{aligned} \quad (\text{A.18})$$

where the variables l_i^* ($i = 1, \dots, 7$) have been identified with the seven remaining “independent” components of $\mathbf{L}^{(1)}$ (relative to the basis $\{\mathbf{e}_i\}$) via

$$l_1^* = L_{1111}^{(1)}, \quad l_2^* = L_{2222}^{(1)}, \quad l_3^* = L_{3333}^{(1)}, \quad l_4^* = L_{1122}^{(1)}, \quad l_5^* = L_{1133}^{(1)}, \quad l_6^* = L_{2233}^{(1)}, \quad l_7^* = L_{1212}^{(1)}. \quad (\text{A.19})$$

In this connection, it should be noted that the conditions (A.18) are satisfied by the tangent modulus of a neo-Hookean material, but not more generally.

Recalling that the composite is statistically isotropic in the undeformed configuration, the expression for \mathbf{P} in the basis $\{\mathbf{e}_i\}$ can be expressed as

$$P_{ijkl} = \frac{1}{4\pi} \int_0^\pi \int_0^{2\pi} (L_{imkn}^{(1)} \xi_m \xi_n)^{-1} \xi_j \xi_l d\theta d\phi, \quad (\text{A.20})$$

where $\xi_1 = \sin(\phi) \cos(\theta)$, $\xi_2 = \sin(\phi) \sin(\theta)$, and $\xi_3 = \cos(\phi)$. Now, making use of the above choice for $\mathbf{L}^{(1)}$, it can be shown that the components of the microstructural tensor \mathbf{P} are given by the analytical expressions

$$\begin{aligned} P_{1111} &= -\frac{1}{3l_7^*(l_1^* - l_3^*)^{3/2}(l_1^* - l_2^*)^2} \left\{ \sqrt{l_2^*}(l_1^* - l_7^*) \{2\chi_1 \Xi_e + l_3^*(l_2^* - l_1^*) \Xi_f\} \right. \\ &\quad \left. - \sqrt{l_1^* - l_3^*} \{ (l_3^* + l_7^* + l_2^*)(l_1^*)^2 - [(3l_2^* + 2l_3^*)l_7^* - (l_2^*)^2 + 2l_3^*l_2^*]l_1^* + l_2^*l_3^*(4l_7^* - l_2^*) \} \right\}, \\ P_{2222} &= -\frac{1}{3l_2^*l_7^*(l_2^* - l_1^*)^2(l_2^* - l_3^*)^2\sqrt{l_1^* - l_3^*}} \left\{ (l_2^* - l_7^*)\sqrt{l_2^*} \{2l_2^*(l_1^* - l_3^*)\chi_2 \Xi_e + l_3^*(l_2^* - l_1^*)[2l_3^*l_2^* + l_1^*(l_2^* - 3l_3^*)] \Xi_f\} \right. \\ &\quad \left. - l_2^*(l_2^* - l_3^*)\sqrt{l_1^* - l_3^*} \{ (l_1^* + l_7^* + l_3^*)(l_2^*)^2 - [(3l_1^* + 2l_3^*)l_7^* + 2l_3^*l_1^* - (l_1^*)^2]l_2^* - l_1^*l_3^*(l_1^* - 4l_7^*) \} \right\}, \\ P_{3333} &= \frac{1}{3l_7^*(l_2^* - l_3^*)^2(l_1^* - l_3^*)^{(3/2)}} \left\{ \sqrt{l_2^*}(l_7^* - l_3^*) \{2\chi_3 \Xi_e - [l_1^*l_3^* + l_2^*(2l_3^* - 3l_1^*)] \Xi_f\} \right. \\ &\quad \left. + \sqrt{l_1^* - l_3^*}(l_2^* - l_3^*)[(l_7^* - l_1^* - l_2^*)l_3^* + l_1^*l_2^*] \right\}, \\ P_{1122} &= \frac{1}{3l_7^*(l_2^* - l_1^*)^2(l_2^* - l_3^*)\sqrt{l_1^* - l_3^*}} (l_4^* + l_7^*) \left\{ \sqrt{l_2^*} \{l_3^*(l_2^* - l_1^*) \Xi_f - \chi_3 \Xi_e\} + (l_1^* + l_2^*)(l_3^* - l_2^*)\sqrt{l_1^* - l_3^*} \right\}, \\ P_{1133} &= \frac{l_1^* - l_7^*}{3l_7^*(l_1^* - l_2^*)(l_2^* - l_3^*)(l_1^* - l_3^*)^{3/2}(l_4^* + l_7^*)} \left\{ \sqrt{l_2^*} \chi_2 \Xi_e - \sqrt{l_2^*} l_3^*(l_2^* - l_1^*) \Xi_f - l_1^*(l_2^* - l_3^*)\sqrt{l_1^* - l_3^*} \right\}, \\ P_{2233} &= -\frac{l_6^* + l_7^*}{3l_7^*(l_1^* - l_2^*)(l_2^* - l_3^*)^2\sqrt{l_1^* - l_3^*}} \left\{ \sqrt{l_2^*} [\chi_1 \Xi_e + 2l_3^*(l_2^* - l_1^*) \Xi_f] - l_2^*(l_2^* - l_3^*)\sqrt{l_1^* - l_3^*} \right\}, \end{aligned} \quad (\text{A.21})$$

where

$$\Xi_f = F \left(\sqrt{\frac{l_1^* - l_3^*}{l_1^*}}, \sqrt{\frac{l_1^*(l_2^* - l_3^*)}{l_2^*(l_1^* - l_3^*)}} \right), \quad \Xi_e = E \left(\sqrt{\frac{l_1^* - l_3^*}{l_1^*}}, \sqrt{\frac{l_1^*(l_2^* - l_3^*)}{l_2^*(l_1^* - l_3^*)}} \right),$$

and $\chi_{1,2,3} = l_{1,2,3}^*(l_{2,1,1}^* + l_{3,3,2}^*) - 2l_{2,1,1}^*l_{3,3,2}^*$. The functions F and E denote the incomplete elliptic integrals of the first and second kinds, respectively (Abramowitz and Stegun, 1965) which are defined in (1.138). It is also remarked that the other non-zero components of the tensor \mathbf{P} do not enter the TSO expression (1.130).

Then, the components of the tensor \mathbf{E} may be computed from the corresponding components of the tensor \mathbf{P} by means of the following relations

$$\begin{aligned}
E_{1111} &= (P_{2222}P_{3333} - P_{2233}^2)\Pi - l_1^*, & E_{2222} &= (P_{1111}P_{3333} - P_{1133}^2)\Pi - l_2^* \\
E_{3333} &= (P_{1111}P_{2222} - P_{1122}^2)\Pi - l_3^*, & E_{1122} &= (P_{2233}P_{1133} - P_{1122}P_{3333})\Pi - l_4^* \\
E_{1133} &= (P_{1122}P_{2233} - P_{1133}P_{2222})\Pi - l_5^*, & E_{2233} &= (P_{1122}P_{1133} - P_{2233}P_{1111})\Pi - l_6^*, \quad (\text{A.22})
\end{aligned}$$

where

$$\Pi = (P_{1111}P_{2222}P_{3333} + 2P_{1122}P_{1133}P_{2233} - P_{1111}P_{2233}^2 - P_{2222}P_{1133}^2 - P_{3333}P_{1122}^2)^{-1}.$$

Next, it is noted that the seven independent components $l_1^*, l_2^*, \dots, l_7^*$ (defined by (A.19)) for a compressible neo-Hookean material are given by

$$l_i^* = \bar{\lambda}_i^{-2} \left[\mu^{(1)}(\bar{\lambda}_i^2 + 1) + \mu'^{(1)}\bar{J}^2 \right]; \quad i = 1, 2, 3, \quad l_i^* = \mu'^{(1)}\bar{\lambda}_i(2\bar{J} - 1); \quad i = 4, 5, 6, \quad (\text{A.23})$$

and $l_7^* = \mu^{(1)}$, where $\bar{J} = \det(\bar{\mathbf{F}}) = \bar{\lambda}_1 \bar{\lambda}_2 \bar{\lambda}_3 = 1$.

Finally, the expression for the relevant components of the tensor \mathbf{E}^I may be obtained by substituting the expressions (A.23) for the l_i^* ($i = 1..7$) into the components of the tensor \mathbf{E} (A.22) and taking the limit as $\mu^{(1)} \rightarrow \infty$. The final expressions are not included here for brevity.

Appendix B

B.1 Calculation of the tensor \mathbf{E}

In this appendix, we recap from Chapter 1 the procedure for calculating the tensor \mathbf{E} for a given stored-energy function $W_\mu^{(1)}$, macroscopic deformation gradient $\bar{\mathbf{F}}$, and shape tensor \mathbf{Z}_0 . Thus,

$$\mathbf{E} = \mathbf{Q}_0 - \mathbf{L}_\mu^{(1)}, \quad (\text{B.1})$$

where

$$\mathbf{Q}_0 = \mathbf{P}_0^\dagger (\mathcal{I} - \mathbf{P}_1 \mathbf{Q}_{-1}) + \sum_{i=1}^3 \mathbf{W}_i \otimes \mathbf{V}_i^{(1)}, \quad (\text{B.2})$$

with

$$\mathbf{Q}_{-1} = \sum_{i=1}^3 \mathbf{W}_i \otimes \mathbf{V}_i^{(0)}. \quad (\text{B.3})$$

In the above equations, $\{\mathbf{W}_1, \mathbf{W}_2, \mathbf{W}_3\}$ is a set of second-order tensor spanning the null space of \mathbf{P}_0 , while the second order tensors $\mathbf{V}_i^{(0)}$ and $\mathbf{V}_i^{(1)}$ are defined by (Avrachenkov et al., 2001)

$$\mathbf{V}_i^{(0)} = \frac{1}{\mathbf{W}_i \cdot \mathbf{P}_1 \mathbf{W}_i} \mathbf{W}_i, \quad (\text{B.4})$$

and

$$\mathbf{V}_i^{(1)} = -\frac{1}{\mathbf{W}_i \cdot \mathbf{P}_1 \mathbf{W}_i} \left\{ (\mathbf{P}_1 \mathbf{P}_0^\dagger)^T \mathbf{W}_i + \left[\mathbf{W}_i \cdot (\mathbf{P}_2 - \mathbf{P}_1 \mathbf{P}_0^\dagger \mathbf{P}_1) \mathbf{W}_i \right] \mathbf{V}_i^{(0)} \right\}, \quad (\text{B.5})$$

where $i = 1, 2, 3$ (no sum), and where the superscript T denotes the usual transpose of a fourth-order tensor (i.e., $(\cdot)_{ijkl}^T = (\cdot)_{klij}$). In addition, \mathbf{P}_0^\dagger is the Moore-Penrose generalized inverse of \mathbf{P}_0 satisfying the properties

$$\begin{aligned} \mathbf{P}_0 \mathbf{P}_0^\dagger \mathbf{P}_0 &= \mathbf{P}_0, & \mathbf{P}_0^\dagger \mathbf{P}_0 \mathbf{P}_0^\dagger &= \mathbf{P}_0^\dagger, \\ (\mathbf{P}_0 \mathbf{P}_0^\dagger)^T &= \mathbf{P}_0 \mathbf{P}_0^\dagger, & (\mathbf{P}_0^\dagger \mathbf{P}_0)^T &= \mathbf{P}_0^\dagger \mathbf{P}_0, \end{aligned} \quad (\text{B.6})$$

where the tensors \mathbf{P}_0 , \mathbf{P}_1 , and \mathbf{P}_2 are given by

$$(P_r)_{ijkl} = \frac{1}{4\pi |\mathbf{Z}_0|} \int_{|\boldsymbol{\xi}|=1} (B_r)_{ik} \xi_j \xi_l \left[\boldsymbol{\xi}^T (\mathbf{Z}_0^T \mathbf{Z}_0)^{-1} \boldsymbol{\xi} \right]^{-\frac{3}{2}} dS, \quad r = 0, 1, 2. \quad (\text{B.7})$$

Note that the tensor \mathbf{P}_0 is the limiting value of the tensor \mathbf{P} (defined in (2.18)) in the incompressible matrix limit. The second-order tensors \mathbf{B}_r , $r = 1, 2, 3$ in (B.7) can be obtained by

$$\begin{aligned} \mathbf{B}_0 &= \frac{1}{d_0} \mathbf{D}_0, \\ \mathbf{B}_1 &= \frac{1}{d_0} \left(\mathbf{D}_1 - \frac{d_1}{d_0} \mathbf{D}_0 \right), \\ \mathbf{B}_2 &= \frac{d_1}{(d_0)^3} (d_1 \mathbf{D}_0 - d_0 \mathbf{D}_1), \end{aligned} \quad (\text{B.8})$$

where d_0 and d_1 are given by

$$\begin{aligned} d_0 &= \frac{1}{6} e_{ijk} e_{pqr} [(K_\mu)_{ip} (K_\mu)_{jq} (K_{-1})_{kr} + (K_\mu)_{ip} (K_{-1})_{jq} (K_\mu)_{kr} + (K_{-1})_{ip} (K_\mu)_{jq} (K_\mu)_{kr}], \\ d_1 &= \det(\mathbf{K}_\mu) = \frac{1}{6} e_{ijk} e_{pqr} (K_\mu)_{ip} (K_\mu)_{jq} (K_\mu)_{kr}, \end{aligned} \quad (\text{B.9})$$

and the tensors \mathbf{D}_0 and \mathbf{D}_1 have components

$$\begin{aligned} (D_0)_{ik} &= e_{irs} e_{kpq} (K_\mu)_{rp} (K_{-1})_{sq}, \\ (D_1)_{ik} &= \frac{1}{2} e_{irs} e_{kpq} (K_\mu)_{rp} (K_\mu)_{sq}. \end{aligned} \quad (\text{B.10})$$

Finally, the second-order tensors \mathbf{K}_μ and \mathbf{K}_{-1} in (B.9) and (B.10) are the parts of the acoustic tensor \mathbf{K} (defined in the context of (2.18)) associated with the "incompressible" and "compressible" parts of the moduli tensor $\mathbf{L}^{(1)}$. These two parts of the tensor $\mathbf{L}^{(1)}$, denoted by $\mathbf{L}_\mu^{(1)}$ and $\mathbf{L}_{-1}^{(1)}$, respectively, defined in (2.6). Hence, the tensors \mathbf{K}_{-1} and \mathbf{K}_μ are determined by the following relations

$$(K_\mu)_{ik} = (L_\mu)_{ijkl}^{(1)} \xi_j \xi_l, \quad (K_{-1})_{ik} = (L_{-1})_{ijkl}^{(1)} \xi_j \xi_l. \quad (\text{B.11})$$

In general, a Gaussian quadrature technique can be implemented for the numerical computations of the integrals (B.7) over the surface of the unit sphere, $|\boldsymbol{\xi}| = 1$. However, it is noted that, for a given microstructure, and for certain types of matrix behaviors and loading conditions, these integrals can be calculated analytically, leading to closed-form expressions for the components of the tensor \mathbf{E} . This is the case for spheroidal particles in a neo-Hookean matrix subjected to aligned loadings. The relevant components of the tensors \mathbf{P}_r for this case are given in Appendix C.

B.2 Calculation of the tensors \mathbf{P}_r for spheroidal particles embedded in a generalized neo-Hookean matrix under non-aligned loadings

In this appendix, we briefly address the numerical calculation of the integrals (B.7) for the case of spheroidal particles embedded in an incompressible matrix of the form (2.21) subjected to non-aligned loadings (2.24) (note that $\bar{\theta}_1 = 0^\circ$). For this purpose, we make use of polar cylindrical coordinates, and parametrize the unit vector $\boldsymbol{\xi}$ in (B.7) as

$$\xi_1 = \sqrt{1-z^2} \cos(\theta), \quad \xi_2 = \sqrt{1-z^2} \sin(\theta), \quad \xi_3 = z, \quad (\text{B.12})$$

in which θ and z vary over the intervals $0 \leq \theta \leq \pi$ and $0 \leq z \leq 1$. Now, making use of (B.12), and setting $\mathbf{Z}_0 = \text{diag}(1, 1, w)$ for the spherical particles, the integrals (B.7) yield to the following double integrals

$$(P_r)_{ijkl} = \frac{w}{4\pi} \int_0^\pi \int_0^1 \frac{(B_r)_{ik}}{[1 + (w^2 - 1)z^2]^{3/2}} d\theta dz, \quad r = 0, 1, 2. \quad (\text{B.13})$$

In order to compute the above integrals, it proves helpful to provide the corresponding analytical expression for the tensors \mathbf{B}_r , $r = 1, 2, 3$, which can be determined from those of the second-order tensors \mathbf{D}_0 and \mathbf{D}_1 as well as the scalars d_0 and d_1 by using relations (B.8). For general non-aligned loadings (2.24) and general matrix behavior (2.21), the analytical expressions for \mathbf{D}_0 , \mathbf{D}_1 , d_0 and d_1 are too cumbersome to be included here, and instead, we present the expressions for the tensors \mathbf{K}_μ and \mathbf{K}_{-1} from which the corresponding expressions for \mathbf{D}_0 , \mathbf{D}_1 , d_0 and d_1 can be easily obtained with the help of relations (B.9) and (B.10). In this case, the components of the symmetric, second-order tensors \mathbf{K}_μ and \mathbf{K}_{-1} read as

$$\begin{aligned} (K_\mu)_{11} &= 2g_I + 4(V_1\xi_1 - V_3\xi_3)^2 g_{II} + (V_2\xi_1 + V_3\xi_3)^2 \bar{\lambda}_2^2 h_{JJ}, & (K_\mu)_{22} &= 2g_I + (4\bar{\lambda}_2^2 g_{II} + h_{JJ}/\bar{\lambda}_2^2)\xi_2^2, \\ (K_\mu)_{33} &= 2g_I + 2(V_3\xi_1 - V_2\xi_3)^2 g_{II} + (V_3\xi_1 + V_1\xi_3)^2 \bar{\lambda}_2^2 h_{JJ}, \\ (K_\mu)_{12} &= [4\bar{\lambda}_2(V_1\xi_1 - V_3\xi_3)g_{II} + (V_2\xi_1 + V_3\xi_3)h_{JJ}] \xi_2, \\ (K_\mu)_{23} &= [4\bar{\lambda}_2(V_2\xi_3 - V_3\xi_1)g_{II} + (V_3\xi_1 + V_1\xi_3)h_{JJ}] \xi_2, \\ (K_\mu)_{13} &= 4[(2V_3^2 + \bar{\lambda}_2^{-1})\xi_1\xi_3 - V_3(V_1\xi_1^2 + V_2\xi_3^2)]g_{II} + \bar{\lambda}_2^2 [(2V_3^2 + \bar{\lambda}_2^{-1})\xi_1\xi_3 + V_3(V_1\xi_3^2 + V_2\xi_1^2)]h_{JJ}, \end{aligned}$$

and

$$\begin{aligned} (K_{-1})_{11} &= (V_2\xi_1 + V_3\xi_3)^2 \bar{\lambda}_2^2, & (K_{-1})_{22} &= \xi_2^2/\bar{\lambda}_2^2, & (K_{-1})_{33} &= (V_3\xi_1 + V_1\xi_3)^2 \bar{\lambda}_2^2, \\ (K_{-1})_{12} &= (V_2\xi_1 + V_3\xi_3)\xi_2, & (K_{-1})_{23} &= (V_3\xi_1 + V_1\xi_3)\xi_2, \\ (K_{-1})_{13} &= [(2V_3^2 + \bar{\lambda}_2^{-1})\xi_1\xi_3 + (V_2\xi_1^2 + V_1\xi_3^2)V_3] \bar{\lambda}_2^2, \end{aligned} \tag{B.14}$$

where

$$\begin{aligned} V_1 &= \bar{\lambda}_1 \cos(\bar{\theta})^2 + (\bar{\lambda}_1\bar{\lambda}_2)^{-1} \sin(\bar{\theta})^2, & V_2 &= \bar{\lambda}_1 \sin(\bar{\theta})^2 + (\bar{\lambda}_1\bar{\lambda}_2)^{-1} \cos(\bar{\theta})^2 \\ V_3 &= [\bar{\lambda}_1 - (\bar{\lambda}_1\bar{\lambda}_2)^{-1}] \sin(\bar{\theta}) \cos(\bar{\theta}). \end{aligned}$$

For the special case of neo-Hookean matrix given by (2.23), the final expressions for d_0 , d_1 and \mathbf{D}_0 , \mathbf{D}_1 can be simplified considerably. In this case, the expressions for d_0 and d_1 are given by

$$d_0 = (\mu^{(1)})^2 (u_2\xi_1^2 + u_3\xi_1\xi_3 + u_1\xi_3^2 + t^2 \bar{\lambda}_1^4 \xi_2^2) \bar{\lambda}_2^2, \quad d_1 = \mu^{(1)} d_0 + (\mu^{(1)})^3. \tag{B.15}$$

Also, the corresponding components of the symmetric matrices \mathbf{D}_0 and \mathbf{D}_1 read as

$$\begin{aligned} (D_0)_{11} &= \mu^{(1)} \bar{\lambda}_2^2 (V_3^2 \xi_1^2 + t^2 \bar{\lambda}_1^4 \xi_2^2 + V_1^2 \xi_3^2 + 2V_1 V_3 \xi_1 \xi_3), & (D_0)_{22} &= \mu^{(1)} \bar{\lambda}_2^2 (u_2 \xi_1^2 + u_3 \xi_1 \xi_3 + u_1 \xi_3^2), \\ (D_0)_{33} &= \mu^{(1)} \bar{\lambda}_2^2 (V_2^2 \xi_1^2 + t^2 \bar{\lambda}_1^4 \xi_2^2 + V_3^2 \xi_3^2 + 2V_2 V_3 \xi_1 \xi_3), \\ (D_0)_{12} &= -\mu^{(1)} \xi_2 (V_2 \xi_1 + V_3 \xi_3), & (D_0)_{23} &= -\mu^{(1)} \xi_2 (V_3 \xi_1 + V_1 \xi_3), \\ (D_0)_{13} &= -\mu^{(1)} \bar{\lambda}_2^2 [V_2 V_3 \xi_1^2 + (2V_3^2 + \bar{\lambda}_2^{-1})\xi_1 \xi_3 + V_1 V_3 \xi_3^2], \end{aligned}$$

and

$$\begin{aligned} (D_1)_{11} &= \mu^{(1)}(D_0)_{11} + (\mu^{(1)})^2, & (D_1)_{22} &= \mu^{(1)}(D_0)_{22} + (\mu^{(1)})^2, & (D_1)_{33} &= \mu^{(1)}(D_0)_{33} + (\mu^{(1)})^2, \\ (D_1)_{12} &= \mu^{(1)}(D_0)_{12}, & (D_1)_{13} &= \mu^{(1)}(D_0)_{13}, & (D_1)_{23} &= \mu^{(1)}(D_0)_{23}, \end{aligned} \quad (\text{B.16})$$

where $t = (\bar{\lambda}_1 \bar{\lambda}_2)^{-2}$, and

$$u_1 = \bar{\lambda}_1^2 \cos^2(\bar{\theta}) + t \sin^2(\bar{\theta}), \quad u_2 = t \cos^2(\bar{\theta}) + \bar{\lambda}_1^2 \sin^2(\bar{\theta}), \quad u_3 = (\bar{\lambda}_1^2 - t) \sin(2\bar{\theta}). \quad (\text{B.17})$$

Finally, it is noted that for the special case of aligned loadings (2.34) with matrix behavior given by (2.21), we can make use of the analytical expressions for the tensors \mathbf{D}_0 and \mathbf{D}_1 and the scalars d_0 and d_1 provided in Chapter 1 for the case of spherical particles embedded in a matrix of the form (2.21) under isochoric, triaxial loadings of the form (2.34). This is because the tensors \mathbf{D}_0 and \mathbf{D}_1 and the scalars d_0 and d_1 do not contain any information about the shape of particles and depend only on the matrix behavior and loading conditions. These expressions are available in relations (1.131) and (1.132).

In general, a Gaussian quadrature technique with a rather high numbers of Gauss points is needed for the numerical integrations of (B.13). However, for the special case of a neo-Hookean matrix subjected to aligned loadings, the integrals (B.13) can be evaluated analytically, and will be given in Appendix C.

B.3 Normal components of the tensor \mathbf{P}_r , $r = 1, 2, 3$ for spheroidal particles embedded in a neo-Hookean matrix under general aligned loading

In this appendix, we present explicit expressions for the normal components of the tensor \mathbf{P}_r , $r = 1, 2, 3$, associated with a spheroidal particle embedded in a neo-Hookean material subjected to the isochoric, aligned deformation of the form (2.34). It is recalled that these analytical expressions for the components of the tensors \mathbf{P}_r , defined by (B.7), are needed to find the corresponding analytical expressions for the \mathbf{E} -tensor, using Eqs. (B.1)-(B.6). In turn, a corresponding analytical expression for the effective stored-energy function (2.35) is obtained by substituting the \mathbf{E} -tensor components. Making use of the neo-Hookean model (2.23) into equations (B.8)-(B.11), it follows that the normal

components of \mathbf{P}_r , $r = 1, 2, 3$, after some algebra, can be expressed as

$$\begin{aligned}
(P_0)_{1111} &= \bar{\lambda}_1^2 (2 \mu^{(1)} l_3^2 \omega_1^2 \omega_2 \omega_3^4)^{-1} \left\{ \omega_1^2 \omega_2 \omega_3 [w (2 \bar{\lambda}_1^2 \bar{\lambda}_2^6 - l_4) A_1 + \omega_3 (w^2 l_4 - 2 \bar{\lambda}_1^2 \bar{\lambda}_2^6)] \right. \\
&\quad \left. - 2 w \bar{\lambda}_1 \bar{\lambda}_2 \left\{ \omega_2^4 \omega_3^2 \Xi_{e1} - \omega_2^2 \left[w^2 \left(\frac{1}{2} L + 1 \right) + \bar{\lambda}_1^2 \bar{\lambda}_2^2 T_{1,0}^{\bar{2},1} \right] \Xi_{f1} + l_2^2 \omega_1^2 \Xi_{p3} \right\} \right\}, \\
(P_0)_{2222} &= \bar{\lambda}_2^2 (2 \mu^{(1)} l_3^2 \omega_2 \omega_3^4)^{-1} \left\{ \omega_2 [w \omega_3 (2 \bar{\lambda}_1^6 \bar{\lambda}_2^2 - l_4) A_1 + \omega_3^2 (w^2 l_4 - 2 \bar{\lambda}_1^6 \bar{\lambda}_2^2)] \right. \\
&\quad \left. - 2 w \bar{\lambda}_1 \bar{\lambda}_2 (\omega_1^2 \omega_3^2 \Xi_{e1} + l_1 \omega_1^2 \Xi_{f1} + l_1^2 \Xi_{p3}) \right\}, \\
(P_0)_{3333} &= (\mu^{(1)} \omega_1^2 \omega_2 \omega_3^5)^{-1} \left[\omega_1^2 \omega_2 \omega_3^2 (w A_1 - \omega_3) - w \bar{\lambda}_1^3 \bar{\lambda}_2^3 \omega_3^3 \Xi_{e1} - w \bar{\lambda}_1^3 \bar{\lambda}_2^3 \omega_3 \omega_1^2 \Xi_{p3} \right. \\
&\quad \left. - w \bar{\lambda}_1^3 \bar{\lambda}_2^3 \omega_3 (\bar{\lambda}_1^4 \bar{\lambda}_2^2 - 2 w^2 + 1) \Xi_{f1} \right], \\
(P_0)_{1122} &= -\bar{\lambda}_1 \bar{\lambda}_2 (2 \mu^{(1)} l_3^2 \omega_2 \omega_3^4)^{-1} \left\{ \omega_2 \omega_3 [w (2 \bar{\lambda}_2^4 \bar{\lambda}_1^4 - l_4) A_1 + \omega_3 (w^2 l_4 - 2 \bar{\lambda}_2^4 \bar{\lambda}_1^4)] \right. \\
&\quad \left. - 2 w \bar{\lambda}_1 \bar{\lambda}_2 (\omega_2^2 \omega_3^2 \Xi_{e1} + l_2 \omega_1^2 \Xi_{f1} + l_1 l_2 \Xi_{p3}) \right\}, \\
(P_0)_{1133} &= \bar{\lambda}_1^2 \bar{\lambda}_2^2 (\mu^{(1)} l_3 \omega_1^2 \omega_2 \omega_3^5)^{-1} \left\{ w \bar{\lambda}_1 \omega_3 [(\bar{\lambda}_2^4 \bar{\lambda}_1^2 - \omega_2^2 - 1) w^2 + \omega_2^2 - \bar{\lambda}_1^6 \bar{\lambda}_2^6 + \bar{\lambda}_1^4 \bar{\lambda}_2^2] \Xi_{f1} \right. \\
&\quad \left. + w \omega_2^2 \bar{\lambda}_1 \omega_3^3 \Xi_{e1} - w \bar{\lambda}_1 \omega_3 l_2 \omega_1^2 \Xi_{p3} + \bar{\lambda}_2 \omega_1^2 \omega_2 \omega_3^2 (w A_1 - \omega_3) \right\}, \\
(P_0)_{2233} &= -\bar{\lambda}_1^2 \bar{\lambda}_2^2 (\mu^{(1)} l_3 \omega_2 \omega_3^5)^{-1} \left[\bar{\lambda}_1 \omega_2 \omega_3^2 (w A_1 - \omega_3) + w \bar{\lambda}_2 \omega_3 (\omega_3^2 \Xi_{e1} - \omega_1^2 \Xi_{f1} - l_1 \Xi_{p3}) \right], \\
\\
(P_1)_{1111} &= \bar{\lambda}_1^2 \bar{\lambda}_2 (2 \mu^{(1)} l_3^2 \omega_1^4 \omega_2)^{-1} \left[w \bar{\lambda}_1 \omega_2^2 (w^2 T_{\bar{3}}^1 + \bar{\lambda}_1^4 \bar{\lambda}_2^2 l_4) \Xi_{e1} - w \bar{\lambda}_1^3 \bar{\lambda}_2^2 l_3 (w^2 T_{\bar{3}}^2 + \bar{\lambda}_1^4 \bar{\lambda}_2^4) \Xi_{f1} \right. \\
&\quad \left. + \bar{\lambda}_2^3 \omega_1^2 \omega_2 (2 w^2 - \bar{\lambda}_1^4 l_4) \right], \\
(P_1)_{2222} &= \bar{\lambda}_1 \bar{\lambda}_2^2 (2 \mu^{(1)} l_3^2 \omega_2^3)^{-1} \left[w \bar{\lambda}_1^2 \bar{\lambda}_2^5 l_3 \Xi_{f1} - w \bar{\lambda}_2 (w^2 T_{\bar{1}}^3 - \bar{\lambda}_1^2 \bar{\lambda}_2^4 l_4) \Xi_{e1} + \bar{\lambda}_1^3 \omega_2 (2 w^2 - \bar{\lambda}_2^4 l_4) \right], \\
(P_1)_{3333} &= \bar{\lambda}_1 \bar{\lambda}_2 (2 \mu^{(1)} \omega_1^3 \omega_2^4)^{-1} \left[w (w^4 + w^2 \bar{\lambda}_1^2 \bar{\lambda}_2^2 l_4 - 3 \bar{\lambda}_1^6 \bar{\lambda}_2^6) \Xi_{e2} - w \bar{\lambda}_1^2 \bar{\lambda}_2^2 (w^2 T_{\bar{2}}^1 - 3 \bar{\lambda}_2^4 \bar{\lambda}_1^4) \Xi_{f2} \right. \\
&\quad \left. - \bar{\lambda}_1^3 \bar{\lambda}_2^3 \omega_1 \omega_2^2 \right], \\
(P_1)_{1122} &= \bar{\lambda}_1^2 \bar{\lambda}_2^2 (2 \mu^{(1)} l_3^2 \omega_1^2 \omega_2)^{-1} \left[w (w^2 l_4 - 2 \bar{\lambda}_1^4 \bar{\lambda}_2^4) \Xi_{e1} - w \bar{\lambda}_1^4 \bar{\lambda}_2^2 l_3 \Xi_{f1} - 2 \bar{\lambda}_1 \bar{\lambda}_2 \omega_2 \omega_1^2 \right], \\
(P_1)_{1133} &= \bar{\lambda}_1^3 \bar{\lambda}_2^2 (2 \mu^{(1)} l_3 \omega_1^4 \omega_2)^{-1} \left[\bar{\lambda}_1 \bar{\lambda}_2 \omega_2 \omega_1^2 - w (w^2 T_{\bar{1}}^2 - \bar{\lambda}_1^4 \bar{\lambda}_2^4) \Xi_{e1} + w l_3 (\bar{\lambda}_1^4 \bar{\lambda}_2^2 + w^2) \Xi_{f1} \right], \\
(P_1)_{2233} &= -\bar{\lambda}_1^2 \bar{\lambda}_2^3 (2 \mu^{(1)} l_3 \omega_1 \omega_2^4)^{-1} \left[\bar{\lambda}_1 \bar{\lambda}_2 \omega_1 \omega_2^2 + w (w^2 T_{\bar{2}}^1 + \bar{\lambda}_1^4 \bar{\lambda}_2^4) \Xi_{e2} - w l_3 (\bar{\lambda}_2^4 \bar{\lambda}_1^2 + w^2) \Xi_{f2} \right],
\end{aligned}$$

$$\begin{aligned}
(P_2)_{1111} &= -\bar{\lambda}_1^2 \bar{\lambda}_2 (8\mu^{(1)} l_3^2 \omega_1^6 \omega_2)^{-1} \left\{ w \bar{\lambda}_1 \left[\left(Y_{3,0}^{\bar{3},\bar{6}} + T_{12}^4 \right) w^6 + \left(Y_{3,12}^{\bar{7},12} + P_{0,0}^{\bar{7},9} + 12 \bar{\lambda}_1^2 \bar{\lambda}_2^6 \right) w^4 \right. \right. \\
&\quad - w^2 \bar{\lambda}_1^4 \bar{\lambda}_2^2 \left(Y_{6,4}^{\bar{1},\bar{3}} + P_{0,9}^{\bar{2},\bar{3}} + L_{16}^4 \right) + \bar{\lambda}_1^8 \bar{\lambda}_2^6 \left(4L_0^2 + T_{1,4}^{\bar{1},0} \right) \left. \right] \Xi_{e1} - w \bar{\lambda}_1 l_3 \left[\left(\frac{8}{12} L_0^9 + T_{3,9}^{\bar{3},0} \right) w^4 \right. \\
&\quad - \bar{\lambda}_1^4 \bar{\lambda}_2^2 \left(\frac{8}{16} L_0^1 + T_6^5 \right) w^2 + \bar{\lambda}_1^8 \bar{\lambda}_2^6 R_{1,0}^{\bar{4},1} \left. \right] \Xi_{f1} + \bar{\lambda}_2 \omega_1^2 \omega_2 \left[8 w^4 \bar{\lambda}_2^2 - \bar{\lambda}_1^2 \left(4L_0^6 + T_{5,8}^{\bar{3},0} \right) w^2 \right. \\
&\quad \left. \left. + \bar{\lambda}_1^6 \bar{\lambda}_2^2 \left(4L_0^2 + T_{1,4}^{\bar{1},0} \right) \right] \right\}, \\
(P_2)_{2222} &= -\bar{\lambda}_1 \bar{\lambda}_2^2 (8\mu^{(1)} l_3^2 \omega_1^2 \omega_2^5)^{-1} \left\{ \bar{\lambda}_1 \omega_1^2 \omega_2 \left[8 w^4 \bar{\lambda}_1^2 + \bar{\lambda}_2^2 \left(T_{3,8}^{\bar{5},0} + \frac{12}{4} L_6^0 \right) w^2 + \bar{\lambda}_1^2 \bar{\lambda}_2^2 \left(T_{1,4}^{\bar{1},0} + 4L_2^0 \right) \right] \right. \\
&\quad + w \bar{\lambda}_2 \left[\left(T_{4}^{\bar{1},2} + Y_{3,0}^{\bar{3},\bar{6}} \right) w^6 + \left(P_{7,9}^{\bar{0},0} + Y_{7,12}^{\bar{3},12} + 12 \bar{\lambda}_1^6 \bar{\lambda}_2^2 \right) w^4 + \bar{\lambda}_2^4 \bar{\lambda}_1^2 \left(P_{2,3}^{\bar{0},9} + Y_{1,4}^{\bar{6},3} + L_{14}^{\bar{1},6} \right) w^2 \right. \\
&\quad + \bar{\lambda}_2^8 \bar{\lambda}_1^6 \left(4L_2^0 + T_{1,4}^{\bar{1},0} \right) \left. \right] \Xi_{e1} - w \bar{\lambda}_2 l_3 \left[\left(\frac{0}{4} L_6^3 + T_{3,3}^{\bar{3},0} \right) w^4 + \bar{\lambda}_1^2 \bar{\lambda}_2^6 \left(3L - Y_{0,0}^{\bar{4},4} - 6 \bar{\lambda}_1^6 + 1 \right) w^2 \right. \\
&\quad \left. - \bar{\lambda}_1^6 \bar{\lambda}_2^8 R_{1,2}^{\bar{4},\bar{3}} \right] \Xi_{f1} \left. \right\}, \\
(P_2)_{3333} &= (8\mu^{(1)} \bar{\lambda}_1 \bar{\lambda}_2 \omega_1^5 \omega_2^6)^{-1} \left\{ \bar{\lambda}_1^3 \bar{\lambda}_2^3 \omega_1 \omega_2^2 \left[w^4 R_{1,4}^{\bar{4},4} - \bar{\lambda}_1^2 \bar{\lambda}_2^2 \left(4L + T_{3,8}^{\bar{3},0} \right) w^2 + \bar{\lambda}_1^6 \bar{\lambda}_2^6 R_7^{\bar{4}} \right] \right. \\
&\quad - w \left[w^8 R_{2,1}^{\bar{4},1} + \bar{\lambda}_1^2 \bar{\lambda}_2^2 \left(T_{7,3}^{\bar{7},0} + L_7^7 \right) w^6 - \bar{\lambda}_1^4 \bar{\lambda}_2^4 \left(Y_{3,16}^{\bar{3},\bar{13}} + P_{0,20}^{\bar{0},20} + L_4^4 \right) w^4 + \bar{\lambda}_1^8 \bar{\lambda}_2^8 \left(T_{10,21}^{\bar{10},0} + \frac{16}{16} L \right) w^2 \right. \\
&\quad - 3 \bar{\lambda}_1^{12} \bar{\lambda}_2^{12} R_5^{\bar{4}} \left. \right] \Xi_{e2} + w \bar{\lambda}_1^2 \bar{\lambda}_2^2 \left[\left(T_{1,3}^{\bar{1},0} + 4L_5^4 \right) w^6 - \bar{\lambda}_1^2 \bar{\lambda}_2^2 \left(Y_{9,24}^{\bar{3},3} + P_{3,13}^{\bar{0},11} + L_8^4 \right) w^4 \right. \\
&\quad \left. + 2 \bar{\lambda}_1^6 \bar{\lambda}_2^6 \left(T_{10,6}^{\bar{5},0} + \frac{8}{10} L_3^0 \right) w^2 + 3 \bar{\lambda}_1^{10} \bar{\lambda}_2^{10} R_{5,1}^{\bar{4},0} \right] \Xi_{f2} \left. \right\}, \\
(P_2)_{1122} &= \bar{\lambda}_1^2 \bar{\lambda}_2^2 (8\mu^{(1)} l_3^2 \omega_1^2 \omega_2^4)^{-1} \left\{ \bar{\lambda}_1 \bar{\lambda}_2 \omega_2^2 \left[8 w^4 + \left(\frac{8}{8} L_1^1 - T_1^1 \right) w^2 - \bar{\lambda}_1^4 \bar{\lambda}_2^4 R_{2,1}^{\bar{8},1} \right] \omega_1 \right. \\
&\quad - w \left[\left(Y_{1,0}^{\bar{1},\bar{2}} + T_4^4 \right) w^6 + \left(P_{1,0}^{\bar{1},0} + Y_{2,16}^{\bar{2},2} - L_4^4 \right) w^4 - 2 \bar{\lambda}_1^4 \bar{\lambda}_2^4 \left(\frac{6}{6} L_1^1 - l_4 \right) w^2 + \bar{\lambda}_1^8 \bar{\lambda}_2^8 R_{2,1}^{\bar{8},1} \right] \Xi_{e2} \\
&\quad \left. + w l_3 \left[\left(\frac{0}{4} L_2^1 + T_{0,1}^{\bar{1},1} \right) w^4 - \bar{\lambda}_2^6 \bar{\lambda}_1^2 \left(2 \bar{\lambda}_1^6 - 4 \bar{\lambda}_1^4 - R_{1,0}^{\bar{4},1} \right) w^2 - \bar{\lambda}_2^8 \bar{\lambda}_1^6 R_{1,0}^{\bar{4},\bar{1}} \right] \Xi_{f2} \right\}, \\
(P_2)_{1133} &= -\bar{\lambda}_1 \left(8\mu^{(1)} l_3 \omega_1^6 \omega_2^3 \right)^{-1} \left\{ \bar{\lambda}_1^3 \bar{\lambda}_2^3 \omega_1^2 \omega_2 \left[\left(T_1^3 + 4 \right) w^4 + \left(T_{1,2}^{\bar{4},0} - 4L_0^{\bar{1}} \right) w^2 + \bar{\lambda}_1^4 \bar{\lambda}_2^4 R_{3,0}^{\bar{4},\bar{1}} \right] \right. \\
&\quad - w \left[\left(\frac{8}{4} L_2^7 + T_{1,3}^{\bar{1},0} \right) w^6 + \bar{\lambda}_1^2 \bar{\lambda}_2^2 \left(P_{0,7}^{\bar{1},\bar{11}} + Y_{1,8}^{\bar{7},3} + L_4^{\bar{8}} \right) w^4 - 2 \bar{\lambda}_1^6 \bar{\lambda}_2^6 \left(\frac{6}{0} L_0^1 - T_{3,1}^{\bar{6},0} \right) w^2 - \bar{\lambda}_1^{10} \bar{\lambda}_2^{10} R_{3,0}^{\bar{4},\bar{1}} \right] \Xi_{e1} \\
&\quad \left. + w \bar{\lambda}_1^2 \bar{\lambda}_2^2 l_3 \left[\left(T_1^3 + 4 \right) w^6 + \left(\frac{0}{4} L_0^5 - T_{1,4}^{\bar{5},0} \right) w^4 - \bar{\lambda}_1^4 \bar{\lambda}_2^2 \left(4 \bar{\lambda}_1^4 \bar{\lambda}_2^2 + T_{6,5}^{\bar{3},0} \right) w^2 + \bar{\lambda}_1^8 \bar{\lambda}_2^6 R_{3,0}^{\bar{4},0} \right] \Xi_{f1} \right\}, \\
(P_2)_{2233} &= -\bar{\lambda}_2 \left(8\mu^{(1)} l_3 \omega_1^4 \omega_2^5 \right)^{-1} \left\{ \bar{\lambda}_1^3 \bar{\lambda}_2^3 \omega_1^2 \left[\left(T_3^1 - 4 \right) w^4 + \left(T_{4,2}^{\bar{1},0} + 4L_1^0 \right) w^2 - \bar{\lambda}_1^4 \bar{\lambda}_2^4 R_{3,\bar{1}}^{\bar{4},0} \right] \omega_2 \right. \\
&\quad - w \left[\left(\frac{4}{8} L_7^2 + T_{1,3}^{\bar{1},0} \right) w^6 - \bar{\lambda}_1^2 \bar{\lambda}_2^2 \left(P_{1,11}^{\bar{0},7} + Y_{7,8}^{\bar{1},3} + L_8^{\bar{4}} \right) w^4 - 2 \bar{\lambda}_1^6 \bar{\lambda}_2^6 \left(\frac{0}{6} L_1^0 + T_{6,1}^{\bar{3},0} \right) w^2 + \bar{\lambda}_1^{10} \bar{\lambda}_2^{10} R_{3,\bar{1}}^{\bar{4},0} \right] \Xi_{e1} \\
&\quad \left. + w \bar{\lambda}_1^2 \bar{\lambda}_2^2 l_3 \left[\left(T_3^1 + 4 \right) w^6 + \left(\frac{4}{4} L_1^1 - T_{4,3}^{\bar{2},0} \right) w^4 + 2 w^2 \bar{\lambda}_1^4 \bar{\lambda}_2^4 R_{3,\bar{1}}^{\bar{2},\bar{1}} + \bar{\lambda}_1^{10} \bar{\lambda}_2^{10} \right] \Xi_{f1} \right\},
\end{aligned}$$

where

$$\begin{aligned}
l_1 &= \bar{\lambda}_1^4 \bar{\lambda}_2^2 - 1, & l_2 &= \bar{\lambda}_1^2 \bar{\lambda}_2^4 - 1, & l_{3,4} &= \bar{\lambda}_1^2 \mp \bar{\lambda}_2^2, \\
\omega_1 &= \sqrt{w^2 - \bar{\lambda}_1^4 \bar{\lambda}_2^2}, & \omega_2 &= \sqrt{w^2 - \bar{\lambda}_1^2 \bar{\lambda}_2^4}, & \omega_3 &= \sqrt{w^2 - 1},
\end{aligned}$$

and the symbols

$$\begin{aligned}
{}^a\mathbf{L}_d^c &= a\bar{\lambda}_1^4\bar{\lambda}_2^2 + b\bar{\lambda}_1^2\bar{\lambda}_2^4 + c\bar{\lambda}_1^6\bar{\lambda}_2^2 + d\bar{\lambda}_1^2\bar{\lambda}_2^6, & \mathbf{P}_{b,d}^{a,c} &= a\bar{\lambda}_1^8\bar{\lambda}_2^2 + b\bar{\lambda}_1^2\bar{\lambda}_2^8 + c\bar{\lambda}_1^6\bar{\lambda}_2^4 + d\bar{\lambda}_1^4\bar{\lambda}_2^6, \\
\mathbf{R}_{b,d}^{a,c} &= c\bar{\lambda}_1^4\bar{\lambda}_2^2 + d\bar{\lambda}_1^2\bar{\lambda}_2^4 + a\bar{\lambda}_1^2\bar{\lambda}_2^2 + b, & \mathbf{T}_{b,d}^{a,c} &= a\bar{\lambda}_1^2 + b\bar{\lambda}_2^2 + c\bar{\lambda}_1^2\bar{\lambda}_2^2 + d\bar{\lambda}_1^4\bar{\lambda}_2^4, \\
\mathbf{Y}_{b,d}^{a,c} &= a\bar{\lambda}_1^4 + b\bar{\lambda}_2^4 + c\bar{\lambda}_1^2\bar{\lambda}_2^2 + d\bar{\lambda}_1^4\bar{\lambda}_2^4, & \mathbf{L}_d^c &= {}_0^0\mathbf{L}_d^c, \quad {}^a\mathbf{L}_b = {}_b^a\mathbf{L}_0^0, \quad \mathbf{T}_b^a = \mathbf{T}_{b,0}^{a,0},
\end{aligned}$$

are introduced for brevity, with barred subscript/superscript indicating negative coefficients. Moreover, $\Xi_{f1,2}$, $\Xi_{e1,2}$, Ξ_{p3} are given in terms of the incomplete elliptic integrals of the first, second and third kind (Abramowitz and Stegun, 1965), respectively, via

$$\begin{aligned}
\Xi_{f1} &= F\left(\frac{\omega_2}{w}, \omega_4\right), & \Xi_{f2} &= F\left(\frac{\omega_1}{w}, \omega_5\right), \\
\Xi_{e1} &= E\left(\frac{\omega_2}{w}, \omega_4\right), & \Xi_{e2} &= E\left(\frac{\omega_1}{w}, \omega_5\right), & \Xi_{p3} &= P\left(\frac{\omega_2}{w}, \frac{\omega_3^2}{\omega_2^2}, \omega_4\right),
\end{aligned}$$

where $\omega_{4,5} = \sqrt{\omega_{1,2}^2/\omega_{2,1}^2}$, the functions F and P are defined in (2.44), and the function E is defined by

$$E(a, b) = \int_0^a \frac{\sqrt{1-b^2t^2}}{\sqrt{1-t^2}} dt. \quad (\text{B.18})$$

It is important to note that the components of the \mathbf{P}_r tensors, given in this appendix, are valid for both prolate ($w > 1$) and oblate ($w < 1$) shapes of particles, and for all positive stretches $\bar{\lambda}_1$, and $\bar{\lambda}_2$. However, for the axisymmetric case with the condition $\bar{\lambda}_1 = \bar{\lambda}_2$ suitable limits must be taken. The final results for this case (in terms of the components of the \mathbf{E} tensor) are given in Subsection 2.4.2. Finally, it should be pointed out that the remaining non-zero components of the tensors \mathbf{P}_r , such as $(P_r)_{1313}$ and $(P_r)_{1113}$, have not been provided here since they do not enter the process for calculating the appropriate components of the tensor \mathbf{E} , required for determining the effective stored-energy function (2.35).

B.4 On the modulus tensor \mathbf{L}^c for the incompressible composites with the effective stored-energy function $\widehat{\Phi}(\bar{\lambda}_1, \bar{\lambda}_2, \bar{\theta}_2, \bar{\theta}_1)$ subjected to non-aligned loadings

In this appendix, we spell out the explicit expressions for the all traces of the effective incremental moduli tensor \mathbf{L}^c which appear in the condition (2.47). Note that in the incompressibility limit of the composite, these (3-D) moduli traces remain finite while some components of the tensor $\widehat{\mathbf{L}}^c$ tend to infinity. Also, these traces, associated with the loading condition (2.24) (recall that $\bar{\theta}_1 = 0^\circ$), can be given in terms of kinematical variables $\bar{\lambda}_1$, $\bar{\lambda}_2$, $\bar{\theta} (= \bar{\theta}_2)$, as well as the derivatives of the effective potential $\widehat{\Phi}(\bar{\lambda}_1, \bar{\lambda}_2, \bar{\theta}_1, \bar{\theta}_2)$, with respect to its arguments, calculated at $\bar{\theta}_1 = 0^\circ$. Moreover, the explicit expressions for the corresponding moduli can be provided in a simpler and shorter form if they are given in a coordinate basis $\{\mathbf{e}'_i\}$ which is aligned with the loading axes (see Fig 3.3.2(a)). In this case, the components of the moduli tensor $\widehat{\mathbf{L}}^c$ in the basis $\{\mathbf{e}'_i\}$ and $\{\mathbf{e}_i\}$ can be related to

each other through the following transformation rule

$$\widehat{L}'_{ijkl}(\bar{\mathbf{F}}) = \bar{Q}_{mi}\bar{Q}_{nj}\bar{Q}_{pk}\bar{Q}_{ql}\widehat{L}'_{mnpq}(\bar{\mathbf{F}}), \quad (\text{B.19})$$

where $\bar{\mathbf{Q}} = \cos(\bar{\theta}) (\mathbf{e}_1 \otimes \mathbf{e}_1 + \mathbf{e}_3 \otimes \mathbf{e}_3) + \sin(\bar{\theta}) (\mathbf{e}_1 \otimes \mathbf{e}_3 - \mathbf{e}_3 \otimes \mathbf{e}_1) + \mathbf{e}_2 \otimes \mathbf{e}_2$, and the primed components denote those relative to the basis $\{\mathbf{e}'_i\}$. Making use of this transformation, the aforementioned traces of $\widehat{\mathbf{L}}^c$ in the basis $\{\mathbf{e}'_i\}$ read as

$$\begin{aligned} \widehat{L}'_{1^*} &= \frac{\bar{\lambda}_1^2 \bar{\lambda}_2 \left[(\bar{\lambda}_1^4 \bar{\lambda}_2^2 + 3) \widehat{\Phi}_{,\bar{\theta}_2} - \bar{\lambda}_1 l_1 \widehat{\Phi}_{,\bar{\lambda}_1 \bar{\theta}_2} \right]}{l_1^2} \\ \widehat{L}'_{2^*} &= \frac{\bar{\lambda}_1^2 \bar{\lambda}_2 \left[(3 \bar{\lambda}_1^4 \bar{\lambda}_2^2 + 1) \widehat{\Phi}_{,\bar{\theta}_2} - \bar{\lambda}_1 l_1 \widehat{\Phi}_{,\bar{\lambda}_1 \bar{\theta}_2} \right]}{l_1^2} \\ \widehat{L}'_{3^*} &= \frac{\bar{\lambda}_1 \left(\bar{\lambda}_1 l_1^2 \widehat{\Phi}_{,\bar{\lambda}_1 \bar{\lambda}_1} - 2 l_1 \widehat{\Phi}_{,\bar{\lambda}_1} - 2 \bar{\lambda}_1^3 \bar{\lambda}_2^2 \widehat{\Phi}_{,\bar{\theta}_2 \bar{\theta}_2} \right)}{l_1^2} \\ \widehat{L}'_{1313} &= \frac{\bar{\lambda}_1 \left(\bar{\lambda}_1^3 \bar{\lambda}_2^2 \widehat{\Phi}_{,\bar{\theta}_2 \bar{\theta}_2} + l_1 \widehat{\Phi}_{,\bar{\lambda}_1} \right)}{l_1^2} & \widehat{L}'_{3131} &= \frac{\bar{\lambda}_1^4 \bar{\lambda}_2^2 \left(\widehat{\Phi}_{,\bar{\theta}_2 \bar{\theta}_2} + \bar{\lambda}_1 l_1 \widehat{\Phi}_{,\bar{\lambda}_1} \right)}{l_1^2} \end{aligned} \quad (\text{B.20})$$

$$\begin{aligned} \widehat{L}'_{3232} &= \frac{\bar{\lambda}_1^2 \bar{\lambda}_2^4 \left(\cos^2(\bar{\theta}) \widehat{\Phi}_{,\bar{\theta}_1 \bar{\theta}_1} + \bar{\lambda}_2 l_2 \widehat{\Phi}_{,\bar{\lambda}_2} + \sin(\bar{\theta}) \cos(\bar{\theta}) \widehat{\Phi}_{,\bar{\theta}_2} \right)}{l_2^2} \\ \widehat{L}'_{2323} &= \frac{\bar{\lambda}_2 \left(\bar{\lambda}_1^2 \bar{\lambda}_2^3 \cos^2(\bar{\theta}) \widehat{\Phi}_{,\bar{\theta}_1 \bar{\theta}_1} + l_2 \widehat{\Phi}_{,\bar{\lambda}_2} + \bar{\lambda}_1^2 \bar{\lambda}_2^3 \sin(\bar{\theta}) \cos(\bar{\theta}) \widehat{\Phi}_{,\bar{\theta}_2} \right)}{l_2^2} \\ \widehat{L}'_{2121} &= - \frac{\bar{\lambda}_1^2 \left[l_3 \left(\bar{\lambda}_2 \widehat{\Phi}_{,\bar{\lambda}_2} - \bar{\lambda}_1 \widehat{\Phi}_{,\bar{\lambda}_1} \right) + \bar{\lambda}_2^2 \sin(\bar{\theta}) \cos(\bar{\theta}) \widehat{\Phi}_{,\bar{\theta}_2} - \bar{\lambda}_2^2 \sin^2(\bar{\theta}) \widehat{\Phi}_{,\bar{\theta}_1 \bar{\theta}_1} \right]}{l_3^2} \\ \widehat{L}'_{1212} &= - \frac{\bar{\lambda}_2^2 \left[l_3 \left(\bar{\lambda}_2 \widehat{\Phi}_{,\bar{\lambda}_2} - \bar{\lambda}_1 \widehat{\Phi}_{,\bar{\lambda}_1} \right) + \bar{\lambda}_1^2 \sin(\bar{\theta}) \cos(\bar{\theta}) \widehat{\Phi}_{,\bar{\theta}_2} - \bar{\lambda}_1^2 \sin^2(\bar{\theta}) \widehat{\Phi}_{,\bar{\theta}_1 \bar{\theta}_1} \right]}{l_3^2} \end{aligned} \quad (\text{B.21})$$

$$\begin{aligned} \widehat{L}'_{4^*} &= \frac{\left(\bar{\lambda}_2 l_2^2 \widehat{\Phi}_{,\lambda_2 \lambda_2} - 2 l_2 \widehat{\Phi}_{,\bar{\lambda}_2} - 2 \bar{\lambda}_1^2 \bar{\lambda}_2^3 \sin(\bar{\theta}) \cos(\bar{\theta}) \widehat{\Phi}_{,\bar{\theta}_2} - 2 \bar{\lambda}_1^2 \bar{\lambda}_2^3 \cos^2(\bar{\theta}) \widehat{\Phi}_{,\bar{\theta}_1 \bar{\theta}_1} \right) \bar{\lambda}_2}{l_2^2} \\ \widehat{L}'_{5^*} &= -(l_1^2 l_2^2 l_3^2)^{-1} \left\{ \bar{\lambda}_1^2 \bar{\lambda}_2^2 \left(\bar{\lambda}_1^4 \bar{\lambda}_2^8 + \bar{\lambda}_1^4 \bar{\lambda}_2^2 - 4 \bar{\lambda}_1^2 \bar{\lambda}_2^4 + \bar{\lambda}_2^6 + 1 \right) l_1^2 \sin(\bar{\theta}) \cos(\bar{\theta}) \widehat{\Phi}_{,\bar{\theta}_2} \right. \\ &\quad + \bar{\lambda}_1^2 \bar{\lambda}_2^2 l_1^2 \left[(\bar{\lambda}_1^4 \bar{\lambda}_2^8 + \bar{\lambda}_1^4 \bar{\lambda}_2^2 - 4 \bar{\lambda}_1^2 \bar{\lambda}_2^4 + \bar{\lambda}_2^6 + 1) \cos^2(\bar{\theta}) - l_2^2 \right] \widehat{\Phi}_{,\bar{\theta}_1 \bar{\theta}_1} \\ &\quad \left. - \bar{\lambda}_1 \bar{\lambda}_2 l_1^2 l_2^2 l_3^2 \widehat{\Phi}_{,\bar{\lambda}_1 \bar{\lambda}_2} + \bar{\lambda}_1^4 \bar{\lambda}_2^2 l_2^2 l_3^2 \widehat{\Phi}_{,\bar{\theta} \bar{\theta}} - \bar{\lambda}_1^3 l_1 l_2^3 l_3 \widehat{\Phi}_{,\bar{\lambda}_1} + \bar{\lambda}_2^3 l_1^3 l_2^2 l_3 \widehat{\Phi}_{,\bar{\lambda}_2} \right\} \end{aligned} \quad (\text{B.22})$$

$$\begin{aligned}
\widehat{L}'_{2312} &= \widehat{L}'_{3212} = \widehat{L}'_{3221} = - \frac{\left[(l_1 \cos^2(\bar{\theta}) - \bar{\lambda}_1^2 \bar{\lambda}_2^2 l_3) \widehat{\Phi}_{,\bar{\theta}_2} - \sin(\bar{\theta}) \cos(\bar{\theta}) l_1 \widehat{\Phi}_{,\bar{\theta}_1 \bar{\theta}_1} \right] \bar{\lambda}_1^2 \bar{\lambda}_2^3}{l_1^2 l_2^2 l_3} \\
\widehat{L}'_{2321} &= - \frac{\left[(\bar{\lambda}_2^2 l_1 \cos^2(\bar{\theta}) - \bar{\lambda}_1^2 + \bar{\lambda}_2^2) \widehat{\Phi}_{,\bar{\theta}_2} - \sin(\bar{\theta}) \cos(\bar{\theta}) \bar{\lambda}_2^2 l_1 \widehat{\Phi}_{,\bar{\theta}_1 \bar{\theta}_1} \right] \bar{\lambda}_1^2 \bar{\lambda}_2}{l_3 l_2^2 l_1^2}
\end{aligned} \tag{B.23}$$

$$\begin{aligned}
\widehat{L}'_6 &= -(l_1^2 l_2 l_3)^{-1} \bar{\lambda}_1^2 \bar{\lambda}_2 \\
&\times \left\{ \left[\bar{\lambda}_2^2 l_1^2 \cos^2(\bar{\theta}) - l_3 (2 \bar{\lambda}_1^6 \bar{\lambda}_2^6 - l_1) \right] \widehat{\Phi}_{,\bar{\theta}_2} + \bar{\lambda}_2 l_1 l_2 l_3 \widehat{\Phi}_{,\lambda_2 \theta} - \bar{\lambda}_2^2 l_1^2 \sin(\bar{\theta}) \cos(\bar{\theta}) \widehat{\Phi}_{,\bar{\theta}_1 \bar{\theta}_1} \right\} \\
\widehat{L}'_7 &= -(l_3 l_2 l_1^2)^{-1} \bar{\lambda}_1^2 \bar{\lambda}_2 \\
&\times \left\{ \left[\bar{\lambda}_2^2 l_1^2 \cos^2(\bar{\theta}) - l_3 (\bar{\lambda}_1^6 \bar{\lambda}_2^6 + \bar{\lambda}_1^2 \bar{\lambda}_2^4 - 2) \right] \widehat{\Phi}_{,\bar{\theta}_2} + \bar{\lambda}_2 l_1 l_2 l_3 \widehat{\Phi}_{,\bar{\lambda}_2 \bar{\theta}} - \bar{\lambda}_2^2 l_1^2 \sin(\bar{\theta}) \cos(\bar{\theta}) \widehat{\Phi}_{,\bar{\theta}_1 \bar{\theta}_1} \right\} \\
\widehat{L}'_8 &= -(l_3 l_2 l_1^2)^{-1} \bar{\lambda}_1^2 \bar{\lambda}_2 \\
&\times \left\{ \left[\bar{\lambda}_2^2 l_1^2 \cos^2(\bar{\theta}) - l_3 (5 \bar{\lambda}_1^6 \bar{\lambda}_2^6 - 4 \bar{\lambda}_1^4 \bar{\lambda}_2^2 + \bar{\lambda}_1^2 \bar{\lambda}_2^4 - 2) \right] \widehat{\Phi}_{,\bar{\theta}_2} + l_1 l_2 l_3 \left(\bar{\lambda}_1 \widehat{\Phi}_{,\lambda_1 \bar{\theta}} + \bar{\lambda}_2 \widehat{\Phi}_{,\bar{\lambda}_2 \bar{\theta}} \right) \right. \\
&\quad \left. - \bar{\lambda}_2^2 l_1^2 \sin(\bar{\theta}) \cos(\bar{\theta}) \widehat{\Phi}_{,\bar{\theta}_1 \bar{\theta}_1} \right\}
\end{aligned} \tag{B.24}$$

Note that for axisymmetric shear loadings with the condition $\bar{\lambda}_1 = \bar{\lambda}_2 = \bar{\lambda}$, suitable limits must be taken for the traces involving the terms $(\bar{\lambda}_1 - \bar{\lambda}_2)$ in the denominator. Taking these limits for the pertinent traces appearing in the strong ellipticity condition (2.56) yields

$$\begin{aligned}
\widehat{L}'_{2121} &= \frac{1}{8} \bar{\lambda} \left[\bar{\lambda} \sin^2(\bar{\theta}) \widehat{\Phi}_{,\bar{\lambda}_1 \bar{\lambda}_1 \bar{\theta}_1 \bar{\theta}_1} + 6 \bar{\lambda} \widehat{\Phi}_{,\bar{\lambda}_1 \bar{\lambda}_1} + 2 \bar{\lambda} \widehat{\Phi}_{,\bar{\lambda}_2 \bar{\lambda}_2} - 2 \bar{\lambda} \widehat{\Phi}_{,\bar{\lambda} \bar{\lambda}}^{AS} + 8 \widehat{\Phi}_{,\bar{\lambda}_1} \right. \\
&\quad \left. - 2 \widehat{\Phi}_{,\bar{\lambda}}^{AS} - \bar{\lambda} \sin(\bar{\theta}) \cos(\bar{\theta}) \widehat{\Phi}_{,\bar{\lambda}_1 \bar{\lambda}_1 \bar{\theta}} \right] \Big|_{\bar{\lambda}_1 = \bar{\lambda}_2 = \bar{\lambda}} \\
\widehat{L}'_{2321} &= -\frac{1}{2} \bar{\lambda}^2 (\bar{\lambda}^6 - 1)^{-2} \left\{ 2 \bar{\lambda} (2 \bar{\lambda}^6 \cos^2(\bar{\theta}) - 1) \widehat{\Phi}_{,\bar{\theta}} + \bar{\lambda}^2 (\bar{\lambda}^6 - 1) \cos^2(\bar{\theta}) \widehat{\Phi}_{,\bar{\lambda}_1 \bar{\theta}} \right. \\
&\quad \left. - \bar{\lambda}^2 \sin(\bar{\theta}) \cos(\bar{\theta}) \left[(\bar{\lambda}^6 - 1) \widehat{\Phi}_{,\bar{\lambda}_1 \bar{\theta}_1 \bar{\theta}_1} + 4 \bar{\lambda}^5 \widehat{\Phi}_{,\bar{\theta}_1 \bar{\theta}_1} \right] \right\} \Big|_{\bar{\lambda}_1 = \bar{\lambda}_2 = \bar{\lambda}}
\end{aligned}$$

For the special case of aligned loadings ($\bar{\theta} = 0^\circ$), the above expressions for the moduli traces simplify considerably. For convenience in using these traces in the SE condition (2.50) (associated with aligned loadings), we provide the simplified expressions. The relevant, non-zero traces in the basis $\{\mathbf{e}_i\}$ (note that $\widehat{L}'_{ijkl} = \widehat{L}^c_{ijkl}$ for aligned loadings) read as

$$\begin{aligned}
\widehat{L}'_3 &= \frac{\bar{\lambda}_1 \left(\bar{\lambda}_1 l_1^2 \widehat{\Phi}_{,\bar{\lambda}_1 \bar{\lambda}_1} - 2 l_1 \widehat{\Phi}_{,\bar{\lambda}_1} - 2 \bar{\lambda}_1^3 \bar{\lambda}_2^2 \widehat{\Phi}_{,\bar{\theta}_2 \bar{\theta}_2} \right)}{l_1^2}, \\
\widehat{L}'_{1313} &= \frac{\bar{\lambda}_1 \left(\bar{\lambda}_1^3 \bar{\lambda}_2^2 \widehat{\Phi}_{,\bar{\theta}_2 \bar{\theta}_2} + l_1 \widehat{\Phi}_{,\bar{\lambda}_1} \right)}{l_1^2}, \quad \widehat{L}'_{3131} = \frac{\bar{\lambda}_1^4 \bar{\lambda}_2^2 \left(\widehat{\Phi}_{,\bar{\theta}_2 \bar{\theta}_2} + \bar{\lambda}_1 l_1 \widehat{\Phi}_{,\bar{\lambda}_1} \right)}{l_1^2},
\end{aligned} \tag{B.25}$$

$$\begin{aligned}
\widehat{L}_{3232}^c &= \frac{\bar{\lambda}_1^2 \bar{\lambda}_2^4 \left(\widehat{\Phi}_{,\bar{\theta}_1 \bar{\theta}_1} + \bar{\lambda}_2 l_2 \widehat{\Phi}_{,\bar{\lambda}_2} \right)}{l_2^2}, & \widehat{L}_{2323}^c &= \frac{\bar{\lambda}_2 \left(\bar{\lambda}_1^2 \bar{\lambda}_2^3 \widehat{\Phi}_{,\bar{\theta}_1 \bar{\theta}_1} + l_2 \widehat{\Phi}_{,\bar{\lambda}_2} \right)}{l_2^2}, \\
\widehat{L}_{2121}^c &= \frac{\bar{\lambda}_1^2 \left(\bar{\lambda}_1 \widehat{\Phi}_{,\bar{\lambda}_1} - \bar{\lambda}_2 \widehat{\Phi}_{,\bar{\lambda}_2} \right)}{l_3^2}, & \widehat{L}_{1212}^c &= \frac{\bar{\lambda}_2^2 \left(\bar{\lambda}_1 \widehat{\Phi}_{,\bar{\lambda}_1} - \bar{\lambda}_2 \widehat{\Phi}_{,\bar{\lambda}_2} \right)}{l_3},
\end{aligned} \tag{B.26}$$

$$\begin{aligned}
\widehat{L}_4^* &= \frac{\bar{\lambda}_2 \left(\bar{\lambda}_2 l_2^2 \widehat{\Phi}_{,\bar{\lambda}_2 \bar{\lambda}_2} - 2 l_2 \widehat{\Phi}_{,\bar{\lambda}_2} - 2 \bar{\lambda}_1^2 \bar{\lambda}_2^3 \widehat{\Phi}_{,\bar{\theta}_1 \bar{\theta}_1} \right)}{l_2^2}, \\
\widehat{L}_5^* &= (l_1^2 l_2^2 l_3)^{-1} \left[\bar{\lambda}_1 \bar{\lambda}_2 l_1^2 l_2^2 l_3 \widehat{\Phi}_{,\bar{\lambda}_1 \bar{\lambda}_2} - \bar{\lambda}_1^2 \bar{\lambda}_4^2 l_1^2 l_3 \widehat{\Phi}_{,\bar{\theta}_1 \bar{\theta}_1} - \bar{\lambda}_1^4 \bar{\lambda}_2^2 l_2^2 l_3 \widehat{\Phi}_{,\bar{\theta}_2 \bar{\theta}_2} + \bar{\lambda}_1^3 l_1 l_2^3 \widehat{\Phi}_{,\bar{\lambda}_1} - \bar{\lambda}_2^3 l_2 l_1^3 \widehat{\Phi}_{,\bar{\lambda}_2} \right].
\end{aligned} \tag{B.27}$$

Again, note that for axisymmetric shear loadings with the condition $\bar{\lambda}_1 = \bar{\lambda}_2 = \bar{\lambda}$, suitable limits must be taken for the traces involving the terms $(\bar{\lambda}_1 - \bar{\lambda}_2)$ in the denominator. Taking these limits for the pertinent traces appearing in the SE condition (2.50) yields

$$\begin{aligned}
\widehat{L}_{1212}^c &= \widehat{L}_{2121}^c = \frac{1}{2} \bar{\lambda} \left[\frac{1}{2} \widehat{\Phi}_{,\bar{\lambda}}^{AS} + \bar{\lambda} \left(2 \widehat{\Phi}_{,\bar{\lambda}_1 \bar{\lambda}_1} - \frac{1}{2} \widehat{\Phi}_{,\bar{\lambda} \bar{\lambda}}^{AS} \right) \Big|_{\bar{\lambda}_1 = \bar{\lambda}_2 = \bar{\lambda}} \right], \\
\widehat{L}_5^* &= \frac{1}{4} \bar{\lambda} \left[(\bar{\lambda}^{13} - 2 \bar{\lambda}^7 + \bar{\lambda}) \widehat{\Phi}_{,\bar{\lambda} \bar{\lambda}}^{AS} - 4 \bar{\lambda}^5 \left(\widehat{\Phi}_{,\bar{\theta}_1 \bar{\theta}_1} + \widehat{\Phi}_{,\bar{\theta} \bar{\theta}} \right) - (\bar{\lambda}^{12} + 2 \bar{\lambda}^6 - 3) \widehat{\Phi}_{,\bar{\lambda}}^{AS} \right].
\end{aligned}$$

Appendix C

C.1 The Hashin-Shtrikman-Willis variational estimates

Hashin and Shtrikman (1963) introduced a variational technique to estimate the effective behavior of linear-elastic composites with statistically isotropic microstructures. This work was extended later by Willis (1977, 1981) for composites with more general anisotropic microstructures. For the particulate material systems of interest in this work, consisting of random distributions of ellipsoidal inclusions in a given matrix, more explicit estimates have been given by Ponte Castañeda and Willis (1995). Given the well-known analogy between the governing equations for a linear-elastic solid and a linearly viscous fluid, Kailasam et al. (1997) and Kailasam and Ponte Castañeda (1998) applied and generalized the PCW theory to estimate the instantaneous response of two-phase linearly and nonlinearly viscous composites subjected to simple flows, assuming that surface tension, buoyancy and dynamical effects could be neglected. In this appendix, we demonstrate how this earlier work for viscous composites can still be further generalized to provide corresponding estimates for the class of suspensions of finitely deforming, viscoelastic particles considered in this work.

We begin by recalling expressions (4.23) and (4.25) defining the local dissipation potential W of the suspension. We then introduce a homogeneous “comparison” Newtonian fluid with viscosity η^0 , whose dissipation potential is given by

$$W^0(\mathbf{D}) = \eta^0 \mathbf{D} \cdot \mathbf{D}, \quad \text{tr}(\mathbf{D}) = \mathbf{0}. \quad (\text{C.1})$$

Suppose for now that $\eta^0 \geq \eta^{(1)}, \eta^{(2)}$, so that $W - W^0$ is a concave function of \mathbf{D} . Then, following Talbot and Willis (1985), the Legendre-Fenchel transform of this difference potential can be defined as

$$(W - W^0)_*(\mathbf{x}, \boldsymbol{\Xi}) = \inf_{\mathbf{D}} \{ \boldsymbol{\Xi} \cdot \mathbf{D} - [W(\mathbf{x}, \mathbf{D}) - W^0(\mathbf{D})] \}. \quad (\text{C.2})$$

Note that the stationary condition associated with this relation is

$$\boldsymbol{\Xi} = \boldsymbol{\tau} - 2\eta^0 \mathbf{D}, \quad (\text{C.3})$$

where we have used the fact that $\boldsymbol{\tau} = \partial W / \partial \mathbf{D}$. As a consequence, the quantity $\boldsymbol{\Xi}$ is known as the “polarization” stress tensor relative to the comparison fluid. Noting that $(W - W^0)_*$ is concave, we deduce from (C.2), by Legendre duality, that

$$W(\mathbf{x}, \mathbf{D}) = \inf_{\boldsymbol{\Xi}} \{ W^0(\mathbf{D}) + \boldsymbol{\Xi} \cdot \mathbf{D} - (W - W^0)_*(\mathbf{x}, \boldsymbol{\Xi}) \}. \quad (\text{C.4})$$

Substituting (C.4) into expression (4.31), and interchanging the order of infima over \mathbf{D} and $\boldsymbol{\Xi}$, we obtain

$$\widetilde{W}(\bar{\mathbf{D}}) = \inf_{\boldsymbol{\Xi}} \left\{ \min_{\mathbf{D} \in K} \left[\int_{\Omega} (W^0(\mathbf{D}) + \boldsymbol{\Xi} \cdot \mathbf{D}) \, dV \right] - \int_{\Omega} (W - W^0)_*(\mathbf{x}, \boldsymbol{\Xi}) \, dV \right\}, \quad (\text{C.5})$$

as first shown by Talbot and Willis (1985) in the context of linear elasticity. Now, taking the polarization stress field as given, it follows that the Euler-Lagrange equation for the “inner” minimum

problem over the field \mathbf{D} is given by

$$\eta^0 \nabla^2 \mathbf{v} - \nabla p = -\nabla \cdot \boldsymbol{\Xi}, \text{ and } \nabla \cdot \mathbf{v} = 0 \text{ in } \Omega, \text{ and } \mathbf{v} = \bar{\mathbf{L}}\mathbf{x} \text{ on } \partial\Omega. \quad (\text{C.6})$$

The above differential equation corresponds to the Stokes equation for a homogeneous Newtonian fluid with viscosity η^0 subjected to the body force distribution $\nabla \cdot \boldsymbol{\Xi}$ in the domain Ω , along with the affine condition $\mathbf{v} = \bar{\mathbf{L}}\mathbf{x}$ on the boundary $\partial\Omega$. After choosing η^0 to be equal to $\eta^{(1)}$, the above equations turns out to be the same as those considered by Gao et al. (2011) in the context of dilute suspensions. As discussed in section 3 of Gao et al. (2011), the solutions for the strain rate and vorticity fields in the domain Ω can be expressed in terms of the Green's function $\mathbf{G}(\mathbf{x}, \mathbf{x}')$ as

$$D_{ij}(\mathbf{x}) = \bar{D}_{ij} + \int_{\Omega^{(2)}} \Gamma_{ijpq}(\mathbf{x}, \mathbf{x}') \Xi_{pq}(\mathbf{x}') d\mathbf{x}', \quad \text{and} \quad (\text{C.7})$$

$$W_{ij}(\mathbf{x}) = \bar{W}_{ij} + \int_{\Omega^{(2)}} \Lambda_{ijpq}(\mathbf{x}, \mathbf{x}') \Xi_{pq}(\mathbf{x}') d\mathbf{x}', \quad (\text{C.8})$$

respectively, where $\Gamma_{ijpq} = (\partial^2 G_{ip}/\partial x_j \partial x'_q)|_{(ij),(pq)}$ and $\Lambda_{ijpq} = (\partial^2 G_{ip}/\partial x_j \partial x'_q)|_{[ij],[pq]}$ with the parentheses and square brackets (enclosing indices) denoting symmetric and anti-symmetric parts, respectively. The above solution requires information on the polarization stress field in the particle phase (note that $\boldsymbol{\Xi}$ is zero in the matrix because of the choice $\eta^0 = \eta^{(1)}$.) For the case of dilute suspensions of ellipsoidal neo-Hookean particles, it was shown by Gao et al. (2011), building on earlier work by Willis (1977) in linear elasticity, that the polarization field in the particles is uniform. On the other hand, for non-dilute suspensions, the polarization field is not expected to be uniform in the particles. However, again building on earlier work (Willis, 1977; Ponte Castañeda and Willis, 1995), it is reasonable to make use of piecewise constant polarization trial fields in the sense of a variational approximation. Thus, the use of the trial stress polarization $\boldsymbol{\Xi}(\mathbf{x}) = \chi^{(2)}(\mathbf{x}) \boldsymbol{\Xi}^{(2)}$, where $\chi^{(2)}(\mathbf{x})$ is the characteristic function of the particle phase, and $\boldsymbol{\Xi}^{(2)}$ the corresponding (uniform) stress polarizations in the inclusion phase (recall that $\boldsymbol{\Xi}^{(1)} = \mathbf{0}$, due to the choice $\eta^0 = \eta^{(1)}$), leads to the result that

$$\widetilde{W}(\bar{\mathbf{D}}) \leq \inf_{\boldsymbol{\Xi}^{(2)}} \left\{ \min_{\mathbf{D} \in K} \left[\int_{\Omega} (W^0(\mathbf{D}) + \boldsymbol{\Xi} \cdot \mathbf{D}) dV \right] - \int_{\Omega} (W - W^0)_*(\mathbf{x}, \boldsymbol{\Xi}) dV \right\}. \quad (\text{C.9})$$

Making use of this approximation of uniform polarizations in the particles, and under the *separation of length scales* and *no long-range order* hypothesis for the random distribution of the particle phase (Willis, 1981; Ponte Castañeda and Willis, 1995; Ponte Castañeda, 2005), the tensors Γ_{ijpq} and Λ_{ijpq} in relations (C.7) and (C.8) may be replaced by the corresponding tensors constructed from the infinite-body Green's function. Then, for the case of ellipsoidal particles distributed with ellipsoidal symmetry (i.e., such that the two-point correlation functions for the distribution of the particle centers exhibit ellipsoidal angular dependence), it can be shown (Ponte Castañeda and Willis, 1995; Ponte Castañeda, 2005) that the averages over the particle phase of the strain rate and

vorticity tensors in (C.7) and (C.8) are given by

$$\bar{\mathbf{D}}^{(2)} = \bar{\mathbf{D}} - (1 - c) \mathbb{P} \boldsymbol{\Xi}^{(2)}, \quad \bar{\mathbf{W}}^{(2)} = \bar{\mathbf{W}} - (1 - c) \mathbb{R} \boldsymbol{\Xi}^{(2)}, \quad (\text{C.10})$$

respectively, where $c = c^{(2)}$ is the volume fraction of the particle phase, and \mathbb{P} and \mathbb{R} are fourth-order microstructural tensors defined by

$$\mathbb{P} = \frac{1}{4\pi |\mathbf{Z}|} \int_{|\boldsymbol{\xi}|=1} \mathbb{H}(\boldsymbol{\xi}) |\mathbf{Z}^T \boldsymbol{\xi}|^{-3} dS, \quad \text{and} \quad \mathbb{R} = \frac{1}{4\pi |\mathbf{Z}|} \int_{|\boldsymbol{\xi}|=1} \mathbb{T}(\boldsymbol{\xi}) |\mathbf{Z}^T \boldsymbol{\xi}|^{-3} dS. \quad (\text{C.11})$$

In these expressions, the fourth-order tensor \mathbb{H} and \mathbb{T} are in turn defined by

$$H_{ijkl} = (M_{ik} \xi_j \xi_l)|_{(ij)(kl)}, \quad T_{ijkl} = (M_{ik} \xi_j \xi_l)|_{[ij](kl)}, \quad (\text{C.12})$$

where $\mathbf{M} = \eta^{(1)}(\mathbf{I} - \boldsymbol{\xi} \otimes \boldsymbol{\xi})$.

Having solved for the strain-rate in the ‘‘inner’’ minimum problem, we next need to find the optimal (uniform) stress polarization $\boldsymbol{\Xi}^{(2)}$ in the inclusions. By evaluating the derivative of the integrals in (C.9) with respect to $\boldsymbol{\Xi}^{(2)}$, and solving for $\boldsymbol{\Xi}^{(2)}$, we obtain the result

$$\boldsymbol{\Xi}^{(2)} = \bar{\boldsymbol{\tau}}^{(2)} - 2\eta^{(1)} \bar{\mathbf{D}}^{(2)}, \quad (\text{C.13})$$

where $\bar{\boldsymbol{\tau}}^{(2)}$ is the average of the extra stress in the particles at the current instant.

Substituting $\boldsymbol{\Xi}^{(2)}$, as determined by relation (C.13), in relations (C.10), we obtain the following expressions for the average strain rate and vorticity tensors in particles

$$\bar{\mathbf{D}}^{(2)} = \left[\mathbb{I} - 2(1 - c) \eta^{(1)} \mathbb{P} \right]^{-1} \left\{ \bar{\mathbf{D}} - (1 - c) \mathbb{P} \bar{\boldsymbol{\tau}}^{(2)} \right\}, \quad (\text{C.14})$$

and

$$\bar{\mathbf{W}}^{(2)} = \bar{\mathbf{W}} + (1 - c) \mathbb{R} \left(2\eta^{(1)} \bar{\mathbf{D}}^{(2)} - \bar{\boldsymbol{\tau}}^{(2)} \right). \quad (\text{C.15})$$

As mentioned earlier, in this work, we consider suspensions of KV particles with a linear viscous part ($\boldsymbol{\tau}_v^{(2)} = 2\eta^{(2)} \mathbf{D}$). It follows that the total average extra stress tensor in the KV particles reads as (see relation (4.1))

$$\bar{\boldsymbol{\tau}}^{(2)} = \bar{\boldsymbol{\tau}}_e^{(2)} + \bar{\boldsymbol{\tau}}_v^{(2)} = \bar{\boldsymbol{\tau}}_e^{(2)} + 2\eta^{(2)} \bar{\mathbf{D}}^{(2)}. \quad (\text{C.16})$$

Then, making use of this decomposition in relations (C.14) and (C.15), we arrive at the results (4.33) and (4.34) for the averages of the strain rate and vorticity tensors, respectively, in the particles. With this result, it can be shown that the effective (modified) dissipation potential (C.9) can be written in the form (4.32). Finally, it should be noted that under the assumption that $\eta^0 \geq \eta^{(1)}, \eta^{(2)}$, it follows from (C.9) that the right-hand side of (4.32) is a rigorous upper bound (see also Lahellec et al., 2011) for the effective (modified) dissipation potential $\widetilde{W}(\bar{\mathbf{D}})$. On the other hand, if it is assumed instead that $\eta^0 \leq \eta^{(1)}, \eta^{(2)}$, the expression in the right-hand side of (4.32) can alternatively be shown to provide a lower bound for $\widetilde{W}(\bar{\mathbf{D}})$, even if the corresponding expressions for $\bar{\mathbf{D}}^{(2)}$ and $\bar{\boldsymbol{\tau}}_e^{(2)}$ do not change. However, in this work, we will not insist on the bounding properties of the estimate (4.32),

and we make use of an equality in expression (4.32), in the sense of an approximation.

C.2 Governing equations for extensional flows

In this appendix, we present simplified evolution equations for the initially spherical particles subjected to the extensional flow defined by (4.58). Because of the flow symmetry, the initially spherical particles remain fixed in orientation, evolving into prolate spheroidal particles with aspect ratios $w = w_1 = w_2$. Also, the symmetry implies that $\bar{\tau}_{33}^{(2)} = \bar{\tau}_{22}^{(2)}$ and $\bar{D}_{22}^{(2)} = \bar{D}_{33}^{(2)} = -\bar{D}_{11}^{(2)}/2$, where the second equality follows from the incompressibility in the particles.

With the above-mentioned simplifications, and for the case of KV particles with Gent elastic behavior, the system of equations (4.33), (4.39), (4.42), and (C.16) can be shown to reduce to

$$\left. \begin{aligned} \frac{d\bar{\tau}_{e11}^{(2)}}{dt} &= \frac{2}{\mu J_m} \bar{D}_{11}^{(2)} \left(\bar{\tau}_{e11}^{(2)} + \mu \right) \left(\bar{\tau}_{e11}^{(2)} - \bar{\tau}_{e22}^{(2)} + \mu J_m \right), \\ \frac{d\bar{\tau}_{e22}^{(2)}}{dt} &= -\frac{1}{\mu J_m} \bar{D}_{11}^{(2)} \left(\bar{\tau}_{e22}^{(2)} + \mu \right) \left[2 \left(\bar{\tau}_{e22}^{(2)} - \bar{\tau}_{e11}^{(2)} \right) + \mu J_m \right], \\ \bar{\tau}_{ij}^{(2)} &= \bar{\tau}_{eij}^{(2)} + 2\eta^{(1)} \bar{D}_{ij}^{(2)}, \quad i, j = 1, 2, 3, \quad \frac{dw}{dt} = -\frac{3}{2} w \bar{D}_{11}^{(2)} \\ \bar{D}_{11}^{(2)} &= \frac{w^2 (1-c) [(w^2+2)\omega_2 - 6\omega_1] \left(\bar{\tau}_{11}^{(2)} - \bar{\tau}_{22}^{(2)} \right) - 4\omega_1^5 \eta^{(1)} \dot{\gamma}}{\{2\omega_1 [9(1-c)w^2(\eta^{(2)} - \eta^{(1)}) - 2\omega_1^4 \eta^{(1)}] - 3(1-c)w^2(w^2+2)\omega_2(\eta^{(2)} - \eta^{(1)})\}}, \end{aligned} \right\} \quad (\text{C.17})$$

where $\omega_1 = \sqrt{1-w^2}$ and $\omega_2 = 2 \ln(\omega_1 + 1) - 2 \ln(w)$. Moreover, for the special case of neo-Hookean elastic response for the KV particles, the above system of ODEs for $\bar{\tau}_e^{(2)}$ simplify further reducing to

$$\frac{d\bar{\tau}_{e11}^{(2)}}{dt} = 2\bar{D}_{11}^{(2)} \left(\bar{\tau}_{e11}^{(2)} + \mu \right), \quad \frac{d\bar{\tau}_{e22}^{(2)}}{dt} = -\bar{D}_{11}^{(2)} \left(\bar{\tau}_{e22}^{(2)} + \mu \right), \quad (\text{C.18})$$

while Eqs. (C.17)₃₋₅ remain the same.

C.3 Governing equations for shear flows

In this appendix, we provide simplified evolution equations for the initially spherical particles, when subjected to the shear flow conditions defined by (4.67). For simplicity, we provide equations only for the case of KV particles with neo-Hookean elastic response. Recall that the particles take on general ellipsoidal shapes characterized by the aspect ratios w_1 and w_2 , but rotate only in the shear plane, the rotation being described by the angle θ . Then, the system of equations (4.39), (4.40),

(4.42), and (C.16) can be shown to simplify to

$$\left. \begin{aligned} \dot{\bar{\tau}}_{e11}^{(2)} &= 2(\bar{D}_{12}^{(2)} + \bar{W}_{12}^{(2)})\bar{\tau}_{e12}^{(2)} + 2(\bar{\tau}_{e11}^{(2)} + \mu)\bar{D}_{11}^{(2)}, \\ \dot{\bar{\tau}}_{e22}^{(2)} &= 2(\bar{D}_{12}^{(2)} - \bar{W}_{12}^{(2)})\bar{\tau}_{e12}^{(2)} + 2(\bar{\tau}_{e22}^{(2)} + \mu)\bar{D}_{22}^{(2)}, \quad \dot{\bar{\tau}}_{e33}^{(2)} = -2(\bar{\tau}_{e33}^{(2)} + \mu)(\bar{D}_{11}^{(2)} + \bar{D}_{22}^{(2)}), \\ \dot{\bar{\tau}}_{e12}^{(2)} &= (\bar{D}_{12}^{(2)} - \bar{W}_{12}^{(2)})\bar{\tau}_{e11}^{(2)} + (\bar{D}_{12}^{(2)} + \bar{W}_{12}^{(2)})\bar{\tau}_{e22}^{(2)} + \bar{\tau}_{e12}^{(2)}(\bar{D}_{11}^{(2)} + \bar{D}_{22}^{(2)}) + 2\mu\bar{D}_{12}^{(2)}, \\ \bar{\tau}_{ij}^{(2)} &= \bar{\tau}_{eij}^{(2)} + 2\eta^{(2)}\bar{D}_{ij}^{(2)}, \quad i, j = 1, 2, 3 \\ \frac{dw_1}{dt} &= -2w_1\bar{D}_{11}^{(2)}, \quad \frac{dw_2}{dt} = -w_2\bar{D}_{11}^{(2)}, \quad \frac{d\theta}{dt} = \left(\frac{1+w_1^2}{1-w_1^2}\right)\bar{D}_{12}^{(2)} - \bar{W}_{12}^{(2)}. \end{aligned} \right\} \quad (\text{C.19})$$

The above equations are complemented by relations (4.33) and (4.34) for the average strain rate $\bar{\mathbf{D}}^{(2)}$ and vorticity $\bar{\mathbf{W}}^{(2)}$ in the particles, respectively.

In the context of equations (C.19), it is noted that these equations are written relative to a fixed coordinate system which is instantaneously aligned with the principal axes of particles. As pointed out by Gao et al. (2011) (see Appendix A in that paper), because of the rotation of particles in shear flow, one must account for the rotation of this coordinate system in order to integrate the above system of equations. One simple way to account for this rotation is to express the stress tensor in the rotating principal axes of the particles (i.e., $\{\mathbf{n}_1, \mathbf{n}_2, \mathbf{n}_3\}$) as

$$\bar{\boldsymbol{\tau}}_e^{(2)} = \bar{\tau}_{e11}^{(2)}\mathbf{n}_1\mathbf{n}_1 + \bar{\tau}_{e22}^{(2)}\mathbf{n}_2\mathbf{n}_2 + \bar{\tau}_{e33}^{(2)}\mathbf{n}_3\mathbf{n}_3 + \bar{\tau}_{e12}^{(2)}(\mathbf{n}_1\mathbf{n}_2 + \mathbf{n}_2\mathbf{n}_1) \quad (\text{C.20})$$

Taking the time derivative from both sides of the above relation, we can express the time derivative of the stress components in the fixed coordinates in terms of the time derivative of those in the rotating principal coordinates as (see relations (A 10) and (A 11) in Gao et al. (2011))

$$\begin{aligned} \dot{\bar{\tau}}_{e11}^{(2)} &= \frac{d\bar{\tau}_{e11}^{(2)}}{dt} - 2\bar{\tau}_{e12}^{(2)}\frac{d\theta}{dt}, \quad \dot{\bar{\tau}}_{e22}^{(2)} = \frac{d\bar{\tau}_{e22}^{(2)}}{dt} + 2\bar{\tau}_{e12}^{(2)}\frac{d\theta}{dt}, \\ \dot{\bar{\tau}}_{e33}^{(2)} &= \frac{d\bar{\tau}_{e33}^{(2)}}{dt}, \quad \dot{\bar{\tau}}_{e12}^{(2)} = \frac{d\bar{\tau}_{e12}^{(2)}}{dt} + (\bar{\tau}_{e11}^{(2)} - \bar{\tau}_{e22}^{(2)})\frac{d\theta}{dt}. \end{aligned} \quad (\text{C.21})$$

After substituting the above relations into the system of equations (C.19), we can directly apply an implicit (or explicit) time-discretization procedure to integrate the equations.

C.4 The tensors \mathbb{P} and \mathbb{R} for an ellipsoidal inclusion

In this appendix, explicit analytical expressions are given for the components of the tensors \mathbb{P} and \mathbb{R} for a general ellipsoidal particle suspended in an incompressible, isotropic, linear viscous matrix with the viscosity constant $\eta^{(1)}$. The final expressions for the components of the tensor \mathbb{P} in the principal coordinate system of the particle read as (Eshelby, 1957; Kailasam, 1998)

$$\begin{aligned} \mathbb{P}_{1111} &= h_1(6I_{11} - y_1), \quad \mathbb{P}_{2222} = h_1(6I_{22}w_1^2 - y_2), \quad \mathbb{P}_{3333} = h_1(6I_{33}w_2^2 - y_3), \\ \mathbb{P}_{1122} &= h_1(2w_1^2I_{12} - 3I_{11} - w_2^2I_{13}), \quad \mathbb{P}_{1133} = h_1(2w_2^2I_{13} - 3I_{11} - w_1^2I_{12}), \\ \mathbb{P}_{2233} &= h_1(2w_2^2I_{23} - 3w_1^2I_{22} - I_{12}), \quad \mathbb{P}_{1212} = h_2(1 + w_1^2)I_{12}, \quad \mathbb{P}_{1313} = h_2(1 + w_2^2)I_{13}, \end{aligned} \quad (\text{C.22})$$

and $\mathbb{P}_{2323} = h_2 (w_1^2 + w_2^2) I_{23}$ where $h_1 = (24 \pi \eta^{(1)})^{-1} a^2$ and $h_2 = (16 \pi \eta^{(1)})^{-1} a^2$. In the above expressions the following variables have been introduced for brevity

$$y_1 = w_1^2 I_{12} + w_2^2 I_{13}, \quad y_2 = I_{12} + I_{23} w_2^2, \quad y_3 = I_{13} + I_{23} w_1^2, \quad (\text{C.23})$$

and the rest of the variables are defined as

$$\begin{aligned} I_1 &= 4 \pi w_1 w_2 \left[(1 - w_1^2) \sqrt{1 - w_2^2} \right]^{-1} (F - E), \quad I_2 = 4 \pi - I_1 - I_3, \\ I_3 &= 4 \pi w_1 w_2 \left[(w_1^2 - w_2^2) \sqrt{1 - w_2^2} \right]^{-1} \left[w_1 w_2^{-1} \sqrt{1 - w_2^2} - E \right], \\ I_{12} &= \frac{1}{a^2(1 - w_1^2)} (I_2 - I_1), \quad I_{13} = \frac{1}{a^2(1 - w_2^2)} (I_3 - I_1), \quad I_{23} = \frac{1}{a^2(w_1^2 - w_2^2)} (I_3 - I_2), \\ I_{11} &= \frac{1}{3} \left(\frac{4 \pi}{a^2} - I_{12} - I_{13} \right), \quad I_{22} = \frac{1}{3} \left(\frac{4 \pi}{a^2 w_1^2} - I_{12} - I_{23} \right), \quad I_{33} = \frac{1}{3} \left(\frac{4 \pi}{a^2 w_2^2} - I_{13} - I_{23} \right), \end{aligned} \quad (\text{C.24})$$

in which the functions F and E denote the incomplete elliptic integrals of the first and second kinds, respectively, and are defined as

$$F = \int_0^{\sin(\Theta)} \frac{1}{\sqrt{1 - t^2} \sqrt{1 - \kappa^2 t^2}} dt, \quad E = \int_0^{\sin(\Theta)} \frac{\sqrt{1 - \kappa^2 t^2}}{\sqrt{1 - t^2}} dt, \quad (\text{C.25})$$

where $\Theta = \sin^{-1}(\sqrt{1 - w_2^2})$, and $\kappa = \sqrt{1 - w_1^2} / \sqrt{1 - w_2^2}$. Moreover, the three independent components of the tensor \mathbb{R} in the principal coordinate systems of the particle read as

$$\mathbb{R}_{ijij} = \frac{1}{16 \pi \eta^{(1)}} (I_j - I_i), \quad \text{for } i, j = 1, 2, 3, \text{ and } j > i. \quad (\text{C.26})$$

The remaining non-zero components of the tensor \mathbb{R}_{ijkl} are obtained by recalling that this tensor is symmetric with respect to the first two indices ($\mathbb{R}_{jikl} = \mathbb{R}_{ijkl}$) and anti-symmetric with respect to the last two indices ($\mathbb{R}_{ijlk} = -\mathbb{R}_{ijkl}$).

Appendix D

D.1 Governing equations for the deformation of spherical particles in a shear flow

In this appendix, we provide simplified evolution equations for the initially spherical, Gent particles, when subjected to the shear flow conditions defined by (5.62). Recall that the particles take on general ellipsoidal shapes characterized by the aspect ratios w_1 and w_2 , but rotate only in the shear plane, the rotation being described by the angle θ . Then, the system of equations (5.50), (5.51), and (5.54) can be shown to simplify to

$$\left. \begin{aligned}
 \dot{\bar{\tau}}_{11}^{(2)} &= 2(\bar{D}_{12}^{(2)} + \bar{W}_{12}^{(2)})\bar{\tau}_{12}^{(2)} + 2(\bar{\tau}_{11}^{(2)} + \mu)\bar{D}_{11}^{(2)} + (\bar{\tau}_{11}^{(2)} + \mu)\Sigma, \\
 \dot{\bar{\tau}}_{22}^{(2)} &= 2(\bar{D}_{12}^{(2)} - \bar{W}_{12}^{(2)})\bar{\tau}_{12}^{(2)} + 2(\bar{\tau}_{22}^{(2)} + \mu)\bar{D}_{22}^{(2)} + (\bar{\tau}_{22}^{(2)} + \mu)\Sigma, \\
 \dot{\bar{\tau}}_{33}^{(2)} &= -2(\bar{\tau}_{33}^{(2)} + \mu)(\bar{D}_{11}^{(2)} + \bar{D}_{22}^{(2)}) + (\bar{\tau}_{33}^{(2)} + \mu)\Sigma, \\
 \dot{\bar{\tau}}_{12}^{(2)} &= (\bar{D}_{12}^{(2)} - \bar{W}_{12}^{(2)})\bar{\tau}_{11}^{(2)} + (\bar{D}_{12}^{(2)} + \bar{W}_{12}^{(2)})\bar{\tau}_{22}^{(2)} \\
 &\quad + \bar{\tau}_{12}^{(2)}(\bar{D}_{11}^{(2)} + \bar{D}_{22}^{(2)}) + 2\mu\bar{D}_{12}^{(2)} + \bar{\tau}_{12}^{(2)}\Sigma, \\
 \frac{dw_1}{dt} &= -2w_1\bar{D}_{11}^{(2)}, \quad \frac{dw_2}{dt} = -w_2\bar{D}_{11}^{(2)}, \quad \frac{d\theta}{dt} = \left(\frac{1+w_1^2}{1-w_1^2}\right)\bar{D}_{12}^{(2)} - \bar{W}_{12}^{(2)}.
 \end{aligned} \right\} \quad (\text{D.1})$$

where

$$\Sigma = [(\bar{\tau}_{11} - \bar{\tau}_{33})\bar{D}_{11}^{(2)} + (\bar{\tau}_{22} - \bar{\tau}_{33})\bar{D}_{22}^{(2)} + 2\bar{D}_{12}^{(2)}\bar{\tau}_{12}]/(J_m\mu).$$

The above equations are complemented with two equations (5.36) and (5.37) for unknown variables $\eta^{(1)}$ and \hat{D}_{eq} . The resulting system of equations, together with relations (5.41) and (5.42) for the average strain-rate $\bar{\mathbf{D}}^{(2)}$ and vorticity $\bar{\mathbf{W}}^{(2)}$ in the particles, respectively, can be integrated numerically for the time-dependent solution. The components of the shape tensors \mathbb{P} and \mathbb{R} , required for this integration, are available from Appendix D in Avazmohammadi and Ponte Castañeda (2014).

Appendix E

E.1 Two-Phase thermoelastic composites

In this appendix, we provide expressions for the effective properties as well as the associated concentration tensors for a two-phase thermoelastic composite defined by the local stress potential (6.11). For this composite, the effective stress potential is defined by (6.23), and the Levin relations (Levin, 1967) for the effective properties $\tilde{\boldsymbol{\gamma}}$ and \tilde{g} are given by

$$\tilde{\boldsymbol{\gamma}} = \bar{\boldsymbol{\gamma}} + \left(\tilde{\mathbb{M}} - \bar{\mathbb{M}} \right) (\Delta \mathbb{M})^{-1} (\Delta \boldsymbol{\gamma}), \quad (\text{E.1})$$

and

$$\tilde{g} = \frac{1}{2} (\Delta \boldsymbol{\gamma}) \cdot (\Delta \mathbb{M})^{-1} \left(\tilde{\mathbb{M}} - \bar{\mathbb{M}} \right) (\Delta \mathbb{M})^{-1} (\Delta \boldsymbol{\gamma}), \quad (\text{E.2})$$

respectively, where $\bar{\mathbb{M}} = (1 - c) \mathbb{M}^{(1)} + c \mathbb{M}^{(2)}$, $\Delta \mathbb{M} = \mathbb{M}^{(1)} - \mathbb{M}^{(2)}$ and $\Delta \boldsymbol{\gamma} = \boldsymbol{\gamma}^{(1)} - \boldsymbol{\gamma}^{(2)}$. Also, according to Levin's relation, the strain-rate concentration tensors $\mathbb{A}^{(1)}$ and $\mathbf{a}^{(1)}$ are expressed as

$$\begin{aligned} \mathbb{A}^{(2)} &= \mathbb{I} - \frac{1}{c^{(2)}} (\Delta \mathbb{L})^{-T} \left(\tilde{\mathbb{L}} - \bar{\mathbb{L}} \right)^T, \quad \text{and} \\ \mathbf{a}^{(2)} &= -\frac{1}{c^{(2)}} (\Delta \mathbb{L})^{-1} \left(\tilde{\mathbb{L}} - \bar{\mathbb{L}} \right) (\Delta \mathbb{L})^{-1} \Delta \boldsymbol{\gamma}, \end{aligned} \quad (\text{E.3})$$

where $(\Delta \mathbb{L})^{-1} = \mathbb{L}^{(1)} - \mathbb{L}^{(2)}$ and $\tilde{\mathbb{L}} = (\tilde{\mathbb{M}})^{-1}$ denotes the effective viscosity of the composite. The concentration tensors $\mathbb{A}^{(1)}$ and $\mathbf{a}^{(1)}$ can be, in turn, obtained from relations (6.26).

E.2 An incremental form for the second moment of stress

In the context of Willis estimates for two-phase composites consisting of a matrix and a distribution of ellipsoidal particles, the stress phase averages are given by

$$\bar{\boldsymbol{\sigma}}^{(r)} = \mathbb{B}^{(r)} \bar{\boldsymbol{\sigma}}, \quad r = 1, 2, \quad (\text{E.4})$$

where the stress-concentration tensors $\mathbb{B}^{(r)}$ are defined by (Ponte Castañeda and Willis, 1995)

$$\mathbb{B}^{(2)} = \left[\mathbb{I} - c^{(1)} \mathbb{Q}_e \Delta \mathbb{S} \right]^{-1}, \quad \text{and} \quad \mathbb{B}^{(1)} = (c^{(2)})^{-1} (c^{(2)} \mathbb{B}^{(2)} - \mathbb{I}). \quad (\text{E.5})$$

In the above expressions, the microstructural tensor \mathbb{Q}_e is defined by the same relation (6.29) with $\mathbb{P}^{(1)}$ and $\mathbb{L}^{(1)}$ being replaced by $\mathbb{P}_e^{(1)}$ and $\mathbb{C}^{(1)}$, respectively.

Also, the second moment of the stress in the matrix phase is obtained as Ponte Castañeda (2005)

$$\langle \sigma_{eq}^2 \rangle^{(1)} = \frac{3}{2 c^{(1)}} \bar{\boldsymbol{\sigma}} \cdot \frac{\partial \tilde{\mathbb{S}}^{Ws}}{\partial \mathbb{S}^{(1)}} \bar{\boldsymbol{\sigma}}. \quad (\text{E.6})$$

Making use of expression (6.44) in the above definition, the second moment will take the functional form

$$\langle \sigma_{eq}^2 \rangle^{(1)} = g(\bar{\boldsymbol{\sigma}}, \mathbb{S}^{(1)}, \mathbb{S}^{(2)}, \mathcal{S}), \quad (\text{E.7})$$

where \mathcal{S} is the set of variables characterizing the microstructure of the composite (such as volume fraction and shape of the particles).

For the special case of two-phase composites with incompressible isotropic phases, making use of relations (E.4) and the identity $\bar{\boldsymbol{\sigma}} = c^{(1)} \bar{\boldsymbol{\sigma}}^{(1)} + c^{(2)} \bar{\boldsymbol{\sigma}}^{(2)}$ in the form (E.7), it is possible (at least for the case of spheroidal particles) to re-write the second moment in the form of

$$\langle \sigma_{eq}^2 \rangle^{(1)} = h(\bar{\boldsymbol{\sigma}}^{(1)}, \bar{\boldsymbol{\sigma}}^{(2)}, \mathcal{S}), \quad (\text{E.8})$$

Therefore, a rate-type relation for this quantity is obtained as given in relation (6.45).

Bibliography

- M. Abramowitz and I. Stegun. *Handbook of Mathematical functions with formulas, graphs, and mathematical tables*. Dover, New York, 1965.
- M. Agoras, O. Lopez-Pamies, and P. Ponte Castañeda. A general hyperelastic model for incompressible fiber-reinforced elastomers. *J. Mech. Phys. Solids*, 57:268–286, 2009a.
- M. Agoras, O. Lopez-Pamies, and P. Ponte Castañeda. Onset of macroscopic instabilities in fiber-reinforced elastomers at finite strain. *J. Mech. Phys. Solids*, 57:1828–1850, 2009b.
- A.N. Alexandrou, T.M. McGilvrey, and G. Burgos. Steady herschel–bulkeley fluid flow in three-dimensional expansions. *J. Non-Newton. Fluid Mech.*, 100(1):77–96, 2001.
- C. Ancey and H. Jorrot. Yield stress for particle suspensions within a clay dispersion. *J. Rheol.*, 45(2):297–319, 2001.
- N. Aravas and P. Ponte Castañeda. Numerical methods for porous metals with deformation-induced anisotropy. *Comput. Meth. Appl. Mech. Engng.*, 193:3767–3805, 2004.
- R. Avazmohammadi and R. Naghdabadi. Strain energy-based homogenization of nonlinear elastic particulate composites. *Int. J. Eng. Sci.*, 47(10):1038–1048, 2009.
- R. Avazmohammadi and R. Naghdabadi. Effective behavior of porous elastomers containing aligned spheroidal voids. *Acta Mech.*, 224(9):1901–1915, 2013.
- R. Avazmohammadi and P. Ponte Castañeda. Tangent second-order estimates for the large-strain, macroscopic response of particle-reinforced elastomers. *J. Elasticity*, 112:139–183, 2013.
- R. Avazmohammadi and P. Ponte Castañeda. Homogenization approach to the rheology of non-dilute suspensions of viscoelastic particles in viscous uniform flows. *J. Fluid Mech.*, Under Review, 2014.
- R. Avazmohammadi and P. Ponte Castañeda. On the macroscopic response, microstructure evolution, and macroscopic stability of short-fibre-reinforced elastomers at finite strains: I—analytical results. *Philos. Mag.*, 94(10):1031–1067, 2014a.
- R. Avazmohammadi and P. Ponte Castañeda. On the macroscopic response, microstructure evolution, and macroscopic stability of short-fiber-reinforced elastomers at finite strains: II—representative examples. *Philos. Mag.*, 94(10):1068–1094, 2014b.

- R. Avazmohammadi, R. Naghdabadi, and G.J. Weng. Finite anti-plane shear deformation of non-linear elastic composites reinforced with elliptic fibers. *Mech. Mat.*, 41(7):868–877, 2009.
- K.E. Avrachenkov, M. Haviv, and P.G. Howlett. Inversion of analytic matrix functions that are singular at the origin. *SIAM J. on Matrix Analysis and Applications*, 22:1175–1189, 2001.
- D. Barthès-Biesel. Motion of a spherical microcapsule freely suspended in a linear shear flow. *J. Fluid Mech.*, 100:831–853, 1980.
- D. Barthès-Biesel and J. M. Rallison. The time-dependent deformation of a capsule freely suspended in a linear shear flow. *J. Fluid Mech.*, 113:251–267, 1981.
- G. K. Batchelor. The stress system in a suspension of force-free particles. *J. Fluid Mech.*, 41:545–570, 1970.
- G. K. Batchelor and J.T. Green. The determination of the bulk stress in a suspension of spherical particles to order c^2 . *J. Fluid Mech.*, 56:401–427, 1972.
- J.S. Bergstrom and M.C. Boyce. Mechanical behavior of particle-filled elastomers. *Rubber Chem. Technol.*, 72:633–656, 1999.
- B. A. Bilby and M. L. Kolbuszewski. The finite deformation of an inhomogeneity in two-dimensional slow viscous incompressible flow. *Proc. R. Soc. Lond. A.*, 355:335–353, 1977.
- B. A. Bilby, J.D. Eshelby, and A. K. Kundu. The change of shape of a viscous ellipsoidal region embedded in a slowly deforming matrix having a different viscosity. *Tectonophysics*, 28:265–274, 1975.
- M. Bouchart, V. Brieu, N. Bhatnagar, and D. Kondo. A Multiscale approach of nonlinear composites under finite deformation: experimental characterization and numerical modeling. *Int. J. Solids Structures*, 47:1737–1750, 2010.
- J.F. Brady and G. Bossis. The rheology of concentrated suspensions of spheres in simple shear flow by numerical simulation. *J. Fluid Mech.*, 155(JUN):105–129, 1985.
- L. Brassart, L. Stainier, I. Doghri, and L. Delannay. Homogenization of elasto-(visco) plastic composites based on an incremental variational principle. *Int. J. Plasticity*, 36:86–112, 2012.
- D.E. Brooks, J.W. Goodwin, and G.V. Seaman. Interactions among erythrocytes under shear. *J. Appl. Physiol.*, 28(2):172–177, 1970.
- M. Brun, O. Lopez-Pamies, and P. Ponte Castañeda. Homogenization estimates for fiber-reinforced elastomers with periodic microstructures. *Int. J. Solids Struct.*, 44:5953–5979, 2007.
- R. Cerf. On the frequency dependence of the viscosity of high polymer solutions. *J. Chem. Phys.*, 20:395–402, 1952.
- X. Chateau, G. Ovarlez, and K.L. Trung. Homogenization approach to the behavior of suspensions of noncolloidal particles in yield stress fluids. *J. Rheol.*, 52:489–506, 2008.

- H. Chen, Y. Liu, X. Zhao, Y. Lanir, and G.S. Kassab. A micromechanics finite-strain constitutive model of fibrous tissue. *J. Mech. Phys. Solids*, 59:1823–1837, 2011.
- S.A. Chester and L. Anand. A thermo-mechanically coupled theory for fluid permeation in elastomeric materials: Application to thermally responsive gels. *J. Mech. Phys. Solids*, 59(10):1978–2006, 2011.
- J.R. Clausen and C.K. Aidun. Capsule dynamics and rheology in shear flow: Particle pressure and normal stress. *Phys. Fluids*, 22:123302, 2010.
- J.R. Clausen, D.A. Reasor, and C.K. Aidun. The rheology and microstructure of concentrated non-colloidal suspensions of deformable capsules. *J. Fluid Mech.*, 685:202–234, 2011.
- G. deBotton. Transversely isotropic sequentially laminated composites in finite elasticity. *J. Mech. Phys. Solids*, 53:1334–1361, 2005.
- G. deBotton and P. Ponte Castañeda. On the ductility of laminated materials. *Int. J. Solid Structures*, 29:2329–2353, 1992.
- G. deBotton, I. Hariton, and E.A. Socolsky. Neo-Hookean fiber-reinforced composites in finite elasticity. *J. Mech. Phys. Solids*, 54:533–559, 2006.
- A. Einstein. A new determination of molecular dimensions. *Ann. Physik*, 19:289–306, 1906.
- I. Ekeland and R. Témam. *Convex Analysis and Variational Problems*. SIAM., Philadelphia, PA, 1999.
- J.D. Eshelby. The determination of the elastic field of an ellipsoidal inclusion and related problems. *Proc. R. Soc. Lond. A*, 241:376–396, 1957.
- J. Finlaysh and K. Shek. Computational plasticity and viscoplasticity for composite materials and structures. *J. Composites*, 29B:613–619, 1998.
- N.A. Frankel and A. Acrivos. On the viscosity of a concentrated suspension of solid spheres. *Chem. Eng. Sci.*, 22:847–853, 1967.
- H. Fröhlich and R. Sack. Theory of the rheological properties of dispersions. *Proc. R. Soc. Lond. A*, 185:415–430, 1946.
- T. Gao, H.H. Hu, and P. Ponte Castañeda. Rheology of a suspension of elastic particles in a viscous shear flow. *J. Fluid Mech.*, 687:209–237, 2011.
- T. Gao, H.H. Hu, and P. Ponte Castañeda. Shape dynamics and rheology of soft elastic particles in a shear flow. *Phys. Rev. Lett.*, 108:058302, 2012.
- T. Gao, H.H. Hu, and P. Ponte Castañeda. Dynamics and rheology of elastic particles in an extensional flow. *J. Fluid Mech.*, 715:573–596, 2013.

- T. Gao, H.H. Hu, and P. Ponte Castañeda. Rheology of a suspension of elastic particles in a viscous shear flow. *J. Fluid Mech.*, 687:209–237, 2011.
- A.N. Gent. A new constitutive relation for rubber. *Rubber Chem. Tech.*, 69:59–61, 1996.
- G. Geymonat, S. Müller, and N. Triantafyllidis. Homogenization of nonlinearly elastic materials, microscopic bifurcation and macroscopic loss of rank-one convexity. *Arch. Rat. Mech. Anal.*, 122: 231–290, 1993.
- G. Ghigliotti, T. Biben, and C. Misbah. Rheology of a dilute two-dimensional suspension of vesicles. *J. Fluid Mech.*, 653:489–518, 2010.
- J. D. Goddard. An elastohydrodynamic theory for the rheology of concentrated suspensions of deformable particles. *J. Non-Newton. Fluid*, 2(2):169–189, 1977.
- J.D. Goddard and C. Miller. Nonlinear effects in the rheology of dilute suspensions. *J. Fluid Mech.*, 28:657–673, 1967.
- C. Gonzalez, J. Segurado, and J. Llorca. Numerical simulation of elasto-plastic deformation of composites: evolution of stress microfields and implications for homogenization models. *J. Mech. Phys. Solids*, 52:1573–1593, 2004.
- I. Hariton and G. deBotton. The nearly isotropic behaviour of high-rank nonlinear sequentially laminated composites. *Proc. R. Soc. Lond. A*, 459:157–174, 2003.
- Z. Hashin and S. Shtrikman. A variational approach to the theory of the elastic behavior of multi-phase materials. *J. Mech. Phys. Solids*, 11:127–140, 1963.
- W.H. Herschel and R. Bulkley. Konsistenzmessungen von gummi-benzollösungen. *Kolloid-Zeitschrift*, 39(4):291–300, 1926.
- R. Hill. On constitutive macro-variables for heterogeneous solids at finite strain. *Proc. Roy. Soc. Lond. A*, 326:131–147, 1972.
- C.C. Honeker and E.L. Thomas. Impact of morphological orientation in determining mechanical properties in triblock copolymers. *Chemistry of Materials*, 8:1702–1714, 1996.
- M.I. Idiart. Modeling the macroscopic behavior of two-phase nonlinear composites by infinite rank laminates. *J. Mech. Phys. Solids*, 56:2599–2617, 2008.
- M.I. Idiart and P. Ponte Castañeda. Field statistics in nonlinear composites. I. Theory. *Proc. R. Soc. Lond. A*, 463:183–202, 2007.
- G. B. Jeffery. The motion of ellipsoidal particles immersed in a viscous fluid. *Proc. R. Soc. Lond. A*, 102:161–179, 1922.
- D.J. Jeffrey and A. Acrivos. The rheological properties of suspensions of rigid particles. *AIChE Journal*, 22:417–432, 1976.

- D.D. Joseph. *Fluid dynamics of viscoelastic liquids*. Springer-Verlag, New York, NY, 1990.
- M Kailasam. *A general constitutive theory for particulate composites and porous materials with evolving microstructures*. PhD thesis, Ph. D. thesis, University of Pennsylvania, 1998.
- M. Kailasam and P. Ponte Castañeda. A general constitutive theory for linear and nonlinear particulate media with microstructure evolution. *J. Mech. Phys. Solids*, 46:427–465, 1998.
- M. Kailasam, P. Ponte Castañeda, and J.R. Willis. The effect of particle size, shape, distribution and their evolution on the constitutive response of nonlinearly viscous composites. I. Theory. *Phil. Trans. R. Soc. Lond. A*, 355:1835–1852, 1997.
- S.R. Keller and R. Skalak. Motion of a tank-treading ellipsoidal particle in a shear flow. *J. Fluid Mech.*, 120:27–47, 1982.
- I.M. Krieger. Rheology of monodisperse latices. *Adv. Colloid Interface Sci.*, 3:111–136, 1972.
- I.M. Krieger and T.J. Dougherty. A mechanism for non-newtonian flow in suspensions of rigid spheres. *J. Rheology*, 3:137, 1959.
- E. Lac, D. Barthès-Biesel, N.A. Pelekasis, and J. Tsamopoulos. Spherical capsules in three-dimensional unbounded stokes flows: effect of the membrane constitutive law and onset of buckling. *J. Fluid Mech.*, 516:303–334, 2004.
- N. Lahellec and P. Suquet. Effective behavior of linear viscoelastic composites: a time-integration approach. *Int. J. Solids Struct.*, 44(2):507–529, 2007.
- N. Lahellec and P. Suquet. On the effective behavior of nonlinear inelastic composites: I. Incremental variational principles. *J. Mech. Phys. Solids*, 55:1932–1963, 2007a.
- N. Lahellec and P. Suquet. Effective response and field statistics in elasto-plastic and elasto-viscoplastic composites under radial and non-radial loadings. *Int. J. Plasticity*, 42:1–30, 2013.
- N. Lahellec, P. Ponte Castañeda, and P. Suquet. Variational estimates for the effective response and field statistics in thermoelastic composites with intra-phase property fluctuations. *Proc. R. Soc. Lond. A*, 467(2132):2224–2246, 2011.
- N. Lahellec, F. Mazerolle, and J.-C. Michel. Second-order estimate of the macroscopic behavior of periodic hyperelastic composites: theory, experimental validation. *J. Mech. Phys. Solids*, 52: 27–49, 2004.
- J. Laven and H.N. Stein. The einstein coefficient of suspensions in generalized newtonian liquids. *J. Rheol.*, 35(8):1523–1549, 1991.
- L.L. Leblanc. *Filled Polymers: Science and Industrial Applications*. CRC Press, New York, 2010.
- S-B Lee, RA Lebensohn, and Anthony D Rollett. Modeling the viscoplastic micromechanical response of two-phase materials using fast fourier transforms. *International Journal of Plasticity*, 27(5):707–727, 2011.

- J. Lemaitre and J. Chaboche. *Mechanics of solid materials*. Cambridge university press, 1994.
- V.M. Levin. Thermal expansion coefficients of heterogeneous materials. *Mekh. Tverd. Tela.*, 2:83–94, 1967.
- G. Limbert and J. Middleton. A constitutive model of the posterior cruciate ligament. *Medical Eng. Phys.*, 28:99–113, 2006.
- M.V. Loocke, C.G. Lyons, and C.K. Simms. A validated model of passive muscle in compression. *J. Biomech.*, 39:2999–3009, 2006.
- O. Lopez-Pamies and M.I. Idiart. Fiber-reinforced hyperelastic solids: a realizable homogenization constitutive theory. *J. Engng. Math.*, 68:57–83, 2010.
- O. Lopez-Pamies and P. Ponte Castañeda. Second-order estimates for the macroscopic response and loss of ellipticity in porous rubbers at large deformations. *J. Elasticity*, 76:247–287, 2004.
- O. Lopez-Pamies and P. Ponte Castañeda. Second-order homogenization estimates incorporating field fluctuations in finite elasticity. *Math. Mech. Solids*, 9:243–270, 2004b.
- O. Lopez-Pamies and P. Ponte Castañeda. On the overall behavior, microstructure evolution, and macroscopic stability in reinforced rubbers at large deformations: I - Theory. *J. Mech. Phys. Solids*, 54:807–830, 2006a.
- O. Lopez-Pamies and P. Ponte Castañeda. On the overall behavior, microstructure evolution, and macroscopic stability in reinforced rubbers at large deformations: II - Application. *J. Mech. Phys. Solids*, 54:831–863, 2006b.
- O. Lopez-Pamies and P. Ponte Castañeda. Homogenization-based constitutive models for porous elastomers and implications for macroscopic instabilities: I – Analysis. *J. Mech. Phys. Solids*, 55: 1677–1701, 2007a.
- O. Lopez-Pamies and P. Ponte Castañeda. Homogenization-based constitutive models for porous elastomers and implications for macroscopic instabilities: II – Results. *J. Mech. Phys. Solids*, 55: 1702–1728, 2007b.
- O. Lopez-Pamies and P. Ponte Castañeda. Microstructure evolution in hyperelastic laminates and implications for overall behavior and macroscopic stability. *Mech. Mater.*, 41:364–374, 2009.
- O. Lopez-Pamies, T. Gouzarzi, and T. Nakamura. The nonlinear elastic response of suspensions of rigid inclusions in rubber: I An exact result for dilute suspensions. *J. Mech. Phys. Solids*, 61: 1–18, 2013a.
- M. Lowenberg and E.J. Hinch. Numerical simulation of concentrated emulsion in shear flow. *J. Fluid Mech.*, 321:395–419, 1996.
- F. Mahaut, P. Chateau, Coussot, and G. Ovarlez. Yield stress and elastic modulus of suspensions of noncolloidal particles in yield stress fluids. *J. Rheol.*, 52:287–313, 2008.

- J.C. Michel, O. Lopez-Pamies, P. Ponte Castañeda, and N. Triantafyllidis. Microscopic and macroscopic instabilities in finitely strained fiber-reinforced elastomers. *J. Mech. Phys. Solids*, 58:1776–1803, 2010.
- G.W. Milton. *The Theory of Composites*. Cambridge University Press, Cambridge, U.K., 2002a.
- G.W. Milton. *The Theory of Composites*. Cambridge University Press, Cambridge, UK, 2002b.
- A.K. Miri, N.Y.K. Li, R. Avazmohammadi, S.L. Thibeault, R. Mongrain, and L. Mongeau. Study of extracellular matrix in vocal fold biomechanics using a two-phase model. *Biomech. Model. Mechan.*, pages 1–9, 2014.
- J. Moraleda, J. Segurado, and J. Llorca. Finite deformation of incompressible fiber-reinforced elastomers: A computational micromechanics approach. *J. Mech. Phys. Solids*, 57:1596–1613, 2009.
- JE O’connor. Short-fiber-reinforced elastomer composites. *Rubber Chemistry and Technology*, 50(5):945–958, 1977.
- R.W. Ogden. *Non-linear Elastic Deformations*. Dover, New York, 1997.
- R.W. Ogden, G. Saccomandi, and I. Sgura. Fitting hyperelastic models to experimental data. *Computational Mechanics*, 34:484–502, 2004.
- J. G. Oldroyd. The elastic and viscous properties of emulsions and suspensions. *Proc. R. Soc. Lond. A*, 218:122–132, 1953.
- R. Pal. Rheology of concentrated suspensions of deformable elastic particles such as human erythrocytes. *J. Biomech.*, 36:981–989, 2003.
- R. Pal. *Rheology of particulate dispersions and composites*. CRC Press, 2010.
- C. Park, J. Yoon, and E.L. Thomas. Enabling nanotechnology with self-assembled block copolymer patterns. *Polymer*, 44:6725–6760, 2003.
- T.N. Phung, J.F. Brady, and G. Bossis. Stokesian dynamics simulations of browning suspensions. *J. Fluid Mech.*, 313:181–207, 1996.
- P. Ponte Castañeda. The overall constitutive behavior of nonlinearly elastic composites. *Proc. R. Soc. Lond. A*, 422:147–171, 1989.
- P. Ponte Castañeda. The effective mechanical properties of nonlinear isotropic composites. *J. Mech. Phys. Solids*, 39:45–71, 1991.
- P. Ponte Castañeda. Bounds and estimates for the properties of nonlinear heterogeneous systems. *Phil. Trans. R. Soc. Lond. A*, 340:531–567, 1992.
- P. Ponte Castañeda. Exact second-order estimates for the effective mechanical properties of nonlinear composite materials. *J. Mech. Phys. Solids*, 44:827–862, 1996.

- P. Ponte Castañeda. Second-order homogenization estimates for nonlinear composites incorporating field fluctuations. I. Theory. *J. Mech. Phys. Solids*, 50:737–757, 2002.
- P. Ponte Castañeda. On the homogenized behaviour of reinforced and other bingham composites. *Phil. Trans. R. Soc. Lond. A*, 361(1806):947–964, 2003.
- P. Ponte Castañeda. *Heterogeneous materials. Lecture Notes*. Department of Mechanics, Ecole Polytechnique, 2005.
- P. Ponte Castañeda and E. Galipeau. Homogenization-based constitutive models for magnetorheological elastomers at finite strain. *J. Mech. Phys. Solids*, 59(19):194–215, 2011.
- P. Ponte Castañeda and M. H. Siboni. A finite-strain constitutive theory for electro-active polymer composites via homogenization. *Int. J. of Nonlinear Mech.*, 47(2):293–306, 2012.
- P. Ponte Castañeda and P. Suquet. Nonlinear composites. *Adv. Appl. Mech.*, 34(998):171–302, 1998.
- P. Ponte Castañeda and E. Tiberio. A second-order homogenization method in finite elasticity and applications to black-filled elastomers. *J. Mech. Phys. Solids*, 48:1389–1411, 2000.
- P. Ponte Castañeda and J.R. Willis. The effect of spatial distribution on the effective behavior of composite materials and cracked media. *J. Mech. Phys. Solids*, 43:1919–1951, 1995.
- P. Ponte Castañeda and J.R. Willis. Variational second-order estimates for nonlinear composites. *Proc. R. Soc. Lond. A*, 455:1799–1812, 1999.
- K.M. Quapp and J.A. Weiss. Material characterization of human medial collateral ligament. *J. Biomech. Eng.*, 120:757–763, 1998.
- V. Racherla, O. Lopez-Pamies, and P. Ponte Castañeda. Macroscopic response and stability in lamellar nanostructured elastomers with "oriented" and "unoriented" polydomain microstructures. *Mech. Mater.*, 42:451–468, 2010.
- S. Ramanujan and C. Pozrikidis. Deformation of liquid capsules enclosed by elastic membranes in simple shear flow: large deformations and the effect of fluid viscosities. *J. Fluid Mech.*, 361:117–143, 1998a.
- S. Ramanujan and C. Pozrikidis. Deformation of liquid capsules enclosed by elastic membranes in simple shear flow: large deformations and the effect of capsule viscosity. *J. Fluid Mech.*, 361:117–143, 1998b.
- E. Reina-Romo and J.A. Sanz-Herrera. Multiscale simulation of particle-reinforced elastic-plastic adhesives at small strains. *Comput. Methods Appl. Mech. Eng.*, 200(25):2211–2222, 2011.
- R. Roscoe. On the rheology of a suspension of viscoelastic spheres in a viscous liquid. *J. Fluid Mech.*, 28:273–293, 1967.
- M.H. Siboni and P. Ponte Castañeda. Fiber-constrained, dielectric-elastomer composites: Finite-strain response and stability analysis. *J. Mech. Phys. Solids*, 68:211–238, 2014.

- M.H. Siboni, R. Avazmohammadi, and P. Ponte Castañeda. Electromechanical instabilities in fiber-constrained, dielectric-elastomer composites subjected to all-around dead-loading. *Math. Mech. Solids*, page 1081286514551501, 2014.
- R. Skalak, N. Ozkaya, and T.C. Skalak. Biofluid mechanics. *Annu. Rev. Fluid. Mech.*, 21:167–200, 1989.
- P. Snabre and P. Mills. Rheology of concentrated suspensions of viscoelastic particles. *Colloids Surf., A*, 152:79–88, 1999.
- J.J. Stickel and R.L. Powell. Fluid mechanics and rheology of dense suspensions. *Annu. Rev. Fluid Mech.*, 37:129–149, 2005.
- D.R.S. Talbot and J.R. Willis. Variational Principles for Inhomogeneous Non-linear Media. *IMA J Appl Math*, 35:39–54, 1985.
- G. I. Taylor. The viscosity of a fluid containing small drops of another fluid. *Proc. R. Soc. Lond. A*, 138:41–48, 1932.
- N. Triantafyllidis and B.N. Marker. On the comparison between microscopic and macroscopic in stability mechanisms in a class of fiber-reinforced composites. *J. Appl. Mech.*, 52:794–800, 1985.
- N. Triantafyllidis, M.D. Nestorovic, and M.W. Schraad. Failure surfaces for finitely strained two-phase periodic solids under general in-plane loading. *J. Appl. Mech.*, 73:505–516, 2006.
- M.M. Villone, F. Greco, M.A. Hulsen, and P.L. Maffettone. Simulations of an elastic particle in newtonian and viscoelastic fluids subjected to confined shear flow. *J. Non-Newton. Fluid Mech.*, 2014a.
- M.M. Villone, M.A. Hulsen, P.D. Anderson, and P.L. Maffettone. Simulations of deformable systems in fluids under shear flow using an arbitrary lagrangian eulerian technique. *Comput. Fluids*, 90: 88–100, 2014b.
- M.J. Wang, P. Zhang, and Mahmud K. Carbon Silica dual phase filler, a new generation reinforcing agent for rubber: Part IX. application to truck tire tread compound. *Rubber Chem. Tech.*, 74: 124–137, 2001.
- S. Wang and J.E. Mark. Generation of glassy ellipsoidal particles within an elastomer by in situ polymerization, elongation at an elevated temperature, and finally cooling under strain. *Macromolecules*, 23(19):4288–4291, 1990.
- E. D. Wetzel and C. L. Tucker. Droplet deformation in dispersions with unequal viscosities and zero interfacial tension. *J. Fluid Mech.*, 426:199–228, 2001.
- J.R. Willis. Bounds and self-consistent estimates for the overall moduli of anisotropic composites. *J. Mech. Phys. Solids*, 25:185–202, 1977.

- J.R. Willis. Variational and related methods for the overall properties of composites. *Adv. Appl. Mech.*, 21:1–78, 1981.
- M. Zaidman and P. Ponte Castañeda. The finite deformation of nonlinear composite materials II. Evolution of the microstructure. *Int. J. Solids Struct.*, 33:1287–1303, 1996.
- L. Zee and E. Sternberg. Ordinary and strong ellipticity in the equilibrium theory of incompressible hyperelastic solids. *Arch. Rat. Mech. Anal.*, 83:53–90, 1983.